U.PORTO

FEUP FACULDADE DE ENGENHARIA
UNIVERSIDADE DO PORTO

Remediation of emergent contaminants using Metal Organic Frameworks immobilized onto Fique fibers

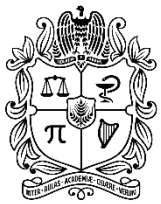
Karen Giovanna Bastidas Gómez

Universidade do Porto

Faculty of Engineering, Department of Chemical Engineering

Porto, Portugal

2020



UNIVERSIDAD
NACIONAL
DE COLOMBIA

Remediation of emergent contaminants using Metal Organic Frameworks immobilized onto Fique fibers

Karen Giovanna Bastidas Gómez

Universidad Nacional de Colombia

Faculty of Engineering, Department of Chemical and Environmental Engineering

Porto, Portugal

2020

Remediation of emergent contaminants using Metal Organic Frameworks immobilized onto Fique fibers

Karen Giovanna Bastidas Gómez

Thesis presented as a partial requirement to qualify for the title of:
Doctor of Engineering - Chemical Engineering (Universidad Nacional de Colombia)
Doctor of Engineering - Environmental Engineering (Universidade do Porto)

Advisors:
Ph.D. Hugo Ricardo Zea Rámirez
Ph.D. Manuel Fernando Ribeiro Pereira
Co-advisor:
Ph.D.

Research Groups:
Materials, Catalysis, and environmental (GICATMA)
LSRE-LCM Catalysis and carbon materials

Universidade do Porto
Faculty of Engineering
Department of Chemical Engineering
Porto, Portugal
2020

Be persistent, be resilient, and never give up chasing the dreams that make your life fly. Only you can make the darkness shine, according to the love present in your heart.

Karen G. Bastidas G.

Acknowledgments

By stopping and looking at the work done up to this point, it is gratifying to confirm that I was always accompanied by experiences and people who gave me incredible learnings. I would like to thank God for allowing me to grow in this stage of my life, for having the opportunity to see the world through the eyes of many cultures, professions, and people. Thank you for teaching me to be resilient and for allowing me to continue dreaming, to provide solutions from us to make this world a better one.

I am also grateful to my family (uncles, aunts, cousins, and grandparents), especially my sister for always believe and encourage me. In addition, my mum, for her emotional support and motivation to be brave, patient, and persistent, without which, my time far away from home would have been more difficult. A special thanks to Kogui, because he was with me regardless of the time, distance, or country where I was, who has provided a supportive ear making my PhD life less demanding and happier, always motivating me to be the best version of me.

I would like to extend my gratitude to my advisors, Manuel Fernando Pereira, and Cesar Sierra, who provide me with constant support and guidance in this path. Particularly thanks to Prof. Hugo Ricardo Zea, who was the guide and counselor to encouraged me to think before speaking with strong and forceful arguments. He shared with me not only knowledge, but he also provided me fundamental human values to be a better person and scientist as part of society, which is constantly changing. Besides, I would like to dedicate this work to Prof. Janet L Scott who taught me and demonstrated how to be a successful woman scientist, with nothing but confidence and credibility in ourselves. A special mention to the researcher Emilie Engel and Inmaculada Velo, who shared with me other approaches to solve research problems using innovative tools. I am beyond grateful to the technician staff in each university where I worked.

It is also a pleasure to thank all my friends for useful academic discussions, friendships, and particular adventures that enriched my way of perceiving the world from different cultures and

outlooks. Thanks, Poli, Jisus, Latin lover, Rajesh, Nachito, Pimon, Andreo, Rasho, Darks, Yu, Alejito, Ele, Jakubito, Pachini, Carli, Tristan, Lucca, Loli, Glau, Yoko, Young, Sinatra, Sofi, Only Ze, Catia, Eli and Lioness. All of you were my home when I was abroad from home. A particular mention to Chucks, for setting a good example of the person with the biggest heart in the world, who care for me independent of the distance and he demonstrated to me the friendship it is only the feeling to be connected in mind and heart. He was always my example to follow, his appropriated words and perspective of seeing the glass half full and not half empty, thank you for always being there.

Finally, I am very grateful for the financial support of the National University of Colombia and Colciencias through the grant number 757 of “Programa de Doctorados Nacionales, 2016 “, the University of Bath with “the Global Challenge Research Found 17/18 “, and the partial support by “Base Funding - UIDB/50020/2020 of the Associate Laboratory LSRE-LCM “ at the University of Porto.

Abstract

The fique fiber was studied as a support in the synthesis of hybrid materials with metal-organic frameworks (MOFs) such a HKUST-1, with potential applications in the remediation of liquid effluents with the presence of emerging contaminants. First, a complete physicochemical characterization of the fiber was made to know its characteristics and properties. Second, to obtain a cleaner and more homogeneous surface, three pretreatments were evaluated: acid, alkali and organosolv. The last one allowed to keep the structural and chemical properties of the fiber, which was confirmed by chemical, mechanical, morphological, and thermal characterizations. Subsequently, a third stage consisted on the biomass surface functionalization to increase the percentage of active functional groups. Two chemical modifications were evaluated: carboxymethylation and oxidation mediated by TEMPO, which obtained degrees of substitution close to 11.3% of carboxymethyl ether groups and 9.32% of carboxylate, respectively. Regarding the MOF, two methods of HKUST-1 synthesis were evaluated: solvothermal and green, the last one considered changes in solvents and operating conditions (room temperature and pressure). The crystals obtained by each synthesis confirmed their identity through morphological characterization, crystallinity, and surface area. Crystals of the green synthesis were further modified with crystalline poisons to include thiol groups in their structure, thus increasing hydrolytic stability. For this, two crystal poisons were evaluated: thiosalic acid (TSA) and mercaptobenzoic acid (MBA). MBA did not distort the crystal structure of MOFs, including thiol groups and improving the crystals hydrolytic stability. The growth of the MOFs in the functionalized fiber was carried out with the methodologies of direct anchoring and secondary growth, a physical deposition was obtained using the direct methodology and chemical anchoring with secondary growth. The materials obtained were tested in heavy metal removal applications such as mercury, the hybrid materials with MOFs and thiol proved to be most selective. In the treatment of organic compounds, such as carbamazepine and metoprolol, the materials were used as catalysts for the ozonation reaction, proving to have catalytic activity. Finally, the antibacterial activity of the materials with Escherichia coli was demonstrated, reducing the death times of the bacteria for treatments of 5 minutes. The development of these new materials can be an alternative to contribute to the solution of water pollution worldwide.

Keywords: Emerging contaminants, fique fiber, MOFs, hybrid materials, water treatment.

Resumen

Se estudiaron las características de la fibra de fique como soporte en la sintesis de materiales híbridos con redes orgánico – metálicas como el MOF HKUST-1, con aplicaciones potenciales en la remediación de efluentes líquidos con presencia de contaminantes emergentes. Primero, se hizo la caracterización fisicoquímica de la fibra para conocer sus características y propiedades. Segundo, obtener una superficie más limpia y homogénea tres pretratamientos se evaluaron: acido, álcali y organosolv. Este último permitió conservar las propiedades estructurales y químicas de la fibra, confirmadas mediante caracterizaciones químicas, mecánicas, morfológicas y térmicas. Posteriormente, la tercera etapa consistió en la funcionalización de la superficie de la biomasa para aumentar el porcentaje de grupos funcionales activos. Se evaluaron dos modificaciones químicas: carboximetilación y oxidación mediada por TEMPO, los cuales obtuvieron grados de sustitución de11.3% de grupos carboximetil éter y 9.32% de carboxilato, respectivamente. En cuanto a los MOF, se evaluaron dos métodos de sintesis de HKUST-1: solvotermal y verde, este último consideraba cambios en los solventes y las condiciones de operación (temperatura y presión ambiente). Los cristales obtenidos por cada sintesis confirmaron su identidad por medio de la caracterización morfológica, cristalinidad y área superficial. Cristales de la sintesis verde, fueron adicionalmente modificados con venenos cristalinos para incluir grupos tiol en su estructura, y así aumentar la estabilidad hidrolítica. Para ello dos venenos cristalinos se evaluaron: ácido tiosalico (TSA) y ácido mercaptobenzoico (MBA). MBA, demostró no distorsionar la estructura cristalina de los MOFs incluyendo los grupos tiol y mejorando la estabilidad hidrolítica de los cristales. El crecimiento de los MOFs en la fibra funcionalizada se llevo a cabo con las metodologías de anclaje directo y crecimiento secundario, se obtuvo deposición física utilizando la metodología directa y anclaje químico con crecimiento secundario. Los materiales obtenidos fueron probados en aplicaciones de eliminación de metales pesados como mercurio, los materiales híbridos con MOFs y tiol demostraron ser más selectivos en la remoción. En el tratamiento de compuestos orgánicos como carbamazepina y metoprolol, los materiales se utilizaron como catalizadores de la reacción de ozonización, demostrando tener actividad catalítica. Finalmente, se demostró la actividad antibacterial de los materiales con *Escherichia coli* reduciendo los tiempos de muerte de la bacteria a 5 minutos luego del tratamiento. El desarrollo de estos nuevos materiales puede ser una alternativa para contribuir con la solución de la contaminación del agua a nivel mundial.

Palabras clave: Contaminantes emergentes, fique, MOFs, materiales híbridos, tratamiento de aguas.

Resumo

A fibra fique foi estudada como suporte na síntese de materiais híbridos com redes metalo-orgânicas (MOFs) como o HKUST-1, com potenciais aplicações na remediação de efluentes líquidos com a presença de contaminantes emergentes. Primeiramente, foi feita a caracterização físico-química da fibra para conhecer suas características e propriedades. Em segundo lugar, para obter uma superfície mais limpa e homogénea, foram avaliados três pré-tratamentos: ácido, álcali e organosolv. Este último permitiu manter as propriedades estruturais e químicas da fibra, comprovadas por caracterizações químicas, mecânicas, morfológicas e térmicas. Posteriormente, a terceira etapa consistiu na funcionalização da superfície da biomassa para aumentar a percentagem de grupos funcionais ativos. Foram avaliadas duas modificações químicas: a carboximetilação e a oxidação mediada por TEMPO, que obtiveram graus de substituição próximos de 11,3% de grupos carboximetil éter e 9,32% de carboxilato, respectivamente. Em relação ao MOF, foram avaliados dois métodos de síntese do HKUST-1: solvotérmico e verde, o último considerando mudanças nos solventes e nas condições de operação (temperatura e pressão ambiente). Foi confirmadaa identidade dos cristais obtidos em cada síntese por meio da caracterização morfológica, cristalinidade e área superficial. Os cristais da síntese verde foram posteriormente modificados com venenos para incluir grupos tiol na sua estrutura, aumentando assim a estabilidade hidrolítica. Para isso, foram avaliados dois venenos de cristal: ácido tiossálico (TSA) e ácido mercaptobenzóico (MBA). O MBA não distorceu a estrutura cristalina dos MOFs, incluindo grupos tiol e melhorando a estabilidade hidrolítica dos cristais. O crescimento dos MOFs na fibra funcionalizada foi realizado com as metodologias de ancoragem direta e crescimento secundário, foi obtida a deposição física utilizando a metodologia direta e a ancoragem química com o crescimento secundário. Os materiais obtidos foram testados em aplicações de remoção de metais pesados como o mercúrio, os materiais híbridos com MOFs e tiol mostraram ser os mais seletivos. No tratamento de compostos orgânicos como a carbamazepina e o metoprolol, os materiais foram utilizados como catalisadores para a reação de ozonização, demonstrando possuir atividade catalítica. Por fim, foi demonstrada a atividade antibacteriana dos materiais com Escherichia coli, reduzindo o tempo de morte da bactéria para 5 minutos de tratamento. O desenvolvimento destes novos materiais pode ser uma alternativa para contribuir para a solução da poluição das águas em todo o mundo.

Palavras-chave: Contaminantes emergentes, fique, MOFs, materiais híbridos, tratamento de água.

Content

Abstract ..... **XI**

List of figures ..... **XIX**

List of tables ..... **XXVI**

Preface **1**

1. Contextualization and theoretical framework..... 7

1.1 Water pollution **7**

1.2 Emerging contaminants **10**

1.2.1 Contamination by pharmaceutical compounds 20

1.2.2 Contamination by heavy metals 22

1.3 Development of new materials **22**

1.3.1 Methods of synthesis in hybrid materials 25

1.4 Biomass **25**

1.4.1 Lignocellulosic biomass 26

1.4.1.1 Structure of the cell wall: 27

1.4.1.2 Chemical structure 27

1.4.2 Biomass pretreatments 31

1.5 Biomass functionalization **37**

1.5.1 Physical approaches: 38

1.5.2 Chemical approaches: 39

1.6 Fique: example of lignocellulosic biomass **41**

1.7 Metal organic frameworks (MOFs) **44**

1.7.1 Design and synthesis of MOFs 45

1.7.2 Anchored and deposition of MOFs 48

1.7.3 MOFs stability 54

1.7.4 Potential applications of MOFs in water treatment: 61

1.7.5 MOF HKUST-1 or MOF-199 66

1.8 References **68**

2. Fique fiber characterization ***83***

2.1 Abstract **83**

2.2 Introduction **83**

2.3 Materials and methods **85**

2.3.1 Chemicals and materials ... 85
2.3.1. Characterization ... 86
2.4 Results and Discussion ... 89
2.5 Conclusions ... 99
2.6 References ... 100
3. Pretreatment evaluation of fique fiber to increase the exposure of hydroxyl groups onto the surface ... 105
3.1 Abstract ... 105
3.2 Introduction ... 106
3.3 Materials and methods ... 109
3.3.1 Chemicals and materials ... 109
3.3.2 Experimental set-up and procedure ... 109
3.3.3 Statistical analysis ... 110
3.3.4 Characterization ... 110
3.4 Results and Discussion ... 113
3.5 Conclusions ... 129
3.6 References ... 129
4. Functionalization of the cellulose fiber surface by carboxymethylation and TEMPO oxidation reactions ... 135
4.1 Abstract ... 135
4.2 Introduction ... 136
4.3 Materials and methods ... 138
4.3.1 Chemicals and materials ... 138
4.3.2 Experimental set-up and procedure ... 138
4.3.3 Characterization ... 142
4.4 Results and Discussion ... 144
4.4.1 Carboxymethyl cellulose (CMC) ... 144
4.4.2 TEMPO Oxidation ... 158
4.5 Conclusions ... 168
4.6 References ... 168
5. Development of hybrid materials combining MOFs and natural fibers ... 173
5.1 HKUST-1 synthesis and functionalization with thiol by using crystal poisons as modifiers ... 173
5.1.1 Abstract ... 173
5.1.2 Introduction ... 174
5.1.3 Materials and methods ... 177
5.1.3.1 Chemicals and materials ... 177
5.1.3.2 Experimental set-up and procedure ... 177
5.1.3.3 Characterization ... 178
5.1.4 Results and Discussion ... 181
5.1.4.1 HKUST-1 synthesis ... 181

5.1.4.1 HKUST-1 functionalization ... 188
5.1.5 Conclusions ... 200
5.1.6 References ... 201

5.2 Anchoring of HKUST-1 and SH-HKUST-1 onto fique fiber ... 205
5.2.1 Abstract ... 205
5.2.2 Introduction ... 205
5.2.3 Materials and methods ... 207
5.2.3.1 Experimental set-up and procedure ... 207
5.2.3.2 Characterization ... 208
5.2.4 Results and Discussion ... 212
5.2.4.2 Functionalization fiber influence ... 219
5.2.4.3 Evaluation of two types of surface functionalization: CMC and TEMPO ... 223
5.2.4.4 Characterization of WET1-199 and WET1-SH ... 227
5.2.5 Conclusions ... 253
5.2.6 References ... 254

6. Potential application of hybrid materials combining MOFs and natural fibers in the water treatment of emerging contaminants. ... ***259***

6.1. Mercury (II) adsorption from wastewater using hybrid material combining fique fiber and metal-organic frameworks ... 259
6.1.1 Abstract ... 259
6.1.2 Introduction ... 260
6.1.3 Materials and methods ... 263
6.1.3.1 Chemicals and materials ... 263
6.1.3.2 Instrumentation ... 263
6.1.3.3 Experimental set-up and procedure ... 264
6.1.3.4 Models analysis ... 265
6.1.4 Results and Discussion ... 270
6.1.5 Conclusions ... 289
6.1.6 References ... 289

6.2 Organic compounds degradation under ozonation reaction catalyzed by hybrid material combining fique fiber and metal-organic frameworks based on copper ... 295
6.2.1 Abstract ... 295
6.2.2 Introduction ... 296
6.2.3 Materials and methods ... 298
6.2.3.1 Chemicals and materials ... 298
6.2.3.2 Catalytic test ... 298
6.2.3.3 Analytic methods ... 299
6.2.3.4 O_3 /Cu^{2+} kinetic modeling study ... 300
6.2.3.5 Materials characterization after the ozonation reaction ... 300
6.2.4 Results and Discussion ... 301
6.2.4.1 Adsorption capacity ... 301
6.2.4.2 Catalytic activity ... 304
6.2.4.3 Kinetic study of O3/Cu2+ reaction based on the simulation of chemical reactions ... 313
6.2.4.4 Materials characterization after ozonation processes ... 319
6.2.5 Conclusions ... 323
6.2.6 References ... 323

6.3. Antibacterial activity on *Escherichia coli* of metal-organic frameworks anchored onto fique fiber 329
6.3.1. Abstract 329
6.3.2. Introduction 329
6.3.3. Materials and methods 331
6.3.3.1 Chemicals and materials 331
6.3.3.2 Experimental set-up and procedure 331
6.3.3.3 Statistical Analysis 333
6.3.4. Results and Discussion 333
6.3.5. Conclusions 339
6.3.6. References 340

7. Conclusions and perspectives 343

7.1 Conclusions 343

7.2 Perspectives 346

List of figures

Pag.

Figure 1.1. Water sources available on the planet. Modified from UNEP 2015 [1]…… 8
Figure 1.2. Removal mechanisms in conventional WWTP [4]…….. 14
Figure 1.3. Main removal mechanisms of micropollutants in conventional WWTPs (example of the polycyclic musk galaxolide) [24]…….. 15
Figure 1.4. Representative sources and routes of micropollutants in the environment [38]…….. 21
Figure 1.5. Relationship between hybrid materials structure, functionally and chemical bonds…… 23
Figure 1.6. Biomass classification [82]…….. 26
Figure 1.7. Structure of the cell wall of lignocellulosic biomass [81]…….. 27
Figure 1.8. Structure and main components of lignocellulosic biomass [84]…… 28
Figure 1.9. Schematic representation of the effect of pretreatment on the lignocellulosic biomass structure. Modified [84]…… 31
Figure 1.10. Common modification chemistries of lignocellulose biomass [125]…….. 38
Figure 1.11. a) *Furcraea Andina* plant b) Fique fiber, c) Raw fique fiber micrograph 250X…….. 41
Figure 1.12. Flexible assembly process of MOFs from metal nodes and organic linkers[160]…….. 44
Figure 1.13. Different modification approaches used to provide a MOF with additional functionality……..…. 59
Figure 1.14. Publications number on MOFs and HMs adsorption based on data in the Scopus database [183]…… 63
Figure 1.15. HKUST-1 coordinatively saturated structure, each crystallographic unit cell features Cu•••Cu paddlewheel motifs…… 66
Figure 1.16. a) Outline of the main structure of HKUST-1 before activation shows the paddlewheel structure that is formed by the union of two Cu^{2+} ions and four benzene molecules of the linker 1,3,5-tricarboxylate linker (BTC), b) hydrated cage of HKUST-1 before the activation, c) activated cage of HKUST-1 (dehydrated) [181]…….. 66
Figure 1.17. Schematic representation of the SBU interaction between the HKUST-1 with a water molecule, which promotes the hydrolysis of the Cu-O bond, generating the release of a carboxylate bridge and the formation of a Cu^{1+} center [181]…….... 68
Figure 2.1. a) *Furcraea Andina* plant, b) Fique fiber, c) Raw fique fiber micrograph 250X…….. 84
Figure 2.2. EDX profile of raw fique fibers……... 91
Figure 2.3. SEM micrographs of the raw fiber, a) 250X, b) 500X, c) 2000X, d) 5000X.. 91
Figure 2.4. Adsorption isotherm for raw fique fiber…….. 92
Figure 2.5. pHzpc for the raw fiber…… 93
Figure 2.6. FTIR - ATR spectrum of raw fique fiber between 4000 and 600 cm^{-1}……... 94

Figure 2.7. a) Optical micrographs of liquid bridges formed between two raw fique fibers and resulting menisci, and b) measurement of the distance (d) and height of the spherical menisci formed (h)…….. 95
Figure 2.8. XRD diffractogram of raw fiber…….. 95
Figure 2.9. TGA (Thermogravimetric analysis) and DSC (Differential Scanning Calorimetry) for raw fique fiber under a) air and b) nitrogen atmosphere…….. 97
Figure 3.1. Cellulose, hemicellulose and lignin present in the solid fiber after dilute acid pretreatments……... 114
Figure 3.2. Contour plot of the effect of acid concentration and pretreatment time on cellulose after dilute acid pretreatment……. 115
Figure 3.3. Contour plot of the effect of acid concentration and pretreatment time on hemicellulose after dilute acid pretreatment……. 115
Figure 3.4. Contour plot of the effect of acid concentration and pretreatment time on lignin after dilute acid pretreatment…… 116
Figure 3.5. Contour plot of the effect of alkali concentration and pretreatment time on cellulose after alkali pretreatment…….. 118
Figure 3.6. Contour plot of the effect of alkali concentration and pretreatment time on hemicellulose after alkali pretreatment……. 118
Figure 3.7. Contour plot of the effect of alkali concentration and pretreatment time on lignin after alkali pretreatment……. 119
Figure 3.8. a) Raw fique fibers 200X, b) fibers pretreated using water 250X, c) fibers pretreated using ethanol 250X, d) fibers pretreated under two extraction steps using water + ethanol 250X…….. 121
Figure 3.9. 1H-NMR spectra obtained from the extractives after the organosolv pretreatment using water (red spectra) and ethanol (blue spectra) as solvents…….. 122
Figure 3.10. HSQC spectrum obtained from the extractives after the organosolv pretreatment. a) HSQC of water extractives and b) HSQC of ethanol extractives…….. 123
Figure 3.11. FTIR spectra obtained for the raw fiber and extractives after the organosolv pretreatment using water (W), ethanol (E), water and ethanol (WE) as solvents. Where: a) O-H, b) C-H, c) C=O, d) calcium oxalate, e) CH_2, f) C-O, g) C-O-C and h) ß glycosidic bond……. 125
Figure 3.12. Diffractogram of pretreated fibers by organosolv using different solvents.. 126
Figure 3.13. TGA (Thermogravimetric analysis) and DSC (Differential Scanning Calorimetry) under nitrogen for pretreated fique WE…… 128
Figure 4.1. Functionalization procedures used to produce CMC on the surface of the fique fiber, following the methodologies of a) HNZ and b) WNG…… 139
Figure 4.2. Scheme of CMC substitution degree…… 139
Figure 4.3. FTIR-ATR spectra of functionalized CMC fique fibers, following the HNZ and WNG methodology, using isopropanol as solvent and stirring during the etherification reaction…….. 146
Figure 4.4. Residual plots for DS calculated from the data summarized in Table 4.3 to check the assumptions to apply the ANOVA statistical study……. 149
Figure 4.5. Contour plot of NaOH concentration % w/v vs sodium chloroacetate %w/v and DS…….. 151
Figure 4.6. Contour plot of time (minutes) vs NaOH concentration % w/v and DS……. 152
Figure 4.7. Contour plot of temperature (°C) vs NaOH concentration % w/v and DS…. 152
Figure 4.8. Contour plot of time (minutes) vs sodium chloroacetate %w/v and DS……. 153
Figure 4.9. Contour plot of temperature (°C) vs sodium chloroacetate %w/v and DS…. 153
Figure 4.10. FTIR-ATR spectra of the CMC fique fibers and pretreated fiber, following the conditions synthesis of run 4 from Table 4.3…….. 154

Figure 4.11. EDX of the CMC fique fiber following the conditions synthesis of run 4 from Table 4.3…….. 155
Figure 4.12. X-ray diffraction spectra of CMC and pretreated fiber, following the conditions synthesis of run 4 from Table 4.3…… 156
Figure 4.13. Micrographs after the CMC functionalization process, a) 500X (WE), b) 2000X, following the conditions synthesis of run 4 from Table 4.3…… 157
Figure 4.14. TGA of CMC and pretreated fiber, following the conditions synthesis of run 4 from Table 4.3…… 158
Figure 4.15. Formation of carboxylate groups (-COONa) on cellulose by TEMPO oxidation [30]…… 159
Figure 4.16. Quantification of the oxidation degree percentage (OD) in raw (R) and pretreated fibers by organosolv using water (W), ethanol (E) and water/ethanol (WE), before and after TEMPO reaction using a NaOCl:AGU molar ratio of 1…… 160
Figure 4.17. Functionalization degree in fiber pretreated (WE) modulating the NaOCl:AGU molar ratio, all the experiments were performed in triplicate…… 161
Figure 4.18. ATR-FTIR spectra for pretreated (WE) and functionalized (WET1) fique fiber, at pH=10 and a molar ratio of NaOCl:AGU of 1…….. 162
Figure 4.19. Chemical groups produced after TEMPO oxidation of cellulose. Modified from [37]……... 163
Figure 4.20. EDX of functionalized (WET1) fique fiber, at pH=10 and a molar ratio of NaOCl:AGU of 1…….. 163
Figure 4.21. Micrographs before and after the functionalization process, a) pretreated fique fibers 2000X (WE), b) functionalized fiber 2000X (WET1)……. 164
Figure 4.22. Diffractogram of pretreated fique fibers (WE) and functionalized fiber (WET1) mediated by TEMPO……. 165
Figure 4.23. pHzpc of pretreated fique fibers (WE) and functionalized fiber (WET1) mediated by TEMPO……... 166
Figure 4.24. TGA of pretreated fique fibers (WE) and functionalized fiber (WET1) mediated by TEMPO……... 167
Figure 5.1.1. The schematic synthesis procedure of a) HKUST-1 using copper nitrate (solvothermal) or copper acetate (green method) as metal source, and b) the HKUST-1 functionalization by the modification trough crystal poison (TSA, left or MBA, right) to add a thiol group into the MOF structure…….. 178
Figure 5.1.2. XRD diffraction pattern of HKUST-1 synthesized by solvothermal and green method…….. 182
Figure 5.1.3. Micrographs of HKUST-1 obtained by the solvothermal method a) 2000x, b) 7000X and by the green method c) 10000X, d) 50000X……..... 183
Figure 5.1.4. HKUST-1 EDX after the a) solvothermal and b) green synthesis method, and the atomic / weight compositional percentage…….. 184
Figure 5.1.5. Infrared spectra of HKUST-1 synthesis by the solvothermal and green method…….. 185
Figure 5.1.6. N_2 adsorption-desorption isotherms of HKUST-1 synthesis by the a) solvothermal and b) green method (inset BJH pore size distribution)…… 186
Figure 5.1.7. The pH of zero points of charge pHzpc for HKUST-1 under the green method synthesis……. 187
Figure 5.1.8. Thermogravimetric analysis profiles of HKUST-1 synthesis by the a) solvothermal and b) green method…… 188
Figure 5.1.9. XRD diffraction pattern for the functionalization of HKUST- (green method) using crystal poisons…… 190
Figure 5.1.10. Micrographs of SH-HKUST-1 obtained by the green method using MBA 5%wt a) 10000X and b) 50000X…… 191

Figure 5.1.11. EDX spectra of the thiol HKUST-1 modified using MBA 5%wt……. 192
Figure 5.1.12. FTIR spectra of the thiol HKUST-1 modified using MBA 5%wt (orange spectrum) and HKUST-1 synthesized using the green method (purple spectrum) …….. 193
Figure 5.1.13. Zero-point of charge pHzpc for HKUST-1 under the green method synthesis modified using MBA 5%wt……. 193
Figure 5.1.14. N_2 adsorption-desorption isotherms and BJH pore size distribution inset of SH-HKUST-1 (Surface area, pore-volume, and pore size of SH-HKUST-1 by the solvothermal and green synthesis for nitrogen adsorption experiments) …….. 194
Figure 5.1.15. TGA y DSC of SH-HKUST-1…… 195
Figure 5.1.16. XRD patterns of HKUST-1(up) and SH-HKUST-1 (down) samples, exposed to water for 6 (pink curve), 24 (green curve), and 48 h (blue curve)…….. 196
Figure 5.1.17. SEM images of HKUST-1(up) and SH-HKUST-1 (down) samples, exposed to water for 6, 24, and 48 hours…….. 197
Figure 5.1.18. ICP-OES measurement of copper in solution after being in contact with water and HKUST-1(purple data) or SH-HKUST-1 (orange data) until 6, 24 and 48 hours……. 198
Figure 5.1.19. UV-VIS measurement of BTC in solution after being in contact with water and HKUST-1(purple data) or SH-HKUST-1 (orange data) until 6, 24 and 48 hours….. 199
Figure 5.2.1. Diagram of the methodology used to anchor HKUST-1 and HKUST-1-SH onto fique fibers…… 208
Figure 5.2.2. SEM images of HKUST-1 supported onto fique fiber functionalized with carboxylate groups (-COONa), following the direct (a and b) and secondary (c and d) growth…….. 213
Figure 5.2.3. XRD diffractograms of HKUST-1 anchored by two approaches: direct and secondary growth…… 214
Figure 5.2.4. Diagram of the methodology used to anchor HKUST-1 onto fique fibers 215
Figure 5.2.5. SEM micrographs of HKUST-1 attached onto fique fiber under solvothermal conditions…….. 217
Figure 5.2.6. XRD diffractograms of HKUST-1 anchored by the direct approaches following the solvothermal synthesis……. 217
Figure 5.2.7. Diffractogram of HKUST-1 synthesized by the green method and anchored onto raw (R-199), pretreated (WE-199) and functionalized fique fibers (RT1-199, WET1-199, WET2-199)……. 220
Figure 5.2.8. Types of surfaces functionalized with groups: carboxymethyl ether and carboxylate, obtained from the carboxymethylation (CMC) and oxidation (TEMPO) reactions, respectively……. 223
Figure 5.2.9. SEM images of CMC fiber after green synthesis of MOF 199 under the conditions reported in Table 5.2.2. Where, a) step 1st (CMC+ Copper acetate), step 2nd (BTC + TEA), b) step 1st (CMC+ Copper acetate + BTC), step 2nd (TEA), c) step 1st (CMC+ Copper acetate), step 2nd (BTC), d) step 1st (CMC+ BTC)…… 224
Figure 5.2.10. Comparison of the XRD samples synthesized under green methodology using CMC by the conditions reported in Table 5.2.2. Where, a) step 1st (CMC+ Copper acetate), step 2nd (BTC + TEA), b) step 1st (CMC+ Copper acetate + BTC), step 2nd (TEA), c) step 1st (CMC+ Copper acetate), step 2nd (BTC), d) step 1st (CMC+ BTC)…. 225
Figure 5.2.11. SEM micrographs of HKUST-1 anchored to the CMC fiber by the secondary growth (procedure C, Table 5.2.2)…….. 226
Figure 5.2.12. HKUST-1 color change in hybrid materials synthesized by the green methodology and approach of secondary growth after the activation process (purple), being in atmospheric pressure during: 1 minute (blue), and 5 minutes (turquoise)…….. 228

Figure 5.2.13. a) Outline of the main structure of HKUST-1 before activation shows the paddlewheel structure that is formed by two Cu2+ ions and four benzene molecules of the linker 1,3,5-tricarboxylate linker (BTC), b) hydrated cage of HKUST-1 before the activation, c) activated cage of HKUST-1 (dehydrated) [29]…… 229
Figure 5.2.14. X-ray diffraction patterns for the hybrid materials synthesized: WET1-199 and SH-WET1-199…….. 229
Figure 5.2.15. FESEM images of the hybrid materials synthesized: WET1-199 (blue square, 5.2.15a, b,c) and SH-WET1-199 (orange square, 5.2.15d, e, f)……. 230
Figure 5.2.16. EDX of the hybrid materials synthesized: WET1-199 and SH-WET1-199…… 232
Figure 5.2.17. X-ray (EDX) elemental mapping analysis for the hybrid materials synthesized: WET1-199 and SH-WET1-199…… 234
Figure 5.2.18. Schematic synthesis procedure of a) HKUST-1 and b) SH-HKUST-1…. 236
Figure 5.2.19. Thermogravimetric analysis (TGA) and Differential Scanning Calorimetry (DSC) of hybrid materials synthesized: WET1-199 and SH-WET1-199….. 237
Figure 5.2.20. pHzpc of hybrid materials synthesized: WET1-199 and SH-WET1-199... 239
Figure 5.2.21. FTIR spectra obtained from the hybrid materials synthesized: WET1-199 and SH-WET1-199…….. 241
Figure 5.2.22. XPS X-ray photoelectron spectroscopy (XPS) of the functionalized fiber WET1, impregnated fiber Cu-WET1, and the hybrid materials synthesized: WET1-199 and SH-WET1-199…….. 242
Figure 5.2.23. C 1s spectra of the functionalized fiber WET1, impregnated fiber Cu-WET1, and the hybrid materials synthesized: WET1-199 and SH-WET1-199……. 243
Figure 5.2.24. O 1s spectra of the functionalized fiber WET1, impregnated fiber Cu-WET1, and the hybrid materials synthesized: WET1-199 and SH-WET1-199……. 244
Figure 5.2.25. Cu 2p spectra of the functionalized fiber WET1, impregnated fiber Cu-WET1, and the hybrid materials synthesized: WET1-199 and SH-WET1-199……. 245
Figure 5.2.26. S 2p spectra of the functionalized fiber WET1, impregnated fiber Cu-WET1, and the hybrid materials synthesized: WET1-199 and SH-WET1-199……. 246
Figure 5.2.27. XRD patterns of WET1-199 (up) and SH- WET1-199 (down) samples, exposed to water for 24, 48 and 72 hours……. 247
Figure 5.2.28. SEM micrographs of WET1-199 (up) and SH- WET1-199 (down) samples, exposed to water for 24, 48 and 72 hours……. 249
Figure 5.2.29. AAS measurement of copper in solution after being in contact with water and HKUST-1(purple data), SH-HKUST-1 (orange data), WET1-199 (turquoise data) and SH-WET1-199 (pink data) for 72 hours…….. 251
Figure 5.2.30. UV-VIS measurement of BTC in solution after being in contact with water and HKUST-1(purple data), SH-HKUST-1 (orange data), WET1-199 (turquoise data) and SH-WET1-199 (pink data) for 72 hours……. 252
Figure 6.1.1. Effect of contact time on mercury adsorption onto functionalized fiber (WET1). Experimental conditions: initial Hg2+ concentration: 40 μg L^{-1}, adsorbent dose: 0.4 g WET1 L^{-1}, pH: 7, temperature: 20 °C, stirring: 100 rpm……. 271
Figure 6.1.2. Effect of WET1 dosage on mercury adsorption. Experimental conditions: contact time: 30 min, initial Hg2+ concentration: 40 μg L-1, pH: 7, temperature: 20 °C, stirring: 100 rpm……... 272
Figure 6.1.3. Effect of stirring in the mercury adsorption on WET1. Experimental conditions: contact time: 30 min, initial Hg2+ concentration: 40 μg L-1, pH: 7, temperature: 20 °C, adsorbent dose: 0.4 g WET1 L-1……. 273
Figure 6.1.4. Uptake capacity of mercury (II) and efficiency adsorption on raw (R), pretreated (WE), functionalized (WET1), functionalized fiber with HKUST-1 anchored (WET1-199), functionalized fiber with HKUST-1 modified to include thiol groups (SH-

WET1-199). Experimental conditions: contact time: 30 min, initial Hg2+ concentration: 40 µg L-1, pH: 7, temperature: 20 °C, adsorbent dose: 0.4 g WET1 L-1, stirring: 100 rpm…… 274
Figure 6.1.5. Residual plots for the analysis of the cross effect between the pH and initial mercury concentration using WET1 as adsorbent. a) Normal probability plot, b) Versus fits, c) Histogram and d) Versus order…….. 282
Figure 6.1.6. Pareto chart of the experimental and calculated results from the of experimental design for mercury removal using as adsorbent WET1…….. 283
Figure 6.1.7. Response surface of the cross effect in the mercury removal from the pH and solution initial concentration to be treated using WET1 as adsorbent following the DOE (Table 6.1.5)…… 284
Figure 6.1.8. Effect of temperature in mercury adsorption on functionalized fiber (WET1). Experimental conditions: contact time: 30 min, initial Hg2+ concentration: 68.28 µg L-1, pH: 7, adsorbent dose: 0.4 g WET1 L-1, stirring: 100 rpm…….. 288
Figure 6.2.1. Adsorption capacity of CBZ and MET (Co = 10 mg L-1), during 120 min in contact with 0.1 g of the materials: WET1, Cu-WET1, WET1-199 and SH-WET1-199, room temperature and pH = 6.45, separately…… 303
Figure 6.2.2. Degradation kinetics of CBZ and MET in ozonation heterogeneous processes catalyzed by the materials WET1, Cu-WET1, WET1-199 and SH-WET1-199. Besides, degradation kinetics of CBZ and MET in ozonation homogeneous processes catalyzed by Cu2+. Both catalysis at room temperature and pH = 6.45, separately……..…….. 305
Figure 6.2.3. Degradation efficiency of CBZ and MET in ozonation processes catalyzed by the materials WET1, Cu-WET1, WET1-199 and SH-WET1-199, room temperature and pH = 6.45, separately…….. 307
Figure 6.2.4. Normalized Total organic carbon (TOC) measured as blank for the materials: WET1, Cu-WET1, WET1-199 and SH-WET1-199……. 309
Figure 6.2.5. Normalized TOC of CBZ and MET (Co = 10 mg L-1), after 120 min in contact with 0.1 g of the materials: Cu-WET1, WET1-199 and SH-WET1-199, room temperature and pH = 6.45, separately…… 310
Figure 6.2.6. Oxalic (OXL) and oxamic (OXM) acid concentration measured during the a) CBZ and b) MET (Co = 10 mg L-1) ozonation, after 120 min to be in contact with 0.1 g of the materials: Cu-WET1, WET1-199 and SH-WET1-199, separately…… 311
Figure 6.2.7. Simulation of the copper species development along the ozonation reaction catalyzed by Cu2+-WET1…… 316
Figure 6.2.8. Simulation of the oxidant radical's concentration along the ozonation reaction catalyzed by Cu-WET1……. 317
Figure 6.2.9. Hydrogen peroxide measured during the ozonation reaction, after 60 min in contact with 0.1 g of Cu-WET1, 0.25 mL of aqueous solution (only miliQ water)……. 318
Figure 6.2.10. XRD diffractograms of WET1, Cu-WET1, WET1-199 and SH-WET1-199, after 120 min of reaction……. 319
Figure 6.2.11. SEM micrographs of WET1, Cu-WET1, WET1-199 and SH-WET1-199, after 120 minutes to ozonation reaction and their initial condition…….. 320
Figure 6.2.12. Cycle use of Cu-WET1 for degradation of CBZ and MET, after each run of 120 min in contact with 0.1 g of the catalyst material, room temperature and pH = 6.45, separately…… 322
Figure 6.3.1. Modified ASTM-2149-13A procedure scheme……. 332
Figure 6.3.2. Reduction percentage of E. Coli using as positive control ampicillin (C+), growth control (CC), raw (R), pretreated (WE) and functionalized (WET1), HKUST-1 or

SH-HKUST-1 MOFs anchored onto fique fibers, WET1-199 and SH-WET1-199, respectively…….. 333
Figure 6.3.3. Reduction percentage of E. Coli using, HKUST-1 or SH-HKUST-1 MOFs anchored onto fique fibers, WET1-199 and SH-WET1-199, respectively……. 335
Figure 6.3.4. Schematic illustration of the antibacterial mechanism proposed by Rajeshkumar et al. [20]…… 338
Figure 6.3.5. Illustration of the chemistry involved in cellular damage caused by oxidative stress in E. Coli bacteria during the antibacterial activity of materials with MOFs. Modified from [24]…… 339

List of tables

Pag.

Table 1.1. Emerging contaminants classification…… 11
Table 1.2. Possibilities of structure and composition of hybrid materials [77]……..…….. 23
Table 1.3. Classification of hybrid materials applications [79]……..……..…. 24
Table 1.4. Constitutive elements properties of hybrid materials……..……... 24
Table 1.5. Sources of lignocellulosic biomass [82]……...……..…….. 26
Table 1.6. Chemical composition of selected lignocellulosic biomass materials [81]…..... 28
Table 1.7. Cellulose characteristics at different structural levels……..….. 29
Table 1.8. Configurations of xylan……...……...….... 30
Table 1.9. Performance pretreatment summary……...…...… 32
Table 1.10. Average distribution of components, percentage used and applications in fique [145]……...……...…….. 42
Table 1.11. Synthesis methods used to produce metal-organic frameworks……..... 46
Table 1.12. Parameters that affect the crystal size and morphology……...……. 49
Table 1.13. Direct growth approaches……...….. 51
Table 1.14. LBL growth approaches……...…. 52
Table 1.15. Growth approaches by electrochemical deposition……..……..…. 53
Table 1.16. Growth approaches by interfacial synthesis……..……..……. 54
Table 1.17. Flow chart of structural factors governing water stability in MOFs [186]…...… 56
Table 1.18. Physicochemical properties of adsorbates, adsorbents, and water quality properties……...……..……. 62
Table 1.19. Factors that affect the adsorption process…….. 64
Table 1.20. Metal-organic frameworks used as adsorbent to remove Hg^{2+} from water……...……...…… 65
Table 2.1. Chemical composition of raw jute fibers analyzed by NREL……...…. 89
Table 2.2. CHNS/O results for the raw fique fiber analyzed in this work……..….... 90
Table 2.3. Results of the acidic and basic sites in the fique fiber……..…… 93
Table 3.1. Factors assessed in the acid and alkali pretreatment of raw fique fiber…..... 110
Table 3.2. Chemical composition and correlation severity of the pretreated fibers by organosolv and raw fique fibers quantified by NREL methodology…… 120
Table 3.3. Percentage of cellulose crystallinity index (CI) for the fibers pretreated by organosolv using different solvents ……...… 126
Table 3.4. Values of Young´s Moduli (E) for pretreated fibers by organosolv using different solvents measured by DMA…… 127
Table 3.5. BET surface area measured by nitrogen adsorption for pretreated fibers by Organosolv ……. 128
Table 4.1. Factors assessed in CMC functionalization of fique fiber pretreated…….. 141
Table 4.2. Experimental design to identify the CMC methodology that reached the higher DS in the fique fiber quantified by USP method, considering the evaluation of

fiber type (raw, R or pretreated, WE), the solvent used in the basification step (isopropyl alcohol, OH or water, H_2O), and with or without stirring during the etherification step…..... 145
Table 4.3. Results of the Box-Behnken experimental design of the degree substitution (DS) after the carboxymethylation functionalization onto fique fiber pretreated (SC is Sodium chloroacetate)…… 148
Table 5.2.1. FESEM micrographs in pretreated fibers after TEMPO functionalization under different NaOCl:AGU molar ratio plus HKUST-1 anchored ……..…. 222
Table 5.2.2. Experimental procedure followed for the formation of HKUST-1 onto CMC fiber functionalized……..……...…..… 224
Table 5.2.3. BET surface area of the hybrid materials synthesized: WET1-199 and SH-WET1-199……... 231
Table 5.2.4. Amount of copper measurement by FAAS in the hybrid materials synthesized: WET1-199 and SH-WET1-199…… 234
Table 5.2.5. CHNS / O elemental analysis in the hybrid materials synthesized: WET1-199 and SH-WET1-199…….. 235
Table 5.2.6. Percentage of metal-organic frameworks HKUST-1 and SH-HKUST-1 were anchored onto the fique fiber, quantified by FAAS and TGA……. 238
Table 6.1.1. Factors assessed in mercury removal using an adsorbent from fique fiber.. 265
Table 6.1.2. pH at the point of zero charge (pH_{PZC}) of the materials evaluated as adsorbents in mercury removal…….. 275
Table 6.1.3. Adsorption isotherm model constants derived from the Langmuir, Freundlich and Temkin models, fitted for raw (R), pretreated (WE), functionalized (WET1), functionalized fiber with HKUST-1 anchored (WET1-199), functionalized fiber with HKUST-1 modified to include thiol groups (SH-WET1-199)…… 277
Table 6.1.4. Kinetic constants for the pseudo first – order, pseudo second- order and Elovich equations, fitted for raw (R), pretreated (WE), functionalized (WET1), functionalized fiber with HKUST-1 anchored (WET1-199), functionalized fiber with HKUST-1 modified to include thiol groups (SH-WET1-199)…….. 277
Table 6.1.5. Adsorption uptake, removal percentage and results for the statistical model fitted, analyzing the cross between the pH and initial mercury concentration using WET1 as adsorbent. Experimental conditions: contact time: 30 min, temperature: 20 °C, adsorbent dose: 0.4 g WET1 L^{-1}, stirring: 100 rpm…….. 281
Table 6.1.6. Analysis of variance (ANOVA) for mercury removal by MiniTab 16 Statistical Software…….. 282
Table 6.1.7. Adsorption isotherm model constants derived from the Langmuir, Freundlich and Temkin models, fitted for functionalized fiber (WET1), under conditions described above in Table 6.1.5…….. 286
Table 6.1.8. Kinetic constants for the pseudo first – order, pseudo second- order and Elovich equations, fitted for functionalized fiber (WET1), under conditions described above in Table 6.1.5…… 286
Table 6.1.9. Thermodynamic parameters calculated for the adsorption of Hg^{2+} onto WET1…… 288
Table 6.2.1. Physical and chemical properties of CBZ and MET [9]……. 302
Table 6.2.2. pH_{ZPC} of all the materials used as adsorbents to remove CBZ and MET… 302
Table 6.2.3. Important reaction mechanism of oxidant species with reactive chemical groups of CBZ and MET……. 308
Table 6.2.4. Ions quantified from the CBZ and MET (Co = 10 mg L^{-1}) ozonation, after 120 min to be in contact with 0.1 g of the materials: Cu-WET1, WET1-199 and SH-WET1-199, separately…… 312
Table 6.2.5. Summary of results obtained from the ozone catalytic system and hybrid materials with copper for the treatment of CBZ and MET…… 312

Table 6.2.6. Copper leached from the catalysts used in the ozonation reaction of MET and CBZ, quantified by ICP-OES…….. 321
Table 6.3.1. Reduction percentage of *E. Coli* using different materials. Using the Tukey method, means do not share a letter are significantly different (Tukey, $p<0.05$)…….. 334

Preface

"The value of the water is not appreciated until the well dries" (English proverb)

Paradoxically, Paradoxically, despite the knowledge of the importance of water for life, human civilization seems not to have become aware yet of the need to preserve this resource. Despite this, according to the WHO, the real access that human populations have to drinking water sources are worrisome. In 2015, there were still about 1800 million people who consumed water contaminated with feces. Likewise, it is expected that approximately 50% of the human population will live in areas with severe water scarcity, either by drought associated with climate change or simply by the irrecoverable contamination of drinking water sources, causing important political, territorial and social conflicts, without counting that it would put at risk the existence of these populations.

Therefore, as long as modern society continues to have comfortable and safe access to water sources, it will not be aware how each of its activities has a negative or positive influence on the consumed water, until the moment when scarcity makes it understand the immense value of this loss. There is a need not to forget that water and its cycle is the very reason of life, its contamination means the end of all life on the planet, so the care of this element should not be understood like a good action or a simple militancy to nature, but as an act of prevention and self-care.

Within the problematic of the contamination of water sources, there are new challenges, such as the new pollutants class known as emerging contaminants (ECs), which are also persistent in the environment, have high toxicity and high capacity for bioaccumulation along food chain. These ECs include pharmaceutical compounds, flame retardants, personal care products, nanotechnology waste, pathogens, heavy metals, among others. The problem of ECs, related to the use and disposal of pharmaceutical compounds, can be analyzed from different perspectives: lack of information about this class of contaminants in water resources (identification and monitoring), absence of studies around chemical species from pharmaceuticals present in

wastewater discharges (origin, transformation and effects of these pollutants on aquatic species and human health), and limited regulation caused by ignorance of the effects of this type of pollutants.

Likewise, consumption patterns of medicines associated with the increase in age of population, development of new molecules for the treatment of chronic diseases, the nonexistence of handling and disposal methodologies of pharmaceuticals in domestic and health institutions, as well as irrational methods of synthesis and poor control of industrial wastes from pharmaceutical industries are the main sources of pollution of a city's water resources by pharmaceutical compounds. They generate an increase in the toxicity of the effluents, affecting individuals in the ecosystems such as the case of feminization of the marine fish *Mugil cephalus*.

The problem consists on the fact that these pharmaceutical residues are not removed or treated by conventional methods as biological processes present in WWTPs (wastewater treatment plants). This type of pollutants affects significantly municipal wastewater causing the limits of potabilization to be exceeded. Consequently, it is necessary to implement new technologies that allow the decontamination of water sources, eliminating or reducing ECs such as pharmaceutical compounds.

This an opportunity to solve the problem from the area of environmental catalysis, as an alternative to provide technical solutions in emissions control and reduce the impact of existing technologies, contributing to the development of new processes and materials that result less polluting. Each effluent requires a unique and specific treatment process, depending on load or content of analytes, impurities and physicochemical properties.

Nowadays there are different alternatives for wastewater treatment, including biological procedures, incineration, photo-oxidation, wet oxidation processes, ozonation, among others. However, many of these processes have problems related to high costs of production and efficiency. To overcome this problem, recent research has shown the possibility of producing new materials, capable of responding to current needs or applications.

These materials are the result of technologies that arise from the synergy of chemistry, applied physics, engineering and materials science. One example of this is hybrid materials that combine the properties of two or more elements. Namely, those that benefit from the attachment of

nanometer scale polymers such as MOFs (Metal Organic Frameworks) with biodegradable compounds such as natural fibers. These hybrid materials can act as adsorbents or catalysts, synthesized at atomic, molecular and macromolecular scale, in which new properties are generated. Their applications are already in the experimental stage in fields such as the control of environmental pollution.

The development of novel materials capable of performing effective water treatment is a current need. Consequently, the potential use of fibers such as fique as new materials gives an added value to a subproduct that currently is a waste, generated by the absence of Good Agricultural Practices (GAP). In addition, being at the forefront in the use of lignocellulosic materials, it is a promising alternative in the synthesis of sustainable materials with new types of morphologies such as microfibrillated cellulose (MFC), obtained through a process of homogenization. On the other hand, the use of nanoscale materials such as MOFs takes advantage of physical, chemical and structural properties, giving an infinity of applications. For example, MOFs have been used in the environmental field for wastewater treatment, allowing the pollutants removal, degradation or mineralization by reaction processes (i.e. accoupling π-π between the pollutant and MOF) or adsorption (physicochemical interactions), complementing the knowledge acquired from the basic sciences, engineering (chemical, environmental and materials) and pharmaceutical chemistry.

Hence, the aim of this thesis was the development of new materials for the treatment of ECs. This was achieved with the synergistic effect obtained from an active and physicochemical stable hybrid material formed by lignocellulosic fibers and metal-organic frameworks (MOFs). The treatment efficiency of ECs with this biomass nanostructured material was improved with parameters such as homogeneity, size and distribution of MOFs on the lignocellulosic fibers surface, increasing the surface area available for physicochemical reactions or specific chemisorption interactions in aqueous media.

This work was carried out in collaboration between Universidad Nacional de Colombia, Universidade do Porto and University of Bath, synergistically combining knowledge from different research groups such as materials, environmental engineering and chemistry, respectively. For this purpose, a novel hybrid material was developed which combines the properties of two or more elements, thus benefiting from the attachment of nanometer scale polymers such as MOFs with biodegradable compounds such as natural fibers. Then, the materials synthesized were

tested in applications related to water remediation of organic, inorganic and pathogen pollutants. Among the main contributions of this doctoral thesis, the following can be highlighted:

- A methodology for the modification of the physicochemical properties of the fique fiber was established to create suitable surface conditions that allow its use as a solid support for the anchoring of nanoparticles.
- A stepwise synthesis method of metal organic frameworks (MOFs) over pretreated fique fibers was design, that ensures: i) stability in aqueous conditions, and ii) formation of a chemical interaction between MOFs and fique fiber.
- The efficiency of the prepared materials on the removal of ECs was evaluated and analyzed.

Therefore, this document is divided into six chapters. Chapter 1 is a literature review that summarizes the main concepts that will be used in the rest of the document, Chapters 2, 3, 4 and 5 are related to the hybrid material synthesis. Specifically, chapter 2 includes a complete characterization of the fique fiber, to identify the benefits and weaknesses of this lignocellulosic biomass, to improve its properties in the next stages.

Chapter 3 is related to the evaluation of three pretreatments in fique fiber: acid, alkali and organosolv. Trough chemical, morphological, thermal, mechanical, and physicochemical characterization, the best pretreatment to clean the lignocellulosic biomass and homogenize the surface of the fibers was identified, without change its mechanical structure. Then, chapter 4 explains the most appropriate functionalization process in relation to the properties expected to be obtained on the pretreated fiber surface with a specific charge in order to facilitate the metal organic framework (MOF) anchoring process. Here two types of functionalization were considered to obtain an active chemical surface, with groups -COONa (sodium carboxylate) and $-CH_2OCH_2COONa$ (sodium carboxymethylcellulose); a complete chemical, morphological, thermal, mechanical, and physicochemical characterization was done to understand the characteristics of each potential fiber to be used as matrix of hybrid materials in the next stages.

Chapter 5 is divided into two subchapters. The subchapter 5.1 includes a definition of the powder MOF synthesis method (green or solvothermal). Here, it is important to consider one of the biggest challenges to use MOF in applications related to water, which is improving the hydrolytic,

chemical, and mechanical stability of the frame. Consequently, an approach with simultaneous synthesis and functionalization was implemented to increase the MOF stability, by the employment of crystal poison to include thiol groups (-SH) into the frame structure. Furthermore, a complete characterization of the synthesized MOFs is carried out. The 5.2 subchapter describes the MOF anchoring onto functionalized fiber. This stage incorporates the best MOF synthesis method established in subchapter 5.1, after which two types of anchoring methodologies are analyzed, consisting in direct and secondary growth. In addition, factors like reagents order addition, synthesis solvent, metal precursor, use or not of a deprotonating agent, and use of both types of functionalized fiber (chapter 4) were investigated to generate chemical interactions between the fique and the porous network, to guarantee the anchor of MOF over the fiber. Parameters such as homogeneity, size, and distribution of MOF particles on the lignocellulosic fibers surface are discussed.

In chapter 6, an evaluation of the hybrid materials synthesized is presented in applications related to wastewater treatment of different ECs, including inorganic and organic compounds, and pathogens. The applications are summarized in three subchapters: in 6.1. the material is used as adsorbent of heavy metals like mercury, here the process performance was followed by electrochemistry; in 6.2. the prepared materials are employed as catalyst for the ozonation reaction to eliminate organic contaminants like pharmaceutical compounds (carbamazepine and metopropol); and in subchapter 6.3., the antibacterial activity was tested on *Escherichia coli* bacteria.

A final chapter with conclusions and future work will be in the last part. Finally, as academic outputs, this research originated so far 1 paper published (Bastidas, K., Sierra, C. & Zea, H. Heterogeneous Fenton oxidation of Orange II using iron nanoparticles supported on natural and functionalized fique fiber. *J. Environ. Chem. Eng.* **6**, 4178–4188 (2018)) and several others in preparation, 3 posters and 4 oral presentations (in national and international events).

1. Contextualization and theoretical framework

The problem of water contamination with emerging pollutants, related to the use and disposal, can be analyzed from different perspectives: lack of information about this class of contaminants in water resources (identification and monitoring), absence of studies concerning chemical species present in wastewater discharges (origin, transformation, and effects of these pollutants on aquatic species and human health), and limited regulation caused by ignorance of pollutants.

Consequently, it is necessary to implement new technologies that allow the decontamination of water sources, eliminating or reducing these emerging pollutants. The area of environmental catalysis can play an important role in this subject, as an alternative to provide technical solutions in emissions control and reduce the impact of existing technologies, contributing to the development of new processes and materials that result less polluting. Each effluent requires a unique and specific treatment, depending on load or content of analytes, impurities, and physicochemical properties.

1.1 Water pollution

Water is the most important resource to support life on earth. Of the total water resources available on the planet (Figure 1.1) only 3% is sweet water, and 1% of this is affordable for use and extraction [1]. Access to water is a fundamental right and a necessity to which 884 million people are constrained by issues of sanitation and water potabilization. Even in the 21st century, 765.000 people die annually due to diseases caused by contaminated water [2].

The global water crisis is evident respect to quantity and quality, caused by the increasing population, fast industrialization, reduction in the amount of food available, increase life expectancy and reduced strategies for reusing water [2]. Water resources are directly related to the economic development of a country (40% of the population depends economically on water).

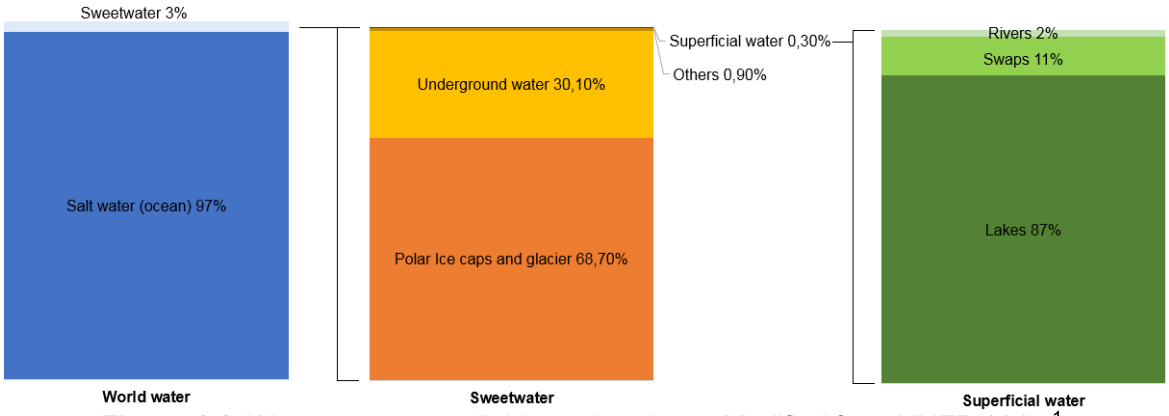


Figure 1.1. Water sources available on the planet. Modified from UNEP 2015 [1].

In addition to the problems previously mentioned, also scarcity of water is greatly affected by pollution from 500 million tons of wastewater discharged in rivers, seas and oceans [3]. One of the main sources of pollution are industries that do not rationalize the amount of water used in processes such as water services and the possible integration of processes to reduce its consumption. Contaminated water contains material from natural and industrial origin such as microorganisms, organic and inorganic pollutants; these elements deteriorate water quality and make it useless for certain uses. Sewages contain pollutants such as infectious agents, plant nutrients, chemicals, hydrocarbons, sediments, inorganic minerals and radioactive substances [1].

As a result of the problems described above, it is essential to perform efficient wastewater management [4]. Without the development of new solutions, the water access gap could increase in the next decades. The water problem in Latin America has become evident in the last two decades, and despite the large reserves of freshwater (about 31% of the world total) [5], there are many challenges regarding the management of water resources. Approximately 40 million people lack of drinking water and 125 million people do not have sanitation services [5]. The people most vulnerable to water pollution in Latin America are inhabitants of rural areas, women, children and fishermen, caused by intensification and expansion of agriculture, as well as more connections to the sewer system with effluents without or under treatment [7].

According to the UN for 2050, it is likely that at least 1 in 4 people could live in a country with a shortage of water suitable for consumption [6]. Therefore, corrective actions must be taken to guarantee the possibility of having quality water for future generations. This can be achieved by developing technologies that mitigate pollution and recover the quality of rivers.

Colombia is the sixth country with the highest water supply in the world thanks to the three mountain ranges, two oceans, tropical forest, and strategic location. Although the Ministry of

Environment calculated that half of the water resources have quality problems, about 9 thousand tons of polluting organic matter per year are generated and discharged to aquifers by the industrial sector, agricultural and domestic waters [8]. As a result, Colombia ranks 24th in the world ranking of water quality [9]. The problem has increased due to lack of wastewater treatment plants (WWTPs). Moreover, most of the existing ones were not properly designed to meet the quality standards for the effluents discharge. Additionally, the National Water Study [9] clearly concludes that part of the Colombian water system has been altered by the transport of sediments and toxic substances, attributed to industrial corridors that finally reach the most important areas: Bogotá–Soacha, Medellín–Itagüí, Cali–Yumbo, Sogamoso–Duitama–Nobsa, Barranquilla–Soledad and Cartagena–Mamonal.

Particularly, the Bogotá river is one of the water streams that reflects more truly and closely the problem of emerging pollutants in Colombia, especially of pharmaceutical nature. One of the few studies conducted in the Bogotá river identified approximately 1000 emerging contaminants (EC); with a great amount of licit and illicit drugs and their metabolites[10]. The use of veterinary medicines and pharmaceutical compounds in major cities differs temporally and spatially between regions, due to differences in marketing, regulations, prescribing practices, among others [11]. Therefore, medicines used in Latin America may differ from those prescribed or consumed in Europe and North America. Consequently, analyzes carried out in each country could ignore important pollutants from other countries.

The concern about the presence of these pollutants is because these rivers not only flow through high biodiversity areas, but also because surface water is used for agriculture and human consumption. This is the reason why it is mandatory to know how to select contaminants to define priority compounds and then establish objective methodologies for their supervision [12,13].

In surface water, the presence of pharmaceutical products was more notable in samples collected from the Tunjuelo river. In this area, around 2.5 million inhabitants discharge their wastewater directly into the river without any treatment. Furthermore, the urban solid waste landfill (Doña Juana landfill) is located there and the potential lixiviation of its leachates contribute surely to the contamination in the area, explaining the profile of emerging pollutants in these surface waters [10]. The results obtained for the Salitre WWTP were similar, reflecting the medicament consumption by a large part of the population (2.5 to 3 million inhabitants). In contrast, the irrigation area of La Ramada, supplied by the Bogotá River in its northern part is affected by industrial and urban

discharges. Although with smaller population (around 600.000 inhabitants), the surface water samples had several contaminants in common with the Tunjuelo river samples and with wastewater samples; nevertheless, the number of compounds detected was noticeably lower.

All previous descriptions shows the importance of the implementation of monitoring mechanisms focused on appropriate identification, characterization, quantification and tracing of these emerging pollutants, because their presence can have undesirable consequences in public health, mainly considering that these waters are used for human consumption and agricultural irrigation.

1.2 Emerging contaminants

Emerging contaminants (ECs) are defined as: “Chemical or non-chemical material with great potential to present a potential risk for the environment and human health" [14]. The awareness of the existence of ECs should be attributed to the mid of 1962, when Rachel Carson in her book "silent spring" [15], showed convincingly that the widespread use of DDT (dichloride diphenyl trichloroethane) for the elimination of mosquitoes and other pests, caused the death and disappearance of many birds. Carson was harshly criticized at that time for challenging the benefits from the use of pesticides and specifically of DDT. As a result of the Carson’s initiative, DDT was prohibited.

Contaminants are "emerging", because within a broader context are recently appeared, generating new concerns. They are also known to be emergent because some compounds have shown new information, throwing other perspectives on the worries of ancient pollutants. Furthermore, they are persistent compounds in the environment, with high toxicity and great capacity for bioaccumulation along food chains[16].

The emerging pollutants approach seeks: i) identify new compounds or molecules that were not previously known or that have recently appeared in the scientific literature, ii) emerging contaminants already known but for which environmental contamination has not been fully analyzed and iii) approach issues about "old" pollutants, ie, situations that seek to understand risks to the environment and human health related to inherited contaminants.

Because ECs are closely related to environmental quality criteria, as a new compound begins to cause concerns, it will be critical to start the collection of data about its chemical accumulation, ecotoxicological and human toxicity, as well as its epidemiology, allowing government to take

actions to establish guidelines or environmental criteria that guarantee adequate protection. Nonetheless, referring to the ECs, it must be clear that this connotation includes different types of pollutants, which have been classified as described in Table 1.1. However, there are limitations in studies since the spatial distribution within the same basin is provisionally evaluated [17], evidencing the dependence to a discrete selective sampling due to the number of sites that are monitored at the same time.

Table 1.1. Emerging contaminants classification.

ECs	Example of chemical product that produces it
Surfactants	Widely used in domestic applications, detergents and cleaning products, personal care, textiles, additives for paints, lacquers and plastics.
Pharmaceutical products	The estimated total concentration of pharmaceutical products is around 70 mg day^{-1} $person^{-1}$ in sewers, which corresponds to around 200-250 µg L^{-1} [18]. The fate of pharmaceutical products in WWTPs depends on their characteristics, i.e. affinity for adsorption and biodegradability. Most of the pharmaceutical products studied have removal efficiencies of less than 50%, depending on the compound.
Illicit drugs	As amphetamine, cocaine, and its main metabolite benzoylecgonine, MDMA (ecstasy) or THC-COOH (metabolite of cannabis) are present on average 100 to 2000 ng L^{-1} in wastewater. These illicit compounds are well eliminated in conventional WWTPs (from 79% to > 98%), except for MDMA (0-26%) [19].
Personal care products	Shampoo, wash lotions, skincare products, dental care products, sunscreen agents, cosmetics, perfumes and hair care.
Industrial and household chemicals	Sweeteners, anticorrosive or chelates, plasticizers, flame retardants, per fluorinated compounds, anticorrosive [20].
Biocides, pesticides, and persistent organic pollutants (POPs)	They can be found in concentrations of 100 to 1 µg L^{-1} [21], in WWTP the removal efficiency is close to 50%, these herbicides such as glyphosate and mecoprop are present in 500 ng L^{-1}, another type of POP are the polychlorinated biphenyls (PCB), they are used as heat exchange fluids in electrical transformers, additives in paint and oil, they are still found in municipal wastewater despite their banned in countries from 1970-1990.
Heavy metals	Elements that are not biodegradable tend to accumulate in living organisms and are toxic at excessive levels, including metals of special concern in wastewater: zinc (Zn), copper (Cu), nickel (Ni), mercury (Hg), cadmium (Cd), lead (Pb) and chromium (Cr) [22].
Polycyclic aromatic hydrocarbons (PAH)	Family of more than 100 organic compounds formed by two or more benzene rings condensed without any heteroatom, come mainly from incomplete combustion or pyrolysis of organic material such as oil, petroleum, coal and wood. They are used in products such as lubricants, bath products, deodorant discs, wood preservatives, fungicides and concrete plasticizers [23].
Volatile organic compounds (VOC)	They are widely used in fuels, paints, aerosols, cosmetics, solvents, disinfectants and pesticides, some examples are benzene, toluene, ethylbenzene, xylene, and styrene (BTEXS group) [20].

More than 70% of relatively hydrophobic contaminants such as metals, POP (persistent organic pollutants), household chemicals, and various personal care products are eliminated, especially by adsorption in WWPT. Likewise, easily biodegradable contaminants such as surfactants, plastic additives, hormones, various PPCPs (pharmaceuticals and personal care products) and some household chemicals are eliminated by biodegradation / transformation. By contrast, most of the pharmaceutical products and pesticides are not significantly eliminated [24].

Factors affecting most of the characterization and technological advance in EC management is data collection by the available monitoring options, affecting sampling by two types of variations: i) intra–day, concentrations change in a single day [25], i.e, specific cases of pharmaceutical products show a concentration peak between 07:00 and 9:00 h, situation explained by the dosage management and accumulation of drugs administered in urine during sleep [25], ii) inter–day, is affected by a sample taken for several days of a week, as well as, collected data reveal a greater trend for some compounds on weekends, such as illicit drugs. Likewise, some ECs have seasonal uses indicate the polluting load will vary throughout the year [26].

To solve the drawbacks concerning the removal methods in WWTP, two alternatives have been proposed: 1) improvement and optimization of existing treatment systems and 2) addition of advanced treatments. For the first alternative, optimization of conventional treatments has been proposed, in which physical processes such as adsorption could be biologically mediated with enzymatic reactions [27]. Regarding the second alternative, the insignificant elimination of some ECs it is not feasible by optimization of existing conventional treatments, then complementary treatments are required. So far, mainly advanced physicochemical processes are available, such as adsorption using activated carbon, membrane filtration (nanofiltration, reverse osmosis) or chemical treatment, mainly by oxidation with ozone, OH radicals, ferrate and UV / H_2O_2.

Currently, there are two technologies with potential application in terms of efficiency, cost and energy: (1) oxidation with ozone and (2) adsorption on activated carbon [28]. These two technologies have been tested on a pilot scale, showing good elimination efficiency of a wide range of micropollutants [29]. However, they still have limitations because adsorption does not work if the net exchange between biomass or sediment and specific medium for a EC is zero [30].

Regarding photolysis, it is a method susceptible to differences in the chemical structure of pollutants [31], but to carry out the elimination of the original compound by photolysis does not

indicate complete mineralization. On the contrary, it is possible to convert the parent pharmaceutical compounds in more polluting byproducts, with an increase of the toxicity.

- Effects of ECs

ECs have biological activity on organisms, their persistence in environment and bioaccumulation is determined by physicochemical properties such as: water solubility, vapor pressure, octanol-water coefficient, Log P (partition coefficient for ionizable compounds), biodegradation reactions, adsorption, hydrolysis and photo oxidation. Particularly, physicochemical parameters such as the octanol-water distribution coefficient (Dow), Henry's constant and the dissociation constant allow to describe its chemical and dynamic equilibrium, providing information about the ideal analytical procedure for their identification [32]. Most ECs are weak acids or bases, so their distribution depends on the medium pH and the acidity constant (Ka).

Although ECs are found in very low concentrations, their effects might be significant, so it is necessary to implement adequate designs of water treatments for their efficient removal. Some studies have reported significant effects on human and animal health. The effects of the pharmaceutical contaminants reported previously depend on the system attacked, moment and the organism. Surely, they can also bioaccumulate in the trophic chain.

- Instrumental techniques for ECs quantification:

As a consequence of the low concentrations (ppt to ppm) of the ECs usually found in real samples and the absence of regulations in most of the countries [33], the identification and quantification of EC is the first stage in making decisions to preserve the water resources. Gas chromatography (GC) and liquid chromatography coupled with mass spectrometry (LC/MS) have been the most used techniques for the analysis of EC, which allow to determine very low concentrations of these compounds (μg or ng L^{-1}) [33].

It is important to identify and evaluate the efficiency of other techniques for pharmaceutical pollutants in water treatment, in order to propose alternatives to minimize the presence of EC through environmental, energy and low-cost benefits [24]. A new method consists in a solid phase extraction procedure followed by ultra-high-performance liquid chromatography coupled to tandem mass spectrometry (SPE-UHPLC-MS/MS), which was optimized using ecological solvents, reaching detection limits below 0.20 ng L^{-1}. The validation method considers the parameters: selectivity, linearity, scope, detection limits, quantification, precision, precision and recovery [34].

- Regulations of ECs quantification:

Although there is no explicit regulation on the legal limits in micropollutants discharge, some regulations have been published, such as The Directive 2000/60/EC. It was the first European policy for water, which aimed to organize a strategy to define and prioritize the risk of substances [35], then 33 substances were ratified as priorities by this directive [36]. In 2010, the European Union Directive 2013/39/EU, recommended pay attention to monitoring and treatment of 45 PSs (priority substances) [37]. This was corrected in 2015 through the European Union Directive 2015/495/EU, substances were included (diclofenac, EE2 y E2), three macrolides antibiotics (azithromycin, clarithromycin and erythromycin), the natural hormone E1, some pesticides, UV filters and food antioxidants [38].

- Treatment methods of ECs:

The water treatment and WWTP are systems and unit operations of physical, chemical or biological type, with the purpose of eliminating and reducing undesirable characteristics in natural, supply, process or residual water. The selection of WWTP depends mainly on characteristics of the raw water, contamination type, required effluent quality and land availability. The wastewater treatments include the following sequence (Figure 1.2).

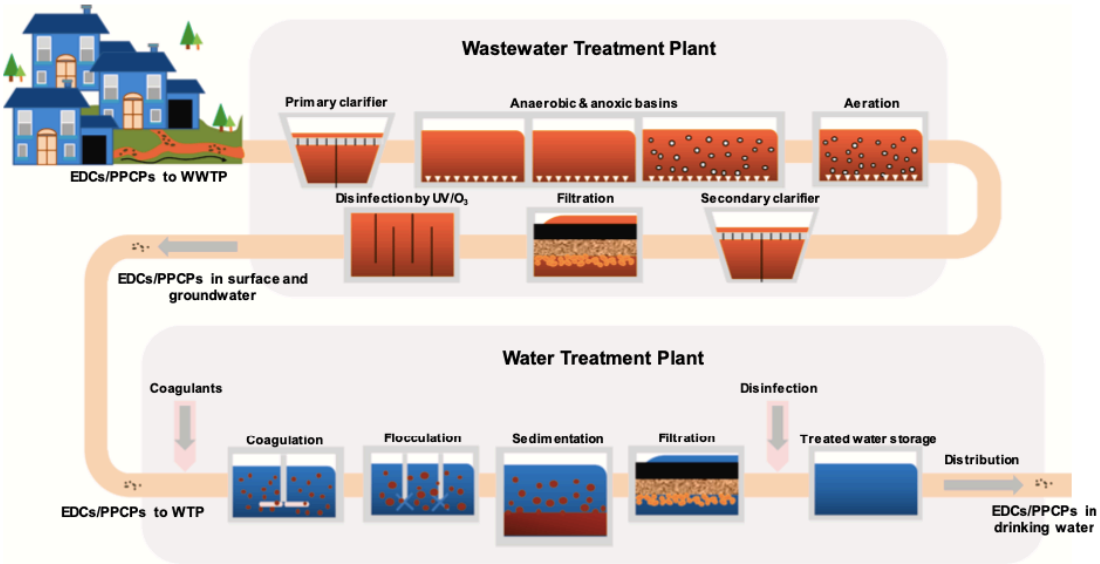


Figure 1.2. Removal mechanisms in conventional WWTP [40].

– Pretreatment: the residual water facilitates treatment, also preserves erosion and clogging installations. It includes grilles, sieves, grit chambers and degreasers.

- Primary treatment (physicochemical treatment): reduces suspended matter by means of precipitation or sedimentation, with or without reagents and different oxidation types (solids removal or screening, sand removal, maceration, sedimentation).
- Secondary treatment (biological treatment): eliminates dissolved organic contamination, requires high costs for the use of aerobic oxidation or anaerobic elimination, produces sludge that must be treated later (includes roughing, activated sludge, filter or oxidation beds, rotating plates, biological reactor, aerated filters, membranes, secondary sedimentation).
- Tertiary treatment (biological, physical and/or chemical treatment): it makes the water suitable for supplying agricultural, industrial and potabilization needs (filtration, lagoning, wetlands, nutrient removal, disinfection).

As consequence of low efficiency in conventional treatments used in the WWTP, new methods have been implemented for the treatment of contaminated water, evaluated through the octanol/water distribution coefficient (Dow), a coefficient that defines hydrophobicity and ionicity[39]. WWTP are not designed for microcontaminants removal because they are usually not affected by physical or biological processes.

The main mechanisms currently used to remove EC during wastewater treatment (Figure 1.3), include volatilization, dispersion, diffusion, adsorption, photolysis, degradation and transformation [38], depending on the physical-chemical characteristics (hydrophobicity, biodegradability, volatility) of the analytes that are sought to attack.

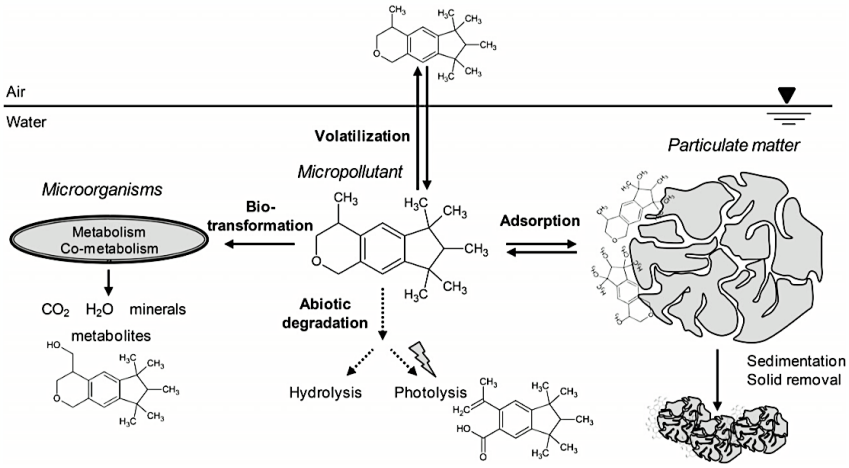


Figure 1.3. Main removal mechanisms of micropollutants in conventional WWTPs (example of the polycyclic musk galaxolide) [24].

Nevertheless, this type of compounds is mostly eliminated by adsorption in particulate material such as activated carbon [41], biological degradation and volatilization process. These treatments can play an important role in the elimination of these components (around 10 to 15%). A brief discussion about some of these methods is given below.

- Adsorption:

Important mechanism for removal of hydrophobic or positively charged compounds, and little biodegradable. In sludge two types of processes can be differentiated: i) Hydrophobic interactions between a hydrophobic pollutant and suspended solids, extracellular polymeric substances (EPS) or lipophilic cell membranes, ii) electrostatic interactions between positively charged groups of contaminants and negatively charged surfaces of microorganisms [24]. Adsorption is defined as pollutants transfer from liquid phase to the surface of a solid phase, the fate of contaminants adsorbed depends on the solid disposal (incineration, landfill, or agriculture reuse).

The tendency to accumulate in mud solids can be evaluated using the partition coefficient octanol/water (K_{OW}). Rogers *et al.* [42] proposed the following guide to evaluate the adsorption potential of organic pollutants: low ($\log K_{OW} < 2.5$), medium ($2.5 < \log K_{OW} < 4.0$) and high ($\log K_{OW} > 4.0$). However, it must consider the prediction of adsorption on solids is mainly applicable to non-polar compounds.

- Biological treatment:

For many hydrophilic organic micropollutants, biological transformation is the main elimination mechanism in wastewater treatment. It usually requires the presence of other growth substrates (carbon and energy sources) to bio-transform pollutants traces. Two types of processes are mainly used: i) Metabolic reactions in mixed substrate use organic micropollutants like substrate for growth; these substrates use energy (catabolic) and/or carbon source (anabolism) to cell development (maintenance, growth and reproduction), ii) Co-metabolic reactions in which micropollutants are not used as growth substrates, but they are biologically transformed through secondary reactions catalyzed by nonspecific enzymes (mono- or di-oxygenases, N-acetyltransferases and hydrolases) or cofactors produced during the microbial conversion of substrate growth [24].

The pollutant fraction eliminated by biodegradation (metabolism or co-metabolism) depends on the microorganisms amount present, microorganisms' type, contaminant biodegradability and

hydraulic retention time inside the reactor (usually, the degradation follows a pseudo-first order kinetic model). Likewise, the biodegradation rate can be influenced by temperature, pH, redox conditions, and co-substrate availability.

- Abiotic degradation:

It is not expected to contribute to a significant elimination; organic micro-pollutants can be

degraded by abiotic reactions such as photolysis or hydrolysis. Photolysis occurs when a photon is absorbed by a compound that leads to the chemical bond cleavage. There is a low surface to volume ratio available for sunlight irradiation and high wastewater turbidity, limiting the light penetration in water. Hydrolysis is the result of chemical bond excision by substitution of one or more atoms from organic compound per molecule (or hydroxide ion) in water [24].

- Volatilization:

It occurs significantly on the surface and happens through aeration, the pollutant transfer from water to air depends on the compound volatility (kH and Henry's law), and process operating conditions (aeration, stirring, temperature and atmospheric pressure), it is a limited method because in some cases it can promote atmospheric pollution.

By itself, the treatments described above have proved to be inefficient in the elimination of micropollutants[43]. Consequently, more advanced and effective treatments are necessary to be able to transform ECs into less dangerous compounds or even mineralize them, through simple operational parameters that use low amounts of energy, since in average these advanced treatments increase costs and electricity consumption by 30% representing an annual increase of approximately 20 € per capita [44]. Advanced treatment processes include technologies as refining in final stages, like membrane technologies, powder activated carbon, ozonation and advanced oxidation processes have shown different degrees of efficiency for pharmaceutical wastewater treatment.

- Treatments by conventional processes:

The most commonly used processes are conventional activated sludge (CAS) and membrane biological reactors (MBRs). Their efficiency depends on contaminants characteristics and the treatments themselves, which are implemented during the secondary treatment [45]. CAS depends on nature of the microbial community, physicochemical characteristics of the substances and operational factors such as temperature, hydraulic retention time (HRT) and sludge retention time

(SRT) [46]. MBRs reduce the chemical oxygen demand (COD), being more efficient in the ECs elimination (approximately 60%) [45].

– Membrane technologies:

The elimination in membrane processes can occur through multiple mechanisms. First, the elimination can be regulated by adsorption, where hydrophobic compounds or with strong hydrogen bonding characteristics, are easily adsorbed to the membranes in initial stages of filtration. However, in many cases, removal can occur through steady-state rejection due to steric effects for uncharged solutes or the combined steric and electrostatic effects for charged solutes. This mechanism is a function of the compounds physico-chemical properties to be treated (molecular weight, pKa, polarity and partition coefficient octanol/water (Kow), the solution in which they are dissolved (pH, ionic strength), and own membrane characteristics (material, surface morphology, pore size) [47].

The most common membrane technologies include low pressure systems such as microfiltration (MF) and ultrafiltration (UF) operated at pressures of 5 to 10 bar, respectively, or high-pressure systems known as nanofiltration (NF) operated at 50 bar and reverse osmosis (RO) up to 70 bar [48]. Particularly, high pressure systems have been shown to be more effective in eliminating ECs (some antibiotics with efficiencies higher than 99%), due to the pore size range used of 0.001 and <0.001 mm, for NF and RO, respectively[49]. Nevertheless, there are disadvantages such as high implementation costs, easy plugging leading to electrostatic rejection of many ionic species and concentrated contents production of all retained compounds, constituting a potential problem for ecosystems [47.50].

- Powder active carbon (PAC):

The adsorption treatment with activated carbon is used to eliminate many hydrophobic pharmaceutical products [47]. The removal efficiency of the activated carbon adsorption treatment system depends on the adsorbent properties (specific surface area, porosity, surface polarity and material shape), compound characteristics (shape, size, charge and hydrophobicity) and initial concentrations of effluent (pH, temperature and presence of other species in solution) [51]. Interactions such as Van der Waals forces and π-π bonds are the dominant mechanism for elimination of non-polar antibiotic compounds using PAC (log K_{OW}> 2), the efficiency of this treatment reported reductions around 49-99% after 4 h of contact time with 10 and 20 mg L^{-1} [52].

- Ozonation:

The mechanism of ozonation takes advantage of strong oxidative properties of hydroxyl radicals produced spontaneously from the ozone decomposition at high pH (non-selective for electron-rich organic molecules), with reported effective degradation ozone doses of 3-8 mg L^{-1} were reported [29]. A possible disadvantage is the formation of unknown reactive by-products, caused by partial oxidation of compounds and reaction with matrix components, potentially increasing effluent toxicity because full EC mineralization is not achieved[44].

- Advanced oxidation processes (AOPs):

This treatment is based on the reactive oxidant species production, such as hydroxyl radicals ($OH^{\bullet}$) used in organic pollutants treatment without selectivity. This includes Fenton and photoFenton processes, wet catalytic oxidation with peroxide/air, catalytic ozonation, heterogeneous photocatalysis, electrochemical oxidation or combinations between them. In general terms, they have the disadvantage of generating byproducts that can be more toxic than the starting contaminants, as a result of partial mineralization or frequent presence of scavenging species in wastewater [38]. Different catalysts have been evaluated, with metal oxides of different metals (Ti, Cu, Zn, Mn, Fe, Co y Bi), supported metals (Ru, Pt, Pd, Ir y Rh) or sometimes metal-free carbon materials such as activated carbon, carbon xerogels, carbon nanotubes, carbon foams, carbon fibers and graphite [53].

Among the examples of AOPs, one of the most important is the Fenton process [54], which uses H_2O_2 and a precursor like iron, generating $OH^{\bullet}$ radicals at atmospheric pressure and room temperature, with high efficiency, relatively cheap reagents, and peroxide does not need activation energy. Therefore, it is easy to implement and operate, but generally generates secondary waste (sludge) and has a limited operating pH range (2.5 to 3). Fenton process variations, consist of photo-Fenton assisted with UV light, which contributes to a faster Fe^{2+} production, [55] and electro-Fenton where Fe^{2+} is produced from sacrificial iron anodes [56] or also photoelectro-Fenton [57].

The catalytic wet oxidation combined with peroxide and metals as catalyst (i.e. iron, platinum, titanium and ruthenium) at temperatures around 50-70 ºC, generates heterogeneous photocatalysis. This type of catalysis is produced by electrons and gaps (and subsequent chains of reactions including $OH^{\bullet}$), when it is irradiated with photons of higher energy than the semiconductor band-gap (i.e., $h\nu > EG$) [58]. Finally, sonolysis performs oxidation with supercritical water, through radiation, γ-rays, microwaves and light rays with electron beats [59].

Therefore, these technologies are promising solutions and would be a great opportunity to expand knowledge in this area of research, contributing to the development of materials and efficient processes that can be applied under conditions of ambient temperature and pressure, making technology a viable alternative for wastewater and surface water treatment.

1.2.1 Contamination by pharmaceutical compounds

The contamination caused by pharmaceutical residues is mainly due to two sources: medicines thrown away in trash or toilet and medicines that, being not fully assimilated by the body (in humans and animals), are excreted by individuals through urine and feces [60].

The problem of emerging pollutants can be analyzed from different points of view: poor regulation by ignorance of the effects of this type of pollutants, the lack of an "inventory" of all chemical species present in the environment, low predictability of the health effects on humans and aquatic organisms (for lack of incidence information, risk concentration and ecotoxicology) [61] and inefficiency of conventional methods used in wastewater treatment plants (WWTP). All of the above generates the necessity to increase knowledge regarding origin, transformation and effects of this new generation of pollutants so that quality of water is guaranteed for human beings and aquatic organisms [62], as well as the development of effective methods to treat pollutants [63].

Within the reported chronic effects of pharmaceutical contaminants, it has been found estrogenic (substance with effects like natural estrogens), genotoxic (harmful to DNA), cancerogenic (produces cancer) and teratogenic (increases risk of malformations in fetus), as well as antibiotic resistance. For example, Bisphenol A has an estrogenic effect [64], increasing the probability of breast cancer in women and in men acts as antiandrogen causing feminizing effects [64,65]; Diclofenac affects gill and kidney tissues in freshwater fish [66]; Penicillin, sulfonamides and tetracyclines cause resistance in bacterial pathogens [64].

In addition, several studies reported for some pharmaceutical analytes the chemical characteristics (functional group and chemical structure), types of use (industrial or consumption), effect types, action mechanisms, source and exposure route [62]. In general, medicines and abuse drugs as emerging contaminants are a problem that has been affecting humanity for years. Still, these have not been studied yet in depth, and novel techniques are needed to detect them in water bodies, but also techniques for their elimination because the current water treatment systems in various countries do not even consider these substances as pollutants [67,68].

The wastewater from a hospital is a complex mixture capable of generating serious environmental problems, which can be 5 to 15 times more toxic than domestic wastewater [69,70], due to the presence of toxic chemical compounds, drug residues, multiresistant pathogens to antibiotics, radioactive elements and radioisotopes, heavy metals and organo-halogen compounds. And generally, these compounds are disposed without proper treatments in the public sewage network, affecting water quality and endangering human health at risk.

Likewise, in the industrial sector (Figure 1.4) water supply is a critical raw material in manufacturing operations, requiring high volumes of water for production, processing, and cooling, implying a great cost to the companies and generating the need for alternatives to measure and optimize the use of this resource. Product purification and equipment cleaning are among the industrial operations with the highest impact on water quality, being responsible for 10 to 20% of the contaminated water produced[68]. In addition, pharmaceutical residues can also be generated in urban sewer systems through human excretion (urine and feces) by inadequate disposal [71,72].

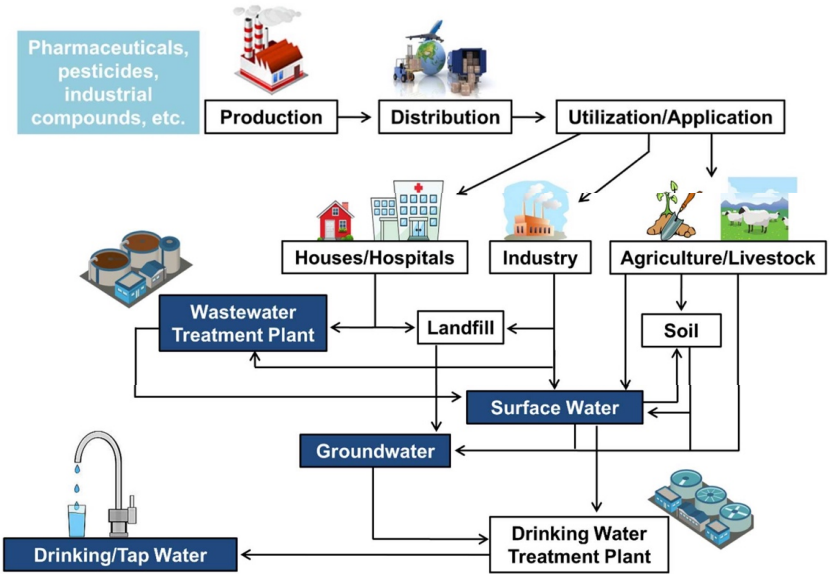


Figure 1.4. Representative sources and routes of micropollutants in the environment [38].

Once in the environment, the decomposition reactions are carried out by "inert agents of the environment" (water, oxygen or light), during periods of months or years. The most important types of degradation by pharmaceutical compounds in the environment are hydrolysis, oxidation, and photolysis. Emerging pollutants in wastewater are not efficiently treated in WWTPs, because these were not designed to treat this kind of substances [73].

1.2.2 Contamination by heavy metals

Heavy metal (HMs), design as a metal with a density greater than 5 g cm^{-3} [74], they have become an important environmental problem since they generate acute toxicity in humans and aquatic organisms, through the food chain [75]. There are two sources of heavy metals in liquid effluents:

- Geological Sources:
  Present in nature in water tanks, the atmosphere, or the soil. As a consequence of rocks interaction (igneous, sedimentary and metamorphic) with the environment (weathering, erosion, soil formation, and rock cycle), transport occurs and generates an HMs redistribution [76]. Mainly influenced by easily leached metals such as nickel (Ni), cobalt (Co), manganese (Mn), zinc (Zn), copper (Cu) and vanadium (V), metals with intermediate instability such as scandium (Sc), yttrium (Y), uranium (U) and hafnium (Hf) have also been found [76]. Furthermore, biological, chemical, and physical factors such as living organisms, sediment adsorption, organic and inorganic matter, dilution and evaporation, redox potential, pH, and temperature promote the HMs presence. Many HMs are essential for biological systems such as (Cu and Zn) when the maximum tolerable intake is exceeded, the toxicity occurs.
- Anthropogenic sources:
  For humanity, the main source of drinking water supply is groundwater, which is contaminated with organic and inorganic compounds resulting from agricultural, industrial, mining, urban areas, landfills, sewage systems, and railways [76]. These types of emissions are the greatest concern today, because there is no modern legislation regarding these pollutants, specifically for mining that produces high traces of HMs such as: As, Cu, Cd, Pb, Hg.

1.3 Development of new materials

In nature, there are unique structures at the nanometric to millimeter size, in which each level of size has a function, benefiting the complete performance of the material bone and mother-of-pearl are examples of these structures. Understanding the function and composition of these materials has been one of the motivations to carry out studies that imitate their behavior [77]. Recent technological advances generate high demand for new materials, because metals, ceramics or plastics do not satisfy current needs, evidenced by the increase in number of publications and patent applications. Each year new materials are synthesized; scientific visions and new

applications are created. To unify the concept of hybrid material, IUPAC defined: “Material composed of an intimate mixture of inorganic components, organic components, or both types of component”. Note: The components usually interpenetrate on a scale less than 1 μm [77]. There are different combinations of composition and structure that can be obtained from hybrid materials (Table 1.2).

Table 1.2. Possibilities of structure and composition of hybrid materials. [77]

Hybrid material component	Possible forms present
Matrix	Crystalline ↔ Amorphous, Organic ↔ inorganic
Building blocks	Molecules ↔ macromolecules ↔ particles ↔ fibers

In most materials the inorganic part corresponds to elements incorporated into matrix in the form of particles, whiskers, fibers, lamellae, or meshes, whose function is to provide greater resistance to the material. The organic part is responsible for joining the inorganic building blocks and the matrix; it is generally synthesized at room temperature, neutral pH and aqueous environments.

Hybrid materials can be classified into two types depending on the existing interactions: i) Class I, show weak interactions (Van Der Waals forces, hydrogen bonds or weak electrostatic interactions) between two components present, ii) Class II, show strong chemical interactions (coordination, ionic and covalent bonds) between components. Depending on functional characteristics, the binding properties may vary; therefore, another classification type of hybrid materials is distinguished: i) Network modifier: organic rest that contains a functional group, which allows the union to an inorganic network, without producing additional chemical reactions to the formed material, ii) Network builder: two or three anchor groups modify an organic segment, leading to materials in which the inorganic group is an integral part of the hybrid network, iii) Network functionalizer: incorporation of a reactive functional group. According to the relationship between structural hybridization, chemical interactions and functionality, Makishima[78] established that materials with the characteristics shown in Figure 1.5 could be obtained.

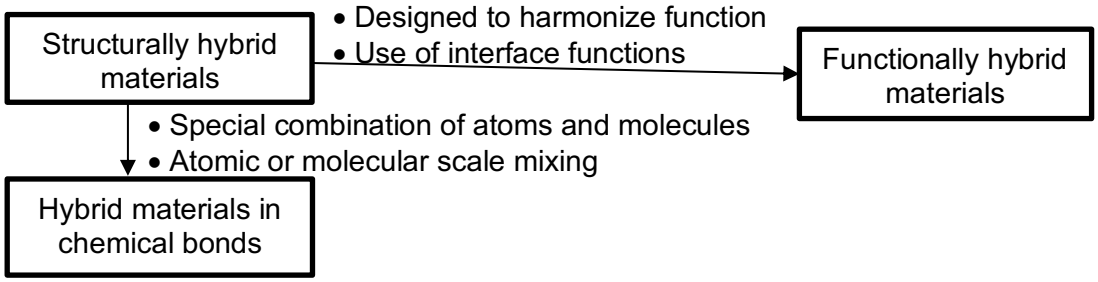


Figure 1.5. Relationship between hybrid materials structure, functionally and chemical bonds.

Consequently, the field of hybrid materials offers the opportunity to invent an almost unlimited set of new materials with a broad spectrum of known and yet unknown properties, being able to develop multifunctional materials with promising applications in various areas (Table 1.3).

Table 1.3. Classification of hybrid materials applications. [79]

Application	Discovered and improved properties
Singular functions	Mass, strength, conductivity, corrosion resistance, etc.
Secondary functions	Thermoelectric, specific strength, heat capacity, etc.
Sensors	Changes in properties corresponding to input signals
Chemical reaction functions	Catalysis, selective permeation, etc.
Intelligent	Self-regeneration, shape memory, memory function, etc.
Environment	Environmental impacts, recycling performance, etc.
Oriented to bio / humans	Toxicity, bioactivity, color, tactile impression, etc.
Specific applications	Cutting, performance of cutting tools

The goal is to combine properties of the organic and inorganic components in a single material (Table 1.4), facilitating its processing, respecting the environment, and consuming less energy with features such as recyclability and reliability.

Table 1.4. Constitutive elements properties of hybrid materials. [79]

Properties	Organic (polymers)	Inorganic (transition metal oxides TMO)
Links nature	Covalent [C-C], Van der Waals, hydrogen bonds	Ionic or covalent [M-O]
Glass transition temperature	Low (−120 °C to 200 °C)	High (>> 200 °C)
Thermal stability	Low (<350 °C–450 °C)	High (>> 100 °C)
Density	0.9-0.12	2-4
Refractive index	1.2-1.6	1.15-2.7
Mechanical properties	Elasticity, plasticity	Hardness, strength, fragility
Hydrophobicity	Hydrophobic	Hydrophilic
Permeability	Hydrophobic ± gas permeable	Low gas permeability
Electronic properties	Conductivity insulation, redox properties	Semiconductor insulator (SiO_2, TMO), redox properties (TMO), magnetic properties
Processability	High (molding, casting, film forming, viscosity control)	Low for powders, high for sol-gel coatings

The transition from macroscopic to microscopic world, nanoscopic and molecular objects leads to changes in the material physical properties, i.e, the so-called quantum-sized effects (i.e. surface area) become important on the surface when objects exist in a very small size, i.e. in nanoparticles (<10 nm) in which almost all the surface atoms can interact with the environment. Therefore, the interacting nature is important, as well as, depending on the intensity of the interaction between the parts, the system will separate thermodynamically and stabilize kinetically through network formation reactions [79].

1.3.1 Methods of synthesis in hybrid materials

Two different approaches can be used for the formation of hybrid materials [77]:

- Approximation by building blocks:

Well-defined preformed building blocks are applied which react with each other to form the final hybrid material in which the precursors at least partially retain their original properties. In general, it does not suffer significant structural changes during the process of matrix formation, and better structural predictions are possible.

- In-situ formation of the components:

Chemical transformation of precursors (simple and commercially available molecules) are used in the materials preparation to multidimensional structures, which show properties totally different from original precursors. The material final internal structure is determined by the composition of these precursors and reaction conditions (change a parameter can often lead to two very different materials).

Nowadays we could say that we are living in the era of biomaterials, which are an example of hybrid materials. They explore the combination of organic compounds such as biomass and nanometer-scale composites as metal organic frameworks (MOFs), and have shown to have interesting applications, each one separately, in water remediation, adsorption processes, sensors, reinforcement of building materials, among others. However, there are few reported investigations found in literature that have explored this combination of materials.

1.4 Biomass

Biomass is considered a renewable source of energy, chemicals and materials, which has become a solution to the oil crisis, rising prices in fuels, climate change, conflict with land and alternative to new materials. It comes from the biodegradable fraction of products, waste and residues of biological origin resulting from agricultural activities (including substances of plants and animal origin), forestry and related industries, as well as the degradable biological fraction of industrial and municipal waste [80]. Biomass is a set of renewable organic matter, accumulated in different organic compounds (polysaccharides, fats, others) along the trophic chain, resulting from the transformation process of solar energy into chemical energy through the photosynthesis process in plants [81].

Figure 1.6. shows the biomass classification according to its composition, origin and state. Particularly, plant biomass is of great interest because it is a suitable raw material in hybrid materials synthesis given the possibility of taking advantage of reactive chemical groups present in cellulose polysaccharides, lignin and hemicellulose. It has been the basis of many applications and derivatives have been given an added value, i.e. liquid and gaseous fuels, construction materials, food, composites and chemical products.

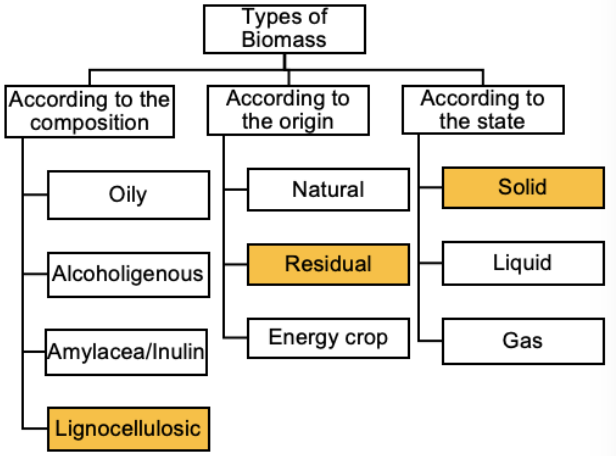


Figure 1.6. Biomass classification [82].

1.4.1 Lignocellulosic biomass

Lignocellulosic biomass is the most abundant organic material on earth, its sources are forests, agricultural crops, agricultural residues and industries such as paper. This biomass is constituted fundamentally by cellulose, hemicellulose, lignin, extractives (mixture of different organic compounds) and inorganic components. It has the advantage of being biodegradable and renewable, while contributes to the CO_2 reduction emissions, avoiding erosion and soil degradation; in addition, it is an alternative to the waste use, mainly in the agricultural sector. Despite the great variety and quantity of lignocellulosic biomass, not all can be used efficiently (Table 1.5), due to its availability, concentration and other factors.

Table 1.5. Sources of lignocellulosic biomass [82].

Forest industries	• Forest residues: Stumps, crowns, branches, foliage, barks • Industrial waste: Sawdust, edges, defects, cuts
Cellulose, paper and boards industry	• Pulps: Chemical, mechanical, chemi-mechanical, semi-chemical, diluent and adsorbent. • Boards: Fiber, particles, pressed, MDF • Cartons and moldings: Corrugated boxes, cardboards, multilayer cardboard, coated cartons, cellulose moldings

Table 1.5. Sources of lignocellulosic biomass [82]. (Cont.)

Cellulose, paper and boards industry	• Printing papers and industrial cartons • Residual liquors from pulping and papermaking: Black liquors and pulp effluents, reject fibers, wastepaper.
Urban sector	• Local solid waste: Boxes, wooden containers, paper and cardboard containers, papers, books, prints, office wastepaper, disposable paper, wooden furniture, food packaging, waste wood instruments. • Debris: Wooden constructions, trees
Derivatives of agricultural productions and food	• Non-timber crops and natural fibers: Cotton, bamboo, Henequen, Kenaf, Flax, Crotolaria, abaca, esparto grass, hemp, miscanthus, energetic cane. • Agricultural residues from crops: Straw and bagasse from sugarcane, coffee pulp, waste from fruit production, straw from cereal crops, waste from wine production, oils and other products.

1.4.1.1 Structure of the cell wall:

The cell walls of plants have layers, which in turn have a complex structure. The vegetal material consists of structural support elements or fibers, vascular elements for the liquid's conduction, such as vessels present in hardwoods, storage cells and specialized cells. Next, the structure of the cell wall will be addressed in more detail [83], which constitutes the lignocellulosic biomass (Figure 1.7).

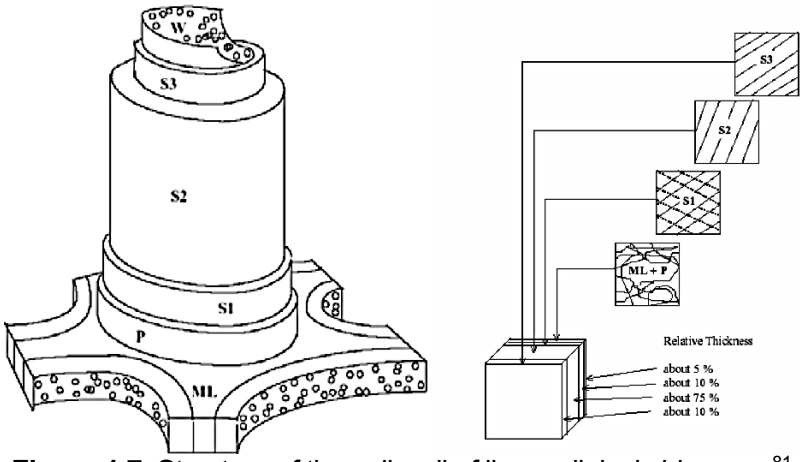


Figure 1.7. Structure of the cell wall of lignocellulosic biomass [81].

1.4.1.2 Chemical structure

The main chemical components present in the lignocellulosic biomass are cellulose, hemicellulose, and lignin, which are high molecular weight organic polymers that constitute more than 75% of the vegetal material; in addition, there are in percentages of less than 10% extractive

and inorganic compounds[84]. Table 1.6. compiles the chemical structure of different lignocellulosic materials.

Table 1.6. Chemical composition of selected lignocellulosic biomass materials [81].

Component (%)	Conifers	Hardwoods	Bagasse cane	Wheatstraw	Rice straw	Cotton	Conifers
Cellulose	40–45	40–45	43–47	38–42	34–36	95–99	40–45
Hemicelluloses	20–27	23–33	28–32	28–32	24–30	——	20–27
Lignin	25–30	18–23	20–22	19–23	22–23	——	25–30
Extractive	4	1.5–2.0	2.5–3.0	3–5	2–3	1–5	4
Ashes	2–4	1.5–3.5	1.5–2.5	4–6	17–19	——	2–4

Figure 1.8. displays the chemical structure of the main compounds that constitute the lignocellulosic biomass, which will be described in more detail below. described in more detail below.

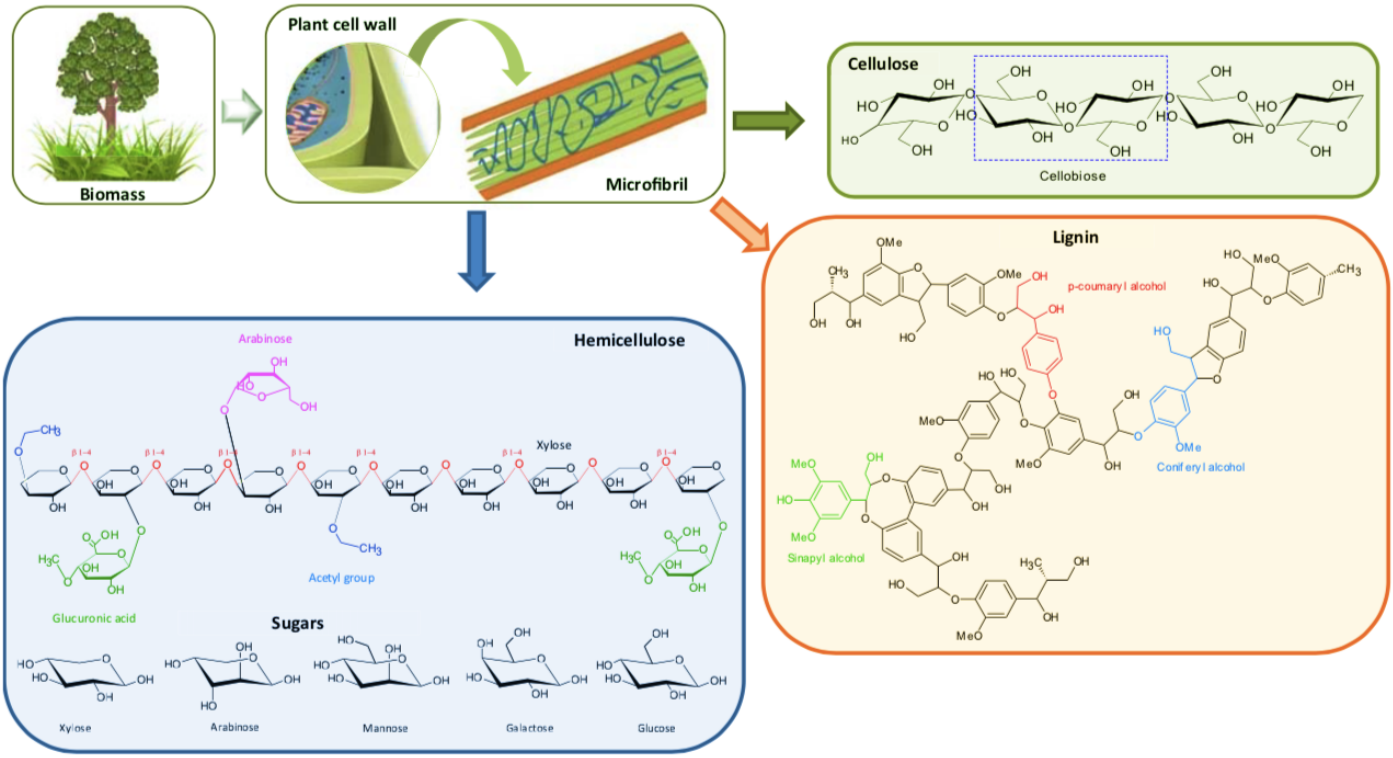


Figure 1.8. Structure and main components of lignocellulosic biomass [84]

The principal characteristics of the lignocellulosic biomass are:

- Cellulose:

Linear chain polymer, formed by D-glucopyranose anhydride units linked by β-1,4-glycosidic bonds, the cellobiose is the repeating unit of the cellulose chains. It has a polymerization degree

that varies depending on its origin, from 1000 to 5000 in the primary wall, 6000 in the secondary wall (S1 and S3) and from 13000 to 14000 in the S2 layer, reaching lengths of up to 6-7 μm and molecular weight of 2000000 [84].

It is a macromolecule with great reactivity in its functional groups, mainly the hydroxyl groups that protrude laterally from this flat ribbon are able to form inter and intramolecular interactions responsible for the mechanical resistance (Figure 1.8). Along with the crystallites size and fibrils, their orientation degree and arrangement determine an imperfect crystalline structure, consequently, to crystalline alternation and amorphous zones within microfibrils. Properly, in the zone S2 there is a higher polymerization degree, so cellulose is more ordered and has a higher crystallinity degree (approximately 66% of cellulose). However, the cellulose crystallinity makes it insoluble in water, despite the high content of OH groups, affecting the pretreatment processes.

The cellulose molecules form fibrillar aggregations of molecules stabilized laterally through hydrogen bonds between hydroxyl groups of adjacent molecules. The microfibrils characteristics vary between species and development stages. These are added in larger fibers reaching thicknesses of 1 nm to 20 nm, confirming the existence of successive protective barriers that hinder the chemical attack and biological agents. Cellulose presents different characteristics depending on the size of microfibrils aggregation, which are described in Table 1.7.

Table 1.7. Cellulose characteristics at different structural levels.

Molecular level	Chemical constitution, steric conformation, molecular weight, molecular weight distribution, intramolecular interactions, presence of functional groups.
Supramolecular level	Chains aggregation of molecules in elementary crystals and fibrils, order degree inside and outside those fibrils, orientation respect to fibrillar axis.
Morphological level	Spatial disposition of crystalline units in the cross-fiber section, existence of layers in the cell wall, presence of interfibrillar interstices or voids.

- Lignin:

The most important amorphous heterogeneous polymer in the cell wall varies in the proportion of its constituent monomers and the type of link between them (depending on the plant, it gives resistance), it serves as a glue to the cell wall and limits the attack of chemicals and microbes [81]. It has a three-dimensional structure, constituted by the monomeric basic unit's association of phenylpropane, linked by carbon-carbon (C-C) and ether (C-O-C) bonds, which alternate in a disorderly manner. The three constituent monomeric units of lignin are three cinnamyl alcohols (Figure 1.8): p-coumaryl (without methoxyls), coniferyl (a methoxylic group), and sinapilic (two

methoxyl groups), generally referred as hydroxyphenyl (H), guayacil (G) and syringyl (S) units [81]; lignin has been reported to have a polymerization degree between 50 and 80. The lignin macromolecule contains few free phenolic hydroxyl groups, as most of them participate in ether bonds between monomeric units, fundamentally with the central carbon of the propyl side chain, which makes it resistant to hydrolytic action. However, it can dissolve when subjected to cold alkali treatments. To achieve the delignification of any lignocellulosic material, the ether bonds must be broken by treatments with oxidizing agents or treatments with chemical agents at high temperatures [85].

- Hemicellulose:

Hemicellulose is a non-cellulose structural polysaccharide with low molecular weight, present in cell walls. It has low polymerization degrees (<200), with small branches that depend on the species. There are two types of hemicelluloses: xylan (contain xylose) and mannose (contain glucomannan) [81]. In plants, xylan is more common (Figure 1.8), which is constituted by a skeleton of xylose units linked by glycosidic bonds β-1,4-xylan, and it has three configurations that are the most found (Table 1.8).

Table 1.8. Configurations of xylan.

Glucurono-Arabinoxylans	They are frequently found in monocots (straws), have L-arabinofuranosyl units linked by bonds (1-3) -glycosidic and glucuronic acid, present in general as 4-O-methyl glucuronic ether linked by (α-1,2) glycosidic bonds between uronic acid and carbon 2 of the principal xylose chain, this bond is the most resistant to acid hydrolysis. Another important substitution group is acetyl; there are 7 acetyl groups every ten xylose units, linked by an ester bond of the positions 2 and 3 from the pentose ring [86].
Glucuronoxylans	Present in hardwoods, they have a similar structure to glucuronoarabinoxylans, with the difference that arabinofuranosyl units are absent [86].
Glucomannan	Linear polymer of glucopyranosyl and mannopyranosyl linked by β-1,4 bonds, it does not present ramifications, reports two types of mannose substituents: acetyl and galactose. In addition, it has a polymerization degree close to 100, the glucose:mannose ratio is 1:2 and the order is completely random, without a repetition pattern in the skeleton, principal component of softwoods [86].

- Extractives:

Organic compounds with low molecular weight, which can be extracted using organic solvents, include resins, terpenes, lignans, aromatics, fats, waxes, fatty acids, alcohols, serpentines, tannins, and flavonoids. They are found mainly in the resinous channels, parenchymal cells, middle lamella, and cell wall of the tracheid, comprise 4 to 10% of the total weight [81].

1.4.2 Biomass pretreatments

Pretreatment is an essential step in the global conversion of lignocellulosic biomass to value-added products (Figure 1.9); its main objective is to make cellulose more accessible with high yields. However, pretreatment remains one of the most expensive steps in the general process of lignocellulosic biomass conversion. To be effective and economical it must meet the following requirements: (1) deconstruct the three-dimensional structure of lignocellulosic biomass, modifying its polymerization degree and decreasing the cellulose crystallinity, (2) increase material surface area and porosity, (3) generate highly digestible solids and promote high sugar yields after hydrolysis, (4) avoid the formation of inhibitory compounds (especially acetic acid of hemicellulose, furfural and hydroxymethylfurfural from sugar degradation, and phenolic compounds of lignin degradation), (5) allow the recovery of hemicellulose and lignin for later use in valuable co-products production, (6) low demand for post-treatment operations such as washing and neutralization, and (7) minimum use of energy, chemical products, water inputs, simple reactors, reasonable size and low cost [87,88].

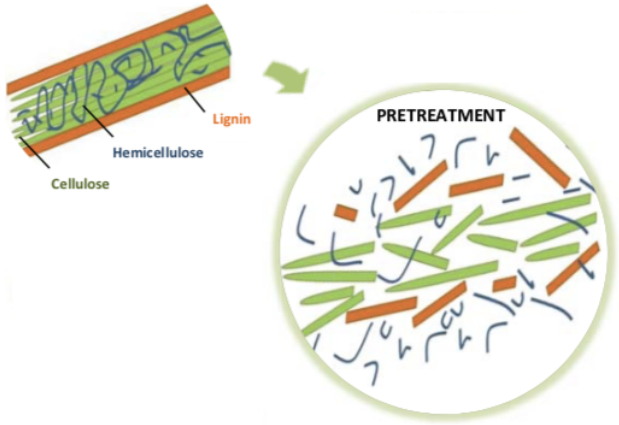


Figure 1.9. Schematic representation of the effect of pretreatment on the lignocellulosic biomass structure. Modified [84]

Many processes have been proposed for the biomass pretreatment, which can be classified into four categories: physical, chemical, physicochemical and biological. In general, combinations of some of these methods are necessary to improve the results since each pretreatment has a different impact on the biomass structure and are not equally effective for all raw materials [89].

Physical pretreatments are intended to reduce the cellulose crystallinity and increase the biomass surface area, while chemical pretreatments usually focus on the lignin removal and crystalline cellulose swelling. Although many technologies for biomass pretreatment have already been

proposed, the choice of the best technology is not an easy task and depends very much on the pretreatment objective (desired products), type of biomass used, and its composition. For the development of an efficient, economically viable and sustainable pretreatment technology is necessary to understand the biomass structure, select the most suitable method for the target components and operate in optimal conditions (Table 1.9). Below there is a complete description of the most important pretreatments.

Table 1.9. Performance pretreatment summary.

Pretreatment	Increases Surface area	Cellulose decrystallization	Hemicellulose removal	Lignin removal	Furfural formation
Liquid hot water	XX		XX		XX
Acid	XX		XX	X	XX
Alkaline	XX		X	XX	XX
Organosolv			X	XX	
Wet oxidation		XX	X	XX	
Steam explosion	XX	XX	XX		X
Ammonia explosion	XX	XX	X	XX	XX
CO_2 explosion	XX		XX		
Mechanical			X	XX	
Biological			XX	XX	
Oxidative (H_2O_2)	XX		X	XX	X

1.4.2.1 Physical pretreatments

- Mechanics:

Efficient method to alter the physicochemical properties of solid phases, includes shock, cutting, pressure, mixing, compression / expansion and other types of mechanical action applied to a solid body. When is applied to a solid body, it produces relaxation of plants cell wall channels creating new available surface, crystal defects, changes in the supramolecular structure, and breaking of Van der Waals forces and covalent bonds. These processes increase the free energy and reactivity of the solid, [90]. In this pretreatment vibratory ball mills are used, which deliver solids with a final size of 0.2-2 mm, likewise mills of blades or hammer are used to obtain a final solid size of 3-6 mm. This type of treatment decreases the crystallinity index and polymerization degree of the cellulose and increases the contact surface [91].

- Pyrolysis:

Process controlled using temperatures above 300 °C and inert atmosphere to convert solids into coke and volatiles with limited amount of water. The lignocellulosic biomass functional groups are thermally degraded into compounds of lower molecular weight (CO, CO_2, CH_4, H_2, among

others), these gases are produced through primary, secondary and even tertiary reactions between reactive intermediates (free radicals), converting this pretreatment into a complex chemical process, numerous simultaneous reactions occur during the thermal treatment. Pyrolysis processes require an elaborate strategy to control the performance and quality of end products [92].

- Microwave:

Hydrothermal fractionation process is carried out at high temperature (around 300 °C), where the pressurized water (also called subcritical and supercritical water) shows physicochemical properties significantly different from water under environmental conditions. The water dielectric constant decreases with increasing temperature and provides greater solubility of low polarity compounds in water [93]. The highly humid biomass is compatible with the hydrothermal treatment because it avoids drying processes that consume a lot of energy, this pretreatment requires controlling variables as: interaction between microwave and irradiated materials, specific dielectric properties of each substrate and microwave frequency.

- Ultrasound:

The biomass treatment with ultrasound is based on the cavitation principle, which is described as the spontaneous formation, growth and subsequent collapse of microscopic cavities/bubbles caused by ultrasonic waves propagation in a liquid medium, usually operating under ambient conditions. The implosion of these cavities produces high temperatures in periods of microseconds, creating an effect of hot spots in the liquid phase [94]. Significantly high energy densities, shock waves and shear in the vicinity of a collapsed cavity can cause substantial alterations in surface morphology, increasing the specific surface area and decreasing the polymerization degree, resulting in a greater degree of pretreatment [95].

- Pulsed electric energy (PEE):

PEE involves a non-thermal pulse treatment of very short duration (from nanoseconds to several milliseconds) and high pulse amplitude ($0.5e^{50}$ kV/cm). There are different techniques such as pulsed electric fields (PEF) and high voltage electric discharges (HVED), which is mainly related to the loss of membrane barrier functions [96].

1.4.2.2 Chemical pretreatments

- Acid:

It uses dilute or concentrated acid solutions to break the rigid structure of lignocellulosic materials. The acid acts as a catalyst, it attacks intermolecular and intramolecular bonds between hemicellulose, cellulose, and lignin, hydrolyzing carbohydrates present in the material structure, especially hemicellulose. This pretreatment is affected by factors, such as acid type and its concentration, solid charge (also called solid/liquid ratio), temperature and reaction time [97].

- Metallic salts:

The pretreatment uses metallic salts as catalysts for lignocellulosic biomass transformation processes. The metallic salt role in biomass transformation is related to its character of Lewis acid (its ability to attract pairs of electrons) [98]. Therefore, the metal cations act like Lewis acids and break glycosidic bonds of the hemicellulose chains [99]. There is little information on the action mechanisms of metal salts in reactions involved in these biomass transformation processes, since factors such as high temperatures, pH and initial concentration of metal have been reported to limit the pretreatment [100].

- Organosolv:

This process uses organic solvents mixture such as methanol, ethanol, acetone, ethylene glycol, triethylene glycol or phenols. It is usually mixed with a small amount of inorganic acid (sulfuric acid or hydrochloric acid) as a catalyst, breaks the internal bonds of lignin and hemicellulose, solubilizing them almost totally [101]. Bases such as sodium hydroxide are also added to the process when it is carried out at temperatures in the range of 100-250 °C [102]. However, it has as main disadvantage the significant losses of the organic solvent, which leads to greater energy and economic investments. In addition, organosolv pretreatments must be carried out under extremely strict and efficient controls due to the organic solvents' volatility. Therefore, the organosolv pretreatment is too expensive to be used at present for biomass pretreatment [103].

- Ionic liquids (IL´s):

It makes use of liquid substances formed exclusively by ions, an example of which are salts such as sodium chloride, which at room temperature is solid, but if it is heated above its melting point (800 °C), melts and becomes a liquid that maintains the ionic character [104]. These ionic liquids are constituted by a cation and an anion, so the properties of conductivity, vapor tension and

thermal stability, are based on the nature of the elements that make them, eliminating mainly lignin by means of the hydro tops solvation process [105].

- Ozonolysis:

Ozone can be used as a method of biomass pretreatment because it has the property of splitting double and triple carbon-carbon bonds [106], due to its oxidation potential (2.07 eV) and electrophilic nature, promotes the reaction of molecular sites with high electron density, as aromatic compounds (hydroxyl or amine groups). The reaction stability is influenced by temperature, pressure, pH and ionic strength of the aqueous solution.

- Alkaline:

In general, this pretreatment is carried out at low temperature and pressure (including environmental conditions), with reaction times in the order of hours or days, particularly, temperature is an important factor that influences performance, since it reduces the reaction time. Pretreatment with alkalis such as sodium hydroxide, potassium hydroxide, calcium hydroxide, hydrazine and anhydrous ammonia, causes swelling, modifies biomass chemical composition and multiscale structure, increasing internal surface area and decreasing the polymerization degree and cellulose crystallinity. The reaction mechanism is based on ester bonds saponification that crosses xylans in hemicellulose and other components such as lignin and cellulose [107].

- Alkaline hydrogen peroxide (AHP):

The treatment with hydrogen peroxide requires an alkaline pH to produce oxidizing radicals necessary to degrade carbonyl and ethylene groups of lignin. In an alkaline pH, powerful hydroxyl (OH) radicals are formed [108], that contribute to the lignin disruption, partial solubilization of hemicellulose and decrease in the cellulose crystallinity. Simultaneously, a part of the hemicellulose can also dissolve as a result of the hydrogen peroxide action [109]. The efficiency of this method depends on the process parameters such as: pH of the reaction mixture (10.5 - 12), temperature (50-70 °C), concentration of hydrogen peroxide (0.4-3%) and reaction time (from minutes to hours), which must be optimized for each type of lignocellulosic raw material [110].

1.4.2.3 Physicochemical pretreatments

- Liquid hot water (LHW or autohydrolysis):

These processes use compressed hot water (pressure above the saturation point) and operating

temperatures between 150 and 230 °C [111], allowing the water hydrolysis through reactions catalyzed by hydronium ions generated *in situ* by autoionization of water and acetic acid resulting in the hemicelluloses depolymerization. Subsequently, hydration of the acetyl groups leads to hydrolyzate acidification and, therefore, the formation of hydrogen ions [112]. This pretreatment is affected by variables such as reaction time, solids concentration, particle size, temperature and pH, which allow a solubilization of hemicelluloses in a large extent and a small lignin portion, together with structural changes in cellulose. In addition, changes in the polymerization degree, crystallinity and molecular mass also give modifications in the oligomers thermal behavior [113].

- Steam explosion process (SE):

In this pretreatment the biomass is brought into contact with saturated water vapor at temperatures ranging between 160 and 260 °C for periods of seconds or several minutes. Later the steam is released suddenly through a relief valve that causes the steam absorbed by lignocellulosic material to expand trying to equalize the surroundings pressure [114]. During the process at such pressures, a reaction of autohydrolysis occurs because organic acids generated from the acetyl groups of the hemicelluloses produce the glycosidic bonds cleavage and the subsequent hemicellulose solubilization. When the pressure is instantly relieved, moisture condensed within the lignocellulosic fibers evaporates again, causing mechanical disruption of the lignocellulosic matrix, resulting in the hemicellulose elimination and part of lignin [115]. Besides the reactions, this pretreatment has mechanical, thermal and chemical effects; the expansion generates forces that disaggregate and break the fibers, such effect depends on the particle size, temperature, humidity and residence time [116].

- Wet explosion pretreatment (WEx):

Processes at temperatures of 140-210 °C and pressures of 0-3.5 MPa using oxidizing agents such as gaseous oxygen, air or hydrogen peroxide as purge in the reactor (increasing the decomposition of lignin and hemicellulose and small amounts of cellulose), for a period of time (5-120 min). The reaction ends by opening a discharge valve to an expansion tank, initiating a sudden decompression of the pretreated material. The severity of WEx can be adjusted by three parameters: temperature, residence time and amount of oxygen added to the reactor. As an oxidizing agent, oxygen/air is preferred because of its low process operating cost and it does not require any additional steps such as detoxification, neutralization or recovery of the chemical used in comparison with other inorganic products [117].

- Pretreatment with CO_2:

It consists of the reaction between CO_2 and H_2O at high pressures (above 20 MPa) and temperatures (above 160 °C). The pressure and temperature can be adjusted to give a high diffusion coefficient, solvation power, diffusivity, selectivity and easy recovery. Carbon dioxide, due to its properties, is able to penetrate the lignocellulosic material structure, decreasing its crystallinity by altering connections between cellulose and hemicellulose, eliminating lignin [118].

- Pretreatment using ammonia:

The application of ammonia as a catalyst in alkaline pretreatment of lignocellulosic biomass has also been proven [119]. The ammonia treatment results from impregnating biomass with ammonia and is subjected to high pressures (2.7 MPa) but at temperatures close to 65 °C and short times, producing the cleavage between phenolic lignin side chains and hemicellulose that allow the elimination of lignin and partially hemicellulose [120]. Different technologies have been developed for pretreatment processes with ammonia, such as soaking in aqueous ammonia (SAA), ammonia filtration (ARP) and fiber explosion/ freezing of ammonia (AFEX) [121]. The treatment conditions can vary, such as ammonia concentration, liquid content, process temperature and pressure.

1.4.2.1 Biological pretreatments

The biological pretreatment, mediated by microorganisms and/or enzymes, is carried out in milder conditions (close to temperature and ambient pressure). Many biological pretreatments take advantage of the ligninolytic enzymatic system: group of oxidoreductases can degrade lignin and improve biomass degradation. This system includes laccases and peroxidases with high redox potential to oxidize the lignin polymer directly, or through the use of low molecular weight organic compounds (mediators), it can diffuse into the pores of the cell wall and attack the lignin structure [122]. Biological pretreatment can be carried out with microorganisms that secrete ligninolytic enzymes, or directly with enzymes to degrade part of the lignin and interrupt its structure, allowing access to holocellulose by hydrolytic enzymes [123].

1.5 Biomass functionalization

Natural fibers are considered a potential replacement for plastic fibers. Although natural fibers have the advantages of low cost and density, they also have a strong polar character that creates

an incompatibility with most matrices. Consequently, the surface functionalization has been investigated to take advantage of chemical interactions, as the good layer adhesion to the base substrate depends on electrostatic interactions and ionic bonds [124]. These surface treatments increase production costs but are potentially capable of overcoming the incompatibility problem [125].

Particularly, the chemical treatment aimed to improve adhesion between the fiber surface and polymer matrix cannot only modify the fiber surface, but also the water absorption of composite materials is reduced, and their mechanical properties are enhanced. Extensive research has been carried out in order to achieve a better interfacial union in natural fibers that can be divided into approaches: physical and chemical [126]. However, it should be noted that it is possible for several types of bonds to occur on the same interface at the same time (Figure 1.10) [127].

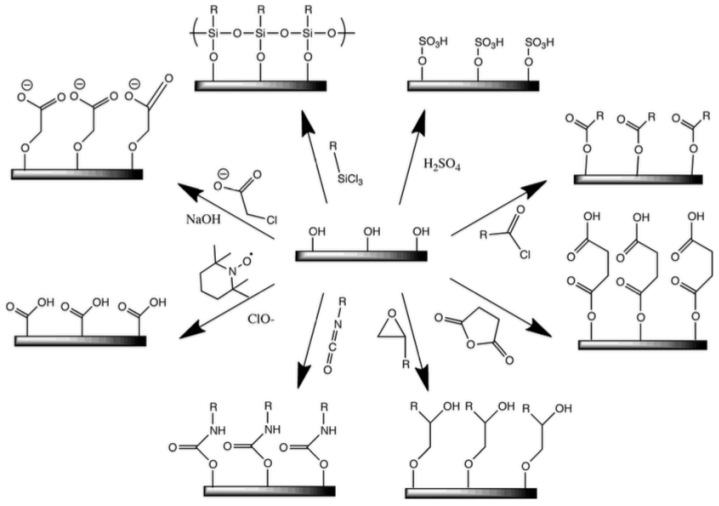


Figure 1.10. Common modification chemistries of lignocellulose biomass [125].

1.5.1 Physical approaches:

Inter-diffusion binding occurs when atoms and molecules of fiber and matrix interact at the interface; functionalization depends on entangled chains length, entanglement degree and the number of chains per area unit [126].

- Corona discharge treatment:

It uses plasma generated by the application of a high voltage to sharp electrodes tips separated by quartz at low temperature and atmospheric pressure. It usually includes the use of oxygen-

containing species, increasing the surface chemical polarity due to a greater amount of carboxyl and hydroxyl groups [128].

- Plasma:

Similar to corona discharge treatment, but is done using a vacuum chamber with gas supplied continuously to maintain the proper gas concentration and pressure [128]. It causes hydrophobicity on fiber surfaces, increases surface roughness and interfacial adhesion [129].

- Thermal treatment:

It involves heating the fibers at temperatures close to fiber degradation, affecting the mechanical properties of fibers, water content, chemical properties, cellulose crystallinity, polymerization degree and physical strength. Similar to corona and plasma treatment, the effect of heat treatment is based on time, temperature and composition of gases involved during the treatment [128].

- Electron radiation:

Improves interfacial bonding with natural fibers and polymers due to the production of free radicals that promote crosslinking between fiber and matrix [130].

1.5.2 Chemical approaches:

Chemical bonds occur when there are functional groups on the fiber surface and the matrix reacts to form bonds. These are propitiated by the use of a coupling agent that acts as a bridge between the fiber and matrix [126]. Generally, chemical coupling agents are molecules with two functions: i) react with the hydroxyl groups of cellulose and ii) react with functional groups of the matrix [131].

- Alkaline treatment:

This modification consists in the hydrogen bonds disruption present in the network structure, which increases the surface roughness. The addition of aqueous sodium hydroxide (NaOH) to the natural fiber promotes the ionization of the hydroxyl group to alkoxide [132]. Consequently, the alkaline treatment has a lasting effect on the mechanical behavior of fibers, especially strength and rigidity [133].

- Silane treatment:

Silane coupling agents can reduce the number of cellulose hydroxyl groups at the fiber-matrix

interface. Silane has different functional groups at each end, the interaction at one extreme can occur with the fiber hydrophilic groups, while the other end can interact with hydrophobic groups in the matrix, to form a bridge between them. Initially, this functionalization involves hydrolysis of alkoxy silane groups with water to form silanol groups (Si-OH), which can then react with hydroxyl groups on the fiber surface [134].

- Acetylation of natural fibers:

Acetylation describes an introduction reaction of acetyl functional group (CH_3COO^-) into an organic compound, in natural fibers is a well-known method of esterification that involves the generation of acetic acid (CH_3COOH). The chemical modification with acetic anhydride (CH_3-C(=O)-O-C(=O)-CH_3) replaces the hydroxyl groups of the cell wall with acetyl groups, making the fiber hydrophobic. Improving interfacial bonding, tensile and flexural strength, stiffness, as well as, thermal stability and resistance to fungal attack [135].

- Maleated coupling agents:

Maleic anhydride modifies the fiber surface, improves the bonding properties at the interface, providing better wettability and adhesion [136].

- Permanganate treatment:

Permanganate contains the group MnO_4^-; this treatment forms cellulose radicals through MnO_3^- ions, which being highly reactive are responsible for initiating the polymerization [137]. As a result of permanganate treatment, the hydrophilic tendency of fibers was reduced, and therefore, water absorption decreased.

- Benzoylation treatment:

Transformation in organic synthesis, benzoyl chloride is used for fiber treatment; this includes benzoyl ($C_6H_5C=O$) and decreases the fiber hydrophilic nature [138]. The fiber benzoylation improves the adhesion and thermal stability, and considerably increases the strength and reduces its water absorption.

- Acrylation and acrylonitrile graft:

Reaction initiated by free radicals of the cellulose molecule leads to strong covalent bond formation and therefore improves mechanical properties, as well as water absorption of the composite materials. Acrylonitrile (AN, ($CH_2=CH–C\equiv N$)) is used to modify fibers [139].

- Peroxide treatment:

Peroxide contains the divalent O-O ion, which tends to decompose easily in free radicals of the RO form, then these react with the hydrogen group of matrix and cellulose fibers, reducing the fiber hydrophilic nature [140].

- Isocyanate treatment:

Isocyanate contains the functional group -N=C=O, which is highly susceptible to react with hydroxyl groups of cellulose and lignin, reducing the hydrophilic character of the composite [137].

- Cellulose carboxymethylation (CMC):

CMC is produced by etherification of hydroxyl groups with sodium monochloroacetate in the presence of an aqueous alkali; this method is based on the Williamson ether synthesis method[141]. CMC reduces the crystallinity degree, caused by the breakdown of accessible chains during pretreatment, which results in a substitution of sodium chloroacetate molecules to cellulose polymers [142].

1.6 Fique: example of lignocellulosic biomass

An example of lignocellulosic material is the Fique fiber (with more than 400 species). *Furcraea Andina*, one of the most abundant Fique species in Colombia, used in several industries, has fibrous fleshy leaves, with or without thorns. Fique plants have long roots, flourish once a year and their size can vary according to the species. Since ancient times, this plant is known as the "Wonderland Plant", because of its different uses, including the extraction of drugs, the production of fermented beverages, mops, among others (Figure 1.11)[143].

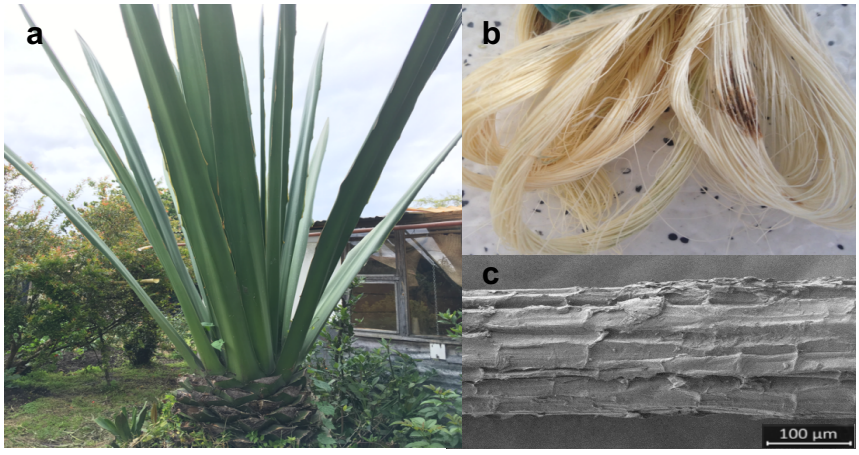


Figure 1.11. a) *Furcraea Andina* plant b) Fique fiber, c) Raw fique fiber micrograph 250X.

In Colombia, fique crops are located mainly in the Andean region, in territories where the climate is temperate. The most relevant departments in terms of fique production are Antioquia, Boyacá, Cauca, Nariño and Santander. In comparison to other types of natural fibers, such as jute and sisal, fique has an intermediate mechanical strength between jute and sisal, making it useful in applications where jute is too weak or sisal is too strong (packaging and textiles) [143].The *Furcraea Andina* plant (Fique), of the *Agavaceae Andina* family (Figure 1.11a), is characterized by an erect stem with an average height of 2 to 7 m and an average width of 10 to 20 cm, the trunk formed by 75 to 100 leaves (from 1 to 3 m long), radially, fleshy, pointed, well toothed and prickly, with greenish-white flowers that only bloom once a year. Fique has a useful life of 10 to 20 years and a production peak of 3 to 6 years [143].

Table 1.10 summarizes the average weight distribution of the fique sheet components, its usable percentage and some of its applications. With the current management practices, most of these byproducts are discomposed in crops or discarded in surface waters, resulting in an environmental contamination problem [144].

Table 1.10. Average distribution of components, percentage used and applications in fique. [145]

Part	Sheets percentage (wt.%)	Percentage used (wt.%)	Uses
Fiber	5	4	Textile industry, packaging
Juice	70	40	Extraction
Tow	8	3	Paper pulp
Bagasse	17	10	Construction materials

Particularly, the fiber is obtained after a cutting process, disheveling and defibering leaves (operation to separate crust from the internal fiber), followed by washing, drying, combing and packing. These fibers are a type of lignocellulosic residual biomass with a high content of impurities, as vegetable pigments, organic and inorganic solid waste (Figure 1.11b). Fique fiber at microscopic level, consists of elementary cellulose fibrils joined by hemicellulose and lignin. Figure 1.11c shows the fique fiber surface, which has a heterogeneous morphology that provides many channels, small pores, and cavities. Authors like Ovalle *et al.* [146], Bastidas *et al.* [147], Peinado *et al.* [143] and Gañan *et al.* [144] characterized this biomass, which may vary according to the species, crop and the region where it grew.

Fique fiber and its byproducts could become excellent raw materials in some chemical and physical process due to their compatibility, low density, biodegradability, flexibility, resistance, low cost, wide availability, mechanical properties (resistance to torsion, flexure and traction) and

thermal insulation, even after its useful life and recycling, production of renewable energy by incineration is an available alternative [148]. The long fique fibers have been used in fabrics production, threads, strings, packaging and handicrafts. Particularly in Colombia, the production of value-added fiber products is not well developed, although it is an important generator of employment in some regions. Nowadays, a good quality fique fiber has a marked value in the order of 0.25 EUR/kg, decreasing incentives for fiber production [145].

Some companies responsible to produce fique fiber packaging materials in Colombia are Cohilados del Fonce LTDA (San Gil), Compañía de Empaques S.A (Medellín), Empaques de Cauca S.A (Popayán) and Hilanderías Colombia LTDA (Pasto). Actually, the fiber is used by Colchones Spring, Colchones El Dorado y Americana de Colchones, to produce slabs as a new material called "microlink®" (agglomerate of fique and cotton), used as thermal insulator and reinforcement structural mattresses [143].

Several studies have reported the use of fique as reinforcement in composite materials. Latorre *et al*. [149] prepared an epoxy polymer matrix with fique fiber used as protection of corrosion pipes. Hidalgo *et al*. [150] improved mechanical properties of composites made of short fique fiber and LDPE (low density polyethylene). Contreras *et al.* [151] explained how fique fiber was used as reinforcement material in polyester matrix, concluding that fique fiber is an excellent alternative to replace synthetic fibers [152]. Gañan *et al.* [144], studied the crystallization process and thermal degradation of a polypropylene thermoplastic matrix reinforced with fique fibers. Other studies have explored not only the mechanical properties of fique fiber but also investigated its chemical properties to use fiber as an adsorbent material, catalyst support and other applications [153,154].

Currently, a growing global trend is to return to use renewable raw materials free of chemicals and not harmful to human health. To continue this path, it is important to implement policies to contribute to the implementation of elements for sustainable development, land use and water. Natural cellulose fibers are attractive as matrices for the *in situ* synthesis of nanomaterials for two reasons: 1) the surface of the fibers has a partial negative charge, due to its high oxygen density that facilitates electrostatic interaction with electropositive transition metal ions, and 2) its small porous and heterogeneous structure, facilitates the control, dispersion and stabilization of nanometric compounds. Some authors hypothesize that composites of hard fibers have improved mechanical strength, compared to raw fibers, due to a similar effect to "vulcanization" in which nanoparticles replace lignin and hemicellulose and act as "glue" between individual strands of microfibers [153].

There are several literature studies in which fiber is used for the synthesis of hybrid materials, using different pretreatments and functionalization. It is possible to deposit nanometer-scale compounds as nanoparticles the surface of the fiber, some examples being: *in situ* synthesis of silver nanoparticles on fique fibers [155], *in situ* synthesis of iron oxide nanoparticles supported on fique fibers and their use in dye degradation such as methylene blue and indigo carmine [156], oil sulfur adsorption using gold nanoparticles supported on fique [157] In situ synthesis of gold nanoparticles using fique natural fibers as support [148], biocomposite of nanostructured MnO_2 and Fique fibers for efficient dye degradation [153], controlled synthesis of ZnO particles on the surface of natural cellulosic fibers: effect of concentration, heating and sonication [158]. Heterogeneous Fenton oxidation of Orange II using iron nanoparticles supported on natural and functionalized fique fiber [154]. Nanostructured MnO_2 catalyst in E. crassipes (*water hyacinth*) for indigo carmine degradation [159].

1.7 Metal organic frameworks (MOFs)

Metal Organic Frameworks (MOFs) or Porous Coordination Polymers (PCPs) are crystalline hybrid networks that result from positively charged metal ions (inorganic building units, IBUs), connected by polygone organic ligands negatively charged (organic building units, OBUs) through coordination bonds, forming a 3D crystalline network, which in many cases has a form of an ordered pores system (Figure 1.12).

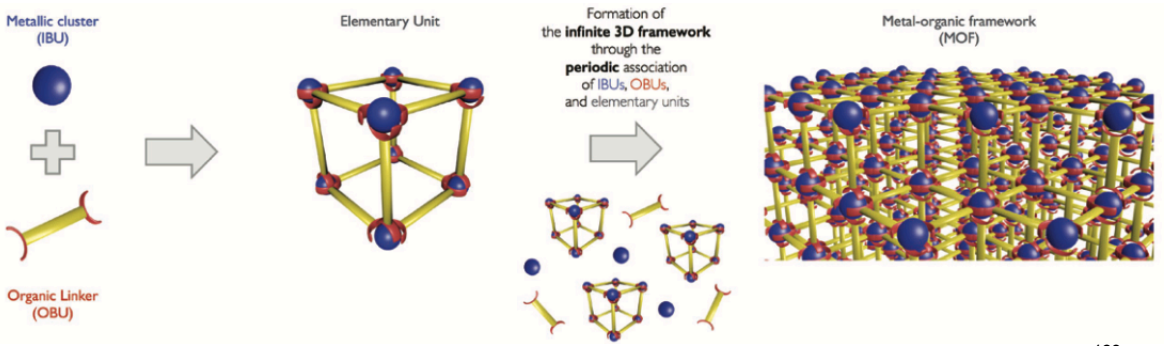


Figure 1.12. Flexible assembly process of MOFs from metal nodes and organic linkers [160].

The organic linkers include aliphatic and aromatic compounds, sometimes substituted by heteroatoms such as (N, O, S), associated with different coordinated functional groups, which may be anionic or neutral, for example carboxylates, phosphonates, sulfonates, imidazolates, pyridines. The inorganic elements, on the other hand, include alkaline earth metals (Ca, Mg), transition metals (Sc, Ti, Zn), *p* metals (Al, Ga, In) and lanthanides, which could form clusters

known as secondary building units (SBUs). There is an unlimited range of inorganic units, organic linkers and their interconnection, giving the possibility of an infinite number of structures, with different properties, including pore diameters [161].

The MOFs size varies according to SBUs and organic ligands that can be used in the synthesis and the different ways to connect them (polymorphism), providing an infinite number of possible combinations, allowing to control the network structure, obtaining MOFs with pore dimensions between ultra-micropores (2-3 Å) up to the range of mesopores (up to 10 nm) [162]. The specific surface areas have reached 7000 m^2/g, which makes them a high porosity material with spatial uniformity, low density, crystallinity, as reflected in adsorption, optical, electrical, magnetic and catalytic properties [161].

MOFs have been successful in applications such as: separation and storage of liquid and gases, sensors, biomedicine and catalysis [162]. However, they exhibit points with poor chemical, hydrolytic and thermal stability, which prevents their potential use in real applications, for which it is desirable to further improve its properties and include new functionalities. For this purpose, different functional materials have been studied that potentiate the characteristics and mitigate deficiencies of both components [163].

1.7.1 Design and synthesis of MOFs

Several methodologies have been developed for the synthesis of MOFs (Table 1.11), including compounds such as: MOF-5, MOF-177, MOF-74, MOF-199 and IRMOF-0 have already been obtained [164,165]. However, the MOF synthesis process still has challenges such as: (1) availability and cost of starting materials, (2) synthesis conditions (low temperature, environmental pressure), (3) working procedure, (4) activation process, (5) high yields, (5) reduce the number of impurities, and (6) use of solvents by implementing principles of green chemistry (i.e. organic solvents). Therefore, there are some important parameters to take into account at the moment to select a synthesis method[166]:

- Temperature: one of the main parameters of the MOF growth is the reaction temperature, as it practically determines the synthesis method to be used.
- Solvent: it is a crucial parameter in the synthesis, since solvent properties such as redox potential, reactivity, solubility or stability determine the thermodynamic and activation energy in the synthesis reaction [166]. Likewise, solvents generate strong interactions inside pores of

the networks and upon activation can lead to the collapse of the structure. Among the most widely used examples of solvents are N, N-dimethylformamide (DMF), diethylformamide, acetonitrile, acetone, methanol and ethanol.

Most MOFs are synthesized in the presence of solvents and, in some cases, unreacted starting materials or by-products become trapped within the pores of the resulting metal-organic frameworks, so MOFs synthesis generally requires final steps of purification and activation. Purification consists of the impurity's removal (metal oxides, recrystallized bonds or dense hybrid compounds), not occluded inside the pores. Many impurities are removed by solvent treatment at elevated temperatures. In the other hand, the activation involves the removal of guest molecules in the pores, in which techniques such as vacuum drying, solvent exchange or supercritical drying are used to obtain the activation of MOFs.

This stage of synthesis is challenging because to achieve the maximum potential of these porous materials, uniform, empty pores must be produced. However, collapse of the structure can also be generated due to high surface tension and capillary forces produced by liquid to gaseous phase transformation of trapped solvent molecules, especially if the solvent has a high boiling point or high surface tension. To avoid this problem, the solvent can be exchanged with a boiling point solvent or lower surface tension before heating under vacuum [170].

Table 1.11. Synthesis methods used to produce metal-organic frameworks.

Method	Description
Conventional (electric heating)	It is generally carried out in liquid phase mixing organic linkers and metal precursor salts of SBU for a time, the reaction product is filtered and evaporated to obtain a purified MOF. Conventional synthesis is classified into two methods: solvothermic and non-solvothermic or hydrothermal. Solvothermal synthesis is done at higher temperatures and pressures (solvothermal approximations), reaction times are usually reduced, and the resulting products are more complicated and diverse [167]. The hydrothermal synthesis is carried out with reactions below the boiling point of the solvent at ambient pressure; the synthesis consists mainly of overcoming the nucleation energy barrier by increasing the concentration of the reagents, requiring long times for an optimal crystallization. It is also a possibility to adjust the reaction conditions (nucleation speed and crystals growth) [168].
Slow evaporation	It occurs at a temperature close to the environment and progressive solvents evaporation of the reaction solution is adopted to control the speed and promote the growth of single crystals, it does not need an external energy supply, which implies very long reaction times compared to other syntheses [169].

Table 1.11. Synthesis methods used to produce metal-organic frameworks (Cont.).

Diffusion	It can be given in the gas, liquid or gel phase, in this method the reaction rate is controlled by the diffusion of the reagents, it is often executed under soft reaction conditions, but requires long reaction times. In gas phase diffusion, a volatile organic linker solution is used as solvent; in liquid phase diffusion, metal ions and organic ligands are dissolved in immiscible solvents; for gel diffusion, MOF formation comes from the mixture of the metal ion solution and organic linker dispersed in a gel substance [75].
Microwave	Very fast method of MOFs synthesis results in greater crystallinity, porosity, reduction of particle size and better morphology control. Microwave-assisted synthesis is based on the interaction between electromagnetic waves and mobile electrical charges (polar solvent molecules or ions in solution) [75]. The parameters to be controlled are solvents, irradiation time, reaction temperature, power level, molar ratio and concentration of reagents. However, a little number of reports typically happened at temperatures greater than 100 °C and reaction times less than 1 hour.
Sono-chemistry	This method relies on ultrasound waves to produce small bubbles or cavities that generate ultrasonic energy (20 kHz-10 MHz) with temperatures close to 5000 K and pressures up to 1000 bar [166]. There are many ultraparameters that govern the formation of cavities, such as the frequency and acoustic intensity (depending on the equipment used) and the liquid selected (vapor pressure, viscosity and chemical reactivity).
Mechano-chemistry	It is based on mechanical agitation and collision between substances to promote the division of intramolecular bonds due to mechanical force followed by chemical transformations, it is a solvent-free procedure at room temperature, resulting in less energy (it is not necessary to heat), high efficiency and simple process. Short reaction times (10-60 min) lead to quantitative yields and products with small particles are generally obtained. One type of mechanochemical synthesis is Liquid Assisted Grinding (LAG), where a small amount of solvent is added to a solid reaction mixture to facilitate grinding [166].
Electro-chemistry	This synthesis was developed by BASF in 2005, it does not require metal salts in the solution, offers continuous MOF production, which is advantageous in an industrial process. The most studied method of electrosynthesis is anodic dissolution, using an electrode as a source of metal ions. The electrode is in a solution with the organic connector and an electrolyte, by applying a voltage or current, the metal dissolves and the metal ions necessary for MOF formation are released near the electrode surface [166].
Ionometric	Using ionic liquids (IL) at room temperature or deep eutectic solvents (DES), the physicochemical properties of MOFs can be controlled by changing the composition of IL which provide thermal stability and a lower melting point but have as a disadvantage the difficult removal of solvents during activation [166].

In addition, the control of the reaction rate by, for example, adjusting the pH, temperature, pressure, molar ratio between reagents and reaction time, can give rise to high quality crystalline products, thus forming a suitable material. Furthermore, to achieve the maximum potential of these porous materials, complete activation of the samples to produce empty and uniform pores is also an essential, but often a challenging task, especially for highly porous MOFs.

The MOF structural characterization is carried out by X-ray diffraction of single crystal or powder X-ray diffraction (PXRD). In order to effectively establish the purity of the crystalline products obtained, nuclear magnetic resonance techniques (NMR) and thermogravimetric analysis (TGA) are also used [165].

1.7.2 Anchored and deposition of MOFs

Different approaches have been applied to improve the compatibility and interaction of MOF-substrates, which has been achieved by the alteration of substrates properties with functional groups, facilitating attachment or deposition of MOF [171]. In many cases, it has been evidenced after the anchorage process, the reduction in MOF sizes and stronger interactions with the matrix are observed, in addition to improved dispersion, as a result of the smaller particles which offer more interfacial area between the substrate and MOF [172]. The chemical modification strategy of the supports improves the heterogeneous nucleation and growth of MOF, allowing the design of new chemical and physical functionalities on surfaces at the molecular level [173]. Surfaces terminated in functional group such as -COOH, -OH, -NH_2, -SH, among others [168], are used to anchored metal nodes or organic linkers, allowing the nucleation and subsequent growth of MOFs.

Currently, this research field is a tendency to understand how to match the substrate functional groups density with the coordination sites number (related to the metal atoms number) per unit area within a certain MOF lattice plane. Also, it has been investigated the way in which the MOF orientation influences into the material where they have been deposited, so it can be related to the possibility of controlling the crystallographic properties, lateral distribution, thickness and homogeneity of MOFs [168]. To fully control the deposition properties of MOFs, other important parameters should be considered, such as: network interpenetration, surface roughness, crystal alignment (orientations in and out of the plane), density and size of crystals, distribution, cohesion and adhesion to substrate, as well as chemical and mechanical properties [168].

Reports of MOFs deposited onto textiles seeking to add or improve properties are limited. In 2011, deposition of MOF-199 on polyester was reported, which gave it good antibacterial properties. In this case, a surface treatment with polyvinylamine/bromoacetic acid was carried out, to generate bonding points (chemical anchor) [174]. In 2014, deposition of MOF-5 on silk was reported using ultrasound [175]. Hinestroza *et al.* reported a new ecological route for the

simultaneous functionalization of textiles by means of MIL-101 (Cr) covalent immobilization, on the nylon fabric surfaceby co-graft polymerization with 2-hydroxyethyl acrylate initiated by irradiation of γ rays [176]. Also, Sierra *et al.* described a mechanism for chemical binding and growth of MOF-199 on cellulosic substrates; they tried to elucidate the role of carboxylate groups on the anionic cellulose surface [177].

- Parameters to control during MOFs anchoring

The controlled synthesis of metallic nanomaterials requires the analysis of certain parameters that significantly affect how particle formation is carried out from a reaction mixture; these are described below:

- Crystal size and morphology

  Table 1.12 describes the parameters that most influence the growth and morphology of MOFs, when they are anchored to various types of substrates.

Table 1.12. Parameters that affect the crystal size and morphology.

Parameter	Description
Composition and process	They include solvent, pH, metal source, reagent concentration, or molar ratio of reagents. Process parameters such as time, temperature, pressure, and heating source can also have a strong influence as well. General trends in crystal size control can not be inferred by changing composition and process parameters, they must be adjusted for each system in a trial-and-error approach.
Temperature program	They influence crystal nucleation and growth rates; in addition, they have been used to synthesize MOF from supersaturated crystallization solutions.
Additives	MOFs can be adsorbed on certain crystal faces and slow down nucleation rates. Molecular blocking agents have been shown to slow crystal growth by adsorption on certain crystal faces. Protection agents can be used to stop crystal growth, while modulators have been used to control the size and morphology of MOF crystals.
Reverse micro-emulsions	In case the dispersed phase is water and continuous is an organic phase, these mixtures are called reverse microemulsions. The starting materials generally dissolve in the aqueous phase and the collision between drops or application of an external stimulus (temperature, microwave, or ultrasound) induces crystallization.

- Quality of the material obtained:

  In heterogeneous systems, the morphology, homogeneity, defects and density of the materials obtained are difficult to control. Hence, it is difficult to determine the importance of these parameters in resulting hybrid materials; optimization of growth conditions will lead to further improvements in the characteristics of these materials [168]. Intrinsic and artificially created defects at the atomic scale within the MOF can generate a break in

coordination links between the organic part and metallic nodes, changing the chemical state of metallic centers or show the absence of linkers or clusters [178].

- Growth and nucleation mechanism:
  The controlled synthesis of nanomaterials from a heterogeneous solution comprises two main stages: nucleation and growth. Nucleation is the process by which nuclei (seeds) act as templates for crystal growth [168]. Nucleation occurs when nuclei settle on the first surface of a foreign body, forming a contact angle θ with the support, if nucleation is established too quickly, very small crystals will grow. In addition, it is affected by experimental variables such as: supersaturation, temperature, and free surface energy. Crystallization is preceded by nucleation, which occurs spontaneously or is incubated by vibration or particles. It begins when the concentration of a compound in a solvent is greater than the solubility product of this compound. However, crystallization is kinetically impeded, and crystals grow only from supersaturated solutions.

- Substrates used for deposition or anchoring:
  Choosing an appropriate substrate and adequate surface modification is crucial for MOF deposition. Different strategies have been developed to support frameworks on solid flat substrates (Si, Au, FTO, ITO), flexible (plastic) and not flat (metal oxide or polymer particles, metal foams, etc).

- Anchorage or deposition methods

Different strategies have been described in the literature to deposit or anchor MOFs on different types of surfaces, which has allowed to increase the number of specific applications [168]. However, there are few studies reporting some advances on the deposition of MOFs in solid supports such as thin films or mixed matrix, so this topic remains a challenge [179]. Since the number of approaches developed is already quite large, it is reasonable to divide them into two different categories: i) deposition based on liquid solutions, ii) vacuum deposition.

Depending on the type of support used, deposition may occur on unmodified support. The matrix is immersed in the growth solution without any crystal or modification previously done to the surface, then nucleation, growth and interpenetration of crystals onto the support occur all in the same manufacturing step. The MOF synthesis takes into account coordination links between the

metal centers and organic ligands; therefore, it is favorable when support is made of the same metal as the MOF that is synthesized, improving the interfacial anchor between MOF and supports [180].

The other alternative consists in using modified support, in which the weak union between substrate and MOFs is a challenge that has been demonstrated. To solve this problem, the supports have been modified chemically to improve the heterogeneous nucleation and direct growth of the MOF membranes. The support preparation process is not direct and often requires multiple steps because the nucleation and growth of MOFs in porous supports are generally not favored.

i) Deposition based on liquid MOF solutions:

Process in which MOF are manufactured on a substrate immersed in solutions containing the reagents, for example, metal precursors and organic ligands. There are different methods, which will be described in more detail below.

- Direct growth:

  This method depends on the support immersion in the reaction solutions containing the precursor metal salts and linkers. The application of heating assisted by electric current or microwaves generates nucleation sites in the supports, which allows the crystals growth in the substrate. These crystals can crosslink to form materials with several micrometers thick.

  Alternatively, the supports can be immersed in a preheated reaction mixture in which nucleation has occurred and crystallization is about to begin. During synthesis, the second material generally serves as a structure-directing agent, leading to the targeted growth of MOF crystals[173]. Different approaches apply to this method are described in Table 1.13.

Table 1.13. Direct growth approaches.

Approach	Characteristics
Solvothermal growth	Most of MOFs known in literature are synthesized by the solvothermal method; it has been extrapolated as a MOF anchoring method, in which the respective substrates are placed in the MOF solutions during the synthesis. However, this strategy is limited in the properties control during deposition, such as morphology, thickness and crystallographic orientation of MOFs. Therefore, the crystallites are oriented randomly, the surface functionalization improves the quality of the deposition, although it does not work with modifications with thiolate because they are not stable under the conditions of solvothermal synthesis, since the desorption of these functional groups starts at 90 °C.

Table 1.13. Direct growth approaches (Cont.).

Crystallization of aged stock solutions	Use the liquid phases of the MOF solvothermal synthesis as the mother solution after most of the product precipitates.
Solvent-induced crystallization	Substrate dissolution in a suitable solvent followed by its evaporation, either by direct contact (two-phase approach) or by phase gas (three-phase approach). The key to this approach is to employ strong co-ordinating solvents for metal ions (or linkers) to form the MOFs, and then the solvent can be removed as desired.

- Layer by layer method (LBL)

  This method involves repeated cycles of immersing a substrate in metal salt and organic linker solutions, at room temperature. Between successive deposition steps, the substrate is rinsed with an appropriate solvent to remove unreacted reaction components. This method leads to homogeneous nanoscale materials with precise control of orientation, thickness and interpenetration of the MOF crystals for each step.

  It should be noted, the selection of metallic nodes is limited to paddlewheel structure metallic precursor salts (copper and zinc acetates). It has the disadvantage to be a tedious method, when the particles must be separated from each reaction or washing solution by filtration or centrifugation [173]. Some approaches to the LBL method are described in Table 1.14.

Table 1.14. LBL growth approaches.

Approach	Characteristics
LBL spray assisted	The modified substrates are alternatively exposed to an aerosol that contains the precursor metal salt for an alternate time with linker solution, allowing growth in the substrate.
LBL Langmuir – Blodgett Deposition	Linkers and metal atoms are deposited together on flat surfaces under ultra-high vacuum conditions, which are then self-assembled in 2D networks [173]. It is not a very suitable approach in LBL, since metal ions bind strongly to substrate, resulting in a redistribution of charges, making it difficult to form 3D bonds.

- Secondary growth or seeded:

  This method consists in the development of a seed layer with metal ions. Different seeding techniques have been used, such as: rubbing, dip coating, erasing, rotation and heating. Mainly sodium carboxylates are used (sodium formate, sodium acetate and sodium oxalate) as a protection reagent to control the resulting MOF crystal size and morphology [181]. Then, the seeded supports are immersed in a MOF reaction solution,

and growth occurs on the seeded surface due to the preexistence of nuclei on the support surface. Therefore, the influence of surface chemistry is eliminated. Due to its low cost and the processing possibility in large areas, this technique is also used in industry. It is an alternative that allows obtaining uniform materials, with thickness and controllable orientation on the support surface, dense and free of defects.

- Electrochemical deposition

  In general, three different approaches to MOF deposition by electrochemical methods have been described, which are listed in detail in Table 1.15.

Table 1.15. Growth approaches by electrochemical deposition.

Approach	Characteristics
Anodic deposition (AD)	It uses a metal electrode, electrochemically dissolving metal anodes with high positive voltages. Metal ions electrochemically generated easily react with organic linkers contained in electrolyte, and MOFs grow on the anode. Not all metals are suitable for anodic deposition, as some are associated with corrosion limiting the growth of homogeneous MOFs [168].
Electro-phoretic deposition (EPD)	Two conductive electrodes are immersed in solutions with charged MOF particles on the surface, applying a voltage between the two electrodes, an electric field drives the MOF particles towards the electrode with opposite charge, causing deposition of MOFs[50].
Cathodic deposition (CD)	In this process, the inert electrodes (WE, working electrode; CE, counter electrode) are used as chemically inert separators; they only act as electron sources without participating in MOF formation reactions. The key step in cathodic deposition is to obtain a local alkaline region near the cathode, where organic linkers are deprotonated.

- Liquid phase epitaxy (LPE)

  LPE is used to grow multilayer semiconductor device structures from molten metallic solutions on monocrystalline semiconductor wafers. It has two key elements: a functionalized substrate and the deposition process where substrates are immersed in solutions containing individual reagents instead of a reagent mixture using conventional solvothermal process.

- Interfacial synthesis:

  It takes place at the interface between two immiscible solutions or at the air-liquid interface through self-coordination of metal ions and organic connectors. In this way, the formation of thin films of independent MOFs is obtained. Table 1.16 describes the two most widely used approaches.

Table 1.16. Growth approaches by interfacial synthesis

Approach	Characteristics
Liquid-liquid interface	Requires difference in solubility of organic and inorganic solvents, as the two solvents are in contact, crystallization is achieved at the liquid-liquid interface, the growth rate of independent MOFs is determined by the different diffusion rates of MOF precursors in the respective solvents.
Air-liquid interface	Molecular construction units are first pre-oriented at the water surface by diffusion of an ethanolic solution into a water subphase. In a second step, the metallic nodes present in the water subphase coordinate with the molecular connectors, thus initiating the formation of MOF.

ii) Vacuum deposition:

Process in which the MOF growth is manufactured on a substrate under vacuum conditions using gas phase reagents.

- Chemical vapor deposition (CVD)

  It involves the adsorption and subsequent chemical reaction of gases with the substrate surface, using curved surfaces or inside tubes.

- Atomic layer deposition (ALD)

  It is based on sequential self-saturated surface gas reactions. The ALD process has two sequential steps: (1) deposition of a volatile metal precursors monolayer onto the substrate and (2) subsequent deposition of the second volatile organic linkers layer. Repeating steps (1) and (2) allows thin films to grow to the desired thickness [181].

1.7.3 MOFs stability

The stability of MOFs depends directly on the bonding strength and characteristics of metal ions and linkers present in the structure. However, each application has different material stability requirements since in real applications the conditions are more complicated. Currently, there are no analysis protocols or specific methodology to study the MOF stability. In this way, parameters like soaking time or solution temperature in each study change a lot and consequently the comparisons between different studies is problematic, making it challenging to characterize the stability of MOFs in water [182]. However, it is common to monitor the MOF stability using characterization methodologies before and after immersing it in aqueous solution, mainly analyzing surface morphology and crystal structure, quantification of leached metals and reuse tests, through techniques such as SEM, nitrogen adsorption-desorption, XRD, AAS, ICP and UV-VIS.

Knowing the mechanisms of MOF degradation in the presence of water or liquid phases is essential. As a result, several theoretical studies have included molecular dynamics and quantum mechanical calculations as tools to understand the possible mechanisms in detail of the water interaction with MOF, as well as some possible reaction routes [183].

The MOFs stability directly influences the feasibility of their practical applications in many fields, including separations. This stability can be thermal, chemical, hydrolytic or mechanical. However, regarding MOF stability in water, there are different levels of stability that are depending on the applications. It may be that they require strict or light stability under humidity environments; therefore, it is important to understand the stability range in MOFs to facilitate the proper selection of materials depending on the application. In literature, the MOF stability is recognized from three perspectives: chemical, thermal, and mechanical.

- Chemical stability: mainly related to water, although it has not been widely explored, there is evidence that coordination links between metal nodes and organic linkers are easily broken by

  chemical reagents, resulting in the linker protonation and formation of metal hydroxide without coordination, promoted by acidic and basic solutions, respectively. The low hydrolytic stability of MOFs is the main limitation for their applications; this behavior has been observed for different humid environments, such as water vapor, liquid water, and acid / base or buffer aqueous media. In general, the MOF is more hydrolytically stable when the pKa for linker deprotonation is higher [184].
- Thermal stability: It is defined as the node-linker bond strength and the number of linkers connected to each node. It can occur in the form of MOF, melting, node dehydration in the cluster and linker hydrogenation/graphitization [183]. Thermal stability is often the first to be evaluated because high thermal stability is synonymous with resistance to other types of stress, although most MOFs are not thermally stable at temperatures above 200 ° C.
- Mechanical stability: it plays a crucial role in compacted forms of MOF, such as pellets, in industrial processes. It is a type of stability inherent in the porosity attributed to these materials, it can manifest as partial pore collapse or even amorphization, in response to a mechanical load. The shear modulus can be a good predictor, along with other properties like volume modulus (uniform compressive strength), hardness, and Young's modulus (linear elasticity resistance along an axis) [185].

Some important characteristics that correlate with water-stable MOF are: (i) highly coordinated metal nodes, (ii) high basicity of the ligand (Zn-imidazolates versus Zn-BDC), (iii) shielding of the coordination site [186]. Low and collaborators reported two main degradation mechanisms of MOFs exposed to water[187]:

- Displacement of the linker:

The insertion of one molecule of water in the MOF metal-linker (M-O) leads the formation of a hydrated cation and the ligand release.

$$M^{n+}\text{-}L^{n-} + H2O \rightarrow M^{n+}\text{-}(OH_2)\ldots.L^{n-}$$

- Hydrolysis:

The metal-linker bond breaks down and water dissociates to form a hydroxylated cation and a free protonated ligand.

$$M^{n+}\text{-}L^{n-} + H2O \rightarrow M^{n+}\text{-}(OH)^{-} + HL^{(n-1)-}$$

Table 1.17 summarizes some of structural factors governing water stability in MOFs, which must be considered when using certain MOFs in applications involving liquids. Nowadays, MOFs such as Bio-MOF-14, MIL-100 (Cr), $Ni_3(BTP)_2$ and ZIF-8 have been shown to be thermodynamically stable mainly because they have an inert metal group that makes it unfavorable for an irreversible hydrolysis reaction to occur under high loads of water; while, MOFs as UiO-66 and MIL-101 exhibit a high kinetic stability of water because they have inert metallic centers that are also combined with the different factors of kinetic stability [186].

Table 1.17. Flow chart of structural factors governing water stability in MOFs [186].

Stability Mechanism	**Governing structural properties**	
Thermodynamic stability (Governed by the free energy of a hydrolysis reaction)		
Unfavorable for irreversible hydrolysis reaction to occur under any water loading. Oxygen in water is a nucleophile, while the metal coordination centers into the MOF are electrophilic. If this metal center is not strong enough, the water can coordinate with the metal assembly and distort or destroy the crystal lattice of the MOF.	**Inertness of Metal Cluster**	
	Metal-ligand bond strength	**Lability with water**
	A metal-ligand coordination link is the key feature that distinguishes MOF from chemically more stable porous materials. As a structure weak point, the strength of this link can be a strong indicator of the MOF hydrolytic stability [187]. • Ligands effects: pk_a of coordinating atom. • Metal effects: oxidation state and ionic radius.	• Lability of the metal cluster towards water: it includes the stability of selected cases (inertia of metal center as opposed to the average metal-oxygen bond strength) [188]. MOF with metallic species that are weaker reducing agents tends to have stronger moisture stability [189], which makes the metal reduction potential another useful predictor. • Coordination geometry: Pauling rules.

Table 1.17. Flow chart of structural factors governing water stability in MOFs [186] (Cont.).

<table>
<tr><th colspan="3">Kinetic stability (it is based on a sufficiently high activation energy barrier, E_a, which is present and depends not only on the product and reactive states, but also on the specific reaction pathway and transition states involved)</th></tr>
<tr><td rowspan="2">Not favorable because water molecules cannot cluster near metal site</td><td colspan="2">Hydrophobicity</td></tr>
<tr><td colspan="2">A hydrolysis reaction can only progress if two different events occur. First, the water molecule must get close enough to the metal to allow interaction between electron orbitals in the electrophilic metal and nucleophilic water. Second, the energy of this interaction must be large enough to overcome the activation energy barrier of this reaction [190].
• Water unable to adsorb in pores: pore hydrophobicity.
• Water unable to cluster near metal: internal hydrophobicity.</td></tr>
<tr><td rowspan="3">Water approaches metal site, but not favorable because of transition state energetics</td><td colspan="2">Steric Factors</td></tr>
<tr><td>Around metal side</td><td>Around labile ligands</td></tr>
<tr><td>Ease of water approach:
• There is greater stability in structures with metals of high coordination numbers, since they create a crowding effect that prevents the formation of water conglomerates near the metal center.
• Structural transitions, i.e., aromatic rings in MOF can exhibit significant rotation dynamics [191].</td><td>Ease of displacing ligand:
The linker functionalization can have a similar impact since bulky functional groups can sterically block the labile linkers to avoid their irreversible displacement.
• Interpenetration.
• Ligand rigidity and sterics.</td></tr>
</table>

The distinction between thermodynamically stable MOFs and those with high kinetic stability is that the former can resist exposure to liquid water conditions, while the later are stable only after exposure to water in the vapor phase. While some MOFs are stable for long periods in moist air without loss of crystallinity or surface area, an immediate structural break can still be observed when exposed to liquid water [192]. This difference in stability can arise from the fact that exposure to liquid water can cause water balance loads in the structure that are greater than what is favored by exposure to water in the vapor phase.

During MOF synthesis, one of the biggest challenges is improving the hydrolytic, chemical, and mechanical stability of the frame, which mainly depends on the inherent lability of metal-linker bonds that allows crystal structures to be formed with correction or improvement of defects. Different useful strategies have been proposed for the modification of synthesized MOFs, with the aim of stabilizing the organometallic networks in aqueous media, including [185]:

- Hydrophobicity improvement: include inside the pores the presence of hydrophobic groups like ester acetate, and use azolate linkers which contain nitrogen (imidazolate, benzolate, triazolate and tetrazolate).
- Linker functionalization: MOFs derived from ligands with methyl groups and polyaromatic rings have been found to be more stable. Likewise, it has been reported that ligand basicity is important.
- Formation of composite materials: it implies the incorporation of MOF in other types of matrices such as polymers.
- Cationic metal exchange: the metal oxidation state in the SBU is important since the high valence ions (Cr^{3+}, Al^{3+}, Fe^{3+}, Zr^{4+}) have a high charge density that allows them to form stronger coordination bonds with the linkers. This combination results in stiffer structures making it less susceptible to water molecules [193].
- Catenation: it refers to the interpenetration or entanglement of networks, which can improve stability through favorable frame-frame interactions [185].

Modular and post-synthetic modifications are among the mechanisms reported to achieve the modifications, although, in practice many functional groups are intolerant to synthesis conditions or incompatible to functionalized linkers during the synthesis, giving rise to unexpected products, hence the importance to select the adequate modification mechanism (Figure 1.13).

- Simultaneous synthesis and functionalization:

It consists in the use of agents that regulate the MOF coordination balance. These modulating agents are chemical species that coordinate metals in a similar way to the linker but with a lower binding, they stop the formation of the frame by inhibiting coordination sites and slow down the formation of nucleation sites. In this way, crystalline defects are regulated, and the product crystallinity is increased in the final product. Among the most used modulating agents are acids (benzoic, hydrochloric, acetic, trifluoroacetic, formic) [194].

In this approach, not only parameters like size, morphology and crystallinity of the products are susceptible to being affected. There are also a variety of factors that influence the modulated synthetic route, the more complex functions to introduce will result in the more difficult synthesis by self-assembly due to its reactivity towards metal precursors [168].

Crystal poison is a type of modulators used currently, its use has kinetically allowed to tune a compound with a structure very similar to the original linker, considering linker substitution rates, the type of crystal poison and the solvent molecules coordination. Crystal poison is any compound that delays the crystals formation in a material that would normally exist in a crystalline state at a given condition. These compounds have different effects: delayed nucleation, development of multiple nucleation sites, retarded growth of successive layers in crystals, reduction in crystal size and can become a steric obstacle [195].

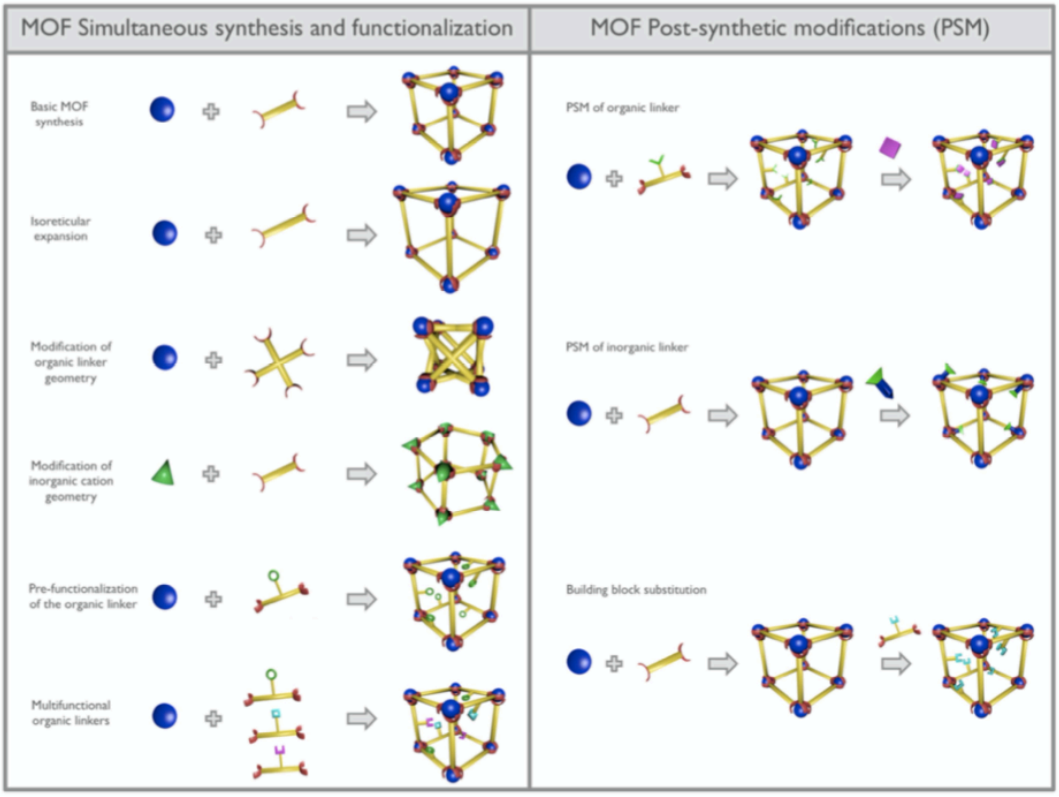


Figure 1.13. Different modification approaches used to provide a MOF with additional functionality. These approaches can be classified in two main concepts: in the first one, at least one building block is modified before MOF synthesis (left), while in the second approach, the structure is synthesized first and then subjected to further post-synthetic modifications (PSM, right) [196].

Crystal formation involves two steps: nucleation and crystal growth. Specifically, nucleation can be of two types: homogeneous (pure and uniform substances are given, the process is random and spontaneous) or heterogeneous (impure substances, in supersaturated concentration and require an initiator for nucleation). After nucleation, a group of nuclei is formed, then it can end in two ways: i) the cluster becomes unstable and dissolves again, ii) the cluster reaches a critical size, stabilizes and forms a nucleus [195].

Crystal growth occurs once the clusters reach the critical size, then an amorphous aggregate is generated, followed by a progression to a more orderly phase to form a microstructure. Next, the formed crystal becomes the convergence point of successive layers (like an onion), this stage can be affected by parameters such as: temperature, pressure, surface tension or stirring [196].

- Post-synthetic modification (PSM):

Describes the MOF functionalization after it has been synthesized, it is a secondary step that allows to have a variation of the mother MOF with identical topology, resulting in new properties without compromising the original structure [194]. Among the most incorporated functional groups in MOFs are –SH, $–NH_2$, RR´C=N-N=CRR´, and quinine. Nevertheless, more complex functional groups have been tried to be included and difficulties have been found because these groups are more reactive, then inside of the pores they can be coordinated with metal centers and participate in the SBU formation, changing the MOF topology.

Additionally, PSM has as disadvantages long reaction times (up to 5 days) and the yields which depend on the diameter sizes. There are three strategies to achieve the MOF modification using PSM:

i) Covalent or dative modification: it is produced by covalent changes to the ligands. For this type of modification, it is desirable that MOF has a reactive chemical group in the linker, which is considered as a label, since it is a stable group and it does not define the structure during MOF formation, but it can be transformed by post-synthetic modification [194]. However, some studies have reported that incorporating very large linkers often results in the network collapse after the activation stage. Despite this, there have been different attempts to increase the steric effect of linkers by improving stability through the synthesis conditions.

ii) Inorganic modification: is produced by the metal exchange of the SBU with another or by the geometry modification of the metal cluster [194]. The metal could develop secondary reactions such as metalation, transmetalation, oxidation or reduction.

iii) Ionic modification or post-synthetic deprotection: method for prevention of penetration in MOF, the concept of deprotection occurs when a functional group is introduced into the organic linker and this, in turn, is included in the MOF under standard solvothermal conditions. At this point, the protective group is removed in a post-synthetic reaction to reveal the desired functionality [196].

1.7.4 Potential applications of MOFs in water treatment:

Porous solid materials, owing to their properties, have shown to have promising applications for separation and water purification. Comparing it with traditional technologies, they have great potential in terms of lower energy consumption and lower carbon footprint and easy operation, since their pores can be controlled by means of inorganic metal linkers and ions. Additionally, the pore surfaces can be easily functionalized through different approaches[179].

For the separation process using adsorption and membranes, the size and shape of the molecules to be separated and the materials interaction, are taken into account. For this, polymer membranes are currently used because they have low production costs and can be used with high flows and mechanical flexibility; however, they have short life times, low thermal and chemical stability and selectivity [197]. However, zeolites, carbon molecular sieves and metal oxides, aluminoforms, activated carbon, activated alumina, carbon nanotubes, silica gel, clays with abutments, inorganic and polymeric resins, porous organic materials and MOFs have been explored as separation and adsorption media [169].

Particularly, MOFs have been found as potential candidates in separation applications as adsorbent materials but also as molecular nanoreactors to perform reactions or stabilize the reaction intermediates in liquid phases, which include liquid chemicals (such as water and organic solvents commonly used) at standard temperature and pressure (STP)[198]. However, in order to be able to use MOFs for practical separation applications, several additional issues must also be solved, including hydrothermal stability in the final work environments, adsorption kinetics studies, continuous cycle of materials (lifetime), associated costs and process manipulation from an engineering support point [179].

Adsorption is the process by which a liquid mixture with solid particles, molecules, or ions is separated. The adsorptive separation is based on three different mechanisms: steric (the adsorbent has pores of such size that allows passing only molecules with a specific size), kinetic (different diffusion rates of compounds in the pores) and equilibrium (adsorbents have different affinities to accommodate different species) [199]. Adsorption is significantly influenced by the physicochemical properties of adsorbates, adsorbents, and water quality properties (Table 1.18). It is used in industrial applications like treatment of contaminated effluent, because compared to other pollution control methods, it has the advantages of low cost, easy design, and recyclability of some adsorbents. Adsorption is determined by the adsorbent-adsorbate interaction characteristics, which can be classified as [199]:

- Physical adsorption or physisorption:

  The interactions take place through van der Waals forces on adsorbent surface, which are not very strong, and the adsorbent regenerates easily through slight changes in the solvent system, pH, or physical treatment. It does not share or transfer electrons, it is a reversible process, with low heat of adsorption.

- Chemical adsorption or chemisorption:

  Interactions are carried out by the chemical bonding of adsorbate surfaces, making the process irreversible, increasing enthalpy, hindering its regeneration and reuse. It occurs only on active centers with high values of adsorption heats.

Table 1.18. Physicochemical properties of adsorbates, adsorbents, and water quality properties.

Solid properties	Surface (a higher adsorbent surface gives greater absorption and greater adsorption). Pore size distribution (determine accessible surface adsorption) and particle size of the adsorbent.
Adsorbate nature	The solubility of the adsorbate in the solvent (high solubility gives low adsorption concentration), adsorbate structure (presence of functional groups promotes solid-solute interactions), the molecular size of the adsorbate (determines the rate of adsorption), and ionic nature of adsorbate (adsorbate net charge).
Liquid phase characteristics	pH (determines the concentration of hydronium and hydroxyl ions in the medium, setting the degree of dissociation), temperature (increasing temperature generates a reduction in adsorption), and nature of the solvent (affinity of the solid by the solvent and adsorbate).
Competition between adsorbates	The presence of multiple adsorbates can influence the adsorption capacity and processing rate.

The adsorption increases with the surface area and the porosity, improving the accessibility to the exchange sites and the diffusion in the material. Viability in practical applications such as water treatment considers the adsorption capacity and selectivity [183]. The heavy metals (HMs) removal from wastewater has found as the main limitation the specificity of adsorbents used owing to hard, smooth, and borderline metal ions [76]. Recently, the performance of innovative materials such as MOF has been studied (Figure 1.14) [183].

Application of MOFs to the adsorption of the emerging contaminants from water has recently increased, due to i) the need to find new materials that contribute to solving the problem through innovative solutions, ii) the textural properties (pore size and surface area), morphology and chemical environment of MOFs, useful in liquid separation applications, iii) the possibility of

modifying the MOFs pores surface utilizing modulating agents or post-synthetic modification (PSM), as a result of the tunable property [169].

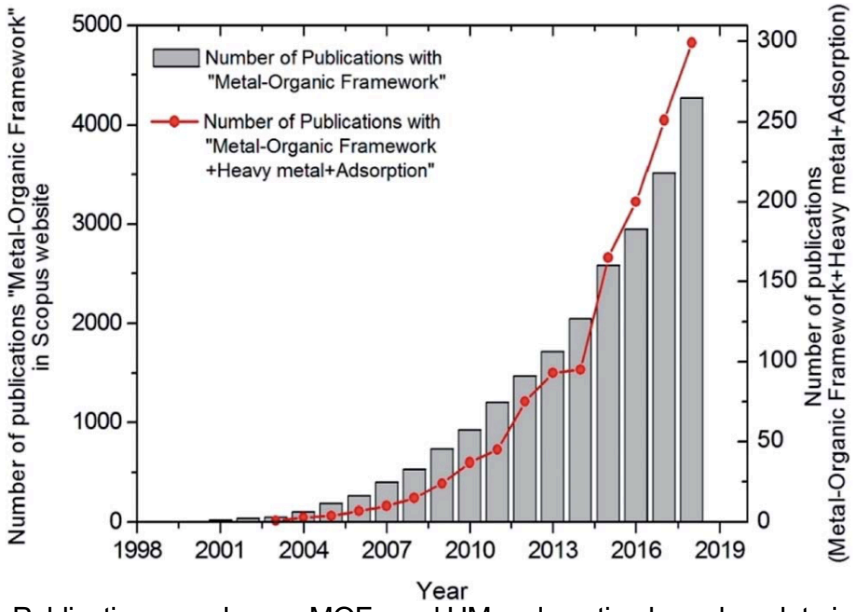


Figure 1.14. Publications number on MOFs and HMs adsorption based on data in the Scopus database [183].

Nevertheless, there are opportunities for more detailed studies to clarify the adsorption mechanism of heavy metals using different MOFs, as well as the combination with other materials that in the future may be used as filters or membranes. Besides, it is necessary to establish standardized criteria in the MOFs evaluation as adsorbents, understanding any desirable properties in metal-organic frameworks to boost the application of these material materials in the future.

Recently, synthesis strategies have been improved to increase the stability of MOFs in water, some examples are: change of metal centers, open metal sites, linkers functionalization, and MOF anchoring[202]. Among the most interesting characteristics of MOFs used as adsorbents, is the possibility of tuning or adapting their surfaces to eliminate specific compounds, due to the hard and soft acids present in linkers, which have specificity for metal ions. However, more functional linkers are able to coordinate with weak acids, so that adsorbents functionalized with hard or soft bases limit the removal efficiency of HMs [203].

Some reports have shown the elements grafting, such as sulfur into adsorbent materials, increases the affinity for contaminants, improves selectivity, and removal of HM ions by up to 100%, due to the coordinating possibility with soft metal centers such as Hg^{2+}. Fundamental and

practical studies of the MOFs application in water have been carried out by Kunsgens *et al.* [193] and Canivet *et al.* [204], who examined a representative set of MOFs and suggested the typical mechanisms of water adsorption by MOF could be: reversible and continuous pore filling, irreversible and discontinuous pore filling through capillary condensation, and irreversibility derived from the flexibility and possible structural modifications of the host material.

Virgin MOFs are synthesized by combining metal centers and organic linkers, which are capable of adsorbing divalent HMs (Pb^{2+}, Cd^{2+}, Hg^{2+}) from aqueous solutions and have demonstrated excellent adsorption capabilities. Virgin MOFs can be modified by synthesis through hybridization or modification with functional groups such as thiol, amino, azine, quinine [200]. Published data has confirmed that virgin MOFs generally achieve lower adsorption capacities compared to modified frames [183].

Within the adsorption mechanisms reported from MOFs interactions (adsorbent) and HMs (adsorbate), they are divided into physical adsorption (electrostatic attraction, van der Waals forces, and diffusion) and chemical (chemical bonds, coordination, and interactions acid-base); in addition, they are a function of the interaction strength developed (see more details in Table 1.19) [200]. Furthermore, the hydrophilic-hydrophobic or polar-apolar character of host molecules also play an important role in approaching the MOF pores surface. Strong interactions between adsorbate and MOF have been reported, causing structural changes or frame modifications, because of breathing and swelling properties of metal-organic frameworks [169]. Research has shown MOFs potential to adsorb inert molecules through hydrogen bonds, which commonly could not be adsorbed by other types of mechanisms [183].

Table 1.19. Factors that affect the adsorption process.

Physisorption	
This kind of adsorption is mainly controlled by the solution pH, in which the MOF surface can be protonated or deprotonated, allowing pollutants to bind, when solution pH < pH_{pzc}, the surface is positively charged. In contrast, when solution pH > pH_{pzc}, the surface is negatively charged causing electrostatic attraction of HMs cations such as Pb^{2+}, Cd^{2+}, Hg^{2+}, Cr^{6+} and As^{6+} [183]. For this type of adsorption, to analyze in-depth the governing mechanism in separation process, adsorption isotherms are used, which from experimental data are adjusted to models such as Langmuir, Freundlich, and Temkin [200], each of these models has assumptions that allow to better infer how the pollutants removal is carried out.	
Interaction	***Characteristics***
Electrostatic	MOF surfaces charged with functional groups such as hydroxyl, thiols, or amines, which are characterized by being rich in electrons, facilitate the electrostatic attraction of anions or cations since during adsorption they play roles as electron donors and acceptors [201].

Table 1.19. Factors that affect the adsorption process (Cont.).

Van Der Waals Forces	It is a distance-dependent interaction between atoms or molecules, these attractions do not result from a chemical electronic bond; they are comparatively weak and therefore more susceptible to disturbance [200].
π-π interactions / stacking	Stack ordering of aromatic molecules, which is adopted due to interatomic interactions, the nonpolar aromatic rings are located one above other. The π-π interactions are caused by the intermolecular overlap of the p orbitals in π conjugate systems, so they become stronger as the number of π electrons increases.
Chemisorption	
It is a kind of adsorption which involves a chemical reaction between the surface and the adsorbate. New chemical bonds are generated at the adsorbant surface (in this case MOF). The strong interaction between the adsorbate and the substrate surface creates new types of electronic bonds.	
Interaction	***Characteristics***
Coordination	They occur between HM ions and functional groups such as amino (-NH_2), carboxyl (-COOH) and thiol (-SH), not determined by the amount of available surface area [76].
Chemical bond	It is a predominant and common mechanism in contaminant removal, generated between HMs and MOFs.
Acid-base interaction	It is based on the high-soft-acid-base theory (HSAB), in which soft acids react strongly with soft bases, while hard acids react strongly with hard bases. Furthermore, this type of interaction is complemented by acid theory- Lewis base, electron donor and acceptor [76].

Specifically, metal-organic frameworks have tested in the mercury removal (Table 1.20). Some studies have shown linker modification with functional groups such as pyridines, carbonates, and organosulfides, but the most promising functional group is thiol (-SH) due to the affinity generated with HMs like Hg^{2+}, Ag^{1+}, Pb^{2+}, as a result of Lewis acid-base interactions [200], improving selectivity and adsorption capacity of Hg^{2+} [217]. Not only the thiol group have been shown to improve selectivity for mercury, but also methylthiol (-SCH_3) groups were able to remove Hg^{2+} from water [221].

Table 1.20. Metal-organic frameworks used as adsorbent to remove Hg^{2+} from water

MOF	Adsorption capacity and conditions
Thiol-$[CU_3(BTC)_2]_n$	714 mg g^{-1}, equilibrium time 120 min [205]
UiO-66-NHC(S)NHMe	Efficiency 99%, equilibrium time 240 min [206]
3D Co(II) MOF	Efficiency 70%, equilibrium time 100 min [207]
FJI-H12	440 mg g^{-1}, equilibrium time 60 min, pH = 7 [208]
PCN-100	Equilibrium time 2880 min [206]
AMOF-1	78 mg g^{-1}, equilibrium time 1440 h, Efficiency 94% [209]
Fe_3O_4@SiO_2@HKUST-1	264 mg g^{-1}, equilibrium time 10 min, pH = 3 [210]
Zn(hip)(L)(DMF)(H_2O)	333 mg g^{-1}, equilibrium time 60 h, Efficiency 85%, pH = 5 [211]
$[Ni(3\text{-}bpd)_2(NCS)_2]_n$	713 mg g^{-1}, equilibrium time 120 min, Efficiency 94% [212]
Cr-MIL-101-AS	Equilibrium time 360 min, Efficiency 99% [213]
Zr-DMBD	Equilibrium time 720 min, Efficiency 100% [214]

Table 1.20. Metal-organic frameworks used as adsorbent to remove Hg^{2+} from water (Cont.).

LMOF-263	380 mg g^{-1}, equilibrium time 30 min, Efficiency 84%, pH = 4-10 [215]
ZIF-90-SH	22 mg g^{-1}, equilibrium time 1440 min, Efficiency 45-90% [16]
SH@SiO_2/$Cu(BTC)_2$	210 mg g^{-1}, equilibrium time 60 min, pH = 6 [217]
BioMOF	900 mg g^{-1}, equilibrium time 120 min, pH = 7 [218]
MOF-74-Z	63 mg g^{-1}, equilibrium time 90 min, pH = 6 [219]
MIL-101-Thymine	52 mg g^{-1}, equilibrium time 200 min, pH = 6 [220]

1.7.5 MOF HKUST-1 or MOF-199

HKUST-1 or MOF-199, its name comes from the Hong Kong University of Science and Technology, has $Cu_3(BTC)_2.(H_2O)_X$, (BTC = Benzene-1,3,5-tricarboxylic acid) as chemical formula, and it is one of the most studied and characterized MOF's so far. For this reason, it is a reference material for research in many of the MOF general properties (Figure 1.15).

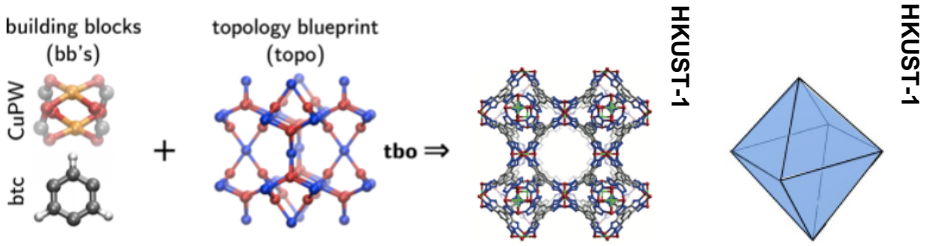


Figure 1.15. HKUST-1 coordinatively saturated structure, each crystallographic unit cell features Cu•••Cu paddlewheel motifs. Modified from [29].

The metal centers in HKUST-1 generally adopt octahedral geometry (Figure 1.16), exhibits a unique turquoise blue color and has a particle diameter of approximately 15-20 μm. The framework has a bimodal pore size distribution, larger pores are hydrophilic and evidenced diameter of 9 Å. The other type of pores is smaller with 6 Å in diameter; they are less hydrophilic since the inside of the pores is made up of four benzene rings [223]. These pores can be evacuated to form a highly porous network (SBET = 1055 $m^2.g^{-1}$), a cubic frame Fm3̲m is characteristic of this material, a cell network and cell volume of 26.34 Å and 18.28 $Å^3$, respectively[29].

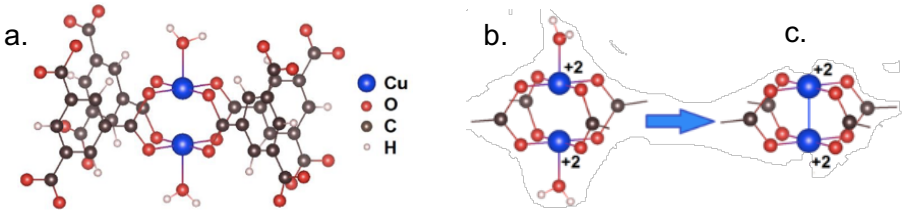


Figure 1.16. a) Outline of the main structure of HKUST-1 before activation shows the paddlewheel structure that is formed by the union of two Cu^{2+} ions and four benzene molecules of the linker 1,3,5-tricarboxylate linker (BTC), b) hydrated cage of HKUST-1 before the activation, c) activated cage of HKUST-1 (dehydrated) [181].

In the HKUST-1 framework, Cu^{2+} ions form dimers, in which each copper atom is coordinated by four oxygens from the BTC linkers, developing a structure known as the paddlewheel unit, which is the heart of the material (also known as secondary building unit, SBU (Figure 1.16a). The fifth binding site on each Cu^{2+} ion (out of plane) is occupied by oxygen from a crystallizing water molecule (Figure 1.16b) that can be easily removed by the activation process (typically consisting of vacuum heat treatment at about 400 K) [222]. The presence of water molecules in the first coordination sphere has suggested the possibility of obtaining a coordination vacancy in Cu^{2+} species (Figure 1.16c) [181].

HKUST-1 has been successfully synthesized using various methods [224], including conventional methods such as hydrothermal/solvothermal, alternative methods such as microwave, ultrasound, mechanochemical and electrochemical methods. Although alternative synthetic methods offer quantitative HKUST-1 yields on the laboratory scale with relatively short reaction times, they generally result in inconsistent yield products, porous structures, and crystallinity [224]. To date, a low number of publications related to HKUST-1 synthesis methods obtained under atmospheric pressure have been evidenced. In this case, the use of dimethyl formamide (DMF) as solvent allowed to obtain yields in the range of 55 to 92%, reaction times of 5 to 18 hours and surface areas close to $1200 m^2. g^{-1}$ [225].

However, the development of greener processes has become a necessity and synthesis of HKUST-1 has not been the exception. There are limited and almost few reports of HKUST-1 green synthesis in which ethanol is used instead of DMF and are adjusted to process temperatures below the solvents boiling point in order to avoid high pressure operation, causing industrial safety problems [225]. Unlike DMF, ethanol does not undergo decomposition and therefore can be recycled. DMF is subject to breakdown when exposed to water and heat, producing amines that are a risk for the enviroment. Unlike DMF, ethanol does not undergo decomposition and therefore can be recycled. Thus, green synthesis results in the significant improvement of the process economy, granting economic viability to the MOFs production [225].

Studies established that long exposure of HKUST-1 to moisture causes the condensation of water molecules inside the MOF cavities, promoting the hydrolysis of Cu-O bonds in the paddlewheels (Figure 1.17), resulting in the collapse of the crystal lattice [181]. HKUST-1 possesses high thermal stability in comparison to many other MOF structures, which is potentially attractive for industrial processes.

This metal-organic framework has shown interesting properties in applications such as hydrogen and methane storage, gas separation, purification and catalysis [226]. This MOF is produced at large scale as Baseolite®.Hydrolytic instability becomes its main weakness, limiting the applications of HKUST-1. However, the robustness of this frame, as well as the possibility to remove and replace linkers in the axial position of the copper dimer, make HKUST-1 a very interesting MOF, since its structure can be adapted through materials chemistry, to improve its water stability.

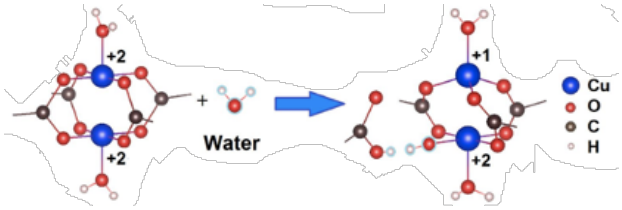


Figure 1.17. Schematic representation of the SBU interaction between the HKUST-1 with a water molecule, which promotes the hydrolysis of the Cu-O bond, generating the realease of a carboxylate bridge and the formation of a Cu^{1+} center [181].

1.8 References

1. UNEP (United Nations Environment Programme). Environmental Data Explorer - The Environmental Database. http://geodata.grid.unep.ch/results.php (2015).

2. Programa de las Naciones Unidas para el Desarrollo (PNUD). Medio ambiente y recursos naturales.http://www.undp.org/content/undp/es/home/ourwork/sustainable-development/ nat ural-capital-and-the-environment.html (2017).

3. USGS Water Science School. How much water is there on, in, and above the Earth? https://water.usgs.gov/edu/earthhowmuch.html (2016).

4. United Nations Department of Economic and social Affairs. UN International Decade for Action 'Water for Life" 2005-2015. 1 http://www.un.org/waterforlifedecade/quality.shtml (2015).

5. Alcamo, J. & Borchardt, D. *Towards a Worldwide Assessment of Freshwater Quality: A UN-Water Analytical Brief*. http://www.wwqa-documentation.info/assets/un _water_ analytical _brief_20161111 _02_web_pages.pdf (2016).

6. Biblioteca Nacional de Chile. La contaminación del agua en América Latina y Chile - Programa Americas. http://www.bcn.cl/observatorio/americas/noticias/la-contaminacion-del-agua-en-america -latina-y-chile (2016).

7. UNEP. *A Snapshot of the World's Water Quality : Towards a global assessment*. (2016).

8. UNPeriodico. El 50% del agua en Colombia es de mala calidad. *UNPeriodico*. **141**, 20 (2015).

9. IDEAM. *Estudio nacional del agua 2014. Ministerio de Medio Ambiente* http://documentacion.ideam.gov.co/openbiblio/bvirtual/023080/ENA_2014.pdf (2014).

10. Hernández, F. *et al.* LC-QTOF MS screening of more than 1,000 licit and illicit drugs and their metabolites in wastewater and surface waters from the area of Bogotá, Colombia. *Anal. Bioanal. Chem.* **407**, 6405–6416 (2015).

11. Boxall, A. *et al.* Pharmaceuticals and personal care products in the environment: what are the big questions? *Environ. Heal. Perspect.* **120**, 1221–1229 (2012).

12. Gros, M., Petrović, M., Ginebreda, A. & Barceló, D. Removal of pharmaceuticals during wastewater treatment and environmental risk assessment using hazard indexes. *Environ. Int.* **36**, 15–26 (2010).

13. Fatta-Kassinos, D., Meric, S. & Nikolaou, A. Pharmaceutical residues in environmental waters and wastewater: Current state of knowledge and future research. *Anal. Bioanal. Chem.* **399**, 251–275 (2011).

14. McCuen, R. Contaminants of Emerging Environmental Concern. *J. Am. Water Resour. Assoc.* **45**, 1-10 (2009).

15. Kaza, S. Rachel Carson: Legacy and Challenge. *Worldviews Glob. Relig. Cult. Ecol.* **14**, 294–297 (2010).

16. Corsolini, S., Borghesi, N., Ademollo, N. & Focardi, S. Chlorinated biphenyls and pesticides in migrating and resident seabirds from East and West Antarctica. *Environ. Int.* **37**, 1329–1335 (2011).

17. Vazquez-Roig, P., Andreu, V., Blasco, C., Morillas, F. & Picó, Y. Spatial distribution of illicit drugs in surface waters of the natural park of Pego-Oliva Marsh (Valencia, Spain). *Environ. Sci. Pollut. Res.* **19**, 971–982 (2012).

18. Belanger, S. *et al.* Aquatic risk assessment of alcohol ethoxylates in North America and Europe. *Ecotoxicol. Environ. Saf.* **64**, 85–99 (2006).

19. Bijlsma, L., Emke, E., Hernández, F. & De Voogt, P. Investigation of drugs of abuse and relevant metabolites in Dutch sewage water by liquid chromatography coupled to high resolution mass spectrometry. *Chemosphere* **89**, 1399–1406 (2012).

20. Kasprzyk-Hordern, B., Dinsdale, R. & Guwy, A. The removal of pharmaceuticals, personal care products, endocrine disruptors and illicit drugs during wastewater treatment and its impact on the quality of receiving waters. *Water Res.* **43**, 363–380 (2009).

21. Singer, H. *et al.* Determination of biocides and pesticides by on-line solid phase extraction coupled with mass spectrometry and their behaviour in wastewater and surface water. *Environ. Pollut.* **158**, 3054–3064 (2010).

22. Fu, F. & Wang, Q. Removal of heavy metal ions from wastewaters: A review. *J. Environ. Manag*. **92**, 407–418 (2011).

23. Fatone, F., Di Fabio, S., Bolzonella, D. & Cecchi, F. Fate of aromatic hydrocarbons in Italian municipal wastewater systems: An overview of wastewater treatment using conventional activated-sludge processes (CASP) and membrane bioreactors (MBRs). *Water Res.* **45**, 93–104 (2011).

24. Margot, J., Rossi, L., Barry, D. & Holliger, C. A review of the fate of micropollutants in wastewater treatment plants. *Wiley Interdiscip. Rev. Water* **2**, 457–487 (2015).

25. Coutu, S., Wyrsch, V., Wynn, H., Rossi, L. & Barry, D. Temporal dynamics of antibiotics in wastewater treatment plant influent. *Sci. Total Environ.* **458**, 20–26 (2013).

26. Health and Social Care Centre. *Prescription Cost Analysis England 2015*. *Health and Social Care Centre* http://content.digital.nhs.uk/catalogue/PUB20200/pres-cost-anal-eng-2015-rep.pdf (2016).

27. Helbling, D., Hollender, J., Kohler, H. P., Singer, H. & Fenner, K. High-throughput identification of microbial transformation products of organic micropollutants. *Environ. Sci. Technol.* **44**, 6621–6627 (2010).

28. Abegglen, C. & Siegrist, H. *Micropolluants dans les eaux usées urbaines. Connaissance de l'environnement n° 1214* https://www.micropoll.ch/fileadmin/user _upload/Redaktion/ Dokum ente /01_Berichte/02_Technische_Verfahren/01_Allgemein/2012_Micropolluants_dans_les _eaux_usees_urbaines03.pdf (2012).

29. Hollender, J. *et al.* Elimination of organic micropollutants in a municipal wastewater treatment plant upgraded with a full-scale post-ozonation followed by sand filtration. *Environ. Sci. Technol.* **43**, 7862–7869 (2009).

30. Petrie, B. *et al.* Diagnostic investigation of steroid estrogen removal by activated sludge at varying solids retention time. *Chemosphere* **113**, 101–108 (2014).

31. Lin, A. & Reinhard, M. Photodegradation of Common Environmental Pharmaceuticals and Estrogens in River Water. *Environ. Toxicol. Chem.* **24**, 1303–1309 (2005).

32. Jiménez, C. Contaminantes orgánicos emergentes en el ambiente: Productos farmacéuticos. *Rev. Lasallista Investig.* **8**, 143–153 (2011).

33. Kuster, M. *et al.* Analysis and occurrence of pharmaceuticals, estrogens, progestogens and polar pesticides in sewage treatment plant effluents, river water and drinking water in the Llobregat river. *J. Hydrol.* **358**, 112–123 (2008).

34. Barbosa, M., Ribeiro, A., Pereira, M. & Silva, A. Eco-friendly LC–MS/MS method for analysis of multi-class micropollutants in tap, fountain, and well water from northern Portugal. *Anal. Bioanal. Chem.* **408**, 8355–8367 (2016).

35. EU Water Framework Directive (WFD). *Directive 2000/60/EC of the European Parliament and of the Council establishing a framework for the Community action in the field of water policy*. http://ec.europa.eu/environment/water/water-framework/index_en.html (2000).

36. Water Framework Directive (WFD). *Directive on Environmental Quality Standards (Directive 2008/105/EC)*.http://ec.europa.eu/environment/water/water-dangersub/pri_substances.htm (2008).

37. European Environment Agency (EEA). *DIRECTIVE 2013/39/EU — European Environment Agency*. https://www.eea.europa.eu/data-and-maps/indicators/emission-intensity-of-manufacturing-industries-1/directive-2013-39-eu (2013).

38. Barbosa, M., Moreira, N., Ribeiro, A., Pereira, M. & Silva, A. Occurrence and removal of organic micropollutants: An overview of the watch list of EU Decision 2015/495. *Water Res.* **94**, 257–279 (2016).

39. Wells, M. Log D OW : Key to Understanding and Regulating Wastewater-Derived Contaminants. *Environ. Chem.* **3**, 439 (2006).

40. Joseph, L. *et al.* Removal of contaminants of emerging concern by metal-organic framework nanoadsorbents: A review. *Chem. Eng. J.* **369**, 928–946 (2019).

41. Ternes, T. Occurrence of drugs in German sewage treatment plants and rivers. *Water Res.* **32**, 3245–3260 (1998).

42. Rogers, K. & Cammarata, A. Superdelocalizability and charge density. A correlation with partition coefficients. *J. Med. Chem.* **12**, 692–3 (1969).

43. De la Cruz, N. *et al.* Degradation of emergent contaminants by UV, UV/H2O2 and neutral photo-Fenton at pilot scale in a domestic wastewater treatment plant. *Water Res.* **47**, 5836–5845 (2013).

44. Margot, J. *et al.* Treatment of micropollutants in municipal wastewater: Ozone or powdered activated carbon? *Sci. Total Environ.* **461**, 480–498 (2013).

45. Verlicchi, P., Al Aukidy, M. & Zambello, E. Occurrence of pharmaceutical compounds in urban wastewater: Removal, mass load and environmental risk after a secondary treatment—A review. *Sci. Total Environ.* **429**, 123–155 (2012).

46. Oulton, R., Kohn, T. & Cwiertny, D. Pharmaceuticals and personal care products in effluent matrices: A survey of transformation and removal during wastewater treatment and implications for wastewater management. *J. Environ. Monit.* **12**, 1956-1978 (2010).

47. Michael, I. *et al.* Urban wastewater treatment plants as hotspots for the release of antibiotics in the environment: A review. *Water Res.* **47**, 957–995 (2013).

48. Coday, B., Yaffe, B., Xu, P. & Cath, T. Rejection of trace organic compounds by forward osmosis membranes: a literature review. *Environ. Sci. Technol.* **48**, 3612–3624 (2014).

49. Dolar, D. *et al.* Removal of emerging contaminants from municipal wastewater with an integrated membrane system, MBR–RO. *J. Hazard. Mater.* **239**, 64–69 (2012).

50. Justo, A., González, O., Sans, C. & Esplugas, S. BAC filtration to mitigate micropollutants and EfOM content in reclamation reverse osmosis brines. *Chem. Eng. J.* **279**, 589–596 (2015).

51. Aksu, Z. & Yener, J. A comparative adsorption/biosorption study of mono-chlorinated phenols onto various sorbents. *Waste Manag.* **21**, 695–702 (2001).

52. Westerhoff, P., Yoon, Y., Snyder, S. & Wert, E. Fate of endocrine-disruptor, pharmaceutical, and personal care product chemicals during simulated drinking water treatment processes. *Environ. Sci. Technol.* **39**, 6649–6663 (2005).

53. Ribeiro, A., Pedrosa, M., Moreira, N., Pereira, M. & Silva, A. Environmental friendly method for urban wastewater monitoring of micropollutants defined in the Directive 2013/39/EU and Decision 2015/495/EU. *J. Chromatogr. A* **1418**, 140–149 (2015).

54. Fenton, H. Oxidation of tartaric acid in presence of iron. *J. Chem. Soc., Trans.* **65**, 899–910 (1894).

55. Ruppert, G., Bauer, R. & Heisler, G. The photo-Fenton reaction — an effective photochemical wastewater treatment process. *J. Photochem. Photobiol. A Chem.* **73**, 75–78 (1993).

56. Nidheesh, P. & Gandhimathi, R. Trends in electro-Fenton process for water and wastewater treatment: An overview. *Desalination* **299**, 1–15 (2012).

57. Brillas, E. *et al.* Aniline mineralization by AOP's: anodic oxidation, photocatalysis, electro-Fenton and photoelectro-Fenton processes. *Appl. Catal. B Environ.* **16**, 31–42 (1998).

58. Frank, S. & Bard, A. Heterogeneous photocatalytic oxidation of cyanide ion in aqueous solutions at titanium dioxide powder. *J. Am. Chem. Soc.* **99**, 303–304 (1977).

59. Ribeiro, A., Mateus, E. & Couto, N. *Electrokinetics across disciplines and continents : new strategies for sustainable development*. (Springer, 2011).

60. Elorriaga, Y., Carriquiriborde, P. & Ronco, A. E. Contaminantes emergentes: productos farmacéuticos en el medio ambiente. *Prod. Farm*. **10**, 1-80 (2012).

61. Petrović, M., Gonzalez, S. & Barceló, D. Analysis and removal of emerging contaminants in wastewater and drinking water. *Trends Anal. Chem.* **22**, 685–696 (2003).

62. Becerril Bravo, J. Optimización de metodologías analíticas para la determinación de contaminantes

emergentes en aguas de abastecimiento y residuales. (Universidad de Santiago de Compostela, 2012).

63. Bila, D. & Dezotti, M. Desreguladores endócrinos no meio ambiente: Efeitos e conseqüências. *Quim. Nova* **30**, 651–666 (2007).

64. García Gómez, C., Gortáres-Moroyoqui, P. & Drogui, Y. Emerging contaminants: effects and removal treatments. *Rev. QuímicaViva.* **2**, 96–105 (2011).

65. Sohoni, P. & Sumpter, J. Several environmental oestrogens are also anti-androgens. *J. Endocrinol.* **158**, 327–339 (1998).

66. Hoeger, B., Köllner, B., Dietrich, D. & Hitzfeld, B. Water-borne diclofenac affects kidney and gill integrity and selected immune parameters in brown trout (Salmo trutta f. fario). *Aquat. Toxicol.* **75**, 53–64 (2005).

67. Alvariño, C., Lloréns, M., Torres, M. & Pellón, A. Tratamiento de las aguas residuales provenientes de la industria de medicamentos. *Rev. CENIC Ciencias Químicas* **36**, 39–34 (2005).

68. Alvariño, C. Los residuos en la industria farmacéutica. *Rev. CENIC Ciencias Biológicas* **37**, 25–31 (2006).

69. Boillot, C. & Perrodin, Y. Joint-action ecotoxicity of binary mixtures of glutaraldehyde and surfactants used in hospitals: Use of the Toxicity Index model and isoblogram representation. *Ecotoxicol. Environ. Saf.* **71**, 252–259 (2008).

70. Emmanuel, E., Pierre, M. & Perrodin, Y. Groundwater contamination by microbiological and chemical substances released from hospital wastewater: Health risk assessment for drinking water consumers. *Environ. Int.* **35**, 718–726 (2009).

71. Huerta-Fontela, M., Galceran, M. T. & Ventura, F. Fast liquid chromatography–quadrupole-linear ion trap mass spectrometry for the analysis of pharmaceuticals and hormones in water resources. *J. Chromatogr. A* **1217**, 4212–4222 (2010).

72. Stackelberg, P. *et al.* Efficiency of conventional drinking-water-treatment processes in removal of pharmaceuticals and other organic compounds. *Sci. Total Environ.* **377**, 255–272 (2007).

73. Dougherty, J., Swarzenski, P., Dinicola, R. & Reinhard, M. Occurrence of herbicides and pharmaceutical and personal care products in surface water and groundwater around Liberty Bay, Puget Sound, Washington. *J. Environ. Qual.* **39**, 1173–80 (2010).

74. Demirbas, A. Heavy metal adsorption onto agro-based waste materials: A review. *J. Hazard. Mater.* **157**, 220–229 (2008).

75. Bedia, J. *et al.* A review on the synthesis and characterization of metal organic frameworks for photocatalytic water purification. *Catalysts.* **9**, 1-43 (2019).

76. Kobielska, P. A., Howarth, A. J., Farha, O. K. & Nayak, S. Metal–organic frameworks for heavy metal removal from water. *Coord. Chem. Rev*. **358**, 92–107 (2018).

77. Kickelbick, G. Introduction to Hybrid Materials. *Hybrid Mater. Synth. Charact.* (Wiley, 2007).

78. Yōgyō Kyōkai, A. & Seramikkusu Kyōkai, N. *Possibility of Hybrids Materials. Ceramics Japan*. **39**, 90-91(Yōgyō Kyōkai, 2004).

79. Nanko, M. Definitions and Categories of Hybrid Materials. *AZojomo.* **6**, 1–8 (2009).

80. Lucas Herguedas, A. *Biomasa, combustibles y sostenibilidad*. (Itagra, 2012).

81. Abril, A. & Navarro, E. *Etanol a partir de biomasa lignocelulósica*. (Aleta Ediciones, 2012).

82. Shankar, J. *et al.* A Review on Biomass Classification and Composition, Co-Firing Issues and Pretreatment Methods. *ASABE.* **1**, 1-31 (2011).

83. Hinestroza, J. & Netravali, A. *Cellulose Based Composites : New Green Nanomaterials.* (Wiley, 2014).

84. Mussatto, S. *Biomass Fractionation Technologies for a Lignocellulosic Feedstock Based Biorefinery*. (Elsevier, 2016).

85. Chua, M. & Wayman, M. Characterization of autohydrolysis aspen (P. tremuloides) lignins. Part 1. Composition and molecular weight distribution of extracted autohydrolysis lignin. *Can. J. Chem.* **57**, 1141–1149 (1979).

86. Thompson, N. HEMICELLULOSE AS A BIOMASS RESOURCE. in *Wood a Agricultural Residues* 101–119 (Elsevier, 1983).

87. Wang, Q., El-Ensashy, H. & Thongchul, N. *Bioprocessing technologies in biorefinery for sustainable production of fuels, chemicals, and polymers*. (Green Processing and Synthesis, 2013).

88. Kumar, P., Barrett, D., Delwiche, M. & Stroeve, P. Methods for pretreatment of lignocellulosic biomass for efficient hydrolysis and biofuel production. *Industrial and Engineering Chemistry Research*. **48**, 3713–3729 (2009).

89. Yang, B. & Wyman, C. Pretreatment: The key to unlocking low-cost cellulosic ethanol. *Biofuels, Bioproducts and Biorefining*. **2**, 26–40 (2008).

90. Bychkov, A. & Lomovskii, O. Mechanical Treatment Effect on the Cellulolytic Specimen Activity. *Russ. J. Appl. Chem.* **83**, 1106–1108 (2010).

91. Sánchez, O. & Cardona, C. Producción biotecnológica de alcohol carburante I: Obtención a partir de diferentes materias primas. *Interciencia* **30**, 22–47 (2005).

92. Bridgwater, A. Review of fast pyrolysis of biomass and product upgrading. *Biomass and Bioenergy* **38**, 68–94 (2012).

93. Pavlovič, I., Knez, Ž. & Škerget, M. Hydrothermal reactions of agricultural and food processing wastes in sub- and supercritical water: A review of fundamentals, mechanisms, and state of research. *J. Agric. Food Chem*. **61**, 8003–8025 (2013).

94. Sawant, S. *et al.* Effect of hydrodynamic cavitation on zooplankton: A tool for disinfection. *Biochem. Eng. J.* **42**, 320–328 (2008).

95. Montgomery, L. & Bochmann, G. Pretreatment of feedstock for enhanced biogas production. *IEA Bioenergy*. (IEA Bioenergy, 2014).

96. Zhu, L. *et al.* Research on the influence of conductivity to pulsed arc electrohydraulic discharge in water. *Journal of Electrostatics*. **72**, 1–6 (2014).

97. Lee, J. & Jeffries, T. Efficiencies of acid catalysts in the hydrolysis of lignocellulosic biomass over a range of combined severity factors. *Bioresour. Technol.* **102**, 5884–5890 (2011).

98. Grzybkowski, W. Nature and properties of metal cations in aqueous solutions. *Polish J. Environ. Stud.* **15**, 655–663 (2006).

99. Kamireddy, S., Li, J., Tucker, M., Degenstein, J. & Ji, Y. Effects and mechanism of metal chloride salts on pretreatment and enzymatic digestibility of corn stover. *Ind. Eng. Chem. Res.* **52**, 1775–

1782 (2013).

100. Marcotullio, G., Krisanti, E., Giuntoli, J. & de Jong, W. Selective production of hemicellulose-derived carbohydrates from wheat straw using dilute HCl or FeCl3 solutions under mild conditions. X-ray and thermo-gravimetric analysis of the solid residues. *Bioresour. Technol.* **102**, 5917–5923 (2011).

101. Hergert, H. *Developments in organosolv pulping – an overview*. *Environmental Friendly Technologies for the Pulp and Paper Industry* (Food and Agriculture Organization of the United Nations, 1998).

102. Mesa, L. *et al.* Preliminary evaluation of organosolv pre-treatment of sugar cane bagasse for glucose production: Application of 23 experimental design. *Appl. Energy* **87**, 109–114 (2010).

103. Zhao, X., Cheng, K. & Liu, D. Organosolv pretreatment of lignocellulosic biomass for enzymatic hydrolysis. *Applied Microbiol. Biotechnol*. **82**, 815–827 (2009).

104. Negi, S. & Pandey, A. Ionic Liquid Pretreatment. in *Pretreatment of Biomass: Processes and Technologies* 137–155 (Elsevier, 2014).

105. Gromov, V., Khrol, Y., Kalninsh, A. & Odincov, P. The mechanism of hydrotropic pulping. *Inst. Lesokhoz. Probl. Khim. Drev. Akad. Nauk Latv.* **25**, 3–27 (1963).

106. Souza-Correîa, J., Ridenti, M., Oliveira, C., Araújo, S. & Amorim, J. Decomposition of lignin from sugar cane bagasse during ozonation process monitored by optical and mass spectrometries. *J. Phys. Chem. B* **117**, 3110–3119 (2013).

107. Bali, G., Meng, X., Deneff, J., Sun, Q. & Ragauskas, A. The effect of alkaline pretreatment methods on cellulose structure and accessibility. *ChemSusChem* **8**, 275–279 (2015).

108. Doner, L. & Hicks, K. Isolation of hemicellulose from corn fiber by alkaline hydrogen peroxide extraction. *Cereal Chem.* **74**, 176–181 (1997).

109. Chen, H., Han, Y. & Xu, J. Simultaneous saccharification and fermentation of steam exploded wheat straw pretreated with alkaline peroxide. *Process Biochem.* **43**, 1462–1466 (2008).

110. Michalsk, K. & Ledakowicz, S. Alkaline hydrogen peroxide pretreatment of energy crops for biogas production. *Chem. Pap.* **68**, 913–922 (2014).

111. Gullón, P., Romaní, A., Vila, C., Garrote, G. & Parajó, J. Potential of hydrothermal treatments in lignocellulose biorefineries. *Biofuels, Bioprod. Biorefining*. **6**, 219–232 (2012).

112. Heitz, M. *et al.* Generalized correlations for the aqueous liquefaction of lignocellulosics. *Can. J. Chem. Eng.* **64**, 647–650 (1986).

113. Heitz, M. *et al.* Fractionation of Populus tremuloides at the pilot plant scale: Optimization of steam pretreatment conditions using the STAKE II technology. *Bioresour. Technol*. **35**, 23–32 (1991).

114. Mosier, N. *et al.* Features of promising technologies for pretreatment of lignocellulosic biomass. *Bioresour. Technol.* **96**, 673–686 (2005).

115. Carvalheiro, F., Duarte, L. & Gírio, F. Hemicellulose biorefineries: A review on biomass pretreatments. *J. Sci. Ind. Res*. **67**, 849–864 (2008).

116. Duff, S. & Murray, W. Bioconversion of forest products industry waste cellulosics to fuel ethanol: A review. *Bioresour. Technol*. **55**, 1–33 (1996).

117. Biswas, R., Uellendahl, H. & Ahring, B. Wet Explosion: a Universal and Efficient Pretreatment Process for Lignocellulosic Biorefineries. *Bioenergy Res*. **8**, 1101–1116 (2015).

118. Santos, A., Kawase, K. & Coelho, G. Enzymatic saccharification of lignocellulosic materials after treatment with supercritical carbon dioxide. *J. Supercrit. Fluids* **56**, 277–282 (2011).

119. Mes-Hartree, M., Dale, B. & Craig, W. Comparison of steam and ammonia pretreatment for enzymatic hydrolysis of cellulose. *Appl. Microbiol. Biotechnol.* **29**, 462–468 (1988).

120. Chundawat, S. *et al.* Multifaceted characterization of cell wall decomposition products formed during ammonia fiber expansion (AFEX) and dilute acid based pretreatments. *Bioresour. Technol.* **101**, 8429–8438 (2010).

121. Brodeur, G. *et al.* Chemical and Physicochemical Pretreatment of Lignocellulosic Biomass: A Review. *Enzym. Res. Enzym. Res.* **2011**, 1-17 (2011).

122. Vasco Correa, J., Ge, X. & Li, Y. Biological Pretreatment of Lignocellulosic Biomass. *Biomass Fractionation Technol. a Lignocellul. Feed. Based Biorefinery* **199**, 561–585 (2016).

123. Shrestha, P., Pometto, A., Khanal, S. & Van Leeuwen, J. Second-Generation Biofuel Production from Corn-Ethanol Industry Residues. *Green Energy Technol.* **62**, 71–87 (2012).

124. Wang, Z., Hauser, P., Laine, J. & Rojas, O. Multilayers of low charge density polyelectrolytes on thin films of carboxymethylated and cationic cellulose. *J. Adhes. Sci. Technol.* **25**, 643–660 (2010).

125. Moon, R., Martini, A., Nairn, J., Simonsen, J. & Youngblood, J. Cellulose nanomaterials review: Structure, properties and nanocomposites. *Chem. Soc. Rev.* **40**, 3941–3994 (2011).

126. Yao, F. *et al.* A review of recent developments in natural fibre composites and their mechanical performance. *Compos. Part A Appl. Sci. Manuf.* **51**, 98–112 (2016).

127. Beckermann, G. & Pickering, K. Engineering and evaluation of hemp fibre reinforced polypropylene composites: Fibre treatment and matrix modification. *Compos. Part A Appl. Sci. Manuf.* **39**, 979–988 (2008).

128. Pickering, K. *Properties and performance of natural-fibre composites*. *Properties and Performance of Natural-Fibre Composites* (Elsevier, 2008).

129. Sinha, E. & Panigrahi, S. Effect of plasma treatment on structure, wettability of jute fiber and flexural strength of its composite. *J. Compos. Mater.* **43**, 1791–1802 (2009).

130. Huber, T., Biedermann, U. & Müssig, J. Enhancing the fibre matrix adhesion of natural fibre reinforced polypropylene by electron radiation analyzed with the single fibre fragmentation test. *Compos. Interfaces* **17**, 371–381 (2010).

131. Li, X., Tabil, L. & Panigrahi, S. Chemical treatments of natural fiber for use in natural fiber-reinforced composites: A review. *J. Polym. Environ.* **15**, 25–33 (2007).

132. Valadez-Gonzalez, A., Cervantes-Uc, J., Olayo, R. & Herrera-Franco, P. Effect of fiber surface treatment on the fiber–matrix bond strength of natural fiber reinforced composites. *Compos. Part B Eng.* **30**, 309–320 (1999).

133. David Chukwudi, A. Comparison of Acetylation and Alkali Treatments on the Physical and Morphological Properties of Raffia Palm Fibre Reinforced Composite. *Sci. J. Chem.* **3**, 72 (2015).

134. Rachini, A., Le Troedec, M., Peyratout, C. & Smith, A. Chemical modification of hemp fibers by silane coupling agents. *J. Appl. Polym. Sci.* **123**, 601–610 (2012).

135. Bledzki, A., Mamun, A., Lucka-Gabor, M. & Gutowski, V. The effects of acetylation on properties of flax fibre and its polypropylene composites. *Express Polym. Lett.* **2**, 413–422 (2008).

136. Joseph, P. *et al.* The thermal and crystallisation studies of short sisal fibre reinforced polypropylene composites. *Compos. Part A Appl. Sci. Manuf.* **34**, 253–266 (2003).

137. Wallenberger, F. *Natural Fibers, Plastics and Composites*. *Journal of Chemical Information and Modeling* (Elsevier, 2004).

138. Follini, E., Leao, A. & Mattoso, L. *Natural polymers and agrofibers based composites*. (Embrapa Instrumentacao Agropecuaria, 2000).

139. Mohanty, A., Misra, M. & Drzal, L. Surface modifications of natural fibers and performance of the resulting biocomposites: An overview. *Compos. Interfaces* **8**, 313–343 (2001).

140. Cyras, V., Vallo, C., Kenny, J. & Vázquez, A. Effect of chemical treatment on the mechanical properties of starch-based blends reinforced with sisal fibre. *J. Compos. Mater.* **38**, 1387–1399 (2004).

141. Tijsen, C., Kolk, H., Stamhuis, E. & Beenackers, A. An experimental study on the carboxymethylation of granular potato starch in non-aqueous media. *Carbohydr. Polym.* **45**, 219–226 (2001).

142. He, X., Wu, S., Fu, D. & Ni, J. Preparation of sodium carboxymethyl cellulose from paper sludge. *J. Chem. Technol. Biotechnol.* **84**, 427–434 (2009).

143. Peinado, J. *et al. Guía ambiental del subsector fiquero. Bogotá DC: Cadena Productiva Nacional del Fique-Cadefique*. (Ministerio de Ambiente, 2006).

144. Gañán, P. & Mondragon, I. Surface modification of fique fibers. Effects on their physico-mechanical properties. *Polym. Compos.* **23**, 383–394 (2002).

145. Castellanos, O., Torres, L. & Rojas, J. *Agenda Prospectiva de Investigación y Desarrollo Tecnológico para la Cadena Productiva de Fique en Colombia*. *Ingeniería e Investigació*. **2**, (2009).

146. Ovalle, S., Blanco, C. & Combariza, M. Exploring the composition of raw and delignified Colombian fique fibers, tow and pulp. *Cellulose* **25**, 151–165 (2018).

147. Bastidas, K., Zea, H. & Sierra, C. Wastewater treatment using an iron nanocatalyst supported on Fique fibers. *Universidad Nacional de Colombia-Sede Bogotá* (Universidad Nacional de Colombia, 2016).

148. Castellanos, L., Blanco Tirado, C., Hinestroza, J. & Combariza, M. In situ synthesis of gold nanoparticles using fique natural fibers as template. *Cellulose* **19**, 1933–1943 (2012).

149. Latorre, G. & Vargas, F. Materiales compuestos orgánicos utilizados como refuerzo. *C.T.F Cienc. Tecnol. Futur.* **1**, (1999).

150. Hidalgo, M., Muñoz, M. & Quintana, K. Análisis mecánico del compuesto polietileno aluminio reforzado con fibras cortas de fique en disposición bidimensional. *Rev. Latinoam. Metal. y Mater.* **32**, 89–95 (2011).

151. Contreras, M. F., Hormaza, W. A. & Marañón, A. Fractografía de la fibra natural extraida del fique y de un material compuesto reforzado con tejido de fibra de fique y matriz resina de poliester. *Rev. Latinoam. Metal. y Mater.* **1**, 57–67 (2009).

152. Paredes, J. & Córdova, M. Estudio de polímeros híbridos estratificados de matriz poliester reforzada con fibra de vidrio y cabuya como material alternativo y su incidencia en las propiedades mecánicas en guardachoques para buses. (Universidad Técnica de Ambato, 2012).

153. Chacón, M., Blanco, C., Hinestroza, J. & Combariza, M. Biocomposite of nanostructured MnO2 and fique fibers for efficient dye degradation. *Green Chem.* **15**, 2920 (2013).

154. Bastidas, K., Sierra, C. & Zea, H. Heterogeneous Fenton oxidation of Orange II using iron nanoparticles supported on natural and functionalized fique fiber. *J. Environ. Chem. Eng.* **6**, 4178–4188 (2018).

155. Sergio, O., Blanco, C. & Combariza, M. Sintesis in situ de nanoparticulas de plata sobre fibras de fique. *Rev. Col. Quim.* **42**, 27 (2013).

156. Ortiz, P., Ovalle, S., Blanco, C. & Combariza, M. Síntesis in situ de nanopartículas de óxidos de hierro soportadas en fibras de fique y su uso en la degradación de colorantes. *Rev. Colomb. Mater.* **5**, 152–158 (2014).

157. Rodas, M., Monsalve, A. & Combariza, M. Adsorción de azufrados del petróleo. *Petrotecnia* **6**, 24–38 (2012).

158. Ovalle, S., Carrillo, V., Blanco, C., Hinestroza, J. & Combariza, M. Controlled synthesis of ZnO particles on the surface of natural cellulosic fibers: effect of concentration, heating and sonication. *Cellulose* **22**, 1841–1852 (2015).

159. Cuervo, T., Sierra, C. & Zea, H. Nanostructured MnO2 catalyst in E. crassipes (water hyacinth) for indigo carmine degradation. *Rev. Colomb. Química* **45**, 30 (2016).

160. Lismont, M., Dreesen, L. & Wuttke, S. Metal-Organic Framework Nanoparticles in Photodynamic Therapy: Current Status and Perspectives. *Adv. Funct. Mater.* **27**, 1-16 (2017).

161. Kärger, J., Ruthven, D. & Theodorou, D. *Diffusion in Nanoporous Materials*. *Diffusion in Nanoporous Materials* (Wiley-VCH, 2012).

162. Cirujano, F. & Llabrés, F. Metal Organic Frameworks as Nanoreactors and Host Matrices for Encapsulation. in *Organic Nanoreactors: From Molecular to Supramolecular Organic Compounds* (Academic Press, 2016).

163. Zhou, H., Long, J. & Yaghi, O. Introduction to metal-organic frameworks. *Chem. Rev.* **112**, 673–674 (2012).

164. Tranchemontagne, D., Hunt, J. & Yaghi, O. Room temperature synthesis of metal-organic frameworks: MOF-5, MOF-74, MOF-177, MOF-199, and IRMOF-0. *Tetrahedron*. **64**, 8553–8557 (2008).

165. Shi, R. *et al.* Cu-based metal–organic framework/activated carbon composites for sulfur compounds removal. *Appl. Surf. Sci.* **394**, 394–402 (2017).

166. Stock, N. & Biswas, S. Synthesis of Metal-Organic Frameworks (MOFs): Routes to Various MOF Topologies, Morphologies, and Composites. *Chem. Rev.* **112**, 933–969 (2012).

167. Functionalisation of Metal-Organic Frameworks via Post-Synthetic Modification (University of Bath, 2017).

168. Liu, J. & Wöll, C. Surface-supported metal-organic framework thin films: Fabrication methods, applications, and challenges. *Chem. Soc. Rev.* **19**, 1-41 (2017).

169. Li, J., Sculley, J. & Zhou, H. Metal–Organic Frameworks for Separations. *Chem. Rev.* **112**, 869–932 (2012).

170. Perry IV, J. J., Perman, J. A. & Zaworotko, M. J. Design and synthesis of metal–organic frameworks

using metal–organic polyhedra as supermolecular building blocks. *Chem. Soc. Rev.* **38**, 1400-1417 (2009).

171. Sosa, J. D. *et al.* Metal–organic framework hybrid materials and their applications. *Crystals* **8**, 1-23 (2018).

172. Lin, R., Ge, L., Diao, H., Rudolph, V. & Zhu, Z. Ionic liquids as the MOFs/polymer interfacial binder for efficient membrane separation. *ACS Appl. Mater. Interfaces* **8**, 32041–32049 (2016).

173. Fechete, I., Wang, Y. & Védrine, J. C. The past, present and future of heterogeneous catalysis. *Catal. Today* **189**, 2–27 (2012).

174. Meilikhov, M. *et al.* Stepwise deposition of metal organic frameworks on flexible synthetic polymer surfaces. *Dalton Trans.* **40**, 4838–4841 (2011).

175. Khanjani, S. & Morsali, A. Ultrasound-promoted coating of MOF-5 on silk fiber and study of adsorptive removal and recovery of hazardous anionic dye 'congo red'. *Ultrason. Sonochem.* **21**, 1424–1429 (2014).

176. Yu, M. *et al.* Covalent immobilization of metal-organic frameworks onto the surface of nylon - A new approach to the functionalization and coloration of textiles. *Sci. Rep.* **6**, 1–9 (2016).

177. da Silva Pinto, M., Sierra, C. & Hinestroza, J. In situ synthesis of a Cu-BTC metal-organic framework (MOF 199) onto cellulosic fibrous substrates: Cotton. *Cellulose* **19**, 1771–1779 (2012).

178. Bunge, M. A., Davis, A. B., West, K. N., West, C. W. & Glover, T. G. Synthesis and Characterization of UiO-66-NH2 Metal-Organic Framework Cotton Composite Textiles. *Ind. Eng. Chem. Res.* **57**, 9151–9161 (2018).

179. Qiu, S., Xue, M. & Zhu, G. Metal-organic framework membranes: From synthesis to separation application. *Chemical Society Reviews*. **43**, 6116–6140 (2014).

180. Kitagawa, S. & Matsuda, R. Chemistry of porous coordination polymers. *Pure Appl. Chem.* **79**, 2155–2177 (2007).

181. Zhuang, J. L., Terfort, A. & Wöll, C. Formation of oriented and patterned films of metal-organic frameworks by liquid phase epitaxy: A review. *Coordination Chemistry Reviews*. **307**, 391–424 (2016).

182. Küsgens, P. *et al.* Characterization of metal-organic frameworks by water adsorption. *Microporous Mesoporous Mater.* **120**, 325–330 (2009).

183. Dhaka, S. *et al.* Metal–organic frameworks (MOFs) for the removal of emerging contaminants from aquatic environments. *Coord. Chem. Rev.* **380**, 330–352 (2019).

184. McHugh, L. N. *et al.* Hydrolytic stability in hemilabile metal–organic frameworks. *Nat. Chem.* **10**, 1096–1102 (2018).

185. Howarth, A. J. *et al.* Chemical, thermal and mechanical stabilities of metal-organic frameworks. *Nature Reviews Materials*. **1**, 1–15 (2016).

186. Burtch, N., Jasuja, H. & Walton, K. Water stability and adsorption in metal-organic frameworks. *Chem. Rev.* **114**, 10575–10612 (2014).

187. Low, J. *et al.* Virtual high throughput screening confirmed experimentally: Porous coordination polymer hydration. *J. Am. Chem. Soc.* **131**, 15834–15842 (2009).

188. García, H. & Navalon, S. *Metal-Organic Frameworks : Applications in Separations and Catalysis*.

(Wiley-VCH, 2018).

189. Liu, J. *et al.* Stability Effects on CO 2 Adsorption for the DOBDC Series of Metal–Organic Frameworks. *Langmuir*. **27**, 11451–11456 (2011).

190. Taylor, J., Vaidhyanathan, R., Iremonger, S. & Shimizu, G. Enhancing water stability of metal-organic frameworks via phosphonate monoester linkers. *J. Am. Chem. Soc.* **134**, 14338–14340 (2012).

191. Kolokolov, D. *et al.* Probing the dynamics of the porous Zr terephthalate UiO-66 framework using 2H NMR and neutron scattering. *J. Phys. Chem. C* **116**, 12131–12136 (2012).

192. Jasuja, H., Burtch, N., Huang, Y., Cai, Y. & Walton, K. Kinetic water stability of an isostructural family of zinc-based pillared metal-organic frameworks. *Langmuir*. **29**, 633–642 (2013).

193. Wang, C., Liu, X., Keser Demir, N., Chen, J. P. & Li, K. Applications of water stable metal-organic frameworks. *Chemical Society Reviews*. **45**, 5107–5134 (2016).

194. Kirchon, A., Feng, L., Drake, H. F., Joseph, E. A. & Zhou, H. C. From fundamentals to applications: a toolbox for robust and multifunctional MOF materials. *Chem. Soc. Rev.* **47**, 8611–8638 (2018).

195. Holder, G. A. & Winkler, J. Crystal-growth poisoning of n-paraffin wax by polymeric additives and its relevance to polymer crystallization mechanisms. *Nature*. **207**, 719–721 (1965).

196. Wuttke, S., Lismont, M., Escudero, A., Rungtaweevoranit, B. & Parak, W. J. Positioning metal-organic framework nanoparticles within the context of drug delivery – A comparison with mesoporous silica nanoparticles and dendrimers. *Biomaterials*. **123**, 172–183 (2017).

197. Jhaveri, J. & Murthy, Z. Nanocomposite membranes. *Desalin. Water Treat.* **12**, 1–17 (2015).

198. Uemura, T., Yanai, N. & Kitagawa, S. Polymerization reactions in porous coordination polymers. *Chem. Soc. Rev.* **38**, 1228–1236 (2009).

199. Masel, R. I. *Principles of adsorption and reaction on solid surfaces*. (*Wiley series in chemical engineering*, 1996).

200. Wen, J., Fang, Y. & Zeng, G. Progress and prospect of adsorptive removal of heavy metal ions from aqueous solution using metal–organic frameworks: A review of studies from the last decade. *Chemosphere*. **201**, 627–643 (2018).

201. Canivet, J., Fateeva, A., Guo, Y., Coasne, B. & Farrusseng, D. Water adsorption in MOFs: Fundamentals and applications. *Chem. Soc. Rev*. **43**, 5594–5617 (2014).

202. Furukawa, H., Cordova, K. E., O'Keeffe, M. & Yaghi, O. M. The chemistry and applications of metal-organic frameworks. *Science.* **341**, 1230444 (2013).

203. Kumar, P., Bansal, V., Kim, K. H. & Kwon, E. E. Metal-organic frameworks (MOFs) as futuristic options for wastewater treatment. *J. Ind. Eng. Chem.* **62**, 130–145 (2018).

204. Canivet, J., Fateeva, A., Guo, Y., Coasne, B. & Farrusseng, D. Water adsorption in MOFs: Fundamentals and applications. *Chem. Soc. Rev.* **43**, 5594–5617 (2014).

205. Ke, F. *et al.* Thiol-functionalization of metal-organic framework by a facile coordination-based postsynthetic strategy and enhanced removal of Hg 2+ from water. *J. Hazard. Mater.* **196**, 36–43 (2011).

206. Saleem, H., Rafique, U. & Davies, R. P. Investigations on post-synthetically modified UiO-66-NH2 for the adsorptive removal of heavy metal ions from aqueous solution. *Microporous Mesoporous*

Mater. **221**, 238–244 (2016).

207. Abbasi, A., Moradpour, T. & Van Hecke, K. A new 3D cobalt (II) metal-organic framework nanostructure for heavy metal adsorption. *Inorganica Chim. Acta* **430**, 261–267 (2015).

208. Liang, L. *et al.* In situ large-scale construction of sulfur-functionalized metal-organic framework and its efficient removal of Hg(II) from water. *J. Mater. Chem. A*. **4**, 15370–15374 (2016).

209. Fang, Q. R. *et al.* Functional mesoporous metal-organic frameworks for the capture of heavy metal ions and size-selective catalysis. *Inorg. Chem.* **49**, 11637–11642 (2010).

210. Huang, L., He, M., Chen, B. & Hu, B. A designable magnetic MOF composite and facile coordination-based post-synthetic strategy for the enhanced removal of Hg2+ from water. *J. Mater. Chem. A*. **3**, 11587–11595 (2015).

211. Luo, F. *et al.* High-performance Hg2+ removal from ultra-low-concentration aqueous solution using both acylamide- and hydroxyl-functionalized metal-organic framework. *J. Mater. Chem. A*. **3**, 9616–9620 (2015).

212. Halder, S., Mondal, J., Ortega-Castro, J., Frontera, A. & Roy, P. A Ni-based MOF for selective detection and removal of Hg2+ in aqueous medium: a facile strategy. *Dalt. Trans.* **46**, 1943–1950 (2017).

213. Liu, T. *et al.* Alkenyl/Thiol-Derived Metal-Organic Frameworks (MOFs) by Means of Postsynthetic Modification for Effective Mercury Adsorption. *Chem. - A Eur. J.* **20**, 14090–14095 (2014).

214. Yee, K. K. *et al.* Effective mercury sorption by thiol-laced metal-organic frameworks: In strong acid and the vapor phase. *J. Am. Chem. Soc.* **135**, 7795–7798 (2013).

215. Rudd, N. D. *et al.* Highly Efficient Luminescent Metal-Organic Framework for the Simultaneous Detection and Removal of Heavy Metals from Water. *ACS Appl. Mater. Interfaces*. **8**, 30294–30303 (2016).

216. Bhattacharjee, S., Lee, Y. R. & Ahn, W. S. Post-synthesis functionalization of a zeolitic imidazolate structure ZIF-90: A study on removal of Hg(ii) from water and epoxidation of alkenes. *CrystEngComm*. **17**, 2575–2582 (2015).

217. Sohrabi, M. R. Preconcentration of mercury(II) using a thiol-functionalized metal-organic framework nanocomposite as a sorbent. *Microchim. Acta* **181**, 435–444 (2014).

218. Mon, M. *et al.* Selective and Efficient Removal of Mercury from Aqueous Media with the Highly Flexible Arms of a BioMOF. *Angew. Chemie Int. Ed.* **55**, 11167–11172 (2016).

219. Xiong, Y. Y. *et al.* Using MOF-74 for Hg2+ removal from ultra-low concentration aqueous solution. *J. Solid State Chem.* **246**, 16–22 (2017).

220. Luo, X. *et al.* Novel thymine-functionalized MIL-101 prepared by post-synthesis and enhanced removal of Hg2+ from water. *J. Hazard. Mater.* **306**, 313–322 (2016).

221. Li, X. *et al.* Water Contaminant Elimination Based on Metal-Organic Frameworks and Perspective on Their Industrial Applications. *ACS Sustainable Chemistry and Engineering*. **7**, 4548–4563 (2019).

222. Todaro, M. *et al.* Decomposition Process of Carboxylate MOF HKUST-1 Unveiled at the Atomic Scale Level. *J. Phys. Chem. C* **120**, 12879–12889 (2016).

223. Lin, S. *et al.* Adsorption behavior of metal-organic frameworks for methylene blue from aqueous

solution. *Microporous Mesoporous Mater.* **193**, 27–34 (2014).

224. Al-Janabi, N. *et al.* Mapping the Cu-BTC metal-organic framework (HKUST-1) stability envelope in the presence of water vapour for CO2 adsorption from flue gases. *Chem. Eng. J.* **281**, 669–677 (2015).

225. McKinstry, C., Cussen, E. J., Fletcher, A. J., Patwardhan, S. V. & Sefcik, J. Scalable continuous production of high quality HKUST-1 via conventional and microwave heating. *Chem. Eng. J.* **326**, 570–577 (2017).

226. Lin, K. S., Adhikari, A. K., Ku, C. N., Chiang, C. L. & Kuo, H. Synthesis and characterization of porous HKUST-1 metal organic frameworks for hydrogen storage. *Int. J. Hydrogen Energy*. **37**, 13865–13871 (Pergamon, 2012).

2. Fique fiber characterization

2.1 Abstract

The use of biomass in the form of fibers has become an interesting alternative to reduce the dependence of contaminating/energy demanding man-made materials. However, for applications where a chemical interaction between the biomass surface and foreigners' molecules is required (i.e. catalyst, wastewater treatment, adsorption), it is necessary to modify the characteristics of the fiber surface. Due to its attractive physicochemical characteristics, low cost and abundance in tropical and subtropical areas, fique fiber (*Furcraea andina spp*) is being widely studied in different processes as support, adsorbent, raw material, among others. This chapter presents a complete characterization of the raw fique fiber, that includes chemical structure, morphological, textural, surface, structural, thermal and mechanical characterizations. From the characterization carried out, it can be concluded the fique is an intermediate fiber, not as hard as sisal but not as soft as jute, with potential in applications related to the use of lignocellulosic biomass, allowing the opportunity to develop new research areas to valorize this fiber, which is currently mainly a residue in Colombia.

Key words: Fique fiber, characterization, cellulose, biomass.

2.2 Introduction

In the COP21 (21st United Nations Climate Change Conference, Paris), regarding the alarming world climate change, biomass was mentioned as a potential solution for many current problems. Biomass is a set of renewable organic matter, accumulated in different compounds (polysaccharides and fats, among others) along the trophic chain, resulting from the transformation process of solar energy into chemical energy through the photosynthesis in plants[1]. Thereby, biomass is considered a renewable source of energy, chemicals, and materials. It comes from biodegradable fraction of wastes, residues and products of biological origin

resulting from agricultural activities, forestry and related industries, as well as the degradable biological fraction of municipal waste [2].

Lignocellulosic biomass is the most abundant organic material on earth; it is constituted fundamentally by cellulose, hemicellulose, lignin, extractives and inorganic components. This type of biomass has the advantage of being biodegradable and renewable, while contributes to the reduction of CO_2 emissions, avoiding erosion and soil degradation [3]. Despite the great variety and quantity of lignocellulosic biomass, not all can be used efficiently, due to its availability, concentration, and chemical composition.

An example of lignocellulosic biomass is the fique fiber, obtained by defibering of *Furcraea Andina spp* leaves (Figure 2.1a). In Colombia fique crops are located mainly in the Andean region, where fique has an important social role providing employment to about 70000 families, and helping to the substitution of illicit crops [45]. In addition, this fiber has shown that can be used in materials such as fabrics, threads, strings, packaging and handicrafts, due to its exceptional properties (biodegradable, flexible, low cost, low density, and excellent thermal and mechanical properties) in comparison to synthetic polymers [4].

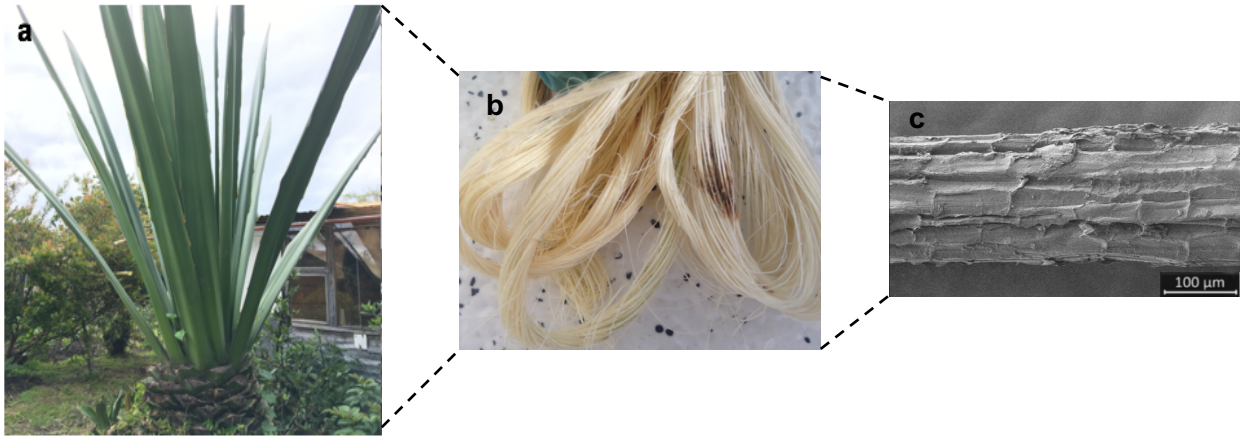


Figure 2.1. a) *Furcraea Andina* plant, b) Fique fiber, c) Raw fique fiber micrograph 250X

Some authors like Peinado [4], Ovalle [5], and Gañan *et al.* [6], have characterized the fiber of fique, which may vary according to the specie, crop and region where it grew. In their reports, the fiber is described as a set of elementary cellulose fibrils joined by hemicellulose and lignin, with a very heterogeneous surface morphology which provides many channels, non-pores and cavities (Figure 2.1c).

Specificaly, cellulose is an attractive natural polymer due to, among others, the presence of a large number of hydroxyl groups which allow to perform a variety of tailor-made chemical modifications giving to biomass specific physicochemical properties according to the desired application. Chacón Patiño [7], Wang [8] and Chattopadhyay *et al.* [9] developed hybrid materials with enhanced chemical, mechanical, thermal and catalytic properties using cellulose extracted from natural fibers, taking advantage of the fact that the fiber surface is negatively charged (due to the presence of oxygen atoms), which facilitates electrostatic interactions with metal ions, also using its porous and heterogeneous structure, characteristics that assist to the control, dispersion and stabilization of nanometric compounds [10].

Hinestroza *et al.* [7] hypothesized that hybrid materials from fibers have improved mechanical, thermal and chemical properties compared to raw fibers, due to an effect similar to "vulcanization", in which nanoparticles replace lignin and hemicellulose and act as a "glue" between individual strands of microfibers. Pretreatments such as ultrasound [7] and alkaline hydrogen peroxide (AHP) [5] are essential in the conversion of lignocellulosic biomass to value added products with enhanced properties. These processes in fibers make cellulose more accessible, exposing approximately 10% more crystalline cellulose, eliminate residues such as pigments, saponins, hecogenins, waxes and calcium salts, increase the number of reactive groups (e.g. hydroxyl) and at the same time the fiber surface tends to be more homogeneous [11,12].

As a preliminary work for subsequent use of raw fique fiber as a solid matrix in the synthesis of hybrid materials, here it is reported a complete characterization of this fiber that includes: crystalline structure, morphology, structural, textural, thermal and mechanical properties.

2.3 Materials and methods

2.3.1 Chemicals and materials

Sulphuric acid (95-97%, MerckMillipore), ethanol absolute (99.8% v/v, Panreac), hydrochloric acid (37%, MerckMillipore), sodium hydroxide pellets (MerckMillipore) and potassium nitrate (Sigma-Aldrich) were used as received. Raw fique fiber with similar moisture, color, length, width, and free of knots, diseases and pests was provided by Compañia de Empaques S.A, who collects the fiber from the Colombian coffee region.

2.3.1. Characterization

- Humidity

Humidity of raw fiber was determined on 1 g of fique using an infrared radiation scale (PMB53-Adam) for 25 min, at 100 °C. Samples did not undergo any other treatment previous to the humidity determination experiment.

- Chemical Structure

The National Renewable Energy Laboratory methodology (NREL) [13] was implemented for the determination of structural components in the fique fiber. NREL consisted of two acid hydrolysis steps to fractionate biomass. The first step allowed the determination of the acid-insoluble lignin in the sample (via standardized gravimetry procedures). The acid-insoluble residue was placed in a crucible and loaded in an oven at 105 °C (Labtech Essa) until constant weight. Then, the samples were removed from the oven and cooled in a desiccator, and their weight was recorded. Finally, the crucibles and residue were placed in a furnace (Thermo Scientific Lindberg/Blue Moldatherm™) at 575 °C for 4 h. The weight of cold samples was recorded again. The second step used UV-Vis spectroscopy to determine acid-soluble lignin, where the absorbance of an aliquot from the hydrolysis products was measured at 320 nm, using a solution of sulfuric acid 4%(v/v) as blank.

A second stage in the NREL characterization involved the fragmentation of the fibers into soluble monomeric forms (glucose, xylose and arabinose), followed by a quantification using HPLC chromatography (VWR-HITACHI ELITE Lachrom system, consisting of a model L-2130 quaternary pump and a IR detector, Model Shodex RI-101). A stainless steel Aminex HPX-87H column (300 x 7.8 mm I.D.) was employed with filtered and degassed HPLC grade sulphuric acid 5 mM as mobile phase. Ezchrom Elite software Chromatography data system was used for data processing and reporting. To achieve reproducibility, an automatic injector (Model L-2220) adjusted to 20 µL was used. The flow rate was kept at 0.6 mL/min with a temperature of 65 °C in the column. Peak identities of the degradation products, both retention time and spectra matching of standard compounds, were confirmed.

In addition, extractives determination was done by the NREL methodology [14] with the purpose to quantify non-structural material in the biomass sample. The methodology includes two steps into the solid/ liquid extraction process made by Soxhlet: first using water and then ethanol as solvent. The results are reported, on a dry weight basis, as a weight percentage of the biomass.

Complementary, with the aim to determine the carbon, hydrogen, nitrogen, sulfur and oxygen mass percentage a CHNS/O elemental analysis was done for the fique fiber using a Micro Cube Analyzer, from Elemental GmbH, Langenselbold, Germany. All the determinations were done in triplicate and the oxygen content were calculated by subtraction.

Additional superficial chemical information of the fiber was obtained using Energy-Dispersive X-ray Spectroscopy (EDX) coupled to a SEM. Chemical elemental analysis performed in a Zeiss Auriga FIB-SEM (GeminiSEM) attached to the Oxford INCA EDS equipment with MAX80 SDD detector system, operating in spectrum collecting mode under high vacuum conditions, 20 kV and approximate at a 5 mm of working distance.

- Surface Characterization

pH_{zpc} was determined using the drift method in which solutions with 45 mL of KNO_3 (1% vol.) were adjusted to an initial pH in the range of 2 to 10 by adding HCl 0.1 M or NaOH 0.1 M. The volume of each solution was completed up to 50mL adding KNO_3 (1% vol.). Once the pH of the solutions was set, 0.1 g of raw fique fiber was added, the resulting suspensions is stirred for 24 h at 25 °C, and the pH of the supernatants is registered [15].

Acidic and basic surface sites were determined by the Boehm titration method [16]. 1 g of fique fiber (raw) was soaked into 50 mL NaOH 0.1 M for acid sites determination or 0.1 M HCl for basic sites determination. Solutions were stirred for 5 days at 30 °C, and then 10 mL from each suspension was titrated with a standard solution. pH data were collected up to a total volume of 25 mL of standard solution added.

Fourier Transform Infrared Spectroscopy (FT-IR) was used to identify changes in the fiber functional groups. FT-IR was determined using an ATR (PIKE) diamond crystal accessory attached to a FT-IR Nicolete iS 10 spectrometer (Thermo Fisher Scientific). Scans of 20 readings were performed by spectrum and data were recorded from 4000 to 600 cm^{-1}.

To analyze the wetting fiber surface a novel method published by Schellbach *et al.* [17] to measure the contact angle was implemented. Two fibers with similar diameter were aligned parallel with a distance ~ 1 mm between them under an Olympus microscope at room temperature. A drop of deionized water was deposited in this small space, in order to measure the hanging bridge to enlarge the lateral dimension of the water bridge and reinforce the spreading of it over the dry sections of the fibers. After the water column enlarged and the spherical menisci stabilized, the high-resolution images were captured using the software cellSens. Five images were captured

for both enlarged and reduced water columns on each sample, the values of the diameter (*d*) and height (*h*) of the meniscus were obtained. The contact angle was calculated using the Eq. 2.1:

$$\theta = 90 - 2\tan^{-1}\left(\frac{2d}{h}\right) \qquad (2.1)$$

- Structural Characterization

Crystalline fique fiber structure was measured at room temperature with an XPert Pro MPD diffractometer with monochromator of crystal graphite using Cu Kα (λ = 1.5406 Å) at 40 kV and 30 mA. Diffraction patterns were obtained in the range of 2theta =10-40°, with a step size of 0.02° and measuring time of 50 s per step. Experimental data were analyzed using PANalytical X'Pert HighScore Plus database.

- Morphological and Textural Characterization

The total surface area was measured by the adsorption of nitrogen at 77 K, using a Quantachrome NOVA e-Series surface area analyzers. N_2 isotherms were performed on raw fiber samples. Before N_2 adsorption, the samples were degassed at 80 °C for 8 h. The calculation of the total surface area was established using the BET method [18].

Morphological characterization of fique fibers was achieved via Field Emission Scanning Electron Microscope (FESEM) and performed on thin-film gold-coated samples using a Zeiss Auriga FIB-SEM (GeminiSEM) scanning electron microscope, coupled to a secondary electrons (SE2) detector. The micrographs were taken at 1.5 kV, working distance (WD) ranging from 4.9 to 5.2 mm, at different magnifications.

- Thermal Characterization

Thermal gravimetric analysis (TGA) and Differential Scanning Calorimetry (DSC) were performed using a simultaneous thermal analyzer (STA 409 PC/4/H Luxx) in a temperature range from 50 to 900 °C at a heating rate of 10 °C/min using an inert (N_2, flow of 50 $cm^3.min^{-1}$) and air (flow of 50 $cm^3.min^{-1}$) atmosphere.

- Mechanical Characterization

Dynamic Mechanical Analysis (DMA) was performed in a Mettler Toledo DMA1 analyzer, one fiber was centered inside the sample holder using single-cantilever clamps, with a free length of 17.5 mm. The DMA was done at room temperature, and the oscillation conditions were fixed at 1Hz and the amplitude was 20 μm (i.e. 0.11% strain), which was well within the linear viscoelastic

region. Storage modulus E (MPa) were collected during the test; the final value includes an average of three measurements for each sample.

2.4 Results and Discussion

- Structural characterization

The chemical composition of raw fique fibers show a value of humidity of 10.3% (Table 2.1), which is related to the water retention reported as an indicator of fibrillation into the fiber. This moisture acts as a separating agent in the fiber when interacts with other interfaces [19]. The value obtained in this study is similar to the value reported for other fibers, such as jute and sisal [20,21].

Table 2.1. Chemical composition of raw jute fibers analyzed by NREL.

Component	Composition percentage (%)
Humidity	10.3 ± 0.9
Ashes	1.1 ± 0.2
Extractives	15.3 ± 0.3
Cellulose	42.1 ± 0.6
Hemicellulose	13.0 ± 0.4
Lignin	18.2 ± 0.8

The ashes percentage measured in fique fiber was 1.1%, value represented by inorganic compounds, including Ca, K, Mg, and Si [22]. A similar value was reported by Peinado *et al.* [4] for fique from the Santander region (northeast of Colombia), such differences in property values are usually related to non comparable agriculture procedures and environmental conditions that varied from region to region.

Additionally, the 15.3% extractives determined includes waxes, steroids (i.e. hecogenine and sapogenine), nitrogenous material and some phenolic substances. In general, extractives are formed by non-structural material responsible for properties like color, smell and resistance to wilt [23]. Some authors have attributed the presence of high amounts of extractives to the type of fertilizer used during cultivation but also to the defibration process employed [24].

Fique analyzed in this study presents 42.1% of cellulose in its composition, which is very different from the 73%, 63% and 52% reported by Peinado [4], Ovalle [5] and Gañan *et al.* [6], respectively. However, the difference between the result in this study and other authors can be attributed to the fact that the current fique characterization includes an extractive analysis which allowed to identify that some components such as non-structural sugars could act as interferers when the

cellulose is quantified [14]. Nevertheless, the cellulose value measured in this study is similar to percentages reported by other authors of 51%, 50% and 44% for fibers similar to fique such as jute [3], sisal [25] and kenaf [26], respectively.

The percentage of hemicellulose (13.0%) is related only to the presence of xylose as monomer. It was confirmed that the hemicellulose configuration present into the fique fiber corresponds to glucuronoxylans, because fique fiber does not have arabinose in its chemical structure. For this reason, this type of fiber is considered from its chemical structure more similar to hardwoods [27]. The percentage obtained for the hemicellulose is similar to reports for fique fiber made by Peinado *et al.* [4], where values close to 10.5% were reported.

Several studies have reported that lignin constitutes between 10 to 25% of the cell wall in most natural fibers [28]. In this work lignin is the 18.2%, value that includes the acid-insoluble lignin (AIL) and acid-soluble lignin (AIS), percentage considerable similar to that reported by Peinado *et al.*[4] of 11.3% and Gañan *et al.* [6] of 14.5%.

The average values of carbon, hydrogen, nitrogen, sulfur and oxygen percentage from the elemental analysis are shown in Table 2.2. Nitrogen and sulfur were not detected; in this way, the fiber is mainly constituted by carbon, oxygen and hydrogen as was expected because natural polymers like cellulose and hemicellulose are organic molecules. The values obtained for raw fique fiber are similar to fibers like jute (C:43.3%, H:5.8%, O:50.1%)[29] and sisal (C:45.7%, H:5.9%, O: 48.1%)[30]. It allowed to concluded that these values are typical for naturals fibers.

Table 2.2. CHNS/O results for the raw fique fiber analyzed in this work.

Element	Content
C (%)	45.3 ± 0.1
H (%)	6.4 ± 0.1
N (%)	0.0 ± 0.0
S (%)	0.0 ± 0.0
O (%)	48.2 ± 0.1

The EDX spectroscopy for raw fiber (Figure 2.2) shows large carbon and oxygen peaks as was expected for an organic material and it was consistent with the elemental analysis reported in Table 2.2. It also agreed with other reports [4]. The EDX spectrum also evidenced the presence of other trace elements such as potassium (K) and aluminum (Al) resulting of the nutrients acquired from the soil by the *Furcraea Andina spp* plant during its cultivation and growth. Particularly, the

presence of calcium (Ca) is due to residues from the defibration process of the plant's leaves, which is typical in lignocellulosic biomass [4,31].

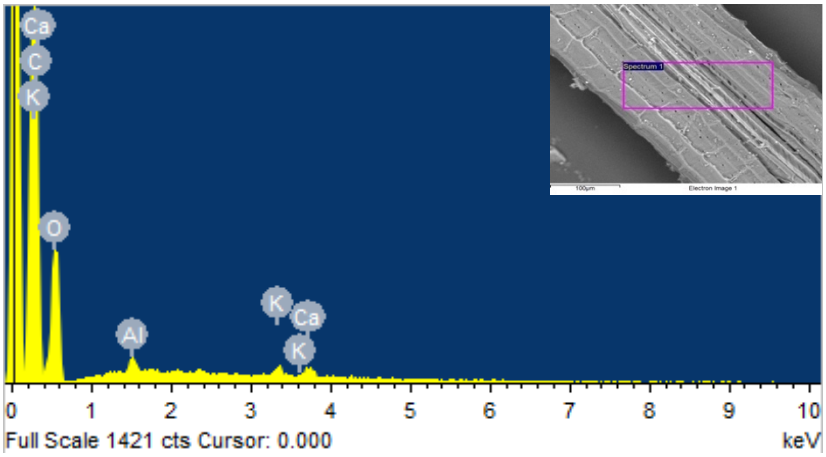


Figure 2.2. EDX profile of raw fique fibers.

- Morphological and textural characterization

The surface of raw fique fiber is covered with scales-like structures tidily packed, rectangular in shape and with an average length and width of 80 µm and 25 µm, respectively (Figure 2.3a). On the surface it can be observed the presence of clusters and aggregates (Figure 2.3b,c), usually associated with waste from the sheet defibration process, and spherical capsules with an approximate size of 1 µm (Figure 2.3d), formations attributed to the presence of *Streptococcus bacteria* [32]. In addition, a heterogeneous surface with a suggestion of roughness can be observed (Figure 2.3) is associated with the presence of lignin and hemicellulose, as reported previously by Chen *e al.* [33].

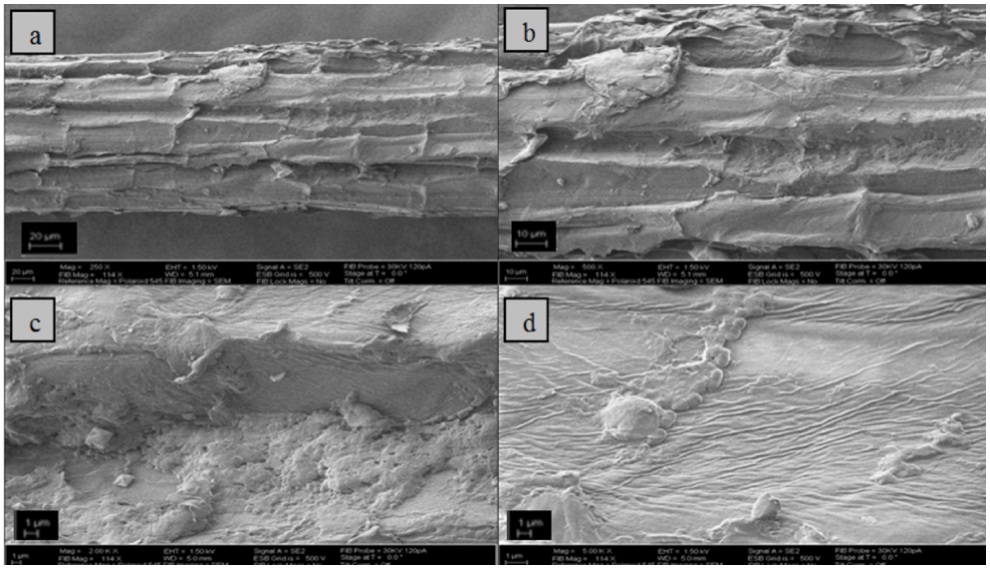


Figure 2.3. SEM micrographs of the raw fiber, a) 250X, b) 500X, c) 2000X, d) 5000X.

From the raw fique fiber isotherm (green dots in Figure 2.4.) is possible to obtain information on the textural properties of this material. It has a characteristic type II shape according to the IUPAC classification which is associated with non-porous solids [34], agreeing with reports by other authors in which the poor and almost null porosity of natural fibers is evidenced [35].

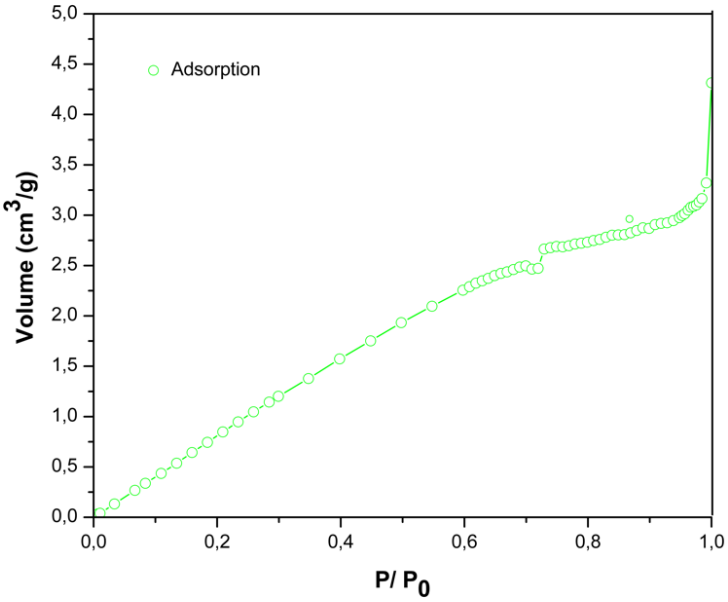


Figure 2.4. Adsorption isotherm for raw fique fiber.

The isotherm in Figure 2.4 has a linear trend in the region of low / medium relative pressures and is convex near saturation pressure, this type of isotherm is a frequent profile in physical adsorption processes in which the interactions are not very specific and fit the BET equation quite well. A surface area of 8.0 ± 0.3 $m^2 g^{-1}$ was obtained for the raw fique fiber, confirming the lack of extended porosity for this type of biomaterials. However, it should be noted that although the fit of the BET model was good, the N_2 adsorption isotherms of natural materials such as natural fibers often do not fully describe the material textural characteristics because of low surface areas of this type of material.

- Surface characterization

Figure 2.5 shows the pH curve used to determinate the pH_{zpc}, the raw fiber presents an intercept with the zero value of the abscise at 5.32, indicating an acid behavior. Probably, this behavior is caused by the presence of different ionizable functional groups such as carboxylic, phenolic, alcoholics and hemiacetal groups [36], contained in the macromolecules of hemicellulose, lignin and cellulose.

The quantification of acidic and basic sites by the Boehm method [16] (Table 2.3) fit very well with

the results obtained in the point of zero charge characterization. The surface sites were calculated in miliequivalents of titrant solution using Eq. 2.2.

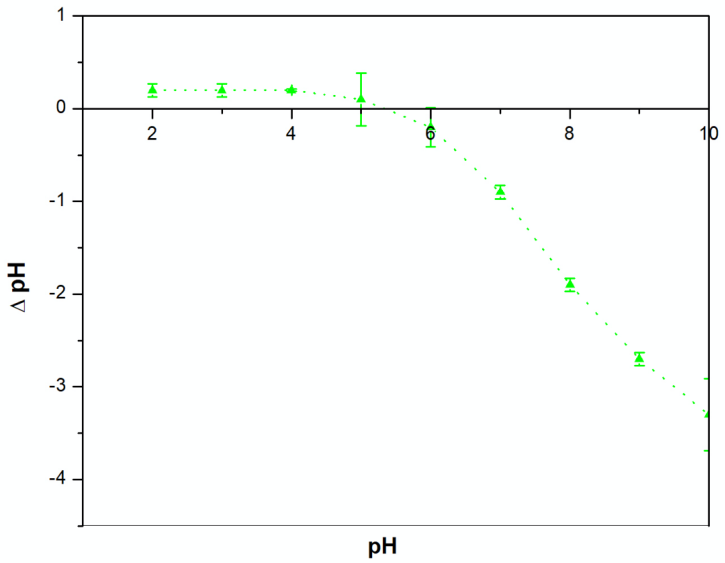


Figure 2.5. pHzpc for the raw fiber.

The quantification of acidic and basic sites by the Boehm method [16] (Table 2.3) fit very well with the results obtained in the point of zero charge characterization. The surface sites were calculated in miliequivalents of titrant solution using Eq. 2.2. Consequently, the difference between initial moles of HCl and moles of HCl consumed by NaOH titration represents the number of acidic sites on fique fiber. Additionally, the difference between initial moles of NaOH and moles of NaOH consumed by HCl titration represents the amount of basic sites on fique fiber, as expressed in Eq. 2.2 [37]:

$$\text{Sites} = \frac{V_T C_T - V_A C_A}{\text{Sample weight}} \qquad (2.2)$$

Where V_T, C_T and C_A, V_A are the concentration and volume of the titrant and analyte solution. The sample weight represents the dry weight of fique fiber before the procedure subjected to the titration.

Table 2.3. Results of the acidic and basic sites in the fique fiber

Sites	me/g
Acids	0.700 ± 0.141
Basics	0.050 ± 0.004

The FTIR – ATR spectrum of the raw fibers shows a band in the region between 3600 and 3200 cm^{-1}, where the OH groups were identified (Figure 2.6). In addition, the bands located at 1730

and 1240 cm^{-1} assigned to C=O linkage in hemicellulose and vibrations of aromatic ether linkages in lignin, were identified, respectively [5,38].

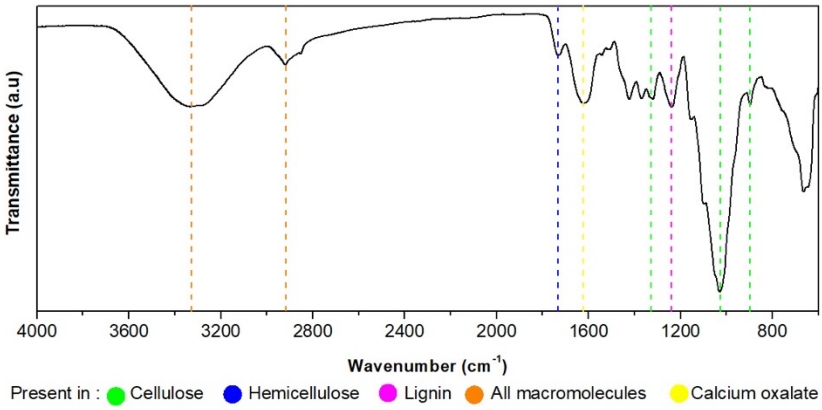


Figure 2.6. FTIR - ATR spectrum of raw fique fiber between 4000 and 600 cm^{-1}.

As expected, the spectra showed characteristic bands for the macromolecules (cellulose, hemicellulose and lignin) present in fique fiber, with OH and CH stretching vibrations approximately over 3300 cm^{-1} and 2910 cm^{-1}, respectively [5,39]. Specifically, important bands for cellulose are present at 898, 1029 and 2920 cm^{-1} which are related to the glycosidic bond β-(1→4), C-O-C anhydroglucose unit skeletal vibration and the CH_2 functional group present in the general chemical formula of monosaccharides like glucose [59]. In addition, there are signs close to 1600 cm^{-1}, which is an indication of the presence of calcium oxalate, from the EDX and NREL described above. It was evidenced that these types of compounds can be found after the defibration process as residues [40].

Another important property to be characterized is the wetness; it will affect the adhesion in the hybrid material between the constituent elements, this will influence the stability, compatibility and mechanical properties of the material [41]. Particularly, the measurement of the contact angle in natural fibers has been a challenge because these types of materials have non-circular and heterogeneous cross-sections, non-uniform diameters (between fibers and their segments), and often rough surfaces [42]. Schellbach *et al.* developed an alternative method to measure the contact angle in the natural fibers with reproducible estimates, through the spherical menisci analysis formed by a small volume of water deposited between two fibers [17]. Figure 2.7a shows a representation of the experimental setup made during the contact angle measurements of fique fibers maintained under an optical stereoscopic microscope, in order to determine the diameter (d) and height (h) of the meniscus on at least one side of the water column. The Olympus

microscope software (Figure 2.7b) was used and the contact angle value was determined using Eq. 2.1.

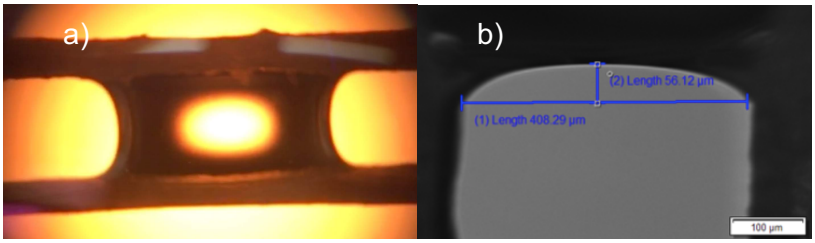


Figure 2.7. a) Optical micrographs of liquid bridges formed between two raw fique fibers and resulting menisci, and b) measurement of the distance (*d*) and height of the spherical menisci formed (*h*).

The contact angle determined for the raw fique fiber was 43.4° ± 6.5° demonstrating a weakly hydrophilic character, attributed to the components of the natural fibers like cellulose and hemicellulose (sugar polymers), lignin (complex polymer of aromatic alcohols) and extractives (waxes, saponins and hecogenins). Specifically, cellulose and hemicellulose are responsible for the fiber hydrophilic nature, and lignin has less water affinity caused by the aromatic rings present in its chemical structure. The only truly hydrophobic component is the waxes present in natural fibers resulting from the structural characteristics of plants to conserve water and keep the mechanical resistance [23]. However, the wetness is governed by the chemical composition and the surface structure of the material. It was evidenced in the SEM micrographs of the raw fique fiber (Figure 2.3) that a heterogeneous surface generates roughness due to the irregularities present, which act as mechanical barriers for the liquid to advance during the contact angle measurements. Similar values of contact angle for fique fiber was reported by Schellbach *et al* [17].

- Structural characterization

XRD profiles for raw fibers are consistent with cellulose diffractograms showing characteristic broad peaks (Figure 2.8), with one centered around 22° associated to polycrystalline cellulose and another at 18° related to amorphous cellulose [43].

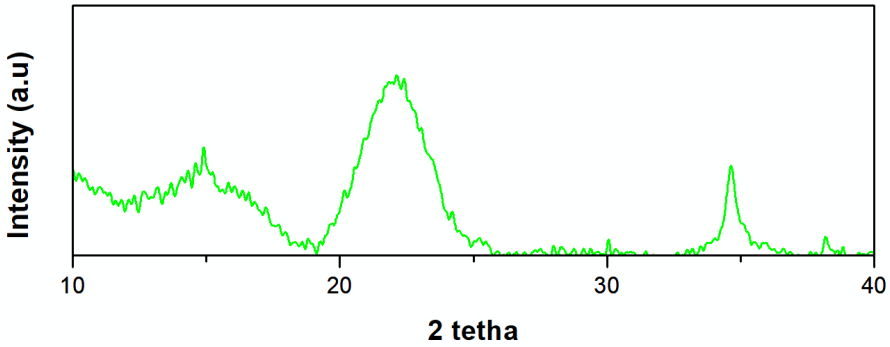


Figure 2.8. XRD diffractogram of raw fiber.

Cellulose has six polymorphs and, particularly, the fique fiber analyzed is classified as crystalline cellulose type I (natural and thermodynamically metastable cellulose) [44]. Plants as fique evidence monoclinic network (Iβ), which presents the (0 0 2), (1 1 0) and (1 1 0) planes [18]. Using Eq. 2.3 is possible to calculate the crystallinity index (C_i), which is a quantification of the percentage of crystalline cellulose in the sample. Where, C_i was calculated as the ratio of the peak heights of I (2 0 0) and the minimum intensity of I_{am} (amorphous), between the peaks of the planes (2 0 0) and (1 1 0):

$$C_i(\%) = \left(1 - \frac{I_{am}}{I_{200}}\right) \times 100 \qquad (2.3)$$

The crystalline cellulose contained in the raw fique fiber reached a value of 60.7%, the crystal index is dependent of the chemical species presents in the cellulose structure, agreeing with results reported by other authors like Ovalle *et al.* [5], who informed for the same raw fiber a value C_i of 63%, similar biomass such as jute and sisal, reported Ci values correspond to 75.7% [45] and 64.6% [46], respectively. The high values of crystallinity index are related to support functions given by the sclerenchyma cells, which owe their properties to the secondary wall present in cellulose, hemicellulose, and lignin in a very organized way, confirming the optimal intrinsic mechanical properties of natural fibers [47].

The average crystallite size (Eq. 2.4) in the cellulose was calculated from XRD data using the Scherrer's equation [24]. Based on the line broadening effect at the full width half maximum (FWHM) of the (0 0 2) peak.

$$D = \frac{k\lambda}{\beta \cos\theta} \qquad (2.4)$$

Where *D* is the average crystallite size, *k* is Scherrer constant, *λ* is wavelength of X-ray, *β* is the FWHM and *θ* is diffraction angle. Results obtained for the diameter of the crystallite cellulose was 7.81 nm, previous reports have calculated a value around 5-6.2 nm [24,48,49] for the crystal size of cellulose using XRD data.

- Thermal characterization

All the fiber analyzed by TGA (Figure 2.9a) presented an approximate 5% of mass loss between 30 °C and 150 °C, attributed to the evaporation of the humidity. This value was confirmed by the NREL analysis reported above in Table 2.1, where the value obtained was 10.3%, the difference could be caused by the ambient exposure of the raw material. A second change was evidenced close to 260 ºC, with approximate 60% of weight loss related to the hemicellulose degradation [50].

Followed by 30% of weight loss between 350 ºC and 500 ºC, generally attributed to the cellulose pyrolysis [51]. Beyond 500 °C, sugar polymers (cellulose and hemicellulose) was expected to be pyrolyzed with some remaining material, frequently related to lignin [50]. In addition, the 5% of the residual mass is related according to the NREL characterization with ashes (approximately 1%) and the EDX (Figure 2.2) revealed the existence of some inorganic compounds like calcium (Ca), potassium (K) and aluminum (Al).

The DSC technique was used to compare the thermal behavior of raw fibers. The results are shown in Figure 2.9, four steps of thermal degradation of fique fiber samples related to humidity, cellulose, hemicellulose and lignin are observed, according to the atmosphere used the change in the nature degradation process.

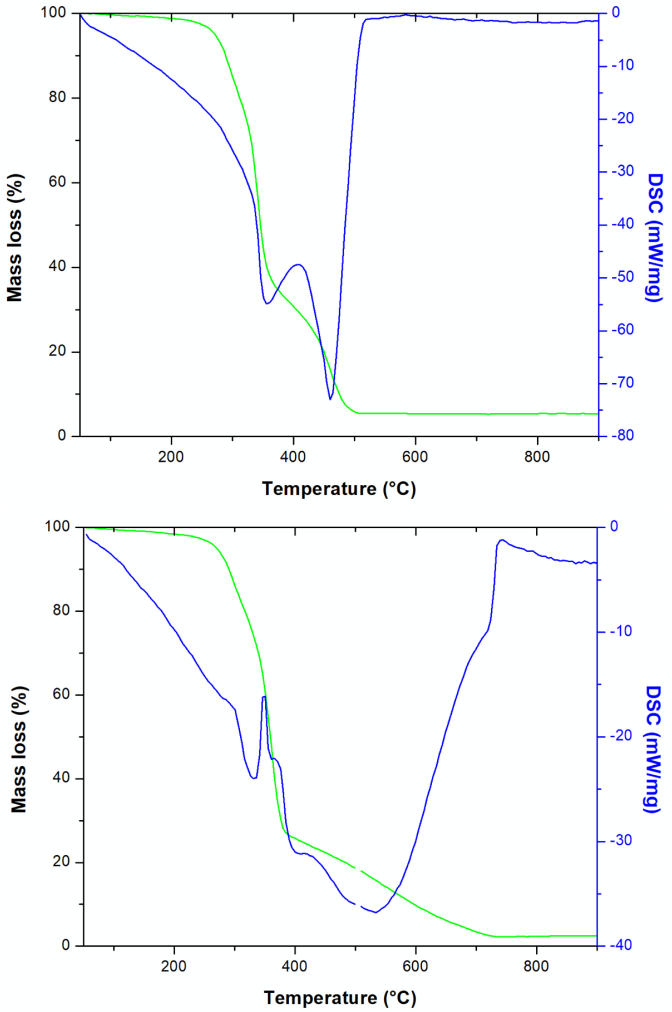


Figure 2.9. TGA (Thermogravimetric analysis) and DSC (Differential Scanning Calorimetry) for raw fique fiber under a) air and b) nitrogen atmosphere.

The thermogram in air (Figure 2.9a) evidenced a tiny endothermic peak between 50 to 110 °C associated with inherent moisture and physically adsorbed water, the small peak size was a result of the low fiber humidity. According to literature, the cellulose decomposition under inert atmosphere is characterized to be an endothermic process related to pyrolysis at 350 °C [52], and that was the behavior evidenced for the raw fique fiber (Figure 2.9b).

The cellulose present into the lignocellulosic biomass is the most resistant against thermal treatment, because of its crystalline structure. The cellulose decomposition also could be identified in thermal analysis under air atmosphere, but in air the decomposition is a more complex process because it includes three primary reactions: thermo-oxidation, dehydration and depolymerization; these reactions happen in the temperature range between 120–350 °C, and resulted in the in glycosane formation [53]. Thermo-oxidation and dehydration are governed by diffusion processes and take place mainly in the amorphous part of the polysaccharides; these reactions are difficult to evidence it in the thermogram. In a parallel way, the cellulose depolymerization reduced the polymerization degree, because the hydroxyl groups were oxidized in carbonyl groups, being this third reaction the dominant in the cellulose decomposition. This reaction is related to an exothermic peak above 300 °C, in the curve of Figure 2.9a the cellulose depolymerization in raw fique evidenced at 360°C.

Regarding, the hemicellulose degradation, some reports identified its depolymerization in the range between 320 and 335 °C in inert atmosphere and at around 312 °C in air [54]. For raw fique fiber no peak in air atmosphere was detected; nevertheless, an exothermic peak was observed in the inert curve at 336 °C, finding a good agreement with the literature data. In addition, partial lignin decomposition occurred simultaneously with hemicellulose and cellulose degradation.

Concerning the lignin decomposition, it included the formation of aromatic hydrocarbons, hydroxyphenolics, guaiacyl and syringyl compounds [55]. An exothermic peak at 464 °C (Figure 2.9a) and the region between 375 to 539 °C (Figure 2.9b) was observed for air and inert atmosphere, respectively. These peaks are included in the reports made by other lignocellulosic biomass that attributed the lignin decomposition is 280–500 °C [55].

Finally, Figure 2.9a and 2.9b shown beyond 550 °C an exothermic peak related to the residual mass attributed to ashes and minor elements like calcium (Ca), potassium (K) and aluminum (Al).

- Mechanical characterization

A dynamic mechanical analysis (DMA) was developed to characterize the stiffness of the fique

natural fiber, trough the Young's modulus or storage modulus. The Young's modulus is defined as the relationship between the force applied to a sample (stress) and the material uniaxial deformation (strain) in the linear elasticity region [6]. The Young's modulus measured on the raw fique fiber was 24.31 GPa, this value depended on the size and geometry of the fique, particularly this fiber has a circular cross section approximately of 170 μm [17]. Jute has a Young's modulus of 26.5 GPa and is more rigid than fique fiber, but less than sisal whose value is in the range of 9 to 22 GPa [56].

In natural fibers, mechanical properties are influenced in a very important way by the cellulose content because the storage modulus is related to intra and intermolecular bonds of H_2, due to the crystal size bulk aligned in parallel along the axis of the fibrils. The number of fibrils of cellulose significantly influences the properties of the resulting compounds: in other words, when the nanocellulose crystallite size is bigger, the Young's modulus and stiffness are greater [44]. Fique fiber presents a cellulose content close to 42% (Table 2.1) a crystallinity index (C_i) of 63% and the diameter of the cellulose crystallite was 7.81 nm, which explained the storage modulus obtained.

2.5 Conclusions

A comprehensive material characterization offers the opportunity to have a starting point of its intrinsic properties, to identify potential novel applications for the materials. Likewise, a good characterization provides the opportunity to work on improving properties with existing approaches or technologies to give additional value to materials. Remarkably, natural fibers have become an alternative to materials such as plastics for being highly contaminating, lignocellulosic biomasses such as fique proved to be interesting biomaterials for their physicochemical properties to be valued in new applications in fields such as wastewater treatment, reinforced materials, raw material from other industrial processes, among others.

Concerning surface characterization, it was confirmed that fique fiber is a lignocellulosic biomass highly attractive, especially due to the presence of many hydroxyl groups useful to perform a tailor-made chemical functionalization and then provide specific physicochemical properties according to the desirable application, as was evidenced by FTIR. Likewise, it was found that the fique surface area can be improved and potentiated. However, the thermal and mechanical properties stand out when compared to similar fibers, such as jute and sisal, opening news

opportunities to use these materials alone or in combination with others like cement, polymers, metals, nanoparticles, and metal-organic frameworks (MOFs).

2.6 References

1. Abril, A. & Navarro, E. *Etanol a partir de biomasa lignocelulósica*. (Aleta Ediciones, 2012).
2. Lucas Herguedas, A. *Biomasa, combustibles y sostenibilidad*. (Itagra, 2012).
3. Mussatto, S. *Biomass Fractionation Technologies for a Lignocellulosic Feedstock Based Biorefinery*. (Elsevier, 2016).
4. Peinado, J. *et al. Guía ambiental del subsector fiquero. Bogotá DC: Cadena Productiva Nacional del Fique-Cadefique*. (Ministerio de Ambiente, 2006).
5. Ovalle, S., Blanco, C. & Combariza, M. Exploring the composition of raw and delignified Colombian fique fibers, tow and pulp. *Cellulose*. **25**, 151–165 (2018).
6. Gañán, P. & Mondragon, I. Surface modification of fique fibers. Effects on their physico-mechanical properties. *Polym. Compos.* **23**, 383–394 (2002).
7. Chacón, M., Blanco, C., Hinestroza, J. & Combariza, M. Biocomposite of nanostructured MnO2 and fique fibers for efficient dye degradation. *Green Chem.* **15**, 2920-2928 (2013).
8. Wang, H. *et al.* Synthesis of Microfiber with Secondary Nanostructure by Cotton Template, Synthesis of Microfiber with Secondary Nanostructure by Cotton Template. *J. Nanotechnologyl.* **20,** 1-5 (2010).
9. Chattopadhyay, D. P. Cationization of cotton for low-salt or salt-free dyeing. *Indian J. Fibre Text. Res.* **26**, 108–115 (2001).
10. Hinestroza, J. & Netravali, A. *Cellulose Based Composites : New Green Nanomaterials.* (Wiley, 2014).
11. Wang, Q., El-Ensashy, H. & Thongchul, N. *Bioprocessing technologies in biorefinery for sustainable production of fuels, chemicals, and polymers*. (*Green Processing and Synthesis*, 2013).
12. Kumar, P., Barrett, D., Delwiche, M. & Stroeve, P. Methods for pretreatment of lignocellulosic biomass for efficient hydrolysis and biofuel production. *Ind. Eng. Chem. Res*. **48**, 3713–3729 (2009).
13. Sluiter, A. *et al. Determination of Structural Carbohydrates and Lignin in Biomass*. *Laboratory Analytical Procedure Technical Report NREL/TP-510-42618* (2008).
14. Sluiter, A., Ruiz, R., Scarlata, C. & Templeton, D. *Determination of extractives in biomass laboratory analytical procedure*. *National Renewable Energy Laboratory* (2005).
15. Dave, S., Damani, M. & Tipre, D. Copper remediation by Eichhornia spp. and sulphate-reducing bacteria. *J. Hazard. Mater.* **173**, 231–235 (2010).
16. Goertzen, S. L. *et al.* Standardization of the Boehm titration. Part I. CO2 expulsion and endpoint determination. *Carbon N. Y.* **48**, 1252–1261 (2010).
17. Schellbach, S. L., Monteiro, S. N. & Drelich, J. W. A novel method for contact angle measurements on natural fibers. *Mater. Lett.* **164**, 599–604 (2016).

18. Arshadi, M., Abdolmaleki, M. K., Mousavinia, F., Foroughifard, S. & Karimzadeh, A. Nano modification of NZVI with an aquatic plant Azolla filiculoides to remove Pb(II) and Hg(II) from water: Aging time and mechanism study. *J. Colloid Interface Sci.* **486**, 296–308 (2017).

19. Hon, D. N.-S. *Chemical modification of lignocellulosic materials*. (CRC Press, 1995).

20. Bledzki, A. K. & Gassan, J. Composites reinforced with cellulose based fibres. *Prog. Polym. Sci.* **24**, 221–274 (1999).

21. Ramesh, T., Rajalakshmi, N. & Dhathathreyan, K. S. Synthesis and characterization of activated carbon from jute fibers for hydrogen storage. *Renew. Energy Environ. Sustain.* **2**, 1–8 (2017).

22. Sun, R. C. *Cereal Straw as a Resource for Sustainable Biomaterials and Biofuels*. (Elsevier, 2010).

23. Milagres, A. M. F., Carvalho, W. & Ferraz, A. Topochemistry, porosity and chemical composition affecting enzymatic hydrolysis of lignocellulosic materials. (Springer, 2011).

24. O'SULLIVAN, A. C. Cellulose: the structure slowly unravels. *Cellulose.* **4**, 173–207 (1997).

25. Morán, J. I., Alvarez, V. A., Cyras, V. P. & Vázquez, A. Extraction of cellulose and preparation of nanocellulose from sisal fibers. *Cellulose*. **15**, 149–159 (2008).

26. Susheel, K. B. & KaithInderjeet, K. *Cellulose Fibers: Bio- and Nano-Polymer Composites*. (Springer, 2011).

27. Thompson, N. Hemicellulose as a biomass resource. *Wood a Agricultural Residues* (Elsevier, 1983).

28. Gardner, K. H. & Blackwell, J. The structure of native cellulose. *Biopolymers.* **13**, 1975–2001 (1974).

29. Wu, H., Fan, S. W., Yuan, X. W., Chen, L. F. & Deng, J. L. Fabrication of carbon fibers from jute fibers by pre-oxidation and carbonization. *Xinxing Tan Cailiao/New Carbon Mater.* **28**, 1-6 (2013).

30. Andrade, M. *et al.* Characterization of the different fractions obtained from the pyrolysis of rope industry waste. *J. Anal. Appl. Pyrolysis.* **95**, 1-7 (2012).

31. Ovalle-Serrano, S. A., Gómez, F. N., Blanco-Tirado, C. & Combariza, M. Y. Isolation and characterization of cellulose nanofibrils from Colombian Fique decortication by-products. *Carbohydr. Polym.* **189**, 169–177 (2018).

32. Ryan, K., Ray, C. G., Ahmad, N., Drew, W. L. & Plorde, J. *Sherris Medical Microbiology,* (McGraw-Hill Medical, 2010).

33. Chen, W., Yu, H., Liu, Y., Zhang, P. & Hai, Y. Individualization of cellulose nanofibers from wood using high-intensity ultrasonication combined with chemical pretreatments. *Carbohydr. Polym.* **83**, 1804–1811 (2011).

34. Brunauer, S., Emmett, P. H. & Teller, E. Gases in Multimolecular Layers. *J. Am. Chem. Soc.* **60**, 309–319 (1938).

35. Yao, F. *et al.* A review of recent developments in natural fibre composites and their mechanical performance. *Compos. Part A Appl. Sci. Manuf.* **51**, 98–112 (2016).

36. Galván, M. V. Mejora de la resistencia de papeles por usos de polielectrolitos sintéticos y naturales. (Consejo Nacional de Investigaciones Científicas y Técnicas, 2012).

37. Moaseri, E., Baniadam, M., Maghrebi, M. & Karimi, M. A simple recoverable titration method for quantitative characterization of amine-functionalized carbon nanotubes. *Chem. Phys. Lett.* **555**,

164–167 (2013).

38. Luzi, F. *et al.* Optimized extraction of cellulose nanocrystals from pristine and carded hemp fibres. *Ind. Crops Prod.* **56**, 175–186 (2014).

39. Munajad, A., Subroto, C. & Suwarno. Fourier transform infrared (FTIR) spectroscopy analysis of transformer paper in mineral oil-paper composite insulation under accelerated thermal aging. *Energies.* **11**, 1–12 (2018).

40. Zaini, L. H., Jonoobi, M., Tahir, P. M. & Karimi, S. Isolation and characterization of cellulose whiskers from kenaf (Hibiscus cannabinus L.) bast fibers. *J. Biomater. Nanobiotechnol.* **4**, 1-37 (2013).

41. Güven, O., Monteiro, S. N., Moura, E. A. B. & Drelich, J. W. Re-Emerging Field of Lignocellulosic Fiber – Polymer Composites and Ionizing Radiation Technology in their Formulation. *Polym. Rev.* **56**, 702–736 (2016).

42. Monteiro, S. N. *et al.* Natural lignocellulosic fibers as engineering materials-An overview. *Metall. Mater. Trans. A Phys. Metall. Mater. Sci.* **42**, 2963-2974 (2011).

43. Ciolacu, D., Ciolacu, F. & Popa, V. I. Amorphous cellulose—structure and characterization. *Cellul. Chem. Technol.* **45**, 1-13 (2011).

44. Moon, R., Martini, A., Nairn, J., Simonsen, J. & Youngblood, J. Cellulose nanomaterials review: Structure, properties and nanocomposites. *Chem. Soc. Rev.* **40**, 3941–3994 (2011).

45. Rabbi, M. A., Rahman, M. M., Minami, H., Habib, M. R. & Ahmad, H. Ag impregnated sub-micrometer crystalline jute cellulose particles: Catalytic and antibacterial properties. *Carbohydr. Polym.* **233**, 1-9 (2020).

46. Krishnaiah, P., Ratnam, C. T. & Manickam, S. Enhancements in crystallinity, thermal stability, tensile modulus and strength of sisal fibres and their PP composites induced by the synergistic effects of alkali and high intensity ultrasound (HIU) treatments. *Ultrason. Sonochem.* **34**, 729–742 (2017).

47. Lamaming, J. *et al.* Isolation and characterization of cellulose nanocrystals from parenchyma and vascular bundle of oil palm trunk (Elaeis guineensis). *Carbohydr. Polym.* **134**, 534–540 (2015).

48. Cataño Rueda, E. H. Obtención y caracterización de nanofibras de celulosa a partir de desechos agroindustriales. Diss. (Universidad Nacional de Colombia, 2009).

49. Gümüskaya, E., Usta, M. & Kirci, H. The effects of various pulping conditions on crystalline structure of cellulose in cotton linters. *Polym. Degrad. Stab.* **81**, 559–564 (2003).

50. Evans, R., Newman, R. H., Roick, U. C., Suckling, I. D. & Wallis, A. F. A. Changes in Cellulose Crystallinity During Kraft Pulping. Comparison of Infrared, X-ray Diffraction and Solid State NMR Results. *Holzforsch. - Int. J. Biol. Chem. Phys. Technol. Wood* **49**, 498–504 (2009).

51. Raveendran, K., Ganesh, A. & Khilar, K. C. Pyrolysis characteristics of biomass and biomass components. *Fuel.* **75**, 987–998 (1996).

52. Milosavljevic, I., Oja, V. & Suuberg, E. M. Thermal effects in cellulose pyrolysis: Relationship to char formation processes. *Ind. Eng. Chem. Res.* **35**, 653–662 (1996).

53. Kačík, F. *et al.* Chemical alterations of pine wood saccharides during heat sterilisation. *Carbohydr. Polym.* **6**, 681–686 (2015).

54. Stevulova, N. *et al.* Thermal degradation of natural and treated hemp hurds under air and nitrogen atmosphere. *J. Therm. Anal. Calorim.* **128**, 1649–1660 (2017).

55. Brebu, M. & Vasile, C. Thermal degradation of lignin - A review. *Cellul. Chem. Technol.* **44**, 353–363 (2010).

56. Gupta, M. K. & Srivastava, R. K. Effect of sisal fibre loading on dynamic mechanical analysis and water absorption behaviour of jute fibre epoxy composite. *Mat. Today Proc.* **9**, 1-6(2015).

3. Pretreatment evaluation of fique fiber to increase the exposure of hydroxyl groups onto the surface

3.1 Abstract

The biomass pretreatments are generally aimed at increasing accessibility to the sugars present in the plant cell wall. In most studies, the approach is to extract as much sugar as possible for use in applications such as biofuel production. However, the focus of this study has as priority the biomass modification to increase the number of hydroxyl groups available on the surface, as well as to obtain a homogenized surface and clean fiber. For this, three different pretreatments: acid, alkali, and organosolv were studied. For the acid and alkaline pretreatments, the effect of catalytic reagent concentration and pretreatment time on the lignocellulosic biomass was analyzed. On the other hand, the organosolv pretreatment investigated the use of different solvents such as water, ethanol, and the water/ethanol combination. All the pretreated biomass was structurally characterized using the NREL methodology, to quantify the percentage of lignin, cellulose, and hemicellulose, and then identify the material in which the amount of hemicellulose and lignin was reduced, while increasing or conserving the cellulose content, without affecting the fiber mechanical structure. Once all the pretreated samples had been characterized by NREL, organosolv using the water/ethanol (WE) combination was the pretreatment that allowed obtaining a more suitable material, without compromising the fiber identity due to the present percentages of lignin, cellulose, and hemicellulose, corresponding to 19.8, 32.8 and 10.5% (w/w), respectively. The fiber pretreated by organosolv was characterized in a much more detail to elucidate the changes compared to the raw fiber, including morphological, mechanical, surface, thermal, and chemical characterization. This study provides data about the pretreatment effect on fique fiber and allowed the identification of organosolv as a process capable of improving the fiber surface characteristics, without changing its identity.

Key words: fique fiber, lignocellulose biomass, pretreatment, acid, alkali, organosolv.

3.2 Introduction

Biomass is considered a renewable source of energy, chemicals and materials, which has become a solution to the oil crisis, rising prices in fuels, climate change, conflict with land and alternative to new materials. It comes from the biodegradable fraction of products, waste and residues of biological origin resulting from agricultural activities (including substances of plants and animal origin), forestry and related industries, as well as the degradable biological fraction of industrial and municipal waste [1]. Biomass is a set of renewable organic matter, accumulated in different organic compounds (polysaccharides, fats, others) along the trophic chain, resulting from the transformation process of solar energy into chemical energy through the photosynthesis process in plants [2].

Particularly, plant biomass is of great interest because it is a suitable raw material in hybrid materials synthesis given the possibility of taking advantage of reactive chemical groups present in cellulose polysaccharides, lignin and hemicellulose. It has been the basis of many applications and derivatives to obtain added-value products, i.e. liquid and gaseous fuels, construction materials, food, composites and chemical products. Lignocellulosic biomass is the most abundant organic material on earth; its sources are forests, agricultural crops, agricultural residues and industries such as paper. This biomass is constituted fundamentally by cellulose, hemicellulose, lignin, extractives (mixture of different organic compounds) and inorganic components. It has the advantage of being biodegradable and renewable, while contributes to the CO_2 reduction emissions, avoiding erosion and soil degradation; in addition, it is an alternative to the waste use, mainly in the agricultural sector.

Pretreatment is an essential step in the global conversion of lignocellulosic biomass into value-added products; its main objective is to make cellulose more accessible with high yields. However, pretreatment remains one of the most expensive steps in the general process of lignocellulosic biomass conversion. To be effective and economical, it must meet the following requirements: (1) deconstruct the three-dimensional structure of lignocellulosic biomass, modifying its polymerization degree and decreasing the cellulose crystallinity, (2) increase material surface area and porosity, (3) generate highly digestible solids and promote high sugar yields after hydrolysis, (4) avoid the formation of inhibitory compounds (especially acetic acid of hemicellulose, furfural and hydroxymethylfurfural from sugar degradation, and phenolic compounds of lignin degradation), (5) allow the recovery of hemicellulose and lignin for later use in valuable co-products production, (6) low demand for post-treatment operations such as

washing and neutralization, and (7) minimum use of energy, chemical products, water inputs, simple reactors, reasonable size and low cost [3,4].

There are different pretreatment methods available to separate and hydrolyze cellulose, hemicellulose, and lignin components. Many processes have been proposed for the biomass pretreatment, which can be classified into four categories: physical, chemical, physicochemical and biological. In general, combinations of some of these methods are necessary to improve the results since each pretreatment has a different impact on the biomass structure and are not equally effective for all raw materials [5]. On the other hand, when specific pretreatment processes are evaluated, other types of objectives are taken into account due to the need for co-design and subsequent processing in other procedures; for example, the cellulose or hemicellulose depolymerization is required to redistribute or partially eliminate other sugars and lignin, or increase the accessibility and porosity of the biomass surface.

Physical pretreatments are intended to reduce the cellulose crystallinity and increase the biomass surface area; these include mechanic [6], pyrolysis [7], microwave [8], ultrasound [9] and pulsed electric energy [10] processes. Chemical pretreatments, usually focus on the lignin removal and crystalline cellulose swelling; these involve acid [11], metallic salts [12], organosolv [13], ionic liquids [14], ozonolysis [15], alkaline [16] and alkaline hydrogen peroxide (AHP) [17]. Several studies address physicochemical (liquid hot water [18], steam explosion process [19], wet explosion [20], CO_2 [21] and ammonia [22]) and biological pretreatments to lignocellulosic biomass.

Although many technologies for biomass pretreatment have already been proposed, the choice of the best technology is not an easy task and depends very much on the pretreatment objective (desired products), type of biomass used, and its composition. For the development of an efficient, economically viable and sustainable pretreatment technology is necessary to understand the biomass structure, select the most suitable method for the target components and operate in optimal conditions.

Specifically, acid pretreatment uses dilute or concentrated acid solutions to break the rigid structure of lignocellulosic materials. The acid acts as a catalyst, it attacks intermolecular and intramolecular bonds between hemicellulose, cellulose and lignin, hydrolyzing carbohydrates present in the material structure, especially hemicellulose. This pretreatment is affected by factors, such as acid type and its concentration, solid charge (also called solid/liquid ratio), temperature and reaction time [11]. On the other hand, alkaline pretreatment is carried out at low

temperature and pressure (including environmental conditions), with reaction times in the order of hours or days; particularly, temperature is an important factor that influences performance, since it reduces the reaction time. Pretreatment with alkalis such as sodium hydroxide, potassium hydroxide, calcium hydroxide, hydrazine and anhydrous ammonia causes swelling, modifies biomass chemical composition and multiscale structure, increasing internal surface area and decreasing the polymerization degree and cellulose crystallinity. The reaction mechanism is based on ester bonds saponification that crosses xylans in hemicellulose and other components such as lignin and cellulose [16].

Regarding the organosolv pretreatment, this process uses organic solvent mixtures such as methanol, ethanol, acetone, ethylene glycol, triethylene glycol or phenols. It is usually mixed with a small amount of an inorganic acid (sulfuric acid or hydrochloric acid) as a catalyst, breaks the internal bonds of lignin and hemicellulose, solubilizing them almost totally [23]. Bases such as sodium hydroxide are also added to the process when temperatures in the range of 100-250 °C are used [24]. However, it has as the main disadvantage the significant losses of the organic solvent, which leads to greater energy and economic investments. In addition, organosolv pretreatments must be carried out under extremely strict and efficient controls due to the organic solvent's volatility. Therefore, the organosolv process is too expensive to be used at present for biomass pretreatment [13].

The previously described pretreatments have been tested on different lignocellulosic biomasses, such as corn stubble, wheat straw, rice straw, stick grass, sugarcane bagasse, Miscanthus, poplar and agave plants, among others [25,26],[24]. However, most of these studies are focused on production and characterization of liqueurs produced during pretreatments, leaving aside effects in resulteded solids. Therefore, it is necessary to focus on the solid by-product, to understand in a global way how they are affected to take advantage of new properties or modifications generated. The pretreatments analyzed from this perspective are really scarce, so it is of great interest to analyze the pretreated biomass to be able to use it as raw material in other types of processes.

In this work, the individual effect of dilute acid, alkali and organosolv pretreatments of fique fiber was investigated, in order to find the pretreatment that provides enhanced properties to the fique fiber to obtain a homogenized surface, clean fiber, and more exposed functional groups of

cellulose, where the cellulose content will increase, while decreasing the contribution of hemicellulose and lignin.

3.3 Materials and methods

3.3.1 Chemicals and materials

Sulphuric acid (95-97%, MerckMillipore), ethanol absolute (99.8% v/v, Panreac), hydrochloric acid (37%, MerckMillipore), sodium hydroxide pellets (MerckMillipore) and potassium nitrate (Sigma-Aldrich) were used as received. Raw fique fiber with similar moisture, color, length, width, and free of knots, diseases and pests was provided by Compañia de Empaques S.A, who collects the fiber from the Colombian coffee region.

3.3.2 Experimental set-up and procedure

- Dilute acid pretreatment

Sulfuric acid was used in three different concentrations (1, 2.5, and 4% v/v), with a solid/liquid ratio of 20 g/L from 5 g of raw fique fiber (on dry basis). Subsequently, biomass and acid were placed in Schott flasks to be autoclaved at 121 °C and 15 psi, during three different times (30, 60, and 90 min), all the experiments were carried out in triplicate. Then, the pretreated solution was filtered, the liquor and solid fraction (pretreated biomass) were obtained, the latter was dried at room temperature and stored for analysis.

- Alkali pretreatment

Sodium hydroxide was used in three different concentrations (1, 2.5, and 4% w/v), with a solid/liquid ratio of 2 g/L from 5 g of raw fique fiber (on dry basis). Subsequently, biomass and alkali were placed in Schott flasks to be autoclaved at 121 °C and 15 psi, during three different times (30, 60, and 90 min), all the experiments were carried out in triplicate. Then, the pretreated solution was filtered, liquor and a solid fraction were obtained, the pretreated biomass was dried at room temperature and stored for analysis.

- Organosolv pretreatment

With the aim to clean, do more homogeneous the surface of raw fique fibers and improve the cellulose accessibility, an organosolv fractionation pretreatment was performed through Soxhlet extraction. This pretreatment was done at room pressure, 8 g of raw fique fibers were located into the extraction thimble, taking in account the height of raw fibers in the thimble must not exceed

the height of the Soxhlet siphon tube [27]. After the Soxhlet apparatus was assembled, 250 mL of solvent was added in the dry boiling flask. Distilled water and ethanol (96% v/v) were evaluated as solvents, the extraction for each solvent was completed after 60 h.

In order to quantify and analyze the effect of the organosolv pretreatment, the liquor obtained from the pretreatment was dried at 50 ± 2 °C under reduced pressure [27]. The extracted solids were dried overnight in a desiccator before weighing. The percentage of extractives in each pretreated sample (Eq. 3.1), were reported as weight percentage of the biomass (dry basis), where ODW_{sample} is the oven dry weight [28].

$$Extractives = \frac{Weight_{\,flask\ plus\ extractives} - Weight_{flask}}{ODW_{sample}} \times 100\% \qquad \text{Eq. 3.1}$$

In addition, to check the effect in the structural composition of the organosolv pretreated material, the solid fraction obtained from the Soxhlet was analyzed according to the NREL methodology "Determination of Structural Carbohydrates and Lignin in Biomass" [29]. To describe the effect of temperature (*T*, °C), time (*t*, min), and pH in the liquor after pretreatment [30], an extend correlation about the severity (*CS*) of organosolv pretreatment was used (Eq. 3.2) [25].

$$CS = \log\left(t \times \exp\left[\frac{T - T_{ref}}{14.75}\right]\right) + |pH - 7| \qquad \text{Eq. 3.2}$$

Where T_{ref} is reference temperature (100 °C).

3.3.3 Statistical analysis

A 2^3 factorial design of experiments was implemented for acid and basic pretreatments evaluation. The effect of two factors was analyzed: catalyst concentration and pretreatment time, each factor with three levels (Table 3.1). The percentages of cellulose, hemicellulose, and lignin were the response variables. The data statistics were analyzed using a one-way analysis of variance (ANOVA) through Minitab 16 Statistical Software.

Table 3.1. Factors assessed in the acid and alkali pretreatment of raw fique fiber.

Factor	Level		
	Low	Medium	High
Catalyst concentration (% v/v or p/v)	1	2.5	4
Pretreatment time (min)	30	60	90

3.3.4 Characterization

- Humidity

Humidity was determinated on 1 g of the material using an infrared radiation scale (PMB53-Adam) for 25 min, at 100 °C. Samples did not undergo any other previous treatment to the humidity determination experiment.

- Chemical Structure

The National Renewable Energy Laboratory methodology (NREL) [29] was implemented for the determination of structural components of the fique fibers. NREL consisted of two acid hydrolysis steps to fractionate biomass. The first step allowed the determination of the acid-insoluble lignin in the sample (via standarized gravimetry procedures). The acid-insoluble residue was placed in a crucible and loaded in an oven at 105 °C (Labtech Essa) until constant weight. Then, the samples were removed from the oven and cooled in a desiccator and their weight was recorded. Finally, the crucibles and residue were placed in a furnace (Thermo Scientific Lindberg/Blue Moldatherm™) at 575 °C for 4 h. The weight of cold samples was recorded again. The second step used UV-Vis spectroscopy to determine acid-soluble lignin, where the absorbance of an aliquot from the hydrolysis products was measured at 320 nm, using a solution of sulfuric acid 4%(v/v) as blank.

A second stage in the NREL characterization involved the fragmentation of the fibers into soluble monomeric forms (glucose, xylose and arabinose), followed by a quantification using HPLC chromatography (VWR-HITACHI ELITE Lachrom system, consisting of a model L-2130 quaternary pump and a IR detector, Model Shodex RI-101). A stainless steel Aminex HPX-87H column (300 x 7.8 mm I.D.) was employed with filtered and degassed HPLC grade sulphuric acid 5mM as mobile phase. Elchrom Elite software Chromatography data system was used for data processing and reporting. To achieve reproducibility, an automatic injector (Model L-2220) adjusted to 20 µL was used. The flow rate was kept at 0.6 mL/min with a temperature of 65 °C in the column. Peak identities of the degradation products, both retention time and spectra matching of standard compounds, were confirmed.

In addition, extractives determination was done by the NREL methodology [27] with the purpose to quantify non-structural material in the biomass sample. The methodology includes two steps into the solid/ liquid extraction process made by Soxhlet: first using water and then ethanol as solvent. The results are reported, on a dry weight basis, as a weight percentage of the biomass.

NMR spectrometry and HSQC analyses were performed using a Bruker BioSpin Gmb operating at 300 MHz both for H and HSQC. The spectra were acquired using NUTS NMR Data Processing software.

- Surface Characterization

pH_{zpc} was determinated using the drift method in which solutions with 45 mL of KNO_3 (1% vol.) were adjusted to an initial pH in the range of 2 to 10 by adding HCl 0.1 M or NaOH 0.1 M. The volume of each solution was completed up to 50 mL adding KNO_3 (1% vol.). Once the pH of the solutions was set, 0.1 g of raw fique fiber was added, the resulting suspensions were stirred for 24 h at 25 °C, and the pH of the supernatants was registered [31]

Fourier Transform Infrared Spectroscopy (FT-IR) was used to identify changes in the fiber functional groups. FT-IR was determined using an ATR (PIKE) diamond crystal accessory attached to a FT-IR Nicolete iS 10 spectrometer (Thermo Fisher Scientific). Scans of 20 readings were performed by spectrum and data were recorded from 4000 to 600 cm^{-1}.

To analyze the wetting fiber surface a novel method published by Schellbach *et al.* [32] to measure the contact angle was implemented. Two fibers with similar diameter were aligned parallel with a distance ~ 1 mm between them under an Olympus microscope at room temperature. A drop of deionized water was deposited in this small space, in order to measure the hanging bridge to enlarge the lateral dimension of the water bridge and reinforce the spreading of it over the dry sections of the fibers. After the water column enlarged and the spherical menisci stabilized, the high-resolution images were captured using the software cellSens. Five images were captured for both enlarged and reduced water columns on each sample, the values of the diameter (*d*) and height (*h*) of the meniscus were obtained. The contact angle was calculated using Eq. 3.3:

$$\theta = 90 - 2\tan^{-1}\left(\frac{2d}{h}\right) \qquad \text{Eq. 3.3}$$

- Structural Characterization

Crystalline fique fiber structure was measured at room temperature with an XPert Pro MPD diffractometer with monochromator of crystal graphite using Cu Kα (λ = 1.5406 Å) at 40 kV and 30 mA. Diffraction patterns were obtained in the range of 2theta =10-40°, with a step size of 0.02° and measuring time of 50 s per step. Experimental data were analyzed using PANalytical X'Pert HighScore Plus database.

- Morphological and Textural Characterization

The total surface area was measured by the adsorption of nitrogen (N_2) at 77 K, using a

Quantachrome NOVA e-Series surface area analyzers. N_2 isotherms were performed on raw fiber samples. Before N_2 adsorption, the samples were degassed at 80 °C for 8 h. The calculation of the total surface area was established using the BET method [33].

Morphologycal characterization of fique fibers was achieved via Field Emission Scanning Electron Microscope (FESEM) and performed on thin-film gold-coated samples using a Zeiss Auriga FIB-SEM (GeminiSEM) scanning electron microscope, coupled to a secondary electrons (SE2) detector. The micrographs were taken at 1.5 kV, working distance (WD) ranging from 4.9 to 5.2 mm, at different magnifications.

- Thermal Characterization

Thermal gravimetric analysis (TGA) and Differential Scanning Calorimetry (DSC) were performed using a simultaneous thermal analyzer (STA 409 PC/4/H Luxx) in a temperature range from 50 to 900 °C at a heating rate of 10 °C/min using an inert (N_2, flow of 50 cm^3 min^{-1}) atmosphere.

- Mechanical Characterization

Dynamic Mechanical Analysis (DMA) was performed in a Mettler Toledo DMA1 analyzer; one fiber was centered inside the sample holder using single-cantilever clamps, with a free length of 17.5 mm. The DMA was done at room temperature, the oscillation conditions were fixed at 1Hz and the amplitude was 20 μm (i.e. 0.11% strain), which was well within the linear viscoelastic region. Storage modulus E (MPa) were collected during the test; the final value includes an average of three measurements for each sample.

3.4 Results and Discussion

- Dilute acid pretreatment

From the factorial design of experiments for the evaluation of acid pretreatment, 9 combinations were tested varying the H_2SO_4 concentration and pretreatment time on the raw fique fiber, according to the conditions established in Table 3.1. Figure 3.1 summarizes the values of lignocellulosic components determined in pretreated fibers following the NREL methodology [29]. The cellulose polymer varied between 62.7 ± 5.9 to 69.0 ± 1.8% (dry basis). Comparing all the pretreatments with the cellulose content in raw fiber, in general, the content increased up to 12%. Neither of the two factors analyzed was statistically significant. From the contour plot of Figure 3.2, the effect of pretreatment on the solid was less strong when short pretreatment times were

used. However, when the time was increased to 90 min, the amount of exposed cellulose in the solid increased for all levels of acid concentration.

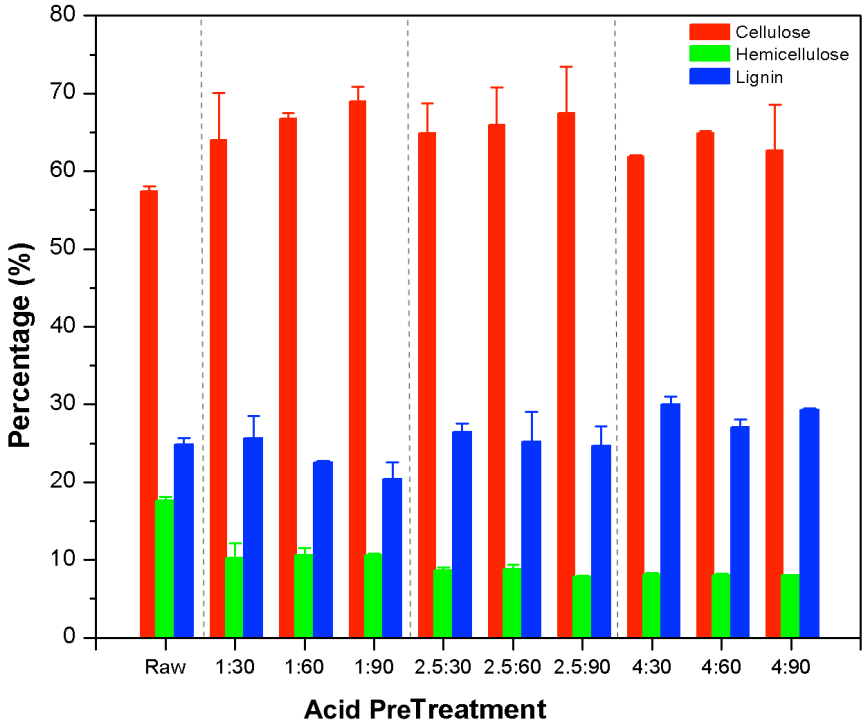


Figure 3.1. Cellulose, hemicellulose and lignin present in the solid fiber after dilute acid pretreatments.

Regarding hemicellulose, as expected the amount of arabinose and xylose present in the lignocellulosic biomass decreased with the acid pretreatment for all the experiments. Figure 3.1 presents values between 7.9 ± 0.1 and 10.7 ± 0.8%, which indicate that, in some pretreatments, hemicellulose hydrolyzed approximately 50% compared to the percentage present in the raw fiber. The lowest value of hemicellulose in the fiber was obtained for the highest concentration of H_2SO_4, corresponding to 4% v / v (Figure 3.3). From the statistical analysis, only the acid concentration exhibited a significant difference ($p = 0.002$). Figure 3.4 presents the hemicellulose contour plot of the effect in acid concentration and the pretreatment time. Also, the highest hemicellulose contents in the fiber were achieved when the lowest acid concentration was used, regardless of the pretreatment time used. Then, as the acid concentration increased, and the pretreatment time was longer, the lignocellulosic biomass was most strongly affected. In fact, the lowest hemicellulose content was reached for the fiber pretreated under these conditions (less than 8%).

The lignin content ranged between 20.4 ± 2.2 and 30.0 ± 1.0% (Figure 3.1). The delignification process was not promoted in this biomass, coinciding with reports by other authors [34], in comparison with the lignin content in raw fiber (24.9 ± 0.8%), the values were very close to each other. The ANOVA indicated the pretreatment time factor did not have a statistically significant difference, the acid concentration (p = 0.017), the lowest lignin values were found when the lowest acid concentrations were used.

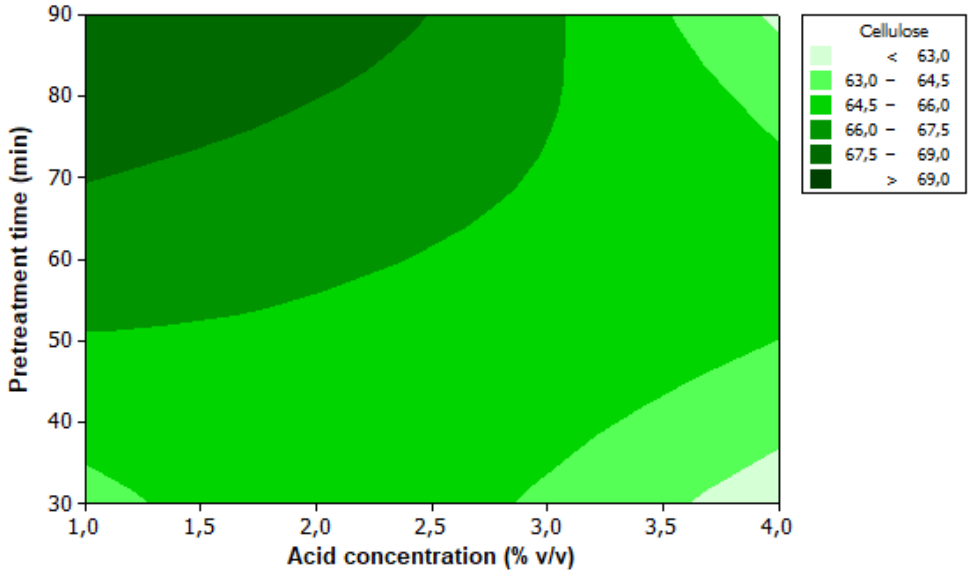


Figure 3.2. Contour plot of the effect of acid concentration and pretreatment time on cellulose after dilute acid pretreatment.

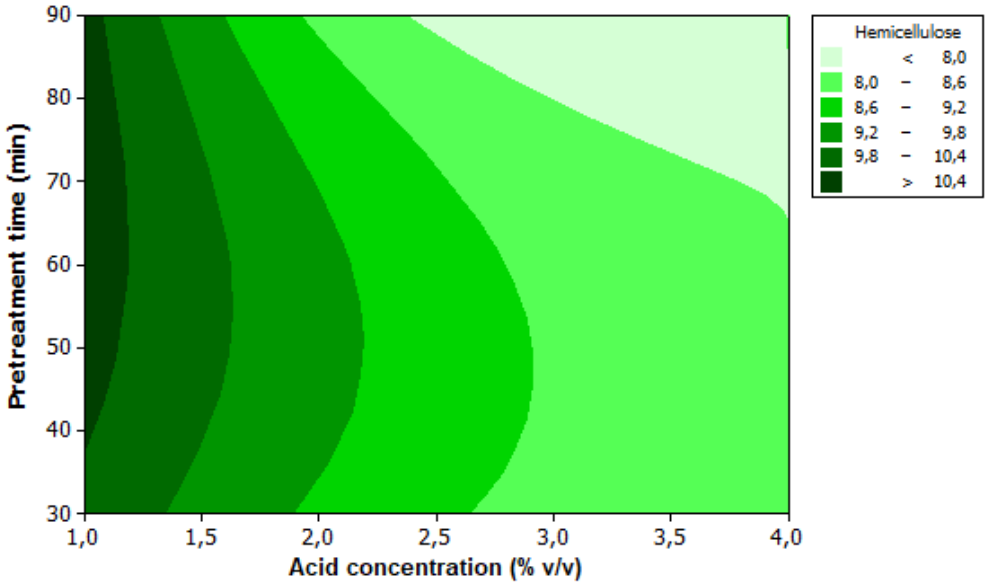


Figure 3.3. Contour plot of the effect of acid concentration and pretreatment time on hemicellulose after dilute acid pretreatment.

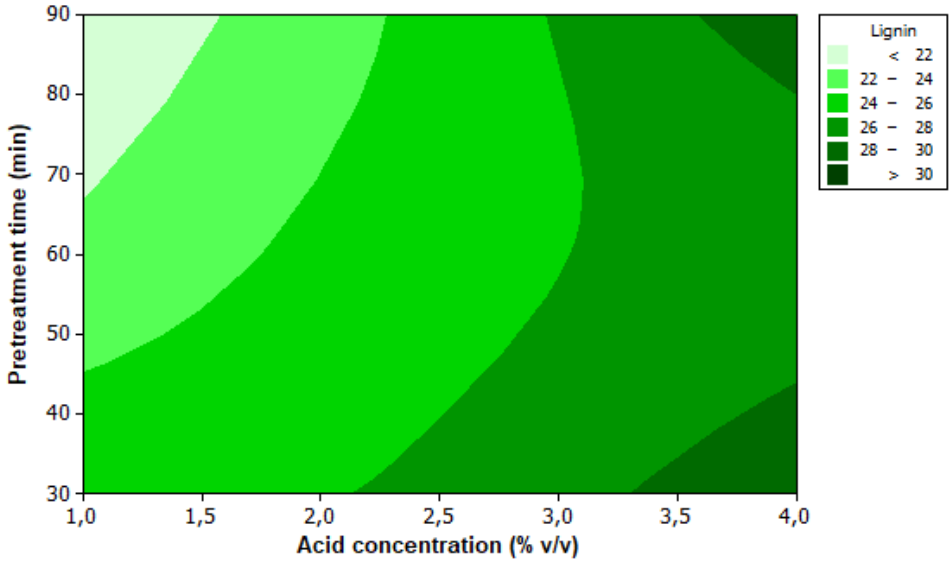


Figure 3.4. Contour plot of the effect of acid concentration and pretreatment time on lignin after dilute acid pretreatment.

The efficiency of the acid pretreatment was mainly focused on the reduction of a considerable amount of hemicellulose, disturbing and disarticulating the lignin, without reducing its content, while increasing the exposed cellulose [35]. The hemicellulose is non-cellulose structural polysaccharide with low molecular weight, present in cell walls, with low polymerization degrees (<200) and slight branches that depend on the species. There are two types of hemicellulose: xylan (contain xylose) and mannose (contain glucomannan). In plants, xylan is more abundant, it is constituted by a skeleton of xylose units linked by glycosidic bonds β-1,4-xylan, and it has three configurations that are the most commonly found. Also, hemicellulose contains acetyl groups; which promoted a much faster decomposition compared to lignin and cellulose, being the most eliminated macromolecule under this pretreatment [36].

In general terms, the results obtained from the dilute acid pretreatment in the fique fiber agreed with reports made by other authors, in which the hemicellulose depolymerization process was mainly achieved after pretreating the biomass. Specifically, in this study independent of the pretreatment time; the acid concentration was the factor statistically significant. Despite milder conditions, that is, less time and acid concentration the effect on the fique structure was evident, since the long fique fibers (30 cm) were converted into fibrils of sizes of approximately 1 cm.

- Alkali pretreatment

From the set of the experiment design, Figure 3.5 summarizes the percentages contained in the

fique fiber after pretreatment with alkali. A low solubilization of cellulose was evidenced, whose values were found in the range of 58.5 ± 0. and 67.8 ± 1.6%, comparing the values obtained after pretreatment with raw fiber. A slight increase in cellulose content could be related to a subtle increase in cellulose accessibility, this behavior was mainly found for concentrations of 2.5 and 4% w/v. From the ANOVA, none of the factors analyzed showed significant differences in the percentage of cellulose. However, Figure 3.5 indicates the contour plot of the alkali effect concentration and pretreatment time. In the level range studied, the highest values of cellulose were obtained at concentrations of 2.5 to 3% w/v and 55 to 75 min of pretreatment.

Concerning hemicellulose, from Figure 3.6 it was confirmed, for all experimental conditions, that the content of this polymer was reduced. Values close to 9.3 ± 0.1 to 13.4 ± 0.4% were obtained, eliminating up to 8% of the hemicellulose compared to the initial content in raw fiber. From the statistical study, only the factor related to alkali concentration showed significant differences on the hemicellulose content ($p = 0.006$). This effect is evident in Figure 3.6 in which, independently of the pretreatment time, at lower alkali concentrations there were higher hemicellulose contents in the fiber, and when the alkali concentration increases the hemicellulose decreases. Additionally, some authors have documented the strong physical connection between cellulose and hemicellulose [5]. Consequently, the hemicellulose solubilization was increased by the rise in pores size of the cellulose structure, which has been attacked by alkali improving its accessibility [37]. Furthermore, throughout the alkali pretreatment, the hemicellulose was separated from the lignin due to the breakdown of α-ether or ester type bonds, resulting from the solubilization of this macromolecule [37].

The lignin percentage was slightly influenced by the treatment with alkali since changes in only approximately up to 5% compared to raw fiber were reached (between 22.4 ± 0.4 and 28.4 ± 3.6%), evident in Figure 3.7. None of the studied factors exhibited significant differences in the percentage of lignin contained in the pretreated biomass. Also, from Figure 3.7, it was confirmed that increasing the alkali concentration, the delignification enlarged regardless of the pretreatment time. However, although the effect of lignin removal was not high enough with this kind of pretreatment, the hemicellulose present in the fique fiber did depolymerize significantly, compromising its physical structure. Some authors agree with the results obtained here and have even reported a growth in the material porosity [16]. This fact could cause an increase in the cellulose release, described above and confirmed in Figure 3.5 for most of the experiments carried out in the factorial design.

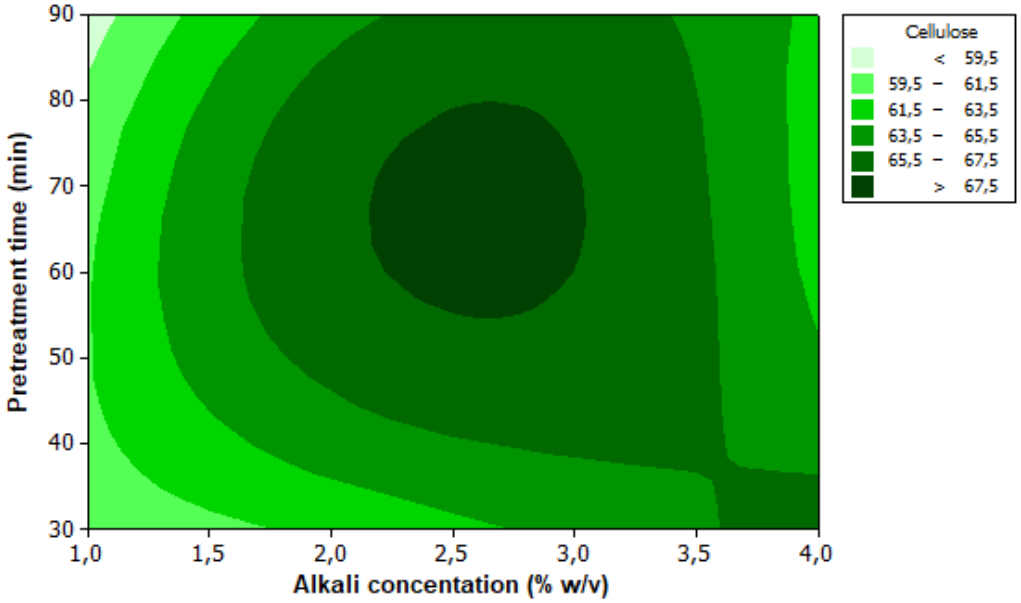


Figure 3.5. Contour plot of the effect of alkali concentration and pretreatment time on cellulose after alkali pretreatment.

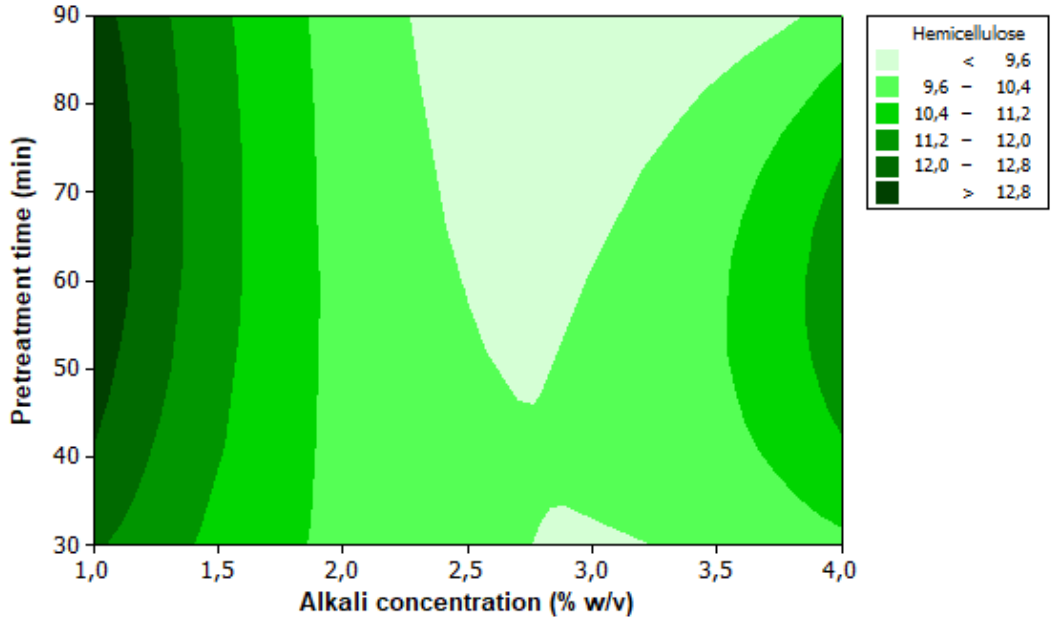


Figure 3.6. Contour plot of the effect of alkali concentration and pretreatment time on hemicellulose after alkali pretreatment.

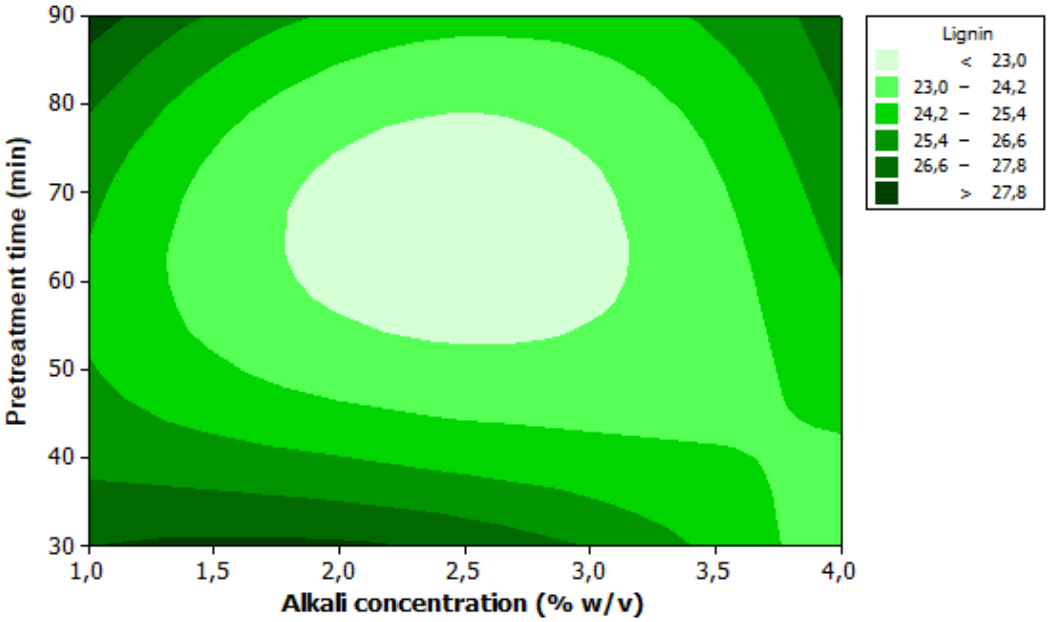


Figure 3.7. Contour plot of the effect of alkali concentration and pretreatment time on lignin after alkali pretreatment.

Although the efficiency of the evaluated pretreatments (acid and alkali) is a function of the biomass intrinsic properties, such as cellulose crystallinity, the polymerization degree of cellulose and hemicellulose, predominant type of hemicellulose in the material structure, surface porosity and amount of accessible cellulose, the degree of surface protection is mainly related to the content of lignin present, the hemicellulose coating to cellulose, and even mechanical properties of the fiber [38]. It was demonstrated these parameters did indeed influence the pretreatment developed in fique fiber.

It was evident the acid pretreatment had a more significant effect compared to the alkali on the fique fiber, due to the significant hydrolysis of the hemicellulose present in the solids after the pretreatment. Regarding the alkali treatment, the delignification was not very high, but the hemicellulose content reduction allowed to intuit the biomass suffered a swelling, due to the increase in the internal surface area of fique fiber, and decrease in the polymerization degree and crystallinity of cellulose, which was confirmed with the growth in its percentage.

Although the two acid and alkali pretreatments were evaluated with the lowest concentration a significant effect in the percentage of cellulose, hemicellulose and lignin were evidenced. Several structural changes confirmed these pretreatments were not ideal to improve the exposed cellulose, create a much larger, homogeneous and cleaner surface, without sacrificing the fiber

physical properties. From these results, another pretreatmen was considered and the results will be reported below.

- Organosolv pretreatment

The main application of pretreatments reported in literature is focused on obtaining a liquor rich in carbohydrates in order to use this one in synthesis of others subproducts. However, a little number of reports are interested in the use the solid fraction resulting from the pretreatment process. Organosolv pretreatment has been a good alternative because it liberates cellulose fibers from lignin and hemicellulose without compromising the mechanical structure of the fibers[13]. Consequently, this research (Table 3.2) the implementation of mild conditions due to partial lignin delignification was necessary (aqueous–organic solvent systems, without catalysts and temperature range of 85–110 °C) [13]. In addition, a process of two extraction steps was analyzed, first 60 h of reflux using as solvent distilled water followed by a reflux during 60 h in ethanol.

Table 3.2. Chemical composition and correlation severity of the pretreated fibers by organosolv and raw fique fibers quantified by NREL methodology.

Pretreatment conditions				**Composition (% w/w)**					
Solvent	Temp (°C)	Time (h)	CS	Humidity	Ashes	Extractives	Cellulose	Hemicellulose	Lignin
Raw	-	-	-	10.3±0.9	1.1±0.2	15.3±0.3	42.1±0.6	12.9±0.4	18.2±0.8
Water	92	60	4.6	27.8±0.9	0.1±0.1	5.0±0.6	35.1±0.2	10.0±0.8	22.0±1.9
Ethanol	76	60	4.0	31.1±1.5	0.1±0.1	2.4±0.6	33.6±1.3	10.4±0.3	22.2±2.2
Water + Ethanol	76	120	4.3	30.6±1.4	0.1±0.1	6.1±0.6	32.8±1.1	10.4±0.6	19.9±1.3

Delignification was not evident as a result of the operational conditions used (without catalyst and low temperature). The percentage of lignin increased only in the range of 1.6 – 4.0% compared with the value reported for the raw fibers. This increase could be attributed to condensation reactions between extractives and carbohydrates or furfural [13,39,40], similar results were reported for olive tree biomass [41] and wheat straw [40]. Also, this behavior may be due to the fact that lignin, being the first macromolecule to be extracted during pretreatment, can react with some derived carbohydrates and subsequently reprecipitate on the surface of the pretreated material [42]. In addition, the β-O-4 and resinol structure (β-β) in the lignin macromolecule are resistant to be removed by organosolv pretreatment [43]. Hemicellulose content was slightly affected by the pretreatment. It was reduced by 2.5% compared to raw fibers; this behavior remained constant for the three conditions evaluated, other studies have reported a removal percentage of 3% [44].

Regarding cellulose, approximately 7.1 to 9.3% was removed in the solid fraction in comparison to the raw fibers. Cellulose solubilization is promoted by the presence of water, because this

solvent is a carrier of protons [45]. Pretreatments using ethanol as solvent result in better cellulose removal, this behavior has been reported for other biomass [46]. Organosolv pretreatment based in aqueous–organic solvents currently uses primary alcohol like ethanol [47], because this solvent has the advantage of being safe, low cost and easy to recover (means low energy consumption). The use of ethanol in high concentration (up to 75%) as solvent, promotes higher cellulose extraction [48]. That is explained by the hydrogen bonding capacities of the solvents and their solubility parameters (Hildebrand parameter, δ1 value) [49], isolated cellulose has a δ1 = 21.6 $(MPa)^{1/2}$ [50], this value is closer to the δ1 of the ethanol than the water (26 and 47.3 $(MPa)^{1/2}$, respectively), for this reason ethanol can solubilize a larger percentage of cellulose [51].

About the combined severity factor (CS), the values obtained for three pretreatment conditions were in the range of 4.0 to 4.6 (so similar between all of them). These allowed a reduction in the glucose content in the solid fiber pretreated varying according to the solvent used, as presented in Table 3.2. In general, minimal hemicellulose and lignin removals were obtained for all pretreatments.

SEM was used to explore changes in the fiber's morphology compared with the raw material (Figure 3.8a). This fiber is compact and has square channels, a heterogeneous surface and some impurities attributed to carbonate compounds originated from the soil or fertilized used to grow.

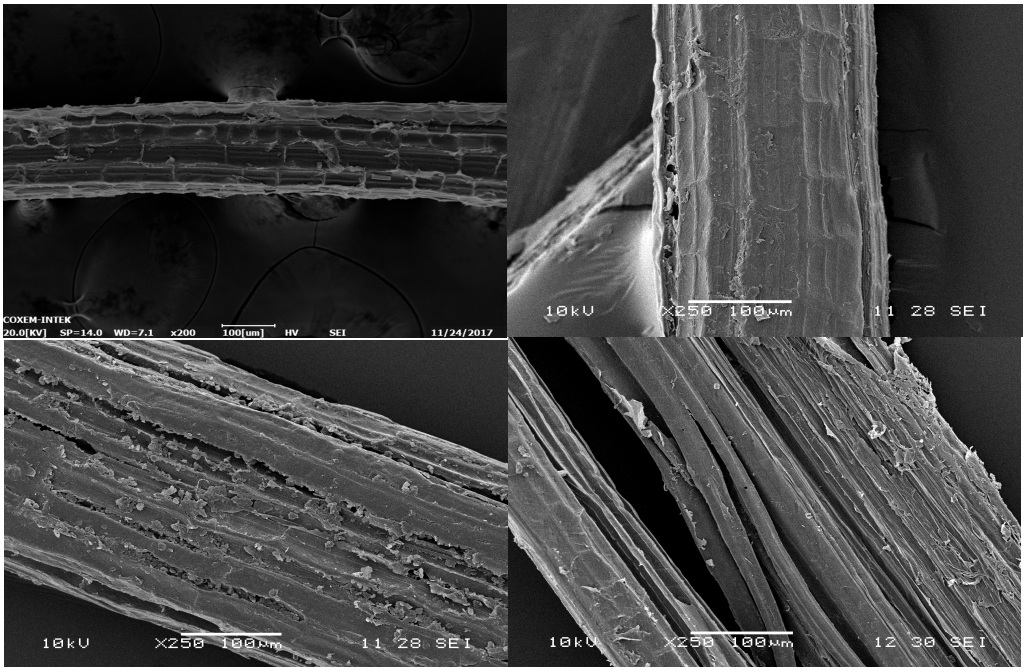


Figure 3.8. a) Raw fique fibers 200X, b) fibers pretreated using water 250X, c) fibers pretreated using ethanol 250X, d) fibers pretreated under two extraction steps using water + ethanol 250X.

Figure 3.8b evidences a cleaner and more homogeneous surface for the fibers pretreated in water, while Figure 3.8c illustrates a surface with an exfoliated surface. This effect is due to ethanol, because this solvent leads to a low hemicellulose solubilization and delignification [45]. The material pretreated under two extraction steps (Figure 3.8d) shows the combination between each individual pretreatment using as solvent water and ethanol. It appears that soft disruption to the cell wall structure has occurred, meaning more accessible, organize and defined microfibrils, confirming the increase of surface area [52,53].

The NMR spectra was used to obtain more structural information on high molecular weight polysaccharides and their building blocks, after implementing the organosolv pretreatment, that included two steps. From the first step (using water as solvent), the water ^{1}H-NMR obtained (red spectra in Figure 3.9) shows a strong signal at 2.5 ppm corresponding to the solvent DMSO. Additionally, a peak in the range of δ 0.5 – 2.4 pmm and δ 3 – 4 pmm could be assign to water-soluble compounds, like: saponins (mainly hecogenin, originated from the leaf-juices after the defibration process) [54], and carbohydrates as cellobiose, respectively. Also, the signal in 4.66 pmm is related to H_β in β-O-4 structures in the lignin macromolecule. Based on the above peak assignments, it can be concluded that saponins and cellobiose chains were removed from the solid material after the pretreatment [55,56].

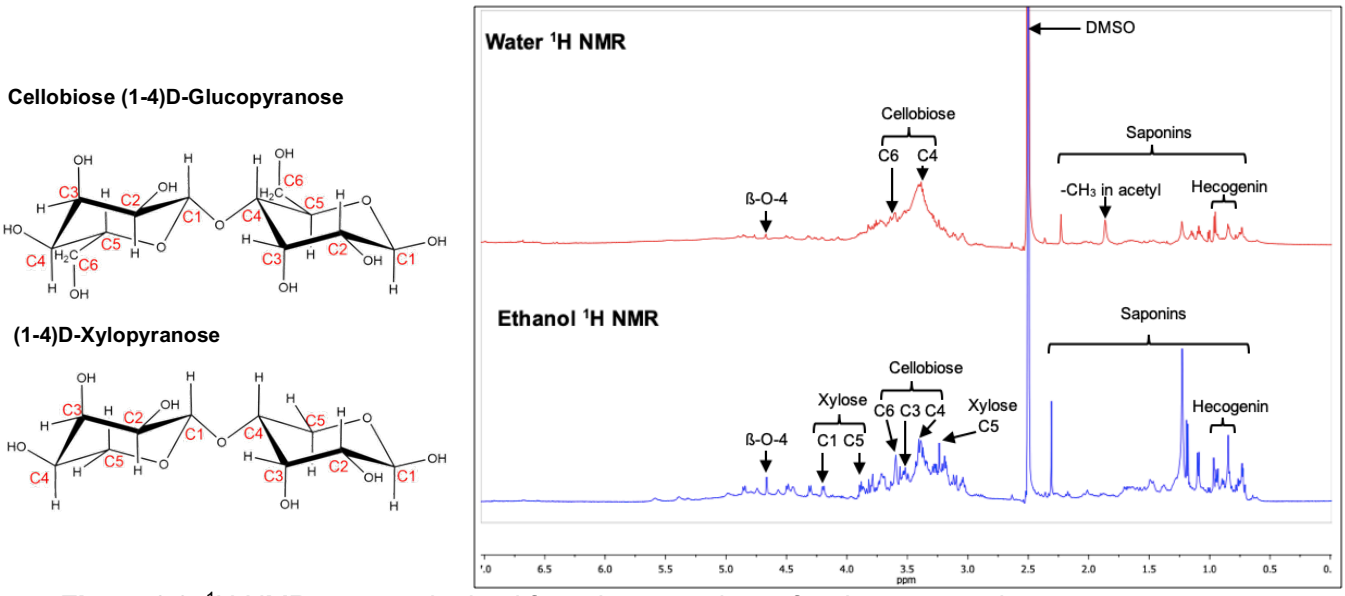
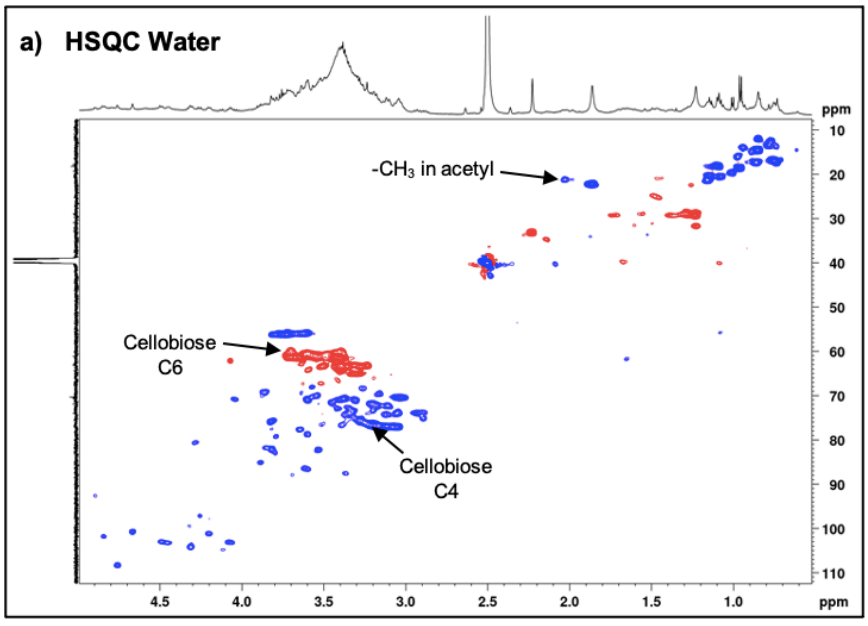


Figure 3.9. ^{1}H-NMR spectra obtained from the extractives after the organosolv pretreatment using water (red spectra) and ethanol (blue spectra) as solvents.

Additionally, in the second step where ethanol was use as solvent, evidenced in the ^{1}H-NMR (blue spectra in Figure 3.9) similar signals to saponins and cellobiose reported in the spectra of water extractives (red spectra in Figure 3.9), but in the ethanol spectra these signals are more intensive. Furthermore, the region between 0.5 and 2.4 ppm related to aliphatic molecules, probably could include materials such as waxes, or other minor components [66]. Additional peaks appeared in the ring proton region (δ 4.5 - 3 ppm), where resonance peaks of most protons showed some overlapped signals, making the identification more difficult [66]. These signals evidenced the removal of cellulose and hemicellulose from the raw fiber after the organosolv pretreatment. Concerning lignin, no significant signal appears in the aromatic region (data not presented), confirming this macromolecule was not affected in a significant way by the pretreatment [65].

To better elucidate the structure of carbohydrates removed by organosolv pretreatment, a 2D NMR was done (Figure 3.10). The majority of the resonances were identified by data reported in literature [55,56,57]. The HSQC spectrum for water (Figure 3.10a) revealed the correlation between the signals δ_C/δ_H cross-peaks at 3.7/61.3 and 3.2/75.8, which were assigned to C-4 and C-6 in the glucose unit (monomer of the cellobiose oligomer), respectively. Meanwhile, the HSQC of ethanol (Figure 3.10b) contained the signals evidenced in the water HSQC for cellobiose, another signal at 3.41/71.11 related to C-3 in the anhydroglucose unit (AGU) of cellulose was showed in the Figure 3.10b. In addition, signals related to C-1 from xylose present in hemicellulose were found at 4.2/101.3 and hecogenin at 1.8/31.3.



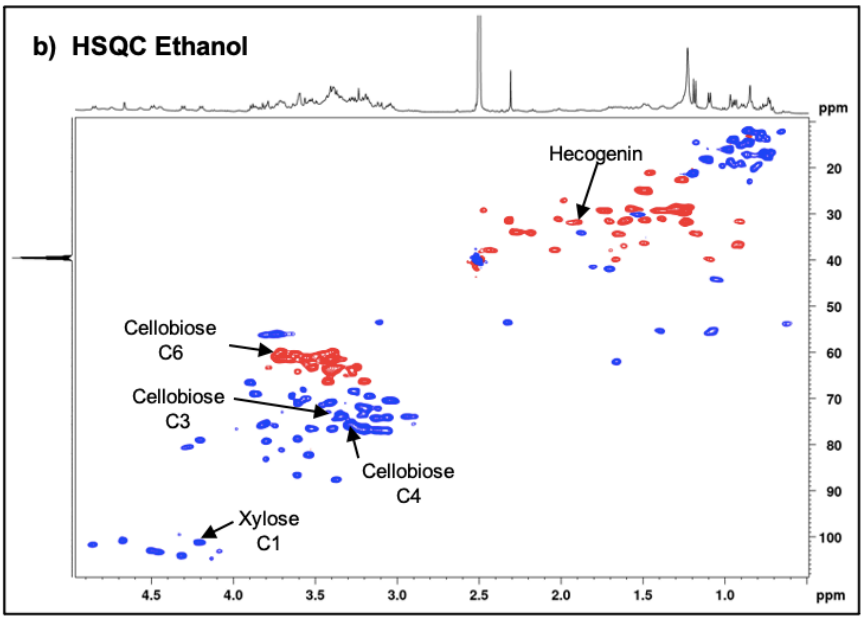


Figure 3.10. HSQC spectrum obtained from the extractives after the organosolv pretreatment. a) HSQC of water extractives and b) HSQC of ethanol extractives.

In summary, these results allowed to confirm a depolymerization of the glucan chains, cellulose, with shorter glucan chains (cellobiose), would form weaker networks and have more reducing ends, increasing in this way the amount of cellulose accessible on the surface and a cleaning process as result of the removal for some compounds like saponins, waxes and carbohydrates from the raw fique fiber.

FTIR was used to investigate changes on the surface chemistry after the organosolv pretreatment; the results are presented in Figure 3.11. The FTIR spectra showed a band at 1736 cm^{-1}, which corresponds to C=O stretching vibration present in hemicellulose, and another at 1236 cm^{-1} assigned to C-O stretch vibration in lignin and carboxylic vibration in xylan [58], both of them were insignificantly reduced after the organosolv pretreatment. Concerning, the band localized at 1622 cm^{-1} associated to calcium oxalate characteristic of the raw fiber [59], a reduction in the intensity was evidenced after the organosolv process suggesting a stage of cleaning as a result of the pretreatment.

Also, a negligible change was observed for the vibration at 3380 and 2928 cm^{-1}, related to -OH groups in the polysaccharide part and non-sterified hydroxyl from the cutin [59], and C-H groups present in all the macromolecules analyzed [58], respectively. The bands reported above allow to infer the chemical structure of the fiber was not modified.

On the other hand, a reduction in the band at 898 cm^{-1} assigned to the C1 frequency in cellulose and hemicellulose was evidenced as consequence of the breakdown of the ß glycosidic bond after the pretreatment [53]. Regarding, the CH_2 present in the cellulose (band at 1326 cm^{-1}) and the C-O-C asymmetric stretch vibration in cellulose and hemicellulose (band at 1165 cm^{-1}) [58], the transmittance was almost unaffected by the pretreatment, in this way confirming that the distribution of cellulose in the pretreated material may have been affected by its defibration.

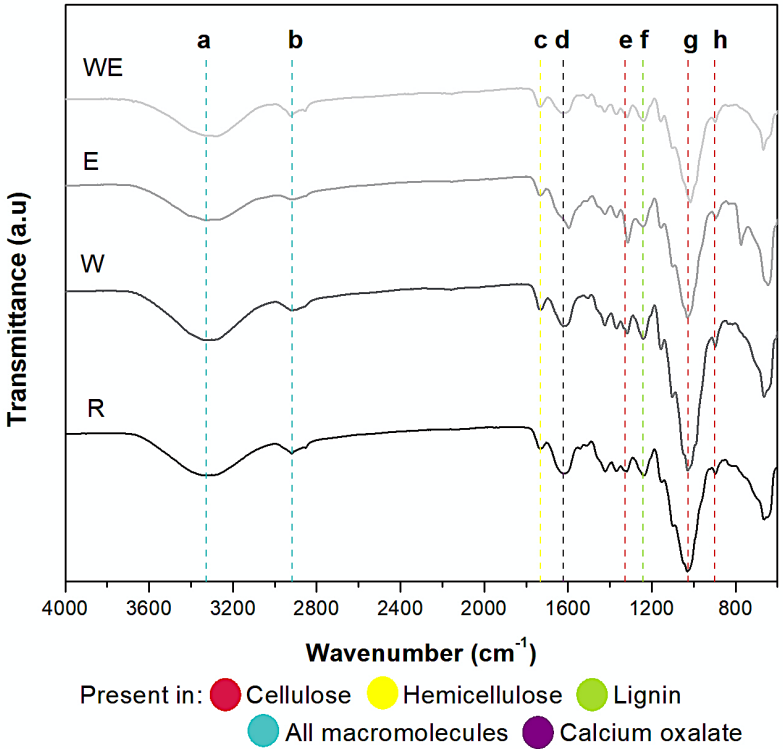


Figure 3.11. FTIR spectra obtained for the raw fiber and extractives after the organosolv pretreatment using water (W), ethanol (E), water and ethanol (WE) as solvents. Where: a) O-H, b) C-H, c) C=O, d) calcium oxalate, e) CH2, f) C-O, g) C-O-C and h) ß glycosidic bond.

The diffractogram (Figure 3.12) for raw, and organosolv pretreatment using as solvents water (W), ethanol (E) and the combination of water + ethanol (WE) showed two characteristic peaks located at 22.6° and 16° assigned to the crystallographic plane (1 0 0) and (2 0 0), respectively [60]. Using the Segal method [61], the crystallinity index (*CI*) was estimated, following Eq. 3.4.

$$CI\ (\%) = \frac{I_{200} - I_{am}}{I_{200}} \times 100 \qquad \text{Eq. 3.4}$$

Where, I_{200} corresponds to the heights of the (2 0 0) peak (indicating crystalline and amorphous cellulose) and the minimum intensity of I_{am} (amorphous), between the peaks of the planes (2 0 0) and (1 1 0).

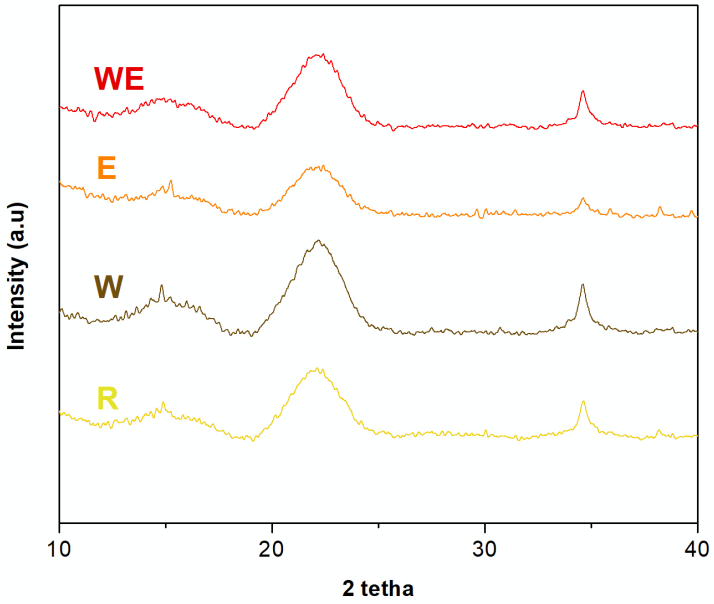


Figure 3.12. Diffractogram of pretreated fibers by organosolv using different solvents

After the organosolv pretreatment, the crystallinity index did not reveal a significant change in the CI value, (only increased close to 4% for the fiber pretreated using water and ethanol as solvents), confirming in this way a small fraction of crystalline cellulose exposure. This data is fully congruent with the characterizations described above in which it was confirmed that chemical structure of the fiber is maintained, while the surface distribution is modified by increasing the number of available hydroxyl groups (Table 3.3).

Table 3.3. Percentage of cellulose crystallinity index (CI) for the fibers pretreated by organosolv using different solvents.

Solvent	CI (%)
Raw	29.1
Water	29.2
Ethanol	31.6
Water + Ethanol	34.4

To characterize the surface charge of the pretreated fiber, the point of zero charge (pH_{zpc}) was determined based on Boehm's method [62], a value of 4.2 ± 0.1 was obtained. Compared to the pH_{zpc} of the raw fique fiber (close to 5.3 [63]), the pH_{zpc} of the fiber decreased as result of the increase in the number of functional groups such as carboxylic, hydroxyl and hemiacetal groups present in cellulose [64], as consequence of more cellulose exposure onto the fiber, resulting in a more acidic surface.

Additionally, the wettability of the pretreated fiber WE under the organosolv process was determined through the measurement of the contact angle following the procedure proposed by Schellbach *et al.*[32] A value of 41.3 ± 9.2° indicated a slight reduction in comparison to the raw fiber, increasing the hydrophilic character of the fiber as a result of the growth in the percentage of accessible cellulose on the fiber surface after pretreatment, which in turn implied an upsurge in the number of hydroxyl groups (-OH) available. Furthermore, as described in Table 3.2, the elimination of extractives such as waxes, sapogenins, and hecogenins, characterized by being strongly hydrophobic, contributed significantly to the improvement of the hydrophilic character of the material [65].

It is important to note that the pretreatment with oraganosolv did not affect the fiber mechanical properties with any of the evaluated solvents (Table 3.4). This statement was supported by the measurement of Young's Moduli (E) for all pretreated fibers using the dynamic mechanical analysis (DMA) technique. No significant changes were evidenced in the magnitude of E. Hence, parameters such as diameter, geometry, and stiffness of the pretreated fibers were maintained. The results reported in Table 3.4 were complemented with those reported with the crystallinity index (CI) values of Table 3.3, since Young's modulus and stiffness increase as CI also take higher values.

Table 3.4. Values of Young´s Moduli (E) for pretreated fibers by organosolv using different solvents measured by DMA.

Solvent	GPa
Raw	24.3
Water	16.8
Ethanol	22.6
Water + Ethanol	24.6

The textural properties of the pretreated fibers were analyzed by nitrogen adsorption isotherms, and the values of surface area were calculated using the BET equation. The results were summarized in Table 3.5. As was described in Chapter 2, lignocellulosic materials such as natural fibers are characterized by not being porous. This minimum porosity was conserved for the pretreatments using water and ethanol. Then, combining these two solvents, the surface area was close to the area contribution of each solvent, which may be a consequence of the fiber increased accessibility through the cellulose polymer. Furthermore, as was displayed in the SEM micrographs in Figure 3.8, ethanol appeared to induce an exfoliation process on the fiber surface, which could be a complementary indicator of the increase in porosity of approximately 10 $m^2 g^{-1}$ for the pretreated fiber (WE) compared to raw fiber. However, it is important to clarify that,

compared to other materials, the porosity value reported by the WE fiber was still considered low, characteristic of biomass such as fique fiber.

Table 3.5. BET surface area measured by nitrogen adsorption for pretreated fibers by organosolv.

Solvent	BET (m^2/g)
Raw	8.0 ± 0.3
Water	6.2 ± 0.2
Ethanol	9.4 ± 0.3
Water + Ethanol	18.2 ± 0.4

Finally, from the thermal characterization carried out on the WE fiber employing DSC and TGA techniques shown in Figure 3.13, the thermogram obtained was very similar to that obtained by the raw fiber in chapter 2. There was an approximate 6% mass loss in the range of 50 to 250 °C, related to the moisture evaporation (correlated to an endothermic peak in the DSC), which was close to the value present in Table 3.2, where the moisture of the pretreated fiber was also calculated under the NREL methodology, whose value was approximately 10%. Subsequently, a second mass loss of 34% was evidenced between 250 and 331 °C, related to the degradation of hemicellulose (confirmed by an exothermic peak at 321 °C in the DSC) [66]. Then, cellulose pyrolysis corresponding to 27% by weight occurred in the region of 331 - 366 °C (evidenced in the DSC as an endothermic peak at 350 °C) [67]. Subsequently, at temperatures higher than 380 °C, a weight reduction of 19.77% was generated, assigned to the lignin decomposition (supported with an exothermic peak at 410 °C) [66]. Finally, approximately 13% of the residual mass was detailed in Figure 3.13, which includes part of the ash and minor elements.

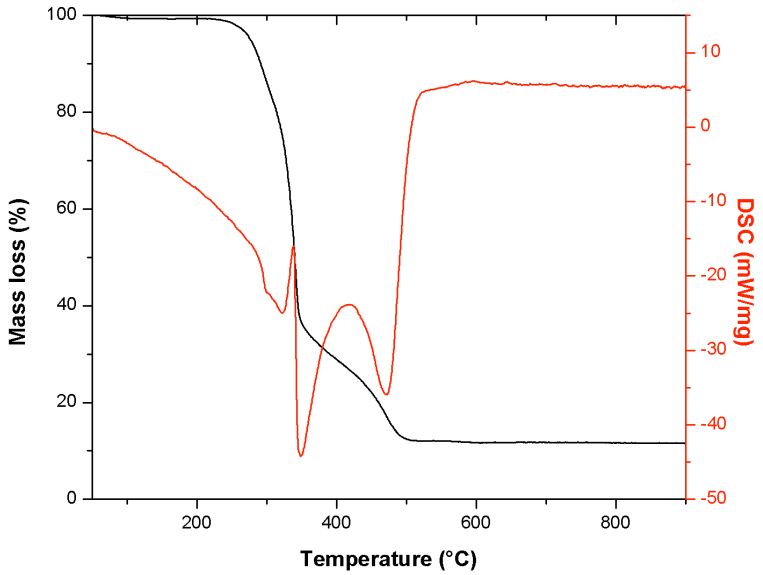


Figure 3.13. TGA (Thermogravimetric analysis) and DSC (Differential Scanning Calorimetry) under nitrogen for pretreated fique WE.

3.5 Conclusions

It was determinate that the alkaline process is mainly affect by reagent concentration and pretreatment time. The fique delignification was not as strong as the alkali concentration and pretreatment time increased, this behavior was confirmed due to the material size and fiber diameter that remained constant. Likewise, a slight change in the structural properties was evidenced, because of a change in the percentage of hemicellulose content in the fiber pretreated under alkali conditions.

On the other hand, the acid pretreatment reached high hydrolysis of hemicellulose, this process was affected in a general way by the acid concentration. Besides, the cellulose accessibility increased while the structural properties of the fiber were sacrificed. Compared with the alkali process, acid pretreatment was much stronger, because, in short times, the fiber size was completely reduced in approximately 1 cm as maximum length.

Subsequently, the organosolv pretreatment allowed controlling the type of solvents to be used (the combination of water and ethanol), to have fique fiber with a higher percentage of exposed cellulose, cleaner, and more homogeneous. This process removed compounds such as waxes, hecogenins, sapogenins, and some residues from the raw fiber. Through different characterization techniques, it was confirmed that the structural, thermal, mechanical, and morphological identity of the fiber were not altered, clearly indicating that any changes in the pretreated fiber were merely physical.

3.6 References

1. Lucas Herguedas, A. *Biomasa, combustibles y sostenibilidad*. (Itagra, 2012).
2. Abril, A. & Navarro, E. *Etanol a partir de biomasa lignocelulósica*. (Aleta Ediciones, 2012).
3. Wang, Q., El-Ensashy, H. & Thongchul, N. *Bioprocessing technologies in biorefinery for sustainable production of fuels, chemicals, and polymers*. (Wiley, 2013).
4. Kumar, P., Barrett, D., Delwiche, M. & Stroeve, P. Methods for pretreatment of lignocellulosic biomass for efficient hydrolysis and biofuel production. *Ind. Eng. Chem. Res*. **48**, 3713–3729 (2009).
5. Yang, B. & Wyman, C. Pretreatment: The key to unlocking low-cost cellulosic ethanol. *Biofuels, Bioprod. Biorefining*. **2**, 26–40 (2008).
6. Bychkov, A. & Lomovskii, O. Mechanical Treatment Effect on the Cellulolytic Specimen Activity. *Russ. J. Appl. Chem.* **83**, 1106–1108 (2010).
7. Bridgwater, A. Review of fast pyrolysis of biomass and product upgrading. *Biomass and Bioenergy*. **38**, 68–94 (2012).

8. Pavlovič, I., Knez, Ž. & Škerget, M. Hydrothermal reactions of agricultural and food processing wastes in sub- and supercritical water: A review of fundamentals, mechanisms, and state of research. *J. Agric. Food Chem*. **61**, 8003–8025 (2013).

9. Montgomery, L. & Bochmann, G. Pretreatment of feedstock for enhanced biogas production. (IEA Bioenergy, 2014)

10. Zhu, L. *et al.* Research on the influence of conductivity to pulsed arc electrohydraulic discharge in water. *J. Electrostat*. **72**, 1–6 (2014).

11. Lee, J. & Jeffries, T. Efficiencies of acid catalysts in the hydrolysis of lignocellulosic biomass over a range of combined severity factors. *Bioresour. Technol.* **102**, 5884–5890 (2011).

12. Marcotullio, G., Krisanti, E., Giuntoli, J. & de Jong, W. Selective production of hemicellulose-derived carbohydrates from wheat straw using dilute HCl or FeCl3 solutions under mild conditions. X-ray and thermo-gravimetric analysis of the solid residues. *Bioresour. Technol.* **102**, 5917–5923 (2011).

13. Zhao, X., Cheng, K. & Liu, D. Organosolv pretreatment of lignocellulosic biomass for enzymatic hydrolysis. *App. Microbiol. Biotechnol*. **82**, 815–827 (2009).

14. Gromov, V., Khrol, Y., Kalninsh, A. & Odincov, P. The mechanism of hydrotropic pulping. *Inst. Lesokhoz. Probl. Khim. Drev. Akad. Nauk Latv.* **25**, 3–27 (1963).

15. Souza-Correîa, J., Ridenti, M., Oliveira, C., Araújo, S. & Amorim, J. Decomposition of lignin from sugar cane bagasse during ozonation process monitored by optical and mass spectrometries. *J. Phys. Chem. B.* **117**, 3110–3119 (2013).

16. Bali, G., Meng, X., Deneff, J., Sun, Q. & Ragauskas, A. The effect of alkaline pretreatment methods on cellulose structure and accessibility. *Chem. Sus. Chem.* **8**, 275–279 (2015).

17. Michalsk, K. & Ledakowicz, S. Alkaline hydrogen peroxide pretreatment of energy crops for biogas production. *Chem. Pap.* **68**, 913–922 (2014).

18. Heitz, M. *et al.* Fractionation of Populus tremuloides at the pilot plant scale: Optimization of steam pretreatment conditions using the STAKE II technology. *Bioresour. Technol*. **35**, 23–32 (1991).

19. Duff, S. & Murray, W. Bioconversion of forest products industry waste cellulosics to fuel ethanol: A review. *Bioresour. Technol*. **55**, 1–33 (1996).

20. Biswas, R., Uellendahl, H. & Ahring, B. Wet Explosion: a Universal and Efficient Pretreatment Process for Lignocellulosic Biorefineries. *Bioenergy Res*. **8**, 1101–1116 (2015).

21. Santos, A., Kawase, K. & Coelho, G. Enzymatic saccharification of lignocellulosic materials after treatment with supercritical carbon dioxide. *J. Supercrit. Fluids.* **56**, 277–282 (2011).

22. Mes-Hartree, M., Dale, B. & Craig, W. Comparison of steam and ammonia pretreatment for enzymatic hydrolysis of cellulose. *Appl. Microbiol. Biotechnol.* **29**, 462–468 (1988).

23. Hergert, H. *Developments in organosolv pulping – an overview*. *Environmental Friendly Technologies for the Pulp and Paper Industry* (Food and Agriculture Organization of the United Nations, 1998).

24. Mesa, L. *et al.* Preliminary evaluation of organosolv pre-treatment of sugar cane bagasse for glucose production: Application of 23 experimental design. *Appl. Energy.* **87**, 109–114 (2010).

25. Pedersen, M. & Meyer, A. S. Lignocellulose pretreatment severity - relating pH to biomatrix opening. *N. Biotechnol.* **27**, 739–750 (2010).

26. Saha, B. C. Hemicellulose bioconversion. *J. Ind. Microbiol. Biotechnol.* **30**, 279–291 (2003).

27. Sluiter, A., Ruiz, R., Scarlata, C. & Templeton, D. *Determination of extractives in biomass laboratory analytical procedure*. (*National Renewable Energy Laboratory*, 2005).

28. Sluiter, A. *et al. Determination of total solids in biomass and total dissolved solids in liquid process samples*. *National Renewable Energy Laboratory (NREL)* https://www.nrel.gov/docs/gen/fy08/42621.pdf (2008).

29. Sluiter, A. *et al. Determination of Structural Carbohydrates and Lignin in Biomass*. *Laboratory Analytical Procedure Technical Report NREL/TP-510-42618* (2008).

30. Chum, H. L., Johnson, D. K., Black, S. K. & Overend, R. P. Pretreatment-Catalyst effects and the combined severity parameter. *Appl. Biochem. Biotechnol.* **24**, 1-10 (1990).

31. Dave, S., Damani, M. & Tipre, D. Copper remediation by Eichhornia spp. and sulphate-reducing bacteria. *J. Hazard. Mater.* **173**, 231–235 (2010).

32. Schellbach, S. L., Monteiro, S. N. & Drelich, J. W. A novel method for contact angle measurements on natural fibers. *Mater. Lett.* **164**, 599–604 (2016).

33. Arshadi, M., Abdolmaleki, M. K., Mousavinia, F., Foroughifard, S. & Karimzadeh, A. Nano modification of NZVI with an aquatic plant Azolla filiculoides to remove Pb(II) and Hg(II) from water: Aging time and mechanism study. *J. Colloid Interface Sci.* **486**, 296–308 (2017).

34. Gupta, R. & Lee, Y. Pretreatment of corn stover and hybrid poplar by sodium hydroxide and hydrogen peroxide. *Biotechnol. Prog.* **26**, 1180–1186 (2010).

35. Carvalheiro, F., Duarte, L. & Gírio, F. Hemicellulose biorefineries: A review on biomass pretreatments. *J. Sci. Ind. Res.* **67**, 849–864 (2008).

36. Jung, Y. & Kim, K. Acidic Pretreatment. *Pretreatment of Biomass: Processes and Technologies* 27–50 (Elsevier, 2014).

37. Bensah, E. & Mensah, M. Chemical pretreatment methods for the production of cellulosic ethanol: Technologies and innovations. *Int. J. Chem. Eng.* **2013**, 1-21 (2013).

38. Brodeur, G. *et al.* Chemical and Physicochemical Pretreatment of Lignocellulosic Biomass: A Review. *Enzym. Res.* **2011**, 1-17 (2011).

39. Cara, C., Ruiz, E., Ballesteros, I., Negro, M. J. & Castro, E. Enhanced enzymatic hydrolysis of olive tree wood by steam explosion and alkaline peroxide delignification. *Process Biochem.* **41**, 423–429 (2006).

40. Huijgen, W. J. J., Reith, J. H. & Den Uil, H. Pretreatment and fractionation of wheat straw by an acetone-based organosolv process. *Ind. Eng. Chem. Res.* **49**, 10132–10140 (2010).

41. Cara, C., Romero, I., Oliva, J. M., Sáez, F. & Castro, E. Liquid hot water pretreatment of olive tree pruning residues. *Appl. Biochem. Biotechnol.* **49**, 10132–10140 (2007).

42. Xu, Y., Li, K. & Zhang, M. Lignin precipitation on the pulp fibers in the ethanol-based organosolv pulping. *Colloids Surfaces A Physicochem. Eng. Asp.* **301**, 255–263 (2007).

43. Zhu, M. Q., Wen, J. L., Su, Y. Q., Wei, Q. & Sun, R. C. Effect of structural changes of lignin during the autohydrolysis and organosolv pretreatment on Eucommia ulmoides Oliver for an effective enzymatic hydrolysis. *Bioresour. Technol.* **185**, 378–385 (2015).

44. Mäki-Arvela, P., Salmi, T., Holmbom, B., Willför, S. & Murzin, D. Y. Synthesis of sugars by hydrolysis

of hemicelluloses- A review. *Chem. Rev.* **9**, 5638–5666 (2011).

45. Díaz, M. J. *et al.* Organosolv pretreatment of olive tree biomass for fermentable sugars. *Holzforschung.* **65**, 177–183 (2011).

46. WJJ, H., Van der Laan, R. R. & Reith, J. H. Modified organosolv as a fractionation process of lignocellulosic biomass for co-production of fuels and chemicals. (16th European Biomass Conference & Exhibition, 2008).

47. Yawalata, D. Catalytic selectivity in alcohol organosolv pulping of spruce wood. (University of British Columbia, 2001).

48. Pan, X. *et al.* Bioconversion of hybrid poplar to ethanol and co-products using an organosolv fractionation process: Optimization of process yields. *Biotechnol. Bioeng.* **94**, 851–861 (2006).

49. Schuerch, C. The solvent properties of liquids and their relation to the solubility, swelling, isolation and fractionation of lignin. *J. Am. Chem. Soc.* **74**, 5061–5067 (1952).

50. Gilbert, M. Relation of Structure to Chemical Properties. (Brydson's Plastics Material, 2016).

51. Zhao, X., Li, S., Wu, R. & Liu, D. Organosolv fractionating pre-treatment of lignocellulosic biomass for efficient enzymatic saccharification: chemistry, kinetics, and substrate structures. *Biofuels, Bioprod. Biorefining.* **11**, 567–590 (2017).

52. Chen, H., Zhao, J., Hu, T., Zhao, X. & Liu, D. A comparison of several organosolv pretreatments for improving the enzymatic hydrolysis of wheat straw: Substrate digestibility, fermentability and structural features. *Appl. Energy.* **150**, 224–232 (2015).

53. Amiri, H. & Karimi, K. Improvement of acetone, butanol, and ethanol production from woody biomass using organosolv pretreatment. *Bioprocess Biosyst. Eng.* **38**, 1959–1972 (2015).

54. Santos, J. D. G., Vieira, I. J. C., Braz-Filho, R. & Branco, A. Chemicals from agave sisalana biomass: Isolation and identification. *Int. J. Mol. Sci.* **16**, 8761–8771 (2015).

55. Le Brech, Y. *et al.* High resolution solid state 2D NMR analysis of biomass and biochar. *Anal. Chem.* **87**, 843−847 (2015).

56. Holding, A. J. *et al.* Solution-State One- and Two-Dimensional NMR Spectroscopy of High-Molecular-Weight Cellulose. *Chem. Sus. Chem.* **9**, 880 – 892 (2016).

57. Pu, Y., Hallac, B. & Ragauskas, A. J. Plant Biomass Characterization: Application of Solution- and Solid-State NMR Spectroscopy. *Aqueous Pretreatment of Plant Biomass for Biological and Chemical Conversion to Fuels and Chemicals.* (Wiley, 2013).

58. Rowell, R. M. *Handbook of wood chemistry and wood composites*. (Tayor & Francis Group, 2012).

59. Ovalle, S., Blanco, C. & Combariza, M. Exploring the composition of raw and delignified Colombian fique fibers, tow and pulp. *Cellulose.* **25**, 151–165 (2018).

60. Ciolacu, D., Ciolacu, F. & Popa, V. I. Amorphous cellulose—structure and characterization. *Cellul. Chem. Technol.* **45**, 1-13 (2011).

61. Segal, L., Creely, J. J., Martin, A. E. & Conrad, C. M. An Empirical Method for Estimating the Degree of Crystallinity of Native Cellulose Using the X-Ray Diffractometer. *Text. Res. J.* **9**, 786–794 (1959).

62. Goertzen, S. L. *et al.* Standardization of the Boehm titration. Part I. CO2 expulsion and endpoint determination. *Carbon N. Y.* **48**, 1252–1261 (2010).

63. Bastidas, K., Zea, H. & Sierra, C. Wastewater treatment using an iron nanocatalyst supported on Fique fibers. *Universidad Nacional de Colombia-Sede Bogotá* (Universidad Nacional de Colombia, 2016).

64. Galván, M. V. Mejora de la resistencia de papeles por usos de polielectrolitos sintéticos y naturales. (Universidad Nacional del Litoral, 2012).

65. Milagres, A. M. F., Carvalho, W. & Ferraz, A. Topochemistry, porosity and chemical composition affecting enzymatic hydrolysis of lignocellulosic materials. (Springer, 2011).

66. Evans, R., Newman, R. H., Roick, U. C., Suckling, I. D. & Wallis, A. F. A. Changes in Cellulose Crystallinity During Kraft Pulping. Comparison of Infrared, X-ray Diffraction and Solid State NMR Results. *Holzforsch. - Int. J. Biol. Chem. Phys. Technol. Wood.* **49**, 498–504 (2009).

67. Milosavljevic, I., Oja, V. & Suuberg, E. M. Thermal effects in cellulose pyrolysis: Relationship to char formation processes. *Ind. Eng. Chem. Res.* **35**, 653–662 (1996).

4. Functionalization of the cellulose fiber surface by carboxymethylation and TEMPO oxidation reactions

4.1 Abstract

The surface of pretreated fique fibers was chemically activated by carboxymethylation reactions (CMC) and oxidation by TEMPO, to produce chemical groups such as sodium carboxymethyl (-CH_2OCH_2COONa) and sodium carboxylate groups (-COONa), respectively. The main difference between these two types of functionalization is the selectivity when interacting with the hydroxyl groups (C6) of cellulose. In terms of the carboxymethyl cellulose functionalization two methodologies and two degrees of substitution quantification methods (DS) were evaluated. Once the methodology and the quantification method were established, the cross effect of variables like sodium hydroxide concentration (basification reaction), temperature, time and the concentration of sodium chloroacetate (etherification reaction) were analyzed through a Box-Behnken response surface design. The combination of 17.5% w/v sodium hydroxide, 10% w/v sodium chloroacetate, 40 °C and 180 min reached the higher DS value (0.14). For the fiber oxidized by TEMPO (a more environmentally friendly methodology), the effect of NaOCl: AGU (anhydrous-glucose units) molar ratio to achieve the highest percentage of oxidation degree (OD) was studied, and it was concluded 1 molar ratio of NaOCl: AGU managed to be the best functionalization condition, accomplishing OD = 9.32%. In both types of functionalization, the importance of using pretreated or raw fiber was determined, and it was confirmed the importance of doing a pretreatment stage before functionalization in both methodologies. For each functionalization, Fourier Transform Infrared Spectroscopy - Attenuated Total Reflectance (FTIR-ATR) characterization technique was used to confirm the presence of the expected functional groups. Besides, to understand how the properties changed after the fiber's functionalization structural, chemical, morphological, thermal, and mechanical characterizations were carried out. CMC affected the fiber identity while TEMPO preserved the fiber nature.

Key words: functionalization, carboxymethyl cellulose, TEMPO oxidation, surface modification, fique fiber.

4.2 Introduction

Cellulose is a linear chain polymer, formed by D-glucopyranose anhydride units linked by β-1,4-glycosidic bonds, the cellobiose is the repeating unit of the cellulose chains. It has a polymerization degree that varies depending on its origin, from 1000 to 5000 in the primary wall, 6000 in the secondary wall (S1 and S3) and from 13000 to 14000 in the S2 layer, reaches lengths of up to 6-7 μm and molecular weight of 2000000.

Cellulose is a macromolecule with great reactivity due to its functional groups, mainly the hydroxyl groups that protrude laterally from the flat ribbon characteristic of the cellulose morphology, being able to form inter and intramolecular interactions responsible for the mechanical resistance. The crystallites size and fibrils, their orientation degree and arrangement determine an imperfect crystalline structure. Consequently, it leads to crystalline alternation and amorphous zones within microfibrils. Properly, in the zone S2 there is a higher polymerization degree, so cellulose is more ordered and has a higher crystallinity degree (approximately 66% of cellulose). However, the cellulose crystallinity makes it insoluble in water, despite the high content of OH groups, affecting the pretreatment processes.

The cellulose molecules form fibrillar aggregations of molecules stabilized laterally through hydrogen bonds between hydroxyl groups of adjacent molecules. The microfibrils characteristics vary between species and development stages, they are added in larger fibers reaching thicknesses of 1 nm to 20 nm, confirming the existence of successive protective barriers that hinder the chemical attack and biological agents.

Natural fibers are considered a potential replacement for plastic fibers. Although natural fibers have the advantages of low cost and density, they also have a strong polar character that creates an incompatibility with most matrices. Consequently, the surface functionalization has been investigated to take advantage of chemical interactions, so a good layer adhesion to the base substrate depends on electrostatic interactions and ionic bonds [1]. These surface treatments increase production costs but are potentially capable of overcoming the incompatibility problem.

Lately, there has been an increase on research dealing with cellulose polyelectrolytes functionalization [2].

Particularly, the chemical treatment improves the adhesion between the fiber surface and polymer matrix, reducing the water absorption of composite materials, and their mechanical properties are enhanced. Extensive research has been carried out in order to achieve better interfacial interactions (physical or chemical) on natural fibers [3]. However, it should be noted the possibility of both types of interactions to occur simultaneously [4].

Carboxymethylation (CMC) and oxidation mediated by TEMPO are some examples of chemical reactions of cellulose reported in the research literature [5], since few functionalization processes are implemented on an industrial scale. Carboxymethylation is an etherification reaction in which condensations are carried out in the presence of organic solvents, the water present in lignocellulosic materials promotes secondary reactions with the etherifying reagent, instead of reacting with the hydroxyl groups of the cellulose [5]. Consequently, this reaction produces significant amounts of by-products (often pollutants for the environment) and requires high temperatures.

On the other hand, some functionalization processes involve newer catalytic reactions, in which room temperature and aqueous conditions are used. An example is the selective oxidation of primary hydroxyl groups (C6) of cellulose to sodium C6 carboxylate groups in water and pH 10, catalyzed by 2,2,6,6-tetramethylpiperidine-1-oxyl (TEMPO) [5]. This reaction is more environmentally friendly and has currently been found as a great alternative to traditional functionalization.

This research evaluated the carboxymethylation and TEMPO oxidation reactions, as alternatives for inserting a negative surface charge to the cellulose present in the pretreated fique fiber, through a simple functionalization, which will increase the reactivity with other chemical species such as metal cations.

4.3 Materials and methods

4.3.1 Chemicals and materials

NaClO, NaBr, TEMPO, acetic acid (> 99%), NaOH, m-cresol (99%), isopropanol (> 99%) and phenolphthalein were purchased from Sigma-Aldrich®, ethanol (analytic grade) was provided by Panreac®, HCl (37%) and silver nitrate were distributed by Merck (Darmstadt, Germany), sodium chloroacetate was acquired from Alfa Aesar®. Aqueous solutions were made up with DI (deionized water). Pretreated fique fiber by Organosolv was obtained from Chapter 3.

4.3.2 Experimental set-up and procedure

- Carboxymethyl cellulose (CMC)

CMC functionalization consists of an ether in which the -OH groups present in the cellulose glucose are converted into a carboxymethyl group. This reaction comprises two stages (Eq 4.1 and 4.2).

Basification:

$$C_6H_7O_2(OH)_3]_n + nNaOH \rightarrow [C_6H_7O_2(OH)_2ONa]_n + nH_2O \quad \text{Eq. 4.1.}$$

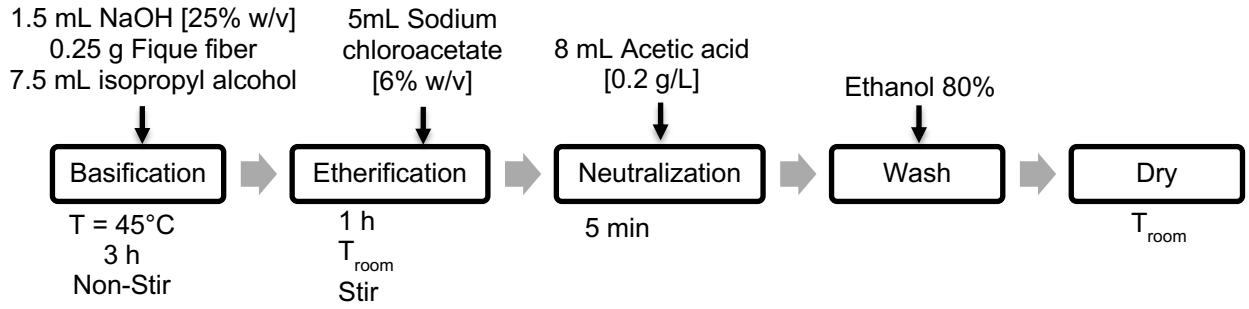
Etherification:

$$[C_6H_7O_2(OH)_2ONa]_n + nClCH_2COONa \rightarrow [C_6H_7O_2(OH)_2OCH_2COONa]_n + nNaCl \quad \text{Eq. 4.2.}$$

However, synthesis methodologies reported differ considerably in the solvent used during the basification reaction (water or isopropanol), and if the etherification reaction changes due to stirring or not. According to literature these variables lead to obtaining materials with different degrees of substitution (DS).

Additionally, other parameters such as sodium hydroxide concentration (basification reaction), temperature, time and concentration of sodium chloroacetate (etherification reaction) have an important influence on the surface modification. However, these 4 parameters were set with equal values in the two methodologies evaluated; the assigned values are common in the reports of each methodology separately. Therefore, to identify the methodology to obtain the highest DS values, two synthesis methodologies were evaluated (HNZ [6] and WNG [1]). Figure 4.1 displays the flow diagram for each methodology.

a) Hinestroza, HNZ (modified from [6])



b) Wang, WNG (modified from [1])

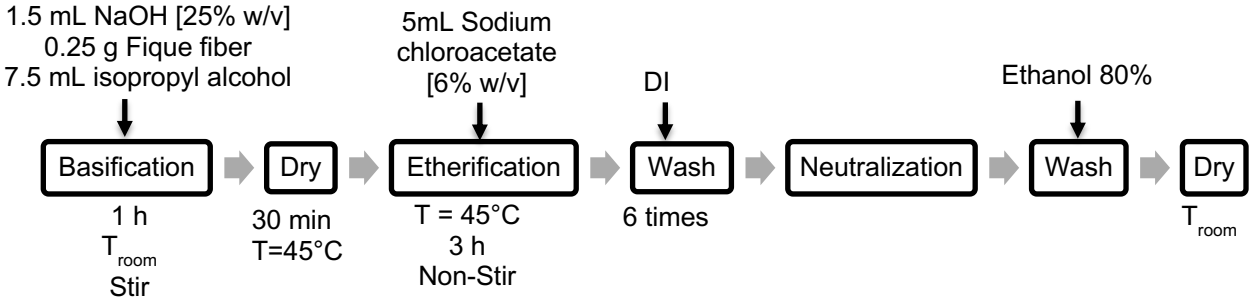


Figure 4.1. Functionalization procedures used to produce CMC on the surface of the fique fiber, following the methodologies of a) HNZ and b) WNG (Cont.).

The degree of substitution (DS) obtained from functionalization (DS = number of hydroxyl groups of glucose unit replaced by carboxymethyl groups) was quantified. However, the etherification reaction is not selective, so there are three hydroxyl groups in each glucose unit, namely C2, C3, and C6, which have the possibility of being functionalized (Figure 4.2).

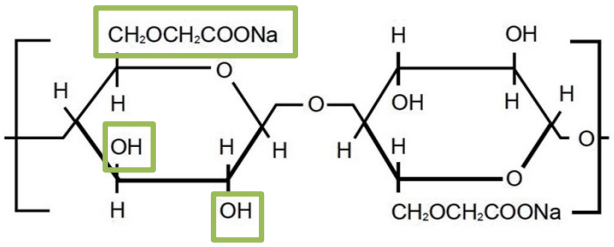


Figure 4.2. Scheme of CMC substitution degree.

Regarding DS quantification, two different methods were evaluated: the first reported by USP XXIII [7] and the second by Wang [1]. In the USP methodology, 0.25 g of the functionalized fiber were weighed and immersed in 75 mL of NaCl (10% w / v), this solution was kept under stirring for 10 min at room temperature. Subsequently, 2 drops of m-cresol were added into 3.75 mL of 0.1 M HCl under constant stirring (it was stopped until the solution turned yellow). After 10 min,

fiber was removed from the solution, and the remaining liquid was titrated with a 0.1 M NaOH solution. Also, the pretreated fiber titration was used as a blank.

The method proposed by Wang was an indirect acid-base titration in which 0.25 g of CMC fiber was immersed in 9 mL (0.5% v/v) for 2 h at room temperature. Subsequently, the fiber was washed with distilled water until no evidence of remaining chlorides was observed (to confirm the absence of chloride, 2 drops of silver nitrate were added). Immediately, the analyzed fiber was dried for 60 min at 105 °C, then immersed in 9 mL of NaOH (0.05 N) for 2 h at room temperature. Subsequently, the fiber was removed from the solution and titrated with HCl (0.05 N), using phenolphthalein as an indicator. To quantify the degree of substitution (*DS*) in a precise and accurate way, some equations are reported. A is the degree of substitution of the carboxymethyl acid (Eq. 4.3), *S* is the degree of substitution of sodium carboxymethyl (Eq. 4.4,) and *DS* is attributed to the degree of total substitution (Eq. 4.5):

$$A = \frac{1150\,M}{(7120 - 412M - 80C)} \quad \text{Eq. 4.3}$$

$$S = \frac{(162 + 58A)C}{(7120 - 80C)} \quad \text{Eq. 4.4}$$

$$DS = A + S \quad \text{Eq. 4.5}$$

Where *M* refers to the base milliequivalents required for the neutralization of carboxymethylcellulose (determined in the titration) and *C* is the ignition percentage of carboxymethylcellulose residues.

Once the best functionalization and quantification methodology to be followed was defined, the four most influential parameters in the carboxymethylation of the fique fiber were evaluated. For this, an experimental design of Box-Behnken was proposed to evaluate the individual and cross effects of sodium hydroxide concentration, sodium chloroacetate concentration, etherification temperature, and etherification time, in three levels for each of them (Table 4.1). The values of each factor level were chosen from the review of several articles on cellulose carboxymethylation by authors such as Da Silva Pinto *et al.* [8], Mousavi *et al.*[9], Adinugraha *et al.*[10], Pushpamalar *et al.* [11], and Zhao *et al.* [12]. Finally, the conditions with the highest DS will be considered as the best conditions to be used in the CMC fiber functionalization.

Table 4.1. Factors assessed in CMC functionalization of fique fiber pretreated.

Factor	Low	Medium	High
[NaOH] %	5	12.5	20
[Sodium chloroacetate] %	5	12.5	20
Etherification Temp (°C)	20	45	70
Etherification time (h)	0.5	1.25	2

MiniTab 16 Statistical Software served to identify the contribution of each variable and its interaction in the degree of substitution (DS) resulted from the carboxymethylation through the respective statistical analysis of the data obtained. Statistical regression was used to fit a second-order polynomial experimental data and identify relevant terms of the model (Eq. 4.6).

$$Y = \beta_0 + \sum \beta_i x_i + \sum \beta_{ii} x_{ii}^2 + \sum \beta_{ij} x_i x_j \qquad \text{Eq. 4.6}$$

Where β_0 is the compensatory term; β_i is the dependent term or the linear effect of factor input x_i; *ii* is the quadratic effect input factor x_i and β_{ij} is the effect of interaction between the linearly input factor x_i and x_j.

- TEMPO oxidation

The surface of the pretreated fique fiber was chemically modified by oxidation to introduce negative charge [13]. Sodium bromide NaBr (0.1 g, 1.0 mmol) and 2,2,6,6-tetramethylpipiridine 1-oxyl radical TEMPO (0.016 g, 0.1 mmol) were added into 200 mL of deionized water in ice bath under constant stirring.

1 g of pretreated fiber was soaked in the solution for 10 min. The initial pH of the sodium hypochlorite solution (NaOCl, 5 vol%) was adjusted to 10 with hydrochloric acid HCl 0.1 $M_{(aq)}$, an equivalent amount into the range of 0.3 to 8 mol equivalents of AGU, drop wise was put on into the fiber pretreated solution while the pH was maintained at 10 with sodium hydroxide NaOH 0.5 $M_{(aq)}$ during the reaction. When the consumption of NaOH was constant (close to 120 min [14]), 10 mL of ethanol were added to stop the reaction. Fibers were washed using DI water and dried.

The carboxylate content in functionalized fiber was determined by conductimetric titrations [13 15]. 50 mg of functionalized fiber were submerged in 15 mL of HCl 10 $mM_{(aq)}$ during 10 min, to ensure protonation of carboxylate groups. Titrant (NaOH, 10 mM) was added in aliquots of 0.5 mL, the conductivity was followed by a Seven Multi Mettler Toledo conductivity probe. Typical conductivity curves have three stages clearly defined, 1) conductivity reduction due to the reaction HCl / NaOH, 2) slow changes in conductivity as a result of the reaction between a weak acid (carboxylic

groups) and NaOH, 3) increases in conductivity owing to all acids (strong and weak) were neutralized, resulting in an excess of NaOH [16]. From the conductivity curve, the value of NaOH consumed can be determined to calculate the value of the oxidation degree following Eq. 4.7:

$$\mathrm{OD}\ (\%) = \left[\frac{162.5 \times C \times (V_2 - V_1)}{w - (35.97 \times C \times (V_2 - V_1))}\right] \times 100 \qquad \text{Eq. 4.7}$$

In addition, surface charge density or carboxyl contents were calculated by Eq. 4.8 [17]:

$$\mathrm{COONa}\ (\mathrm{mmol/g}) = \left[\frac{\left(\frac{80}{30}\right) \times C \times (V_2 - V_1) \times 1000}{w}\right] \qquad \text{Eq. 4.8}$$

Where *C* is the concentration of NaOH solution (M), V_1 and V_2 are the volumes of NaOH (L), *w* is the dry mass of the functionalized fiber (g), 162.15 is the AGU molecular weight and 35.97 is the difference between the AGU molecular weight and the sodium salt of the glucuronic acid group [18]. Measurements were done in triplicate for each fiber, the average value was reported.

4.3.3 Characterization

- Chemical characterization

Fourier Transform Infrared Spectroscopy (FT-IR) was used to identify changes in the fiber functional groups. FT-IR was determined using an ATR (PIKE) diamond crystal accessory attached to a FT-IR Nicolete iS 10 spectrometer (Thermo Fisher Scientific). Scans of 20 readings were performed by spectrum, and data were recorded from 4000 to 600 cm^{-1}.

Energy-dispersive X-ray spectroscopy (EDX) equipment coupled to a SEM was used, this chemical elemental analysis was performed in a JEOL JSM-6480LV, operating in spectrum collecting mode under high vacuum conditions, 10 kV and approximate at a 50 µm of working distance.

- Surface Characterization

Point of zero charge (pH_{zpc}) was determined using the drift method in which solutions with 45 mL of KNO_3 (1% vol.) were adjusted to an initial pH in the range of 2 to 10 by adding HCl 0.1 M or NaOH 0.1 M. The volume of each solution was completed up to 50 mL adding KNO_3 (1% vol.). Once the pH of the solutions was set, 0.1 g of raw fique fiber was added, the resulting suspensions were stirred for 24 h at 25 °C, and the pH of the supernatants is registered [19].

To analyze the wetting fiber surface, a novel method published by Schellbach *et al.* [20] to measure the contact angle was implemented. Two fibers with similar diameter were aligned parallel with a distance ~ 1 mm between them under an Olympus microscope at room temperature. A drop of deionized water was deposited in this small space, in order to measure the hanging bridge to enlarge the lateral dimension of the water bridge and reinforce the spreading of it over the dry sections of the fibers. After the water column enlarged and the spherical menisci stabilized, the high-resolution images were captured using the software cellSens. Five images were captured for both enlarged and reduced water columns on each sample, and the values of the diameter (*d*) and height (*h*) of the meniscus were obtained. The contact angle was calculated using Eq. 4.9:

$$\theta = 90 - 2\tan^{-1}\left(\frac{2d}{h}\right) \qquad \text{Eq. 4.9}$$

- Structural Characterization

Crystalline fique fiber structure was studied at room temperature with an XPert Pro MPD diffractometer with monochromator of crystal graphite using Cu Kα (λ = 1.5406 Å) at 40 kV and 30 mA. Diffraction patterns were obtained in the range of 2theta =10-40°, with a step size of 0.02° and measuring time of 50 s per step. Experimental data were analyzed using PANalytical X'Pert HighScore Plus database.

- Morphological and Textural Characterization

The total surface area was measured by the adsorption of nitrogen (N_2) at 77 K, using a Quantachrome NOVA e-Series surface area analyzer. N_2 isotherms were performed on raw fiber samples. Before N_2 adsorption, the samples were degassed at 80 °C for 8 h. The calculation of the total surface area was established using the BET method [21].

Morphologycal characterization of fique fibers was achieved via Field Emission Scanning Electron Microscope (FESEM) and performed on thin-film gold-coated samples using a Zeiss Auriga FIB-SEM (GeminiSEM) scanning electron microscope, coupled to a secondary electrons (SE2) detector. The micrographs were taken at 1.5 kV, working distance (WD) ranging from 4.9 to 5.2 mm, at different magnifications.

- Thermal Characterization

Thermal gravimetric analysis (TGA) and Differential Scanning Calorimetry (DSC) were performed using a simultaneous thermal analyzer (STA 409 PC/4/H Luxx) in a temperature range from 50 to 900 °C at a heating rate of 10 °C/min using an inert (N_2, flow rate of 50 cm^3 min^{-1}) atmosphere.

- Mechanical Characterization

Dynamic Mechanical Analysis (DMA) was performed in a Mettler Toledo DMA analyzer, one fiber was centered inside the sample holder using single-cantilever clamps, with a free length of 17.5 mm. The DMA was done at room temperature and the oscillation conditions were fixed at 1Hz and the amplitude was 20 μm (i.e. 0.11% strain), which was well within the linear viscoelastic region. Storage modulus E (MPa) were collected during the test; final value includes an average of three measurements for each sample.

4.4 Results and Discussion

4.4.1 Carboxymethyl cellulose (CMC)

The first result reported was related to the DS quantification method to follow the results obtained by the CMC reaction. In general terms, the methodology proposed by Wang did not give coherent DS values, for most of the proposed experiments the indirect acid-base titration reported negative values. Also, only the raw fique fiber sample managed to have DS = 0.14 ± 0.02, which was inconsistent because this fiber had no surface modification. On the contrary, the USP methodology allowed to quantify the two functionalization methodologies proposed by HNZ and WNG, for which the effect of fiber pretreatment, the solvent used in the basification reaction (isopropanol or water) and stirring was analyzed in the etherification reaction. The DS results for both methodologies were summarized in Table 4.2.

From the results presented in Table 4.2, the measurement of a blank was considered, which corresponded to the functionalization process without fique fiber. Likewise, the determination of DS was carried out on the raw and pretreated fibers, which were normalized with the blank. Comparing the DS values obtained by these fibers, DS values were 0.018 and 0.034, respectively. These values were the average number of hydroxyl groups (-OH) in the cellulose structure substituted by carboxymethyl groups. The pretreated cellulose DS was approximately the double compared to raw fiber, since in the pretreated fiber the amount of cellulose exposed on the surface was greater, due to the organosolv pretreatment previously carried out.

Additionally, Table 4.2 highlights the poor DS values obtained using the WNG functionalization methodology when compared to the HNZ methodology. Experiments carried out for the evaluation of each methodology were performed in triplicate. CMC implies two reactions: basification and etherification, the methodologies differ between these two reactions. In the

Wang's case, there was a conventional carboxymethylation separated by a drying stage at 45 °C and a neutralization stage after etherification, which could negatively affect the CMC development. Furthermore, according to Parikh *et al.* [22] the CMC functionalization, where a dried stage was included between the basification and etherification reactions, was mainly focused to have low levels of DS (between 0.002-0.003), coinciding with the results obtained in this research.

Table 4.2. Experimental design to identify the CMC methodology that reached the higher DS in the fique fiber quantified by USP method, considering the evaluation of fiber type (raw, R or pretreated, WE), the solvent used in the basification step (isopropyl alcohol, OH or water, H_2O), and with or without stirring during the etherification step.

Sample	**DS**	
Blank	0.042 ± 0.001	
Raw	0.018 ± 0.008	
Pretreated	0.034 ± 0.001	
Experiment	**DS following HNZ procedure**	**DS following WNG procedure**
R / H_2O /Stir	0.037 ± 0.003	-0.003 ± 0.002
R / H_2O /Non-Stir	0.011 ± 0.001	-0.007 ± 0.002
R / OH /Stir	0.035 ± 0.014	0.005 ± 0.002
R / OH /Non-Stir	0.039 ± 0.007	-0.005 ± 0.002
WE / H_2O /Stir	0.043 ± 0.003	0.024 ± 0.005
WE / H_2O /Non-Stir	0.050 ± 0.003	0.011 ± 0.002
WE / OH/Stir	0.083 ± 0.009	0.020 ± 0.002
WE /OH/Non-Stir	0.076 ± 0.003	0.014 ± 0.002

Meanwhile, HNZ eliminated these two steps and possibly avoided two important facts: i) since the fiber was wet after basification, the swelling/gelling capacity was preserved at the etherification time, and the high content of bound water promoted etherification, ii) the neutralization could eliminate the fiber functionalization achieved, due to a possibly very strong acid-base reaction. Similar behaviors were reported in other studies[22].

Regarding the importance of the pretreatment implemented before functionalization, it was confirmed that both evaluated pretreatment methodologies contribute positively to higher DS values. The HNZ methodology using previously pretreated fibers achieved DS values approximately two times bigger than the ones obtained for raw fiber (see Table 4.2), due to the higher content of hydroxyl groups available on the surface to be converted into carboxymethyl groups (see details in chapter 2).

On the other hand, in the experiments carried out by the HNZ methodology, varying stirring conditions during the etherification reaction proved to be non-influential in the functionalization. Very similar values of DS were achieved under the same experimental conditions of R/OH,

WE/H_2O, and WE/OH, (where R means raw fiber, WE mean fiber pretreated by organosolv; OH and H_2O are related to the isopropanol and water solvents used during the basification reaction). However, the highest value of DS = 0.083 was obtained using stirring, pretreated fiber, and isopropanol as a solvent. Additionally, whenever R was used under the carboxymethylation methodology of HNZ, similar values between the samples were obtained (DS = 0.038). Instead, when WE were used higher values of degrees of substitution were reached compared to R.

On the contrary, a significant effect was corroborated depending on the type of solvent used during the basification reaction (Table 4.2). The importance of using organic solvents during carboxymethylation consists of providing the reagents accessibility in the etherification stage to the anhydrous-glucose units present in cellulose [23]. The organic solvent polarity has been reported to significantly influence in the cellulose carboxymethylation; isopropyl alcohol has lower polarity than water, and as the polarity of the aqueous medium was reduced, the efficiency of basification reaction increased. Similar behaviors were reported by Parikh *et al.* [22].

Figure 4.3 showed the FTIR spectra of the materials with stirring and using isopropanol as a solvent in the basification reaction, for the two proposed methodologies. In the FTIR spectra of CMC synthesis, important changes were evidenced in 3 mainly bands when they were compared to the raw and pretreated fiber spectra.

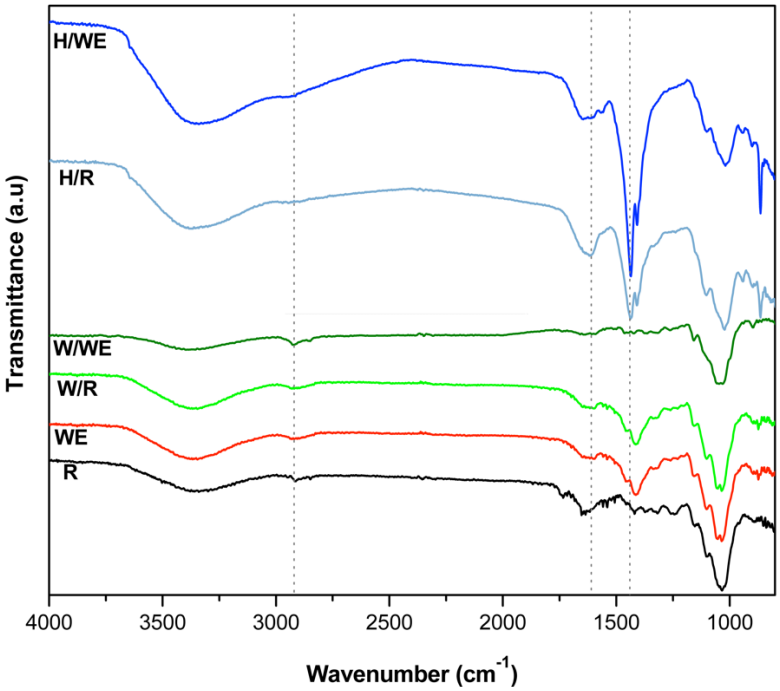


Figure 4.3. FTIR-ATR spectra of functionalized CMC fique fibers, following the HNZ and WNG methodology, using isopropanol as solvent and stirring during the etherification reaction.

The first signal at 2920 cm^{-1} evidenced almost a complete elimination for most experiments due to the substitution that occurs in the CH_2 groups (Figure 4.15). The other two bands confirmed the carboxymethylation, the band located at 1605 cm^{-1} increased its intensity in most experiments with the HNZ methodology compared to raw and pretreated fiber caused because by the presence of the carboxymethyl ether group (associated to stretching vibrations of a carboxylic group). A new band appeared at 1410 cm^{-1} corresponding to the carboxyl salt group (it did not exist in the FTIR spectra of cellulose from raw and pretreated fique fiber), this signal was very strong for HNZ methodology using pretreated fiber.

To conclude up to this moment, the quantification technique to be used will be the reported by the USP. Likewise, it was shown the HNZ methodology allowed to achieve higher values of DS, setting from now on isopropanol as a solvent for the basification reaction, stirring in the etherification reaction and effectively use the fiber pretreated by organosolv. Based on the results obtained previously, the conditions described were constant in the experiments carried out from now on, in which it was sought to analyze the effect of influencing factors on CMC functionalization.

A Box-Behnken response surface design was obtained, using the levels for each factor established in Table 4.1. The order of the cross and individual factors that most affect the functionalization by cellulose carboxymethylation are sodium hydroxide concentration (basification stage) and temperature, time and sodium chloroacetate concentration (etherification stage).

Table 4.3 summarized the experimental conditions of each one of the 27 runs and the degree of substitution (DS) after the functionalization process; also, it includes the three-center point runs. All the experiments were performed randomly to minimize possible systematic errors. The highest value of DS = 0.14 was achieved under the conditions of run 4, where the highest values of each factor evaluated were used, except for the concentration of sodium hydroxide (intermediate). On the contrary, the lowest DS values were obtained for runs 13 and 16, which have in common low temperatures and the lower concentration of sodium chloroacetate used during the etherification reaction.

Table 4.3. Results of the Box-Behnken experimental design of the degree substitution (DS) after the carboxymethylation functionalization onto fique fiber pretreated (SC is Sodium chloroacetate).

Run	[NaOH] w/v %	[SC] w/v%	Temperature of etherification (°C)	Time of etherification (min)	DS
1	30.0	6	40	30	0.12
2	5.0	6	40	180	0.11
3	17.5	10	40	30	0.10
4	17.5	10	40	180	0.14
5	17.5	2	20	105	0.07
6	17.5	6	20	30	0.08
7	17.5	6	40	105	0.09
8	30.0	2	40	105	0.09
9	17.5	6	40	105	0.10
10	5.0	6	40	30	0.10
11	30.0	6	40	180	0.08
12	5.0	2	40	105	0.08
13	30.0	6	20	105	0.06
14	17.5	2	40	180	0.09
15	5.0	10	40	105	0.08
16	5.0	6	20	105	0.06
17	17.5	6	40	105	0.11
18	30.0	10	40	105	0.12
19	17.5	2	60	105	0.09
20	30.0	6	60	105	0.12
21	5.0	6	60	105	0.08
22	17.5	2	40	30	0.07
23	17.5	6	60	180	0.10
24	17.5	10	20	105	0.07
25	17.5	6	20	180	0.07
26	17.5	10	60	105	0.10
27	17.5	6	60	30	0.09

To evaluate the treatment effect on the variability of DS through an analysis of variances (ANOVA) of the results reported in Table 4.3, it was necessary to verify the assumptions of this statistical analysis; the residual plots of DS were summarized in Figure 4.4.

The histogram in Figure 4.4c indicated the data were not biased. The normal probability plot (Figure 4.4a) shows the data were normally distributed, and there were no outliers. From the residuals plot versus adjusted values (Figure 4.4b), it was possible to conclude the variance was constant since there was no linear relationship of the data. From Figure 4.4d, the residuals versus

order of the data allowed corroborating there were no systematic effects on the data owing to the experiments time or the data collection order.

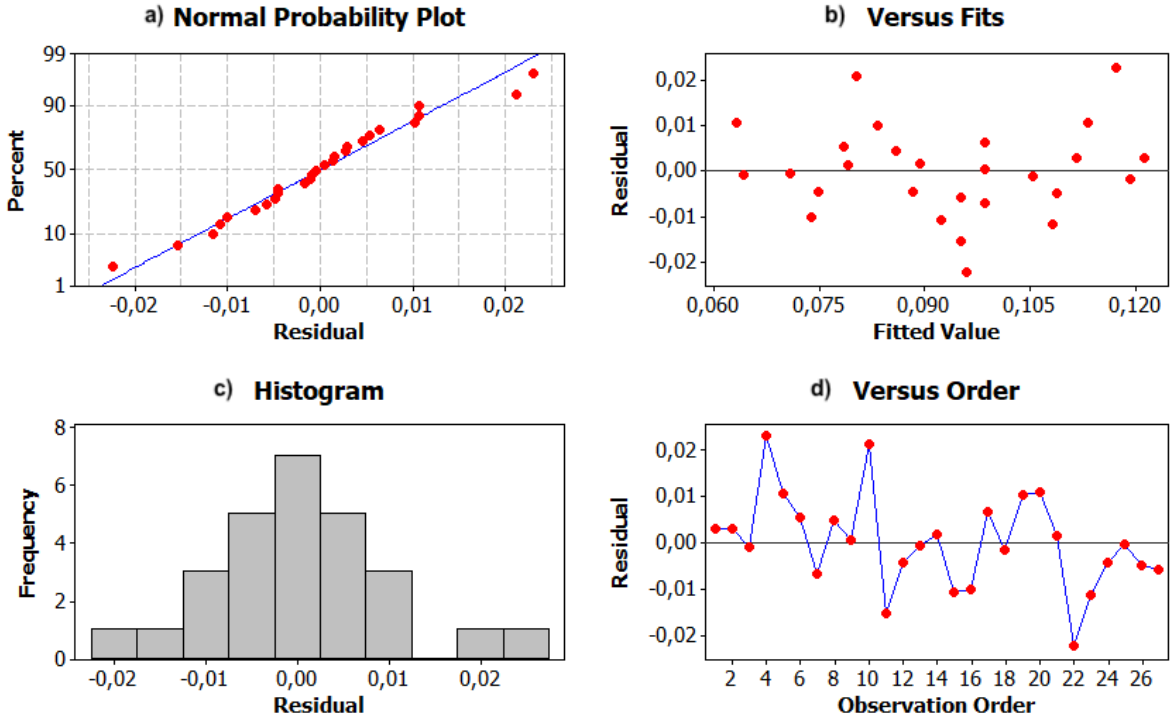


Figure 4.4. Residual plots for DS calculated from the data summarized in Table 4.3 to check the assumptions to apply the ANOVA statistical study.

Once the four assumptions of the ANOVA statistical analysis were verified, it was confirmed that, of the four factors analyzed in the cellulose carboxymethylation process, only the temperature of the etherification reaction proved to be statistically significant (p = 0.008). However, of the variables cross effect, none of the possible combinations between the factors was shown to be statistically significant to affect CMC functionalization.

The statistical adjustment of the equation Eq. 4.6 to the data summarized in Table 4.3, led the experimental description of the degree substitution of the carboxymethyl groups onto the fique fiber after the functionalization stage (Eq. 4.10); where *A*: [NaOH] w/v%, *B:* [Sodium chloroacetate] w/v%, *C*: temperature of etherification (°C) and *D*: time of etherification (min).

$$DS = 0.04 - 3.11\times10^{-4}(A) - 2.77\times10^{-3}(B) + 2.27\times10^{-3}(C) - 1.14\times10^{-4}(D) - 6.37\times10^{-6}(A^2) - 6.72\times10^{-5}(B^2) - 3.73\times10^{-5}(C^2) + 8.07\times10^{-7}(D^2) + 1.46\times10^{-4}(AB) + 4.39\times10^{-5}(AC) - 1.53\times10^{-5}(AD) + 4.31\times10^{-5}(BC) + 1.55\times10^{-5}(BD) + 3.43\times10^{-6}(CD) \quad \text{Eq. 4.10}$$

Given the *DS* obtained in the functionalization, it was concluded that the levels analyzed were adequate. The model fitting between the experimental and calculated data is reflected by the correlation coefficient R^2 = 82.99%. The cross effect of the four variables analyzed in DS (values from Table 4.3) will be described.

Initially, the NaOH concentration effect, described in Figure 4.5, showed to be a limiting factor at low concentrations in the reaction with sodium chloroacetate during the etherification reaction (Eq. 4.2). That was expected since NaOH was the limiting reagent in high concentrations in the basification reaction (approximately between 20 to 30% w/v). This reagent achieved the highest DS values around 0.11 - 0.12.

Figure 4.6 presented the NaOH concentration effect; at low etherification times, the higher the NaOH concentration, the higher the DS values reached (close to 0.12). The etherification temperature complemented the results already described (Figure 4.7), in which higher concentrations of NaOH achieved the highest values of DS. Thus, with values greater than 15% w/v of NaOH and temperatures greater than 35 °C the obtained DS values were greater than 0.10. In general, the cross effect of NaOH concentration with any of the variables always reached the higher DS values of carboxymethyl groups onto the surface of fique fiber.

Sodium chloroacetate being the limiting reagent in the etherification reaction, only in concentrations greater than 4% achieved values of DS = 0.1 (Figure 4.5). Likewise, the etherification reaction allowed to reach higher DS values in longer reaction times, without significant variations from 120 min of reaction (Figure 4.8). From the cross effect of the sodium chloroacetate concentration and the etherification temperature, the directly proportional behavior was confirmed (see Figure 4.9), attaining DS concentration values close to 0.12.

The third variable analyzed (the etherification time) reveals as the etherification time increased, the DS values also improved with the NaOH concentration, reaching a maximum value of 0.12 at 180 min, as observed in Figures 4.6 and 4.8. However, as the concentration of sodium chloroacetate became higher the DS decreased, possibly as an indication that at the beginning of the etherification reaction all the chloroacetate was available to react. Still, the reaction rate was fast during the first 60 min. Additionally, since chloroacetate was the limiting reagent, this may be another evidence of the DS reduction at longer reaction times.

In terms of the etherification temperature (ANOVA statistical analysis confirmed to be the most influential factor in the cellulose carboxymethylation), it was found that regardless of the concentration of either NaOH (Figure 4.7) or sodium chloroacetate (Figure 4.9), only at temperatures greater than 35 °C a significant change could be evidenced in DS values greater than 0.1.

From all the analysis carried out up to this moment, the highest DS value 0.14 (according to the potentiometric titration in terms of oxidation degree, OD = 11.3% ± 1.1) was obtained under 17.5% w/v NaOH concentration, 10% w/v chloroacetate concentration, etherification temperature (40 °C), and 180 min of etherification time, these conditions corresponded to run 4 reported in Table 4.3. The characterization was performed in the functionalized fique fiber with the higher DS.

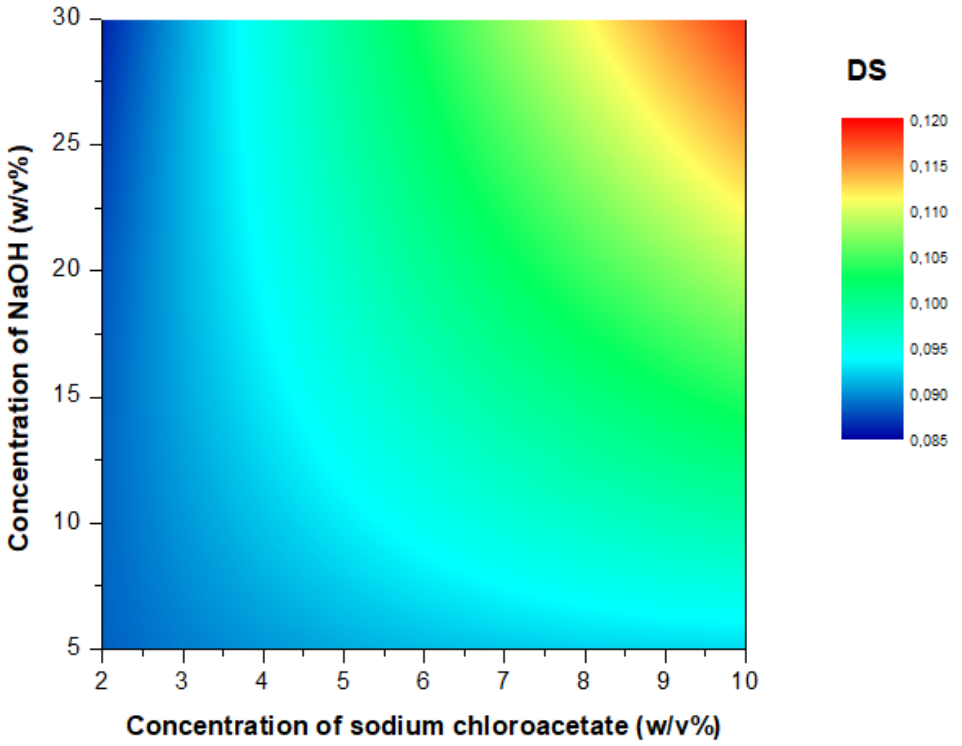


Figure 4.5. Contour plot of NaOH concentration % w/v vs sodium chloroacetate %w/v and DS

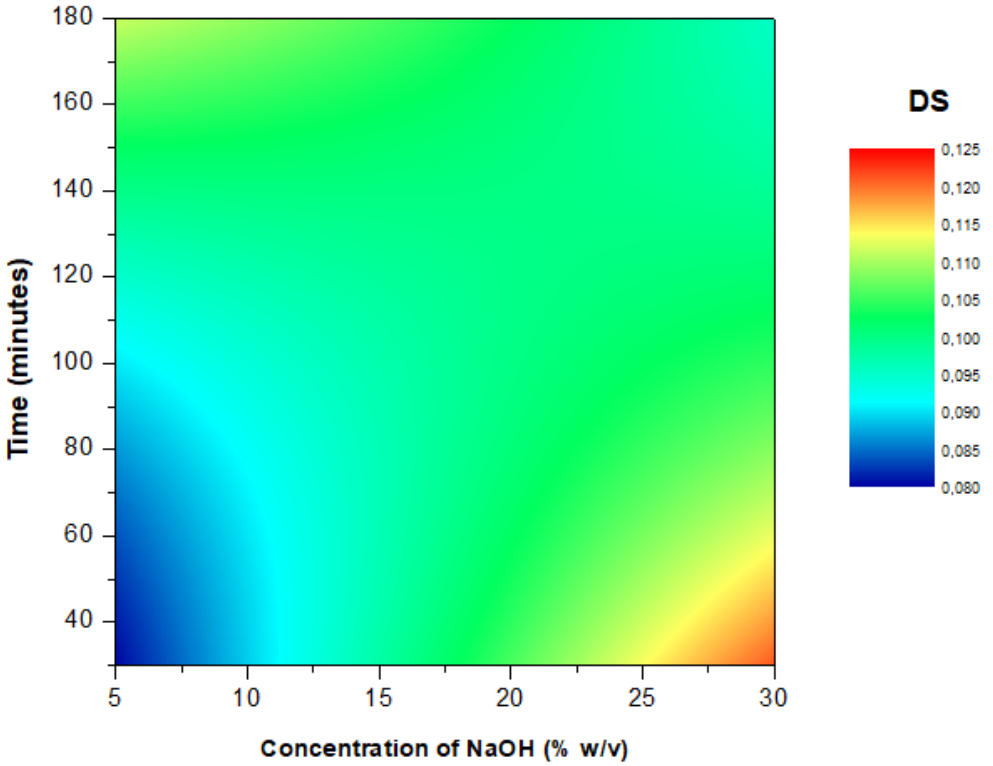


Figure 4.6. Contour plot of time (minutes) vs NaOH concentration % w/v and DS.

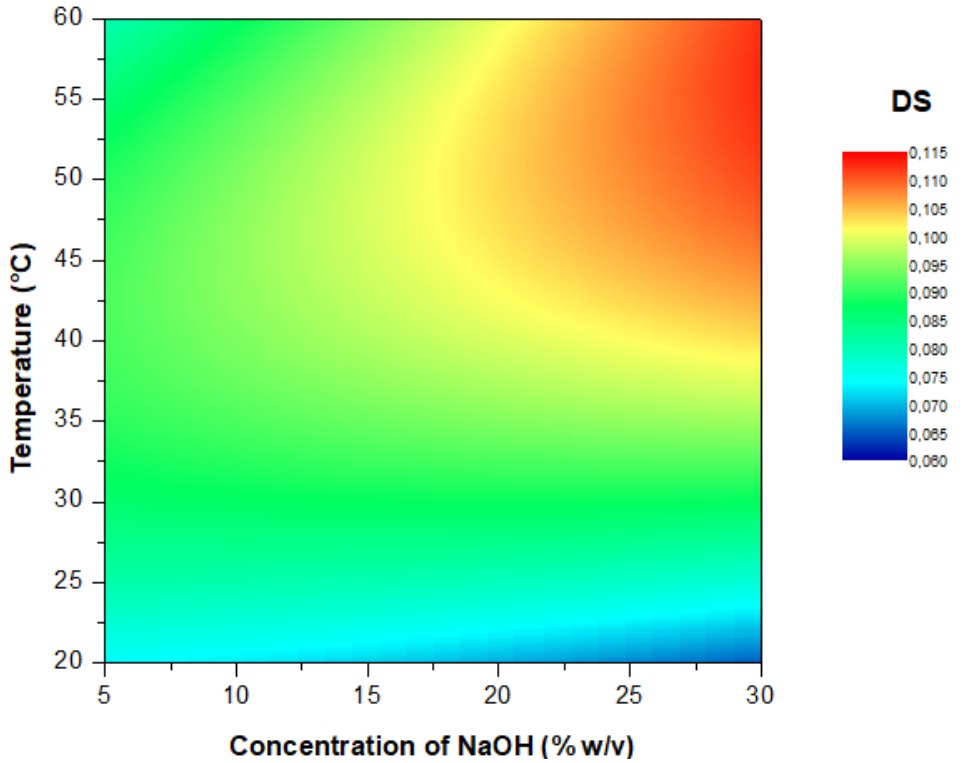


Figure 4.7. Contour plot of temperature (°C) vs NaOH concentration % w/v and DS.

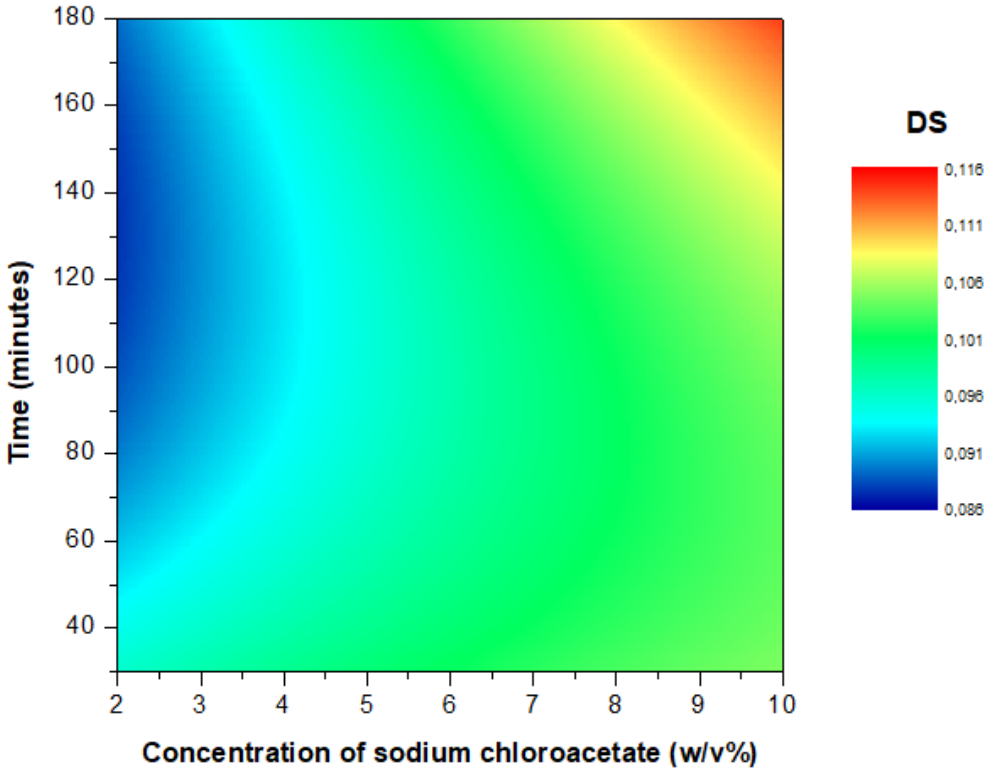


Figure 4.8. Contour plot of time (minutes) vs sodium chloroacetate %w/v and DS.

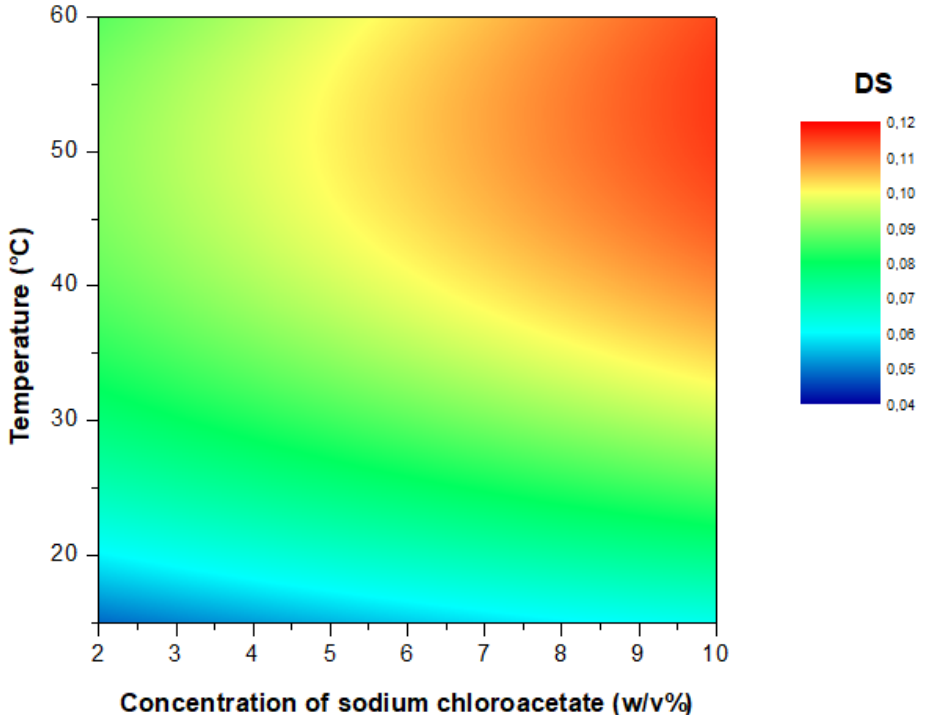


Figure 4.9. Contour plot of temperature (°C) vs sodium chloroacetate %w/v and DS.

- Chemical characterization:

Infrared spectroscopy spectrum of CMC fique fiber with the higher DS of the box-Behnken experimental design is shown in Figure 4.10. The peaks located at 1620 and 1423 cm^{-1} indicated the presence of carboxymethyl groups resulted from the substitution of hydroxyl groups in anhydrous glucose unit in cellulose.

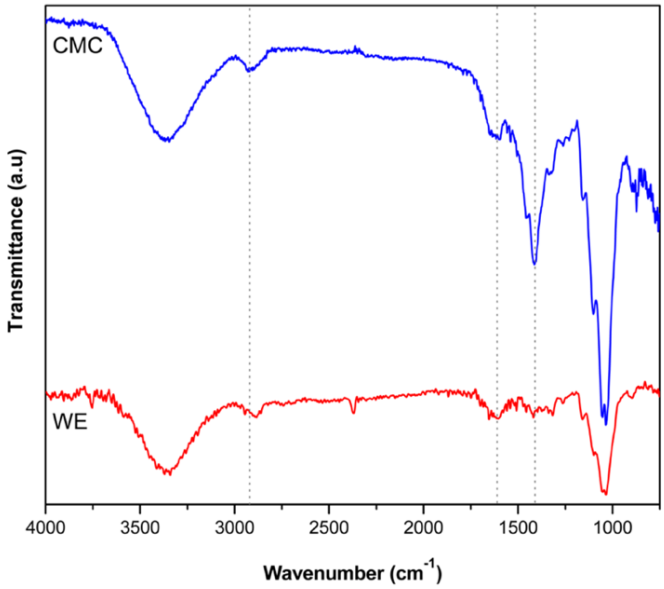


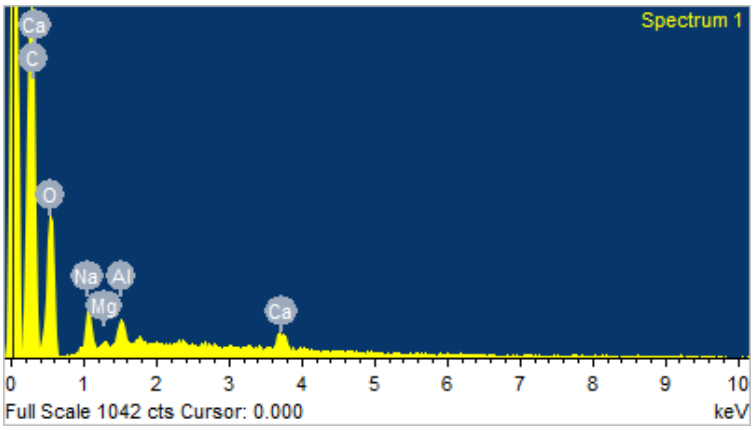
Figure 4.10. FTIR-ATR spectra of the CMC fique fibers and pretreated fiber, following the conditions synthesis of run 4 from Table 4.3.

According to others reports sodium carboxymethyl appears in wavenumbers between 1600 to 1640 cm^{-1} and 1400 to 1450 cm^{-1} [10], the incidence of these groups may suggest the etherification process originating CMC onto the fique fiber pretreated previously. These results were similar to other authors, producing CMC from different types of biomass, such as banana skin [10].

According to the elemental analysis obtained from EDX (see Figure 4.11), no significant changes were perceived in comparison with WE fiber (see Chapter 3). The most abundant elements, as was expected, were oxygen and carbon, which correspond to the main elements present in the lignocellulosic biomass structure. Of the minor elements, sodium was the highest because of the use of sodium hydroxide and sodium chloroacetate during the basification and etherification reactions, respectively.

The other elements such as calcium, aluminum and magnesium are traces of the fique fiber, a result of the conditions used during the process of cultivation of the fique fiber, due to soil conditions in which the fique grew or according to with the type of fertilizer used. In particular,

calcium is the product of calcium carbonate compounds from the shredding process carried out, once the fiber was cut and combed [24].



Element	Atomic (%)	Weight (%)
C	57.4	65.0
O	38.8	33.0
Na	2.0	1.2
Mg	0.2	0.1
Al	0.9	0.4
Ca	0.9	0.3
Total	100	100

Figure 4.11. EDX of the CMC fique fiber following the conditions synthesis of run 4 from Table 4.3.

- Surface characterization

To know how the wettability property changed according to the substituents in CMC, the contact angle of the carboxymethylated fique fiber was measured. A value of Θ = 59.4 ± 6.7° was obtained, which could indicate an amphiphilic character of the functionalized fiber, the contact angle increased approximately 18° compared to the pretreated WE fiber. This change could be a consequence of the hydrophobic polysaccharides content in the fique fiber and the presence of many hydrophilic carboxyl groups resulting from the carboxymethylation reaction.

These hydrophilic groups are inherent to the water-soluble cellulose ethers, which in turn depend largely on the uniformity. When the DS value was less than 0.2, the material has a greater tendency to be insoluble in water [25]. Additionally, the character of the functionalized fique fiber can also be defined by the cellulose structure and reagents used during the synthesis process, such as accessibility to cellulose, the reactivity of the hydroxyl groups presented on the surface, and reagents reactivity.

- Structural characterization

On the structural properties' characterization of the CMC fiber, X-ray diffraction was used to analyze the crystal structure of CMC. As shown in the diffractograms of Figure 4.12, three characteristic peaks of cellulose located at 15°, 22°, and 34° were kept from the WE diffraction, a

reduction in the crystallinity in two of them (22° and 34°), as well as the transformation of a well-defined peak with a diffraction angle of 14°. To determine the change in the CMC crystallinity from Figure 4.12, the Segal method was followed [26].

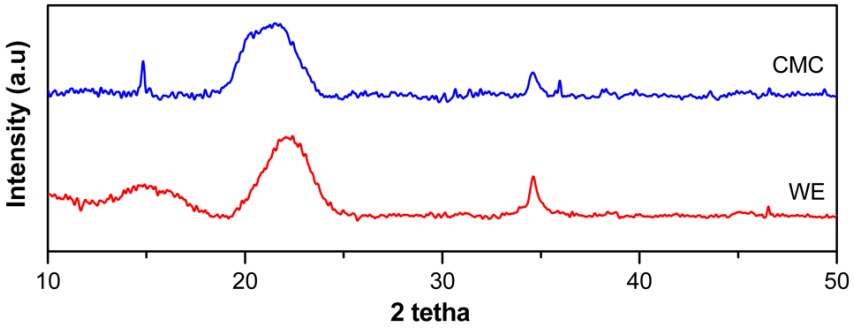


Figure 4.12. X-ray diffraction spectra of CMC and pretreated fiber, following the conditions synthesis of run 4 from Table 4.3.

Using Eq. 4.11 was possible to calculate the crystallinity index (C_i), which is a quantification of the percentage of crystalline cellulose in the sample.

$$C_i(\%) = \left(1 - \frac{I_{am}}{I_{200}}\right) \times 100 \qquad \text{Eq. 4.11}$$

Where C_i was calculated as the ratio of the peaks centered around 22° associated to polycrystalline cellulose and another at 18° related to amorphous cellulose [26]. The crystallinity index was 27.0%, which may suggest a change in the type of cellulose. Isopropyl alcohol has a low dielectric constant, making it a bad solvent for sodium hydroxide. Therefore, the NaOH concentration was maintained constant to interact with the crystalline region of cellulose, promoting a change of the polymorphism from cellulose I to the cellulose II throughout the basification reaction. Similar behaviors were reported by other authors[27].

- Morphological and Textural Characterization

Changes in the morphological characteristics of CMC fibers were analyzed by scanning electron microscopy. Figure 4.13a displayed the homogeneous surface of the fiber after carboxymethylation; likewise, it was possible to observed bundles of threads that form the entire fiber. Detailing the fiber surface in Figure 4.13b, numerous connections of the cellulose fibrils were perceived inside the fiber. Additionally, some clusters were also confirmed on the surface of the fique fiber, possibly the result of the reduction in the cellulose crystallinity percentage, thus complementing the results obtained from the XRD analysis described above.

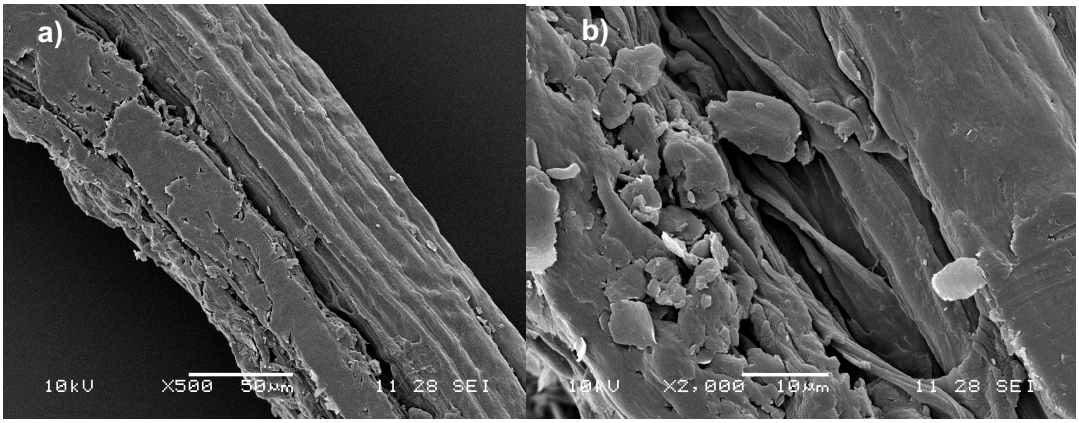


Figure 4.13. Micrographs after the CMC functionalization process, a) 500X (WE), b) 2000X, following the conditions synthesis of run 4 from Table 4.3.

The surface area of the functionalized fique fiber was determined employing the BET method to the nitrogen adsorption isotherms, reaching a minimum value of 3.9 ± 0.5 m^2 g^{-1}. This value allowed to conclude that the functionalization process did not influence the textural properties of the fiber, preserving the non-porous character of lignocellulosic biomass. Furthermore, the value obtained from the CMC surface area was within the limits of the equipment error range, as was described in previous chapters.

- Thermal Characterization

To know if the structure of fiber functionalized by carboxymethylation could influence its thermal properties, thermogravimetric analysis was performed. In Figure 4.14 the thermograms of the fiber before and after functionalization were reported, corresponding to WE and CMC, respectively. TGA curves did not demonstrate important changes in the material thermal stability compared to the pretreated fiber. The degradation was complete in five steps located close to 100, 250, 320 – 350, 420 °C and ashes, associated to moisture loss, hemicellulose degradation, cellulose pyrolysis, lignin decomposition and remaining inorganic species, respectively. However, the only change that happened in the cellulose decomposition for functionalized fiber was confirmed at 320 to 350 °C, a consequence of the change in the cellulose crystallinity due to carboxymethylation which confirmed the results obtained using XRD.

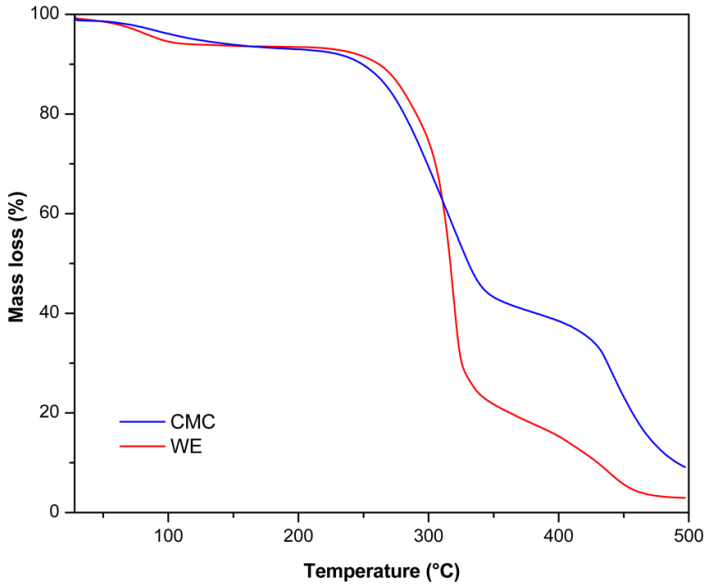


Figure 4.14. TGA of CMC and pretreated fiber, following the conditions synthesis of run 4 from Table 4.3.

- Mechanical Characterization

The carboxymethylation effect on the mechanical properties of the resulting fiber was studied by DMA (dynamic mechanical analysis). The value of Young's Moduli (E) for carboxymethyl cellulose fiber was quantified as 9.39 GPa compared to 24.59 GPa measured in the pretreated fiber. There was a significant reduction in the mechanical properties of the functionalized fiber, because of the CMC fiber crystallinity index decrease during the basification reaction, which negatively affected the material elastic behavior, already confirmed by other characterization techniques like XRD, contact angle and TGA.

4.4.2 TEMPO Oxidation

Cellulose in its natural form has low chemical reactivity. To be able to use the cellulose in fique fibers as a matrix in hybrid materials, it was necessary to functionalize them to create surface groups that facilitate the bonding with other compounds. Some authors like Watanabe *et al*. [28], Wu *et al*.[29] and Schelling *et al*. [6] have confirmed the chemical surface functionalization of cellulose through the introduction of ionic charges promotes the anchoring of other compounds such as mammalian cells, silver nanoparticles and metal-organic frameworks (MOFs), respectively.

In this, the cellulose surface was negatively charged (anionic cellulose) employing a controlled oxidation reaction using the TEMPO / NaOCl / NaBr system, which has advantages in terms of selective position reaction at room temperature under aqueous conditions at pH 10. As shown in

Figure 4.15, in the TEMPO reaction, alcohol groups (C6-OH) accessible on the surface of water-insoluble cellulose are oxidized to C6 sodium carboxylate groups (-COONa).

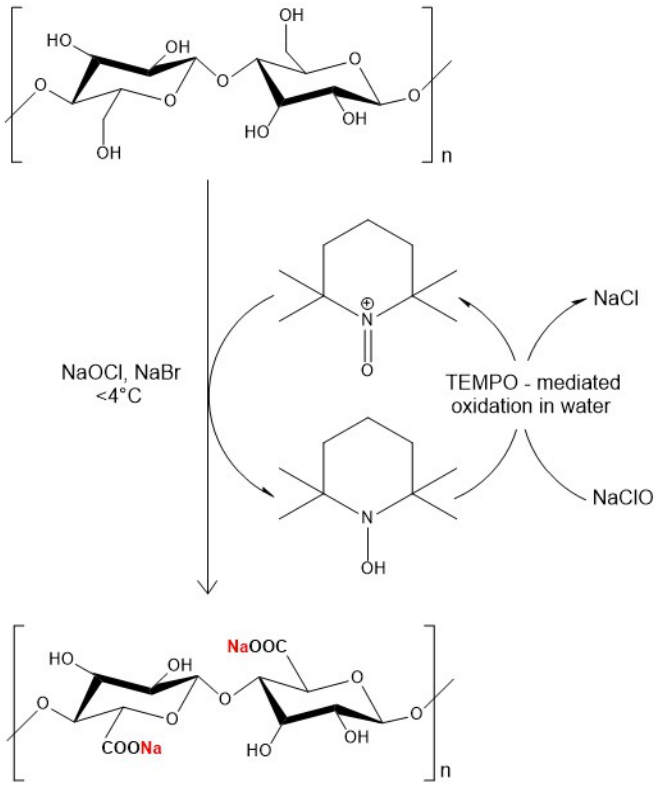


Figure 4.15. Formation of carboxylate groups (-COONa) on cellulose by TEMPO oxidation [30].

After TEMPO oxidation, the modification degree of cellulose surface in terms of number of carboxylic units was determined by conductimetric titrations. Preliminary experiments to quantify the oxidation degree (OD) in the fibers: raw (R) and pretreated with water (W), ethanol (E) and water/ethanol (WE), were performed before and after the TEMPO reaction using a NaOCl:AGU molar ratio of 1. The results obtained are shown in Figure 4.16. Comparing the OD of raw fiber (R) and pretreated (W, E, WE) before oxidation with TEMPO, values of 3.88, 8.42, 6.25 and 0.83% were obtained, respectively, for each of them.

These values of OD percentages are a consequence of the compounds present in each of the fibers Analyzed. As explained in the previous section, raw fiber has compounds such as sapogenins, hecogenins, lignin, cellulose and hemicellulose, while fibers pretreated by organosolv present a reduce content of extractives and cellulose, resulting in a cleaner and homogeneous fibers, with a greater number of hydroxyl groups exposed on the surface. Each of these compounds has functional groups that contribute to the OD intrinsic of the raw and pretreated fibers [3132].

However, after TEMPO oxidation the OD values increased to 4.01, 2.50 and 7.26%, for R, E and WE, respectively (Figure 4.16). This type of effect was expected for most of the functionalized fibers. The WE pretreated fiber had the most significant change in the number of carboxylic groups, confirming the important role of the pretreatment using two stages of Soxhlet (first with water and then ethanol, WE).

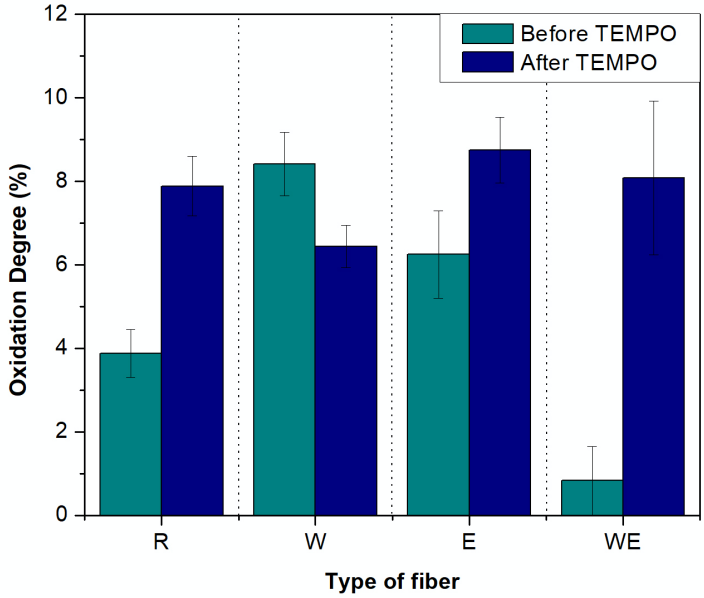


Figure 4.16. Quantification of the oxidation degree percentage (OD) in raw (R) and pretreated fibers by organosolv using water (W), ethanol (E) and water/ethanol (WE), before and after TEMPO reaction using a NaOCl:AGU molar ratio of 1.

The decrease in the OD percentage of R, W and E is related to the compositional analysis of the macromolecules present in the raw and pretreated fique fibers. The presence of macromolecules like hemicellulose and lignin can influence the chemical reactions and properties of the final products [30533], since they could be degraded and removed by the use of NaClO as soluble fractions in water, which consequently decreases the amount of oxidant that remains to react with the TEMPO system [34]. In addition, the presence of water in the initial cellulosic fibers or in the reaction media generates preferential side reactions between water and the etherifying or esterifying reagent instead of reactions between the hydroxy groups (from the AGU) and reagents[35].

Using the fiber pretreated (WE), the modulating effect of the molar ratio of oxidant reagent to AGU was studied (Figure 4.17). The increase in the molar ratio of NaOCl:AGU resulted in a proportionately higher OD (from 4.16% for 0.3 equivalent moles of NaClO to 13.81% for 8 equivalent moles of NaClO). In this way, it was demonstrated that the surface modification degree

could be controlled. A significant increment of 9.32% in the OD value was evidenced between WE and a NaOCl:AGU molar ratio of 1, while a 8:1 NaOCl: AGU ratio was required to achieve a substantial level of substitution close to 13.81%. For that reason, it was decided to select as the functionalized fiber the one obtained using 1:1 molar ratio of oxidant reagent to AGU.

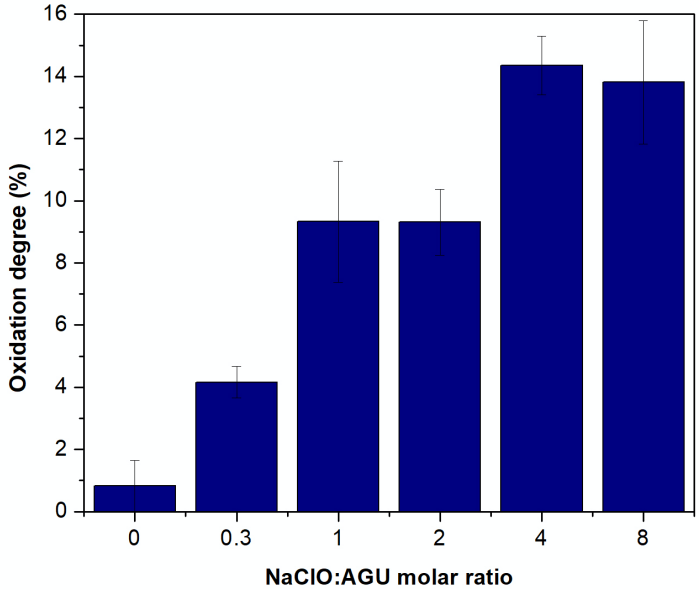


Figure 4.17. Functionalization degree in fiber pretreated (WE) modulating the NaOCl:AGU molar ratio, all the experiments were performed in triplicate.

Regarding the surface charge density of sodium carboxylate (-COONa), WE fibers functionalized reach values between 0.68 to 2.27 mmol/g (for 0.3 to 8 equivalent moles of NaClO, respectively). Other studies reported, for materials derivatized under similar conditions of reaction (8:1 NaOCl: AGU molar ratio), values of 1.6 mmol/g of COONa for fique pretreated by ultrasound and TEMPO oxidation (NaClO, 37 mmol) [16]. Other cellulosic materials like hemp, bamboo, and bleached kraft pulp revealed carboxylate concentrations from 1.5 to 1.7 mmol/g in [36], while eucalyptus, ginkgo and rice straw showed carboxylate contents of 0.8-1.6 mmol/g using 5 to 10 mmol concentrations of NaClO for TEMPO reaction [34].

It is important to consider that chemical properties of derivatized materials can change according to the oxidation reaction conditions and chemical structure of the substrate. Therefore, in general terms anionic units of sodium carboxylate groups (-COONa) are formed in selective and regular way onto the surfaces of cellulose microfibrils, keeping the original cellulose morphology, crystalline structure and width of the crystal [5]. In order to analyze in a detail way changes on the functionalized fiber, a complete material characterization was done.

- Chemical characterization:

Figure 4.18 shows the FTIR spectra of the pretreated (WE) and functionalized (WET1) fique fiber through TEMPO oxidation. Significant changes attributed to the stretching vibrations of carbonyl (C=O) and carboxylic acid (-COOH) groups at 1603 and 1734 cm^{-1}, respectively, were confirmed. . A comparison between the two spectra identified the band intensity of carboxyl groups increased in WET1 compared to WE, confirming that TEMPO reaction was carried out, oxidizing alcohols groups present in cellulose. Additionally, there are no significant differences for the typical lignin, cellulose and hemicellulose signals, corroborating the chemical fiber integrity was not affected by the oxidation reaction.

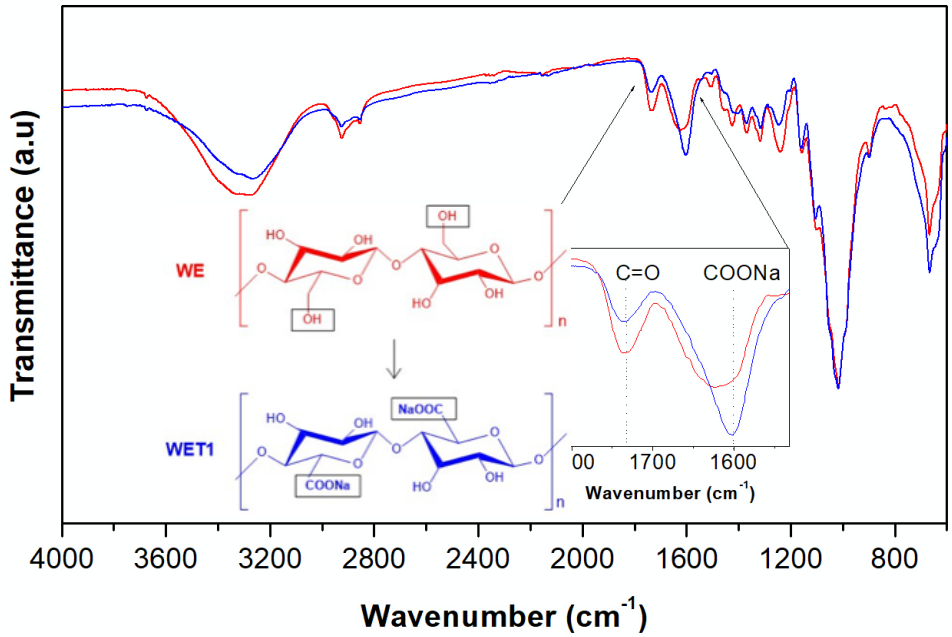


Figure 4.18. ATR-FTIR spectra for pretreated (WE) and functionalized (WET1) fique fiber, at pH=10 and a molar ratio of NaOCl:AGU of 1.

The presence of the band at 1603 cm^{-1} for the functionalized fiber attributed to carbonyl groups coincided with a report made by Takaichi *et al.* [37]. When the TEMPO oxidation was applied to different lignocellulosic materials diverse oxidized products were obtained heterogeneously on the surfaces of cellulose microfibrils (Figure 4.19); i.e., C6 sodium carboxylate groups and C2 / C3 ketones can be obtained as a result of primary and secondary reactions of TEMPO, respectively [38]. Hence, the oxidation degree acquired for WET1 close to 13.81% is probably due to an incomplete transformation of the surface available chemical groups to carboxylic acids.

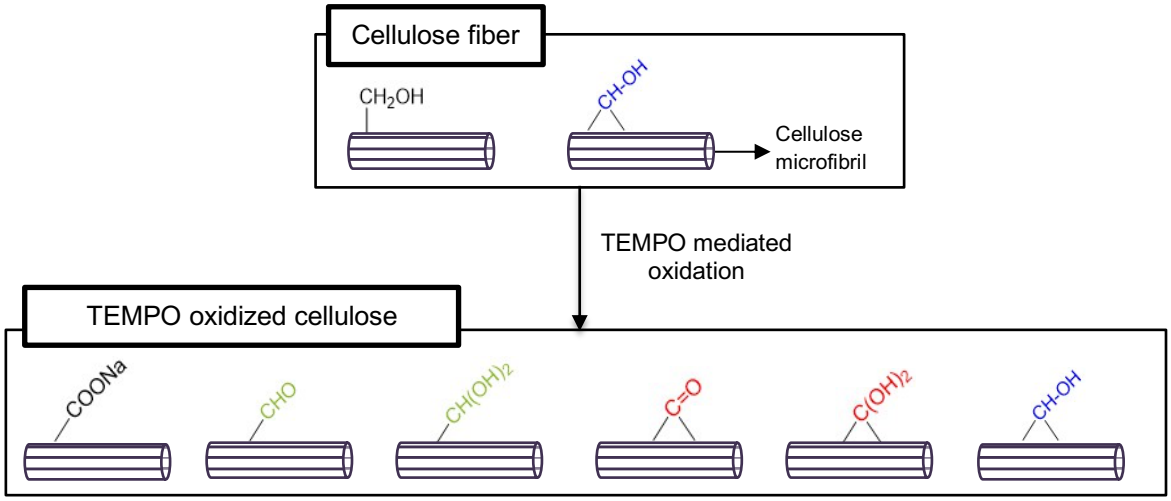
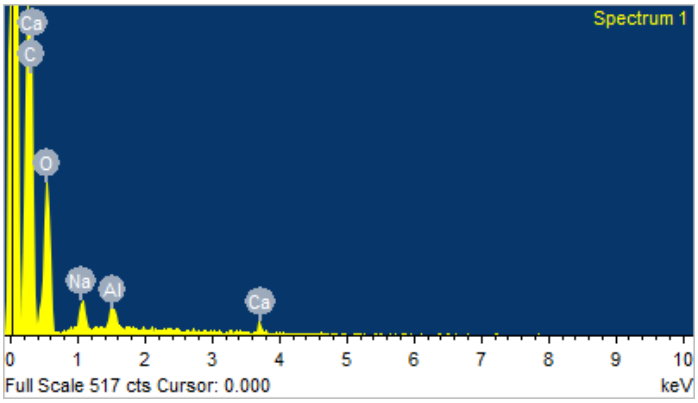


Figure 4.19. Chemical groups produced after TEMPO oxidation of cellulose. Modified [37].

Figure 4.20 displayed the EDX profile of a functionalized fiber by TEMPO (WET1). It revealed a large carbon and oxygen peaks as was expected in an organic material; besides, the spectrum showed a signal for Ca resulted from the carbonate residues in the defibration stage. Other elements such as Na and Al were found at lower levels in the material matrix. The Na contained in units of sodium carboxylate groups (-COONa) indicated a successful functionalization process.



Element	Atomic (%)	Weight (%)
C	58.7	66.8
O	35.46	30.2
Na	2.52	1.50
Al	1.74	0.88
Ca	1.57	0.54
Total	100	100

Figure 4.20. EDX of functionalized (WET1) fique fiber, at pH=10 and a molar ratio of NaOCl:AGU of 1.

- Morphological and Textural Characterization

The morphology before and after the functionalization process is shown in Figures 4.21a and 4.21b, respectively. Figure 4.21b shows how the TEMPO reaction promoted cellulose microfibrils to be released from the surface compared to pretreated fique fiber (Figure 4.21a). This type of functionalization facilitates the fiber surface defibrillation producing the individualization of

cellulosic microfibrils, as a consequence of the anionic groups resulting from chemical modification, which generate electrostatic repulsions in water and have osmotic effects [5].

This has been reported by other authors, who claimed that depolymerization of cellulose molecules is often observed after derivatization with TEMPO [3940]. Micrograph 4.21b evidenced a fiber with some intricate branches and network structures, which is typical of cellulose obtained from leaves such as sisal and abaca [41]. Using the ImageJ ® software, the microfibrils widths were calculated, which on average are 620 to 660 µm and several microns long.

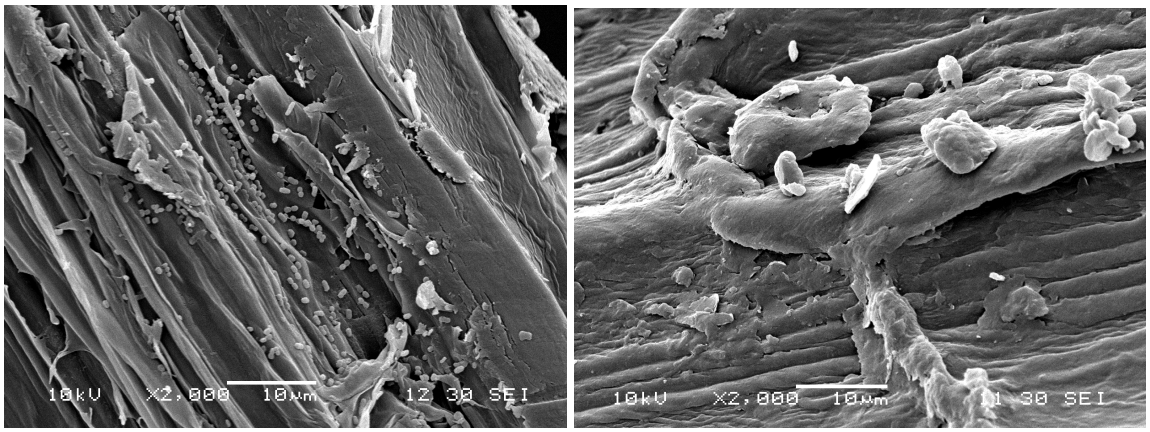


Figure 4.21. Micrographs before and after the functionalization process, a) pretreated fique fibers 2000X (WE), b) functionalized fiber 2000X (WET1).

The value of the BET surface area for WET1 was 16.8 ± 0.2, which is similar to the 18.1 ± 0.4 m^2 g^{-1} obtained to pretreated fiber WE, suggesting a minimum effect of the functionalization process on the surface area.

- Structural Characterization

Regarding the crystallinity structure of the WET1, the diffractogram of Figure 4.22 did not show significant changes in the internal structure of crystalline cellulose microfibrils, due to the highly selective nature of TEMPO reaction in the hydroxyl functional groups (C6-OH) oxidation present into the AGU molecules, allowing the biopolymer structure to remain almost intact [42].

Crystallinity indices (CI) values of 34.4 and 29.6% were obtained for pretreated and functionalized fibers, respectively. A slight decrease in the CI percentage (close to 4.9%) guarantees the mechanical properties of the functionalized fiber will not be compromised. This result was consistent with the work made by Puangsin *et al.* [36], who reported that lignocellulosic materials achieve a maximum of up to 10% change in the crystallinity index as a result of the TEMPO

reaction. For example, corncob [43], jute [44], bamboo pulp [36] and oil palm [45] presented a reduction in the CI of 11.6, 6.2, 4 and 3%, respectively, suggesting the elemental nanofibril mass structure was retained after chemical modification.

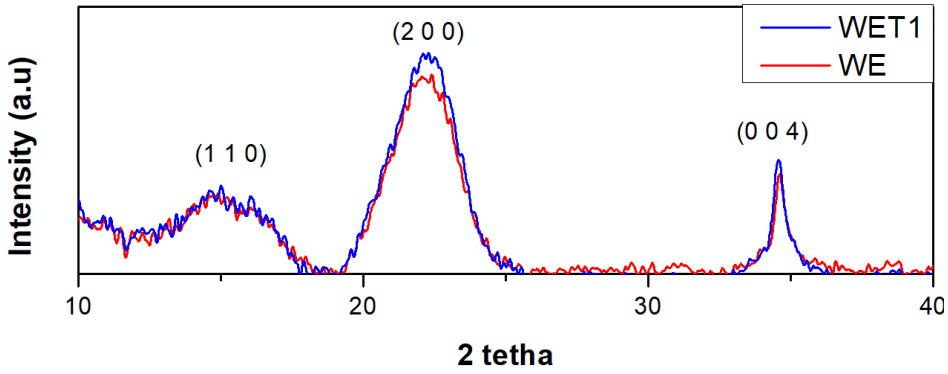


Figure 4.22. Diffractogram of pretreated fique fibers (WE) and functionalized fiber (WET1) mediated by TEMPO.

The average cellulose crystallite size was estimated from XRD data, using the Scherrer's equation (Eq. 4.12) [46]. Based on the line broadening effect at the full width at half maximum (FWHM) of the (0 0 2) peak.

$$D = \frac{k\lambda}{\beta \, Cos \, \theta} \qquad \text{Eq. 4.12}$$

Where *D* is the average crystallite size, *k* is Scherrer constant, λ is the wavelength of X-ray, β is the FWHM and θ is diffraction angle. An average crystallite size of 11.8 nm was reported for raw fique fiber [47], a similar value of 11.3 nm was kept during the pretreatment, but after the functionalization that value decreased to 10.1 nm.

Crystallinity index (CI) and crystallite size have a directly proportional relationship. It explains the behavior describe above, which is consistent with the results obtained in this study. Both characteristics were reduced after the functionalization process, caused by the elimination of intra and intermolecular hydrogen bonds and hydrophobic interactions that are regularly present in lignocellulosic materials. However, the original crystallinity and crystal width of the WET1 fiber cellulose did not change drastically after the oxidation [2].

- Surface Characterization

With the aim to characterize some properties on the surface fiber after TEMPO oxidation, point of zero charge (pH_{zpc}) was measured by Bohem titration [48]. There was a slight increase in the

pH_{ZPC} value of WET1 compared to pretreated fiber (see Figure 4.23). The acid character of the pretreated fiber was reduced in the functionalized fiber (pHzpc = 5.18 ± 0.05), this slight change is related to the presence of Na in units of sodium carboxylate groups (-COONa). Then, pH values above 5.18 and below 5.18 will give to the fiber a negative and positive charge in solution, respectively.

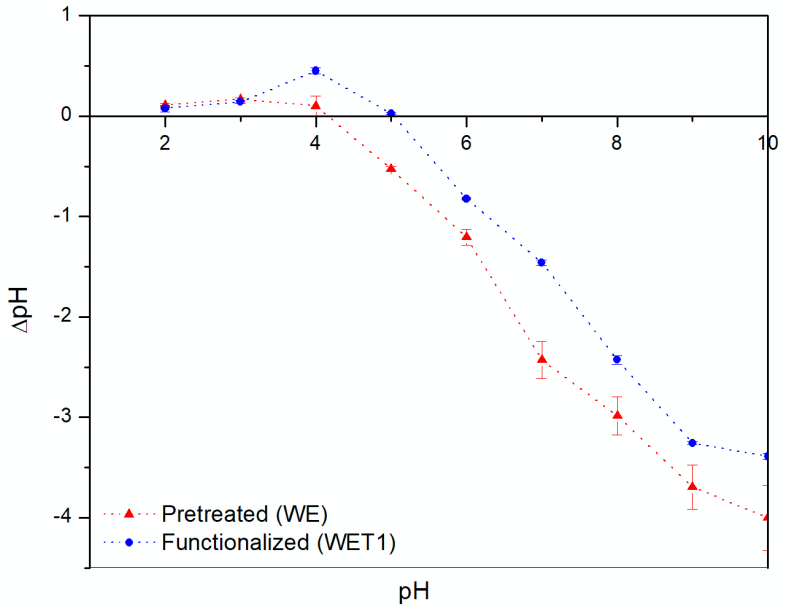


Figure 4.23. pH_{zpc} of pretreated fique fibers (WE) and functionalized fiber (WET1) mediated by TEMPO.

In complement, the contact angle was determined to evaluate changes in the wettability properties. A value of 32.9º ± 1.9° evidenced an increment in the hydrophilic character of WET1 compared to WE, because of the occurrence of ionic species on the cellulose surface like COO^-. Properly, this type of group did not promote the hydrogen bond formation between nanofibrils due to Coulombic repulsion (effect named as 'hydrogen bond lock'), saving the wettability of WET1 [49].

- Thermal Characterization

The thermal characterization of functionalized fiber through TEMPO confirmed the fiber structure did not undergo significant changes compared to the pretreated fiber (Figure 4.24). WET1 showed four important changes. The first, with approximately 1.5% of mass loss was related to dehydration from 50 to 110 °C, a second change corresponded to the hemicellulose degradation starting at 250 °C with a weight loss of up to 18%.

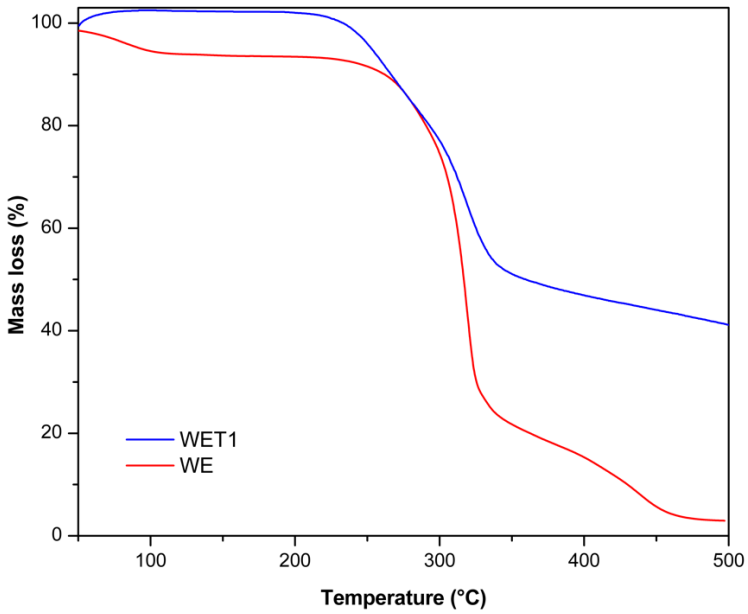


Figure 4.24. TGA of pretreated fique fibers (WE) and functionalized fiber (WET1) mediated by TEMPO.

The third change was the thermal degradation of cellulose from 340 °C, with the greatest weight loss of approximately 30%, the WET1 thermogram indicated a slight shoulder at 320 °C, assigned to the decomposition of the surface carboxylic units product of the functionalization through TEMPO. Other studies have reported similar behaviors with other types of biomass such as rice straw and jute [50] [51]. Compared to the pretreated fiber, a change associated with the lignin decomposition was not evident in WET1 at 450 °C. So, at temperatures higher than 350 °C the weight loss was due to residues of the decomposition reaction, volatiles loss, carbon formation, and ashes. The reaction residues were approximately 40% more than the pretreated fiber, a fact reported by other authors in carbon residues for nano cellulose [52].

- Mechanical Characterization

The mechanical properties of TEMPO functionalized fiber were analyzed using DMA to verify if the oxidation degree influenced the mechanical performance of WET1 compared to the pretreated WE fiber. Young's modulus of WET1 was 23.15 GPa, which is similar to the value of 24.59 GPa obtained for WE fiber. It suggested the chemical functionalization performed did not compromise the mechanical strength or integrity of the material. On the contrary, the high mechanical resistance of the fique was probably preserved. Therefore, TEMPO functionalization leads to modifications only on the surface and not in the bulk of the materials.

4.5 Conclusions

Two functionalization processes were evaluated using physicochemical characterization techniques. The oxidation by TEMPO reaction, showed that the fiber kept its nature without important changes from thermal, mechanical, morphological and structural properties. Both functionalization process confirmed the importance to develop a pretreatment stage, in order to have more hydroxyl groups available to react and be converted in active groups. The fiber with the best conditions was achieved with the highest DS of 0.14 conditions for the carboxymethylation of fique fiber were: isopropyl alcohol as solvent medium, 17.5% w/v NaOH concentration, 10% w/v chloroacetate concentration, etherification temperature (40 °C), and 180 minutes, all the functionalization process was followed by the USP method.

Regarding the functionalization by TEMPO, the best oxidation conditions showed a NaOCl:AGU molar ratio as 1, to get an oxidation degree of 9.32%. In addition, the product was characterized by FTIR-ATR confirming the existence of the sodium carboxylate groups (-COONa) onto the fiber surface. In this way, could be concluded an adequate functionalization process was done and can be used in other applications.

4.6 References

1. Wang, Z., Hauser, P., Laine, J. & Rojas, O. Multilayers of low charge density polyelectrolytes on thin films of carboxymethylated and cationic cellulose. *J. Adhes. Sci. Technol.* **25**, 643–660 (2010).

2. Moon, R., Martini, A., Nairn, J., Simonsen, J. & Youngblood, J. Cellulose nanomaterials review: Structure, properties and nanocomposites. *Chem. Soc. Rev.* **40**, 3941–3994 (2011).

3. Yao, F. *et al.* A review of recent developments in natural fibre composites and their mechanical performance. *Compos. Part A Appl. Sci. Manuf.* **51**, 98–112 (2016).

4. Beckermann, G. & Pickering, K. Engineering and evaluation of hemp fibre reinforced polypropylene composites: Fibre treatment and matrix modification. *Compos. Part A Appl. Sci. Manuf.* **39**, 979–988 (2008).

5. Isogai, A., Hänninen, T., Fujisawa, S. & Saito, T. Review: Catalytic oxidation of cellulose with nitroxyl radicals under aqueous conditions. *Prog. Polym. Sci.* **86**, 122–148 (2018).

6. Schelling, M., Kim, M., Otal, E. & Hinestroza, J. Decoration of cotton fibers with a water-stable metal–organic framework (uio-66) for the decomposition and enhanced adsorption of micropollutants in water. *Bioengineering.* **5**, 1-14 (2018).

7. Rachtanapun, P. & Rattanapanone, N. Synthesis and characterization of carboxymethyl cellulose powder and films from Mimosa pigra. *J. Appl. Polym. Sci.* **122**, 3218–3226 (2011).

8. Da Silva Pinto, M., Sierra, C. & Hinestroza, J. In situ synthesis of a Cu-BTC metal-organic framework (MOF 199) onto cellulosic fibrous substrates: Cotton. *Cellulose.* **19**, 1771–1779 (2012).

9. Mousavi, M., Alizadeh Asl, S. & Mohsen Labbafi. Synthesis and characterization of carboxymethyl cellulose from sugarcane bagasse. *J Food Process Technol.* **8**, 1-8 (2017).

10. Adinugraha, M. P., Marseno, D. W. & Haryadi. Synthesis and characterization of sodium carboxymethylcellulose from cavendish banana pseudo stem (Musa cavendishii LAMBERT). *Carbohydr. Polym.* **62**, 164–169 (2005).

11. Pushpamalar, V., Langford, S. J., Ahmad, M. & Lim, Y. Y. Optimization of reaction conditions for preparing carboxymethyl cellulose from sago waste. *Carbohydr. Polym.* **64**, 312–318 (2006).

12. Zhao, J. *et al.* Design carboxymethyl cotton knitted fabrics for wound dressing applications: Solvent effects. *Mater. Des.* **87**, 238–244 (2015).

13. Courtenay, J. C. *et al.* Surface modified cellulose scaffolds for tissue engineering. *Cellulose.* **24**, 253–267 (2017).

14. Inamochi, T., Funahashi, R., Nakamura, Y., Saito, T. & Isogai, A. Effect of coexisting salt on TEMPO-mediated oxidation of wood cellulose for preparation of nanocellulose. *Cellulose.* **24**, 4097–4101 (2017).

15. Da Silva Perez, D., Montanari, S. & Vignon, M. R. TEMPO-mediated oxidation of cellulose III. *Biomacromolecules.* **5**, 1417–25 (2003).

16. Ovalle-Serrano, S. A., Gómez, F. N., Blanco-Tirado, C. & Combariza, M. Y. Isolation and characterization of cellulose nanofibrils from Colombian Fique decortication by-products. *Carbohydr. Polym.* **189**, 169–177 (2018).

17. Praskalo, J. *et al.* Sorption properties of TEMPO-oxidized natural and man-made cellulose fibers. *Carbohydr. Polym.* **77**, 791–798 (2009).

18. Zaman, M., Xiao, H., Chibante, F. & Ni, Y. Synthesis and characterization of cationically modified nanocrystalline cellulose. *Carbohydr. Polym.* **89**, 163–70 (2012).

19. Dave, S., Damani, M. & Tipre, D. Copper remediation by Eichhornia spp. and sulphate-reducing bacteria. *J. Hazard. Mater.* **173**, 231–235 (2010).

20. Schellbach, S. L., Monteiro, S. N. & Drelich, J. W. A novel method for contact angle measurements on natural fibers. *Mater. Lett.* **164**, 599–604 (2016).

21. Arshadi, M., Abdolmaleki, M. K., Mousavinia, F., Foroughifard, S. & Karimzadeh, A. Nano modification of NZVI with an aquatic plant Azolla filiculoides to remove Pb(II) and Hg(II) from water: Aging time and mechanism study. *J. Colloid Interface Sci.* **486**, 296–308 (2017).

22. Parikh, D. V. Carboxymethylation-cotton for Wound Care Management. *ACS Symp. Ser.* **792**, 115–124 (2001).

23. Najafpour, G. & Noshirvani, B. Catalyst-free conversion of alkali cellulose to fine carboxymethyl cellulose at mild conditions. *World Appl Sci J.* **4**, 564-569(2009).

24. Peinado, J. *et al. Guía ambiental del subsector fiquero. Bogotá DC: Cadena Productiva Nacional del Fique-Cadefique*. (Ministerio de Ambiente, 2006).

25. Doh, S. J., Lee, J. Y., Lim, D. Y. & Im, J. N. Manufacturing and analyses of wet-laid nonwoven consisting of carboxymethyl cellulose fibers. *Fibers Polym.* **14**, 2176–2184 (2013).

26. Segal, L., Creely, J. J., Martin, A. E. & Conrad, C. M. An empirical method for estimating the degree of crystallinity of native cellulose using the x-ray diffractometer. *Text. Res. J.* **9**, 786–794 (1959).

27. He, X., Wu, S., Fu, D. & Ni, J. Preparation of sodium carboxymethyl cellulose from paper sludge. *J. Chem. Technol. Biotechnol.* **84**, 427–434 (2009).

28. Watanabe, K. *et al.* A new bacterial cellulose substrate for mammalian cell culture - A new bacterial cellulose substrate. *Cytotechnology* **13**, 107–14 (1993).

29. Wu, C. N. *et al.* TEMPO-oxidized bacterial cellulose pellicle with silver nanoparticles for wound dressing. *Biomacromolecules* **19**, 544–554 (2018).

30. Saito, T. & Isogai, A. TEMPO-mediated oxidation of native cellulose. The effect of oxidation conditions on chemical and crystal structures of the water-insoluble fractions. *Biomacromolecules* **5**, 1983–1989 (2004).

31. Tava, A., Scotti, C. & Avato, P. Biosynthesis of saponins in the genus Medicago. *Phytochem. Rev.* **10**, 459–469 (2011).

32. Liu, C., Wu, S., Zhang, H. & Xiao, R. Catalytic oxidation of lignin to valuable biomass-based platform chemicals: A review. *Fuel Process. Technol.* **191**, 181–201 (2019).

33. Sang, X. *et al.* Mechanism and kinetics studies of carboxyl group formation on the surface of cellulose fiber in a TEMPO-mediated system. *Cellulose.* **24**, 2415–2425 (2017).

34. Kuramae, R., Saito, T. & Isogai, A. TEMPO-oxidized cellulose nanofibrils prepared from various plant holocelluloses. *React. Funct. Polym.* **85**, 126–133 (2014).

35. Klemm, D., Philipp, B., Heinze, T., Heinze, U. & Wagenknecht, W. *Comprehensive cellulose chemistry: fundamentals and analytical methods*. (Wiley, 1999).

36. Puangsin, B., Yang, Q., Saito, T. & Isogai, A. Comparative characterization of TEMPO-oxidized cellulose nanofibril films prepared from non-wood resources. *Int. J. Biol. Macromol.* **59**, 208–213 (2013).

37. Takaichi, S., Saito, T., Tanaka, R. & Isogai, A. Improvement of nanodispersibility of oven-dried TEMPO-oxidized celluloses in water. *Cellulose.* **21**, 4093–4103 (2014).

38. Takaichi, S., Hiraoki, R., Inamochi, T. & Isogai, A. One-step preparation of 2,3,6-tricarboxy cellulose. *Carbohydr. Polym.* **110**, 499–504 (2014).

39. Shinoda, R., Saito, T., Okita, Y. & Isogai, A. Relationship between length and degree of polymerization of TEMPO-oxidized cellulose nanofibrils. *Biomacromolecules.* **13**, 842–849 (2012).

40. Hiraoki, R., Ono, Y., Saito, T. & Isogai, A. Molecular mass and molecular-mass distribution of TEMPO-oxidized celluloses and TEMPO-oxidized cellulose nanofibrils. *Biomacromolecules.* **16**, 675–81 (2015).

41. Alila, S., Besbes, I., Vilar, M. R., Mutjé, P. & Boufi, S. Non-woody plants as raw materials for production of microfibrillated cellulose (MFC): A comparative study. *Ind. Crops Prod.* **46**, 250–259 (2013).

42. Okita, Y., Saito, T. & Isogai, A. Entire surface oxidation of various cellulose microfibrils by TEMPO-mediated oxidation. *Biomacromolecules.* **11**, 1696–700 (2010).

43. Liu, C. *et al.* Properties of nanocellulose isolated from corncob residue using sulfuric acid, formic acid, oxidative and mechanical methods. *Carbohydr. Polym.* **151**, 716–724 (2016).

44. Cao, X., Ding, B., Yu, J. & Al-Deyab, S. S. Cellulose nanowhiskers extracted from TEMPO-oxidized jute fibers. *Carbohydr. Polym.* **90**, 1075–1080 (2012).

45. Rohaizu, R. & Wanrosli, W. D. Sono-assisted TEMPO oxidation of oil palm lignocellulosic biomass for isolation of nanocrystalline cellulose. *Ultrason. Sonochem.* **34**, 631–639 (2017).

46. O'SULLIVAN, A. C. Cellulose: the structure slowly unravels. *Cellulose* **4**, 173–207 (1997).

47. Bastidas, K., Sierra, C. & Zea, H. Heterogeneous Fenton oxidation of Orange II using iron nanoparticles supported on natural and functionalized fique fiber. *J. Environ. Chem. Eng.* **6**, 4178–4188 (2018).

48. Goertzen, S. L. *et al.* Standardization of the Boehm titration. Part I. CO2 expulsion and endpoint determination. *Carbon N. Y.* **48**, 1252–1261 (2010).

49. Missoum, K., Bras, J. & Belgacem, M. N. Water redispersible dried nanofibrillated cellulose by adding sodium chloride. *Biomacromolecules.* **13**, 4118–4125 (2012).

50. Hu, S., Gu, J., Jiang, F. & Hsieh, Y. Lo. Holistic Rice Straw Nanocellulose and Hemicelluloses/Lignin Composite Films. *ACS Sustain. Chem. Eng.* **4**, 728–737 (2016).

51. Park, J. Y. *et al.* Effects of pH on nanofibrillation of TEMPO-oxidized paper mulberry bast fibers. *Polymers (Basel).* **11**, 1-11 (2019).

52. Rohaizu, R. & Wanrosli, W. D. Sono-assisted TEMPO oxidation of oil palm lignocellulosic biomass for isolation of nanocrystalline cellulose. *Ultrason. Sonochem.* **34**, 631–639 (2017).

5. Development of hybrid materials combining MOFs and natural fibers

5.1 HKUST-1 synthesis and functionalization with thiol by using crystal poisons as modifiers

5.1.1 Abstract

Through the last decade, a great effort has been made in the development of new synthesis methods to improve the chemical and hydrolytic stability of HKUST-1 (or MOF-199), one of the most studied and characterized MOFs. Two synthesis method, one being carried out at room temperature (green method) and the other one at high temperatures (solvothermal method), were evaluated in order to obtain a fundamental understanding on the effect of synthesis conditions on the properties of HKUST-1.

In general, during the HKUST-1 formation it was found that green synthesis tends to suppress impurities formation such as Cu_2O, giving rise to crystals with tendencies to regular shapes and yields of 85.7%. However, the solvothermal method produces materials with higher surface area values, and well-defined octahedral crystals with a maximum yield of 67.7%. In this way, it was shown that green synthesis turned out to be an innovative, simple, fast, economic, and ecological method to prepare high-quality carboxylate-based MOF, as compared to those obtained under conventional conditions such as the solvothermal method.

Additionally, as a result of the low hydrolytic stability of HKUST-1, MOF functionalization was evaluated through the use of crystal poisons such as MBA (4-mercaptobenzoic acid) and TSA (thiosalicylic acid) to include thiol groups in the linker that forms the metal-organic framework, so they act as steric impediments increasing hydrolytic stability. Crystal poisons were investigated in a concentration range of 5 to 10 wt% respect to the linker concentration. Under these conditions, 10 wt% of TSA gave rise to a distorted the network crystallinity. For MBA, the

crystallinity was developed better at lower concentrations (5 wt%). The linker structure modification with the addition of the thiol group in HKUST-1 allowed obtaining the MOF SH-HKUST-1, thus improving its hydrolytic stability from 6 to 48 hours, for HKUST-1 and SH-HKUST-1 respectively. At the same time, new properties were developed with this functionalization, such as increased selectivity towards mercury without modifying its topology and composition, which must be evaluated in real applications.

Different characterization techniques including XRD, FESEM, EDX, FTIR, BET, and TGA were used to characterize and monitor the changes and effects produced throughout the synthesis. A novel hydrolytic stability analysis methodology was developed as in the literature the conditions established for this type of analysis are very diverse.

Keywords: HKUST-1, green synthesis, water stability, crystal poison, modifications.

5.1.2 Introduction

Research related to metal-organic frameworks (MOFs) is still growing rapidly, and there remain many challenges to use MOFs in real world applications. Hence, understanding MOFs structure allows to transcend and examine the structure-property relationships and design the next generation of high-performance MOFs compounds. Several aspects such as synthesis methodology, stability, results obtained in previous applications and literature reports have to be considered in selecting a MOF to be evaluated in a particular application. Depending on the type of synthesis used for the MOFs development, this affects the stability and properties of the products obtained. Among the parameters that most affect the synthesis of MOFs are temperature and solvent, which are directly related to the synthesis methods used[1].

Particularly, the temperature is the parameter that allows the reaction balance to promote the spontaneous self-assembly of the structures by improving the diffusion of the reagent and optimizing the coordination interactions in a thermodynamically favorable way [2]. The energy can be transferred to the reaction system electrically, by electromagnetic radiation [1], microwaves [2], ultrasounds, or mechanically [3]. The energy source is closely related to the duration, pressure, and energy per molecule that is introduced into the system and each of these parameters can have a strong influence on the product formed and its morphology.

Generally, MOFs are synthesized from room temperature to 250 °C, being the solvothermal method one of the most used in the MOFs synthesis. This includes the addition of all reagents (metal salts, ligands, and solvents) in a single step in sealed containers followed by heating, just below subcritical conditions (100 °C <T <250 °C), during a few minutes, hours or days, depending on the type of MOF. Another method that has begun to be implemented is hydrothermal synthesis, which constitutes a more environmentally friendly approach; it substitutes the use of organic solvents for water and is carried out at elevated temperature and pressure. It is an easy, low cost, quickly, and commercially viable alternative [1].

MOF structures are obtained through a self-assembly process that generally begins with isolated metal ions that coordinate with linker molecules during MOF synthesis. There is a possibility to improve the hydrolytic [13], chemical and mechanical stability of the framework that mainly depends on the inherent lability of metal-linker bonds, which allows crystal structures to be formed, correcting or improving defects.

An alternative route of synthesis is related to the employment of modulating agents through the precursor approach [14]. This implies the use of pre-constructed polynuclear coordination complexes that comprise structures and functions similar or identical to the linker that constitutes the MOF structure. There have been different attempts to increase the MOF stability through synthesis conditions, improving the steric effects of linkers. In this case, a novel approach consists in the use of modulators such as crystal poisons, which have allowed kinetically to tune MOFs with a linker very similar to the original, considering linker replacement rates, the type of poison crystal and the coordination of solvent molecules [15].

It should be noted that recent studies have focused on a small number of reference MOFs, such as MOF-5, IRMOF series, HKUST-1, MIL series, and ZIF family. Nonetheless, each of these MOFs has strong and weak characteristics. For example, MOF-5 has shown to be unstable in water; MIL materials are candidates for water adsorption applications, although high concentrations of the adsorbate are needed to achieve effective adsorption [4]. HKUST-1 is a copper MOF with general chemical formula $Cu_3(BTC)_2$ $(H_2O)_X$, (BTC = Benzene-1,3,5-tricarboxylic acid). It has a Cu^{2+} with a dinuclear paddlewheel structure that can accommodate four bidentate ligands (typically carboxylate) as a secondary building unit (SBU) [5], and It includes hydroxyl groups rich in electronegativity, giving it characteristic chemical activity [6].

Several studies report the properties and applications of HKUST-1. Furthermore, it has been produced at industrial-scale as Baseolite F-300®. Several methods have been applied for the HKUST-1 synthesis, and most of which involve the use of organic solvents like DMF under solvothermal conditions [7]. To promote the HKUST-1 greener synthesis, procedures based on aqueous solvents were proposed [8], but some authors have described problems related to morphological control, phase control and reaction performance. High-quality synthesis of HKUST-1 using ethanol as the solvent turned out to be a good and potentially much cheaper alternative, ethanol, unlike DMF, does not decompose and it can be recycled in the synthesis [9].

Additionally, some computational simulations studies performed on HKUST-1 have contributed to understand the phenomena involved in the adsorption or gas separation processes; while liquid separations have shown limitations [4,10,11]. However, this MOF resulted in a material sensitive to high relative humidity and to direct water contact, since water displaces the organic linkers from copper centers causing collapse of the framework, which leads to the irreversible decomposition of the HKUST-1 and therefore the deterioration of its adsorption capacity.

All the previous knowledge about HKUST-1 provides a fundamental understanding to allow the modification of its nature improving its stability in water and increase the selectivity towards other compounds [4]. Particular synthesis approaches, in which the MOFs structures and properties can be adjusted without change connectivity or topology through design strategies such as ligand pre-synthesis, modification of metallic nodes or organic linkers [12].

The main objective of this subchapter is to analyze the solvothermal and green synthesis methods of the HKUST-1 MOF and to establish the conditions leading to the adequate crystallization kinetics, in order to allow nucleation and growth of MOF. The effect of the synthesis conditions, such as temperature, solvents, and reaction times were investigated. Therefore, based on production quality, cost, sustainability, and safety, the best synthesis method was selected to make HKUST-1 more stable by using modulators like crystal poison.

The improvement of the hydrolytic stability of HKUST-1 during the synthesis was achieved by including thiol groups inside the structure. As so, two similar compounds to the linker (1,3,5-benzene tricarboxylic acid, BTC) were evaluated as crystal poisons, these were 4 -mercaptobenzoic acid (MBA) and thiosalisilic acid (TSA). Both of these compounds own a thiol group in the structure of the aromatic ring but in different positions.

5.1.3 Materials and methods

5.1.3.1 Chemicals and materials

Copper (II) acetate monohydrate, copper (II) nitrate trihydrate, 4-mercaptobenzoic acid, and benzene-1,3,5-tricarboxylic acid (H_3BTC) were purchased from Sigma-Aldrich, ethanol absolute and N,N'- dimethylformamide (DMF) were supplied by Merck Millipore. All the chemicals and solvents described above were of analytical grade, obtained from commercial suppliers, and used without further purification.

5.1.3.2 Experimental set-up and procedure

- HKUST-1 solvothermal synthesis:

The solutions of $Cu(NO_3)_2 \cdot 3H_2O$ (4.39 g, 18.1 mmol) and trimesic acid (H_3BTC) (2.36 g, 11.2 mmol) were dissolved separately in a mixture of DMF (15 mL), ethanol (20 mL), and water (15 mL). After 1 mL of the mix solution was put in a vial of 5 mL. The vial was heated to 80 °C in an isothermal oven for 24 h, producing a powder formed by small turquoise crystals. After allowing to cool inside the oven, the solid was filtered and washed with DMF. Following this, the MOF was dried in the oven for 6 h at 60 °C [16]. The reaction yield is 67.7% (HKUST-1, $C_{18}H_6Cu_3O_{12}$, MW: 604.87 g mol^{-1}), based on trimesic acid, obtaining 5 g.

- HKUST-1 green synthesis:

HKUST-1 crystals were synthesized by a green *in situ* method adapted from literature [17]. Briefly, 10 mL of a 20 mM solution of benzene-1,3,5-tricarboxylic acid (BTC) in ethanol was added dropwise to 15 mL of a 20 mM aqueous solution of copper (II) acetate. HKUST-1 was formed within seconds as a light blue precipitate, which was collected by centrifugation and washed several times with ethanol and deionized water. Finally, the product was dried overnight at room temperature. The reaction yield, based on BTC as limiting reagent, was 85.77%.

- HKUST-1 functionalization by crystal poisons:

The green synthesis method described above was used to produce HKUST-1 [17], whereas a crystal poison approach was employed to functionalize HKUST-1 through coordination of thiol groups and BTC linkers in HKUST- 1 (Figure 5.1.1). To maintain the Cu^{2+}: BTC^{3-} (3:2) molar ratio of the HKUST-1 synthesis, in the functionalization with modulating agents, the molar ratio of Cu^{2+}: [BTC^{3-} + crystal poison] (3:2) was also used. The concentration of crystal poison was varied in

the range of 5 to 10% by linker weight. Furthermore, the effect of two crystal poison was evaluated, MBA (4-mercaptobenzoic acid) and TSA (thiosalisilic acid). During the synthesis, three solutions were prepared separately: 15 mL of an aqueous solution with 20 mM of $Cu(CH_3COO)_2 \cdot H_2O$ (solution A), 10 mL of linker solution (solution B), and crystal poison (solution C) using ethanol as solvent taking into account the sum of the molar ratio of B + C = 0.2 mmol. Subsequently, solution B and C were mixed, then the resulting solution (B + C) was added dropwise to solution A under room temperature and pressure. This was left to stand overnight, and the product was washed several times alternating water and ethanol for each wash. Theproduct was collected by centrifugation and finally vacuum dried at room temperature. The reaction yield obtained, calculated from BTC as limit reagent, was of 77.27%.

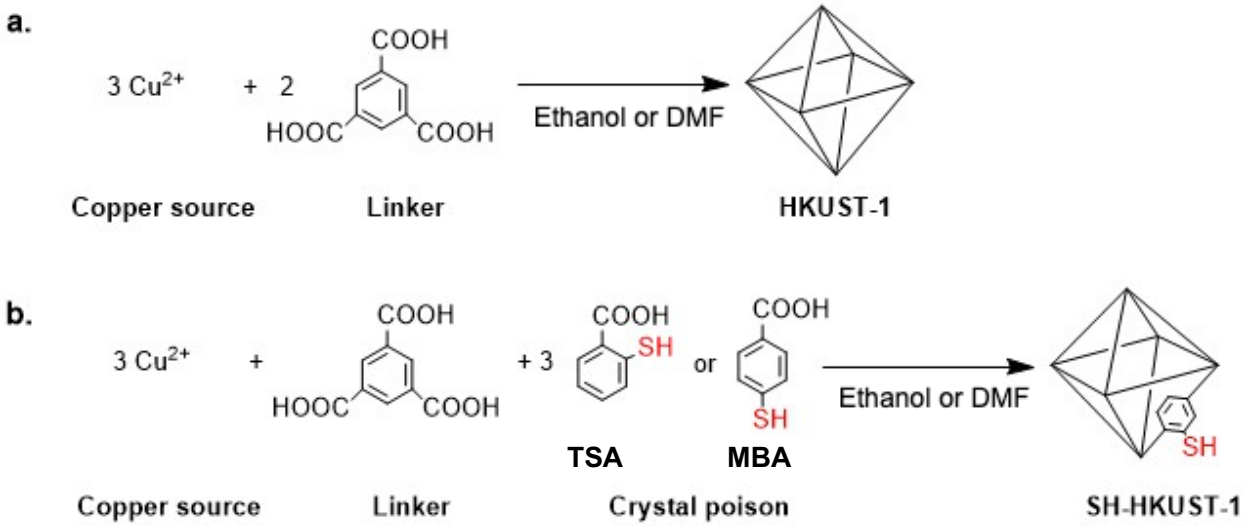


Figure 5.1. The schematic synthesis procedure of a) HKUST-1 using copper nitrate (solvothermal) or copper acetate (green method) as metal source, and b) the HKUST-1 functionalization by the modification trough crystal poison (TSA, left or MBA, right) to add a thiol group into the MOF structure.

5.1.3.3 Characterization

- Chemical structural components

Chemical information about the metallic Cu present in the HKUST-1 synthesized, and to confirm the sulfur was introduced during the MOF functionalization, energy-dispersive X-ray spectroscopy (EDX) equipment coupled to SEM was used. This chemical elemental analysis was performed in a JEOL JSM-6480LV, operating in spectrum collecting mode under high vacuum conditions, at 10 kV and approximate at an 18 mm of working distance.

The Cu content present in the MOFs was determined using flame atomic absorption spectrometry (FAAS) using the injection method. Before the analysis, samples underwent a digestion procedure following the EPA Method 3050B: Acid Digestion of Sediments, Sludge, and Soil [18]. Then, the digested material was analyzed in a Hitachi z-8000 atomic absorption spectrometer equipped with an atomizer with an air-acetylene burner. The wavelength used for the determination of the Cu^{2+} analyte was: 324.7 nm.

- Spectroscopy and surface characterization

Attenuated total reflectance Fourier transform infrared spectrometry (ATR-FT-IR) was performed at room temperature in an IR PerkinElmer Frontier, using a diamond crystal for the characterization of the main functional groups present in the HKUST-1 synthesis and MOF functionalization. The spectra were recorded in the range of 4000 to 600 cm^{-1}, with an accumulation of 30 scans and a resolution of 1 cm^{-1}.

pH_{zpc} was determined using the drift method in which solutions with 10 mL of NaCl (0.01M) were adjusted to an initial pH in the range of 2 to 10 by adding HCl 0.05 M or NaOH 0.05 M. Once the pH of the solutions was set, 0.05 g of the hybrid material was added, the resulting suspensions were stirred for 3 h at 25 °C, and the pH of the supernatantswas registered [19].

- Structural characterization

Powder X-Ray Diffraction (PXRD) was used to confirm the HKUST-1 crystalline structure and its functionalization identity. The equipment STADI P (Cu radiation) Double setup in transmission and reflection mode was operated to obtain the PXRD patterns. The average crystallite size of the MOFs obtained was calculated from XRD data using Scherer's equation [20] (Eq. 5.1.1). Based on the line broadening effect at the full width half maximum (FWHM) of the most intense peak in HKUST-1, which was located close to θ=11.6°.

$$D = \frac{k\lambda}{\beta \cos \theta} \qquad \text{(Eq. 5.1.1)}$$

Where *D* is the average crystallite size, *k* is Scherer constant, *λ* is the wavelength of X-ray, *β* is the FWHM and *θ* is the diffraction angle.

- Morphological characterization

The total surface area was measured by N_2 isotherms of adsorption-desorption at 77 K, using a Quantachrome NOVA e-Series surface area analyzer. N_2 isotherms were performed on MOF powders, which were previously degassed at 80 °C for 8 h before measurements were carried

out. The calculation of the total surface area was established using the BET method [21], the pore size distribution (PSD) was studied by the Barret-Joyner-Halenda method (BJH) and the pore volume was calculated by the t-model plot [30].

Morphological characterization of MOFs was achieved via Field Emission Scanning Electron Microscope (FESEM) and performed on thin-film gold-coated samples using a Zeiss Auriga FIB-SEM (GeminiSEM) scanning electron microscope, coupled to a secondary electrons (SE2) detector. The micrographs were taken at 1.5 kV, working distance (WD) ranging from 4.9 to 5.2 mm, at different magnifications. Besides, the morphology also was inspected by Scanning Electron Microscopy (SEM) using a Hitachi FLEX SEM 1000 model microscope.

- Thermal Characterization

Thermal gravimetric analysis (TGA) and Differential Scanning Calorimetry (DSC) were performed using a simultaneous thermal analyzer (STA 409 PC/4/H Luxx) in a temperature range from 50 to 900 ºC at a heating rate of 10 ºC/min using an inert (N_2, 50 cm^3 min^{-1}) and air (50 cm^3 min^{-1}) atmosphere.

- Hydrolytic stability characterization

In the context of this thesis, hydrolytic stability refers to whether the structure holds up or collapses after being immersed in water. To analyze the water stability of the synthesized MOFs, the materials were immersed in water at room temperature, in an independent experiment lasting for 0, 1, 2, 4, 6, 12, 18, 24, 48, and 72 h. At the end of each experiment, the solutions were filtered and the collected solid was dried at room temperature. The dried powder and the remaining liquid were analyzed separately.

The dried powder was analyzed by XRD, SEM, EDX, FTIR, and adsorption isotherms (under the conditions previously described) to verify how the morphology, chemical structure and crystallinity were affected.

Also, the part regarding the remaining liquid was analyzed to determine if the main components of the MOFs structure (Cu, S, and BTC) were released into the water (*i.e.*, leaching) during the stability analyzes. The linker leaching was continuously monitored using a UV-vis spectrophotometer to track absorbance of the BTC molecule in a quartz cell in a Shimadzu Pharm device. Its concentrations were assessed through a calibration curve in the range of 0.25 to 4 mM obtained at a wavelength of 291 nm.

Inductively Coupled Plasma - Optical Emission Spectrometry (ICP-OES) was used to identify and quantify Cu and sulfur present in the solutions analyzed. All experiments were conducted using an iCAP 7400 ICP-OES instrument (Thermo Fisher Scientific). Plasma conditions were as follows: RF power: 1250 W, auxiliary gas flow: 0.5 dm^3/min, coolant gas flow: 12 dm^3 min^{-1}, nebulizer gas flow: 0.5 dm^3/min, and nebulizer gas pressure: 270 kPa. Spectra were analyzed using Qtegra ISDS (Thermo Fisher Scientific). The iCAP 7400 ICP-OES instrument was calibrated to the following elements: Cu and S, using the respective elemental standard (1 mL) in concentrated HNO_3 with deionized water.

5.1.4 Results and Discussion

5.1.4.1 HKUST-1 synthesis

Understanding the variation of HKUST-1 synthesis methods reflected how different properties can be affected. The HKUST-1 yields obtained by the solvothermal and green synthesis methods were 67.7% and 85.7%, respectively, calculated from the BTC linker as a limiting reagent. X-ray powder diffraction analyzes were performed to ensure the crystallinity of the HKUST-1 material synthesized by the solvothermal (Figure 5.1.2. pink) and green (Figure 5.1.2. purple) methods.

The diffractograms in Figure 5.1.2 show the characteristic peaks of HKUST-1 located at $2\theta \approx 6.5°$ (200), 9.5° (220), 11.6° (222), 13.3° (400), 14.7° (331), 16.2° (422), 17.5° (511), 19° (440) and 20.08° [22], which coincide with the pattern diffractogram (Figure 5.1.2. turquoise). Thus, XRD confirmed the solid products were high-quality HKUST-1 due to the peak indexing intensity and their sharp profile. For HKUST-1 synthesized at room temperature conditions (green method), no diffraction pattern is observed at Bragg angles greater than 21° compared to HKUST-1 synthesized at high temperature (solvothermal method), suggesting the most common impurity phases of Cu, CuO or Cu_2O did not form [23]. At the same time confirms the high purity of the crystalline phases of the synthesized MOF by the green method, in line with the few existing reports of HKUST-1 synthesis in which low temperatures suppress Cu_2O formation during HKUST-1 [24]. In addition, it has been reported that syntheses at high temperatures allow obtaining significant amounts of Cu_2O as a by-product, which can affect the properties of metal-organic frameworks. Besides, if the Cu_2O impurities remain in the MOF pores after the activation process, there are great possibilities that it will result in the blocking of the frame pores [24].

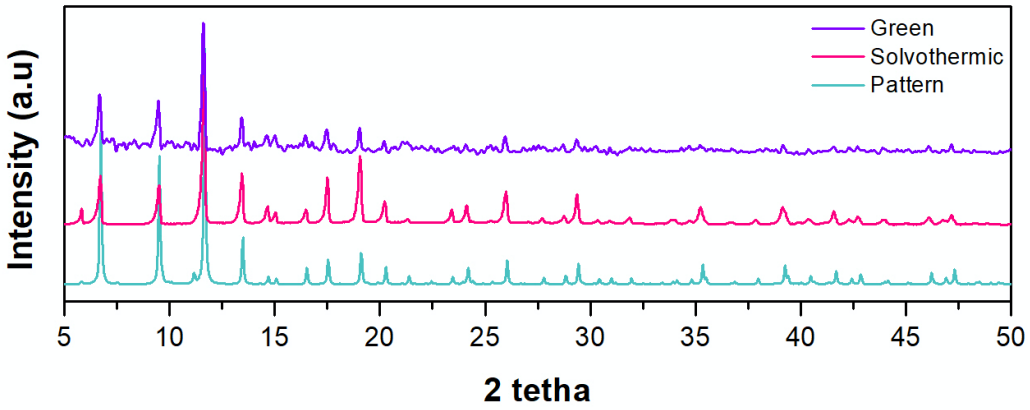


Figure 5.1.2. XRD diffraction pattern of HKUST-1 synthesized by solvothermal and green method.

The average size of the HKUST-1 crystallites was calculated using the Scherrer equation (Eq 5.1), with the strongest peak identified in the diffraction pattern corresponding to the Bragg angle of 11.6°. Values of 81.5 and 56.5 nm were calculated for the solvothermal and green synthesis, respectively. In this way, it was evident the MOF crystal size was strongly affected by the method used for the synthesis, which may be related with the change of solvents or reaction conditions (temperature, pressure, and time).

FESEM micrographs were used to characterize the morphology, microstructures, and size of crystals obtained. As shown in Figure 5.1.3 a,b, the solvothermal synthesis originates octahedral crystals with average diameters of approximately 10 µm with sharp edges and smooth surface, with a homogenous crystal size distribution (Figure 5.1.3a). This is in agreement with XRD data in which the high synthesis temperatures are favorable to produce individual crystals.

On the other hand, the green synthesis produced smaller, more rounded particles of about 100 to 500 nm (Figure 5.1.3d), non-uniform, agglomerated, and rough surface (Figure 5.1.3c). The crystal size difference between both methods could be attributed to the solvents used in each process, which influences the nucleation stages and subsequent crystals growth [25].

FESEM microscopy was combined with energy dispersion spectroscopy (EDX) to determine the elemental qualitative composition of the obtained MOFs. EDX spectra for both HKUST-1 synthesized MOFs revealed the same elemental composition of C, O, and Cu, as shown in Figure 5.1.4.

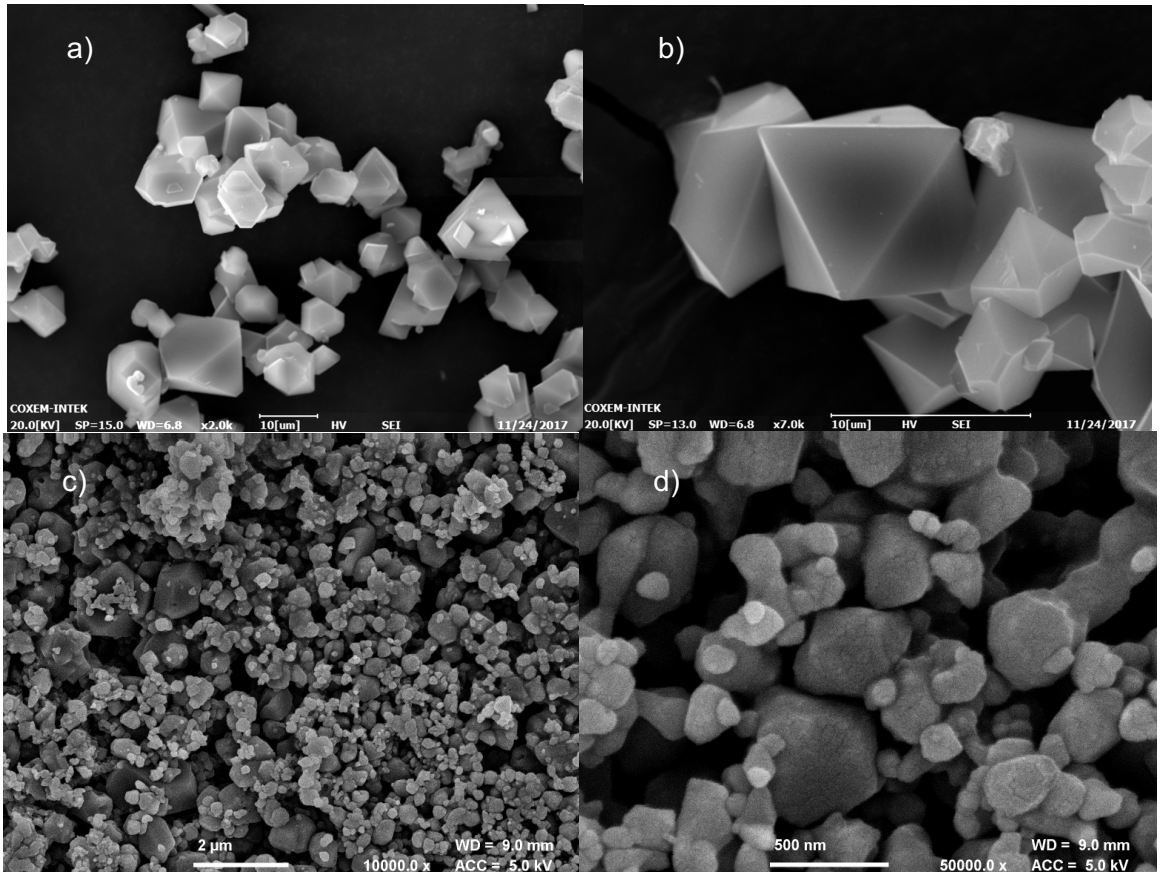


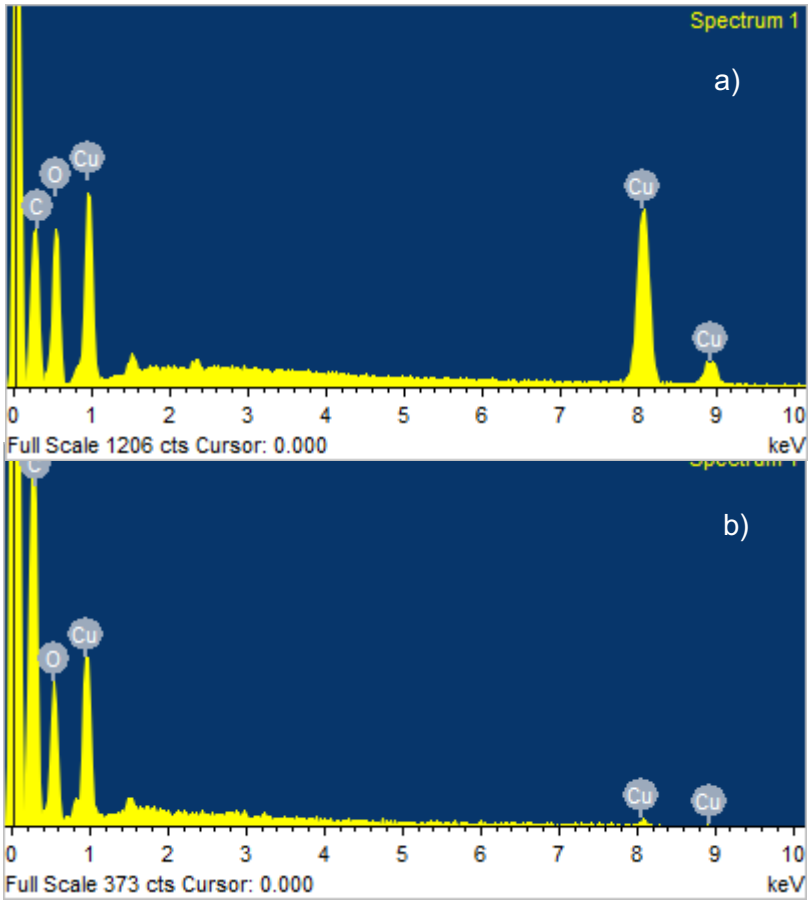
Figure 5.1.3. Micrographs of HKUST-1 obtained by the solvothermal method a) 2000x, b) 7000X and by the green method c) 10000X, d) 50000X.

In general, the element with the highest content in atomic percentage was carbon, followed by oxygen and Cu, as was expected, due to the chemical composition of the reagents used. The oxygen content was similar in the two synthesis methods whereas the atomic percentage of Cu, the value was higher in the material prepared by green synthesis than solvothermal, while the carbon content was higher in the solvothermal synthesis compared to the green one.

Complementary to EDX, the quantification of Cu in the HKUST-1 synthesized by both methods was carried out by FAAS (flame atomic absorption spectrometry). The amount of Cu measured was of 35.3 ± 3.6 and 43.1 ± 4.7% wt, for the solvothermal and green synthesis, respectively. The results obtained by FAAS corroborate the description made by EDX, which, despite being a semiquantitative elemental analysis technique, demonstrated the same behavior.

The Cu content is higher in the green synthesis compared to the solvothermal; this behavior is influenced by the precursor salt that is used as a metal source. Cu acetate is a more efficient metal source compared to Cu^{2+} mononuclear species, such as copper nitrate (II), because the

acetate already contains the paddlewheel structure which differs in the nucleation and growth mechanism of HKUST-1, resulting in the appearance of defects, stages of isotropic growth and differences in crystal size, as was evidenced above by SEM. In HKUST-1, the local environment of Cu^{2+} atoms is very similar to cupric acetate. Hence, HKUST-1 adopts the valence and conduction bands that have cupric acetate [26],which according to electronic structure calculations consist: d-bond state (a closed-layer singlet), a ferromagnetic state (FM) (an open-layer triplet) and an antiferromagnetic state (an open-shell cage) [27].



Solvothermal

Element	Atomic (%)	Weigh t (%)
C	77.31	59.63
O	14.24	16.60
Cu	8.45	23.77
Total	100	100

Green

Element	Atomic (%)	Weight (%)
C	74.08	56.80
O	20.84	20.85
Cu	5.51	22.36
Total	100	100

Figure 5.1.4. HKUST-1 EDX after the a) solvothermal and b) green synthesis method, and the atomic / weight compositional percentage.

The FTIR spectra of both synthesized HKUST-1 (Figure. 5.1.5) showed the characteristic peak signal at 728 cm^{-1} attributed to the Cu-O bond in HKUST-1. The bands at 1644, 1373, and 1447 cm^{-1}, related to stretching vibratory frequencies of the aromatic ester C = O and C-O, as well as O-H flexing of the carboxylic acid, respectively, indicate the presence of the COOH group into the BTC linker. The presence of additional peaks in the green synthesis spectrum (Figure 5.1.5, purple) in the region of 1720–1680 cm^{-1}, suggested that not all the linker carboxylic groups were

unprotonated. The appearance of a wideband at 3700-2700 cm^{-1} is related to the presence of water and -OH groups in the material structure. In general, the vibration bands obtained in Figure 5.1.5 of the HKUST-1 green and thermal synthesis spectra agree with the reports made for this MOF [28].

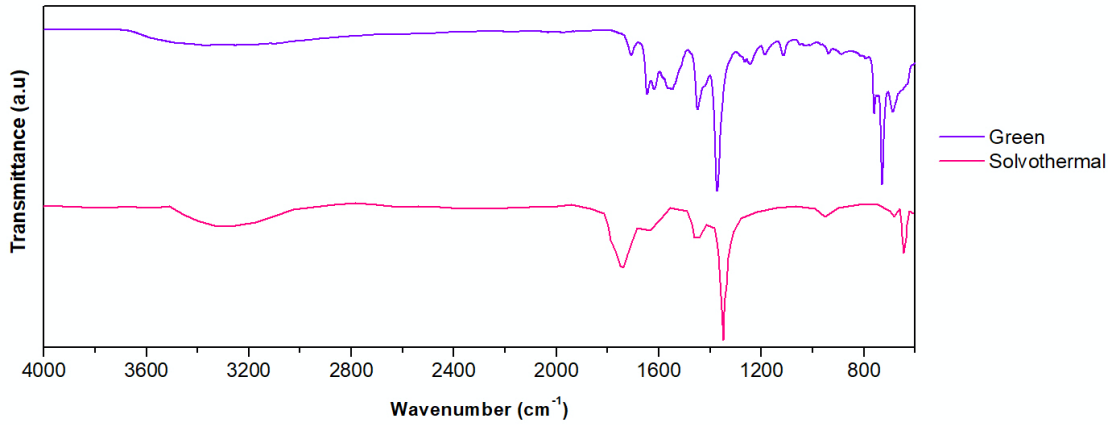


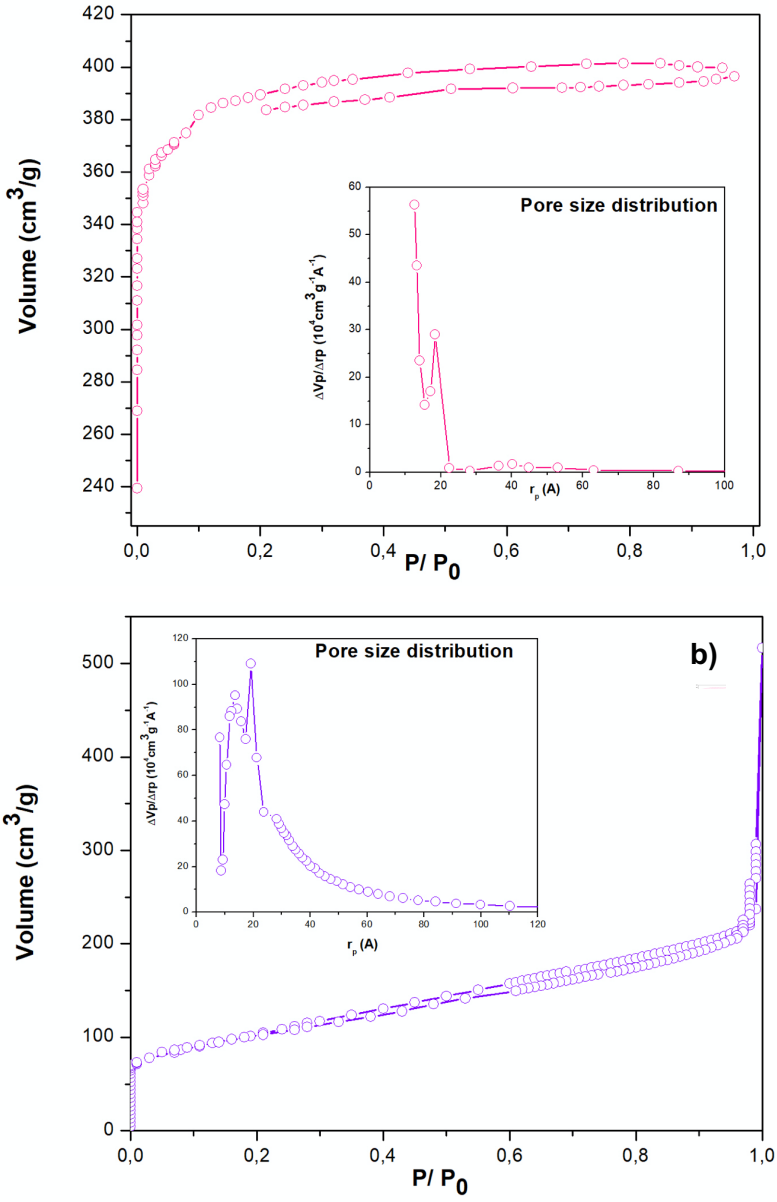
Figure 5.1.5. Infrared spectra of HKUST-1 synthesis by the solvothermal and green method.

N_2 adsorption-desorption isotherms measurements were used to determine the textural parameters such as surface area, volume, average size, and pore distribution of HKUST-1 sinthesized in both synthesis (Figure 5.1.6). Solvothermal synthesis (Figure 5.1.6 a) has a type I isotherm characteristic of microporous frames (<2 nm) [29]. The green synthesis showed a type II isotherm (Figure. 5.1.6b), it evidenced a first upward slope in the low-pressure range (0-0.05 P/P_0) attributed to the filling of smaller pores or primary cages in Cu- BTC, followed by a slightly deeper slope in the relative pressure range between 0.05 and 0.95, corresponding to the filling of larger Cu-BTC cages. Additionally, the green synthesis isotherm presented a hysteresis loop in the region of relatively high pressure, attributed to particle stacking or capillary condensation that occurs in mesopores [29].

The surface area of HKUST-1 obtained by the solvothermal synthesis was 1131 $m^2 g^{-1}$, a high value as was expected for metal-organic frameworks. On opposite, the green synthesis reported a surface area value of 367 m^2g^{-1}, *i.e*, a one third of the value measured with solvothermal synthesis. Also, the pore volume was reduced from 0.52 to 0.02 cm^3g^{-1} for the solvothermal and green synthesis, respectively.

These reductions in textural parameters can be attributed to the washing and activation stage of HKUST-1, since depending on the synthesis method used, they could host solvent molecules

inside the frame pores. For example, the solvothermal synthesis could contain water, ethanol, or DMF, and the green synthesis only water or ethanol. Likewise, other amorphous or non-porous impurities, reagents, or by-products could not be removed from the material, causing blockage of pore channels. As the impurities are removed, the pore volume becomes larger and the blocked channels open, increasing the surface area. Additionally, the surface area of the green synthesis was smaller because of the rapid crystal formation causing the unreacted metal/linker to be retained in some pores, thereby reducing the available surface area.



Surface Area (m^2/g)		
Model	Green	Solvothermal
BET	367	1131
Pore volume (cm^3/g)		
t-Plot	0.02	0.52
Pore size (nm)		
BJH	2.83	2.16

Figure 5.1.6. N_2 adsorption-desorption isotherms of HKUST-1 synthesis by the a) solvothermal and b) green method (inset BJH pore size distribution).

It should be noted, the materials obtained from the solvothermal and green synthesis contained micropores and mesopores (2.16 and 2.83 nm, respectively). The solvothermal HKUST-1 samples present a more uniform pore distribution (Figure 5.1.6 a) compared to the green synthesis sample. Values obtained for the textural parameters are comparable to the previously reported values [31].

Figure 5.1.7. displays the pH curve used to determine the pHzpc of HKUST-1. The value quantified was 4.56 ± 0.15. It indicated an acid behavior, most probably due to the acid character as a result of the linker used into the MOF structure (acid trimesic with a pk_a = 3.17 [32]). This values is consistent with the literature, the value of pHzpc measured by Hassan was 4.8 [19].

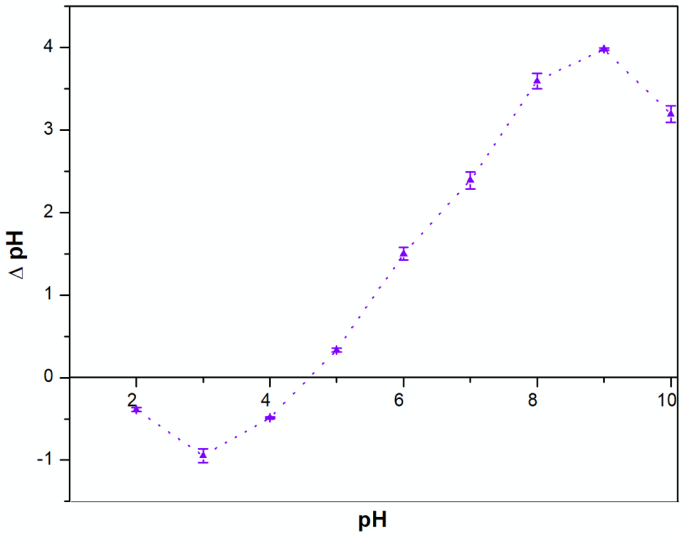


Figure 5.1.7. pH_{zpc} for HKUST-1 under the green method synthesis.

The thermal stability of HKUST-1 synthesized by the solvothermal and green methods was investigated. Both syntheses showed similar thermograms (Figure 5.1.8), three regions of mass loss were detectable. The first stage corresponding to a mass loss close 13% occurred between 30 to 120 °C, attributed to the physisorbed water in the network pores. The second mass change of approximately 7% happened between 120 to 220 °C, related to the release of chemisorbed water to the Cu atoms and solvents hosted in the internal pores of the structure, for both synthesis ethanol and DMF only for solvothermal synthesis. During the third stage, the greatest amount of mass was lost (about 50 to 55%) between 220 to 420 °C, as a consequence of the breakdown of linker/metal coordination bonds and BTC degradation. Finally, there is a remaining mass related to metallic oxides such as CuO and Cu_2O, products of the frame collapse [29].

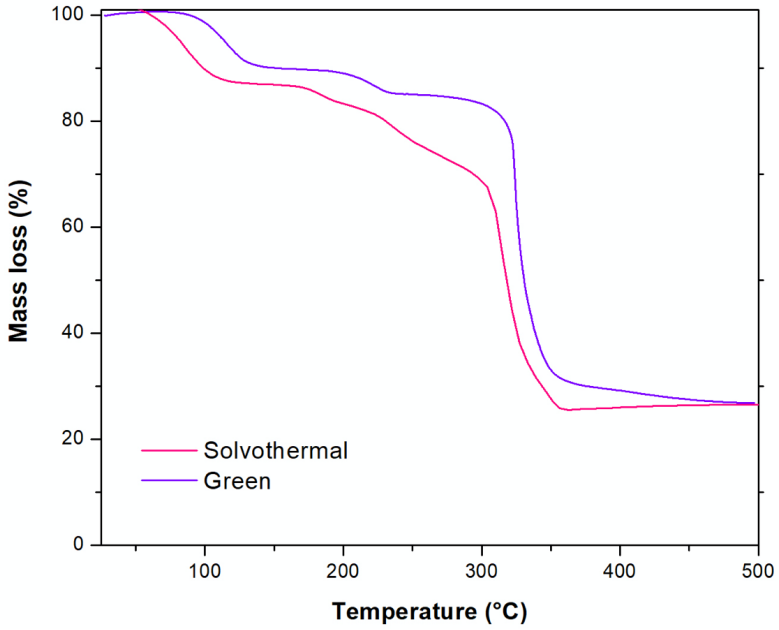


Figure 5.1.8. Thermogravimetric analysis profiles of HKUST-1 synthesis by the a) solvothermal and b) green method.

At this point, it was concluded the synthesis of HKUST-1 is affected by factors such as the metal salt source, type of solvent, temperature, reaction time, and stoichiometric relationship, as evidenced by the textural and morphological properties. However, there is no change in the crystallinity obtained as both materials showed to have very similar peak diffraction, despite having been synthesized through two different methods.

For this reason, from now on the green synthesis was selected as the method to be used in the following research stages, since compared to the solvothermal method it has the advantages of energy-saving (generated under pressure and ambient temperature conditions) and avoids the use of polluting solvents such as DMF, which makes it a potentially scalable and environmentally friendly synthesis method.

5.1.4.1 HKUST-1 functionalization

To improve the hydrolytic stability of HKUST-1 and increase its selectivity in applications related to the removal of ECs, literature studies refer to the linker structure functionalization through the introduction of a target functional group [33]. One type of linker functionalization is the use of modulating agents capable to maintain the structural integrity of MOFs during the reaction media. The modulators approach has advantages compared to conventional synthesis since it allows to

have control of nature and topology in the final product, often through milder synthetic conditions[14].

Crystal poison is a type of modifier that can be incorporated into the MOFs crystal in small concentrations, reducing the nucleation rate and providing a growth step in which the molecules could be grafted into the frames, altering the normal behavior of crystals. One of the main challenges facing the introduction of modulating agents like crystal poison is finding the right concentration. Particularly, there are reports where thiol groups (-SH) have been able to become steric barriers to the addition of solute atoms [5]. In this research, HKUST-1 was modified by the insertion of thiol groups into the linkers coordinated in the structure.

Two crystal poison with the same chemical formula $C_7H_6O_2S$ were evaluated. These compounds have a chemical structure similar to the BTC linker (Figure 5.1.1). They consist of an aromatic ring with a carboxylic acid in position 1, and with a thiol group substituted at different position: *ortho*- for TSA (thiosalicylic acid) and *para*- in MBA (4-mercaptobenzoic acid). In addition, the effect of crystal poison concentration was assessed by varying it from5 to 10% by linker weight, to analyze the effect of the concentration. The functionalized materials was then characterized by several techniques, as discussed below.

According to the XRD patterns (Figure 5.1.9), all the diffraction peaks of functionalized MOFs can be easily indexed with the HKUST-1 diffractogram synthesized by the green method (Figure 5.1.9 purple), which has already been compared against the simulated pattern (Figure 5.1.9 turquoise). In general, new peaks were not evidenced for the thiol functional group in XRD patterns after the MOF modifications (TSA 10%, MBA 5 and 10%), possibly due to the low content of -SH in the frames. In this way, it was confirmed that evaluated modulators (MBA and TSA) compete with linkers, slowing the MOFs growth and giving rise to be included in the same structure.

The Cu coordination as a metallic center depended on the lack of BTC linker protection, which in turn is affected by the type of crystal poison used and its concentration. In particular, the functionalization done with TSA resulted in the loss of the frame crystalline order, as evidenced by the appearance of a significant number of peaks and the deformation of main peaks indexed with the corresponding HKUST-1 structure (Figure 5.1.9 yellow), which could be a consequence of a coordination deficit of MOF constituent units. The diffraction patterns obtained were compared with the pristine MOF (Figure 5.1.9 purple), and differences were found whereby the

TSA structure might not be very stable and possibly contain impurities in the crystals. Since the HKUST-1 crystallographic profile was not developed using TSA as crystal poison, the use of this modulating agent was ruled out.

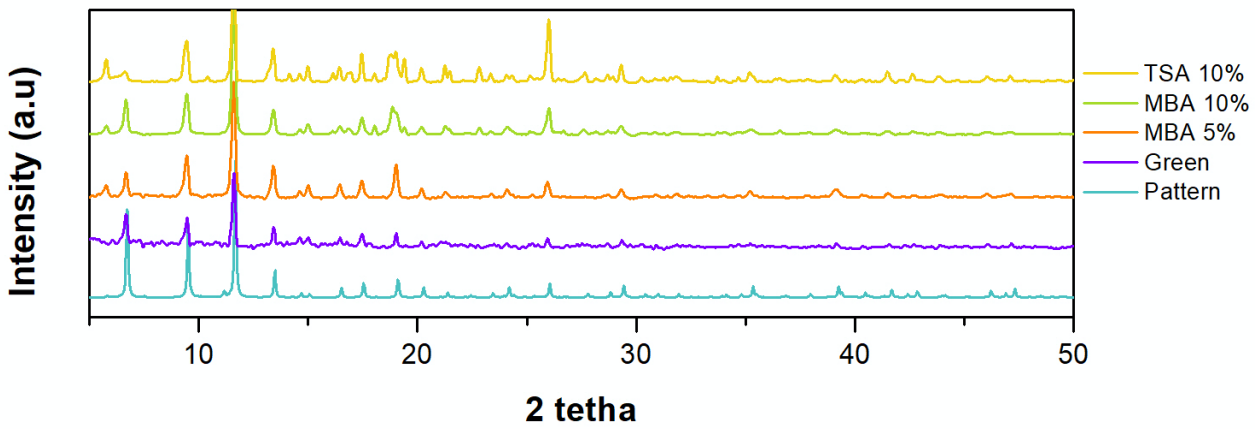


Figure 5.1.9. XRD diffraction pattern for the functionalization of HKUST- (green method) using crystal poisons.

In contrast, the functionalization of HKUST-1 using MBA in the concentration range of 5 to 10% by linker weight, evidenced a better peaks indexation. The modification trough 5% wt of MBA was evident in the diffractogram from (Figure 5.1.9, orange), where more defined XRD patterns and developed peaks are easily indexed with the simulated pattern in (Figure 5.1.9, purple), confirming the appropriate modification of the metal-organic framework. Nevertheless, it is important to take into account the formation of possible impurities, such as Cu_2O attributed to the peaks located at 36.4°, 42.3°, and 43.3° [28]. Using the Scherrer equation (Eq. 5.1.1), the average crystallite size was calculated to be 43.5 nm, which is smaller than those obtained for HKUST-1 employing the green synthesis method (56.5 nm).

However, high concentrations of MBA (10% wt of linker) evidenced a reduction in crystallinity as a consequence of the new diffraction peaks appearance ($2\theta \approx 18°$), amorphization, and widening of others ($2\theta \approx 16°$, 19°, and 21°). In this way, it can be concluded that as the crystal poison concentration increased, the crystallography of modified HKUST-1 decreased. This could be due to high concentrations of modifying agent inhibits the formation of nuclei, affecting the nucleation and preventing the formation of MOF crystals. This behavior agrees with data from other authors when they use acids as modulating agents, in which modulators acted as competitive compounds in coordination equilibria [14].

In addition, it was also verified the position where the thiol group is located into the crystal poison plays an important role in the HKUST-1 functionalization. Meanwhile, the TSA did not show to develop the HKUST-1 crystalline standard under the same experimental conditions as MBA, probably because the ortho- position of thiol could have had some interaction with the Cu metal center. Likewise, it was corroborated the HKUST-1 modification with MBA as a modulating agent is quite sensitive to the substitution percentage of crystal poison by the linker, since after 5% addition of MBA the MOF crystallography was altered. As a result, hereinafter the MOF HKUST-1 functionalized with MBA 5% by weight of BTC will be named as SH-HKUST-1.

Scanning electron microscopy images (Figure 5.1.10) allowed us to investigate the surface morphology of the HKUST-1 functionalized MOF. Crystals obtained from SH-HKUST-1 have a spherical shape and slightly smaller sizes compared to those reported for HKUST-1 synthesized by the green method (Figure 5.1.3. c and d), which are in the range of 50 to 300 nm. Nonetheless, HKUST-1 crystals have a smooth surface which, unlike SH-HKUST-1, showed to be rougher after functionalization. No additional morphologies were found in SEM micrographs, suggesting the complete inclusion of thiol functional groups into the metal-organic framework structure.

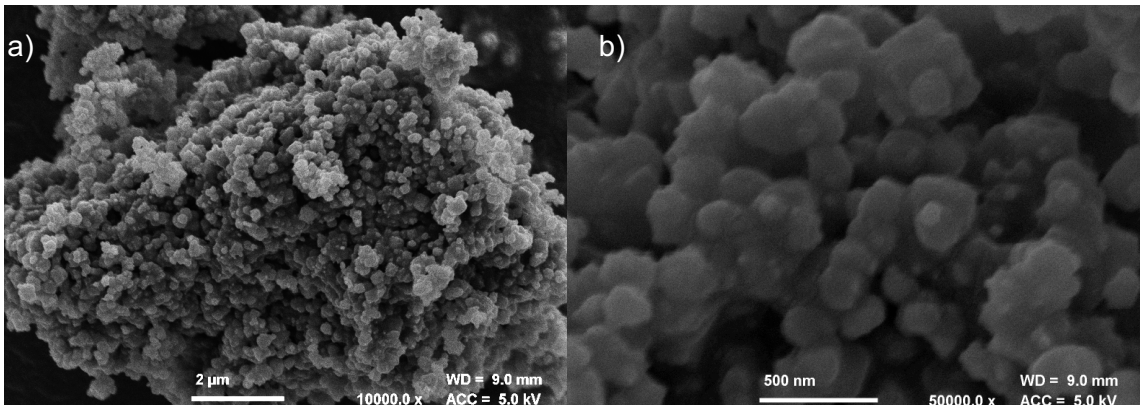


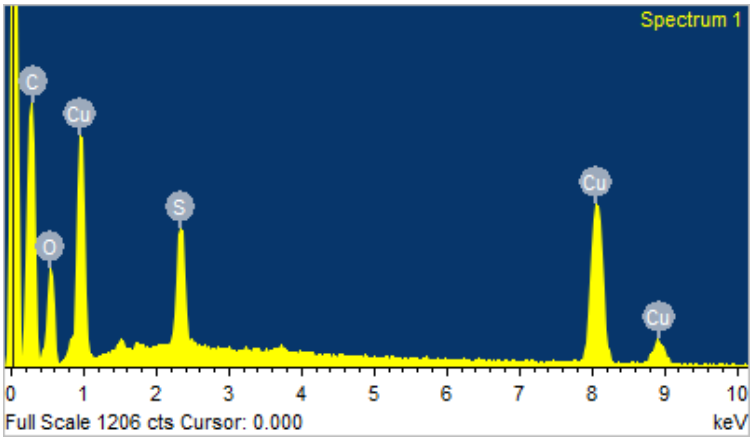
Figure 5.1.10. Micrographs of SH-HKUST-1 obtained by the green method using MBA 5%wt a) 10000X and b) 50000X

It has been argued about the control of crystal shape obtained through functionalization with modulating agents that it is achieved by blocking crystal growth as a consequence of the crystal poison interaction with certain facets of MOF, resulting in the simultaneous interruption of crystal growth in a specific direction [15]. This behavior complemented the results previously reported with XRD, where concentrations of 10% MBA led to obtaining products that were not entirely crystalline. The growth rate of crystals in a certain direction was affected by the crystal poison concentration. Additionally, it is possible the thiol group acted as a steric hindrance by the

reduction of cohesive energy with linkers during the post-nucleation stage, producing a disruption that retarded the SH-HKUST-1 growth.

The presence of sulfur atoms of the thiol group was confirmed in the EDX spectrum of SH-HKUST-1 (Figure 5.1.11), suggesting the content of the –SH group was grafted into the frame. Regarding the Cu content in Figure 5.1.10, the value was reduced regarding the percentage by weight of the non-functionalized MOF, going from 10.68 to 7.36%. The carbon and oxygen values were similar to those reported for HKUST-1 synthesized by the green method (Figure 5.1.4).

FAAS technique was used to quantitatively ratify if the Cu content was reduced in the modified MOF. As so, the amount of Cu in SH-HKUST-1 was measured to be 48.5 ± 5.4% wt, a value very close to the amount in HKUST-1 before being functionalized (43.1 ± 4.7% wt), which was consisted with results obtained by EDX of the low sulfur content in the synthesized MOF samples.



SH-HKUST-1

Element	Atomic (%)	Weight (%)
C	75.30	53.99
O	15.75	15.04
S	1.58	3.03
Cu	7.36	27.94
Total	100	100

Figure 5.1.11. EDX spectra of the thiol HKUST-1 modified using MBA 5%wt.

The material was further charcterized by FTIR (Figure 5.1.12). The spectra of the material functionalized with thiol (SH-HKUST-1) and the bare crystals of HKUST-1 are similar, although SH-HKUST-1 has less defined and intense signals compared to HKUST-1. The spectrum of modified MOF agreed with the characteristic bands of HKUST-1, However, the new bands below 1200 cm^{-1} correspond to vibrations of the BTC linker, from which it can be intuited that some linkers did not fully deprotonated.

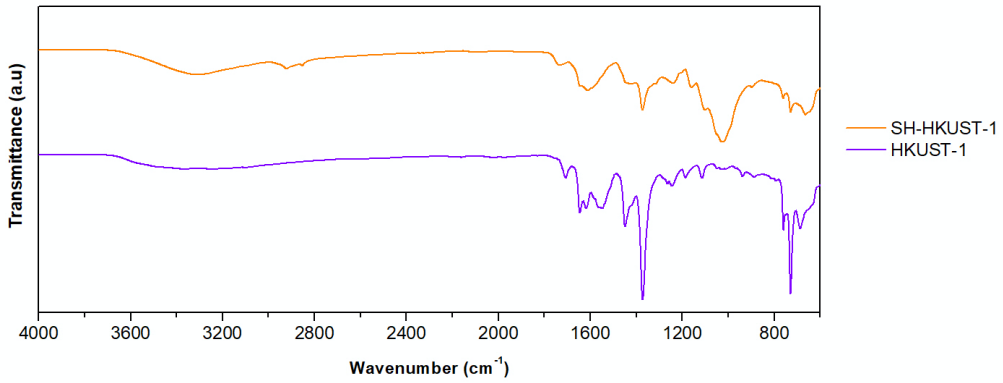


Figure 5.1.12. FTIR spectra of the thiol HKUST-1 modified using MBA 5%wt (orange spectrum) and HKUST-1 synthesized using the green method (purple spectrum).

The pH_{zpc} of SH-HKUST-1 was determined Figure 5.1.13. It presents an intercept with the zero value of the abscissa at 4.69 ± 0.21, which corresponds to the value of pH_{zpc} for SH-HKUST-1. This value is very similar to the one obtained for HKUST-1 (4.56 ± 0.15)., clearly indicating the metal-organic framework modification did not affect the net surface charge.

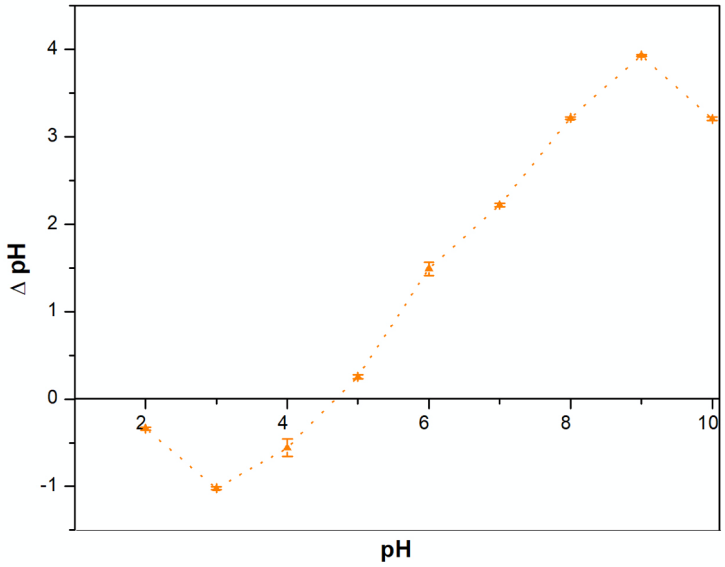
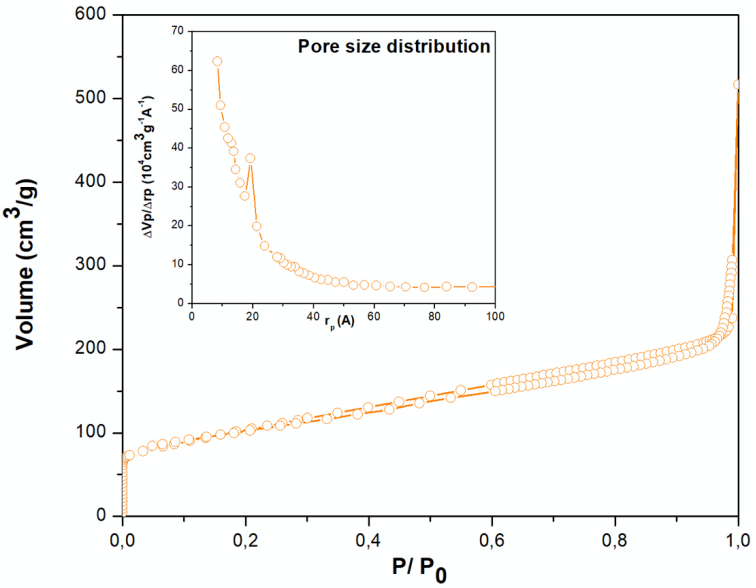


Figure 5.1.13. Zero-point of charge pH_{zpc} for HKUST-1 under the green method synthesis modified using MBA 5%wt.

The result of grafting thiol groups through linkers in the HKUST-1 structure is also visible in the N_2 adsorption isotherm of the new material (Figure 5.1.14). The isotherm confirmed the formation of a mesoporous MOF, similarly to pristine HKUST-1, as a result of the type II isotherm obtained. The thiol-modified samples exhibit a significant increase in surface area, volume and pore size compared to the MOF not functionalized. The SH-HKUST-1 BET surface area increased from

367 to 579 m^2g^{-1}; likewise, the volume increased from 0.02 to 0.17 cm^3g^{-1} and pore size was kept similar from 4.83 to 4.86 nm, respectively (Figure 5.1.14).

The results indicated the SH-HKUST-1 pores were not blocked after thiol inclusion, leaving the pore volume accessible to nitrogen molecules. In this way, it is possible to conclude the -SH groups did not occupy the cavities of the crystals bu,t on the contrary, were found on the surface. One of the possible results of using modifying agents is to affect the crystals growth rate, which was disturbed by the green synthesis method that gave enough time to improve the nucleation and growth stages of the crystals [1].



Surface Area (m^2/g)	
Model	Thiol
BET	579
Pore volume (cm^3/g)	
t-Plot	0.17
Pore size (nm)	
BJH	4.86

Figure 5.1.14. N_2 adsorption-desorption isotherms and BJH pore size distribution inset of SH-HKUST-1 (Surface area, pore-volume, and pore size of SH-HKUST-1 by the solvothermal and green synthesis for nitrogen adsorption experiments).

Additionally, a well-defined hysteresis loop was observed from the desorption curve, suggesting a high homogeneity in the size of the crystals, as was observed in the material SEM micrographs (Figure 5.1.10). From the HKUST-1 functionalization using modulating agents such as crystal poison, the pristine MOF modification was achieved by including thiol functional groups on the structure surface, fully retaining the framework topology after the modification. MBA acted as a competitive ligand in the coordination equilibria during nucleation and growth of the SH-HKUST-1 crystals, which allowed obtaining a modified MOF, with higher selectivity and interesting properties that must be evaluated in different applications.

The thermal characterization of the modified MOF SH-HKUST-1 (Figure 5.1.15) shows the material dehydration of the material took place up to 180 ºC with a total weight loss of 2 wt.%,

related to the three water molecules per Cu center in the framework [34]. DSC result correlated well to the TGA displaying an endothermic peak due to the SH-HKUST-1 dehydration. SH-HKUST-1 was thermally stable up to 250 ºC before starting to gradually disintegrate at higher temperatures [28]. The weight loss of decomposition was measured as 91%, which was related to the formation of Cu_2O and CuO. Two exothermic peaks were discovered by DCS analysis at temperatures higher than 250 ºC, being the first exothermic peak (350–450 ºC) associated with the Cu_2O formation and the second one (500–650 ºC) corresponded to the phase transformation of Cu_2O to CuO [35].

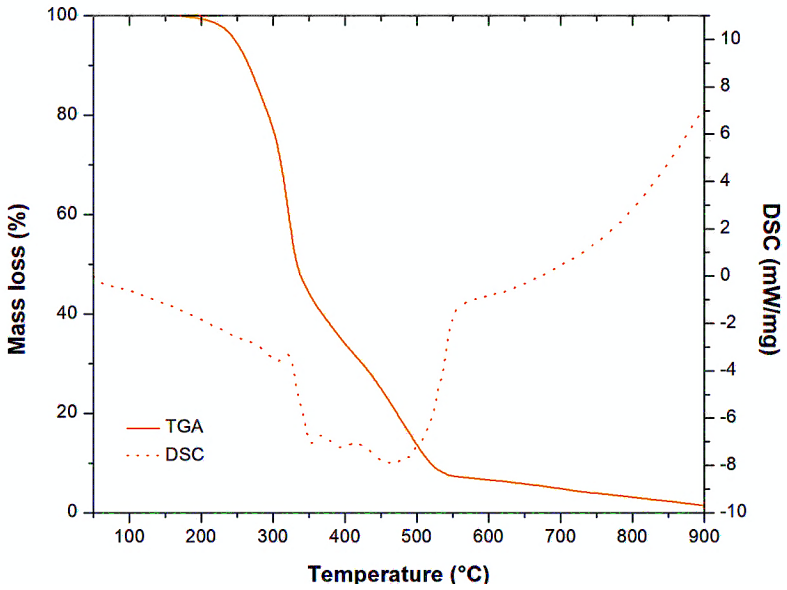


Figure 5.1.15. TGA y DSC of SH-HKUST-1.

- Hydrolytic stability characterization:

From the XRD results of the MOFs synthesized after being in contact with water (Figure 5.1.16), it was evident the characteristic peaks of the SH-HKUST-1 structure after 24 hours of exposure to water. Whereas, the HKUST-1 XRD showed evidence of structure collapse after 6 hours, showing only the peak located at 2θ = 9.5 °, on the contrary, the appearance of new several diffraction peaks were observed. While the metal-organic framework modified using thiol groups kept its characteristic peaks at 2θ = 9.5, 11.5 13, 16, 17.5, 1,9, and 20° after 24 hours, indicating that the crystal structure of SH-HKUST-1 is maintained after contact with water.

XRD patterns also revealed the diffraction of HKUST-1 after the collapse of its structure are very similar to those of SH-HKUST-1 after being in contact with water for 48 hours. Both diffractograms

that confirmed the frames amorphization. HKUST-1 lost all the diffraction peaks characteristic of the crystal structure while SH-HKUST-1 still mantained some characteristic peaks. Besides, both materials developed new diffractions like the 2θ = 22.5, which could be related to the presence of phases like $Cu(OH)_2$ [26].

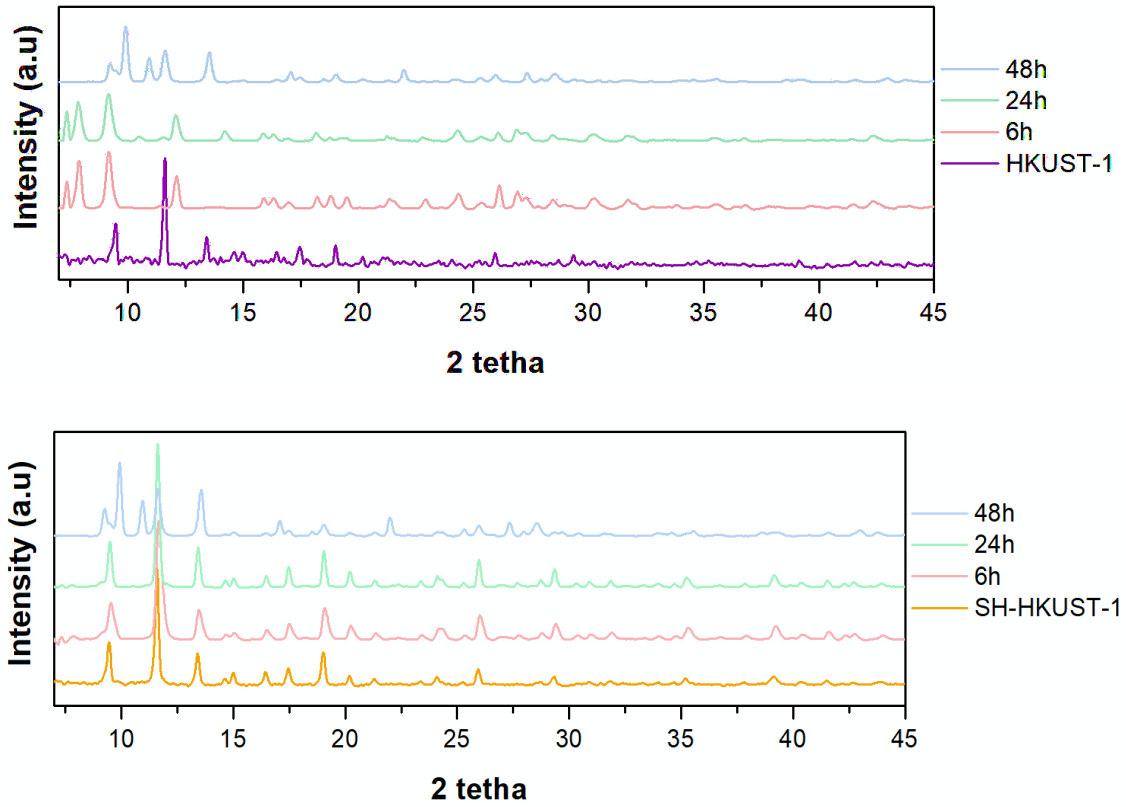


Figure 5.1.16. XRD patterns of HKUST-1(up) and SH-HKUST-1 (down) samples, exposed to water for 6 (pink curve), 24 (green curve), and 48 h (blue curve).

Micrographs of the synthesized HKUST-1 and SH-HKUST-1 materials after different times of exposure to water at room temperature (Figure 5.1.17), showed needle-shaped crystals, exhibiting degradation crystal morphology [26], as a result of the crystallites aggregation. As the contact time increased, it was possible to verify the formation of rectangular, much wider, and flatter structures with defined edges.

These new rectangular shapes became visible in HKUST-1 at 24 hours, while for SH-HKUST-1 they began to be evident at 48 hours. Corroborating the results obtained using XRD, in which greater conservation of the crystal structure by SH-HKUST-1 compared to HKUST-1 was demonstrated. On the other hand, authors like Jimenez *et al.* [36] have reported the rectangular shapes of the micrographs in Figure 5.1.17, and have related them to the $Cu(OH)_2$ compounds

which possess a platelet morphology. This is also in accordance with the crystallographic development of the copper hydroxide phase, previously explained through XRD (FIgure 5.1.16).

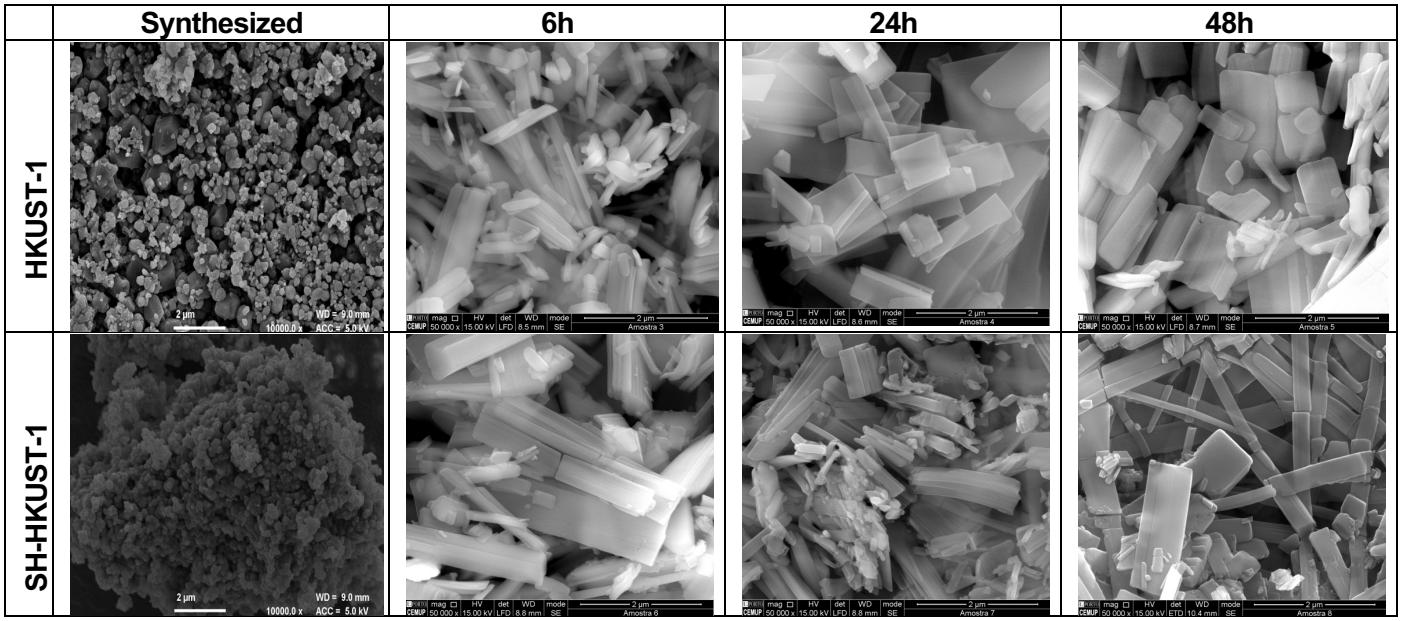


Figure 5.1.17. SEM images of HKUST-1(up) and SH-HKUST-1 (down) samples, exposed to water for 6, 24, and 48 hours.

Regarding the analysis of the BET surface area of the materials in contact with water for 48, these were reduced from 445 to 2.15 m^2g^{-1} and 612 to 5 m^2g^{-1}, for HKUST-1 and SH-HKUST-1, respectively. Due to the network collapse, no isotherm was developed, limiting the calculation of total pore volume and confirming the irreversible damage of the metal-organic frameworks, as was supported by SEM and XRD data.

Nitrogen adsorption of metal-organic frameworks has been described [27]. HKUST-1 is a metal-organic framework formed by two types of large pores connected, the first is mainly hydrophilic and has diameters of 11 and 10 Å, the second are micropores of 4 Å which tend to be mostly hydrophobic [26]. Regarding the water molecule, it has a collision diameter of 4.3 Å (according to the Stockmayer model) [26], capable of spreading so much throughout the porous structure of HKUST-1. Water filling of the pores occurred first in the largest pores and later in the small ones.

Furthermore, materials such as MOFs within their structure contain oxygen that coordinates with metal centers acting as polar sites. Besides, organic linkers provide a strongly non-polar character; they are mainly made up of aromatic molecules and represent the largest fraction of

the internal surface. This type of composition causes water to be adsorbed with greater preference for hydrophilic sites while avoiding hydrophobic zones present on the surface [37].

Molecules that do not bind to any of these sites are possibly linked by hydrogen bonding to the nucleation sites of water, forming small water clusters. Later they grow and combine with other accumulations of water near to pore or within the same pore, leaving a free space above the hydrophobic area. Therefore, characteristics such as surface area and pore volume calculated from the measured data were not reproducible and generated small values, which did not always adequately explain the phenomena that occur in the material [27], suggesting the interaction energy of water is considerably high with the frame.

The remaining liquid produced after submerging the hybrid materials in water allowed the quantification of Cu and BTC in solution, related to the metal centers and linker, respectively. The results of Cu quantification by ICP-OES are presented in Figure 5.1.18. The amount of Cu leached from the metal-organic frameworks in the analyzed period was equivalent to approximately 0.25 wt.% of the MOFs, and it is almost constant from the first hour. This value was insignificant.

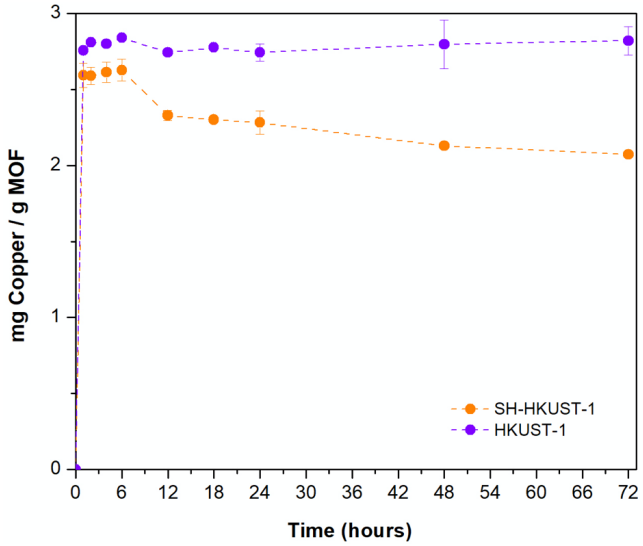


Figure 5.1.18. ICP-OES measurement of copper in solution after being in contact with water and HKUST-1(purple data) or SH-HKUST-1 (orange data) until 6, 24 and 48 hours.

Contrary to this, the linker quantified employing UV-VIS spectrophotometry (Figure 5.1.19), showed an increase in the amount of linker in solution as the contact time increased. Both MOFs

have a similar behavior after 12 hours, later HKUST-1 presented greater leaching of BTC compared to SH-HKUST-1, with values of 130 and 170 mg BTC / g MOF.

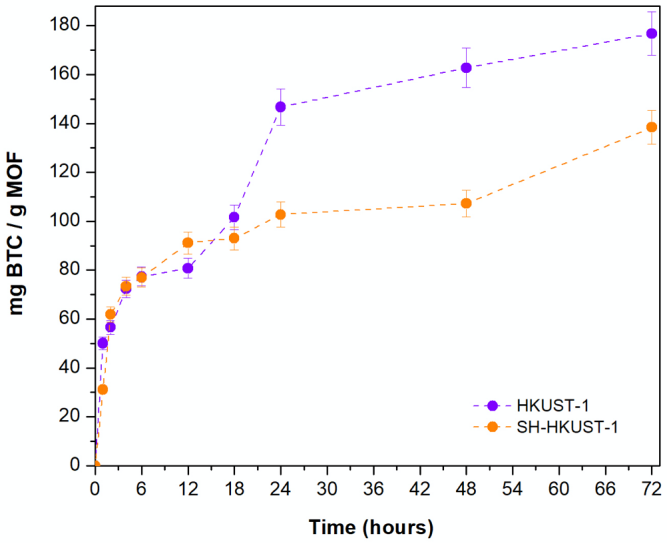


Figure 5.1.19. UV-VIS measurement of BTC in solution after being in contact with water and HKUST-1(purple data) or SH-HKUST-1 (orange data) until 6, 24 and 48 hours.

Low and collaborators [38] reported two main degradation mechanisms of MOFs exposed to water, i) displacement of the linker: the insertion of one molecule of water in the MOF metal-linker (M-O), leads to the formation of a hydrated cation and the ligand release (Eq. 5.1.2), ii) Hydrolysis: the metal-linker bond breaks down and the water dissociates to form a hydroxylated cation and a free protonated linker (Eq. 5.1.3).

$$M^{n+}\text{-}L^{n-} + H2O \rightarrow M^{n+}\text{-}(OH_2)\ldots.L^{n-} \quad \text{(Eq. 5.1.2)}$$

$$M^{n+}\text{-}L^{n-} + H2O \rightarrow M^{n+}\text{-}(OH)^{-} + HL^{(n-1)-} \quad \text{(Eq. 5.1.3)}$$

From the Cu and linker data in solution, it was suggested that the degradation mechanism that caused the instability of the metal-organic frameworks produced in this research was due to the slow hydrolysis of the BTC linker involved in the metal-ligand coordination link. These metal coordination centers into the MOF are electrophilic and could interact with oxygen in water that is a nucleophile [38]. Under the reported experimental conditions implemented in this research, it was possible to occur the aggregation of water molecules near to metallic sites, gradually hydrolyzing the carboxylate groups of BTC (related to C-O bonds), which coordinate with the binuclear cations of Cu^{2+}, causing linker hydrolysis over time. This led to the breakdown of the metal-ligand coordination link and copper hydroxide formation as confirmed by XRD analysis above [26].

In general, three stages of the HKUST-1 decomposition process have been recognized. First, the Cu-free sites coordinate with water to establish a σ bond. During the second stage, the filling of water from large and some small pores was facilitated, since the accessible metallic sites were reduced. Then, in the third stage, the water condensation into the pores occurred. It is important to consider that, during the second and third stage of the process, hydrolysis of C-O bonds was involved, resulting in the MOF crystal lattice irreversibly distortion or destruction [27].

By comparing the hydrolytic stability of the two produced MOFs, it was evident the -SH groups gave to the Cu-based MOF better hydrolytic stability when SH-HKUST-1 was exposed to water. According to the stability characterization carried out, the indiscriminate breakdown of the BTC links that normally end in the degradation of HKUST-1 did not occur so soon. SH-HKUST-1 retained its structural integrity even after being in contact with water for 24 hours, while HKUST-1 a metal-organic framework with a similar composition but lacking the thiol groups lost its crystallinity in less than 6 hours in the same conditions.

The thiol group inclusion acted as a steric effect to repel the BTC linkers of the structure from water. It was a strategy that worked to improve the stability of the Cu-BTC structure and prevent its structural degradation in aqueous conditions. Although the modification of HKUST-1 with thiol groups preserved the new MOFs crystal structure up to 24 hours after being in contact with water, the structural changes became evident. However, minor they maybe they will significantly affect the network morphology.

5.1.5 Conclusions

HKUST-1 was synthesized through self-assembly reactions between linkers and metal salts in solutions from room temperature to 250 °C, which allowed to evaluate two methods of synthesis: solvothermal and green. Characterization techniques such as XRD, SEM, FTIR, BET, and TGA, allow to confirmed that both methods obtained Individual crystalline products as desired, and the most important characteristic: a precise indexation of the diffractogram with patterns and characteristics typical of this type of MOF.

At temperatures close to the environment (green synthesis), slow diffusion of solvents from the solution is often adopted to control the reaction rate and promote the growth of monocrystals. At higher temperatures and pressures (solvothermal synthesis), the products can be more complex

and diverse compared to those achieved at room temperature. For this reason, green synthesis was found as an interesting alternative in the HKUST-1 synthesis, increasing the possibility of scaling its production while implementing more environmentally friendly synthesis methodologies.

Specifically, HKUST-1 has poor stability in contact with water, limiting its applications. The improvement of this MOF hydrolytic stability was achieved through modifications to the BTC linker using crystal poison. The MOF crystallinity changed as a function of the crystal poison molar ratio (relative to the linker). A variation in the crystal poison amount to form crystalline HKUST-1 caused non-crystalline products. TSA did not work to make the HKUST-1 modification because amorphous or low crystallinity products were obtained. However, the linker and metal ion bond were reduced using MBA at high concentrations. MBA concentrations of 5 wt.% was able to include thiol functional groups in the structure of SH-HKUST-1 without modifying its topology. This was verified using XRD, FESEM, FTIR, EDX and BET techniques.

Additionally, hydrolytic stability studies were carried out, and it was shown the HKUST-1 modification by the inclusion of functional groups thiol (-SH) became an effective and practical tool to improve the stability in aqueous media of the Cu-BTC metal-organic framework. A stability analysis methodology described an increase in the hydrolytic stability of SH-HKUST-1 from 6 to 24 h compared to HKUST-1, improving the stability and selectivity of HKUST-1 by the thiol groups' inclusion into the MOF structure, making them more competitive in real applications.

5.1.6 References

1. Stock, N. & Biswas, S. Synthesis of Metal-Organic Frameworks (MOFs): Routes to various mof topologies, morphologies, and composites. *Chem. Rev.* **112**, 933–969 (2012).

2. Shi, R. *et al.* Cu-based metal–organic framework/activated carbon composites for sulfur compounds removal. *Appl. Surf. Sci.* **394**, 394–402 (2017).

3. Bedia, J. *et al.* A review on the synthesis and characterization of metal organic frameworks for photocatalytic water purification. *Catalysts*. **9**, 1–43 (2019).

4. Zhu, Q.-L. & Xu, Q. Metal–organic framework composites. *Chem. Soc. Rev.* **43**, 5468–5512 (2014).

5. Liu, J. & Wöll, C. Surface-supported metal-organic framework thin films: Fabrication methods, applications, and challenges. *Chem. Soc. Rev.* **41**, 5730-5770 (2017)

6. Shekhah, O., Liu, J., Fischer, R. A. & Wöll, C. MOF thin films: Existing and future applications. *Chem. Soc. Rev.* **40**, 1081–106 (2011).

7. Van Vleet, M. J., Weng, T., Li, X. & Schmidt, J. R. *In Situ*, Time-resolved, and mechanistic studies of metal-organic framework nucleation and growth. *Chem. Rev*. **118**, 3681–3721 (2018).

8. Oestreicher, V. & Jobbágy, M. Extremely efficient crystallization of HKUST-1 and Keggin-loaded related phases through the epoxide route. *Chem. Commun.* **53**, 3466–3468 (2017).

9. Loera-Serna, S., Solis, H., Ortiz, E., Martínez-Hernandéz, A. L. & Noreña, L. Elimination of Methylene Blue and Reactive Black 5 from Aqueous Solution Using HKUST-1. *Int. J. Environ. Sci. Dev.* **8**, 241–246 (2017).

10. Furukawa, H., Cordova, K. E., O'Keeffe, M. & Yaghi, O. M. The chemistry and applications of metal-organic frameworks. *Science.* **341**, 1-12 (2013).

11. Andrew Lin, K. Y. & Hsieh, Y. T. Copper-based metal organic framework (MOF), HKUST-1, as an efficient adsorbent to remove p-nitrophenol from water. *J. Taiwan Inst. Chem. Eng.* **50**, 223–228 (2015).

12. García, H. & Navalon, S. *Metal-Organic Frameworks : Applications in Separations and Catalysis*. (Wiley, 2018).

13. Audu, C. *et al.* The dual capture of AsV and AsIII by UiO-66 and analogues. *Chem. Sci.* **7**, 6492–6498 (2016).

14. Kirchon, A., Feng, L., Drake, H. F., Joseph, E. A. & Zhou, H. C. From fundamentals to applications: a toolbox for robust and multifunctional MOF materials. *Chem. Soc. Rev.* **47**, 8611–8638 (2018).

15. Holder, G. A. & Winkler, J. Crystal-growth poisoning of n-paraffin wax by polymeric additives and its relevance to polymer crystallization mechanisms. *Nature.* **207**, 719–721 (1965).

16. Phan, N. T. S., Nguyen, T. T., Ho, P. & Nguyen, K. D. Copper-catalyzed synthesis of α-aryl ketones by metal-organic framework MOF-199 as an efficient heterogeneous catalyst. *ChemCatChem* **5**, 1822–1831 (2013).

17. Wang, C., Qian, X. & An, X. In situ green preparation and antibacterial activity of copper-based metal–organic frameworks/cellulose fibers (HKUST-1/CF) composite. *Cellulose* **22**, 3789–3797 (2015).

18. EPA. *METHOD 3050B: acid digestion of sediments, sludges, and soils*. https://www.epa.gov/sites/produc tion/files/2015-12/documents/3050b.pdf (1996).

19. Hassan, A. F. Synthesis of carbon nano-onion embedded metal–organic frameworks as an efficient adsorbent for cadmium ions: kinetic and thermodynamic studies. *Environ. Sci. Pollut. Res.* **26**, 24099–24111 (2019).

20. Patterson, A. L. The scherrer formula for x-ray particle size determination. *Phys. Rev.* **56**, 978–982 (1939).

21. Arshadi, M., Abdolmaleki, M. K., Mousavinia, F., Foroughifard, S. & Karimzadeh, A. Nano modification of NZVI with an aquatic plant Azolla filiculoides to remove Pb(II) and Hg(II) from water: Aging time and mechanism study. *J. Colloid Interface Sci.* **486**, 296–308 (2017).

22. Zhu, Q. *et al.* High performance HKUST-1@PVA-co-PE/PVA hybrid hydrogel with enhanced selective adsorption. *Compos. Commun.* **10**, 36–40 (2018).

23. Gao, P. & Liu, D. Facile synthesis of copper oxide nanostructures and their application in non-enzymatic hydrogen peroxide sensing. *Sensors Actuators, B Chem.* **208**, 346–354 (2015).

24. Lin, K. S., Adhikari, A. K., Ku, C. N., Chiang, C. L. & Kuo, H. Synthesis and characterization of porous HKUST-1 metal organic frameworks for hydrogen storage. *Int. J. Hydrogen Energy*. **37**, 13865–13871 (Pergamon, 2012).

25. Joseph, L. *et al.* Removal of contaminants of emerging concern by metal-organic framework nanoadsorbents: A review. *Chem. Eng. J.* **369**, 928–946 (2019).

26. Álvarez, J. R. *et al.* Structure stability of HKUST-1 towards water and ethanol and their effect on its CO2 capture properties. *Dalt. Trans.* **46**, 9192–9200 (2017).

27. Todaro, M. *et al.* Decomposition Process of Carboxylate MOF HKUST-1 Unveiled at the Atomic Scale Level. *J. Phys. Chem. C* **120**, 12879–12889 (2016).

28. Al-Janabi, N. *et al.* Mapping the Cu-BTC metal-organic framework (HKUST-1) stability envelope in the presence of water vapour for CO2 adsorption from flue gases. *Chem. Eng. J.* **281**, 669–677 (2015).

29. Chen, Y., Mu, X., Lester, E. & Wu, T. High efficiency synthesis of HKUST-1 under mild conditions with high BET surface area and CO2 uptake capacity. *Prog. Nat. Sci. Mater. Int.* **28**, 584–589 (2018).

30. Wu, X.-W., Ma, H.-W., Li, J.-H., Zhang, J. & Li, Z.-H. The synthesis of mesoporous aluminosilicate using microcline for adsorption of mercury(II). *J. Colloid Interface Sci.* **315**, 555–561 (2007).

31. Azhar, M. R. *et al.* Excellent performance of copper based metal organic framework in adsorptive removal of toxic sulfonamide antibiotics from wastewater. *J. Colloid Interface Sci.* **478**, 344–352 (2016).

32. Trimesic acid - DrugBank. https://www.drugbank.ca/drugs/DB08632 (2020).

33. Functionalisation of Metal-Organic Frameworks via Post-Synthetic Modification — the University of Bath's research portal. https://researchportal.bath.ac.uk/en/studentTheses/functionalisation-of-metal-organic-frameworks-via-post-synthetic- (University of Bath, 2017).

34. Kim, H. K. *et al.* A chemical route to activation of open metal sites in the copper-based metal-organic framework materials HKUST-1 and Cu-MOF-2. *J. Am. Chem. Soc.* **137**, 10009–10015 (2015).

35. Cychosz, K. & Matzger, A. Water stability of microporous coordination polymers and the adsorption of pharmaceuticals from water. *Langmuir* **26**, 17198–17202 (2010).

36. Jiménez-López, A. *et al.* Layered basic copper anion exchangers: Chemical characterisation and X-ray absorption study. *J. Mater. Chem.* **3**, 303–307 (1993).

37. Küsgens, P. *et al.* Characterization of metal-organic frameworks by water adsorption. *Microporous Mesoporous Mater.* **120**, 325–330 (2009).

38. Low, J. *et al.* Virtual high throughput screening confirmed experimentally: Porous coordination polymer hydration. *J. Am. Chem. Soc.* **131**, 15834–15842 (2009).

5.2 Anchoring of HKUST-1 and SH-HKUST-1 onto fique fiber

5.2.1 Abstract

Hybrid materials manufacturing has been reported as an interesting alternative to take advantage of the properties of constituent parts, such as in this case, metal-organic frameworks and lignocellulosic biomass like fique fibers. The immobilization of Cu-based MOFs HKUST-1 and SH-HKUST-1 onto fique fibers was studied. The fiber surfaces were functionalized with carboxymethyl ether or carboxylate group prior to anchoring of the MOFs via two methods: direct growth and secondary growth. In the direct method, the substrate, linker and precursor salt were combined simultaneously to time to carry out the nucleation and growth in a single step. In the secondary growth method, copper metal ions were seeded on cellulose surfaces functionalized by means of ion exchange to create possible nucleation sites. After this impregnation step, the copper seeded fiber was placed in the linker solution to start the MOF crystal growth. Using characterization techniques such as XRD, SEM, TGA, XPS, Nitrogen adsorption, among others, it was possible to confirm the synthesis of hybrid materials with 20 wt.% of metal organic-frameworks anchored to the cellulose surface, evidencing the increase in the lifetime of MOFs in aqueous environments. As a result of the hydrolytic stability improvement via linker modification using crystal poison and implementation of polymers as substrates, a steric effect was created that can slow down the collapse of the network. Anchoring MOFs in organic polymers is an effective strategy to retard frame dissolution in applications involving aqueous solutions.

Key words: HKUST-1, fique, cellulose, thiol functionalization, anchoring.

5.2.2 Introduction

The development of hybrid materials has recently been proposed to merge the advantages of each of the constituent parts, while mitigating the deficiencies. The materials remarkable characteristics resulting from the synergistic combination of compounds at nanometric scale and different types of supports (including metallic nanoparticles, organic and inorganic oxides, quantum dots, polymers, materials based on carbon or silicon, enzymes, among others) [1], make hybrid materials a viable alternative in a wide range of applications.

The organic part is responsible for joining the inorganic building blocks and the matrix. Currently,

lignocellulose biomass is a material widely studied because many times is considered a waste, despite it, natural cellulose fibers are attractive matrices for *in situ* synthesis of nanomaterials for two reasons: 1) the fibers surface has a partial negative charge, due to its high oxygen density, that facilitates electrostatic interaction with electropositive transition metal ions, and 2) its porous and heterogeneous structure facilitates the control, dispersion and stabilization of nanometric compounds. Some authors hypothesize that bionanocomposites of hard fibers have improved mechanical strength, compared to raw fibers, due to a similar effect to "vulcanization" in which nanoparticles replace lignin and hemicellulose and act as "glue" between individual strands of microfibers [2].

An example of lignocellulosic material is the Fique fiber (*Furcraea Andina spp*). It is the national fiber of Colombia, has fibrous fleshy leaves, with or without thorns [3.4]. The long fique fibers have been used in fabrics production, threads, strings, packaging and handicrafts. Particularly in Colombia, the production of value-added fiber products is not well developed, although it is an important generator of employment in some regions. Nowadays, a good quality fique fiber has a market value in the order of 0.3 EUR/kg, decreasing incentives for proper fiber production [5].

The inorganic part corresponds to elements incorporated into the matrix in form of particles, whiskers, fibers, lamellae, or meshes, whose function is to provide greater resistance to the material. Currently, metal-organic frameworks (MOFs) are crystalline hybrid networks that result from positively charged metal ions connected by polygon organic ligands negatively charged through coordination bonds, forming an extended 3D crystalline network that in many cases has a form of an ordered pores system.

HKUST-1 is an example of MOF with specific surface areas close to 2200 m^2/g, which makes them a high porosity material with spatial uniformity, low density, and crystallinity; all of these reflected in adsorption, optical, electrical, magnetic and catalytic properties [6]. This MOF has been successful in applications such as: separation and storage of gases, sensors, biomedicine and catalysis [7]. However, HKUST-1 exhibits poor hydrolytic stability, which prevents its potential use in applications, for which, it is desirable to further improve the properties and include new functionalities.

As a result of the intrinsic hydrophobicity of most MOFs, which has limited their application under aqueous conditions, according to some authors, there are possibilities to improve this deficiency through the deposition of MOFs on functionalized polymer surface [1,8]. The polymer molecule,

through functionalization could have functional groups on the surface capable to bind MOF particles across vacant metal coordination sites on the surface of the particle, electrostatic attraction, or covalent binding to linkers [9]. Among the different methods of MOFs controlled deposition, some approaches have advantages that include easy separation of reaction mixture and matrices use, which may or not be functionalized. However, the MOFs anchoring processes have been limited because they do not result in continuous and homogeneous growth. This is why challenges have been proposed in the way to control characteristics such as morphology, crystallographic orientation, surface roughness, adhesion to the substrate, mechanical properties, and stability [10].

In this subchapter, two approaches for anchoring Cu-based MOFs were described: HKUST-1 and SH-HKUST-1 were fixed onto the surface of cellulose fibers previously functionalized with carboxymethyl-ether or carboxylic acid groups. The first approach was the direct method, in which functionalized fibers were soaked with the precursor salt solution and linker in one step. The second approach was secondary growth, it has two steps. First, the functionalized fiber was impregnated or seeded with copper ions through an ionic exchange with functional groups of cellulose fibers, thus creating possible nucleation points; subsequently, the impregnated fiber was submerged into linker to promote the MOF crystals growth. Additionally, two MOF synthesis methods were analyzed during the frames anchoring: solvothermal and green, under operating conditions previously reported in the subchapter 5.1.

5.2.3 Materials and methods

5.2.3.1 Experimental set-up and procedure

In the hybrid material synthesis (Figure 5.2.1), functionalized fique fibers were used as matrix by means of grafting two types of functional groups: i) using the reaction of TEMPO to produce -COOH groups and ii) carboxymethyl ether (-CH_2OCH_2COONa) groups were produced by the carboxymethylation reaction as was described in Chapter 4. Within the hybrid material as an incorporated element, the anchorage of MOFs like HKUST-1 and SH-HKUST-1 (HKUST-1 modified with thiol groups) were evaluated, which were prepared according to the solvothermal and green synthesis methods reported in the subchapter 5.1.

Two anchoring methods were evaluated: direct growth and secondary or seeded growth. For the evaluation of the HKUST-1 direct growth method, 500 mg of the functionalized fique fiber samples

were immersed in metal precursor solution with linker and left: i) under solvothermal conditions overnight in a reactor hermetically sealed, and ii) for the green synthesis at room conditions overnight in a closed container. The resulting fibers were washed in alternating cycles of DMF / water / ethanol for the solvothermal method and water / ethanol for the green method; both dried at room temperature.

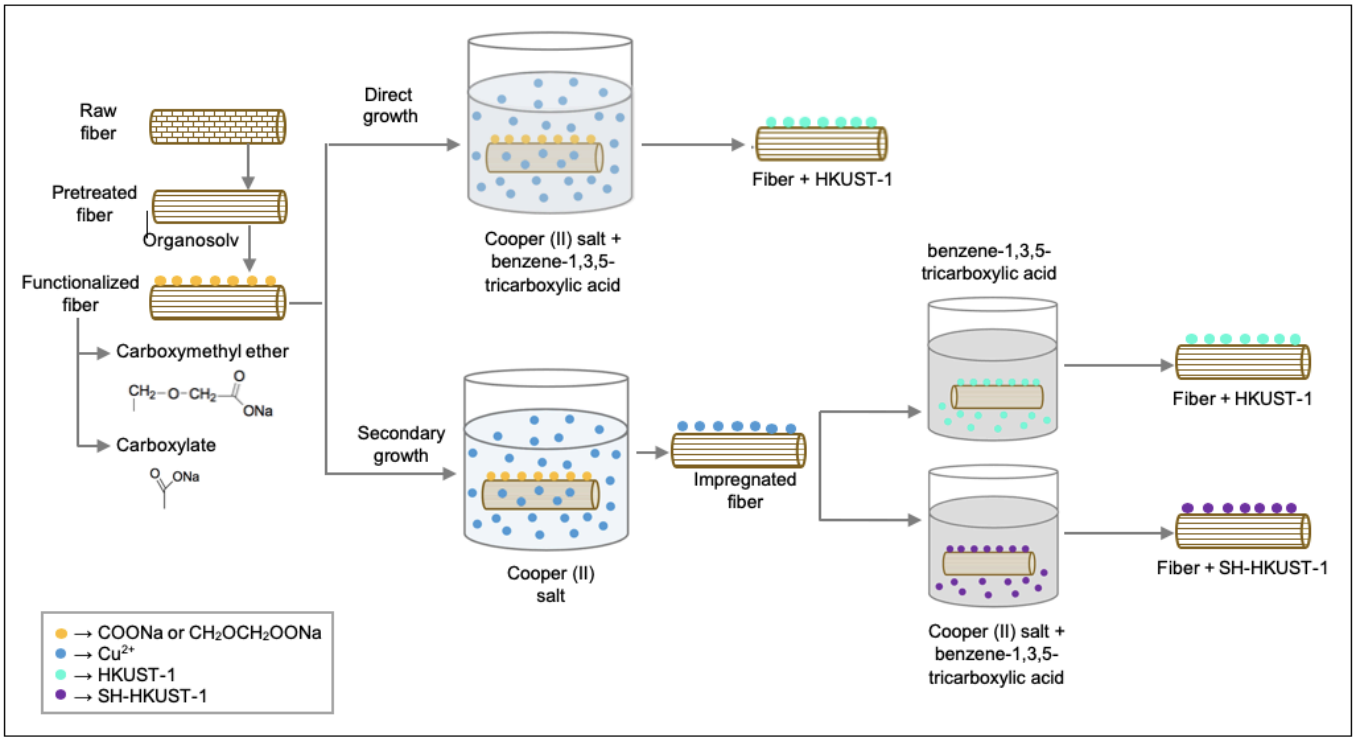


Figure 5.2.1. Diagram of the methodology used to anchor HKUST-1 and HKUST-1-SH onto fique fibers.

The development of the secondary method was carried out in two stages. The first consisted in an impregnation process; 500 mg of functionalized fiber was immersed in the metal precursor salt, in order to seed the surface with copper ions which would be nucleation points. In the second stage, the copper seeded fiber was soaked in the linker solution to carry out the growth of the MOF crystals. It is worth clarifying, the volumes and concentrations of the precursor salts (copper acetate and copper nitrate), the linker solution (1,3,5, Benzene tricarboxylic) and crystal poison MBA (4-mercaptobenzoic acid), kept the values reported in the subchapter 5.1, the only change was the addition of the functionalized fiber as just described.

5.2.3.2 Characterization

- Chemical structural components

Chemical information about the metallic copper present in the hybrid materials synthesized related to the MOFs incorporated, and to confirm the sulfur introduced during the MOF functionalization, Energy-dispersive X-ray spectroscopy (EDX) equipment coupled to a SEM was used. This chemical elemental analysis was performed in a JEOL JSM-6480LV, operating in spectrum collecting mode under high vacuum conditions, 10 kV and approximate at a 50 µm of working distance. In addition, EDX mapping was performed to the surface of the synthesized samples to analyze the atomic distribution on the surface of the hybrid materials.

To have an approximation of the amount of MOF anchored onto the fiber, the copper content of MOFs was determined by flame atomic absorption spectrometry (FAAS) using the injection method. Before the analysis, the fibers with MOFs anchored underwent a digestion procedure following the EPA Method 3050B: Acid Digestion of Sediments, Sludge, and Soil [11]. Then, the material obtained from the digestion procedure was analyzed in a Hitachi z-8000 atomic absorption spectrometer equipped with an atomizer with air-acetylene burner used for the determination of elemental copper. The wavelength used for the determination of the analyte was: 324.7 nm.

Complementary, with the aim to determine the carbon, hydrogen, nitrogen, sulfur and oxygen mass percentage a CHNS/O elemental analysis was done for the hybrid material using a Micro Cube Analyzer, from Elemental GmbH, Langenselbold, Germany. All the determinations were done in triplicate, and the oxygen content was calculated by difference.

- Spectroscopy and surface characterization

Fourier transform infrared spectrometry (ATR-FT-IR) was done at room temperature in an IR PerkinElmer Frontier, using a diamond crystal for the characterization of the main functional groups presents in the HKUST-1 and SH-HKUST-1 anchored onto fique fiber functionalized. The spectra were recorded in the range of 4000 to 600 cm^{-1}, with an accumulation of 30 scans and a resolution of 1 cm^{-1}.

pH_{zpc} was determined using the drift method in which solutions with 10 mL of NaCl (0.01 M) were adjusted to an initial pH in the range of 2 to 10 by adding HCl 0.05 M or NaOH 0.05 M. Once the pH of the solutions was set, 0.05 g of hybrid material was added, the resulting suspensions are stirred for 3 h at 25 °C, and the pH of the supernatants is registered [12].

To analyze the wetting fiber surface, a novel method published by Schellbach *et al*. [13] to measure the contact angle was implemented. Two fibers with similar diameter were aligned parallel with a distance ~ 1 mm between them under an Olympus microscope at room temperature. A drop of deionized water was deposited in this small space, to measure the hanging bridge to enlarge the lateral dimension of the water bridge and reinforce the spreading of it over the dry sections of the fibers. After the water column enlarged and the spherical menisci stabilized, the high-resolution images were captured using the software cellSens. Five images were captured for both enlarged and reduced water columns on each sample, the values of the diameter (d) and height (h) of the meniscus were obtained. The contact angle was calculated using Eq. 5.2.1.

$$\theta = 90 - 2\tan^{-1}\left(\frac{2d}{h}\right) \qquad \text{(Eq. 5.2.1)}$$

X-ray photoelectron spectroscopy (XPS) was performed using Fi Kratos Axis Ultra HAS-VISION with an operating pressure of ~ 2 × 10^{-9} Torr. Monochromatic Al Kα X-rays (1486.6 eV) with a beam size of 1 mm diameter were used. Photoelectrons were collected at an emission angle of 55°. A hemispherical analyzer determined the kinetic energy of the electrons using a step energy of 150 V for panoramic / large scale scans and 50 V for high resolution scans. A flood gun was used to neutralize the charge.

- Structural Characterization

Powder X-Ray Diffraction (PXRD) was used to confirm the MOF identity after the anchoring process and determine its crystalline structure. The equipment STADI P (Cu radiation) Double setup in transmission and reflection mode was operated to obtain the PXRD patterns. The average crystallite size of the metal-organic frameworks was calculated from XRD data using Scherrer's equation [14] (Eq. 5.2.2). Based on the line broadening effect at the full width half maximum (FWHM) of the most intense peak in HKUST-1, located close to θ=11.6°.

$$D = \frac{k\lambda}{\beta \cos\theta} \qquad \text{(Eq. 5.2.2)}$$

Where *D* is the average crystallite size, *k* is Scherrer constant, *λ* is the wavelength of X-ray, *β* is the FWHM and *θ* is diffraction angle.

- Textural and morphological Characterization

The surface area, pore size, and pore volume were measured using N_2 adsorption/desorption

isotherms trough a Quantachrome NOVA e-Series surface area analyzers. The samples of fique fibers with MOF were prepared for analysis at 90 °C during 8 h in high vacuum before the adsorption/desorption measurements with N_2. The calculation of the total surface area was established using the BET method [15], the pore size distribution (PSD) was studied by the Barret-Joyner-Halenda method (BJH) and the pore volume was calculated by the t-model plot [16].

Morphological characterization of MOFs anchored onto natural fibers was achieved via Field Emission Scanning Electron Microscope (FESEM) and performed on thin film gold coated samples using a Zeiss Auriga FIB-SEM (GeminiSEM) scanning electron microscope, coupled to a secondary electrons (SE2) detector. The micrographs were taken at 1.5 kV, working distance (WD) ranging from 4.9 to 5.2 mm, at different magnifications. In addition, the morphology was determined by Scanning Electron Microscopy (SEM) using a Hitachi FLEX SEM 1000 model microscope.

- Thermal Characterization

Thermal gravimetric analysis (TGA) and Differential Scanning Calorimetry (DSC) were performed using a simultaneous thermal analyzer (STA 409 PC/4/H Luxx) in a temperature range from 50 to 900 ^{o}C at a heating rate of 10 ^{o}C/min using nitrogen (flow of 50 cm^3 min^{-1}) atmosphere.

- Mechanical Characterization

Dynamic Mechanical Analysis (DMA) was performed in a Mettler Toledo DMA1 analyzer, one fiber was centered inside the sample holder using single-cantilever clamps, with a free length of 17.5 mm. The DMA was done at room temperature and the oscillation conditions was fixed at 1Hz and the amplitude was 20 µm (i.e. 0.11% strain), which was well within the linear viscoelastic region. Storage modulus E (MPa) were collected during the test; the final value includes an average of three measurements for each sample.

- Hydrolytic stability characterization

Hydrolytic stability in the context of this discussion refers to whether the structure remains or collapses after being immersed in water. To analyze the water stability of the hybrid materials synthesized, fiber with MOFs were immersed in water and monitored every 0, 1, 2, 4, 6, 12, 18, 24, 48 and 72 h at room temperature; then the fibers were separated and dried at room

temperature. The resulting products, the fibers soaked, and the remaining liquid were analyzed separately.

The remaining solid part of the hybrid material was analyzed to verify if its morphology, chemical and crystallinity structure were affected. For this, techniques like XRD, SEM, EDX, FTIR and adsorption isotherms were used, under the conditions described above.

In addition, the remaining liquid part was analyzed to determine if the main components of the MOFs attached (copper, sulfur and BTC) were released into the water during the stability analyzes. The linker leached was continuously monitored using an UV-vis spectrophotometry to track absorbance of the BTC molecule in a quartz cell in a Shimadzu Pharm device; its concentrations were assessed through a calibration curve in the range of 0.25 to 4 mM obtained at a wavelength of 291 nm.

ICP-OES (Inductively Coupled Plasma - Optical Emission Spectrometry) was used to identify and quantify the copper and sulfur present in the solutions analyzed. All experiments were conducted using an iCAP 7400 ICP-OES instrument (Thermo Fisher Scientific). Plasma, the conditions used were as follows: RF power: 1250 W, auxiliary gas flow: 0.5 dm^3/min, coolant gas flow: 12 dm^3/min, nebulizer gas flow: 0.5 dm^3/min, and nebulizer gas pressure: 270 kPa. Spectra were analyzed using Qtegra ISDS (Thermo Fisher Scientific). The iCAP 7400 ICP-OES instrument was calibrated to the following elements: copper and sulfur, using the respective elemental standard (1 mL) in concentrated HNO_3 with deionized water.

5.2.4 Results and Discussion

5.2.4.1 Anchor method analysis

MOF particles have been shown to be incorporated into polymeric matrices, by deposition or anchoring, and their adherence depends on the method used. In this research, the effect of direct and secondary growth was analyzed. For this, a first analysis was made using the fique fiber functionalized with carboxylate groups (-COONa), which reached an oxidation degree (OD) of approximately 9.3 ± 1.9 (%). HKUST-1 was used as the metal-organic framework to be attached onto the fique fibers functionalized following the green synthesis method under the conditions described above in subchapter 5.1, to test the behavior of both anchoring methods.

SEM images of the anchoring methods showed the direct growth (Figure 5.2.2 a and b) developed a small number of MOFs onto the surface of the cellulosic polymer, since the growth rate was very fast. Therefore, only the characteristic morphology of the functionalized fiber with carboxylate groups was observed, confirming the direct growth of HKUST-1 networks was not successful. On the contrary, in Figures 5.2.2 c and d were revealed crystals with similar sizes distributed on the fique fiber surface after using the secondary growth method, preserving the morphology of HKUST-1 powder. It was also evidenced in the micrograph 5.2.2d the crystals seem to be in close contact with the fiber, which could be an early evidence of the anchorage of the metal-organic frameworks onto the cellulosic substrate. The frameworks had a well-defined octahedral shape, and the crystals appear to have a wide size distribution ranging from 250 to 350 nm in characteristic length.

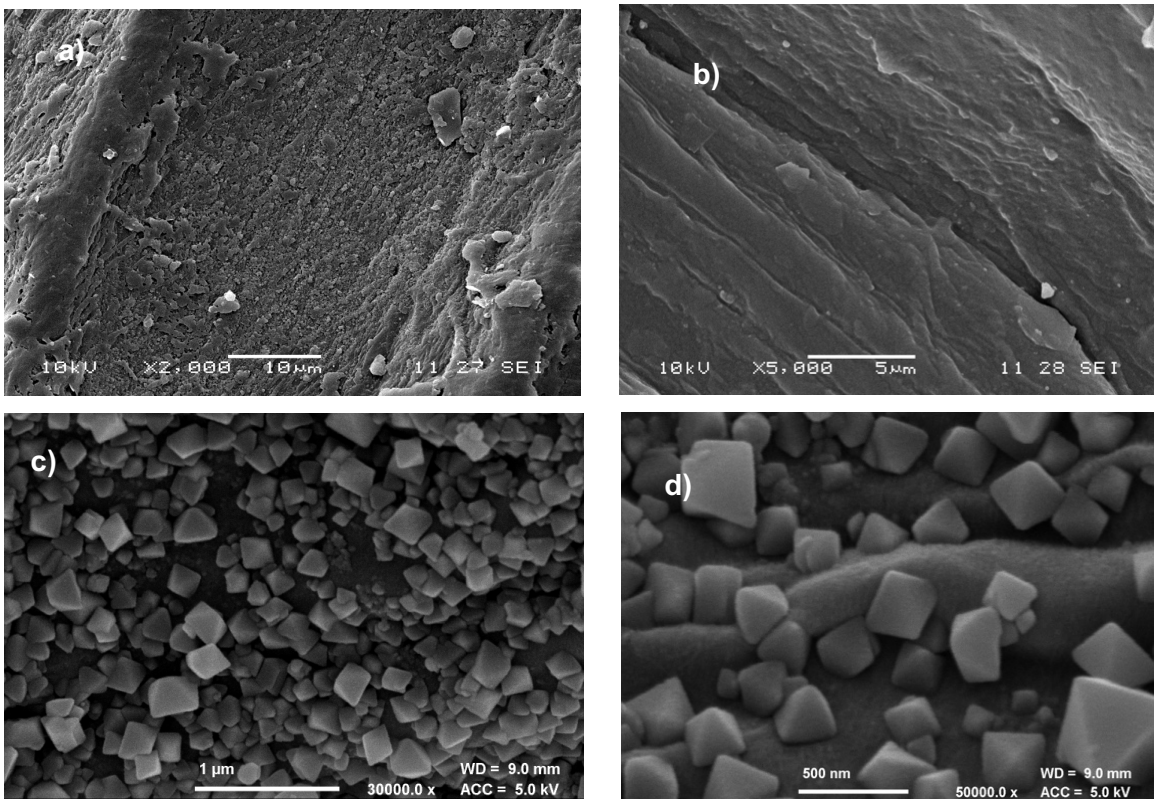


Figure 5.2.2. SEM images of HKUST-1 supported onto fique fiber functionalized with carboxylate groups (-COONa), following the direct (a and b) and secondary (c and d) growth.

Complementary to the results obtained by SEM, X-ray diffraction analysis was carried out to confirm the crystal structure of HKUST-1 grafted on the fique fiber. Figure 5.2.3 contains the diffraction patterns of the functionalized fique fiber samples (blue) and the pure HKUST-1 powder (purple), a clear overlap of the main diffraction peaks of the elements separately from the hybrid

material synthesized can be observed (yellow and turquoise for the direct and secondary method, respectively). The XRD spectra of both anchoring methods showed the characteristic peaks of the carboxylated fique fiber corresponding to cellulose at 22.6° and 34°, while the peak located at 16° was eliminated; all these peaks attributed to the crystallographic planes (2 0 0), (0 0 4) and (1 1 0) of cellulose, respectively [17].

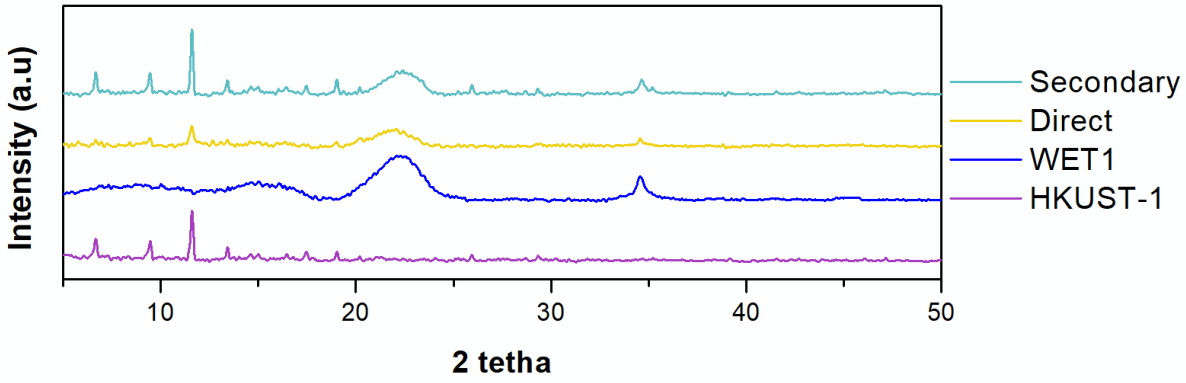


Figure 5.2.3. XRD diffractograms of HKUST-1 anchored by two approaches: direct and secondary growth.

Furthermore, the diffractogram of the secondary anchoring (Figure 5.2.3, turquoise) showed clear combination with the peaks of the metal-organic frameworks HKUST-1 located at 2θ ≈ 6.5° (200), 9.5° (220), 11.6° (222), 13.3° (400), 14.7° (331), 16.2° (422), 17.5° (511), 19° (440) and 20.08° [18], which coincide with the simulated diffractogram of the HKUST-1 powder sample synthesized by the green methodology (subchapter 5.1). It was confirmed the hybrid material maintained the high crystallinity of frames onto the fiber. The crystallite size of the anchored HKUST-1 was calculated from Scherer formula (Eq. 5.2.2) [14] and an average size of 47.11 nm was obtained.

However, the direct anchor diffractogram (yellow) only exhibited a small peak at 2θ ≈ 11.6°, which was consistent with the SEM micrographs in Figure 5.2.2. a and b, in which there was no significant evidence of HKUST-1 on the surface of lignocellulosic biomass, allowing us to affirm the direct anchoring method did not contribute to the embedding of metal-organic frameworks on cellulosic substrates such as fique fiber.

In the direct growth method, the MOFs were synthesized by immersion of the cellulosic substrate together with the metallic precursor (copper acetate) and the organic linker (BTC) at the same time. The reaction rate was so fast thatthe HKUST-1 synthesis was carried out mainly in solution. Afterwards, crystallites synthesized by electrostatic interactions between the carboxylate groups

and the copper metal centers of the MOF allowed a limited number of frames to be deposited (as confirmed by the XRD analysis). Moreover, the reaction was carried out at room temperature, which also limited the development of nucleation sites in the supports, which in turn affected the crystals growth.

In contrast, in the secondary growth method, a route of three-step to anchor frames can be proposed (Figure 5.2.4): first the ion exchange between the functional groups -COONa of the fiber surface functionalized with the ions of Cu^{2+} coming from the metal source, which would form possible nucleation points through the coordination of copper-carboxylate or seeds; the second stage consisted of the growth of the nuclei, and finally the growth of the HKUST-1 crystals occurred in contact with the solution of BTC linker.

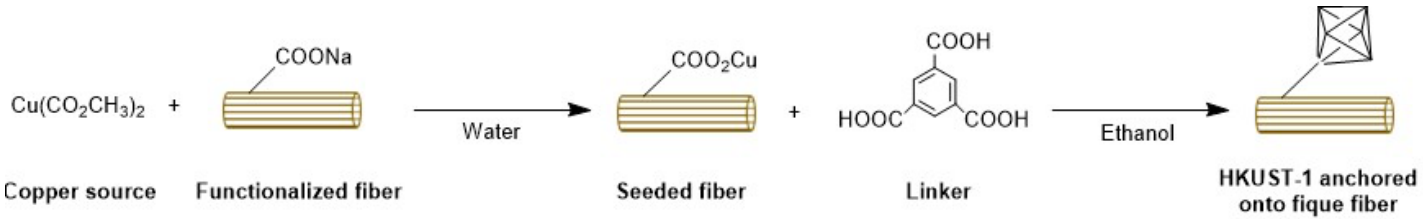


Figure 5.2.4. Diagram of the methodology used to anchor HKUST-1 onto fique fibers.

The results described above allow us to conclude the attaching of HKUST-1 on lignocellulosic surfaces was largely influenced by the anchoring method, namely by the way the two main stages occur in the controlled synthesis of nanomaterials: nucleation and growth. As was described above, in the proposed mechanism for secondary or seeding anchoring method, the nucleation path through the ion exchange between the functional groups of the cellulose surface and copper allowed the creation of seeds (nuclei) that acted as nucleation points in growth. This step did not have enough time to be carried out in the direct method, since the reaction rate prevailed so that the nuclei synthesis will be carried out in solution and not onto the fiber surface.

As crystallization is preceded by nucleation, what happens during nucleation will determine the type of crystals that are obtained. Crystals do not always develop as the direct anchoring, where nucleation established too quickly, and crystallites formed were too small or did not even form on the surface (as confirmed by the XRD in Figure 5.2.3). Therefore, the best way to grow MOF crystals is by slow nucleation that continues while the initial crystallization occurs and the particles grow without new nuclei forming (i.e., nucleation-controlled reactions) [19].

Additionally, during nucleation-controlled reactions, the possibility to create a bond between the carboxylate groups on the fique surface and the first layer of copper atoms could be considered, constituted first evidence of the HKUST-1 immobilization. Nevertheless, this bonding could not be achieved after the formation of the metal-organic framework, possibly because of the contact between two rigid surfaces (substrate and MOF), which are not atomically flat, resulting in localized strut contacts (Figure 5.2.2a and b). Later, it will be discussed how the carboxylate groups acted as strong bonds between the MOF and the cellulosic fiber surface in the secondary anchoring method, thus improving the compatibility between the MOF and the lignocellulosic substrate, giving advantages to the material synthesized in new application.

As previously verified, the direct anchoring method did not allow the MOFs grafting on the fique fibers. In fact, in literature limitations of this anchoring method have been reported, attributed to the synthesis conditions such as: temperature, pressure and type of precursor salt [20], since the crystals MOF size and the nucleation speed will also depend on the synthesis method used. An alternative approach is solvothermal direct growth, in which the respective substrates are placed in the MOF solutions during the synthesis.

In this research, the direct anchorage method with a solvothermal approach was evaluated using the fique fiber functionalized by TEMPO reaction and HKUST-1 was again grafted under the conditions of solvothermal synthesis reported in subchapter 5.1 (Figure 5.2.1). After the solvothermal reaction at 80 °C for 24 h and consuming copper nitrate as the precursor salt, the fique fiber surface functionalized by the TEMPO reaction was covered with well-defined octahedral particles, 6.7 µm in average size and with the characteristic morphology of HKUST-1 (Figure 5.2.5). Nevertheless, the micrograph in Figure 5.2.5b may indicate that the MOF, due to the large size and the morphology of the crystals, were initially formed in the reactive solution and then deposited by electrostatic interactions on the fiber surface; in addition, the presence of some cellulose zones free of MOFs were evidenced.

To verify the crystallographic identity of the metal-organic framework assembled on the anionic cellulose surface, as previously described (Figure 5.2.3), it was expected the diffractogram of the hybrid material obtained to be the combination between the diffraction patterns of cellulose and HKUST-1 reported in literature. The XRD pattern of the HKUST-1 secondary anchoring by solvothermal approach onto the fibers (yellow diffractogram, Figure 5.2.6) allowed to verify the existence of very well defined and intense peaks. They were fully indexed with the simulated

HKUST-1 standard, as well as a highly smoothed peak attributed to the main cellulose diffraction at 22°.

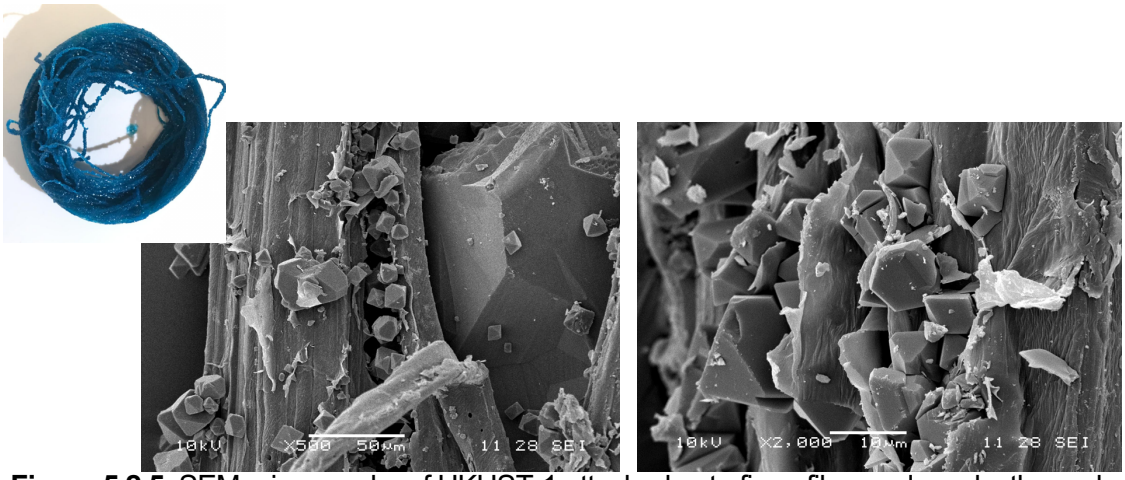


Figure 5.2.5. SEM micrographs of HKUST-1 attached onto fique fiber under solvothermal conditions.

It is interesting to note in the micrographs of Figure 5.2.5, the diffraction peaks related to MOF were much more intense than those of cellulose, even though the cellulose content was much higher in mass than MOF. Probably, it could be a result of the large crystals size and the way they were located onto fiber, which may be an indicative of the possible crystals deposition making the diffraction of HKUST-1 much greater than cellulose. Using the Scherer equation (Eq 5.2.2) from the peak located at θ = 11.6°, the average crystallite size was quantified as 80.7 nm, which is approximately twice the size of the crystallites synthesized by the secondary anchoring method reported above. In addition, this size is bigger than the value reported by other authors [21,22].It is important to consider this value depends on the synthesis method used that change in parameters like temperature, pressure and salt precursor [20].

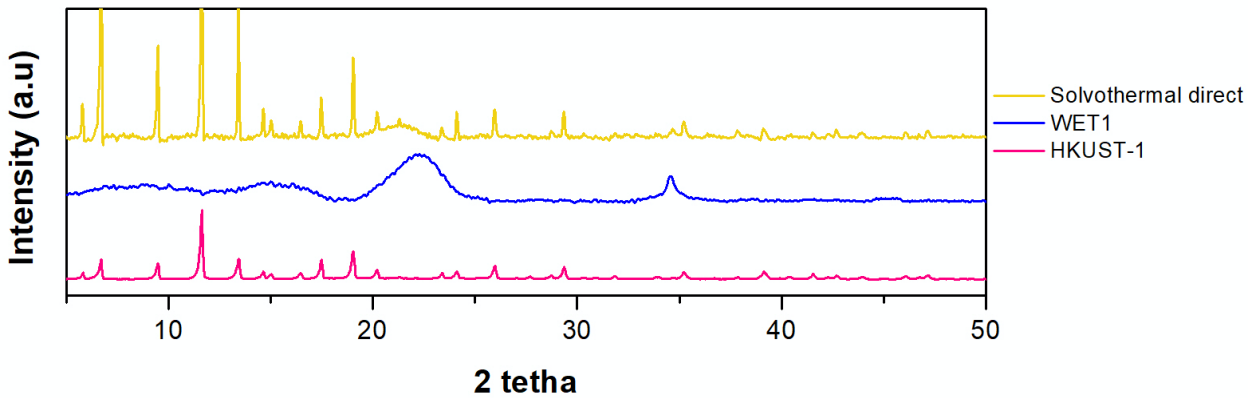


Figure 5.2.6. XRD diffractograms of HKUST-1 anchored by the direct approaches following the solvothermal synthesis.

The result obtained from the possible deposition of MOF on the lignocellulosic substrate from weak physical connections could be the result of concentration gradients between copper metal ions and BTC molecules, which migrated from the fiber to the reaction solution and from the reaction solution to cellulose, respectively. At the time, high concentrations of copper and linker ions were maintained in the functionalized fiber proximity, which was the reaction zone where the growth of MOF crystals would be promoted during the solvothermal synthesis. However, some authors such as Zhu *et al.* [23] have also described similar results, explaining the existence of limitations in this anchorage approach regarding low property control such as morphology, thickness and crystallographic orientation of MOFs. Therefore, the crystallites were oriented randomly; the surface functionalization improves the quality of the deposition, but this weak interaction between the parts reduced the hybrid material functionality since its application is possibly not durable over time.

Comparing the results of the secondary with the direct anchorage under the solvothermal approach, it may indicate the secondary anchorage method achieved the carboxylate-functionalized fique fiber reached copper nucleation by being in contact with the precursor salt and a subsequent crystal growth when reacted with the linker. This kinetics was slower than the HKUST-1 direct solvothermal anchoring, which was due to the temperature difference. While in the solvothermal synthesis the solution was heated to 80 °C, the secondary anchoring method was carried out at room temperature. Therefore, the solvothermal synthesis was faster, the crystals grew in the reaction solution and subsequently settled on the surface of the carboxylated fiber. Which resulted in the size difference of the crystals obtained, while in the direct solvothermal approach the crystals were on the microns range in the secondary method, their dimensions reached nanometers.

Besides the temperature, another difference in the anchor methods consisted of the type of metallic precursors used. The secondary method used copper acetate, which contains the preformed paddlewheel structure, instead of the solvothermal method that used copper nitrate as a metal source. In accordance with the concept of secondary building unit (SBU), it wa suggested that MOF structures should be present in the reaction solution [24], as the HUST-1 Cu paddle wheel structures are preformed, crystal growth is promoted and facilitated.

In conclusion, from the evaluation of the anchoring methods, it was confirmed the hybrid material synthesis that combines these two elements, through the secondary or seeded growth, the metal-

organic framework graft was achieved onto the functionalized support with carboxylate groups (-COONa). From now on, this will be the anchoring method to be used to evaluate the effect of other parameters.

5.2.4.2 Functionalization fiber influence

- Effect of the functionalization degree using TEMPO oxidation

In a preliminary way, some experiments were carried out to analyze the importance of the functionalization process during the metal-organic frameworks anchoring, using fibers with different stages of surface modification. The first group was made up of fibers without functionalization: raw (R) and pretreated (WE) fiber. The second group included fibers that underwent functionalization through the TEMPO reaction described in Chapter 4: raw fiber (RT1), pretreated using 1 as NaOCl:AGU molar ratio (WET1), pretreated using 4 as NaOCl: AGU molar ratio (WET4). Each of these fibers reached oxidation degree (OD) values of 7.89, 8.09, 9.31 and 14.35%, respectively, quantified by conductometric titration (for more details of these materials see chapter 4).

For all the fibers described above, the secondary anchoring method of HKUST-1 was implemented with the green synthesis methodology. The nomenclature for each of the synthesized hybrid materials consists of the fiber type followed by 199 referring to the HKUST anchoring -1 or MOF 199. The XRD technique was used to analyze the results of the HKUST-1 synthesis on the modified fique fibers, the respective diffractograms were gathered in Figure 5.2.7. As expected all show the combination of the main cellulose peaks and the diffraction peaks of HKUST-1. The diffractograms associated with fibers without functionalization (those of green color) have the cellulose peak much more accentuated in θ = 22°, compared to supports subjected to the TEMPO reaction (those of purple color) to which this peak has a much smoother profile.

Properly, the fibers without surface modification developed the main HKUST-1 peak located at θ = 11°, despite it was the only peak fully developed by the raw fiber (R-199) even under careful optimization of the reaction conditions. On the other hand, in the pretreated fiber (WE-199) the MOF developed extra peaks, not too intense, located at θ = 6.5°, 9.5°, 11.6°, 13.3°, 13.3° and 19°, making it evident that surface modifications create more homogenous fiber surface with more exposed cellulose, allowing to grow up more MOFs.

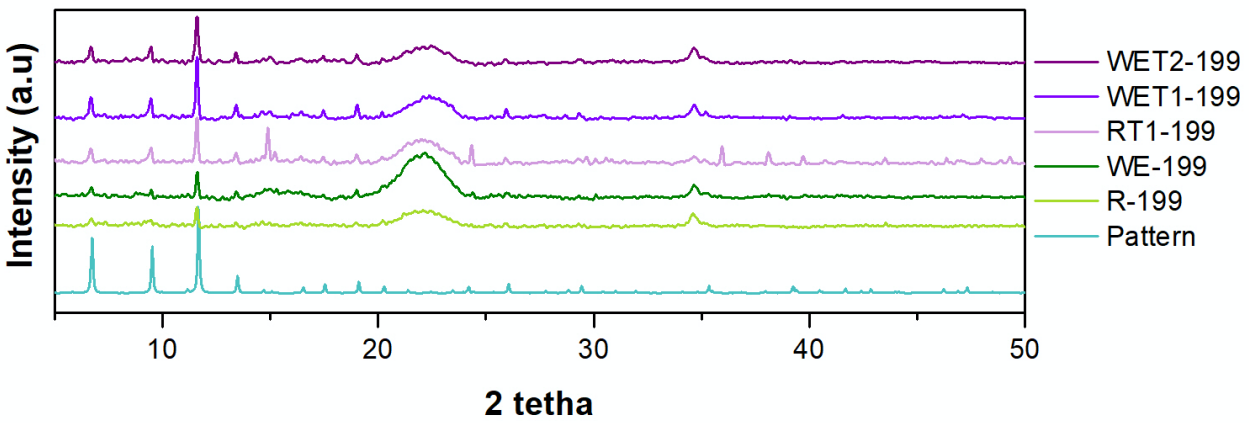


Figure 5.2.7. Diffractogram of HKUST-1 synthesized by the green method and anchored onto raw (R-199), pretreated (WE-199) and functionalized fique fibers (RT1-199, WET1-199, WET2-199).

The surface of these fibers is mainly characterized to have functional groups like carbonyl and hydroxyl, which reduce the interaction with copper ions from the precursor salt, proving HKUST-1 anchoring happened selectively to the organic surface with -COONa groups while -OH-terminated surfaces were nearly inert, corroborating the results obtained in other studies in which the carboxyl groups report greater affinity in the anchorage of metal-organic networks [25].

Regarding the set of chemically modified fibers with carboxylate groups, all showed easily indexable differences with the HKUST-1 pattern, confirming the MOF immobilization onto the different types of functionalized fique fiber. But, the diffractogram of the RT1-199 sample (light purple) allowed to observe the presence of additional peaks to those of the simulated HKUST-1 pattern, which could be attributed to the formation of some impurities in the crystallite structures, as a consequence of the presence of compounds such as sapogenins, hecogenins and sodium carbonates, intrinsic to the raw fiber.

These types of compounds reduced the crystallinity of the obtained material, allowing to conclude the pretreatment stage is necessary to clean and homogenize the fiber surfaces (chapter 3), so during the functionalization process (chapter 4) a better performance was obtained in the degree of surface chemical activation.

From the results obtained, it can be concluded the less strong was the fiber modifications, that is, the less chemically active was the support, the less favorable was the anchoring of metal-organic frameworks, because the interfacial bonding between MOF and the lignocellulosic substrate was limited. This observation validated the assumption that surface functionalization is a mandatory

step to achieve the MOFs anchoring process, and also HKUST-1 preferably grows on surfaces with functional groups -COONa [10,,24].

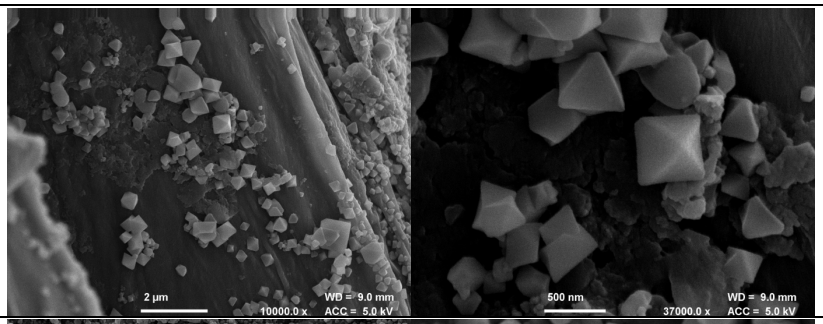
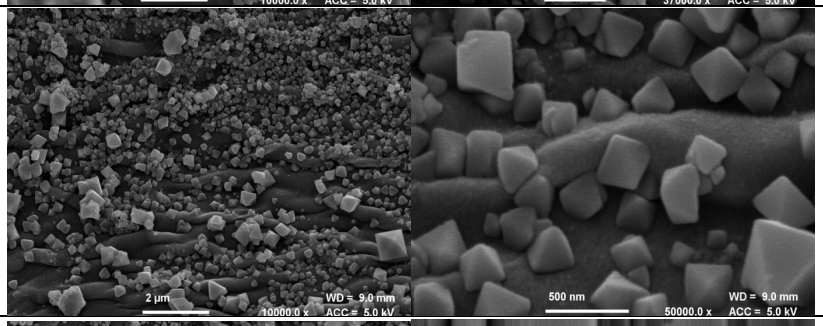
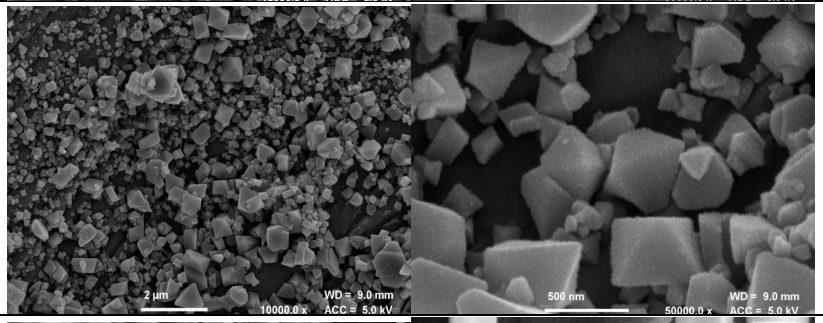
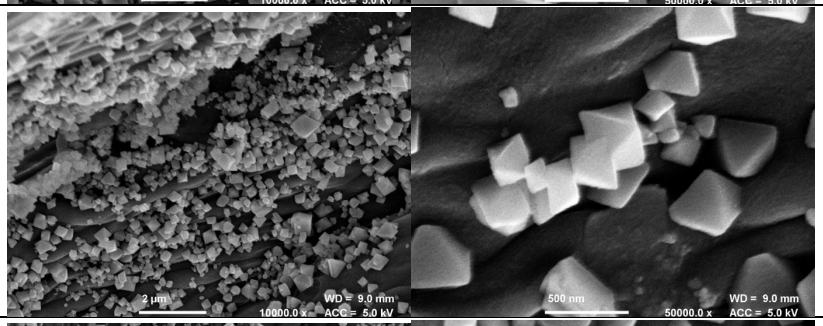
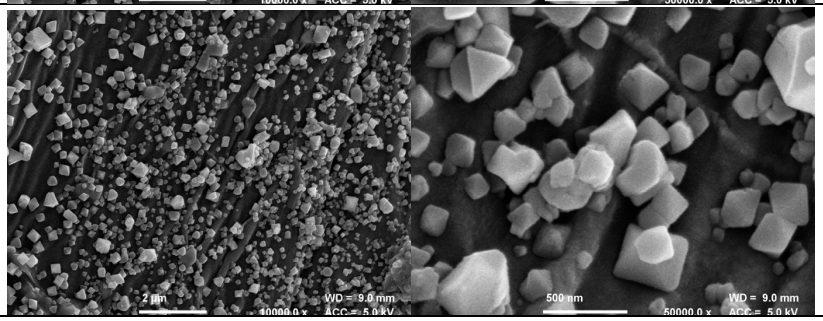
Additionally, it was necessary to evaluate if the higher the degree of functionalization will promote more ion exchange between the metal ions and the surface functional groups present in cellulosic substrate, which would lead to a higher yield of MOFs formed on the surface [26].

In Figure 5.2.7. the diffractograms for two degrees of functionalization are shown, quantified by the degree of oxidation (OD) corresponding to 9.3 and 14.3%, respectively, using 1 and 4 as NaOCl: AGU molar ratio. For both cases, the HKUST-1 pattern was satisfactorily indexed, the diffractograms of the two functionalized fibers (WET1-199 and WET4-199) were very similar in intensity and shape, allowing to ratify the growth of HKUST-1 on the fiber of fique functionalized with -COONa groups. The crystallites size obtained was quantified using the Scherer equation (Eq. 5.2.2), values around 47.1 and 51.4 nm, for WET1-199 and WET4-199, respectively were reported.

Table 5.2.1 summarizes the micrographs obtained for the fibers using different degrees of functionalization. In the first row is the sample prepared by the secondary anchoring method of HKUST-1, showing the metal-organic frameworks developed their morphology but seem to be only deposited but not anchored. Besides, it had a heterogeneous distribution revealing frame-free areas of the cellulose surface, complementing the results obtained by XRD in which it was not possible to fully index the diffractogram with the HKUST-1 pattern.

The other functionalized fibers (WET1-199, WET2-199, WET4-199, WET8-199) showed HKUST-1 crystals that arise from the surface of the TEMPO-modified fique fibers. Crystals were also evident in cell lumens. In general, all the fibers displayed crystals in the octahedra form, in the size of nanometers in the range of 250 to 500 nm, with a relatively homogeneous distribution. In terms of the morphology, the crystals obtained were too similar with those reported for the synthesis of HKUST-1 powder. It was proved the degree of coating did not depend on the level of functionalization, since the WET1-199 functionalization with an oxidation degree of 9.31% presented a uniform coating.

Table 5.2.1. FESEM micrographs in pretreated fibers after TEMPO functionalization under different NaOCl : AGU molar ratio plus HKUST-1 anchored.

(NaOCl:AGU, 0:1)	WE-199	
(NaOCl:AGU, 1:1)	WET1-199	
(NaOCl:AGU, 2:1)	WET2-199	
(NaOCl:AGU, 4:1)	WET4-199	
(NaOCl:AGU, 8:1)	WET8-199	

5.2.4.3 Evaluation of two types of surface functionalization: CMC and TEMPO

The influence of surface chemistry on the HKUST-1 anchoring was investigated. Two types of cellulose surfaces functionalized with groups carboxylates and carboxymethyl ether, with oxidation degree of 9.3 ± 1.9% and 11.3 ± 1.1%, respectively, were studied (Figure 5.2.8). The functional groups exposed on fique fiber substrates were used as supports in hybrid materials for the anchoring of metal-organic frameworks.

They can be designed to specifically interact with metal groups through ion exchange bonds, to control the structures morphology and often the crystallographic orientation formed [10]. In this case, the groups -COONa (carboxylate) and -CH_2OCH_2OONa (carboxymethyl ether) can play different roles in the anchoring process of HKUST-1. Previously, a comprehensive study has been made of how -COONa groups behave during the HKUST-1anchoring process on the surface chemically modified of fique fiber.

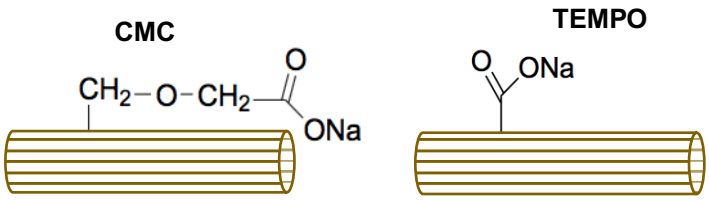


Figure 5.2.8. Types of surfaces functionalized with groups: carboxymethyl ether and carboxylate, obtained from the carboxymethylation (CMC) and oxidation (TEMPO) reactions, respectively.

To elucidate the anchoring of HKUST-1 on functionalized fiber by carboxymethylation (CMC), the methodology proposed by Sierra *et al.* was implemented [26]. It allowed to analyze the order of reagents addition (linker and precursor salt), while the use of triethylamine (TEA) as a linker deprotonating agent was also employed.

The concentrations and reagents reported in the green synthesis from subchapter 5.1 were followed. In Table 5.2.2, four procedures were used to describe the anchoring process, in the case in which the deprotonating agent was used, 0.5 mL of TEA was added immediately after the addition of the BTC.

Table 5.2.2. Experimental procedure followed for the formation of HKUST-1 onto CMC fiber functionalized

Stage	Procedure A	Procedure B	Procedure C	Procedure D
First	CMC fiber + Copper acetate	CMC fiber + Copper acetate + BTC	CMC fiber + Copper acetate	CMC fiber + BTC
Under stirring overnight				
Second	+ BTC + TEA	+ TEA	+ BTC	
Under stirring for 5 hours				
Washed four times alternating water and ethanol each time				

SEM micrographs (Figure 5.2.9) revealed that there was no evidence of crystal formation for procedures B and D. For samples A and C, the formation of much more regular structures in sample C than in sample A was observed. Sample A presented clusters of small particles, irregularly grouped on the fiber, while sample C revealed crystals formation with much more defined octahedral morphology of HKUST-1; the coating was heterogeneous but distributed over the entire lignocellulosic surface.

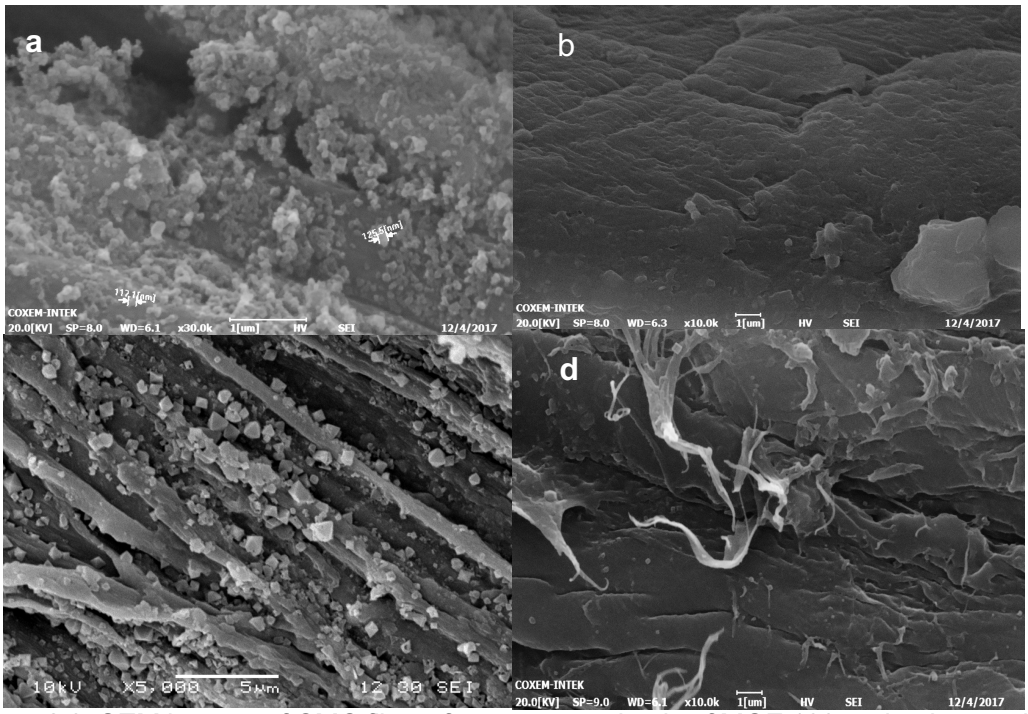


Figure 5.2.9. SEM images of CMC fiber after green synthesis of MOF 199 under the conditions reported in Table 5.2.2. Where, a) step 1st (CMC+ Copper acetate), step 2nd (BTC + TEA), b) step 1st (CMC+ Copper acetate + BTC), step 2nd (TEA), c) step 1st (CMC+ Copper acetate), step 2nd (BTC), d) step 1st (CMC+ BTC).

To confirm if the particles observed in Figure 5.2.10 could be attributed to metal-organic frameworks from HKUST-1, validation was performed using the XRD technique (Figure 5.2.10). For all the diffractograms, the characteristic peaks of the cellulose matrix of fique fiber are found, located at θ = 16° and 22.6°. Only samples A and C anchored with the secondary method showed the development of a small diffraction indexed to the most important peak of the HKUST-1 crystallographic structure at θ = 11°. The appearance of this single peak was the result of the lack of complete development of the MOFs crystal structure; therefore, it was not possible to do full indexing with the HKUST-1 XRD. However, as was described in the previous section, the development of a nucleation stage (first stage in Table 5.2.2) made it possible to carry out the ion exchange process of copper acetate and CMC-functionalized fiber, to produce seed or nucleation points for HKUST-1 crystals to grow.

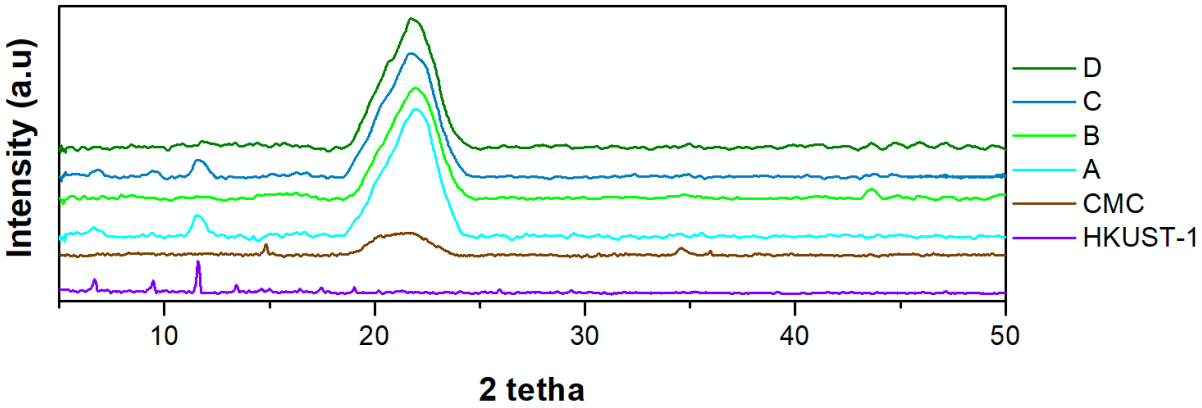


Figure 5.2.10. Comparison of the XRD samples synthesized under green methodology using CMC by the conditions reported in Table 5.2.2. Where, a) step 1st (CMC+ Copper acetate), step 2nd (BTC + TEA), b) step 1st (CMC+ Copper acetate+ BTC), step 2nd (TEA), c) step 1st (CMC+ Copper acetate), step 2nd (BTC), d) step 1st (CMC+ BTC).

Regarding the use of the linker deprotecting agent, it can be concluded the crystal growth was not influenced. The protons were not sufficiently coordinated by TEA as well as the quantity of partially deprotonated BTC. Moreover, the modulation effect cannot impact the coordination equilibrium, mainly in the direct method (procedure B), slowing down the chemical reaction between BTC and metallic copper. Initially, when all the reagents were mixed at the same time; the competition was generated between the aliphatic carboxylate ions (functionalized fiber and precursor salt) for the more acid hydrogen present in tricarboxylic acid. Carboxylate ions in functionalized fique fiber prevailed, causing acidic cellulose did not trap copper ions, promoting the formation of HKUST-1 crystals in the solvent.

At this point, it can be concluded the order of addition of the reagents during the anchoring method had a significant effect on how the nucleation step was mainly carried out. Next, it will be analyzed in more detail how the functionalization of the support with carboxymethylation, influenced the growth of the HKUST-1 crystallites, taking as a reference the material obtained employing procedure C, which was carried out under conditions of green synthesis and anchorage through the secondary method.

The SEM images in Figure 5.2.11 confirmed the HKUST-1 crystals were anchored to the fique fiber surface functionalized by carboxymethylation (procedure C). The -CH_2OCH_2OONa group acted as a nucleation point at which the copper ions from the precursor salt allowed an ion exchange while being closely bound to the surface of the fiber. Subsequently, the benzenetricarboxylic acid linker can promote a coordination link so that the copper carboxylate worked as a starting node in the MOF growth. The micrographs on the right in Figure 5.2.11 shows, after the nucleation process, the crystals growth, which indicated the development of some defects in the structure as a result of the disturbance in the network periodicity, generating changes in the MOFs surface such as: evidence of pitted or chopped holes, half-formed crystals and allowed to suppose a rough surface formed by layers resulting from the forced and tortuous crystal growth.

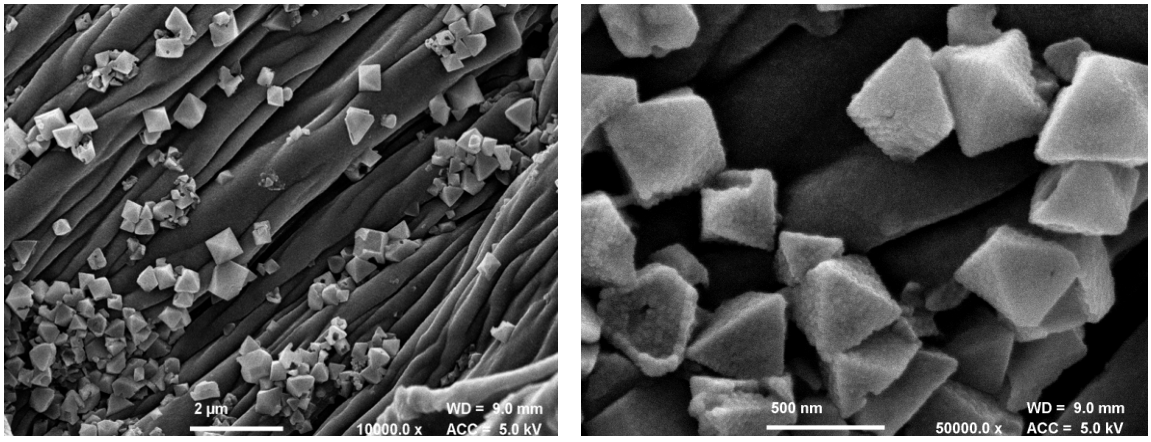


Figure 5.2.11. SEM micrographs of HKUST-1 anchored to the CMC fiber by the secondary growth (procedure C, Table 5.2.2).

In addition, there may be the possibility of defects such as network interpenetration, changes in crystal alignment (in-plane and out-of-plane orientations), changes in cohesion, and even modification in chemical properties. These defects could be the result of the MOFs growth where only the carboxymethyl group was accessible, and there was no presence of the copper metal center, resulting in the linker reaction directly with -CH_2OCH_2OONa. Unexpected reactions could

also occur, such as crosslinking of the fique fiber; therefore, the carboxymethyl group would no longer be available to react with copper ions. This crosslinking trend has already been reported by other authors who maintain that CMC has high favorability of forming micelles [27]. Furthermore, the length of the -CH_2OCH_2OONa link could affect the MOF strength immobilization at the moment of growth, intervening in some way with the coordination links present in the frame.

Also, it can be seen in the micrograph on the left of Figure 5.2.11, the MOF coating was not completely uniform, possibly because of the functionalized percentage of the fiber surface. This reached approximately 11.3% of the total surface, leaving many gaps in which hydroxyl groups can become nucleation points, but were not strong enough to retain the metal-organic frameworks. Probably the anchoring of HKUST-1 on CMC can be optimized, by means of the most exact identification of the precise causes for which the crystalline defects occurred; but that goes beyond the current work.

Comparing the HKUST-1 anchorage using functionalized supports by CMC or TEMPO, the reactivity was shown to be high in the fibers with carboxylate and non-ether groups, which translated into more specific interactions of the lignocellulosic surface with the copper ions or growing nuclei. Although crystal growth was independent of the conditions under the reaction was carried out, it was evident the presence on the surface of -COONa groups prevailed compared to -CH_2OCH_2OONa. This result was in agreement with other authors such as Shekhah *et al.* [24], who demonstrated by XPS the surfaces with -COOH led to the deposition of zinc ions and also to the binding of BDC (1,4-benzenedicarboxylic acid) to immobilize MOF-5.

Regarding the time it took to see the development of the crystals, it was also distinguished that copper acetate was the best source of copper compared to copper nitrate, because of the paddlewheel structures present in the intrinsic initial solution [28]. Finally, from the analyzes carried out previously, a set of synthesis conditions necessary to produce fique fibers with anchored HKUST-1 were identified, which consist of: synthesis by the green methodology, the functionalized substrate trough TEMPO reaction and implementation of the anchoring method by secondary growth, which largely depends on the sequence of reagents addition.

5.2.4.4 Characterization of WET1-199 and WET1-SH

In this section, a complete characterization of the synthesized hybrid materials WET1-199 (fique

fiber functionalized by TEMPO and HKUST-1 anchored) and SH-WET1-199 (fique fiber functionalized by TEMPO and the modified SH-HKUST-1) will be made. This characterization will allow to analyze how the interfacial coordination between the cellulose surface functionalities on the fique fiber and the secondary building unit of the MOF (SBU) occur. The spectrum of possible applications in which these new materials could be used was expanded, but for this, it is important to know their properties.

Both fibers after the synthesis exhibited a characteristic turquoise color of the organic-framework metal HKUST-1 as a result of the presence of Cu•••Cu. As the frame was activated at 60 °C under vacuum, the fiber changed its color to blue and finally turned violet when activation was complete (Figure 5.2.12). This process was completely reversible when activated materials were exposed to ambient conditions.



Figure 5.2.12. HKUST-1 color change in hybrid materials synthesized by the green methodology and approach of secondary growth after the activation process (purple), being in atmospheric pressure during1 minute (blue), and 5 minutes (turquoise).

The fibers color change before and after activation was the result of the water molecules removal covalently attached to the copper centers and π-π transition state of copper ions (Figure 5.2.13) [18]. The dehydration process maintained the crystalline nature of the material, while making the Cu^{2+} sites in the framework available for interaction with other molecules [28]. This color change was consistent with reports in literature by other authors such as Cheng *et al.* [30]*, who* described the color change implied the copper coordination number would decrease from six to four, increasing the ionic character, while the electron density in the carboxylated groups increased [30].

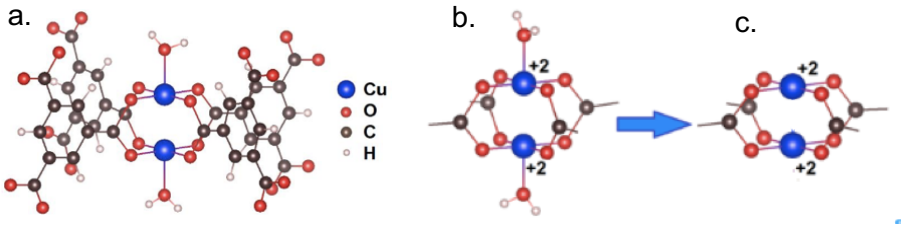


Figure 5.2.13. a) Outline of the main structure of HKUST-1 before activation shows the paddlewheel structure that is formed by two Cu^{2+} ions and four benzene molecules of the linker 1,3,5-tricarboxylate linker (BTC), b) hydrated cage of HKUST-1 before the activation, c) activated cage of HKUST-1 (dehydrated) [29].

- Structural characterization

X-Ray Diffraction allowed to check whether the crystallographic structure of each part that conformed the hybrid material kept its identity. The combination of the diffractograms profiles corresponding to the powdered metal-organic frameworks and the functionalized fique fiber was obtained. From Figure 5.2.14 it can be appreciated grafts of MOFs in the fique fiber (WET1) with HKUST-1 and SH-HKUST1, where the main peaks was evidenced at θ = 22°, associated with cellulose, and five dominant peaks at θ = 9.5°, 11.6°, 13.8°, 17° and 19°, which were possibly indexed with the planes (2 2 0), (2 2 2), (4 0 0), (3 3 3) and (4 4 0) [18]. Both shape and indexing indicated the Cu-BTC structure present in HKUST-1 and SH-HKUST-1 of the powdered frames was well preserved.

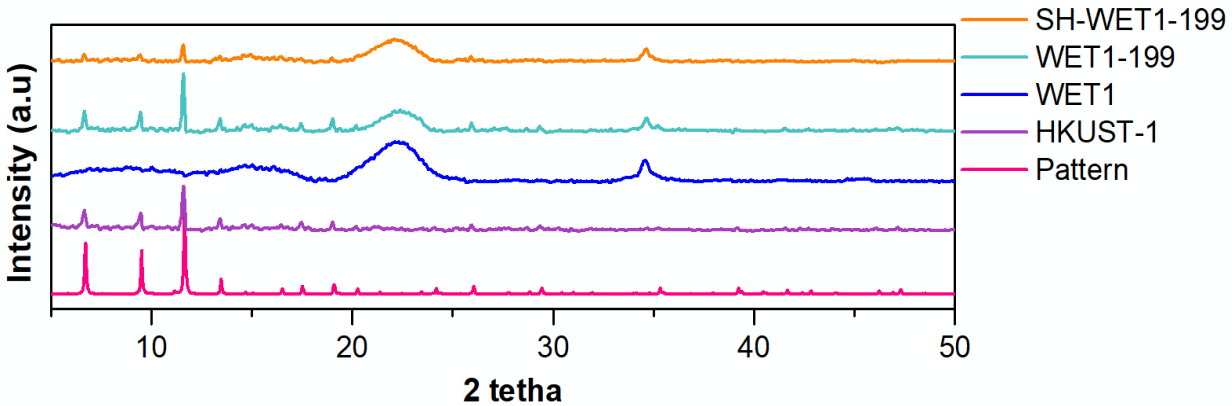


Figure 5.2.14. X-ray diffraction patterns for the hybrid materials synthesized: WET1-199 and SH-WET1-199.

The two metal-organic frameworks samples synthesized on the cellulose support indicated diffraction patterns identical to those of the simulated HKUST-1 pattern, allowing to suppose the copper MOFs stabilization on the functionalized fique fiber. The diffractograms combination suggested the co-existence of the two components in the hybrid material, the average size

crystallites were 47.1 and 50.2 nm, for WET1-HKUST and SH-WET1-199, respectively calculated by the Scherer formula (Eq. 5.2.2).

- Morphological characterization

The morphologies, microstructures and particle size of the MOFs synthesized and anchored on supports were determined by FESEM. As was expected, the micrographs revealed that a crystalline material was obtained (Figure 5.2.15). The crystals of HKUST-1 and its modification SH-WET1-199 achieved by the use of crystal poisons have the form of octahedral shape for both materials, with defined, smooth and undamaged morphologies.

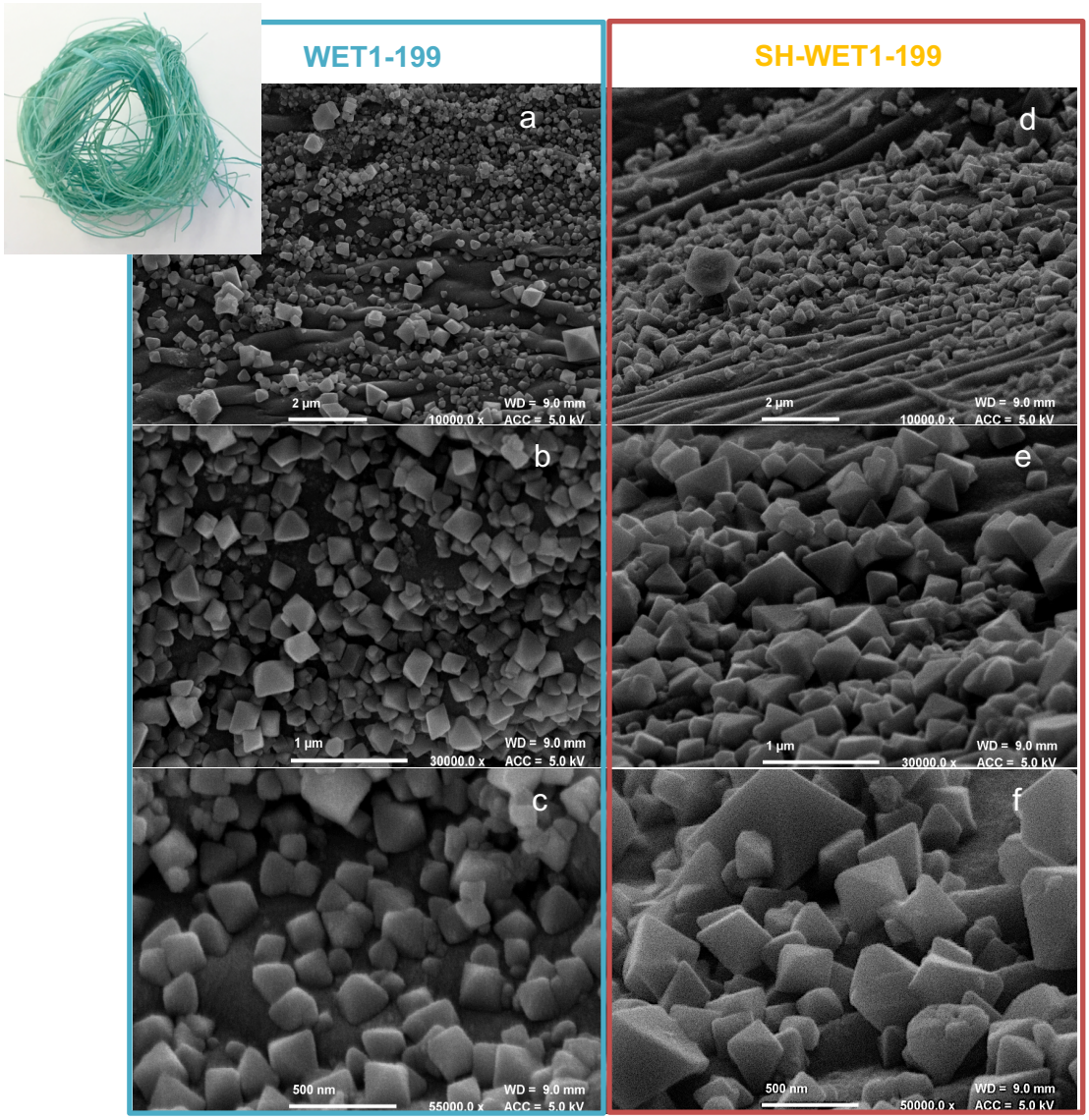


Figure 5.2.15. FESEM images of the hybrid materials synthesized: WET1-199 (blue square, 5.2.15a, b,c) and SH-WET1-199 (red square, 5.2.15d, e, f).

The crystal sizes were on average 250 and 350 nm, respectively, for WET1-199 and SH-WET1-199 (micrographs c and f, Figure 5.2.15). These values of the MOFs crystal sizes were very similar to those obtained when the metal-organic frameworks were synthesized in powder. Therefore, no effect on the size of the octahedra particles was confirmed after they were anchored to the lignocellulosic substrate.

Regarding the distribution of MOFs on the fique fiber (micrographs a and d, Figure 5.2.15), both frames were grafted randomly, leaving some areas of the fiber surface bare. It was also demonstrated the metal-organic frameworks were developed from the cellulosic support, confirming the anchorage and development of hybrid materials. The deposition was homogeneous since only a monolayer of crystals was observed, which can vary a little in size, but there was no evidence of the cluster's formation (micrographs b and e, Figure 5.2.15).

BET surface areas obtained for the synthesized hybrid materials are presented in Table. 5.2.3. It became evident a significant difference in the BET surface area compared to the MOF powders. the fiber with graft of MOFs gave rise to a minimum amount of nitrogen adsorbed (the results were within the measurement error of the equipment), implying that the surface was less porous and even not porous, as a consequence of the significant percentage of fique fiber that constitutes the hybrid materials. A similar behavior was reported by Lawson *et al*. [31], as a result of the MOF-74 immobilization in lambs' monoliths, they reported the surface area reduction of synthesized materials after the frames anchoring on the support. The surface area of the hybrid materials was reduced from 367 to 43.4 $m^2 g^{-1}$ for HKUST-1 and from 579 to 53.7 $m^2 g^{-1}$ for SH-HKUST-1.

Table 5.2.3. BET surface area of the hybrid materials synthesized: WET1-199 and SH-WET1-199.

Surface Area by BET (m^2/g)	
WET1-199	43.4
SH-WET1-199	53.7

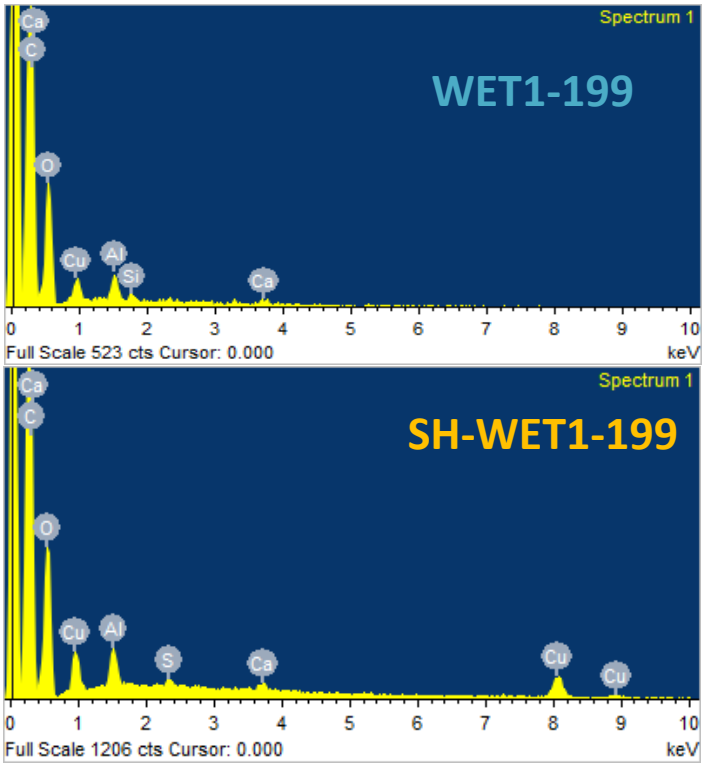
Additionally, to verify if this step was within the anchoring methodology affected the N_2 adsorption measurements were done for the functionalized fiber after the seed step (impregnation) and it revealed the material could not develop any isotherm. Lignocellulosic materials have been described as non-porous materials [32], which is why techniques such as nitrogen adsorption are limited because they are only generally applied for materials with more than 5 $m^2 g^{-1}$.

For this type of materials, the suggestion is to use gases such as argon or krypton as an alternative to nitrogen, but it is quite difficult to obtain consistent results because materials such

as biomass could affect the measurements due to the diameter of the fibers used [33]. Besides, a complete degassing process could not be achieved so the material surface was not free of molecules that may be adsorbed, since there was a limitation in the temperatures used which cannot be higher than 110 °C because it produced structural changes in the fiber.

- Chemical characterization

The qualitative composition of the synthesized hybrid materials was studied by Scanning Electron Microscopy with X-ray Dispersive Energy Spectroscopy (EDX). The spectra obtained in Figure 5.2.16, corresponded to the elements fusion present in each of the constituent parts. In both spectra, the presence of minor elements such as aluminum, calcium and silicon were characteristic of the cellulose matrix; carbon and oxygen result from both parts: structure of cellulose polymer and the organic linker of the metal-organic framework (BTC), besides in the spectrum of MOF SH-WET1-199 to crystal poison (MBA). Comparing the EDX of Figure 5.2.16, both had the presence copper, related to the inorganic component of the synthesized MOFs; the only difference was the presence of sulfur in the SH-WET1-199 sample due to the modification made to include thiol groups (-SH) into the frame structure.



WET1-199

Element	Atomic (%)	Weight (%)
C	69.29	59.58
O	27.84	31.88
Al	1.13	2.19
Si	0.34	0.68
Ca	0.44	1.25
Cu	0.97	4.41
Total	100	100

SH-WET1-199

Element	Atomic (%)	Weight (%)
C	74.95	64.23
O	22.27	25.42
Al	0.69	1.33
Ca	0.10	0.29
S	0.14	0.32
Cu	1.85	8.41
Total	100	100

Figure 5.2.16. EDX of the hybrid materials synthesized: WET1-199 and SH-WET1-199.

In general, the semi-quantitative analysis of the elements presents in the hybrid materials gave the highest values for the carbon and oxygen elements, because the cellulose support was the material found in greater proportion. Traces of aluminum, silicon and calcium existed intrinsic to the fique fiber and were a result of the type of fertilizers and nutrients acquired throughout the plant growth.

Copper presence corroborated the identity of the characteristic metal included in both metal-organic framework structure fixed onto the fiber. It reached values in the range of 0.97 to 1.85 of atomic percentage, which allowed to infer the amount of copper present in the hybrid materials was low. The quantification of the amount of anchored copper was carried out by Flame atomic absorption spectroscopy (FAAS), which will be analyzed later. Concerning to atomic percentage of sulfur, the presence of this element was only evident in sample SH-WET1-199 as expected, since the anchored MOF contained the modification of HKUST-1 by grafting of thiol groups (-SH) through crystal poison. The minimum value reached for sulfur was consequence the amount of MBA used, since as previously discussed, the modification could only involve the use of crystal poison in 5% by weight of the linker to not affect the network structure.

The chemical composition was studied by mapping EDX. Figure 5.2.17 shows the atomic distribution of each element present on the surface of the samples analyzed (WET1, WET1-199 and SH-WET1-199). The presence can be seen throughout all the micrographs for carbon (C) and oxygen (O) atoms, which have similar intensities in the signals attributed to the red and green colors in Figure 5.2.17, due to the organic composition of the biomass lignocellulosic.

Copper (Cu) was only detected in the samples in which the metal-organic frameworks of HKUST-1 were deposited; its signal related to the blue color is an additional evidence of the frames anchoring on the functionalized fibers. The Cu element was homogeneously distributed on the cellulose surface, indicating a good dispersion of possible nucleation points produced during the first stage of the secondary anchoring method. Moreover, for sulfur (yellow signal) a non-uniform distribution in sample SH-WET1-199 was observed, which led to propose the structure modification of HKUST-1 did not happen in all crystals, but only in some of them

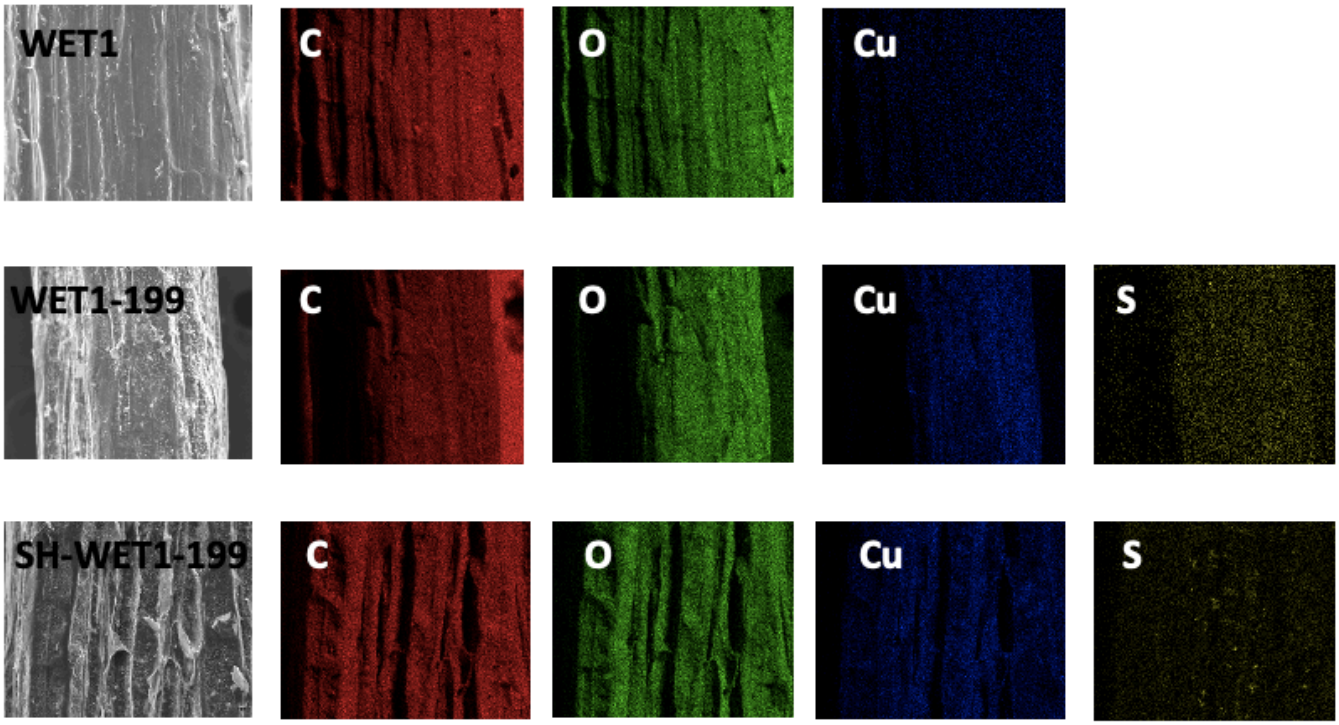


Figure 5.2.17. X-ray (EDX) elemental mapping analysis for the hybrid materials synthesized: WET1-199 and SH-WET1-199.

To complement the chemical characterization performed by EDX and quantify the amount of copper present on the surface of each of the synthesized materials, the flame atomic absorption spectroscopy (FAAS) technique was used. The hybrid materials samples were previously digested by acid. It was important to consider the copper quantification was carried out in the samples of the hybrid materials: WET1-199 and SH-WET1-199, and in the functionalized fiber (WET1) as a blank. In addition, it was analyzed the functionalized fiber after performing the first step of the secondary anchoring method, corresponding to the ion exchange with the copper precursor salt and thus quantifying the amount of copper exchanged to be used as nucleation points. The values obtained for copper content in each one of the analyzed samples are reported in Table 5.2.4; all the measurements were made in triplicate to guarantee the quantification statistics.

Table 5.2.4. Amount of copper measurement by FAAS in the hybrid materials synthesized: WET1-199 and SH-WET1-199.

Treatment	Material	mg Cu / g Fiber	Cu % wt.
Functionalized	WET1	0.0 ± 0.0	0.0 ± 0.0
Impregnated	WET1-Cu	79.6 ± 5.9	7.9 ± 0.6
Fiber + HKUST-1	WET1-199	63.3 ± 23.3	6.3 + 1.0
Fiber + SH-HKUST-1	SH-WET1-199	64.7 ± 16.4	6.5 ± 0.3

The data in Table 5.2.4 indicated that almost the total number of possible nucleation sites produced after the copper impregnation process, approximately 80.36% of the total copper available, was used for the subsequent frames growth. The analysis by FASS indicated a copper loading of 63.97 mg Cu / g fique fiber for both hybrid materials. Also, a CHNS / O elemental analysis was done for the hybrid materials to quantify the amount of sulfur present onto the fiber after the anchor stage. A summary of the values obtained from the samples analyzed are in Table 5.2.5.

Table 5.2.5 CHNS / O elemental analysis in the hybrid materials synthesized: WET1-199 and SH-WET1-199.

Material	C (%)	H (%)	N (%)	S (%)	O (%)
WET1	42.4 ± 0.1	6.3 ± 0.13	0.0 ± 0.0	0.0 ± 0.00	51.5 ± 0.5
WET1-Cu	40.3 ± 1.4	6.0 ± 0.12	0.0 ± 0.0	0.0 ± 0.00	53.6 ± 1.5
WET1-199	43.4 ± 0.2	6.0 ± 0.21	0.0 ± 0.0	0.0 ± 0.00	50.6 ± 0.2
SH-WET1-199	41.9 ± 0.8	5.9 ± 0.10	0.0 ± 0.0	0.02 ± 0.01	52.2 ± 0.9

As previously discussed, from the elemental analysis in Table 5.2.5 the elements with the highest percentages were, as expected, attributed to oxygen (O), carbon (C) and hydrogen (H). Since the matrix was the part that mainly constituted the hybrid material, there was no nitrogen in the samples analyzed. The material SH-WET1-199 was the only one with a sulfur content on the surface of the material of approximately 0.008 ± 0.004 wt%, resulting from the modification of HKUST-1 with the thiol functional groups graft (-SH) using MBA as crystal poison in the synthesis process.

From the copper (Cu) and sulfur (S) data quantified in Tables 5.2.4 and 5.2.5, respectively, the Cu: S ratio was 1: 0.002 in SH-HKUST-1, considering the molecular formula of HKUST-1 as $[Cu_3(C_9H_3O_6)_2]_n$ and based on the asymmetric unit of HKUST-1 and correct according to the amount of thiol present. The molecular formula for SH- HKUST-1 was $[Cu_3(C_9H_3O_6)_{1,998}(C_7H_5O_2S)_{0.006}]_n$, its molecular weight (MW) is 605.385 g mol^{-1}.

From the complete quantification of the synthesized composite materials combining fique fiber and HKUST-1 or SH-HKUST-1 as metal-organic framework, assuming 100% reaction and taking into account the stoichiometry of Figure 5.2.18, the amount of HKUST-1 and SH-HKUST-1 incorporated into the cellulose polymer was calculated. Values close to 201 mg of HKUST-1 / g fique fiber (20.1wt%) and 205 mg of SH-HKUST-1 / g fique fiber (20.5 wt%), were obtained. It was interesting to note, from the percentage by weight of metal-organic framework present into

the hybrid material quantified before, the copper percentage existent in the hybrid material corresponded to a third of the weight percentage of the MOF (Table 5.2.4). This ratio was close to coordination of copper with two oxygens from the linker as was revealed in Figure 5.2.18.

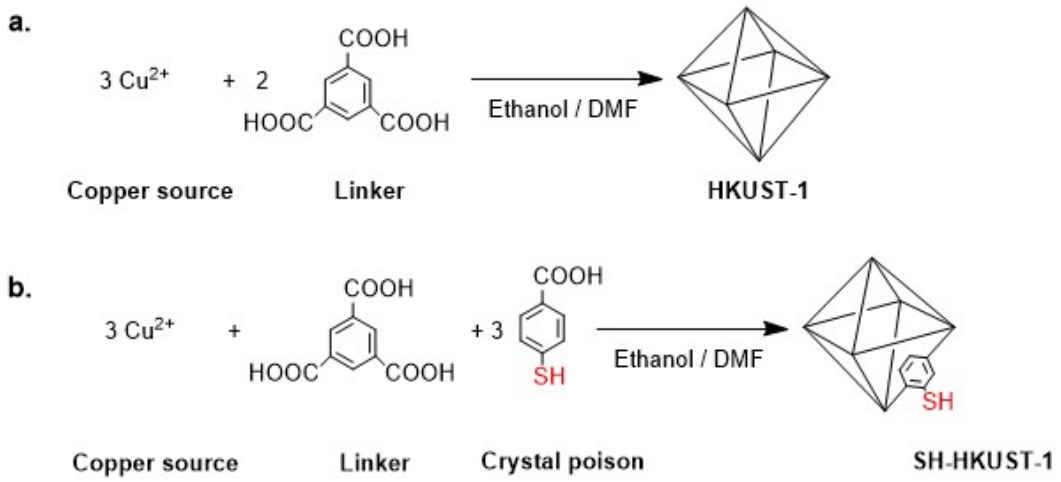


Figure 5.2.18. Schematic synthesis procedure of a) HKUST-1 and b) SH-HKUST-1.

With the aim to support the above information, the amount of each of the MOF presented in the hybrid materials was also analyzed by thermogravimetric (TGA), which will be discussed in the next section.

- Thermal characterization

The thermogravimetric analysis (TGA) and Differential Scanning Calorimetry (DSC) of the hybrid materials are shown in Figure 5.2.19. These were used to quantify the mass fraction of MOF deposited onto the functionalized fiber surface, after the anchoring process, knowing in advance the temperature at which the incorporated MOFs were thermally stable. In general, there were mainly five regions in the decomposition patterns of the two very similar composite materials (5.2.19a and 5.2.19b, for WET1-199 and SH-WET1-199).

The first step between 50 to 120 °C, hydrated materials contain up to 1.04 and 0.36 wt% of water and solvent such as ethanol (WET1-199 and SH-WET1-199, respectively). The weight loss was due to the moisture removal and guest molecules from the MOF, correlated with a very smooth endothermic peak in the DSC of Figure 5.2.19a and b, respectively. Then the WET1-199 sample did not show any significant change in weight, from 120 to 205 °C, after which a second stage was evidenced for both materials with a weight loss between 5.91 and 8.76% attributed to the decomposition of the hemicellulose [34], which is confirmed by the exothermic peak of Figure 5.2.19 at 205 °C

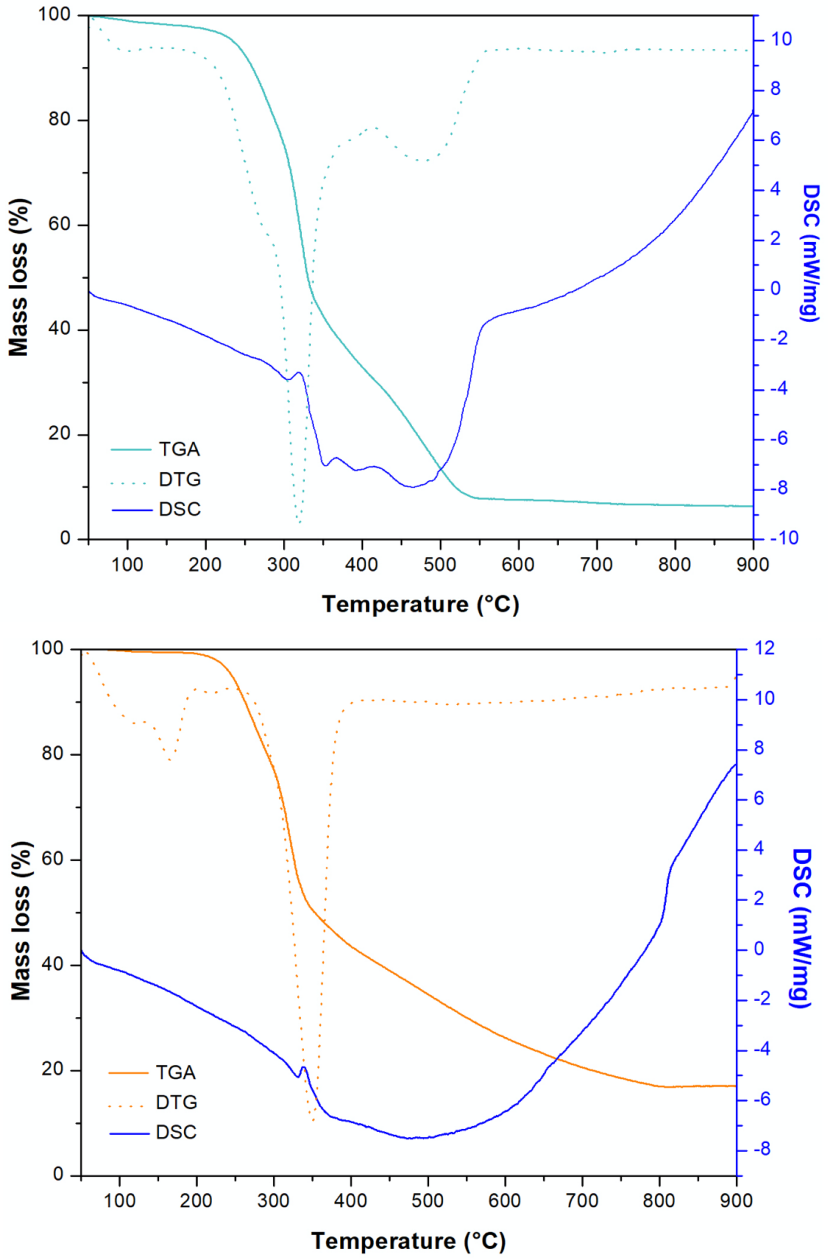


Figure 5.2.19. Thermogravimetric analysis (TGA) and Differential Scanning Calorimetry (DSC) of hybrid materials synthesized: WET1-199 and SH-WET1-199.

.

Subsequently, the exothermic process (Figure 5.2.19b) of linker degradation associated with the metal-organic frameworks anchored began in the third stage from 255 to 287 °C for WET1-199 and from 266 to 305 °C for SH -WET1-199. During this stage, there was a gradual weight loss, close to 11.05% and 14.02% in the hybrid materials WET1-199 and SH-WET1-199, respectively. This result agreed very well with literature reports for HKUST-1 powder in which these frames

have been described to be thermally stable in the 280 to 320 °C range, before they gradually disintegrate at higher temperatures [18].

A fourth change was evidenced from 287 to 415 ºC associated to the cellulose pyrolysis. The weight loss percentage was the highest of all the stages since the lignocellulosic biomass was mainly made up of cellulose, with values of 50.17 and 30.48 wt% for the samples WET1-199 and SH-WET1-199, respectively. These correlated to the exothermic peak of the DSC in Figure 5.2.19b located close to 320 °C, finding a good agreement with the literature data [35]. Concerning the fifth region, mainly the lignin decomposition happened [36], a mass loss close to 22.78 and 26.67 %wt. was reached by WET1-199 and SH-WET1-199, respectively, between 410 to 800 °C in both samples (Figure 5.2.19). In addition, partial lignin decomposition occurred simultaneously during the hemicellulose and cellulose degradation [36].

The materials residual mass, 6.01 and 17.31% corresponded to residues of WET1-199 and SH-WET1-199, they were the result of the frames decomposition and lignocellulosic biomass, which were related to ashes of fique fibers and the formation of the copper oxide CuO from MOFs [18,37].

From the third region described above, related to linker degradation, it was used to calculate the amount of MOFs anchored in each of the synthesized hybrid supports. Assuming all the linker was used in the reaction, approximately 167.58 mg of HKUST-1/g of fiber of fique (16.13 wt%) and 204.70 mg of SH-HKUST-1 / g of fiber of fique (20.47 wt%) were obtained. Table 5.2.6 compared the amount of metal-organic frameworks anchored onto the fiber surface through TGA with those obtained by FAAS, a similar percentage by weight can be evidenced for each one of the hybrid materials. The small difference in the values can be attributed to the fact that in this range of TGA other parallel reactions to the linker degradation like the decomposition of the lignocellulosic substrate could occur.

Table 5.2.6. Percentage of metal-organic frameworks HKUST-1 and SH-HKUST-1 were anchored onto the fique fiber, quantified by FAAS and TGA.

Material	FAAS (wt%)	TGA (wt%)
WET1-199	20.08	16.13
SH-WET1-199	20.53	20.47

The growth and anchoring of MOFs have been shown to be highly sensitive to the experimental conditions of the implemented synthesis and anchoring method, as has been studied throughout this document [38]. Analyzing the amount of MOF anchored to the surface of the fique fiber, it can be seen about 20% by weight of the two metal-organic frameworks was achieved. So, it could be

said, it was possible to match the density of the groups carboxylate available from functionalization (about 11.3 ± 1.1%) with the number of coordination sites created after the seeding stage (first step of the anchoring method). From the total MOFs anchored to the fiber surface corresponding to 20 wt% it may be assumed that about 11.30% correspond to metal-organic frameworks that grew at nucleation sites related to carboxylate groups resulting from functionalization and the other 9% was the rest of the MOFs that possibly grew on fiber parts without functionalization, perhaps on hydroxyl groups available in the cellulose matrix.

- Spectroscopy and surface characterization

Figure 5.2.20 shows the graph plotted between initial pH of the solution and the variation on the initial and final pH. These plots allowed to calculate the zero point of charge of the material produced in this research. The zero-point charge (pH_{zpc}) of the hybrid materials synthesized WET1-199 and SH-WET1-199 was estimated at 4.17 ± 0.09 and 4.12 ± 0.1, respectively. The values of pH_{zpc} obtained are mainly influenced by the zero-point charge of the metal organic frameworks which have pH_{zpc} values of 4.56 ± 0.15 (HKUST-1) and 4.69 ± 0.21 (SH-WET1-199). Also, the acid character of the functionalized fiber (pH_{zpc} = 5.18 ± 0.05) influenced the zero point of charge obtained for the synthesized material. Therefore, for both hybrid materials, the net surface charge will be positive at pH values lower than pH_{zpc} and negative at pH values higher than pH_{zpc}.

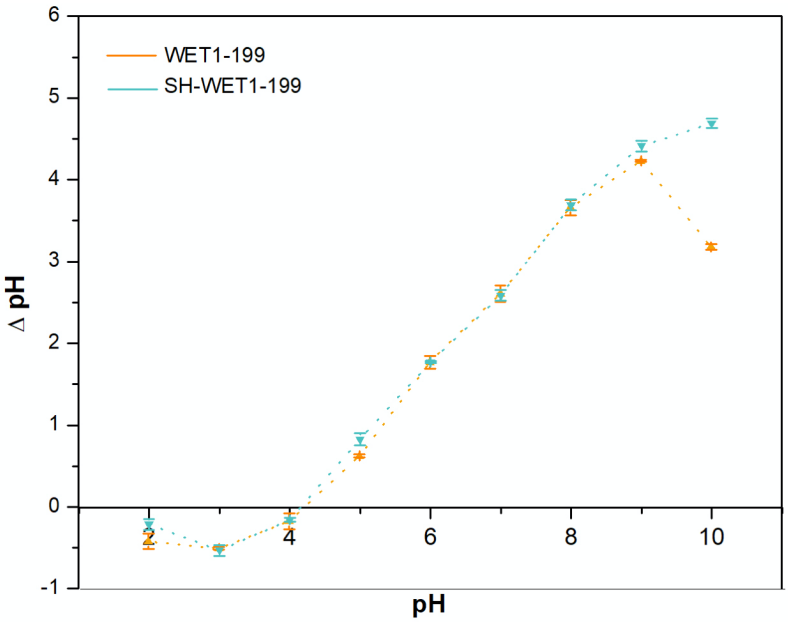


Figure 5.2.20. pHzpc of hybrid materials synthesized: WET1-199 and SH-WET1-199.

In addition, the wetness of the hybrid materials produced was also measured by the contact angle because this will affect the stability, compatibility and mechanical properties [39]. The technique used to quantify the contact angle in natural fibers was described in detail in Chapter 2 because materials as natural fiber due to the non-circular and heterogeneous cross sections needed an alternative measurement [13]. The contact angle values were determined using Eq. 5.2.1, WET1-199 and SH-WET1-199 reported values of 83.5 ± 0.6 and 65.6 ± 6.1, which proved its low hydrophilicity. Each part of the hybrid material contributes with the wetness, in one hand the fiber functionalized and the other is the MOF HKUST-1, which have a contact angle of 32.9° ± 1.9º and 146° [40], respectively. However, the low hydrophilicity tendency of the hybrid material could be related to the highly strong metal-linker bonds or can result from hydrophobic compounds like the BTC linker [40].

Comparing the wetness of the materials obtained using as metal-organic frameworks HKUST-1 and its modification through the grafting of sulfhydryl groups (-SH), it became evident that the material with HKUST-1 was much more low hydrophilicity related to the SH-HKUST-1 MOF, possibly as a consequence of the grafted sulfhydryl group, which contains a sulfur atom. It tends to form two covalent bonds by containing 6 valence electrons, creating a negative partial charge (δ^-) on sulfur and on hydrogen a positive partial charge (δ^+), giving a polar character to the thiol group [41].

The FTIR-ATR spectra (Figure 5.2.21) demonstrated the presence of functional groups in the synthesized hybrid materials, which confirmed to be the combination of the groups from the fique fiber and in HKUST-1, already reported in this document. Specifically, related to the fiber, the presence of peaks around to 1236, 1326, 898 and 1165 cm^{-1}, attributed to the stretching vibration of C-O in lignin and carboxylic vibration in xylan, CH_2 present in cellulose, ß-glycosidic bond and C-O-C asymmetric stretch vibration in cellulose, respectively [42].

In addition, a very important absorption peak was evident in 1734 cm^{-1} related to the carboxylate functional groups resulting of the fiber functionalization through the TEMPO reaction. These functional groups acted as seed coordination sites during the synthesis and nucleation of the metal-organic frameworks, allowing the resulting crystals to be chemically immobilized on the cellulose surface, avoiding the desorption of particles through the chemical anchor.

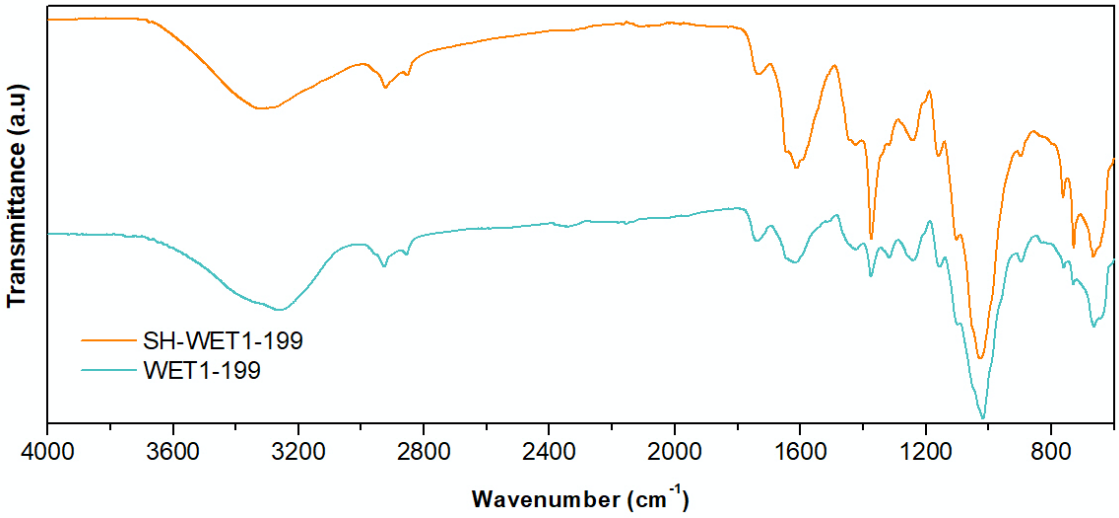


Figure 5.2.21. FTIR spectra obtained from the hybrid materials synthesized: WET1-199 and SH-WET1-199.

Furthermore, peaks related to HKUST-1 were detected in the spectra of Figure 5.2.21, from which the presence of HKUST-1 was confirmed. Functional groups correlated to the aromatic ring of the BTC linker were identified at 1646, 1448 and 1371 cm^{-1}, associated to the stretching vibratory frequencies of C=O of the aromatic esters, -OH and O-C-O flexing of the carboxylic acid. The characteristic stretch vibration of the Cu-O at 747 cm^{-1} corroborated the coordination between oxygen and copper [43], thus ratifying the presence of HKUST-1 on the fique fiber.

The XPS technique was used to explore the electronic properties of the synthesized materials, to verify the chemical bond formed between the coordination forces of the copper metal centers and the carbonyl groups that form the metal-organic frameworks of HKUST-1. Bonds of the carboxylate groups present in functionalized cellulose with at least one pendant carbonyl group of the MOFs were also analyzed (Figure 5.2.22). The spectrum of the functionalized material WET1 showed three characteristic peaks, corresponding to Na 1s (1071 eV) associated with the oxidation process by TEMPO, resulted in sodium carboxylate groups (-COONa), corroborating the results obtained previously. C 1s and O 1s displayed changes in the electron density around 285 and 532 eV, respectively, due to the presence of functional groups associated with the lignocellulosic biomass macromolecules, such as cellulose and hemicellulose.

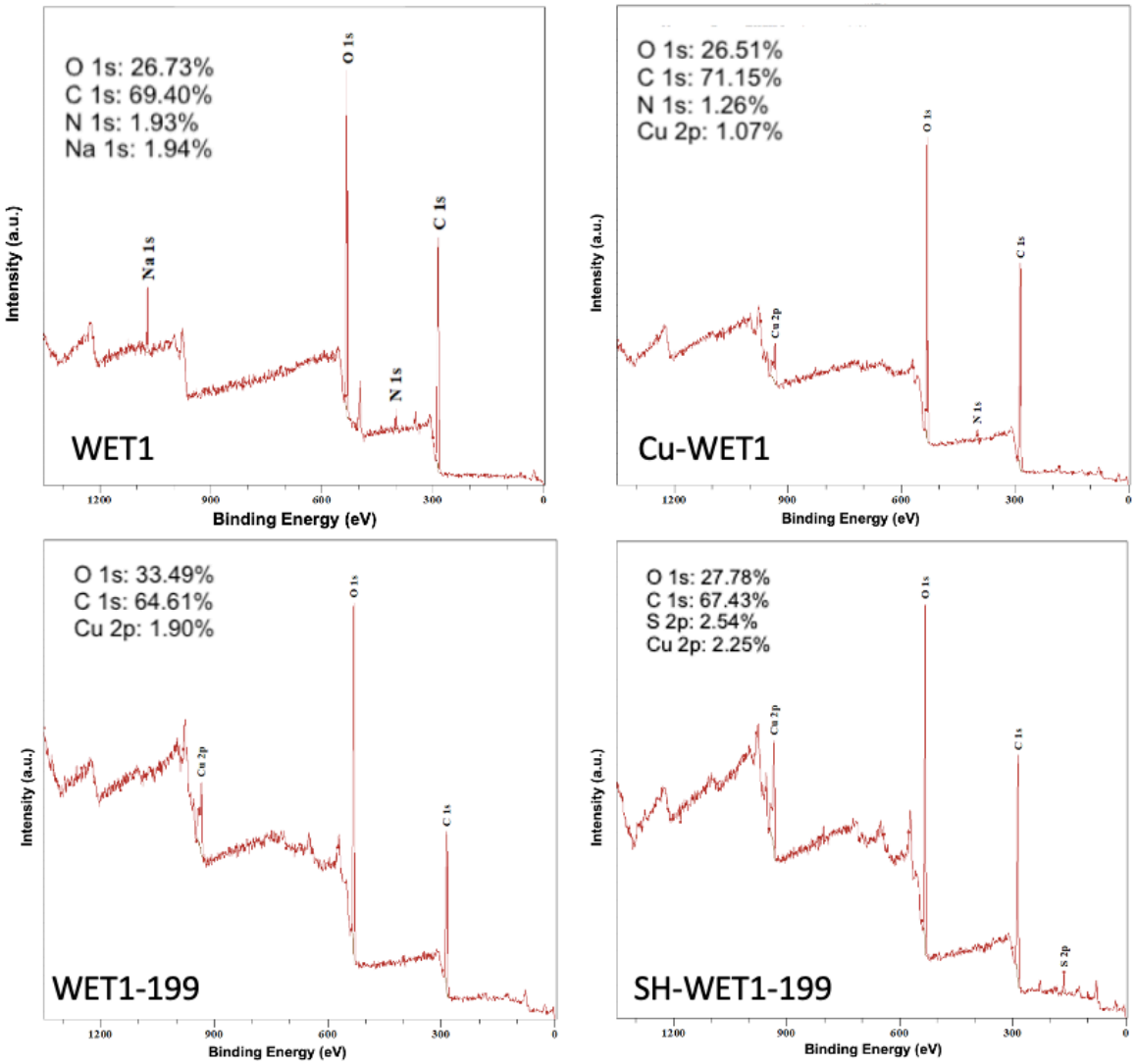


Figure 5.2.22. XPS X-ray photoelectron spectroscopy (XPS) of the functionalized fiber WET1, impregnated fiber Cu-WET1, and hybrid materials synthesized: WET1-199 and SH-WET1-199.

Regarding the spectrum of Cu-WET1 material, three peaks were recognized O 1s (532 eV) and C 1s (285 eV) directly attributed to the fique fiber as previously described. Also, it was confirmed the impregnation process, because the peak related to Na atoms disappeared and, in its replacement, one of Cu 2p appeared at 934 eV after the ionic exchange between these two elements. The spectra of materials with metal-organic frameworks anchored WET-199 and SH-WET1-199, the Cu2p peak was shown to agree with reports made by other authors with the pristine HKUST-1 [26], suggesting the chemical environment of the copper into the synthesized materials was very similar between the impregnated copper and the subsequent MOFs growth. Additionally, for the SH-WET1-199 material, the presence of the S2p peak (164 eV) was

evidenced, a result of the MOF modification previously identified by techniques such as EDX and elemental analysis.

In Figure 5.2.23 the deconvolution of the C 1s peak common for all materials is shown. A total of 5 peaks were obtained in the energy region of 285 to 288 eV, associated with the group's C-C, C-O-C, C-OH, and OH-C = O, related to the structure of cellulose and hemicellulose inherent to fique fiber. Specifically, the OH-C = O group in the WET1-199 and SH-WET1-199 materials can also be related to the groups present in the BTC linker structure of the HKUST-1 metal-organic frameworks. Additionally, there was another common peak for all materials at 289 eV related to carbonate groups, which were particular to natural fibers such as fique as the result of the farming method and other parameters like the fertilizers used.

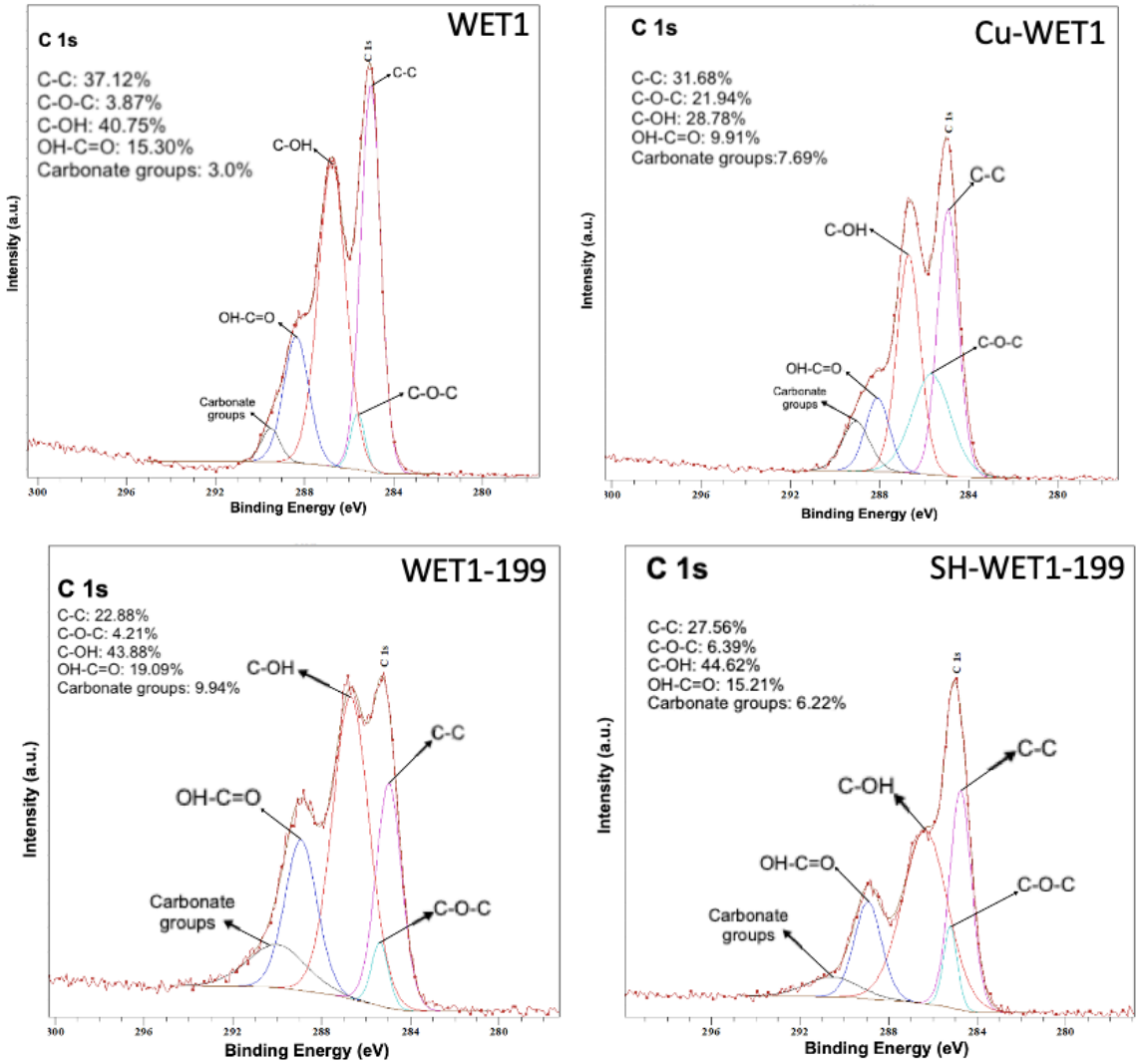


Figure 5.2.23. C 1s spectra of the functionalized fiber WET1, impregnated fiber Cu-WET1, and the hybrid materials synthesized: WET1-199 and SH-WET1-199 (Cont.).

Complementary to the carbon deconvolution (Figure 5.2.23), the O 1s deconvolution was carried out, the results were shown in Figure 5.2.24, in which again there were three peaks attributed to the fiber structure (WET1) corresponding to the binding energies at 530, 531 and 532 eV, recognized to the functional groups of COOR, R-OH, and C-O-C, respectively. Besides, the spectrum of the copper impregnated fiber (Cu-WET1) exposed a peak at 529 eV related to the O-Cu bond, allowing to affirm the seeding stage was carried out through the development of this type of bond, which in later stages became a potential nucleation point in which MOFs would grow onto the fiber surface. The binding energy of the O-Cu bond was maintained in WET1-199 and SH-WET1-199 in which the growth of HKUST-1 frames was carried out. The results obtained coincide with reports made by other authors [44].

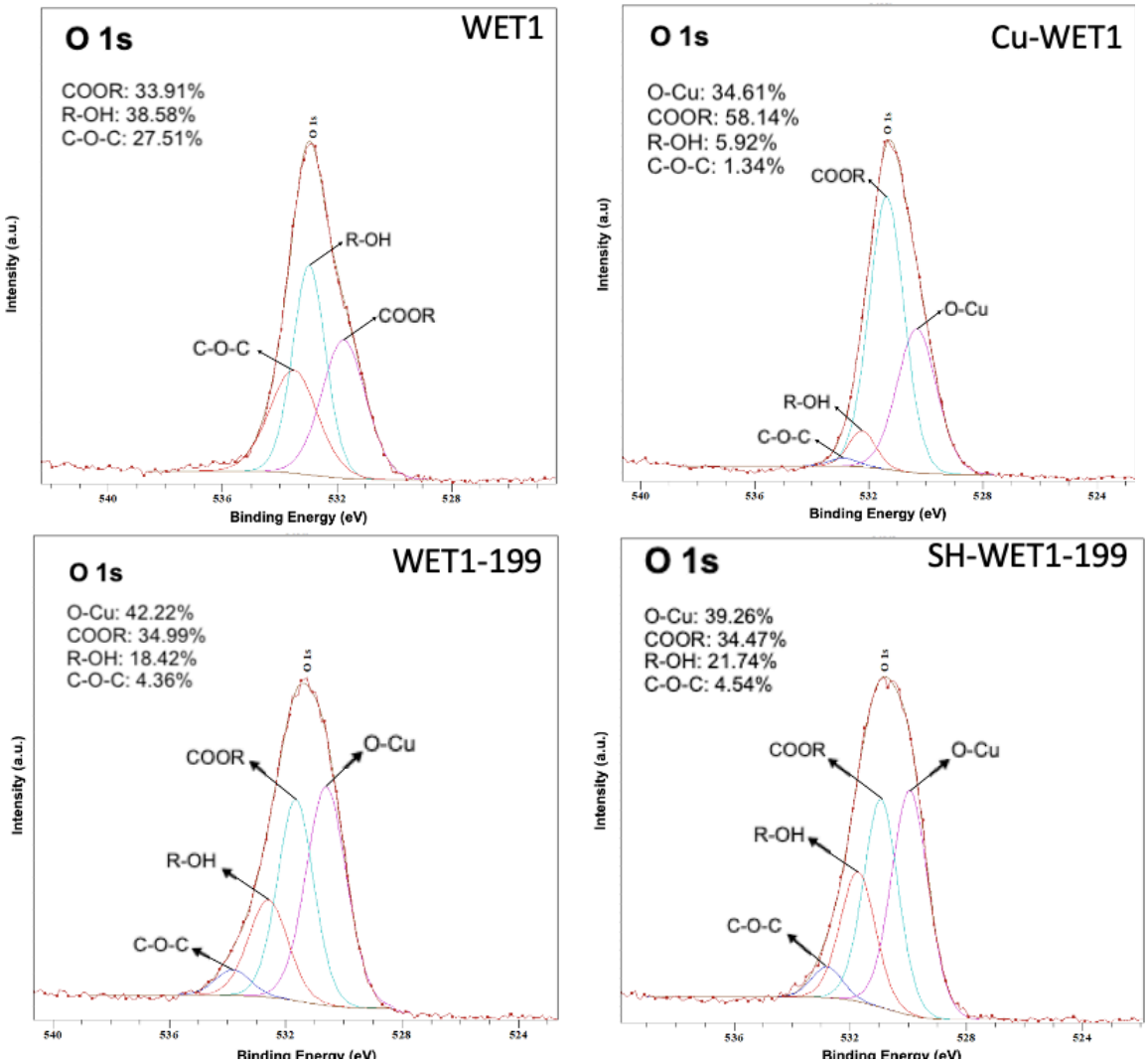


Figure 5.2.24. O 1s spectra of the functionalized fiber WET1, impregnated fiber Cu-WET1, and the hybrid materials synthesized: WET1-199 and SH-WET1-199 (Cont.).

Specifically, in Figure 5.2.25, materials in which a Cu 2p peak has been detected, the presence of two oxidation states in the binding energies located at 933 and 934 eV, correlated to the impregnation stage assigned to the oxidation states of Cu^{2+} $2p_{3/2}$ and Cu^{+} $2p_{3/2}$. Likewise, the appearance of an additional signal corresponding to Cu $2p_{1/2}$ was evidenced at 953 eV, this binding energy may be the result of coordinated copper metal centers within the structure of the metal-organic framework since this signal appeared in the two materials with MOFs anchored to the functionalized fique fiber.

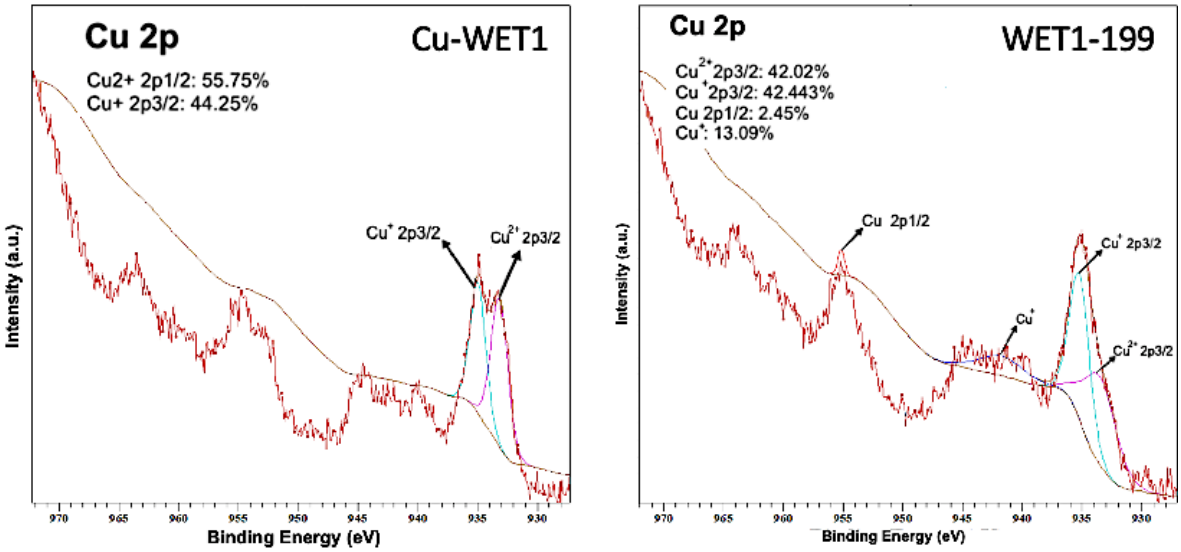


Figure 5.2.25. Cu 2p spectra of the functionalized fiber WET1, impregnated fiber Cu-WET1, and the hybrid materials synthesized: WET1-199 and SH-WET1-199.

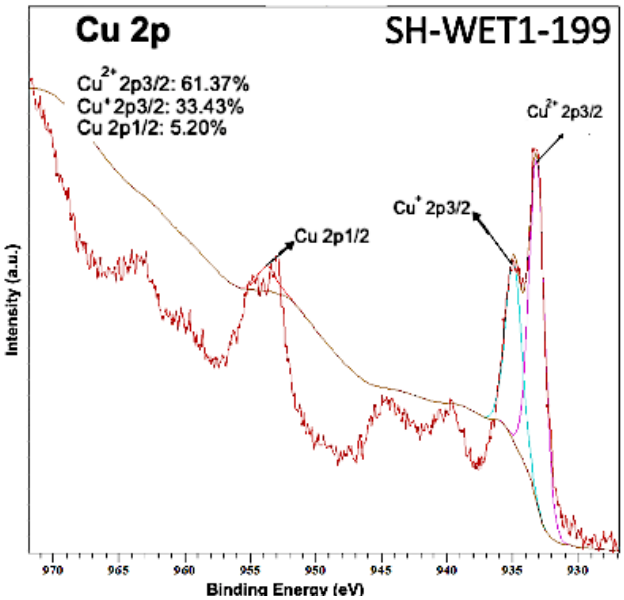


Figure 5.2.25. Cu 2p spectra of the functionalized fiber WET1, impregnated fiber Cu-WET1, and the hybrid materials synthesized: WET1-199 and SH-WET1-199 (Cont.).

Finally, in Figure 5.2.26 the deconvolution of S 2p exposed a peak located at 163.97 eV assigned to the thiol functional group, confirming that indeed the modification carried out utilizing the crystal poisons did allow obtaining this type of functional groups, complementing the information from characterizations made employing EDX.

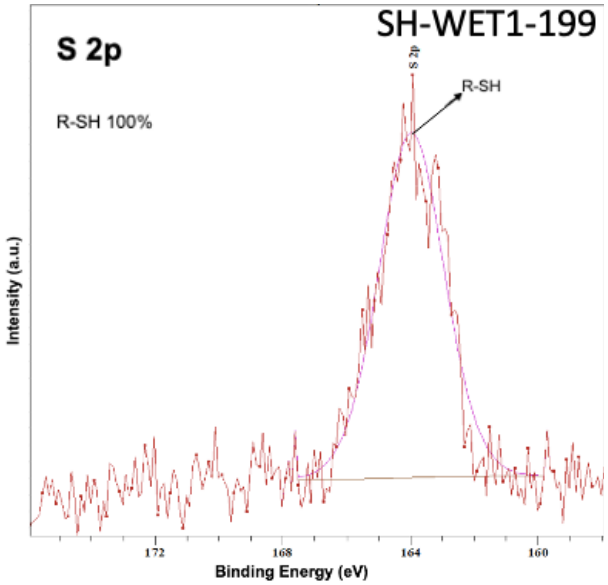


Figure 5.2.26. S 2p spectra of the functionalized fiber WET1, impregnated fiber Cu-WET1, and the hybrid materials synthesized: WET1-199 and SH-WET1-199.

- Mechanical characterization

To characterize the stiffness of the hybrid material produced, the Young's modulus or storage modulus by the dynamic mechanical analysis (DMA) was measured. The values measured on WET1-199 and SH-WET1-199 were 13.43 and 14.61 GPa. These values were lower than the Young's modulus of the functionalized fiber corresponding to 23.15 GPa. Probably, the reduction of the hybrid materials stiffness produced was related to the intra and intermolecular bonds of H_2 within the cellulose fibrils, which were affected by the presence of the metal-organic frameworks [45]. In addition, Dürholt *et al.* [46] reported the presence of mesopores in HKUST-1 reduces the crystals stability, a limitation was inherited from composite materials with fiber as a result of the combination of properties from each of the parts into the final material.

- Hydrolytic characterization

To assess the degradation of the synthesized hybrid materials, different characterization techniques were used to analyze how the solid was affected after being in contact with water;

also, the analysis of the remnant water was performed after the hybrid material was submerged in water.

The XRD patterns obtained for the synthesized hybrid materials after immersion in water at room temperature for 24, 48 and 72 h were reported in Figure 5.2.27. As expected, both materials presented the diffractograms combination of cellulose and metal-organic frameworks (HUST-1 and SH-HKUST-1), with the most important characteristic peaks of each one of the elements, 2 θ = 22° and 34° associated with cellulose and five dominant peaks related to HKUST-1 located at 2θ = 6°, 9.5°, 11.6°, 13.3° and 19°.

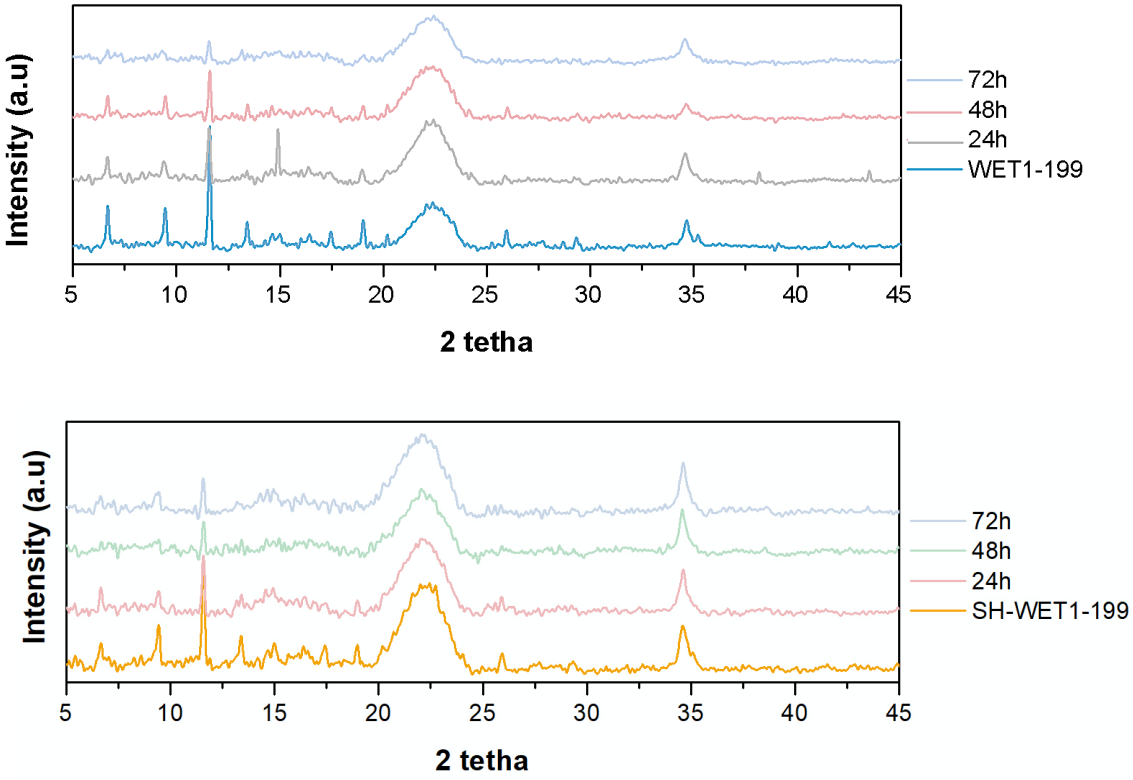


Figure 5.2.27. XRD patterns of WET1-199 (up) and SH- WET1-199 (down) samples, exposed to water for 24, 48 and 72 hours.

Over time the peaks linked to the fique fiber did not change, while the peaks related to MOFs showed variations between the two synthesized materials. SH-WET1-199 retained most of the peaks of the original material compared to WET1-199, for which the revealed peaks intensities became weaker as time got longer, after 72 h many of them disappeared and only the 11.6° Bragg diffraction was preserved, as a consequence of the possible reduction of the crystal

structure of the network caused by the hydration of HKUST-1[18]. From the peak located at 11.6°, constant in all the diffractograms throughout the analysis time, the crystallites size for the materials WET1-199 and SH-WET1-199 was calculated using the Scherer equation (Eq. 5.2.2), obtaining values of 54.1 and 48.5 nm, which did not change significantly during the experiments.

Nevertheless, it was interesting that in none of the materials a displacement of the peaks for higher or lower diffraction angles was perceived, nor was the development of new diffractions related to the existence of phases or copper compounds such as CuO, Cu_2O or $Cu(OH)_2$ [47]. This suggests the MOFs structure anchored to the fiber surface did not completely transform to H_3BTC and $Cu(OH)_2$, implying partial metal-organic frameworks structures degradation of HKUST-1 and SH-HKUST- 1.

Supported by the diffraction peaks preserved by the SH-WET1-199 material (6°, 9.5°, 11.6°, 13.3° and 19°), a profile matched to a type of crystalline phase from SH-HKUST- 1 associated with a layer structure of $[Cu_2OH(BTC)(H_2O)]$ was possible [28], which could be due to the partial hydrolysis of the original structure, also supported by the non-formation of $Cu(OH)_2$. Similar results were suggested by Pérez-Ramírez *et al.* [28]. However, despite a reduction in the crystallinity of both hybrid materials (higher in WET1-199 compared to SH-WET1-199), both retained some crystalline structure associated with powdered synthesized MOFs.
The synthesized materials morphology and their evolution after being in contact with water for 24, 48 and 72 h are presented in Figure 5.2.28. Each of the analyzed materials demonstrated a different behavior (WET1-199 and SH-WET1-199).

The micrographs of WET1-199 did not show significant changes in morphology after 24 h (Figure 5.2.28b) of exposure to water with respect to the original material (Figure 5.2.28a). Then, after 48 h the octahedral morphology of some HKUST-1 frames changed to more elongated shapes without significantly modified size (Figure 5.2.28c). Finally, at 72 h, the MOFs began to lose the sharp edges, maintaining the volume but at the same time showing some holes on the faces of its crystals (Figure 5.2.28d). During all the time when the material was exposed to the water, it was common to recognize changes in the crystallites but always kept the anchor onto the fiber, allowing to confirm the water affected the MOFs structure but not the attachment process.

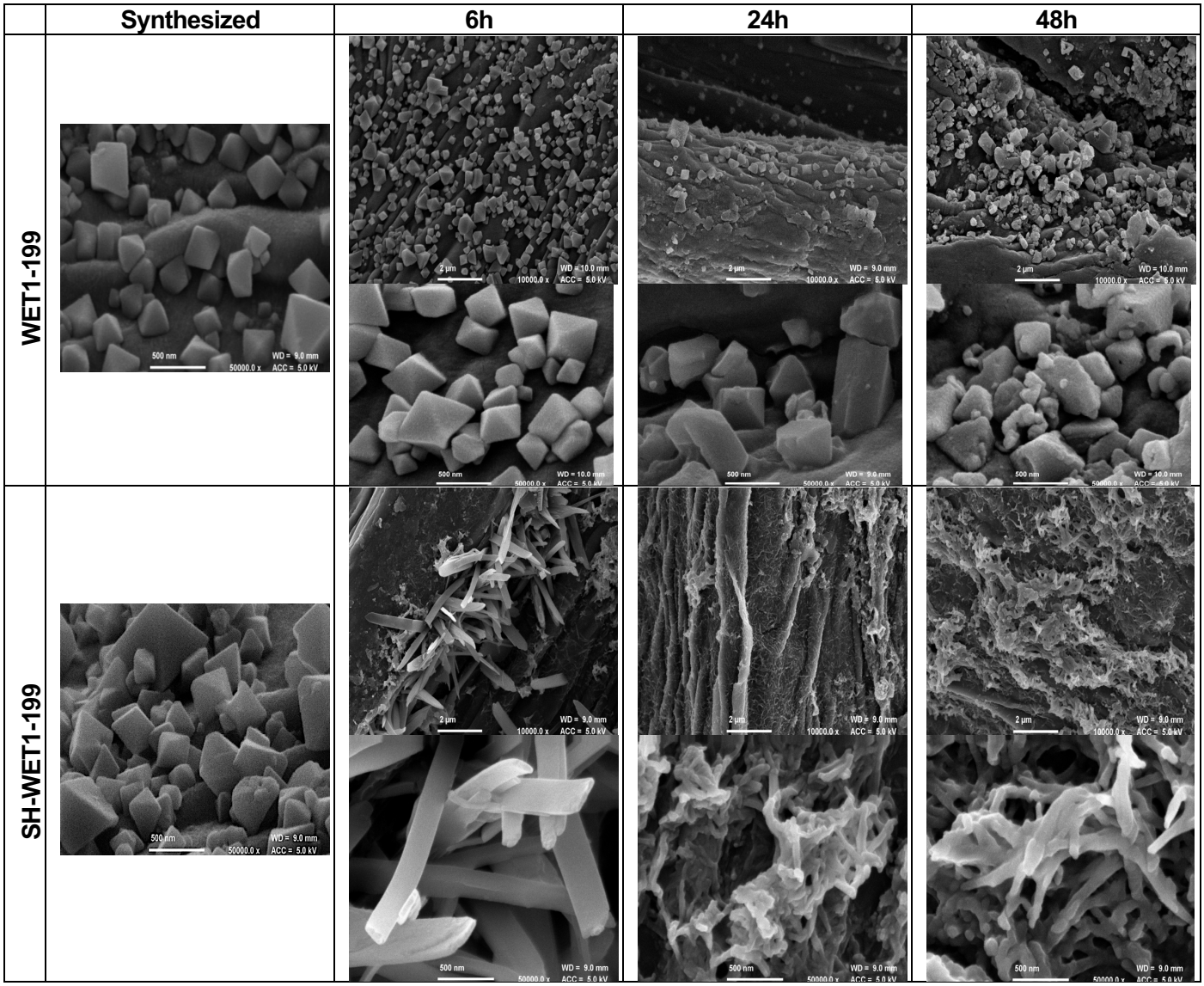


Figure 5.2.28. SEM micrographs of WET1-199 (up) and SH- WET1-199 (down) samples, exposed to water for 24, 48 and 72 hours.

Regarding, the SH-WET1-199 material, the crystals morphology was transformed completely after being submerged in water, from typical octahedral to stalactite-like crystals (Figure 5.2.28f). After 24 h, the new crystal morphology displayed an excellent definition of the contour, as well as the smooth and defect-free surface. The stalactites of the SH-HKUST-1 metal-organic frameworks became less defined after two days with water (Figure 5.2.28g), and finally, after three days the form of the stalactites was softly reduced (Figure 5.2.28h).

In general terms, the morphology changes observed in the two materials were indicators of the dissolution of the crystals, caused by the interaction with water by the variation of the contact time.

For neither of the two materials tested a definitive collapse of the frame was confirmed. Still, to the conversion to other phases or structures of each of the MOFs that formed the hybrid materials, it was even possible in parallel to carried out recrystallization processes.

Concerning the results obtained from the nitrogen adsorption-desorption isotherms, the surface areas were reduced from 43.4 to 12.4 $m^2 g^{-1}$ and from 53.7 to 9.8 $m^2 g^{-1}$ for WET1-199 and SH-WET1-199, respectively. Despite, the data obtained was not useful to contribute to the discussion of the material stability. Two parameters strongly influenced the measurements of these isotherms, which did not adequately describe the change in the structures area, i) natural materials such as natural fibers are characterized to have a non-porous structure and within the synthesized hybrid materials they constituted about 80 wt% of the total composition of the hybrid materials, ii) as already described in the wetness characterization, WET1-199 and SH-WET1-199 are materials with the tendency to have a low hydrophilicity surface, which was why the use of nitrogen as a probe molecule for the determination of surface area and pore distribution from various models was not considered the best alternative when carrying out this type of measurements [48].

The liquid remnant was studied under AAS (atomic absorption spectroscopy) and UV-VIS spectrophotometry. These techniques allowed to quantify the amount of copper and BTC, respectively, which were leftover into the solution. A blank using only the functionalized fique fiber was also performed. Figures 5.2.29 and 5.2.30 indicated the monitoring of the reaction over 72 h of the copper and linker. For the blank experiment, the values measured for both analytes were close to zero, confirming that no quantified amount of BTC or copper was the result of the metal-organic framework anchoring onto the fique fiber.

Figure 5.2.29 illustrated the evolution of the copper amount in solution of the powdered MOFs and of the hybrid materials during the exposure with water at room temperature. In general, all the materials led to a loss of approximately 2.5 mg of copper / g of solid material. These values stabilized after the first hour and did not demonstrate any more changes during the rest of the experiment time (up to 72 h), allowing to conclude the changes could occur in the metal-organic frameworks deposited on the fique were not related to effects produced from the metal centers.

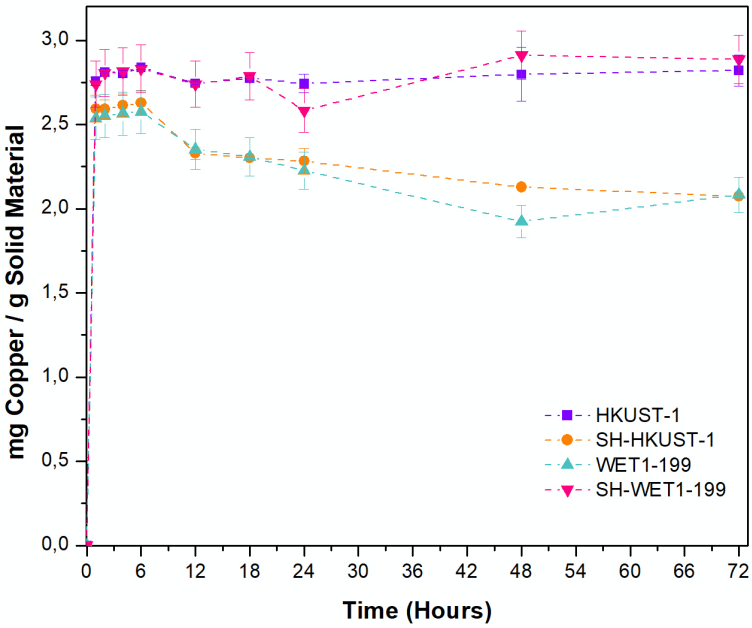


Figure 5.2.29. AAS measurement of copper in solution after being in contact with water and HKUST-1(purple data), SH-HKUST-1 (orange data), WET1-199 (turquoise data) and SH-WET1-199 (pink data) for 72 hours.

To determine the amount of BTC in solution over time, the Beer-Lambert law was used, the results of which are shown in Figure 5.2.30. It can be seen how the powdered metal-organic frameworks (HKUST-1 and SH-HKUST-1), used to be anchored onto the functionalized fiber, have a large amount of linker in solution compared to the crystallites grafted to the fiber, indicating the hybrid material did not behave in a similar way to pure powder, so it influenced the way of BTC was leached.

Furthermore, comparing the two hybrid materials (WET1-199 and SH-WET1-199), the presence of thiol groups reduced the leaching of BTC by approximately half. This is probably as a result of frame degradation because it caused steric effects that could play an important role within the material, confirming the increase in the metal-ligand bond resistance. In fact, a possible steric impediment was one of the feasible justifications for which amorphization of the organometallic network in the presence of water was reduced and slowed down.

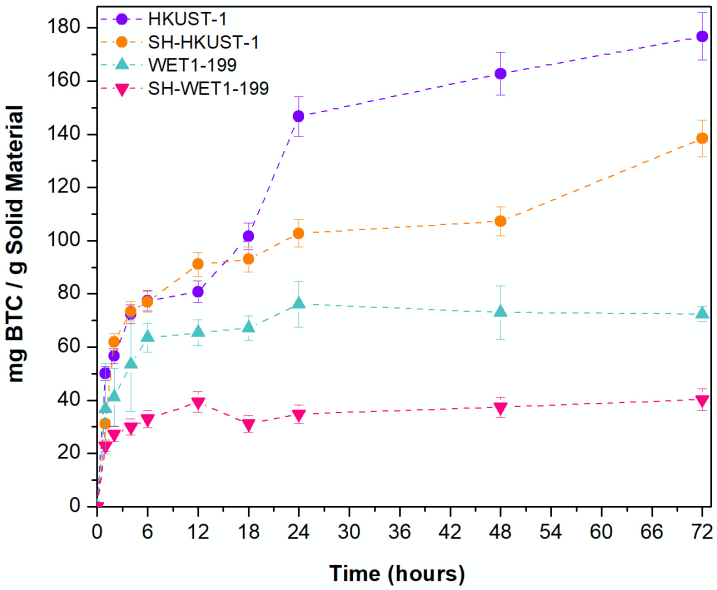


Figure 5.2.30. UV-VIS measurement of BTC in solution after being in contact with water and HKUST-1(purple data), SH-HKUST-1 (orange data), WET1-199 (turquoise data) and SH-WET1-199 (pink data) for 72 hours.

From the analysis and characterization carried out previously, the structure distortion of the MOFs deposited in the material can be suggested, mostly in WET1-199 compared to SH-WET1-199. That was not caused by linker hydrolysis but possibly by displacement of the ligand, due to the absence of copper hydroxide after 72 h of contact with water [49]. Conversely, ligand displacement occurs when a water molecule becomes trapped in the metal-ligand MO bond into the framework leading to a hydrated cation formation of and the release of a free ligand. In this particular case copper (Eq. 5.2.3), which would explain the increase in the concentration of BTC in solution reported by the quantification with UV-VIS spectrophotometry.

$$Mn^{+}{-}Ln^{-} + H_2O \rightarrow Mn^{+} - (OH_2) \cdots Ln^{-} \qquad \text{(Eq. 5.2.3)}$$

Also, the modification of HKUST-1 with thiol groups was a factor that contributed to reduce and slow down the disintegration effects of the network, caused mainly by the water influence on the organic linker. Thus, it was found the thiol groups helped to the chemical control and structural properties of the resulting material due to the steric effect. Similar results were achieved in other studies [23]. Furthermore, the use of supports was another approach that allowed controlling parameters like size, morphology and crystallinity of the products susceptible to be affected. There were also a variety of other factors, more complex functions to introduce will result in a more difficult reactivity towards the metal-linker bond destruction [1].

The average life of the materials produced from the combination of fique fibers and metal-organic frameworks based on Cu-BTC were comparable with the literature reports in terms of days. However, a direct comparison with all the details cannot be established due to differences in the characteristics of the composite materials, the reaction conditions with water and even the definition of stability in water used in this research, which change a lot within other authors. Despite the importance of studying novel materials such as MOFs, there are only a limited number of studies reporting the enhancement in hydrolytic properties. Improving the water stability of HKUST-1 was achieved by taking two of the main approaches, first, the modification of the external MOF surface through crystal poison to include thiol groups in the structure and produce the SH-HKUST-1 metal-organic frameworks; second, the use of supports such as lignocellulosic biomass promoted the MOFs anchoring, creating barriers and tools that serve as impediments to the network collapse or at least retard its destruction.

5.2.5 Conclusions

Pretreated and functionalized fique fibers were used as support of metal-organic frameworks HKUST-1 and SH-HKUST-1. Two anchorage techniques were evaluated: direct and secondary growth. The secondary or seeded growth allowed the anchorage of approximately 20 wt% of MOFs onto the functionalized fique fiber, meanwhile the direct growth non evidenced chemical anchored. The addition order of the reagents during the MOFs deposition was a determining factor to achieve the necessary conditions for the growth and nucleation of the crystallites on the lignocellulosic substrate, which did not happen in the liquid solution. In addition, it was discussed how the MOFs anchoring to the surface could be controlled via experimental parameters of the synthesis process, such as temperature, protonating agents, solvents, among others.

The anchoring strength was influenced by the appropriate support functionalization. The fiber functionalized with carboxylate groups was the one that guaranteed a true anchorage, through bonds that allowed the crystals growth from nucleation points formed by the ion exchange between the metal centers of the precursor salts and the carboxylate groups of the fique fiber. The copper contained in HKUST-1 was easily crosslinked, limiting leaching of MOFs after contact with water. Techniques such as XPS, SEM and ICP confirmed the adequate grafting of the crystallites, to generate the hybrid materials of interest. WET1-199 and SH-WET1-199 presented a relatively homogeneous monolayer distribution of crystals, structurally and morphologically well defined.

A complete chemical, morphological, thermal, mechanical, hydrolytic and surface characterization was performed for the resulting hybrid materials. Both materials were found to have similar wetness, octahedral shape, and size properties (50 to 300 nm). Still, it was relevant to notice, the modification with crystal poison to include thiol groups to HKUST-1 increased the hydrolytic stability of SH-WET1-199 compared to WET1-199, since after 72 h the metal-organic structure did not completely collapse.

5.2.6 References

1. Kirchon, A., Feng, L., Drake, H. F., Joseph, E. A. & Zhou, H. C. From fundamentals to applications: a toolbox for robust and multifunctional MOF materials. *Chem. Soc. Rev.* **47**, 8611–8638 (2018).

2. Chacón, M., Blanco, C., Hinestroza, J. & Combariza, M. Biocomposite of nanostructured MnO_2 and fique fibers for efficient dye degradation. *Green Chem.* **15**, 2920 (2013).

3. Hidalgo, M., Muñoz, M. & Quintana, K. Análisis mecánico del compuesto polietileno aluminio reforzado con fibras cortas de fique en disposición bidimensional. *Rev. Latinoam. Metal. y Mater.* **32**, 89–95 (2011).

4. Arjona, S., Perdomo, F. & Gutiérrez, R. Ecolaminados de pead-fibras de fique. *Rev. Ing. y Compet.* **3**, 43–49 (2001).

5. Castellanos, O., Torres, L. & Rojas, J. *Agenda Prospectiva de Investigación y Desarrollo Tecnológico para la Cadena Productiva de Fique en Colombia*. *Ing. Inv.* **29**, 1-30 (2009).

6. Kärger, J., Ruthven, D. & Theodorou, D. *Diffusion in Nanoporous Materials*. (Wiley, 2012).

7. Cirujano, F. & Llabrés, F. Metal organic frameworks as nanoreactors and host matrices for encapsulation. in *organic nanoreactors.* (Academic Press, 2016).

8. Sosa, J. D. *et al.* Metal–organic framework hybrid materials and their applications. *Crystals.* **8**, 1-23 (2018).

9. Dhaka, S. *et al.* Metal–organic frameworks (MOFs) for the removal of emerging contaminants from aquatic environments. *Coord. Chem. Rev.* **380**, 330–352 (2019).

10. Zhu, Q.-L. & Xu, Q. Metal–organic framework composites. *Chem. Soc. Rev.* **43**, 5468–5512 (2014).

11. EPA. *Method 3050b: acid digestion of sediments, sludges, and soils*. https://www.epa.gov/sites/prod uction/files/2015-12/documents/3050b.pdf (1996).

12. Hassan, A. F. Synthesis of carbon nano-onion embedded metal–organic frameworks as an efficient adsorbent for cadmium ions: kinetic and thermodynamic studies. *Environ. Sci. Pollut. Res.* **26**, 24099–24111 (2019).

13. Schellbach, S. L., Monteiro, S. N. & Drelich, J. W. A novel method for contact angle measurements on natural fibers. *Mater. Lett.* **164**, 599–604 (2016).

14. Patterson, A. L. The Scherrer formula for x-ray particle size determination. *Phys. Rev.* **56**, 978–982 (1939).

15. Arshadi, M., Abdolmaleki, M. K., Mousavinia, F., Foroughifard, S. & Karimzadeh, A. Nano modification of NZVI with an aquatic plant Azolla filiculoides to remove Pb(II) and Hg(II) from water: Aging time and mechanism study. *J. Colloid Interface Sci.* **486**, 296–308 (2017).

16. Barrett, E. P., Joyner, L. G. & Halenda, P. P. The determination of pore volume and area distributions in porous substances. Computations from nitrogen isotherms. *J. Am. Chem. Soc.* **73**, 373–380 (1951).

17. Ciolacu, D., Ciolacu, F. & Popa, V. I. Amorphous cellulose—structure and characterization. *Cellul. Chem. Technol.* **45**, 13 (2011).

18. Al-Janabi, N. *et al.* Mapping the Cu-BTC metal-organic framework (HKUST-1) stability envelope in the presence of water vapour for CO2 adsorption from flue gases. *Chem. Eng. J.* **281**, 669–677 (2015).

19. Fechete, I., Wang, Y. & Védrine, J. C. The past, present and future of heterogeneous catalysis. *Catal. Today* **189**, 2–27 (2012).

20. Stock, N. & Biswas, S. Synthesis of metal-organic frameworks (MOFs): routes to various mof topologies, morphologies, and composites. *Chem. Rev.* **112**, 933–969 (2012).

21. Shi, R. *et al.* Cu-based metal–organic framework/activated carbon composites for sulfur compounds removal. *Appl. Surf. Sci.* **394**, 394–402 (2017).

22. Fan, C. *et al.* Sustainable synthesis of HKUST-1 and its composite by biocompatible ionic liquid for enhancing visible-light photocatalytic performance. *J. Clean. Prod.* **208**, 353–362 (2019).

23. Zhu, Q. L. & Xu, Q. Metal-organic framework composites. *Chem. Soc. Rev*. **43**, 5468-5512 (2014).

24. Liu, J. & Wöll, C. Surface-supported metal-organic framework thin films: Fabrication methods, applications, and challenges. *Chem. Soc. Rev.* **46**, 5730-5770 (2017).

25. Schelling, M., Kim, M., Otal, E. & Hinestroza, J. Decoration of cotton fibers with a water-stable metal–organic framework (UIo-66) for the decomposition and enhanced adsorption of micropollutants in water. *Bioengineering.* **5**, 1-11 (2018).

26. da Silva Pinto, M., Sierra, C. & Hinestroza, J. In situ synthesis of a Cu-BTC metal-organic framework (MOF 199) onto cellulosic fibrous substrates: Cotton. *Cellulose* **19**, 1771–1779 (2012).

27. Liu, J. *et al.* Preparation and characterization of carboxymethylcellulose hydrogel fibers. *J. Eng. Fiber. Fabr.* **13**, 6-13 (2018).

28. Álvarez, J. R. *et al.* Structure stability of HKUST-1 towards water and ethanol and their effect on its CO2 capture properties. *Dalt. Trans.* **46**, 9192–9200 (2017).

29. Todaro, M. *et al.* Decomposition process of carboxylate MOF HKUST-1 unveiled at the atomic scale level. *J. Phys. Chem. C* **120**, 12879–12889 (2016).

30. Cheng, Y. *et al.* Reversible structural change of Cu-MOF on exposure to water and its CO2 adsorptivity. *Langmuir.* **25**, 4510–4513 (2009).

31. Lawson, S., Hajari, A., Rownaghi, A. A. & Rezaei, F. MOF immobilization on the surface of polymer-cordierite composite monoliths through in-situ crystal growth. *Sep. Purif. Technol.* **183**, 173–180 (2017).

32. Occelli, M. L., Olivier, J. P., Petre, A. & Auroux, A. Determination of pore size distribution, surface area, and acidity in fluid cracking catalysts (FCCS) from nonlocal density functional theoretical

models of adsorption and from microcalorimetry methods. *J. Phys. Chem. B.* **107**, 4128–4136 (2003).

33. Brunauer, S., Emmett, P. H. & Teller, E. Gases in multimolecular layers. *J. Am. Chem. Soc.* **60**, 309–319 (1938).

34. Kačík, F. *et al.* Chemical alterations of pine wood saccharides during heat sterilisation. *Carbohydr. Polym.* **6**, 681–6 (2015).

35. Bastidas, K., Zea, H. & Sierra, C. Wastewater treatment using an iron nanocatalyst supported on Fique fibers. (Universidad Nacional de Colombia, 2016).

36. Brebu, M. & Vasile, C. Thermal degradation of lignin - A review. *Cellul. Chem. Technol.* **44**, 353–363 (2010).

37. Gao, P. & Liu, D. Facile synthesis of copper oxide nanostructures and their application in non-enzymatic hydrogen peroxide sensing. *Sensors Actuators, B Chem.* **208**, 346–354 (2015).

38. Hendon, C. H. & Walsh, A. Chemical principles underpinning the performance of the metal-organic framework HKUST-1. *Chem. Sci.* **6**, 3674–3683 (2015).

39. Güven, O., Monteiro, S. N., Moura, E. A. B. & Drelich, J. W. Re-emerging field of lignocellulosic fiber – polymer composites and ionizing radiation technology in their formulation. *Polym. Rev.* **56**, 702–736 (2016).

40. Antwi-Baah, R. & Liu, H. Recent hydrophobic metal-organic frameworks and their applications. *Materials*. **11**, 1-11 (2018).

41. Wang, C., Liu, X., Keser Demir, N., Chen, J. P. & Li, K. Applications of water stable metal-organic frameworks. *Chem. Soc. Rev*. **45**, 5107–5134 (2016).

42. Chattopadhyay, D. P. Cationization of cotton for low-salt or salt-free dyeing. *Indian J. Fibre Text. Res.* **26**, 108–115 (2001).

43. Wang, C., Qian, X. & An, X. In situ green preparation and antibacterial activity of copper-based metal–organic frameworks/cellulose fibers (HKUST-1/CF) composite. *Cellulose.* **22**, 3789–3797 (2015).

44. Zhou, L., Niu, Z., Jin, X., Tang, L. & Zhu, L. Effect of lithium doping on the structures and CO_2 adsorption properties of metal-organic frameworks HKUST-1. *ChemistrySelect*. **3**, 12865–12870 (2018).

45. Gañán, P. & Mondragon, I. Surface modification of fique fibers. Effects on their physico-mechanical properties. *Polym. Compos.* **23**, 383–394 (2002).

46. Dürholt, J. P., Keupp, J. & Schmid, and R. The impact of mesopores on the mechanical stability of HKUST-1: A Multiscale Investigation. *Eur. J. Inorg. Chem.* **2016**, 4517–4523 (2016).

47. Küsgens, P. *et al.* Characterization of metal-organic frameworks by water adsorption. *Microporous Mesoporous Mater.* **120**, 325–330 (2009).

48. Trens, P., Denoyel, R. & Glez, J. C. Comparative adsorption of argon and nitrogen for the characterisation of hydrophobized surfaces. *Colloids Surfaces A Physicochem. Eng. Asp.* **245**, 93–98 (2004).

49. Low, J. *et al.* Virtual high throughput screening confirmed experimentally: Porous coordination polymer hydration. *J. Am. Chem. Soc.* **131**, 15834–15842 (2009).

6. Potential application of hybrid materials combining MOFs and natural fibers in the water treatment of emerging contaminants.

6.1. Mercury (II) adsorption from wastewater using hybrid material combining fique fiber and metal-organic frameworks

6.1.1 Abstract

High concentrations of heavy metals (HMs) such mercury in water bodies create important environmental problems in humans and aquatic organisms, through the food chain. In this study, the removal of mercury from synthetic water by adsorption was evaluated using five materials: fique fiber, raw (R), pretreated (WE), functionalized (WET1), fique fiber with metal-organic framework HKUST-1 (WET1-199), and fiber with SH-HKUST-1 where the BTC linker was modified by thiol groups on the HKUST-1 structure (SH-WET1-199). Adsorption studies were carried out in a batch system using the 5 materials described above under conditions of ambient pressure and temperature, pH = 7, and 40 ppb as initial concentration of mercury. When comparing the materials with anchored MOFs, SH-WET1-199 demonstrated to be more selective for adsorption of Hg^{2+} ions than WET1-199, the adsorption capacities achieved in 30 min were 44.4 and 79.9 mg g^{-1}, respectively. To analyze how adsorption was carried out in the studied materials, data collected experimentally were adjusted to equilibrium and kinetic models.

Pseudo-second order models properly describe the adsorptions on the R, WE, WET1-199 and SH-WET1-199 materials, meanwhile for the WET1 material the Elovich model presents a better fitting. However, of all the materials tested, the functionalized fiber showed the highest Hg^{2+} adsorption in water. For the later material, additional adsorption experiments varying the pH, mercury initial concentration and solid adsorbent/liquid ratio (S/L). Thermodynamic results showed the adsorption on WET1 is a spontaneous and endothermic process, the maximum

adsorption capacity reached was 120 mg g^{-1} at 20 °C without significant changes at 30 min, with a mercury removal efficiency of 94% at pH = 7, S/L ratio of 0.4 g L^{-1}. This process was attributed to the interactions by stacking Π-Π, hydrogen bonds and electrostatic interactions, and was confirmed by adjusting the experimental data of WET1 to the Elovich model. Besides, this material kept high adsorption performance even after six cycles of use, clearly demonstrating the fique fiber functionalized with carboxylate groups onto its surface could act as useful and effective adsorbent to remove HMs ions from contaminated water in the environment. All monitoring of the mercury concentration in solution was carried out employing an electrochemical methodology using a single screen-printed electrode probe; all measurements were validated against atomic absorption spectroscopy (AAS), showing an excellent agreement.

Key words: mercury, fique fiber, metal-organic frameworks, adsorption, removal.

6.1.2 Introduction

Heavy metal (HM) is a metal with a density greater than 5 g cm^{-3} [1], some examples found in water bodies are: lead (Pb), mercury (Hg), cadmium (Cd), arsenic (As), chromium (Cr), uranium (U), selenium (Se), zinc (Zn), silver (Ag), gold (Au) and nickel (Ni). They have become an important environmental problem since they generate acute toxicity in humans and aquatic organisms [2]. Exposure to high concentrations of HMs affects the growth and development of living beings and their environment, causing biochemical disorders [3]. Although these types of metals do not have a role in human homeostasis, they do damage to organs through defects which are classified as carcinogenic [4]. For example, synaptic loss and brain dysfunction through alteration and impairment of fatty acid metabolism, also, can damage central nervous function, lungs, kidneys, liver, and bones [3].

There are two sources of heavy metals in liquid effluents: geological and anthropogenic. The first one is originated in water reservoirs, the atmosphere, or the soil, as a consequence of rocks interaction with the environment, transport occurs and generates an HMs redistribution [5]. The second source is the result of human mismanagement of water resources. The primary origin of drinking water supply is groundwater, which may be contaminated with organic and inorganic compounds resulting from agricultural, industrial, mining, urban areas, landfills, sewage systems, and railways [5]. These types of emissions are the greatest concern today, because there is a lack

of legislation regarding these pollutants, specifically for mining that produces high traces of HMs such as: As, Cu, Cd, Pb, Hg.

From all the HMs present in the environment, the World Health Organization (WHO) has found Pb, Cd, and Hg as the main threats to human health, which is why they are constantly reviewed by international regulatory bodies [6]. This problem is evident throughout the world, developed countries such as the US have been vulnerable, i.e., the water crisis in Flint, Michigan, generated by municipal pipes that leach lead to drinking water. However, in developing countries exposure to HMs is much higher as a result of minimal environmental legislation, lack of resources, and awareness; this fact puts millions of people at risk [4].

The remediation methods of HMs used on an industrial scale are standard, involving chemical precipitation, adsorbents or membranes, but they all have common disadvantages such as high economic and energy costs, low removal efficiency, difficult regeneration, and reduced industrial scaling. Mercury (Hg) is considered an important pollutant in the mining process related to gold (remarkably in illegal extraction). Mercury has a silver color, high density, is liquid at room temperature, and produces toxic effects in humans [7]. Hg presents interesting physicochemical properties like high thermal and electrical conductivity, surface tension, and chemical stability. As a result of these properties, this metal has been used in the manufacturing of thermometers and measuring instruments, dentistry, batteries, electronic, electrical, and lighting components [8].

Mercury could naturally be in the environment mainly by the earth's erosion and volcanic activity [7]. Despite this, most of the Hg released into the environment is related to industrial processes like illegal mining, coal burning, and chlorination plants [9]. The main mercury species are inorganic, Hg^{2+}, and methylmercury (CH_3Hg (I)), although it can also be in the metallic form [10]. The most common in water sources is methylmercury, this compound goes into the human body through food and develops a high risk due to its storage in the autotrophs organism membranes; the heterotrophic organisms are feed with autotrophs organism, and it generates the bioaccumulation in the food chain, that finally are consumed by humans [10].

Mercury is a potentially harmful substance in the ecosystems; it depends on the compound state (organic, elemental, inorganic), exposure degree, exposure source, absorption route concentration, and interaction with other compounds. It can produce health issues like brain

damage, kidney damage, lung, digestive system problems, tremors, changes in vision and hearing, insomnia, memory disorders, nausea, vomit, diarrhea, seizures, among others [11].

Recent reports have reported the presence of mercury (Hg^{2+}) in liquid effluents in a concentration range of 200 - 100,000 ppb and methylmercury with approximately 50 ppb [12]. The permissible limit of mercury in drinking water is 2 ppb according to the US Environmental Protection Agency (EPA), [12] and 6 ppb for the WHO [6]. Communities close to the gold mining industry in developing countries are exposed to high mercury concentrations, generating public health problems, due to the absence of restrictive regulations and the use of rudimentary practices, [7]. One of the main Colombian mining areas is located in Antioquia, where small-scale mining processes are additionally controlled by guerrillas [13].

This problem is alarming since to obtain 1 kg of gold, after the amalgamation process, between 3 to 5 kg of mercury is released into the environment [14]. This fact has put Colombia in the third-largest source of mercury emissions in the world, after China and Indonesia [13]. Gold mining is an important economic activity in the country, with an average production of 30 tons per year; however, this process produces irreversible environmental damage, evidenced by the discharge of approximately 19.86 kg of mercury per month into the environment, including the atmosphere and rivers of Segovia and Remedios [15]. Another similar case is the Choco department, where gold mining is promoted through the burning of amalgam [16]. In consequence, the law National Legislative Decree 3930 of 2010 allows as the maximum concentration of mercury in drink water as 2 ppb [17].

To evaluate the application of novel materials in the treatment of effluents contaminated with HMs such as mercury, in this study mercury adsorption removal from synthetic water was evaluated using five materials synthesized from fique fiber, raw (R), pretreated (WE), functionalized (WET1), fique fiber with metal-organic framework HKUST-1 (WET1-199), and fiber with SH-HKUST-1, MOF corresponding to the HKUST-1 modification by inserting thiol groups in BTC linker (SH-WET1-199). Also, the effect of parameters like initial concentration of mercury, solid/liquid ratio, temperature, and pH was explored for the adsorption process. In addition, the monitoring of mercury concentrations was done by an electrochemistry technique, validated after using atomic absorption spectroscopy coupled with a hydride generator.

6.1.3 Materials and methods

6.1.3.1 Chemicals and materials

Hydrochloric acid (37%) and mercury standard solution (1000 mg/L) as a model contaminant were provided from Merck KGaA, Germany. The mercury solution was prepared with deionized water (>18 MΩ/cm, Milli-Q) obtained from a water purification system. The pH of the working solution was adjusted with HCl (0.1 M) and stored at a temperature below 4 °C after the electrochemical analysis. (Reagents used in atomic absorption).

6.1.3.2 Instrumentation

Square wave anodic stripping voltammetry (SWASV) was performed with a potentiostat Gamry 1000T ® using Gamry Echem Analyst software. Electrodes screen-printed (DRP-220BT) with low-temperature curing ink were used. Working (4 mm diameter) and counter electrodes are made of gold and the reference electrode is made of silver, as well as the electrical contacts. Plastic containers (20 mL) were used to store the working solutions during the electrochemical analysis. A Toledo LE427 pH-meter was used for the measurement of the pH.

The potentiostat was calibrated using the Gamry UDC4 Calibration Circuit, which was protected with a faraday cage to eliminate ambient noise. Then, the electrodes were conditioned through cyclic voltammetry (CV) applying 5 cycles with a potential sweep between -0.1 to +0.8 V at a step size of 4 mV. Cyclic voltammetry was performed with a conditioning potential of +0.7 V and a scan rate of 49.9 mV/s for 15 s in 0.1 M HCl solution, according to previous works [1].

The validation of the electrochemical method was determined by cold vapor atomic absorption spectrometry (CVAAS) in a Hitachi z-8000 atomic absorption spectrometer equipped with a hydride generator, using the injection method of an aliquot of 1000 µL. The T-cell quartz tube was placed (Length 120 mm and ID 5mm) directly onto the nitrous oxide/acetylene burner, which was equipped with a T-cell tube holder. The wavelength used for the analyte determination was: Hg 253.7 nm, with a 0.5 nm spectral bandpass, the solution of 0.3% (w/v) sodium borohydride in 0.5% (w/v) NaOH was prepared as a reducing agent.

6.1.3.3 Experimental set-up and procedure

Fique fiber under five different conditions were tested, these include: raw (R), pretreated (WE), functionalized (WET1), fique fiber with metal-organic framework HKUST-1 (WET1-199), and fiber with SH-HKUST-1, MOF corresponding to the HKUST-1 modification by inserting thiol groups in BTC linker (SH-WET1-199).

Mercury solutions of 250 mL and a mass of fiber were introduced in a jacketed glass batch reactor, with continuous agitation controlled by the motor IKA 260; all the experiments were done in triplicate. Each run lasted 30 min. All experiments were performed at 20 °C and 551 mmHg. Every 5 min an aliquot was taken and analyzed by electrochemistry. Preliminary experiments were performed to determine the effect of the solid/liquid ratio (50, 100, 200 mg of material) and the stirring (50, 100, 200 rpm) on the adsorption and to establish proper operational conditions.
The metal ion adsorption capacity in solution was determined for each value of initial concentration, with experimental data equilibrium concentration and initial concentration, using the following Eq.6.1.1.

$$q_e = \frac{(C_i - C_e)V}{w} \qquad \text{(Eq. 6.1.1)}$$

Where q_e is the equilibrium adsorption capacity (mg/g), C_i is the initial mercury concentration (adsorbate) in solution (mg/L), C_e is the solute concentration in the equilibrium (mg/L), V is the mercury solution and (L) w is the adsorbent mass (g).

The removal percentage of the mercury (II) was expressed as Eq. 6.1.2:

$$\text{Removal}\ (\%) = \frac{(C_o - C_e)}{C_0} x\ 100\% \qquad \text{(Eq. 6.1.2)}$$

Where, C_o and C_e are the initial and equilibrium concentrations of mercury (II) ions in solution.
After identifying the material with the best adsorption capacity; A Box- Behnken design of experiments with response surface (DOE) was implemented, which used the maximum and minimum levels of the three factors evaluated in the mercury removal. This type of DOE includes a triplicate center point, for a total of 15 experiments. A summary of the experimental condition for the DOE is presented in Table 6.1.1. Minitab 16 Statistical Software served to identify the contribution of each variable and its interaction in the removal of mercury through the respective statistical analysis of the data obtained. A linear regression method, as the one described in

Equation 6.1.3, was used to set the second-order polynomial experimental data and to identify relevant terms of the model.

$$Y = \beta_0 + \sum \beta_i x_i + \sum \beta_{ii} x_{ii}^2 + \sum \beta_{ij} x_i x_j \qquad \text{Eq. 6.1.3}$$

Where β_0 is the compensatory term; β_i is the dependent term or the linear effect of factor input x_i; *ii* is the quadratic effect input factor x_i and β_{ij} is the effect of interaction between the linear input factor x_i and x_j.

Before starting the adsorption experiments, the initial pH was measured using a Toledo LE427 pHmeter. The initial pH of the solutions to be treated was adjusted with the addition of a diluted solution of NaOH or HCl; then the adsorbent material was added to the solution and this was the zero time.

Table 6.1.1. Factors assessed in mercury removal using an adsorbent from fique fiber.

Factor	Level		
	Low	**Medium**	**High**
pH	4	7	10
$[Hg]_o$ (ppb)	20	40	60

The DOE provided the conditions under which the mercury removal was the most efficient to perform two new sets of experiments, the first one investigates the temperature effect (20, 45 and 60 °C), the second set of experiments evaluated the adsorbent life cycles. Besides, regeneration study was done using a Bransonic Ultrasonic ultrasound at 42 kHz and 100 W, 100 mg of fiber tested in mercury removal was submerged in an Erlenmeyer containing 100 mL of miliQ water for 15 min to promote the desorption of mercury ions from the fiber. The material regenerated was finally dried at room temperature during the night to be reused in the next adsorption cycle.

6.1.3.4 Models analysis

The removal of mercury from synthetic water solution consists of many steps:

a) Transport of mercury from the bulk solution to the adsorbent interface.
b) Mass transport across the limit film layer by diffusion.
c) Adsorption onto external surface sites of the adsorbent.
d) Internal mass transport of mercury within the pores of the adsorbent

To investigate the mercury (II) adsorption mechanism onto the adsorbent from aqueous solutions, kinetic and adsorption isotherm models were analyzed.

- Adsorption isotherms

1) Langmuir isotherm

Langmuir isotherm model [18] describes monolayer adsorption and the adsorption sites have equal affinity towards adsorbate. The mathematical expression for this model can be represented as the equation (6.1.4):

$$q_e = \frac{q_m a_L C_e}{1 + a_L C_e} \qquad (\text{Eq. } 6.1.4)$$

Where q_m (mg g^{-1}) is the maximum adsorption capacity of the material, a_L (L mg^{-1}) is the Langmuir constant that describes the adsorption/desorption equilibrium for each reactant in contact with a surface, q_e (mg g^{-1}) is the equilibrium adsorption capacity of the adsorbent and C_e (mg L^{-1}) is the equilibrium concentration of the adsorbate in the solution. The linear transformation of the Langmuir isotherm is in the Eq. 6.1.5

$$\frac{C_e}{q_e} = \frac{1}{q_m} C_e + \frac{1}{q_m a_L} \qquad (\text{Eq. } 6.1.5)$$

A mathematical expression developed by Webber and Chak- ravorti (Eq. 6.1.6) has been used to test the adsorption process favorability [19]:

$$R_L = \frac{1}{1 + K_L C_O} \qquad (\text{Eq. } 6.1.6)$$

Where R_L is the separation factor, it is a dimensionless term and *Co* is the adsorbate initial concentration (mg L^{-1}). R_L indicates the adsorption nature to be unfavorable ($R_L > 1$), linear ($R_L = 1$), favorable ($0 < R_L < 1$), or irreversible ($R_L = 0$).

2) Freundlich isotherm

The Freundlich isotherm is an empirical equation [20] given as Eq. 6.1.7; it describes multilayer adsorption that takes place on a heterogeneous surface, and adsorption capacity is related to the metal ions concentration at equilibrium.

$$q_e = K_f C_e^{1/n} \qquad (\text{Eq. } 6.1.7)$$

Where K_F (mg g^{-1} $(L/mg)^{1/n}$) is the Freundlich isotherm constant, n adsorption intensity, C_e (mg L^{-1}) equilibrium concentration of mercury (II) and q_e (mg g^{-1}) amount of metal adsorbed per gram of adsorbent at equilibrium. The linear form of this isotherm is given by the Eq. 6.1.8.

$$\log(q_e) = \frac{1}{n}\log(C_e) + \log(K_f) \qquad (\text{Eq. } 6.1.8)$$

Plotting log (q_e) versus log (*Ce*) allowed to calculate the Freundlich constant K_F and 1/*n* from the intercept and slope, respectively. The constant K_F is an indicator of the sorption capacity, the constant n represents the strength of the adsorptive bond (heterogeneity factor) [21]. If *n* = 1, the partition between two phases is independent of concentration, *n*>1 indicates favorable adsorption with high heterogeneity, and *n*<1 shows cooperative adsorption.

3) Temkin isotherm

This model contains a factor that explicitly takes into account of mercury (II) ions – adsorbent interactions [22]. Assumes the heat of adsorption of all molecules in the layer linearly decreases with the coverage on the adsorbent surface, ignoring very low and large concentration values. The Temkin isotherm is stated as Eq. 6.1.9 and 6.1.10.

$$q_e = B\ln(A_T) + B\ln(C_e) \qquad (\text{Eq. } 6.1.9)$$

$$B = \frac{R\mathrm{T}}{b_T} \qquad (Eq. 6.1.10)$$

Where q_e (mg g^{-1}) is the equilibrium adsorption capacity, C_e (mg L^{-1}) is the equilibrium concentration of adsorbate, A_T (L mg^{-1}) is the Temkin isotherm equilibrium binding constant (corresponding to the maximum binding energy), *B* (J/mol) is the constant related to adsorption heat, *R* universal gas constant (8.314 J mol^{-1} K^{-1}), *T* (K) absolute temperature and b_T is the Temkin isotherm constant (J mol^{-1}). The fitting to Temkin Isotherm was carried out by plotting q_e versus ln(C_e) and the constants were determined from the slope and intercept, respectively.

- Kinetic models

Different models of diffusion were studied, including single steps of external or intra-particle diffusion. Also, three kinetical chemical expressions were used to describe the solid/liquid adsorption such as the pseudo-first-order, pseudo-second-order and the Elovich models.

1) Pseudo first-order model

The pseudo first-order equation was proposed by Lagergren [23], it is expressed following the Eq. 6.1.16:

$$\frac{dq_t}{dt} = k_1\,(q_e - q_t) \qquad (\text{Eq. } 6.1.16)$$

Where q_e and *qt* (mg. g^{-1}) are the amount of mercury (II) adsorbed on fibers at equilibrium and at certain time *t*, respectively, k_1 (min^{-1}) is the pseudo-first-order rate constant. Integrating Eq.

6.1.16, for the initial conditions t=0 to t=t and qt = 0 to $q_t = q_t$, the linearized form is obtained is the Eq. 6.1.17.

$$\log(q_e - q_t) = \log(q_e) - \frac{k_1}{2.303}t \qquad \text{(Eq. 6.1.17)}$$

From the slope and intercept of the linear plot of log($q_e - q_t$) versus t the values of the rate constant k_1 and the adsorption capacity at equilibrium q_e can be calculated, respectively.

2) Pseudo-second-order model

This model was described by Ho and McKay [24], and explained the adsorption kinetics of divalent metal ions onto adsorbent, is widely applied to the adsorption processes of metal ions, dyes, herbicides, oils, and organics from solutions [25]. In this model, the adsorption mechanism is related to a cation exchange between metal ions and adsorbents that have polar functional groups as aldehydes, ketones, acids, and phenolic [26]. The principal assumption was that the adsorption may be of second-order and the limiting step could be chemical adsorption, including covalent forces by share or electrons exchange between the adsorbent and divalent metal ions [25]. Nevertheless, sometimes the pseudo-second-order rate equation established on chemical adsorption cannot be correctly tested in processes where the physical adsorption is the main driving force (for example organics adsorption by nonpolar adsorbents) or combined processes of physisorption and chemisorption (for instance, metal ions adsorption by carbon materials) [25]. The pseudo-second-order kinetic model can be represented as Eq. 6.1.18.

$$\frac{dq_t}{dt} = k_1 (q_e - q_t)^2 \qquad \text{(Eq. 6.1.18)}$$

Where k_2 (g mg^{-1} min^{-1}) is the pseudo-second-order rate constant. Eq. 6.1.19 is the integrated rate for a pseudo second-order reaction, for the boundary conditions t=0 to t=t and qt = 0 to $q_t = q_t$.

$$\frac{1}{(q_e - q_t)} = \frac{1}{q_e} + k_2 t \qquad \text{(Eq. 6.1.19)}$$

The reorganized form of the Eq. 6.1.19 allows to obtain Eq. 6.1.20, which is the linearized form.

$$\frac{t}{q_t} = \frac{1}{k_2 q_e^2} + \frac{1}{q_e}t \qquad \text{(Eq. 6.1.20)}$$

The equilibrium adsorption capacity (q_e) and the second-order constant k_2 can be determined from the slope and intercept of plot t/q_t versus t, respectively.

3) Elovich equation

This equation explains chemisorption processes without desorption products, it was established

by Zeldowitsch (1934) to describe the rate of gas adsorption on solids that decreases exponentially with an increase in the amount of gas adsorbed [25]. This model is appropriate for materials with heterogeneous surface active sites; consequently, it has different activation energies for chemisorption[27]. This model can be used to describe metal ions adsorption from the liquid phase into solid matrixes [28]. Elovich equation is given by Eq. 6.1.21.

$$\frac{dq_t}{dt} = \alpha_e \exp(-\beta_e q_t) \qquad (\text{Eq. } 6.1.21)$$

Where q_t (mg. m^{-1}) is the amount of mercury (II) adsorbed at time *t*, α_e and β_e are Elovich constants (mg g^{-1} min^{-1}). Specifically, α_e is associated with the initial adsorption rate (chemical adsorption at zero coverage) and β_e is related to the level of surface coverage (desorption constant) and the activation energy of chemisorption [25]. The integration of Eq. 6.1.21 assuming q_t=0 at *t*=0 becomes Eq. 6.1.22.

$$q_t = \frac{1}{\beta_e}\ln(1 + \alpha_e\beta_e.t) \qquad (\text{Eq. } 6.1.22)$$

The Eq. 6.1.22 can be simplified assuming that $[\alpha_e\beta_e t]>>1$ and using the boundary conditions of q_t=0 at *t*=0 and $q_t = q_t$ [29], to obtain the Eq. 6.1.23.

$$q_t = \frac{1}{\beta_e}\ln(t) + \frac{1}{\beta_e}\ln(\alpha_e\beta_e) \qquad (\text{Eq. } 6.1.23)$$

Plotting q_t versus *t* the constants for the Elovich equation can be obtained from the slope and intercept.

- Error analysis

The models fit (R^2) was verified by the sum of the squared errors [30] (Eq. 6.1.24).

$$SSE = \sum \frac{\left(q_{t,e} - q_{t,m}\right)^2}{q_{t,e}^2} \qquad (\text{Eq. } 6.1.24)$$

Where $q_{t,e,}$ and $q_{t,m}$ are the experimental mercury adsorption capacities (mg/g) at time t and the corresponding values obtained from the kinetic models.

- Thermodynamic analysis:

The fundamental thermodynamics of adsorption allows to calculate the parameters that describe the feasibility ($\Delta G°$), spontaneity ($\Delta H°$) and nature ($\Delta S°$) of adsorbent/adsorbate interactions, and it was computed through Eq. 6.1.25:

$$\Delta G° = -RT\ln K_c \qquad \text{Eq. } 6.1.25$$

Where *R* is the universal gas constant (8.3144 J mol^{-1} K^{-1}), *T* is the absolute temperature (K), and *Kc* is the equilibrium dimensionless constant, calculated as Eq. 6.1.26 and Eq. 6.1.27 [31]:

$$K_e = \frac{q_e}{C_e} \qquad \text{Eq. 6.1.26}$$

$$K_c = K_e \times 55.5 \times 200.59 \qquad \text{Eq. 6.1.27}$$

Where q_e is the amount of Hg uptake at equilibrium (mg g^{-1}), C_e is the Hg^{2+} concentration in the solution at equilibrium (mg L^{-1}), the factor 55.5 is the number of moles of pure water per liter (dividing 1000 g L^{-1} by 18 g mol^{-1}), 200.59 is the adsorbate molecular weight (g mol^{-1}) and K_e is the constant dimensionless.

The relationship of *ΔG°* to *ΔH°* and *ΔS°* was described as Eq. 6.1.28:

$$\Delta G° = \Delta H° - T\Delta S° \qquad \text{Eq. 6.1.28}$$

The well-known van't Hoff equation, Eq. 6.1.29, is obtained by substituting Eq. 6.1.28 into Eq.6.1.25:

$$Ln\, K_c = -\frac{\Delta H°}{R} \times \frac{1}{T} + \frac{\Delta S°}{R} \qquad \text{Eq. 6.1.29}$$

A plot of Ln *Kc* versus 1/*T* should give a linear graph and *ΔH°* and *ΔS°* can be calculated from the slope and intercept, respectively.

6.1.4 Results and Discussion

The square wave anodic stripping voltammetry (SWASV) was implemented as a method to monitor the mercury removal from contaminated waters with this heavy metal, which has proven to achieve high analytical sensitivity and was preliminarily implemented as a fast and efficient method for the detection and on-site monitoring of mercury in water [32]. The calibration curve used from the optimization of the SWASV. To validate the measurements made employing the SWASV electrochemical method, Cold Vapor-Atomic Absorption (CVAAS) was used.

Before research the kinetics of mercury adsorption by different adsorbents, it was decided to examine the operational parameters with which the adsorption experiments were to be carried out. These included residence time, solid/liquid ratio (S / L), load of adsorbent and stirring speed.

- Effect of residence time

From Figure 6.1.1, a typical experiment showed the mercury adsorption capacity with WET1 increased rapidly up to 59 mg g^{-1} in the first 10 min (corresponding to a mercury removal rate of 60%). In this experimental scenario, the adsorption process became slower between 10 and 20

min when it reached q_e = 80 mg g^{-1} (removal efficiency of 82%), and after 20 min the number of mercury ions continued to increase slightly. The adsorption capacity and removal efficiency of Hg^{2+} achieved the highest value of 82.2 mg g^{-1} and 83.9%, respectively, at 30 min of contact time.

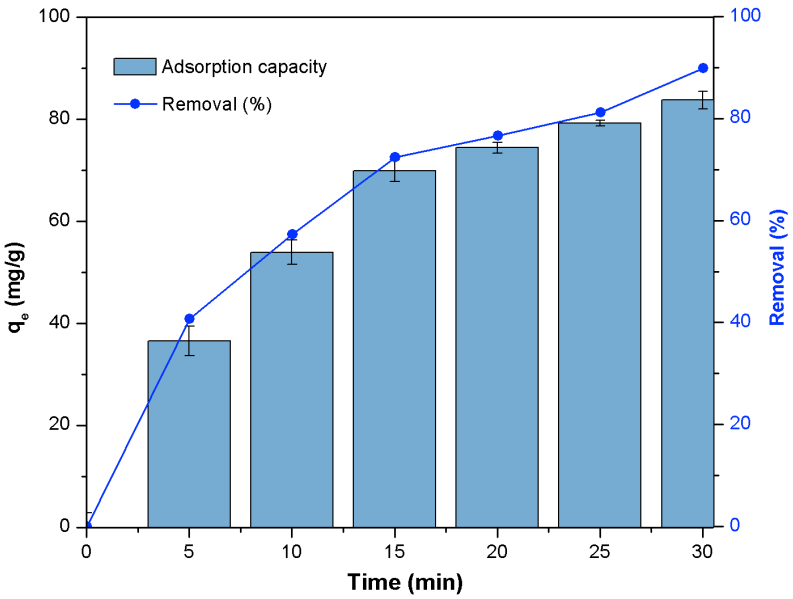


Figure 6.1.1. Effect of contact time on mercury adsorption onto functionalized fiber (WET1). Experimental conditions: initial Hg^{2+} concentration: 40 µg L^{-1}, adsorbent dose: 0.4 g WET1 L^{-1}, pH: 7, temperature: 20 °C, stirring: 100 rpm.

In the initial stage, the functionalized fiber surface had a large number of available binding sites leading to a rapid increase in adsorption; after a while, the adsorption process became slower and more stable because, gradually, the active sites of the adsorbent WET1 surface became saturated and, besides, the concentration gradient between the mercury ions in solution and those adsorbed on WET1 decreased [33]. This trend was similar to the results reported by other authors for mercury removal [34,35].

- Effect of adsorbent dose:

To evaluate the effect of adsorbent dose on mercury adsorption with WET1, the experiments were carried out at a different S / L ratio from 0.2 to 0.8 g L^{-1} and the experimental conditions were at pH = 7, a contact time of 30 min, and initial mercury concentration of 40 ppb. The results are presented in Figure 6.1.2, which showed the very stable mercury removal percentage from 81 to 87%, corresponding to WET1 dose in the range of 0.2 to 0.8 g L^{-1}, this percentage of mercury ion removal was attributed to the available surface area and active sites to carry out adsorption.

Furthermore, the adsorption capacity of Hg^{2+} ions on WET1 tends to decrease from 133 to

29 mg g^{-1} when the S/L ratio was in the range 0.2 to 0.8 g L^{-1}, reducing the adsorption capacity to major S / L might be due to the aggregation of functionalized fique fibers. Additionally, due to the heterogeneity of the chemistry and surface morphology of the functionalized fiber, active sites available for adsorption have different binding energies, as a result of the presence of functional groups such as carboxylates and hydroxyl identified from the characterization carried out in Chapter 4; then at lower S / L ratios all types of active sites are fully available, therefore saturation with Hg^{2+} ions could be faster [36]. The results obtained were consistent with other studies in which the importance of S/L ratio in adsorption processes was also verified [36,33]. Therefore, an intermediate ratio of 0.40 g L^{-1} was adopted for the rest of the experiments in this study.

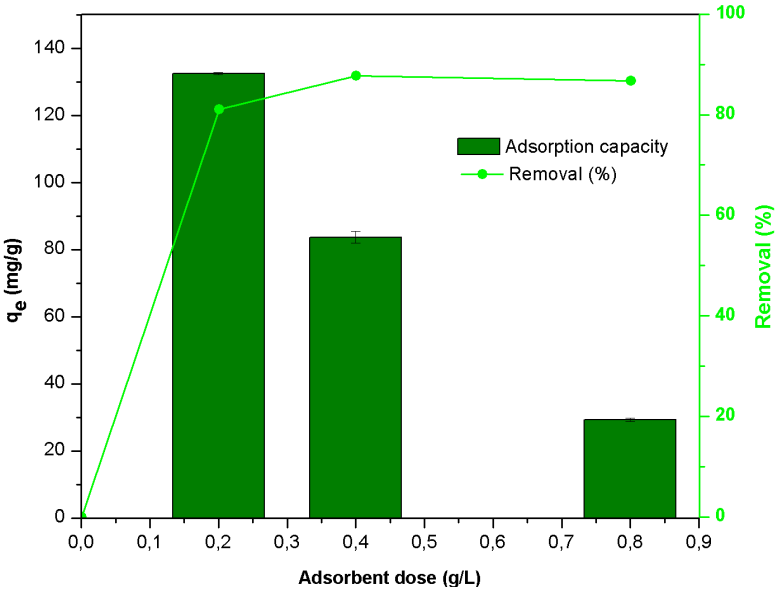


Figure 6.1.2. Effect of WET1 dosage on mercury adsorption. Experimental conditions: contact time: 30 min, initial Hg^{2+} concentration: 40 µg L^{-1}, pH: 7, temperature: 20 °C, stirring: 100 rpm.

- Effect of stirring speed:

The effect of stirring speed on the mercury adsorption was carried out at pH = 7, a contact time of 30 min, and mercury initial concentration of 40 ppb, using the functionalized fiber WET1 as adsorbent, the stirring speed was varied in the range of 50 to 200 rpm and the results obtained are in Figure 6.1.3. In batch adsorption processes, stirring speed plays an important role since it can affect the outer film boundary layer resistance and distribution of adsorbate ions in aqueous solution [37]. The results increased the adsorption capacity as the stirring speed improved, reaching values of 71, 84, and 93 mg g^{-1}, for the stirring of 50, 100, and 200 rpm, respectively.

However, for the same stirring speeds, mercury removal percentages of 69, 88, and 87% were

achieved in the same order. These observations were the result of minimum mass transfer resistance of the boundary layer, thus homogeneous mixing in the experimental conditions allowing the diffusion of the mercury ions from the bulk of the fluid to the surface of WET1. Since Hg^{2+} adsorption was not significantly influenced by stirring speed, 100 rpm was set as the speed for all subsequent experiments.

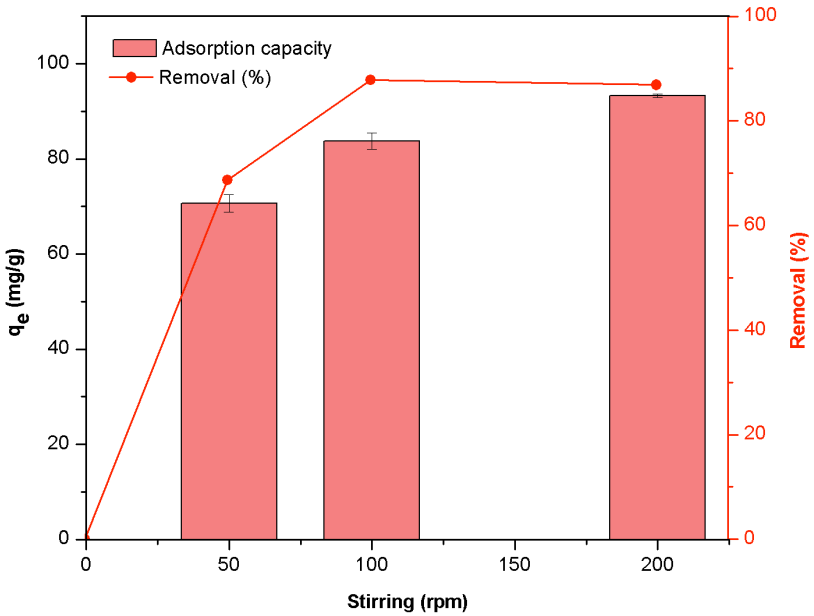


Figure 6.1.3. Effect of stirring in the mercury adsorption on WET1. Experimental conditions: contact time: 30 min, initial Hg^{2+} concentration: 40 µg L^{-1}, pH: 7, temperature: 20 °C, adsorbent dose: 0.4 g WET1 L^{-1}.

From the results obtained previously, the experimental conditions to carry out the experiments were defined from now on, contact time: 30 min, adsorbent dose 0.4 g L^{-1} (defined as 100 mg of adsorbent in 250 mL mercury solution), and stirring speed of 100 rpm.

- Materials evaluation in mercury adsorption:

Figure 6.1.4 revealed the Hg^{2+} adsorption kinetics of all the materials evaluated. In general, the mercury adsorption was very fast in all the materials, which reached equilibrium after 20 min. The lowest adsorption capacity was 43.2 mg g^{-1} for WET1-199, followed by two materials with very similar behaviors, raw (R) and pretreated fiber (WE), with q_e values corresponding to 59.9 and 66.3 mg g^{-1}, respectively. Both materials had in common the fact that they were not subjected to processes of surface chemical modification, since the R material was the fiber obtained after the defibration process and WE correspond to the fiber with an organosolv pretreatment process,

described in detail in Chapter 3. This fiber has more exposed glucose units from cellulose, as well as a much more homogeneous and cleaner surface.

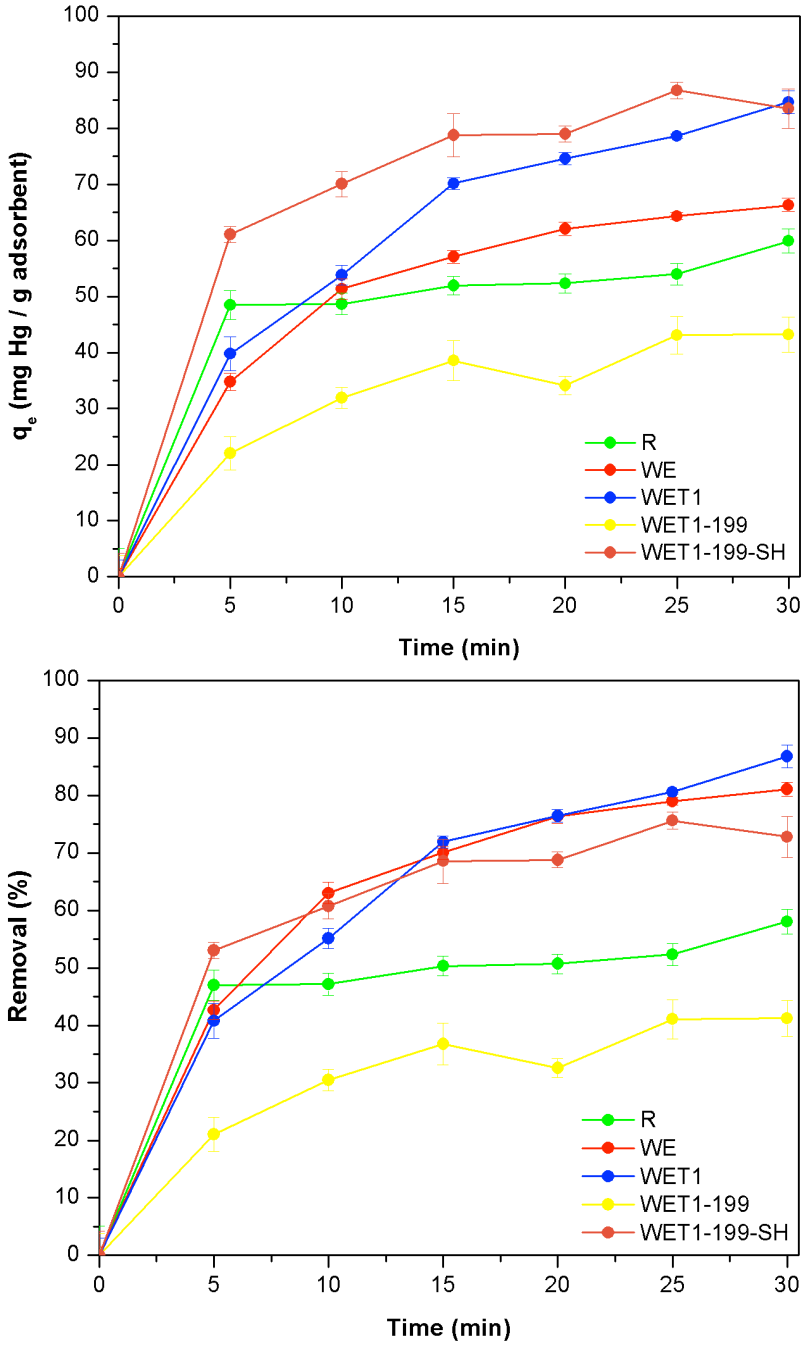


Figure 6.1.4. Uptake capacity of mercury (II) and efficiency adsorption on raw (R), pretreated (WE), functionalized (WET1), functionalized fiber with HKUST-1 anchored (WET1-199), functionalized fiber with HKUST-1 modified to include thiol groups (SH-WET1-199). Experimental conditions: contact time: 30 min, initial Hg^{2+} concentration: 40 µg L^{-1}, pH: 7, temperature: 20 °C, adsorbent dose: 0.4 g WET1 L^{-1}, stirring: 100 rpm.

On the other hand, materials with the best adsorption capacities were the functionalized WET1 fiber and fiber with MOF modified by the thiol groups grafting SH-WET1-199, each of them achieved a q_e of 84.6 and 83.5 mg g^{-1}. Furthermore, the removal efficiencies for almost all materials followed the same order as the removal capacities, except WE and SH-WET1-199. Here, were described from lower to higher removal efficiency: WET1-199 <R <SH-WET1-199 <WE <WET1, with removal percentages of 41.2, 58.1, 72.8, 81.0, and 86.8%, respectively.

The adsorption pH was one of the most influential parameters, since it not only affected the surface charge of adsorbents due to the speciation of functional groups present [38], but also influenced the species distribution that can take metallic elements such as mercury. In many reports, the impact of pH considers the material point of zero charge (pH_{PZC}); the pH_{PZC} values of the adsorbents evaluated are summarized in Table 6.1.2.

Table 6.1.2. pH at the point of zero charge (pH_{PZC}) of the materials evaluated as adsorbents in mercury removal.

Material	pH_{PZC}
R	5.31 ± 0.06
WE	4.18 ± 0.11
WET1	5.18 ± 0.05
WET1-199	4.17 ± 0.19
SH-WET1-199	4.12 ± 0.11

Then, when the pH of the solution to be treated was close to the material pH_{PZC}, the interaction with Hg^{2+} ions was minimal due to the lack of significant electrostatic interactions. However, when the solution pH was lower than the material pH_{PZC}, their surfaces were positively charged, exerting electrostatic attractions of negative compounds, which in this case was not ideal since mercury is a divalent cation. Instead, when the pH was higher than the pH_{PZC} (which was what happened for all the adsorbents studied), the mercury adsorption was favored since the surfaces were negatively charged, attracting Hg^{2+} ions.

It should be clarified that the pH ≈ 7 used in all adsorption experiments was chosen due to the possible chemical instability of the MOFs materials (WET1-199 and SH-WET1-199). Other authors have reported very acidic or basic pH values can cause partial and even complete degradation of the frame structure, changing the crystalline phases and affecting the adsorption capacity [2].

The material with the highest mercury removal efficiency and the best adsorption capacity was WET1, compared to SH-WET1-199, which reached an adsorption capacity very similar to WET1 but the removal efficiency was reduced by approximately 15%. To understand the reasons to develop mercury adsorption, an adsorption study was carried out which allowed to establish the mechanism, either physisorption (from relatively weak interactions) or chemisorption (involves electron transfer).

- Adsorption isotherms and kinetics studies

3 models were used to analyze the adsorption isotherms data (Langmuir, Freundlich, and Temkin) and another 3 models were implemented to understand the kinetics studies (pseudo-first-order, pseudo-second-order, and Elovich). Tables 6.1.3 and 6.1.4 summarize the correlation coefficients, and all the model's parameters, for the 5 materials synthesized in previous chapters: raw (R), pretreated (WE), functionalized (WET1), WET1 with the metal-organic framework HKUST-1 anchored onto the surface (WET1-199) and with HKUST-1 modified by grafting thiol groups (SH-WET1-199).

In general terms, the Freundlich and Tempkin adsorption isotherm models did not adjust very well to any of the evaluated materials (low correlation coefficients). Although for the R, WE, and SH-WET1-199 materials the Langmuir model achieved R^2 values close to 0.98 - 0.99 (Table 6.1.3), analyzing the Langmuir constant data (a_L), negative values were observed for all of them, possibly because the adsorbents did not follow all the assumptions of the Langmuir model. Another reason could be due to the small values of q_e dependent on the low initial concentrations of the adsorbates. Then, calculated errors are even smaller, which is why no adsorption mechanism associated with physisorption was considered for the materials tested.

Analyzing the kinetic results, a possible competition of mechanisms could exist for the adsorption on R and WE. Both pseudo-first-order and pseudo-second-order kinetic models can be used to fit the removal of Hg^{2+} by WE, with very similar R^2 values for R and WE. Comparing the adsorption pseudo-second-order kinetics of R and WE, both fibers were shown to have high adjustment coefficients (0.986 and 0.999), adequately representing the experimental data, suggesting the adsorption mechanism was chemically rate controlling. The error obtained for both materials was close to 3.2 and 7.8%, for R and WE, respectively, validating the applicability of these kinetic models.

Table 6.1.3. Adsorption isotherm model constants derived from the Langmuir, Freundlich and Temkin models, fitted for raw (R), pretreated (WE), functionalized (WET1), functionalized fiber with HKUST-1 anchored (WET1-199), functionalized fiber with HKUST-1 modified to include thiol groups (SH-WET1-199).

Material	Langmuir				Freundlich				Temkin			
	$q_{m,cal}$ (mg g^{-1})	a_L (L g^{-1})	R^2	SSE %	k_f (mg g^{-1} (L mg^{-1})$^{1/n}$)	n	R^2	SSE %	b_T (J mol^{-1})	A_T (L mg^{-1})	R^2	SSE %
R	51.6	-7.76	0.99	0.07	0.01	333	0.01	0.1	573177	0.0	0.01	108.9
WE	37.2	-1.12	0.98	0.6	0.84	-5.2	0.84	0.7	-28000	0.0	0.89	82.4
WET1	35.0	-0.64	0.96	154.4	0.84	-3.1	0.84	0.1	-52613	0.0	0.85	89.1
WET1-199	24.6	-2.47	0.94	14.3	0.36	-11.8	0.36	6.1	-18469	0.0	0.37	78.1
SH-WET1-199	61.3	-2.91	0.99	2.3	0.33	-24.7	0.33	0.3	-22830	0.0	0.31	78.9

The value of the adsorption rate constant (k_2) was lower for WE than R (Table 6.1.4), but the adsorption capacity was higher for WE compared to R, maybe, caused by the functional groups present in each one of the materials, as well as the morphology. In WE, a more significant number of Hg^{2+} ions could compete to occupy adsorption sites with greater interaction. For example, R is a fiber with heterogeneous surface morphology, with the presence of molecules such as sapogenins, hecogenins, calcium carbonates, and hydroxyl groups of the lignocellulosic structure; on the contrary, the pretreated fiber is characterized to have a surface much more homogeneous, cleaner, and predominantly with more available hydroxyl groups, (check Chapters 2 and 3 of this document).

Table 6.1.4. Kinetic constants for the pseudo first – order, pseudo second- order and Elovich equations, fitted for raw (R), pretreated (WE), functionalized (WET1), functionalized fiber with HKUST-1 anchored (WET1-199), functionalized fiber with HKUST-1 modified to include thiol groups (SH-WET1-199).

Material	qe_{exp} (mg g^{-1})	Pseudo-first order rate law			Pseudo-second order rate law			Elovich			
		k_f (min^{-1})	R^2	SSE (%)	k_2 (g mg^{-1} min^{-1})	R^2	SSE (%)	β_e (mg g^{-1})	α_e (mg g^{-1} min^{-1})	R^2	SSE (%)
R	55.42	0.08	0.71	0.71	0.007	0.99	3.21	0.17	6742.42	0.64	0.02
WE	67.38	0.14	1.00	1.00	0.002	1.00	7.80	0.05	31.36	0.64	0.04
WET1	79.25	0.12	0.96	0.96	0.001	1.00	17.46	0.04	21.29	0.99	0.01
WET1-199	44.38	0.18	0.73	0.73	0.003	0.96	4.75	0.09	17.68	0.89	0.16
SH-WET1-199	79.93	0.16	0.96	0.96	0.004	0.99	3.25	0.07	222.15	0.94	0.08

According to the data shown in Table 6.1.4, the mercury adsorption on WET1 followed the kinetics proposed by the Elovich model due to the favorable fit between the experimental and calculated values of q_e (R^2 = 0.986), this implied the chemisorption could be the rate-limiting step

in the mercury adsorption process. The initial Hg^{2+} concentration might have been the driving force necessary to overcome the mass transfer resistances between the aqueous solution with the mercury ions and the solid adsorbent. The values of the Elovich constants α_e and β_e, related to the chemical adsorption at zero coverage and the desorption constant, are shown in Table 6.1.4.

For both materials with metal-organic frameworks anchored, the pseudo-second-order chemical reaction kinetics provided the best correlation with the experimental data. Here the chemical reaction seemed significant in the rate-controlling step; the values of the constants are listed in Table 6.1.4. Although the WET1-199 had the unmodified HKUST-1 frames, it did not show much binding affinity to Hg^{2+}. However, the modification with thiol groups made on the SH-WET1-199 MOFs led to reach a significant increase in the binding capacity for mercury. The rate constant for a kinetic model of pseudo-second-order was higher for SH-WET1-199 compared to WET1-199, calculated at 0.0036 and 0.0027 g mg^{-1} min^{-1}, respectively.

In hybrid materials with metal-organic frameworks anchored onto the surface, all-metal centers and organic linkers can be used as adsorption sites. Besides, strong interactions between adsorbate and MOF have been reported, causing structural changes or frame modifications, because of the breathing and swelling properties of metal-organic frameworks [39]. In the WET1-199 material, the low adsorption favorability by Hg^{+2} could be a consequence of the HKUST-1 presence, which limits the removal process because even the raw fiber managed to have a greater removal capacity (Figure 6.1.4), possibly due to high material hydrophobic nature, intuited from the characterization made employing the material contact angle, explained in more detail in chapter 5.2.

The result for SH-WET1-199 possibly implied interactions between the mercury ions and the frame, such as: electrostatic, intermolecular, hydrogen bridges, π-π of the benzene rings of the MOF linkers and the mercury ions, hydrophobic and acid-base by effects of the metal centers of Cu^{2+} and Hg^{2+} [38], likewise interactions "host-host", all the previous interactions agree with the results obtained by other authors for the frame HKUST-1 [4041]. The improvement in the adsorption capacity of Hg^{2+} attributed to the thiol groups present in the MOFs structure was presumably the result of a metal complex formation[42].

Like in this research, in other reports, modified MOFs with thiol groups have been used for the removal of Hg (II), demonstrating to have a beneficial effect on the removal of this heavy metal, since the adsorption capacities always increased compared to the frames without modification. Some examples of MOFs, such as UiO-66, UiO-66-NH_2, $Zr_6O_4(OH)_4(BDC\text{-}NH_2)_{3.84}(BDC\text{-}NHCH_2C_3H_2N_2SH)_{2.16}$ and $Zr_6O_4(OH)_4$ $(BDC\text{-}NH_2)_{4.74}(BDC\text{-}NHCH_2C_3H_2N_2SH)_{1.26}$, have been evaluated in the removal of mercury, reporting efficiency percentages of 11, 23, 50, and 99%, for four MOFs; the last two were modified with thiol groups and were the ones that showed higher percentages of mercury removal [43]. However, for the studies reported in the literature, the concentrations of the analytes to be removed, as well as a load of metal-organic frameworks used as adsorbents, can vary from 30 to 6000 ppm; therefore, to make direct comparisons between the results obtained was, very often, not possible.

Framed materials did not show a direct correlation between adsorption and textural properties, agreeing with other authors, such as Khan *et al.* [44], who used different MOFs for pollutant adsorption like sulfur and nitrogen-containing compounds in fuels, organic contaminants, and heavy metals in wastewater. In general terms, it was suggested adsorption on materials with anchored MOFs was the result of acid-base interactions since the size of mercury ions to be removed (approximately 1.1 Å) had sizes not significantly smaller than the HKUST-1 pore windows (this framework has a bimodal pore size distribution, larger pores are hydrophilic and evidenced diameter of 9 Å, others are smaller with 6 Å in diameter) [45]. Therefore, it has been suggested this parameter was not decisive in the mercury adsorption processes with MOFs; however, it is one of the topics widely studied today.

On the contrary, the presence of functional groups or specific molecules allowed controlling the adsorption mechanisms, in which the type of interaction was a function of the pollutant type to be treated and the metal-organic frame structure explored [46]. Consequently, the importance of modifying MOFs through the post and pre-synthetic techniques has recently been reported as a useful tool to improve MOFs / adsorbate interactions.

Mercury removal through adsorption has been reported using other types of adsorbents, among which the adsorption capacities of carbon nanotubes functionalized with sulfur (q_e = 131 mg g^{-1}) [47], metallic nanoparticles (q_e = 714 mg g^{-1}) [48], silica (q_e = 47.5 mg g^{-1}) [49], xerogels (q_e = 95 mg g^{-1}) [50], coconut residues (q_e = 144.4 mg g^{-1}) [51] and pillared clay (q_e = 49.75 mg g^{-1}) [52], suggesting the results obtained in this study were in line with other studies. Additionally, most of these studies

coincided the pseudo-second-order kinetic model is the best to describe the adsorption process with different materials as adsorbent. Thefefore, it has been widely applied to describe the adsorption kinetics of divalent metal ions like Hg^{2+} onto adsorbents [25].

In this model, the adsorption mechanism is related to a cation exchange between metal ions and adsorbents that have polar functional groups as aldehydes, ketones, acids, and phenolic [26]. The principal assumption was that the adsorption may be of second-order and the limiting step could be chemical adsorption, including covalent forces by share or electrons exchange between the adsorbent and divalent metal ions [25]. For all the materials evaluated, it can be indicated chemical adsorption was the dominant step to control the reaction rate in the heterogeneous system because the pseudo-second-order kinetic and Elovich models consider the chemical adsorption process implied share and transfer electrons between the adsorbent and Hg^{2+} [25].

Although the SH-WET1-199 material corresponding to fique fiber with metal-organic frameworks modified by the inclusion of thiol groups exhibited chemical and hydrolytic stability, compared to WET1-199, reusing the material became a challenge in materials with MOFs after the adsorption of heavy metals, due to the difficulty to regenerate the hybrid material evaluated. SH-WET1-199 reached a mercury adsorption capacity similar to WET1 fiber only functionalized with carboxylate groups (Table 6.1.4), and both materials achieved significant percentages of mercury removal from water, 72.78 to 84.54% for SH-WET1-199 and WET1, respectively.

Then, the WET1 material displayed more advantages, including fewer synthesis processes, easy recovery, reuse after adsorption, chemical and hydrolytic stability, reasons why it was chosen as the material with the best performance compared to the other materials studied. Therefore, it was selected as the adsorbent for the effective analysis of other parameters in the removal of Hg^{2+} from water.

- Analysis of the cross effect of pH and initial concentration in the mercury removal

To analyze the individual and cross-over effect of pH and initial mercury concentration in the removal of this pollutant through the adsorption process, a Box - Behnken design of experiments (DOE) was proposed. It included the evaluation of 13 experiments with five central points to guarantee the statistics of analysis. Each one of the factors studied comprised 3 levels (Table 6.1.1). Table 6.1.5 summarizes the experimental conditions, removal percentage and adsorption

capacity (experimental and adjusted by the statistical model), for each DOE experiment. These experiments were performed randomly to minimize possible systematic errors.

Table 6.1.5. Adsorption uptake, removal percentage and results for the statistical model fitted, analyzing the cross between the pH and initial mercury concentration using WET1 as adsorbent. Experimental conditions: contact time: 30 min, temperature: 20 °C, adsorbent dose: 0.4 g WET1 L^{-1}, stirring: 100 rpm.

Run	Conditions		Code values		Removal (%)	Experimental values	Model predicted values	SSE %
	pH	[Hg] ppb	PyType	Blocks		q_e(mg g^{-1})	q_e (mg g^{-1})	
1	7	40	0	1	83.87	82.21	85.80	0.19
2	4	20	1	1	62.31	31.50	21.90	9.30
3	7	40	0	1	89.70	87.07	85.80	0.02
4	10	20	1	1	54.35	23.59	34.23	20.34
5	7	40	0	1	78.97	86.49	85.804	0.01
6	7	68.28	-1	1	77.12	120.48	109.62	0.81
7	7	11.71	-1	1	81.99	24.68	25.93	0.26
8	4	60	1	1	42.48	67.17	66.12	0.02
9	11.24	40	-1	1	93.60	85.93	66.81	4.95
10	2.74	40	-1	1	20.52	18.71	28.22	25.83
11	7	40	0	1	82.62	87.01	85.80	0.02
12	10	60	1	1	71.43	89.16	108.36	4.64
13	7	40	0	1	81.36	86.24	85.80	0.01

To examine the results obtained from the design of the experiments summarized in Table 6.1.5, the data obtained was validated through an analysis of variances (ANOVA). Figure 6.1.5a verified the assumption of residuals are normally distributed, Figure 6.1.5b shows residuals have a constant variance, it means homoscedasticity. Figure 6.1.5c confirms residues followed a normal distribution; half of the data took positive values (over 50%), and the other half negative values (below 50%). Then, there were no significant deviations of residuals from the normal distribution; likewise, in Figure 6.1.5d it was evidenced residuals were not correlated with each other.

Complying with the previously described ordinary least squares assumptions, the ordinary least squares regression was achieved, which produced estimates of coefficients without minimum variance bias, summarized in Table 6.1.6, from which it is concluded the pH factors and initial mercury concentration were statistically significant ($p < 0.05$). From the results reported in Table 6.1.4 it was possible to estimate the linear regression coefficients, squares, and interaction of the adsorption capacity q_e, to generate a statistical model, which allowed studying the effect of pH (A) and initial concentration of mercury (B) .Eq. 6.1.30 describes the relationship of the variables.

$$q_e \text{ (mg g}^{-1}) = 85.804 + 13.643A + 29.59B - 19.14A2 - 9.011B2 + 7.475AB \quad \text{Eq. 6.1.30.}$$

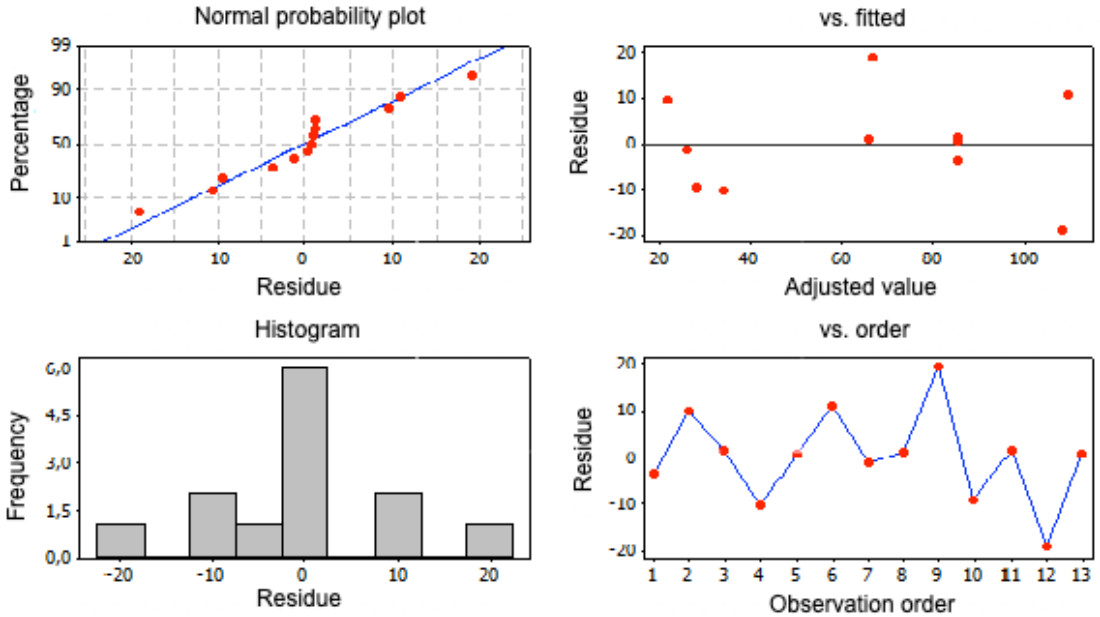


Figure 6.1.5. Residual plots for the analysis of the cross effect between the pH and initial mercury concentration using WET1 as adsorbent. a) Normal probability plot, b) Versus fits, c) Histogram and d) Versus order.

Table 6.1.6. Analysis of variance (ANOVA) for mercury removal by MiniTab 16 Statistical Software.

Source	DF	Seq SS	Adj SS	Adj MS	F	P
Regression	5	11566.1	11566.1	2313.2	13.87	0.002
Linear	2	8493.7	8493.7	4246.85	25.47	0.001
pH	1	1489.0	1489.1	1489.06	8.93	0.020
$[Hg]_0$ ppb	1	7004.6	7004.6	7004.64	42.01	0.000
Square	2	2848.9	2848.9	1424.47	8.54	0.013
pH*pH	1	2284.1	2548.6	2548.65	15.29	0.006
$[Hg]_0$ ppb*$[Hg]_0$ ppb	1	564.8	564.8	564.82	3.39	0.108
Interaction	1	223.5	223.5	223.50	1.34	0.285
AB	1	223.5	223.5	223.50	1.34	0.285
Total	12	12733.2				

Figure 6.1.6. reports the comparison between experimental data of mercury adsorption capacity and values predicted by the statistical model (Table 6.1.4). The parity figure evidenced a good fit of the experimental and calculated data, reflected by the correlation coefficient R^2 = 90.83% and R^2 adjusted = 84.29%, on average the predicted adsorption capacity values differed by less than 5% (Table 6.1.4), thus being an efficient model to predict the adsorption capacities of experimental conditions within levels of the variables analyzed.

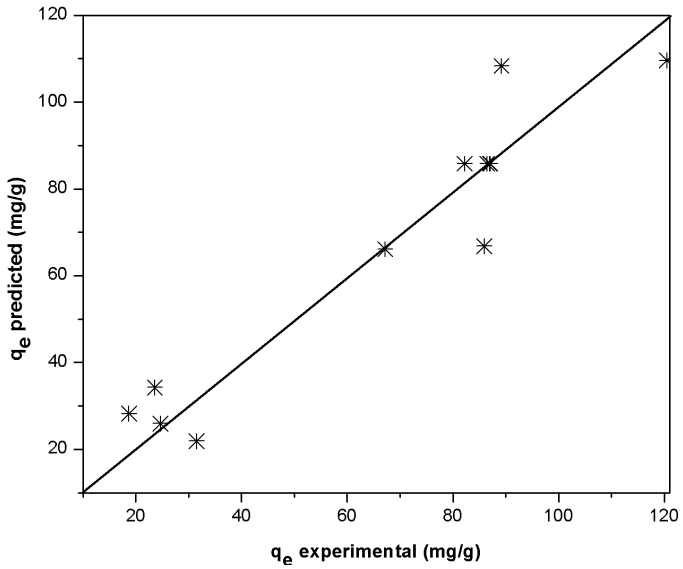


Figure 6.1.6. Pareto chart of the experimental and calculated results from the of experimental design for mercury removal using as adsorbent WET1.

From Eq. 6.1.30. the response surface of Figure 6.1.7 was generated, which displayed the cross effect of the variables of pH and initial mercury concentration, although both variables studied affect the adsorption process. The variable that most affected the adsorption capacity was the initial mercury concentration within the range of low values (less than 25 ppb), while the pH can also be a limiting factor (as will be described later in more detail). At pH values higher than the WET1 point of zero charge (5.18 from Table 6.1.2), adsorption was directly favored because the surface was negatively charged. From the response surface, it can be concluded pH values between 5 and 10.5 combined with initial concentrations of mercury greater than 38 ppb were conditions at which the highest mercury adsorption capacities were achieved using the functionalized fique fiber as adsorbent material.

From the effect analysis of each o variable, Figure 6.1.7 indicated how the adsorption capacity of WET1 changes against the pH value. It was discovered the adsorbed amounts increased between pH values from 3 to 9, indicating the material was stable in a wide range of acidic and basic pH. As the solution pH was higher than 5.18 (adsorbent pH_{PZC}, Table 6.1.2), the surface charge of WET1 became more negative, probably due to the presence of functional groups that contain oxygen, such as sodium carboxylate (-COONa) from the functionalization and hydroxyl groups (-OH) of the anhydrous-glucose structures present in the fiber, which ionized and improved the deposition of mercury cations. According to the species diagram, this metal exists in positive form as Hg^{2+} or $HgOH^{+}$ [53].

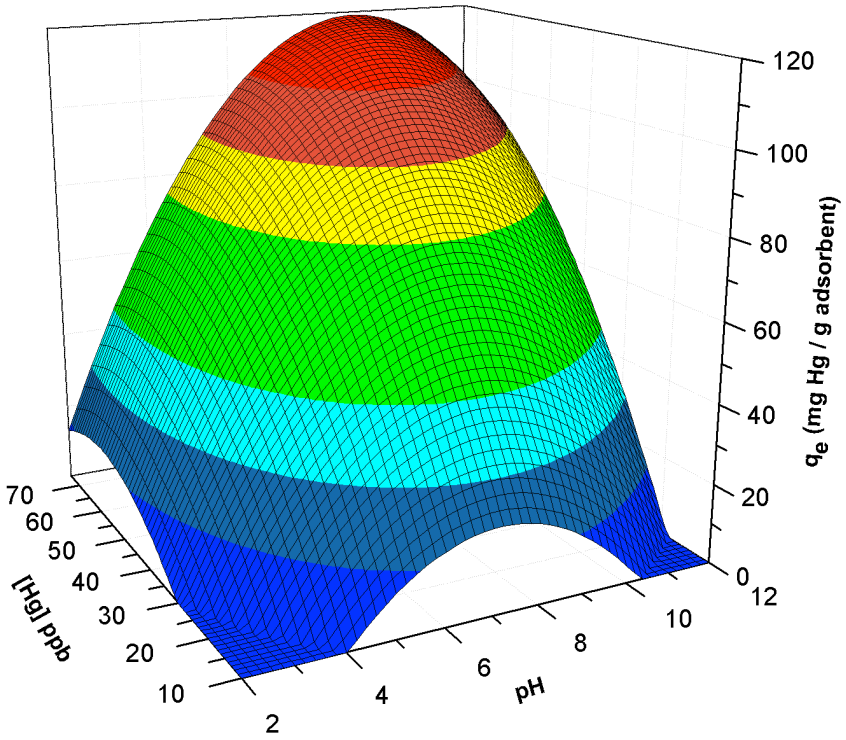


Figure 6.1.7. Response surface of the cross effect in the mercury removal from the pH and solution initial concentration to be treated using WET1 as adsorbent following the DOE (Table 6.1.5).

The adsorption of Hg^{+2} on WET1 was shown to be higher at pH values close to 7, because the adsorbent was more likely to be in the anionic form. The maximum adsorption capacity was 120.48 mg g^{-1}. However, it is very important to consider pH was a variable that proved to have a strong dependence on the initial mercury concentration values, which will be discussed later.

Furthermore, the mercury adsorption at pH less than 4 was reduced to almost zero, due to the protonation of active sites on the adsorbent surface, disfavoring the electrostatic interactions with the Hg^{2+} ions by electrostatic repulsion of species. Also, for pH values greater than 9.5, the mercury removal was significantly limited, probably because at these pH values, according to the mercury species diagram, mercury is present in solution as $Hg(OH)_2$ [53], a consequence of the high concentration of OH^- ions in the aqueous medium. The results described above suggested the mercury removal using WET1 as adsorbent was due to electrostatic adsorbate/adsorbent interactions, as has been described by other authors [54,41].

The initial concentration of mercury was the factor that most influenced the adsorption process. The effect of the initial concentration of Hg^{2+} ions was studied in the range of concentrations from

20 to 70 ppb, defined from preliminary studies of in-situ monitoring of the mercury levels contamination in the Amazon river, quantified through electrochemical techniques [32]. The results obtained were in agreement with Figure 6.1.7; the adsorption capacity of Hg^{2+} increased as the mercury ions concentration in solution improved and due to the cross effect of the variables with the pH, as was explained above when the solution pH was lower than the pH_{PZC} value of WET1, the surface was protonated, and the adsorption process was limited.

At a pH greater than 7, a maximum adsorption capacity was reached in the range of 89 to 120 mg g^{-1}. Meanwhile, the mercury removal efficiency for this same range was around 78.97 to 93.60% for concentrations between 40 and 70 mg L^{-1}. Due to lower concentrations, the mercury concentration gradient in solution and the ions on the material surface eventually became very low, which was why the movement of the ions from the solution to the adsorbent did not have enough driving force to break the concentration gradient, promoting the adsorption process, as reported in other studies [33].

- Kinetic fit of DOE data

The adsorption capacity data obtained from the DOE were adjusted to 3 models of adsorption isotherms (Langmuir, Freundlich, and Tempkin) and 3 models of kinetic equations (pseudo-first-order, pseudo-second-order, and Elovich), the parameters of each model are summarized below in Tables 6.1.7 and 6.1.8, respectively. From the data previously reported on the mercury adsorption on WET1 (Figure 6.1.4), and after adjusting the models associated with the kinetic (Table 6.1.3) and equilibrium (Table 6.1.4). It was determined the kinetic controlled the step in the mercury removal.

However, it was necessary to do again an analysis to confirm, despite the significant effect on the mercury removal capacity caused by the change in pH or initial concentration of the adsorbate, that chemisorption was the predominant mechanism to describe adsorption. The results of Table 6.1.7 established none of the physisorption models adequately described the Hg^{2+} adsorption mechanism, coinciding with the results obtained from Table 6.1.3 above. From the DOE experimental data, the best kinetic model adjusted was Elovich, most of the runs of Table 6.1.8 indicated correlation coefficients R^2 greater than 0.95. Only those in which the pH was very low were not adjusted, indicating the adsorption of Hg^{2+} ions followed the chemisorption mechanism. The maximum adsorption capacity of WET1 at pH = 7 and initial mercury concentration of 68.3

ppb was calculated at 109.6 mg g^{-1}, while the experimental value reached 120.5 mg g^{-1}, which corresponds to the capture of 77.1% of mercury in solution.

Table 6.1.7. Adsorption isotherm model constants derived from the Langmuir, Freundlich and Temkin models, fitted for functionalized fiber (WET1), under conditions described above in Table 6.1.5.

Run	Langmuir				Freundlich				Temkin		
	$q_{m,cal}$ (mg g^{-1})	a_L (L g^{-1})	R^2	SSE %	k_f (mg g^{-1} (L mg^{-1})$^{1/n}$)	n	R^2	SSE %	b_T (J mol^{-1})	R^2	SSE %
1	41.32	-0.86	0.98	9.12	76.91	-7.53	0.63	0.71	-30223	0.67	84.3
2	13.18	-8.16	0.37	30.3	17.62	-7.14	0.18	18.2	-25062	0.27	86.4
3	38.17	-0.66	0.92	0.12	81.92	-5.71	0.29	1.41	-96667	0.23	91.8
4	9.785	-5.49	0.51	24.3	15.14	-5.17	0.18	12.9	-32875	0.18	88.9
5	27.70	-0.96	0.81	5.25	57.62	-6.22	0.40	5.64	-36853	0.48	87.3
6	58.48	0.69	0.10	36.5	103.8	-4.04	0.01	20.8	-1740001	0.03	99.6
7	10.64	-3.85	0.68	0.98	15.78	-7.15	0.14	7.83	-45876	0.09	91.8
8	32.57	-2.87	0.69	27.4	71.96	-3.40	0.32	17.8	-93632	0.31	92.8
9	54.65	-1.63	0.99	1.03	89.95	-7.08	0.85	0.06	-28828	0.84	83.3
10	23.87	-1.36	0.99	33.4	22.46	11.5	0.17	0.09	30412	0.15	111
11	39.45	-0.78	0.95	5.78	79.34	-6.93	0.46	0.99	-55678	0.54	87.1
12	58.14	-1.29	0.92	0.13	53.49	10.4	0.20	2.78	69205	0.23	102
13	42.54	-0.87	0.97	8.75	78.43	-6.19	0.54	1.11	-76734	0.45	89.9

Table 6.1.8. Kinetic constants for the pseudo first – order, pseudo second- order and Elovich equations, fitted for functionalized fiber (WET1), under conditions described above in Table 6.1.5.

Run	qe_{exp} (mg^{-1} g)	Pseudo-first order rate law			Pseudo-second order rate law			Elovich			
		k_f (min^{-1})	R^2	SSE (%)	k_2 (g mg^{-1} min^{-1})	R^2	SSE (%)	β_e (mg g^{-1})	α_e (mg g^{-1} min^{-1})	R^2	SSE (%)
1	82.21	0.18	0.96	9.93	0.0013	0.99	8.02	0.04	28.90	0.97	0.00
2	31.50	0.21	0.71	251.06	0.0001	0.30	201.05	0.07	4.33	0.99	0.26
3	87.07	0.08	0.95	0.14	0.0007	0.96	28.04	0.04	20.08	0.95	0.10
4	23.59	0.1q	0.94	8.88	0.0004	0.76	303.23	0.09	3.47	0.98	0.02
5	86.49	0.19	0.87	48.33	0.0007	0.96	31.13	0.04	13.96	0.97	0.01
6	120.48	0.08	0.92	4.97	0.0001	0.01	11.34	0.02	13.75	0.96	0.50
7	24.68	0.10	0.78	8.28	0.0008	0.80	72.28	0.11	3.719	0.90	0.35
8	67.17	0.15	0.85	11.87	0.0004	0.91	44.56	0.01	12.21	0.96	0.84
9	85.93	0.19	0.94	1.32	0.0026	0.99	5.93	0.06	81.67	0.96	0.06
10	18.71	0.09	0.38	67.43	0.0158	0.88	1.91	0.01	0.01	0.19	0.00
11	87.01	0.13	0.97	5.76	0.0009	0.97	15.89	0.05	24.32	0.96	0.07
12	89.16	0.05	0.27	9.59	0.0013	0.76	2.11	0.06	35.77	0.46	5.56
13	86.24	0.15	0.96	4.56	0.0012	0.98	10.33	0.03	26.98	0.07	0.01

Elovich's kinetic model adequately described how the adsorption process was carried out since this model has been widely used to describe the adsorption of metal ions like mercury from the liquid phase into solid matrixes like fique fiber functionalized as WET1 [28]. Additionally, it was an appropriate model for materials with heterogeneous surface-active sites, such as WET1, as described in the characterization of this material in chapter 4.

From the surface chemistry of this fiber, approximately 11% of its surface was sodium carboxylate groups (-COONa) product of the functionalization carried out by TEMPO oxidation, and the other 89% corresponded to hydroxyl groups (-OH) intrinsic to the fiber, coming from the lignocellulose structure of polymers such as cellulose and hemicellulose. Both classes of functional groups were considered as potential active sites in which mercury adsorption can take place, making this assumption fully valid under current experimental conditions. The values of Elovich constants α_e and β_e, associated with the initial adsorption rate (chemical adsorption at zero coverage) and level of surface coverage (desorption constant) are listed in Table 6.1.8 for the various experimental conditions used. In general, α_e increased from 3.72 to 117.1 mg g^{-1} min^{-1}, when the initial concentration of mercury also enlarged from 11.7 to 60 ppb. On the other hand, the value of β_e reached similar values in the range of 0.05 to 0.11 mg g^{-1} for all concentrations.

- Temperature effect on mercury removal

To evaluate the temperature influence on the mercury removal process, experiments were performed at different temperatures (20, 45 and 60 °C), using 0.1 g of WET1 and 0.25 L of mercury solution, under DOE conditions with the highest adsorption capacity (run 6), pH = 7 and initial mercury concentration 68.28 ppb. Figure 6.1.8 collected the adsorption isotherms of these experiments, which reached q_e values of 120.5, 110.3, and 92.8 mg g^{-1} for the temperatures of 20, 45, and 60 °C, respectively. It can be verified that as the temperature rose the adsorption capacity was slightly reduced, revealing adsorption was an exothermic process, and equilibrium at higher temperatures was reached much faster.

For the experiment at 20 °C, the adsorption capacity changed over 30 min, achieving the maximum value with a removal efficiency close to 77.1%. Once the temperatures were increased to 45 and 60 ° C, they reached the equilibrium adsorption capacity after approximately 5 min, with removal efficiencies of 98.7 and 100%, respectively, which was not surprising, due to the exponential dependency of the Arrhenius factor with temperature. However, due to the large volume of wastewater usually generated with this type of contaminant, the option to use high

temperatures to reduce the time is not practical due to operating costs. It is necessary to consider possibly other phenomena happen over time and can affect the adsorbent.

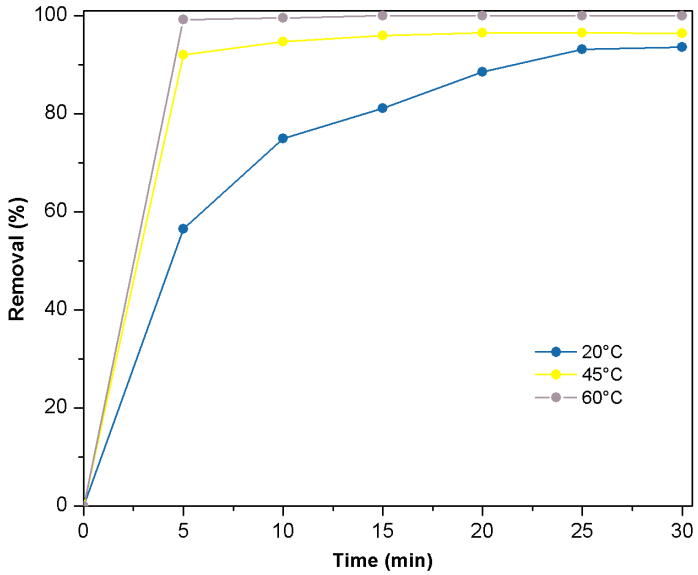


Figure 6.1.8. Effect of temperature in mercury adsorption on functionalized fiber (WET1). Experimental conditions: contact time: 30 min, initial Hg^{2+} concentration: 68.28 µg L^{-1}, pH: 7, adsorbent dose: 0.4 g WET1 L^{-1}, stirring: 100 rpm.

- Thermodynamic of adsorption

The analyzes of the thermodynamic parameters of ΔG°, ΔH° and ΔS°, provided detailed information on the internal energy changes associated with the mercury adsorption on WET1. The parameters were calculated at three different temperatures 20, 45 and 60 ° C for 30 min, the results were summarized in Table 6.1.9. The Gibbs free energy (ΔG°) at all temperatures was negative, indicating the adsorption process of Hg^{2+} on WET1 was spontaneous within the evaluated temperature range.

Table 6.1.9. Thermodynamic parameters calculated for the adsorption of Hg^{2+} onto WET1

Temperature (°C)	**20**	**45**	**60**
ΔG° (KJ mol^{-1})	-29.84	-35.55	-41.77
ΔH° (KJ mol^{-1})	-54.87		
ΔS° (J mol^{-1} K^{-1})	287.89		

However, as the temperature increased, the value of ΔG° decreased, which meant the adsorption process was less favorable at higher temperatures. The negative value of enthalpy (ΔH°) suggested the development of an exothermic process because the energy absorbed in the breakage of bonds was lower compared to the total energy released during the formation of

bonds between Hg^{2+} and WET1, generating extra energy in the form of heat. Regarding the positive entropy (ΔS°), it indicated randomness with the adsorption of Hg^{2+}.

- Regeneration

The material after an adsorption cycle the material WET1 was regenerated under sonication for 20 minutes. Then, a new adsorption experiment at pH = 7 and initial concentration of 40 ppb reached a mercury removal of 65%, reducing only approximately in 10% its removal efficiency.

6.1.5 Conclusions

Materials based on fique fiber and its modification to obtain hybrid composite with metal-organic structures were tested as adsorbents for the removal of mercury from aqueous solutions. Of all the materials with MOF anchored tested, SH-WET1-199 showed the best performance as a result of the introduction of thiol groups in the structure of HKUST-1, which markedly improved the selectivity for mercury with adsorption capacities from 43.2 mg g^{-1} for WET1-199 to almost double for SH-WET1-199 with 83.5 mg g^{-1}.

However, the adsorption processes using the WET1 material reached adsorption capacities similar to SH-WET1-199 thanks to the fiber surface functionalization through TEMPO oxidation reactions, which originate carboxylate functional groups. These groups enhance theelectrostatic interactions promoting the mercury removal from the aqueous solutions. The mercury adsorption process in WET1 was highly dependent on the initial Hg^{2+} concentration and the pH value. In this study, the highest adsorption of Hg^{2+} using WET1 as adsorbent (120 mg g^{-1}) was obtained for a pH of 7 and an initial mercury concentration of 68.28 ppb. Furthermore, none of the adsorption equilibrium models tested was adequate to describe the adsorption process; on the contrary, Elovich's model presented the best fit for adsorption kinetics with a correlation coefficient of 0.96, which allowed to conclude that the main Mercury (II) adsorption mechanism in WET1 was ion exchange between adsorbate and adsorbent.

6.1.6 References

1. Demirbas, A. Heavy metal adsorption onto agro-based waste materials: A review. *J. Hazard. Mater.* **157**, 220–229 (2008).

2. Bedia, J. *et al.* A review on the synthesis and characterization of metal organic frameworks for photocatalytic water purification. *Catalysts*. **9**, 1–43 (2019).

3. Kumar, P., Bansal, V., Kim, K. H. & Kwon, E. E. Metal-organic frameworks (MOFs) as futuristic

options for wastewater treatment. *J. Ind. Eng. Chem.* **62**, 130–145 (2018).

4. Sun, D. T. *et al.* Rapid, Selective Heavy Metal Removal from Water by a Metal-Organic Framework/Polydopamine Composite. *ACS Cent. Sci.* **4**, 349–356 (2018).

5. Kobielska, P. A., Howarth, A. J., Farha, O. K. & Nayak, S. Metal–organic frameworks for heavy metal removal from water. *Coord. Chem. Rev*. **358**, 92–107 (2018).

6. Wen, J., Fang, Y. & Zeng, G. Progress and prospect of adsorptive removal of heavy metal ions from aqueous solution using metal–organic frameworks: A review of studies from the last decade. *Chemosphere*. **201**, 627–643 (2018).

7. US EPA, O. Mercury in your environment. https://www.epa.gov/mercury (2016).

8. Hadi, P., To, M.-H., Hui, C.-W., Lin, C. S. K. & McKay, G. Aqueous mercury adsorption by activated carbons. *Water Res.* **73**, 37–55 (2015).

9. Hilson, G. Abatement of mercury pollution in the small-scale gold mining industry: Restructuring the policy and research agendas. *Sci. Total Environ.* **362**, 1–14 (2006).

10. Driscoll, C. T., Mason, R. P., Chan, H. M., Jacob, D. J. & Pirrone, N. Mercury as a global pollutant: sources, pathways, and effects. *Environ. Sci. Technol.* **47**, 4967–4983 (2013).

11. US EPA, O. Health Effects of Exposures to Mercury https://www.epa.gov/mercury/effects(2016).

12. Sohrabi, M. R. Preconcentration of mercury(II) using a thiol-functionalized metal-organic framework nanocomposite as a sorbent. *Microchim. Acta.* **181**, 435–444 (2014).

13. Cordy, P. *et al.* Mercury contamination from artisanal gold mining in Antioquia, Colombia: The world's highest per capita mercury pollution. *Sci. Total Environ.* **410**, 154–160 (2011).

14. Semana. La fiebre minera se apoderó de Colombia. https://www.semana.com/nacion/articulo/la-fiebre-minera-apodero-colombia/246055-3 (2011).

15. Academia. Gestion minero ambiental. https://www.academia.edu/7673547/Gestion_minero_ambiental (2012).

16. El Espectador. Alarma por altos niveles de mercurio en etnias amazónicas. https://www.elespectador.com/noticias/medio-ambiente/alarma-por-altos-niveles-de-mercurio-en-etnias-amazonicas (2015).

17. Alcaldía mayor de Bogotá. Regimen legal aguas. https://www.alcaldiabogota.gov.co/sisjur/normas/Norma1 .jsp?i=1 (2019).

18. Langmuir, I. The adsorption of gases on plane surfaces of glass, mica and platinum. *J. Am. Chem. Soc.* **40**, 1361-1403 (1918).

19. Weber, T. W. & Chakravorti, R. K. Pore and solid diffusion models for fixed-bed adsorbers. *AIChE J.* **20**, 228-238 (1974)

20. H.M. Freundlich. Over the adsorption in solution. *J. Phys. Chem.* **57**, 385–470 (1906).

21. E. Voudrias, K. Fytianos & E. Bozani. Sorption - desorption isotherms of dyes from aqueous solutions and wastewaters with different sorbent materials. *Glob. Nest Int. J* **4**, 75–83 (2002).

22. M.J. Temkin, V. P. Recent modification to Langmuir isotherms. *Acta Physicochim.* **URSS**, 217–225 (1940).

23. Yuh-Shan, H. Citation review of Lagergren kinetic rate equation on adsorption reactions. *Scientometrics* **59**, 171–177 (2004).

24. Ho, Y. S. & McKay, G. A Two-stage batch sorption optimized design for dye removal to minimize contact time. *Process Saf. Environ. Prot.* **76**, 313–318 (1998).

25. Ribeiro, A., Mateus, E. & Couto, N. *Electrokinetics across disciplines and continents : new strategies for sustainable development*. (Springer, 2011).

26. Cheung, C. ., Porter, J. . & Mckay, G. Sorption kinetic analysis for the removal of cadmium ions from effluents using bone char. *Water Res.* **35**, 605–612 (2001).

27. and, R.-S. J. & Chen, M.-L. Application of the elovich equation to the kinetics of metal sorption with solvent-impregnated resins. **36**, 813–820 (1997).

28. Rudzinski, W. & Panczyk, T. The langmuirian adsorption kinetics revised: a farewell to the xxth century theories. *Adsorption.* **8**, 23–34 (2002).

29. Ho, Y. S. & McKay, G. Sorption of copper(ii) from aqueous solution by peat. *Water, Air, Soil Pollut.* **158**, 77–97 (2004).

30. Lata, H., Garg, V. K. & Gupta, R. K. Adsorptive removal of basic dye by chemically activated Parthenium biomass: equilibrium and kinetic modeling. *Desalination* **219**, 250–261 (2008).

31. Tran, H. N., You, S. J. & Chao, H. P. Thermodynamic parameters of cadmium adsorption onto orange peel calculated from various methods: A comparison study. *J. Environ. Chem. Eng.* **4**, 2671–2682 (2016).

32. Bernalte, E. *et al.* Rapid and on-site simultaneous electrochemical detection of copper, lead and mercury in the Amazon river. *Sensors Actuators, B Chem.* **307**, 127620 (2020).

33. Trinh, V. T. *et al.* Phosphate Adsorption by silver nanoparticles-loaded activated carbon derived from tea residue. *Sci. Rep.* **10**, 1–13 (2020).

34. Xiong, Y. Y. *et al.* Using MOF-74 for Hg2+ removal from ultra-low concentration aqueous solution. *J. Solid State Chem.* **246**, 16–22 (2017).

35. Luo, F. *et al.* High-performance Hg2+ removal from ultra-low-concentration aqueous solution using both acylamide- and hydroxyl-functionalized metal-organic framework. *J. Mater. Chem. A* **3**, 9616–9620 (2015).

36. Lin, K. Y. A., Liu, Y. T. & Chen, S. Y. Adsorption of fluoride to UiO-66-NH2 in water: Stability, kinetic, isotherm and thermodynamic studies. *J. Colloid Interface Sci.* **461**, 79–87 (2016).

37. Sakin Omer, O., Hussein, M. A., Hussein, B. H. M. & Mgaidi, A. Adsorption thermodynamics of cationic dyes (methylene blue and crystal violet) to a natural clay mineral from aqueous solution between 293 and 323 K. *Arab. J. Chem.* **11**, 615–623 (2018).

38. Joseph, L. *et al.* Removal of contaminants of emerging concern by metal-organic framework nanoadsorbents: A review. *Chem. Eng. J.* **369**, 928–946 (2019).

39. Li, J., Sculley, J. & Zhou, H. Metal–Organic Frameworks for separations. *Chem. Rev.* **112**, 869–932 (2012).

40. Chen, Q. *et al.* Controlled release of drug molecules in metal–organic framework material HKUST-1. *Inorg. Chem. Commun.* **79**, 78–81 (2017).

41. Mon, M. *et al.* Selective and efficient removal of mercury from aqueous media with the highly flexible

arms of a BioMOF. *Angew. Chemie Int.* **55**, 11167–11172 (2016).

42. Sohrabi, M. R. Preconcentration of mercury(II) using a thiol-functionalized metal-organic framework nanocomposite as a sorbent. *Microchim. Acta* **181**, 435–444 (2014).

43. Saleem, H., Rafique, U. & Davies, R. P. Investigations on post-synthetically modified UiO-66-NH2 for the adsorptive removal of heavy metal ions from aqueous solution. *Microporous Mesoporous Mater.* **221**, 238–244 (2016).

44. Khan, N. A., Hasan, Z. & Jhung, S. H. Adsorptive removal of hazardous materials using metal-organic frameworks (MOFs): A review. *J. Hazard. Mater.* **244**–**245**, 444–456 (2013).

45. Lin, S. *et al.* Adsorption behavior of metal-organic frameworks for methylene blue from aqueous solution. *Microporous Mesoporous Mater.* **193**, 27–34 (2014).

46. Hindelang, K., Kronast, A., Vagin, S. I. & Rieger, B. Functionalization of metal-organic frameworks through the postsynthetic transformation of olefin side groups. *Chem. - A Eur. J.* **19**, 8244–8252 (2013).

47. Bandaru, N. M. *et al.* Enhanced adsorption of mercury ions on thiol derivatized single wall carbon nanotubes. *J. Hazard. Mater.* **261**, 534–541 (2013).

48. Sheela, T., Nayaka, Y. A., Viswanatha, R., Basavanna, S. & Venkatesha, T. G. Kinetics and thermodynamics studies on the adsorption of Zn(II), Cd(II) and Hg(II) from aqueous solution using zinc oxide nanoparticles. *Powder Technol.* **217**, 163–170 (2012).

49. Arsuaga, J. M., Aguado, J., Arencibia, A. & López-Gutiérrez, M. S. Aqueous mercury adsorption in a fixed bed column of thiol functionalized mesoporous silica. *Adsorption* **20**, 311–319 (2014).

50. Katok, K. V. *et al.* Synthesis and application of hydride silica composites for rapid and facile removal of aqueous mercury. *ChemPhysChem*. **14**, 4126–4133 (2013).

51. Johari, K., Saman, N., Song, S. T., Heng, J. Y. Y. & Mat, H. Study of hg(ii) removal from aqueous solution using lignocellulosic coconut fiber biosorbents: equilibrium and kinetic evaluation. *Chem. Eng. Commun.* **201**, 1198–1220 (2014).

52. Eloussaief, M., Sdiri, A. & Benzina, M. Modelling the adsorption of mercury onto natural and aluminium pillared clays. *Environ. Sci. Pollut. Res.* **20**, 469–479 (2013).

53. Anagnostopoulos, V. A., Manariotis, I. D., Karapanagioti, H. K. & Chrysikopoulos, C. V. Removal of mercury from aqueous solutions by malt spent rootlets. *Chem. Eng. J.* **213**, 135–141 (2012).

54. Chiarle, S., Ratto, M. & Rovatti, M. Mercury removal from water by ion exchange resins adsorption. *Water Res.* **34**, 2971–2978 (2000).

6.2 Organic compounds degradation under ozonation reaction catalyzed by hybrid material combining fique fiber and metal-organic frameworks based on copper

6.2.1 Abstract

Developing new hybrid materials with potential applications in the catalytic ozonation of organic contaminants in water attracts much attention. Herein, three hybrid materials based on copper were explored for the catalytic ozonation reaction of pharmaceutical emerging contaminants (ECs) like carbamazepine (CBZ) and metoprolol (MET). One of these three catalysts has anchored Cu^{2+} onto the fiber surface (Cu-WET1) and the other two have copper into the structure of the HKUST-1 metal-organic framework supported onto fique fiber (WET1-199) and its modification with thiol groups (SH-WET1-199). The evolution of the degradation of CBZ and MET as model compounds, the Total Organic Carbon (TOC) related to mineralization, and the formation of the by-product was monitored. All the Cu-catalysts showed to have a better catalytic performance on the degradation of MET than CBZ. Moreover, the ozonation catalyzed by Cu-WET1 demonstrated the highest activity in terms of degradation percentage (43.4 ± 3.6 and 52.81 ± 1.4 % for CBZ and MET) and TOC removal (51.4 ± 12.3 and 63.5 ± 13.1 % for CBZ and MET), probably because of the copper availability onto the surface.

In terms of the two materials with metal-organic frameworks grafted, SH-WET1-199 performed better than WET1-199, perhaps due to the Lewis Acid Sites (LAS) increment that the thiol modification produces on the material, improving its interaction with compounds like ECs and also acting as active sites for ozone decomposition. Preliminary simulation (*Kintecus* software) was implemented to understand the O_3/Cu^{2+} catalytic interaction; it was found that the formation of radical oxygen species (ROS), like hydroxyl and hydrogen peroxide from ozone decomposition catalyzed by copper, could reach high concentrations. Also, the influence of the O_3/Cu^{2+} ratio was found to be an important parameter because it can affect the amount of hydrogen peroxide produced, determining which advanced oxidation process (AOP) will happen. If the concentration of H_2O_2 is low, ozonation will be the main reaction. On the contrary, if the concentration is higher than that ofO_3, it will tend to be Fenton-like reaction. The material stability also was studied following morphological and structural changes using SEM and XRD and also by tracking the amount of copper leached (less than 1.5 ppm).

Keywords: catalytic ozonation, fique fiber, metal-organic frameworks, emerging contaminants, copper.

6.2.2 Introduction

The increase in drug consumption has resulted in contamination of aqueous effluents with pharmaceuticals and their partial decomposition compounds, causing damage to ecosystems, mainly in aquatic and human organisms[1]. Currently, they are classified as emerging contaminants (ECs) because they are in concentrations of ng L^{-1}; then, many times they are not recognized as toxic substances and do not have a defined regulation [2]. Factors like the number of drugs prescribed, frequency of use, excretion forms (metabolites or compounds), and the treatment effectiveness, affect the characterization and technological advance in the ECs management [3].

Two of the most frequently detected compounds in aquatic environments are carbamazepine (CBZ) and metoprolol (MET); they belong to the families of antiepileptics and beta-blocker, respectively. Both compounds are excreted in urine as metabolites and some percentage of the initial compound, CBZ reaches average concentrations of 84 - 790 ng L^{-1} and MET 745 – 5000 ng L^{-1} [4]. Different studies have confirmed the ECs resistance to conventional treatments carried out in wastewater treatment plants, making evident the need to develop new technologies or materials capable of contributing to the efficient elimination of this type of contaminants [5].

Advanced oxidation processes (AOPs) are an alternative technology effective in destroying organic molecules such as ECs present in aqueous solutions [6]. AOPs are based on the production of reactive oxidant species, such as hydroxyl radicals (•OH) used in organic pollutants treatment through the implementation of UV radiation / H_2O_2 or O_3, H_2O_2 (hydrogen peroxide), or O_3. These types of processes allow complete mineralization of organic compounds in carbon dioxide and water, or partial oxidation in simpler molecules such as alcohols, aldehydes, or carboxylic acids [1].

Ozonation is a technique applied to wastewater treatment, capable of removing ions such as manganese and iron, it has disinfecting properties and it has also been proved to have high efficiency in the degradation of pharmaceutical ECs, as a result of the molecular ozone reactions and radicals derived from the auto-decomposition of ozone or reactions of ozone with pharmaceutical pollutants [7]. However, it remains a challenge to improve the efficiency of the ozonation process, understand the mechanisms that allow the degradation of organic molecules to achieve mineralization, and improve the economic viability of the process [8].

Intending to improve the ECs mineralization, the ozonation process has explored new catalysts based on metals or metal compounds to promote the ozone conversion into much more reactive oxygen species (ROS), specifically heterogeneous catalysts with transition metals supported oxidize and then regenerate to their initial form, decreasing deactivation and facilitating post-reaction separation [9]. For example, using 4 mg L^{-1} of Cu^{2+} showed high catalytic activity for the mineralization of 5 mM maleic acid [10]. However, few reports clarify the species present in the oxidation or possible transformations that occur between various species present, being an interesting opportunity to elucidate what happens during ozonation when copper is used as a catalyst.

Innovative composite materials such as metal-organic frameworks have just recently been investigated as catalysts in AOPs for the degradation of organic compounds [11]. The few studies available focused on the use of iron based MOFs (i.e. MIL-88B, MIL-100, MIL-53) in Fenton processes for the degradation of dyes, phenol, and antibiotics [12,11]. In particular, MIL-88A (Fe) was used in the treatment of 4-nitrophenol by photocatalytic ozonation reaching a TOC removal of 75.4% [11]. Another report evaluated different types of frames, revealing the Rhodamine B (RhB) degradation; the first-order reaction rate constant was calculated to be 5.76 min^{-1} with MIL- 53 (Fe), 1.82 min^{-1} with MIL-88B (Fe), 1.40 min^{-1} with MIL- 101 (Fe), and 0.87 min^{-1} with MIL-100 (Fe) [13].

Applications reported with catalytic ozonation processes using MOFs are limited to gaseous effluents and not much with liquids, because of the MOFs low stability in aqueous media [14,15]. Consequently, the efficiency and mechanisms of catalytic ozonation with different types of MOFs have not been explored yet, which could be interesting in applications with ozone due to the high concentration of Lewis acid surface sites observed in the materials synthesized in this study and its beneficial effect on the ozone decomposition into ROS [13].

The present work aimed to explore the catalytic activity of hybrid materials combining metal-organic frameworks based on copper supported onto fique fibers, in the degradation of pharmaceutical ECs like CBZ and MET by ozonation. From these results, the kinetic reactions that took place in the Cu-MOF-fique/O_3 catalytic system were investigated. It allowed to analyze which oxidizing species probably prevailed in the reaction system and a kinetic model was developed to elucidate the reactions involved in the CBZ and MET degradation.

6.2.3 Materials and methods

6.2.3.1 Chemicals and materials

Ammonium chloride (≥99%), nitric acid (90%), oxalic acid (≥99%), oxamic acid (≥96%), sodium nitrate (≥99%), 2,6-pyridine dicarboxylic acid (≥99%), sodium carbonate (≥99%), acetonitrile (≥99%) and formic acid (98%–100%), $TiO(SO_4)$ (15 wt% in H_2SO_4), also carbamazepine (CBZ) and metoprolol (MET) analytic standards were purchased from Sigma Aldrich. Sodium nitrite (≥99%) was provided by Fluka, and sulfuric acid (95%–98%) from Labor. The standard solutions, as well as pollutant solution and eluents, were prepared with ultrapure water obtained from the Direct-Q Millipore system.

6.2.3.2 Catalytic test

The CBZ and MET degradation by ozonation reaction in aqueous solution was studied in batch experiments using a glass laboratory cylinder reactor (60 mm diameter, 250 mm height). Three hybrid materials and one blank were tested as catalysts: Cu-WET1 (functionalized fiber + Cu^{2+}), WET1-199 (functionalized fiber + HKUST-1), SH-WET1-199 (functionalized fiber + SH-HKUST-1), and as blank was used WET1 (functionalized fiber by TEMPO oxidation). Ozone (O_3) was produced from pure oxygen using a BMT 802X ozone generator; its concentration was continuously measured with a BMT 964 analyzer (BMT MESSTECHNIK GMBH, Stahnsdorf, Germany).

In a typical run, the reactor was filled with 250 mL of CBZ or MET solution (10 $mg \cdot L^{-1}$) and 0.1 g of hybrid material, the reactions were kept under magnetic agitation of 250 rpm, and the pH (≈ 6.4) was not modified avoiding to add more reagents to control the pH. The O_3 stream (75 $cm^3 \cdot min^{-1}$) was bubbled trough a ceramic diffusor (1 cm in diameter) with a concentration of 50 $g \cdot m^{-3}$; the residual O_3 was removed and collected in vessels with potassium iodide (KI 20%). To reach a homogeneous O_3 concentration into the liquid solution, the hybrid material was added after 5 min, which was established as zero reaction time. Aliquots were collected from the reactor regularly for 2 h to be analyzed by HPLC; at the end of each run, a sample was taken to quantify the TOC. Additionally to catalytic runs, the individual processes were tested for comparative purposes; they included: adsorption, ozonation, blank (O_3 + WET1) and pharmaceutical ozonation (O_3 + ECs).

The pollutant adsorption capacity in solution was determined for each value of initial concentration, with experimental data equilibrium concentration and initial concentration, using Eq.6.2.1.

$$q_e = \frac{(C_i - C_e)V}{w} \qquad \text{(Eq. 6.2.1)}$$

Where q_e is the adsorption capacity (mg g^{-1}), C_i is the initial pollutant concentration (adsorbate) in solution (mg L^{-1}), C_e is the solute concentration in the equilibrium (mg L^{-1}), V (L) is the volume of the pollutant solution and w is the adsorbent mass (g).

The degradation percentage of the emerging contaminants (ECs) was expressed by Eq. 6.2.2:

$$\text{Degradation}\ (\%) = \frac{(C_o - C_e)}{C_0} x\ 100\% \qquad \text{(Eq. 6.2.2)}$$

Where, C_o and C_e are the initial and equilibrium concentrations of CBZ or MET in solution.

6.2.3.3 Analytic methods

CBZ and MET concentrations were followed by high-performance liquid chromatography (HPLC) using a Shimadzu Corporation HPLC (Tokio, Japan) equipment with two detectors, fluorescence FD (RF-20A xs) and diode array detector DAD (SPD-M20A), two pumps (LC-30AD), an autosampler (SIL-30AC), an oven (CTO-20AC), a degasser (DGU-20A 5R), a system controller (CBM-20A) and the software LC Solution Version 5.41SP1. The stationary phase was composed by KinetexTM 1.7 µm XB-C18 100 Å (100 × 2.1 mm i.d.) column, and the mobile phase was a gradient (50:50, CBZ and 80:20, MET) of 0.1% formic acid and acetonitrile at 0.2 mL·min^{-1} with a total run time of 4 min and injection volume of 50 µL. CBZ and MET were identified by DAD (wavelength 285 nm) and FD (at 230 nm excitation and 290 nm emission), respectively.

Oxalic and oxamic acids were analyzed in an isocratic HPLC Hitachi Elite LaChrom (Hitachi High-Technologies Corporation, Kagoshima, Japan) system, equipped with the Alltech AO-1000 (Fisher Scientific, Hampton, NH, USA) separation column (300 × 6.5 mm) equilibrated with 5 mM sulfuric acid – water, 50:50 (v/v) at flow rate 0.5 mL·min^{-1} and injection volume of 15 µL. The separation column was kept at ambient temperature. The detection was carried out with a UV detector and the wavelength was set at 200 nm.

Ion chromatography (IC) was implemented to investigate the ion species produced after the ozonation reaction (ammonium, nitrates and nitrites). This identification was performed on a

Metrohm 881 Compact IC Pro equipment. Nitrates (NO_3^-) and nitrites (NO_2^-) were detected in the Metrosep A Supp 7 column (250 × 4 mm) with a Metrosep P2 Guard/3.5 pre-column at 45 °C, using as mobile phase solution of 3.6 mM sodium carbonate, flow rate of 0.7 mL·min^{-1}, and injection volume of 20 µL. Ammonium (NH_4^+) ions were quantified by a Metrosep C4 column (250 × 4.0 mm) from Metrohm with Metrosep C4-S-Guard/4.0 pre-column at 25 °C, the eluent was a solution of 0.7 mM of 2,6-pyridine dicarboxylic acid and a solution of 1.7 mM of nitric acid at 0.7 mL·min^{-1}, and injection volume of 20 µL.

The detection of Total Organic Carbon (TOC) was done using a Shimadzu L-TOC Total Organic Carbon Analyzer coupled to a Shimadzu ASI-L auto sampler, by the Non-Purgable Organic Carbon (NPOC). The samples were collected after 2 h of reaction and were analyzed without any pretreatment.

Hydrogen peroxide produced along the reaction was determined through a colorimetric method [16]. An aliquot of 1 mL, was acidified with 1 mL of sulfuric acid (0.5 M) and then 0.1 mL of $TiO(SO_4)$ (15 wt% in dilute H_2SO_4) was added. The solution prepared before was measured by UV-VIS spectrometer at 405 nm. A calibration absorption curve of H_2O_2 from 0.03 to 2.94 mM was prepared by diluting a standard mixture of 30 wt% H_2O_2.

6.2.3.4 O_3 /Cu^{2+} kinetic modeling study

The concentrations interpretation of oxidant radicals and the ozone catalysis process evolution using the Cu-WET1 catalyst (it is the only one with 100% copper as Cu^{2+}) was established using Kintecus 6.51 software [17]. All the reaction rate constants were collected from the literature. Only the reactions of inorganic compounds were considered in the kinetic model, due to the high concentrations of the pollutants tested and the subproducts released could affect the steady-state ROS concentrations.

6.2.3.5 Materials characterization after the ozonation reaction

Hybrid materials were characterized after the ozonation reactions by X-ray diffraction (XRD), performed by a PANalytical X'Pert PRO diffractometer with a Cu Ka radiation source (λ = 1.54 nm). The voltage and current used were 50 kV and 40 mA, respectively. The diffractions were collected between 2θ = 10° to 50°. The Rietveld refinement was used to analyze the results.

In addition, morphological characterization of samples was performed via Scanning Electron Microscope (SEM) implemented on thin film gold coated samples using a Zeiss Auriga FIB-SEM (GeminiSEM) scanning electron microscope, coupled to a secondary electrons (SE2) detector. The micrographs were taken at 1.5 kV, working distance (WD) ranging from 4.9 to 5.2 mm, at different magnifications.

ICP-OES (Inductively Coupled Plasma - Optical Emission Spectrometry) was used to identify and quantify the copper present in the solutions analyzed after the ozonation reactions. All experiments were conducted using an iCAP 7400 ICP-OES instrument (Thermo Fisher Scientific). Plasma conditions were as follows: RF power: 1250 W, auxiliary gas flow: 0.5 dm^3/min, coolant gas flow: 12 dm^3/min, nebulizer gas flow: 0.5 dm^3/min, and nebulizer gas pressure: 270 kPa. Spectra were analyzed using Qtegra ISDS (Thermo Fisher Scientific). The iCAP 7400 ICP-OES instrument was calibrated to copper, using the respective elemental standard (1 mL) in concentrated HNO_3 with deionized water

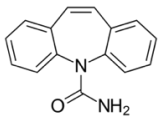
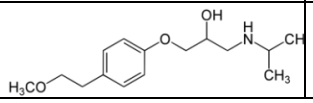
6.2.4 Results and Discussion

6.2.4.1 Adsorption capacity

To determine if the fiber functionalized (WET1), HKUST-1+fiber (WET1-199), SH-HKUST-1+fiber (SH-WET1-199) and impregnated fiber (Cu-WET1) adsorb carbamazepine (CBZ) and metoprolol (MET) effectively, a batch process was conducted, keeping the operational conditions implement in the ozonation reaction.

Figure 6.2.1 shows the adsorption capacity (q_e) reached for all materials after 2 h. CBZ was less adsorbed than MET; MET has in its chemical structure functional groups such as amines, hydroxyl, ether, methyl, and methoxy, which increase the electrostatic interaction with the surface of the materials evaluated as adsorbents, while CBZ is a condensed monocyclic compound (Table 6.2.1) that hardly interacts with the material's surface since it only has one amide group available to interact.

Table 6.2.1. Physical and chemical properties of CBZ and MET [9].

ECs	Structural formula	Chemical formula	Molecular weight (g mol^{-1})	Solubility in water at 25°C (mg L^{-1})	pK$_a$	Log K$_{OW}$	Concentration measured in effluents (mg L^{-1})
CBZ		$C_{15}H_{12}N_2O$	236	17.7	-3.8, 15.96	2.45	1 x 10^{-6} – 1.1 x 10^{-2}
MET		$C_{15}H_{25}NO_3$	267	1.7 x 10^4	9.7, 14,09	1.88	5 x 10^{-6} – 3 x 10^{-3}

Additionally, both CBZ and MET at pH = 7 are in their neutral form given the corresponding pKa values (15.96 and 9.7 respectively), limiting possible electrostatic interactions with the evaluated materials. Also, the low adsorption observed for WET1, WET1-199, SH-WET1-199 and Cu-WET1 may be due to the negatively charged surface that all the materials have under the experiment pH = 7, when compared to the zero-point charge of each material, values previously obtained in chapters 3 and 5.2, and summarized in Table 6.2.2.

Table 6.2.2. pHpzc of all the materials used as adsorbents to remove CBZ and MET

Material	pHpzc
WET1	5.18 ± 0.05
Cu-WET1	4.85 ± 0.05
WET1-199	4.17 ± 0.09
SH-WET1-199	4.12 ± 0.1

In particular, in the case of the CBZ adsorption (Figure 6.2.1), the fiber impregnated with Cu^{2+} reached the highest adsorption capacity, with a value of 17.29 µg CBZ / g material, followed by SH-WET1-199 with q_e = 9.95 µg CBZ / g material and the other two materials WET1 and WET1-199 obtained similar values of adsorption capacity, 6.37 and 7.50 95 µg CBZ / g material, respectively. The low adsorption observed for CBZ can be a consequence of interactions such as Van der Waals forces and π-π bonds, these are the dominant mechanism for elimination of non-polar pollutants compounds like CBZ using PAC (powder active carbon) (log K_{OW}> 2), the efficiency of this treatment reported reductions around 49-99% after 4 h of contact time with 10 and 20 mg L^{-1} [18]. Similar studies like Akpinar *et al.* [19] used an initial CBZ concentration of 100 mg L^{-1} with the metal-organic framework UiO-66 and active carbon; after 120 min the equilibrium uptake of CBZ was found to be 82.61 mg g^{-1} and 75 mg g^{-1}-Comparing the adsorption capacity of the materials produced in this investigation with others, it is noticeable the materials with fique fiber failed to adsorb CBZ significantly.

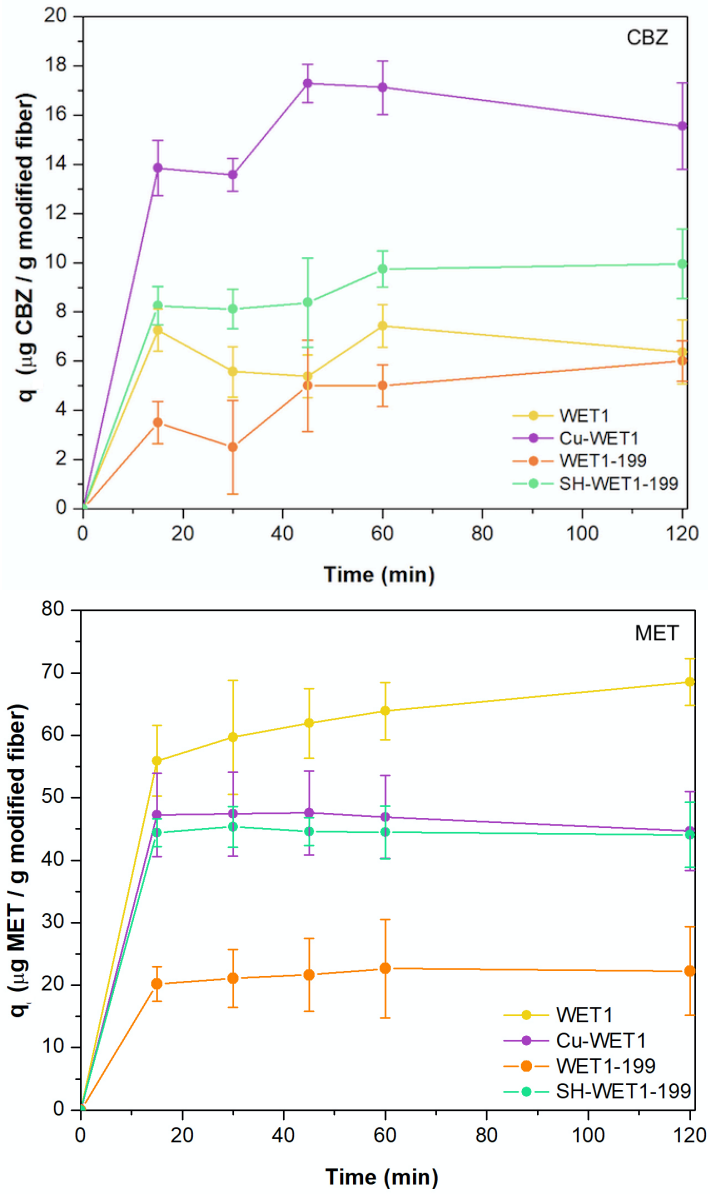


Figure 6.2.1. Adsorption capacity of CBZ and MET (C_o = 10 mg L^{-1}), during 120 min in contact with 0.1 g of the materials: WET1, Cu-WET1, WET1-199 and SH-WET1-199, room temperature and pH = 6.45, separately.

Regarding MET, all the materials demonstrated to reach the saturation after 15 min, WET1 reported the highest value of adsorption capacity (68.55 µg MET / g material), while Cu-WET1 and WET1-199 reported q_e values corresponding to 44.65 and 22.67 µg MET / g material; the lowest adsorption capacity was reported for WET1-199. Similar studies reporting the adsorption of MET using 100 mg L^{-1}, pH = 8 and 1.5 g of active carbon, obtained an adsorption capacity of MET of 120 mg g^{-1} after 60 min [20], contrasting with the smaller adsorption capacities observed for the materials produced with fique fiber and metal-organic frameworks [21].

Under the experimental adsorption conditions in which the synthesized materials were evaluated in this study, the adsorption efficiency percentage of CBZ and MET were very low for both compounds. This fact, is explained by the solid adsorption prediction guide applicable to non-polar compounds that suggests a low adsorption potential of organic pollutants with an octanol / water partition coefficient (log K_{OW}) of less than 2.5 [22], like CBZ or MET (Table 6.2.1). Finally, it can be indicated the adsorption process did not contribute significantly to the CBZ or MET removal, so from now on the contribution to the pharmaceutical removal by this process can be assumed to be negligible.

6.2.4.2 Catalytic activity

As previously described, the CBZ or MET adsorption on the materials evaluated as catalysts was practically zero throughout the entire reaction, for which all the degradation results obtained were attributed to the ozonation reaction. The ECs elimination in AOPs such as ozonation can occur in two ways, direct oxidation of organic molecules by O_3 at pH <4 or indirect oxidation with ROS (Eq. 6.2.3) formed from the ozone decomposition at pH> 9. Then, under the experimental conditions in which the experiments in this research were carried out, the two mechanisms could coexist at the same time [6].

While direct oxidation is selective and slow or even null with some species, reaction rate constants are lower, resulting in oxidation/reduction, cycloaddition, substitution or nucleophilic addition reactions [7]. On the contrary, $^{\bullet}OH$ have high oxidation rate constants, which means very rapid and non-selective oxidation of organic compounds; besides, $^{\bullet}OH$ radicals react quickly with molecular O_3, contributing to its auto-catalytic decomposition [23,24].

The degradation of CBZ and MET are shown in Figure 6.2.2, which stabilized after 10 min for CBZ and 30 min for MET, for all the catalysts analyzed. The experiments performed only with O_3 catalyzed with hybrid materials with copper (impregnated or coordinated in MOFs) managed to have a higher reduction for MET than CBZ, and the degradation of both ECs increased compared to the use of only O_3 in 44 and 27%, respectively. Confirming the literature reports in which the oxidative capacity of ozone is insufficient to achieve complete degradation of this type of pollutants [25,26]. Regarding the homogeneous ozonation reaction, CBZ and MET were reduced 98 and 99% due to the copper catalytic activity. However, the hybrid materials studied favored the partial removal of the ECs of interest, with better results compared to the reaction only with O_3.

The heterogeneous reaction process was lower compared to the homogeneous, because of the copper accessibility during the ozonation reaction.

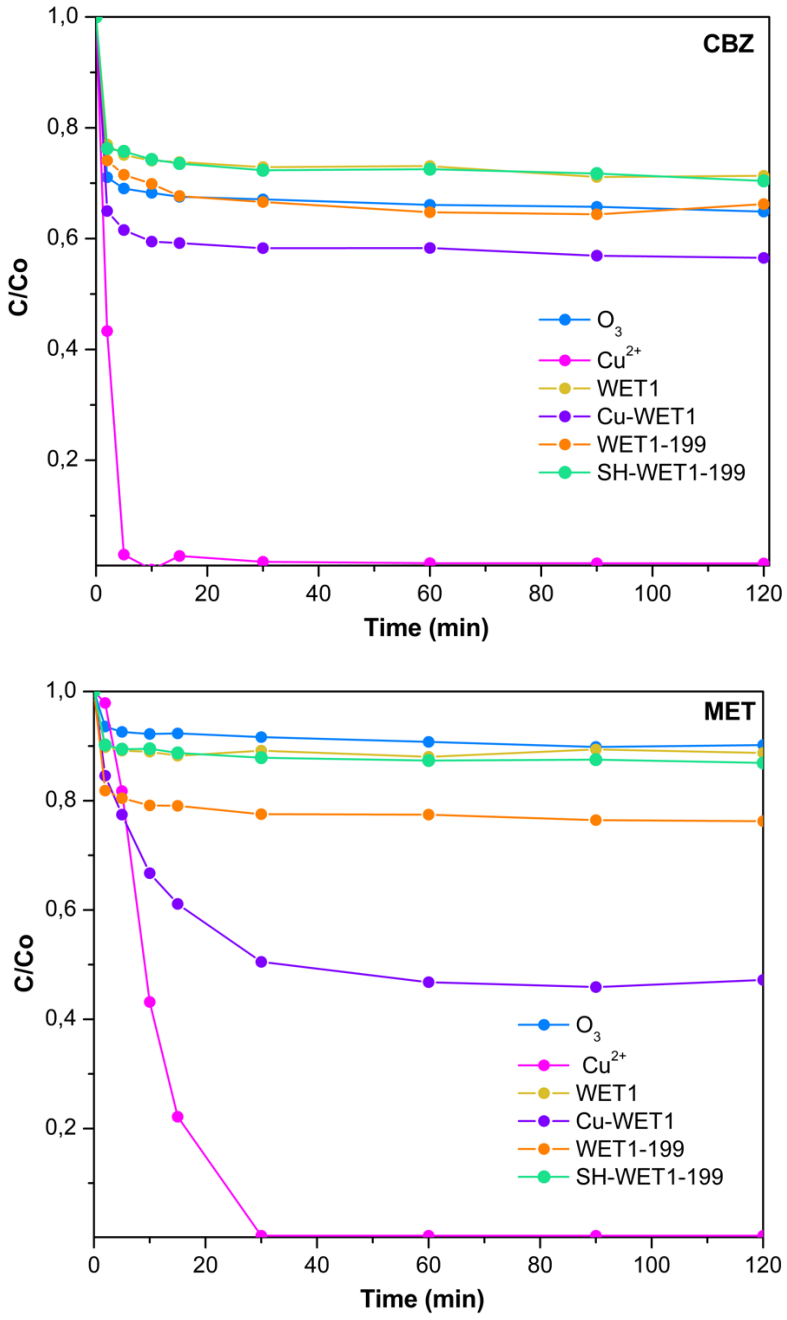


Figure 6.2.2. Degradation kinetics of CBZ and MET in ozonation heterogeneous processes catalyzed by the materials WET1, Cu-WET1, WET1-199 and SH-WET1-199. Besides, degradation kinetics of CBZ and MET in ozonation homogeneous processes catalyzed by Cu^{2+}. Both catalysis at room temperature and pH = 6.45, separately.

The best degradation rate was observed for materials with supported copper (Cu-WET1), since transition metals such as Cu(II) act as catalysts for reactions with ozone, improving self-decomposition, accelerating the generation of active free radicals or increased molecular reactions of ozone [27]. On the other hand, the reaction of the materials with supported metal-organic frameworks (WET1-199 and SH-WET1-199) was reduced compared to Cu-WET1, intuitively due to the lower ozone decomposition, since copper could be playing two roles at the same time, acting as metallic coordination centers in the frame structures and as catalysts of the reaction with O_3.

The degradation of CBZ and MET carried out by the systems O_3/ WET1-199 and O_3/ SH-WET1-199 could be the result of many active sites available and the facility of diffusion within these frames, a consequence of the material's porosity, which improves the accessibility to active sites, increasing the ozonation efficiency. According to some authors, functionalization's MOFs develop the content of active sites in the frames, which results in improvements in catalytic reactions due to increased selectivity [28]. However, SH-WET1-199 contained a metal-organic frame functionalized with thiol groups (-SH) which did not serve as a decisive element for the evaluated catalytic system, since both CBZ and MET in Figure 6.2.2 showed to have a behavior very similar to the support functionalized of fique fibers (WET1), allowing to affirm that thiol groups interfere negatively in the catalysis of copper with ozone [29].

On the contrary, the material WET1-199, which contains MOFs of HKUST-1, a frame with copper metal centers and trimesic acid (BTC) linkers, gave it the character of an acid catalyst which serves to promote the reaction with molecules that contain nitrogen such as MET and CBZ [28]. According to previous characterization (subchapter 5.1), MOFs such as HKUST-1 possess Lewis Acid Sites (LAS), which have an important role in the O_3 decomposition since it can be easily adsorbed in LAS and subsequently decomposed in reactive oxidation. LAS are also active sites for hydrogen peroxide (H_2O_2) and the activation of reactions similar to Fenton, thus achieving some performance in catalytic ozonation [13].

Comparing the ozonation systems used for the degradation of CBZ and MET, Figure 6.2.3. shows higher degradation efficiencies in systems that included copper compared to those only using ozone as an oxidant, confirming the catalytic copper effect, shown in Figure 6.2.2 of the ECs analyzed. This behavior is due to reactions with O_3 and CBZ or MET that mainly involve hydroxyl radicals ($^{\bullet}OH$) as oxidizing species, while the copper-catalyzed system also generates

ROS as superoxide ($^{\bullet}O_2^-$), hydroperoxyl ($HO_2^{\bullet}$), and hydrogen peroxide (H_2O_2), facilitating the degradation of these pollutants.

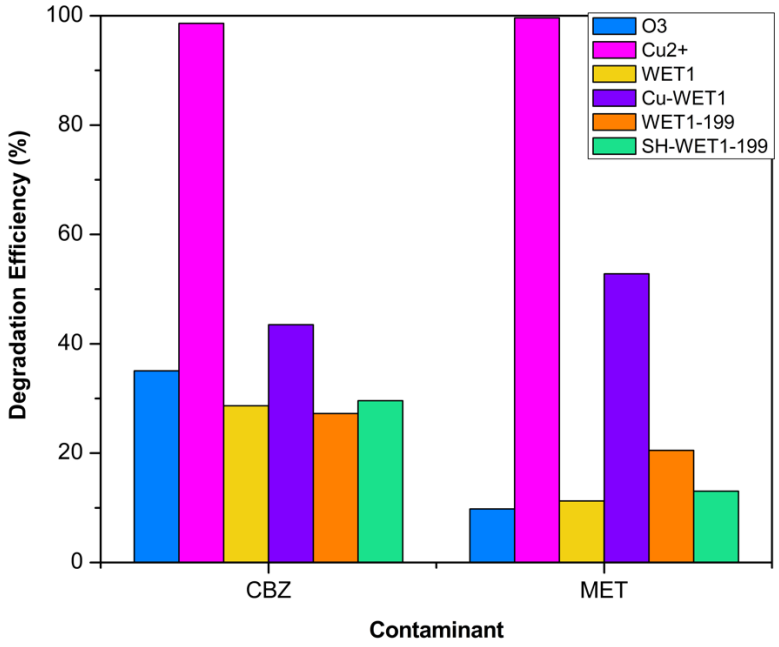


Figure 6.2.3. Degradation efficiency of CBZ and MET in ozonation processes catalyzed by the materials WET1, Cu-WET1, WET1-199 and SH-WET1-199, room temperature and pH = 6.45, separately.

Regarding the degradation efficiency of the heterogeneous system catalyzed by copper, it was lower compared to the homogeneous. The radicals concentration in heterogeneous was much lower than in homogeneous, so there was less degradation of pollutants as a consequence of more competition from $^{\bullet}OH$ radicals than H_2O_2.

Specifically, the contribution of MOFs in the degradation efficiency of CBZ was not positive since, as previously explained, the chemical structure of this compound (*i.e* presence of reactive groups) allows the $^{\bullet}OH$ radicals to attack the EC molecules through three types of reactions: i) radicals addition to double bonds, but not to C = O, ii) hydrogen abstraction, iii) electron transfer [30]. Table 6.2.3 summarizes the possible functional groups that could be attacked in the compounds of interest employing ozone and hydroxyl radicals, catalyzed by hybrid materials (MOF / fiber fibers).

On the contrary, it was discovered that, of all the materials evaluated in the ozone catalytic reaction, Cu-WET1 (fique fiber functionalized with carboxylate groups, impregnated with Cu^{2+} ions) presents the best performance, since it managed to increase the degradability of both pollutants. In particular, the MET oxidation was a more efficient process compared to CBZ, due

to the presence of amino functional groups, aromatic rings, double bonds (electron donors), while CBZ is much more recalcitrant because of the presence of an amide group that has the role of capturing electrons, which means it is less easily oxidized by ozone.

Table 6.2.3. Important reaction mechanism of oxidant species with reactive chemical groups of CBZ and MET.

Active compound	Important reaction mechanism	Reactive groups		Important groups with limited reactivity	
		CBZ	MET	CBZ	MET
$^{\bullet}$OH radicals	Radical addition to double bods	C=C	C=C	C=O	O-H
	Hydrogen abstraction related to the R-H bond dissociation energy	Tertiary C-H > secondary C-H	Tertiary C-H > secondary C-H > primary C-H		
O_3	Direct oxidation, cycloaddition, electrophilic substitution	Electron-rich functional groups: C=C, amines (N-R_3, NH_2-R)	Electron-rich functional groups: C=C, methoxy, amines (NH-R_2)	Electron-withdrawing functional groups: amides	------
	Decomposition to generate $^{\bullet}$OH radicals through electron transfer to electron-rich organic moieties in organic matter	Activated aromatic compounds, amines (N-R_3, NH_2-R), C=C	Activated aromatic compounds, amine (NH-R_2), C=C	------	------

Ozonation leads to the formation of by-products, caused by partial oxidation of CBZ or MET, only partially mineralizing the ECs. To carry out the adequate TOC quantification in reactions with ozone, it was necessary to perform normalization respect to the measurement of total organic carbon, since the lignocellulosic supports contributed to a certain amount of TOC, as a consequence of the releasing of functional groups present in their structures to the solution. For example, the functionalized fiber WET1 had a process of chemical activation through TEMPO oxidation to generate carboxylate groups, and in the materials with metal-organic frameworks, the organic linkers of trimesic acid could contribute with the value of TOC in solution (Figure 6.2.4).

The ECs mineralization was monitored with the changes in TOC (Figure 6.2.5) The non-catalytic ozonation (only with O_3) led to a minimal elimination of both pollutants (blue bar Figure 6.2.5), with values of 1.27 and 4.42% for CBZ and MET, respectively. In general, when the catalytic system with ozone and copper was used as catalyst, either within MOFs or impregnated in Cu^{2+} form, mineralization increases for both pollutants, in all systems. Specifically, when the catalysis was carried out using MOFs, the degradability of CBZ increased by 18.1 and 34.6%, using

WET1-199 and SH-WET1-199, respectively. The highest mineralization percentage reduction for both contaminants were reached by the homogeneous system catalyzed by copper (Figure 6.2.5 pink).

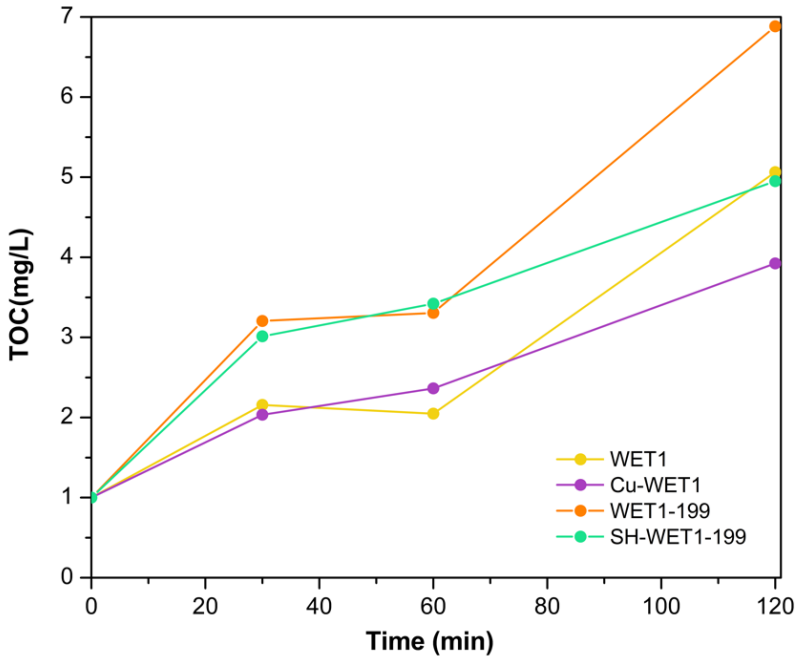


Figure 6.2.4. Normalized Total organic carbon (TOC) measured as blank for the materials: WET1, Cu-WET1, WET1-199 and SH-WET1-199.

On the other hand, MET achieved greater mineralization compared to CBZ using the same MOFs, values of 21.7 and 54.3% of partial mineralization were obtained by WET1 and SH-WET1-199, confirming transition metals such as copper acted as catalysts (characterized before in the sub-chapter 5.2). It was interesting to see between the two frames, SH-HKUST-1 contained both metals (copper and sulfur) achieved the best TOC reduction for MET, it could be attributed to the by-products generated during ozonation which were attacked and mineralized.

However, the oxidizing capacity changes when copper was not coordinated within the MOFs but is completely available on the surface in the form of Cu^{2+}, as is the case of the Cu-WET1 material, which achieved the greatest reduction of TOC in both pollutants (Figure 6.2.5), reaching values of 50.2 and 59.2% elimination of TOC after 120 min for CBZ and MET, respectively. In this case, the probable reaction mechanism involved is the interaction of ECs with the sites on the oxidized surface, proving the performance obtained by the materials with MOFs was limited because the metallic centers of these structures were not fully available to interact with the oxidizing species

in solution. However, regardless of the catalyst used, none achieved complete mineralization of CBZ or MET; it was found MET is a less refractory drug than CBZ.

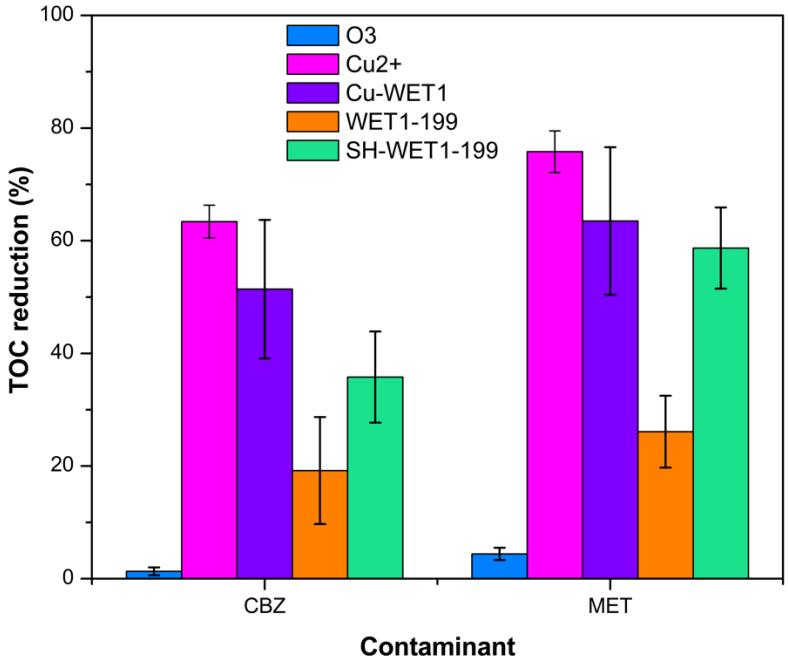


Figure 6.2.5. Normalized TOC of CBZ and MET (C_o = 10 mg L^{-1}), after 120 min in contact with 0.1 g of the materials: Cu-WET1, WET1-199 and SH-WET1-199, room temperature and pH = 6.45, separately.

It is important to mention that the surface chemistry and textural properties of the evaluated materials had an important role in the O_3 decomposition. The lignocellulosic materials are rich in oxygenated groups (characterization reported in previous chapters), which do not contribute to O_3 decomposition. In comparison, when carbon materials are used as catalysts, the ozonation reaction is favored with large surfaces and high porosity, the contrary of the hybrid materials evaluated [31].

To identify if the degradation evidenced by TOC (Figure 6.2.5) could be attributed to complete mineralization or it was the generation of by-products due to the attack of certain functional groups in the structure (Table 6.2.3), the quantification of carboxylic acids such as oxalic (OXL) and oxamic (OXM) was carried out. These are characteristic by-products of degraded organic molecules through advanced oxidation processes due to their highly refractory character. The results are shown in Figure 6.2.6, where it was distinguished the formation of OXM and OXL during the first 5 min of reaction, only in systems in which copper was present inthe catalyst (Cu-WET1-199, WET1-199, and SH- WET1-199).

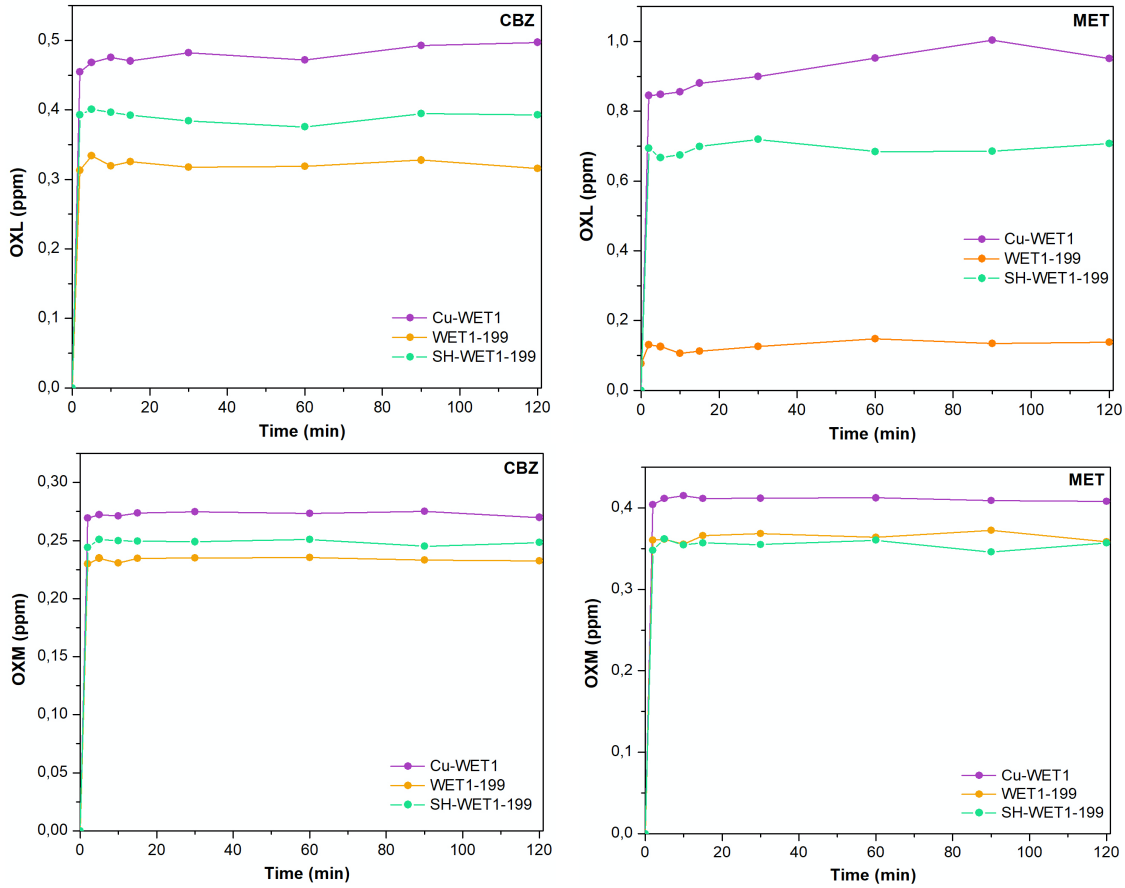


Figure 6.2.6. Oxalic (OXL) and oxamic (OXM) acid concentration measured during the a) CBZ and b) MET (C_o = 10 mg L^{-1}) ozonation, after 120 min to be in contact with 0.1 g of the materials: Cu-WET1, WET1-199 and SH-WET1-199, separately.

In general, both by-products reached a maximum concentration with CBZ and MET, after which it became constant after 120 min of treatment, presumably involving the cleavage of the aromatic rings in CBZ and MET contaminants, which in turn generated intermediate compounds in solution, including carboxylic acids, which would mean the partial mineralization of these contaminants.

Additionally, Table 6.2.4 shows the quantification of nitrate, nitrite, and ammonium ions after ozonation when partial mineralization was evidenced. The results support the data obtained for the OXM and OXL acids, in which the heterogeneous resulted in more stable reaction by-products; then, limiting the TOC reduction.

Regarding the two anions analyzed, there was no presence of nitrites, but rather nitrates, the more oxidized form, which present similar values when carrying out the degradation of CBZ or MET with and without a catalyst. In addition, in all the pollutants reactions, either only with O_3 or

catalyzed with copper, the formation of small ammonium concentrations was identified after 120 min of treatment. Slightly higher values were obtained in the presence of a catalyst, which probably occurred due to the attack of functional groups such as amines present in CBZ and MET molecules.

Table 6.2.4. Ions quantified from the CBZ and MET (C_o = 10 mg L^{-1}) ozonation, after 120 min to be in contact with 0.1 g of the materials: Cu-WET1, WET1-199 and SH-WET1-199, separately.

Materials	Nitrates (NO_3^-) (mg L^{-1})		Nitrites (NO_2^-) (mg L^{-1})		Ammonium (NH_4^+) (mg L^{-1})	
	CBZ	MET	CBZ	MET	CBZ	MET
O_3	1.45	1.74	0	0	9.34	9.06
O_3 / Cu-WET1	1.38	2.50	0	0	14.5	11.1
O_3 / WET1-199	1.94	1.38	0	0	11.8	13.5
O_3 / WET1-199-SH	1.38	3.25	0	0	11.1	11.6

According to the results summarized in Table 6.2.5., MET was able to be degraded in a greater extent compared to CBZ, although both compounds have aromatic rings in the structure and their reactivity with ozone is low (CBZ [32]: 3.0 x 10^5 M^{-1} s^{-1} and MET [33]: 2.0 x 10^3 M^{-1} s^{-1}). MET contains electron-donating substituents, such as hydroxyl, alkyl and amine groups (Table 6.2.3), which allowed increasing reactivity with ozone. On the contrary, CBZ has electron-withdrawing groups, e.g. amide, which deactivates the benzene ring producing a significant reactivity decrease; then, it was found that the presence of active groups increased in pollutant degradation. However, the TOC reduction was not complete because possibly CBZ and MET were attacked on the C = C groups of the benzoic rings of their chemical structures, generating their rupture and although these remain reactive to ozone they can be transformed into more stable carbonyl by-products such as quinone or hydroxy compounds of the benzene ring [34].

Table 6.2.5. Summary of results obtained from the ozone catalytic system and hybrid materials with copper for the treatment of CBZ and MET.

Catalytic system	% Degradation		% TOC reduction		k_{obs} (s^{-1})			
	CBZ	MET	CBZ	MET	CBZ	R^2	MET	R^2
O_3	35.0 ± 1.6	9.8 ± 2.5	1.3 ± 0.7	4.4 ± 1.1	$8.7x10^{-2}$	0.87	$1.8x10^{-2}$	0.89
O_3/Cu-WET1	43.4 ± 3.6	52.8 ± 1.4	51.4 ± 12.3	63.5 ± 13.1	$1.1x10^{-1}$	0.89	$5.6x10^{-2}$	0.96
O_3/WET1-199	27.2 ± 2.2	20.5 ± 2.8	19.3 ± 9.5	26.1 ± 6.4	$7.9x10^{-2}$	0.88	$5.1x10^{-2}$	0.87
O_3/WET1-199-SH	29.6 ± 1.7	13.1 ± 1.3	35.8 ± 8.1	58.7 ± 7.2	$6.7 x10^{-2}$	0.85	$2.6x10^{-2}$	0.87

Additionally, in Table 6.2.5 the kinetic reaction constants (k_{obs}) observed during the first 5 minutes are shown, the time where degradation rate was higher for both pollutants, capable of increasing the pollutants mineralization (confirmed with the TOC reduction), after this time the reaction in all

materials stabilized. When comparing the k_{obs} of each of the contaminants of interest treated in this study, the reaction rate of CBZ was slightly faster with all catalyst systems compared to MET, when WET1 was used (except Cu-WET1). Furthermore, of all the catalysts evaluated, it was Cu-WET1 that could have generated additional by-products, allowing the CBZ and MET to be less refractory, through the best reduction in the percentage of degradation and TOC values.

Although there are reports in which copper is used as a catalyst for the ozone reaction, most of the literature refers to homogeneous catalysis [24] and few to heterogeneous [35]. Independently of the type of catalysis carried out, there is an agreement on the beneficial effect of the catalyst on the decomposition of ozone to generate active oxidants, improving the oxidation of organic molecules [10,35]. However, other reports state that the previous statement is true to a certain extent because, although the formation of hydroxyl radicals is evident, the formation of other oxidizing species cannot be ignored, such as hydrogen peroxide or superoxide radicals[36]. It is necessary to analyzed in more detail if they can also have a ROS scavenger effect. The Cu (II) catalyzed ozonation process is complex, and there are still not many reports that allow to fully elucidate the mechanism [27].

6.2.4.3 Kinetic study of O3/Cu2+ reaction based on the simulation of chemical reactions

In order to elucidate which ROS were involved in the degradation of ECs, and the plausible mechanism involved in the ozonation process with and without catalyst in the O_3 / Cu^{2+} system, a kinetics analysis on the obtained data was performed using the Kintecus 6.51 software [17]. O_3 can be broken down by two reaction mechanisms: i) Direct decomposition in the aqueous medium initiated by hydroxyl ions (OH^-), producing hydroperoxyl ($HO^{\bullet}_2$) and superoxide ($^{\bullet}O_2^-$) radicals (Eq. 6.2.3), ii) via reactive oxygen species (ROS) such as $^{\bullet}OH$, $^{\bullet}O_2^-$ and other intermediate radicals such as $HO^{\bullet}_2$ also produced (Eq. 6.2.4 and 6.2.5).

In addition, the transformation of some ROS is also contemplated (Eq. 6.2.6 to 6.2.10) as well as the production of hydrogen peroxide (H_2O_2) by radical recombination reactions (produced between the radicals, described in Eq. 6.2 .11 and 6.2.12). H_2O_2 reactions as a radical scavenger were included (Eq. 6.2.13 and 6.2.15) [24]. From literature data, the main reactions are detailed below with their rate constants used to describe the decomposition of O_3 in water [24], at pH ≈ 7.

$O_3 + OH^- \rightarrow HO^{\bullet}_2 + {}^{\bullet}O_2^-$	$7.0 \times 10^1\ M^{-1}\ s^{-1}$	Eq. 6.2.3 [37]
$O_3 + HO_2^- \rightarrow OH^{\bullet} + {}^{\bullet}O_2^- + O_2$	$5.5 \times 10^6\ M^{-1}\ s^{-1}$	Eq. 6.2.4 [37]
$O_3 + {}^{\bullet}OH \rightarrow HO^{\bullet}_2 + O_2$	$2.0 \times 10^9\ M^{-1}\ s^{-1}$	Eq. 6.2.5 [38]
${}^{\bullet}OH + HO^{\bullet}_2 \rightarrow H_2O + O_2$	$7.1 \times 10^9\ M^{-1}\ s^{-1}$	Eq. 6.2.6 [39]
${}^{\bullet}OH + {}^{\bullet}O_2^- \rightarrow OH^- + O_2$	$8.5 \times 10^9\ M^{-1}\ s^{-1}$	Eq. 6.2.7 [39]
$HO^{\bullet}_2 \rightarrow H^+ + {}^{\bullet}O_2^-$	$1.6 \times 10^5\ M^{-1}\ s^{-1}$	Eq. 6.2.8 [40]
$H^+ + {}^{\bullet}O_2^- \rightarrow HO^{\bullet}_2$	$5.0 \times 10^{10}\ M^{-1}\ s^{-1}$	Eq. 6.2.9 [41]
${}^{\bullet}O_3^- + {}^{\bullet}OH \rightarrow HO^{\bullet}_2 + {}^{\bullet}O_2^-$	$8.5 \times 10^9\ M^{-1}\ s^{-1}$	Eq. 6.2.10 [42]
$HO^{\bullet}_2 + HO^{\bullet}_2 \rightarrow H_2O_2 + O_2$	$1.2 \times 10^7\ M^{-1}\ s^{-1}$	Eq. 6.2.11 [43]
${}^{\bullet}OH + {}^{\bullet}OH \rightarrow H_2O_2$	$5.0 \times 10^9\ M^{-1}\ s^{-1}$	Eq. 6.2.12 [43]
${}^{\bullet}OH + H_2O_2 \rightarrow HO^{\bullet}_2 + H_2O$	$2.7 \times 10^7\ M^{-1}\ s^{-1}$	Eq. 6.2.13 [43]
${}^{\bullet}O_2^- + H_2O_2 \rightarrow HO^{\bullet} + OH^- + O_2$	$6.5 \times 10^{-1}\ M^{-1}\ s^{-1}$	Eq. 6.2.14 [44]
$HO^{\bullet}_2 + H_2O_2 \rightarrow HO^{\bullet} + H_2O + O_2$	$3.0 \times 10^0\ M^{-1}\ s^{-1}$	Eq. 6.2.15 [43]

To improve the O_3 decomposition, transition metals like copper have been tested as catalyst of O_3 to promote the elimination of the O_3 chain decomposition process, which may or not be significant depending on the mechanism in which O_3 decomposes (direct or by radicals), which in turn is a function of the solution pH to be treated. Eq. 6.2.16 describes the mechanism carried out when the O_3/Cu^{2+} catalytic system has direct interaction between the metal and the ozone molecule [23].

$Cu^{2+} + O_3 + H^+ \rightarrow Cu^{3+} + {}^{\bullet}OH + O_2$	$6 \times 10^{-2}\ M^{-1}\ s^{-1}$	Eq. 6.2.16 [24]

From Eq. 6.2.17 to 6.2.24, it is evident that if copper is in excess, it would eliminate the ${}^{\bullet}OH$ radicals produced, so the oxidant/catalyst ratio is vital for the O_3/Cu^{2+} catalytic ozonation system; likewise, the development of parallel secondary reactions can also be fostered, such that some ROS could become scavenger species. The regeneration of the reduced copper ions occurs through oxidation by ${}^{\bullet}HO_2^-$ radicals, formed during the ozone decomposition (Eq. 6.2.19), the Cu^{2+} reactions and ROS species involved are:

$Cu^{2+} + {}^{\bullet}OH \rightarrow Cu^{3+} + OH^{-+}$	$3.5 \times 10^8\ M^{-1}\ s^{-1}$	Eq. 6.2.17 [45]
$Cu^{2+} + HO^{\bullet}_2 \rightarrow H^+ + Cu^+ + O_2$	$1.2 \times 10^9\ M^{-1}\ s^{-1}$	Eq. 6.2.18 [45]
$Cu^+ + HO^{\bullet}_2 + H^+ \rightarrow Cu^{2+} + H_2O_2$	$2.3 \times 10^9\ M^{-1}\ s^{-1}$	Eq. 6.2.19 [24]
$Cu^{2+} + H_2O_2 \rightarrow Cu^+ + {}^{\bullet}O_2^- + 2H^+$	$4.7 \times 10^2\ M^{-1}\ s^{-1}$	Eq. 6.2.20 [46]
$Cu^+ + H_2O_2 \rightarrow Cu^{3+} + 2OH^-$	$6.1 \times 10^1\ M^{-1}\ s^{-1}$	Eq. 6.2.21 [47]
$Cu^+ + H_2O_2 \rightarrow Cu^{2+} + {}^{\bullet}OH + OH^-$	$4.0 \times 10^5\ M^{-1}\ s^{-1}$	Eq. 6.2.22 [48]
$Cu^{3+} + H_2O_2 \rightarrow Cu^{2+} + {}^{\bullet}O_2^- + 2H^+$	$1.3 \times 10^5\ M^{-1}\ s^{-1}$	Eq. 6.2.23 [23]
$Cu^+ + {}^{\bullet}OH \rightarrow Cu^{2+} + OH^{-+}$	$2.0 \times 10^{10}\ M^{-1}\ s^{-1}$	Eq. 6.2.24 [49]

Additionally, the reaction of organic pollutants such as CBZ and MET with ${}^{\bullet}OH$ radicals are not selective and have high rate constants (constants Eq. 6.2.25 and 6.2.27) ; on the contrary, in the selective oxidation with O_3 the values of the rate constants are lower compared to those of the

•OH radicals. The nature of the catalysis is not only influenced by the type of mechanism that attacks the pollutants but also the fact that MET and CBZ are compounds characterized by being highly recalcitrant, so the half-life of these contaminants in the water is prolonged, which ends up making it difficult to complete mineralization.

$CBZ + O_3 \rightarrow$ Products	$3.0 \times 10^5\ M^{-1}\ s^{-1}$	Eq. 6.2.25 [32]
$CBZ + {}^{\bullet}OH \rightarrow$ Products	$8.8 \times 10^9\ M^{-1}\ s^{-1}$	Eq. 6.2.26 [32]
$MET + O_3 \rightarrow$ Products	$2.0 \times 10^3\ M^{-1}\ s^{-1}$	Eq. 6.2.27 [33]
$MET + {}^{\bullet}OH \rightarrow$ Products	$8.1 \times 10^9\ M^{-1}\ s^{-1}$	Eq. 6.2.28 [50]

For the present case study, it could be suggested both O_3 decomposition mechanisms may be intervening, because of the working pH solution ≈7. For the current study, the equations written would allow to describe and analyze how copper present in the synthesized hybrid materials can influence the ozonation reaction for the treatment of emerging pharmaceutical contaminants. Due to the results obtained in the evaluation of the three catalytic materials Cu-WET1, WET1-199 and SH-WET1-199, it was found the material with the highest catalytic activity corresponded to Cu-WET1, possibly as a consequence of the availability of ions Cu^{2+} on the surface of the material. Consequently, the results obtained with this material allowed us to analyze better the reaction between O_3 and Cu^{2+}, without the addition of other components such as the linkers of the metal-organic frameworks.

Copper catalysis was an advantageous process because the most oxidizing radicals in the system, like •OH, were generated directly (Eq. 6.2.15), and the decomposition of O_3 also involves $HO^{\bullet}_2$ and ${}^{\bullet}O_2^-$ radicals (Eq 6.2.3) [42]. However, in the literature, there are reports of three different hypotheses of the decomposition reaction products of O_3 (Eq. 6.2.29 to 6.2.31) [37].

Hypothesis I	$O_3 + OH^- \rightarrow HO^{\bullet}_2 + {}^{\bullet}O_2^-$	Eq. 6.2.29 [51]
Hypothesis II	$O_3 + OH^- \rightarrow HO_2^- + O_2$	Eq. 6.2.30 [37]
Hypothesis III	$O_3 + OH^- \rightarrow {}^{\bullet}O_3^- + {}^{\bullet}OH$	Eq. 6.2.31 [37]

Then the presence of Cu^{2+} promoted the generation of ${}^{\bullet}O_2^-$ radicals through a reaction similar to Fenton-like between Cu^{3+} and H_2O_2 (Eq. 6.2.22), which besides ROS produced could help to treat the pollutants. Additionally, Cu^{2+} can be regenerated from the oxidation of Cu^+ with H_2O_2 (Eq. 6.2.20), at the same time (Figure 6.2.7), $HO^{\bullet}_2$ radicals ensure the catalytic loop of the Cu^+/Cu^{2+} pair produces enough Cu^{2+} to propagate reactions with •OH radicals (Eq. 6.2.17), similar results were reported by Perez-Benito *et al.* [36], who developed the mechanisms for the ozone catalysis using silver and copper as transition metals.

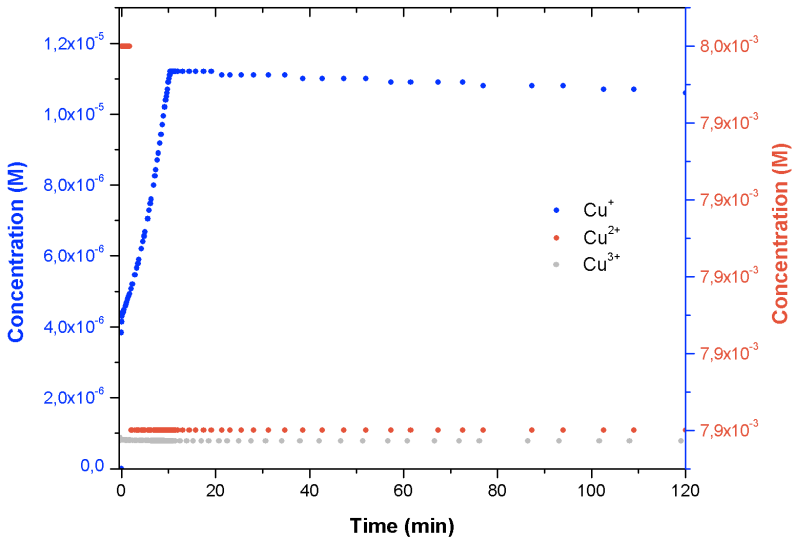


Figure 6.2.7. Simulation of the copper species development along the ozonation reaction catalyzed by Cu^{2+}-WET1.

Kintecus [17] was used as a tool to explain the kinetics of the O_3/Cu^{2+} reaction system; the ozonation reaction began with Eq. 6.2.16, in which radicals •OH were produced. When the concentration of •OH radicals is very high, in AOPs a recombination reaction of two •OH originates H_2O_2 (Eq. 6.2.12); Figure 6.2.8 shows how the H_2O_2 concentration evolution depends mainly on the concentration of •OH radicals and to a lesser extent on $HO^{\bullet}_2$ radicals (Eq. 6.2.11). As a result of the model, it was observed the concentration of H_2O_2 in the first minutes was of the same order as the O_3 concentration; besides, the constant ratio of Fenton-like was higher than the copper catalysis, promoting the system to behave as Fenton-Like system.

However, in the peroxone system (O_3/ H_2O_2) the hydroxyl radical's production can be significantly affected by the presence of other ROS generated from secondary reactions; they end up attacking each other and not the proper pollutant of interest, becoming scavengers and reducing efficiency of the CBZ and MET transformation, as occurs in other advanced oxidation processes (AOPs) [10]. In this case, the identification and quantification of hydrogen peroxide in solution allowed to verify the results proposed by the preliminary simulation in which, indeed, H_2O_2 was being generated in the reaction with ozone catalyzed by copper. Many times, this class of oxidants was assumed to be negligible in catalytic systems with ozone, but, in this investigation, they have an important effect on the degradation of CBZ and MET.

Analyzing the concentrations of the ECs used in the CBZ degradation experiments (10 mg L^{-1} = 4.23 x10^{-5} M) and MET (10 mg L^{-1} = 3.74x10^{-5} M), they were lower than the concentrations of H_2O_2 (9.86 x 10^{-4} M) obtained from the simulation with Kintecus in Figure 6.2.8. The generated

H_2O_2 could compete as a scavenger for ROS, and therefore the degradation became constant because neither CBZ nor MET and even their by-products were found in higher concentrations than H_2O_2 (Eq. 6.2.13 to Eq. 6.2.15).

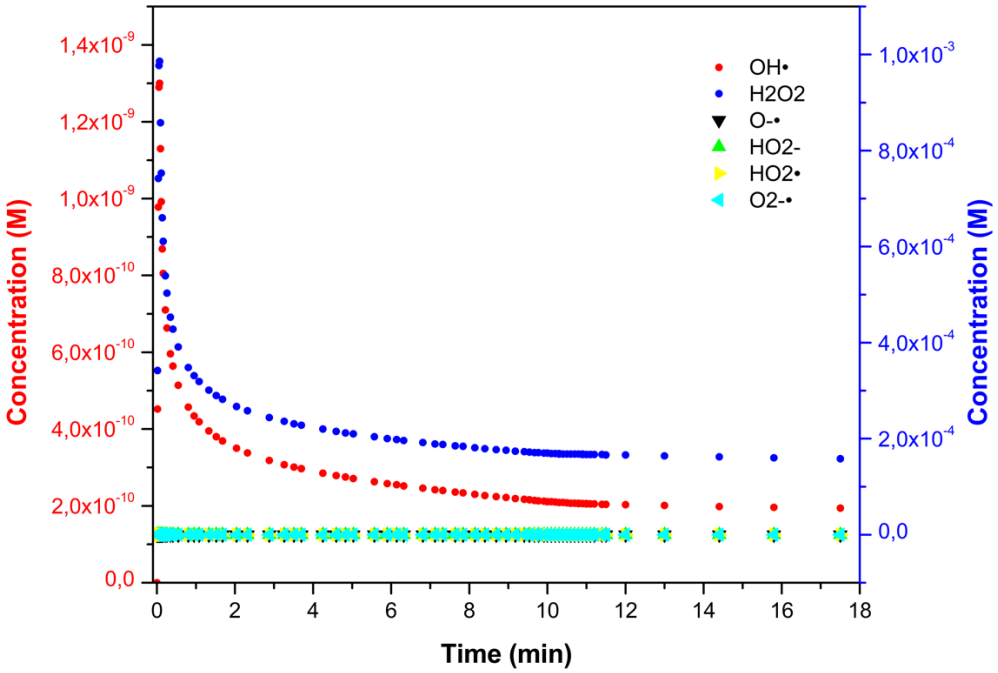


Figure 6.2.8. Simulation of the oxidant radical's concentration along the ozonation reaction catalyzed by Cu-WET1.

AOPs usually happens with the presence of H_2O_2, because it reacts with radicals $^{\bullet}OH$ ($k = 3.3 \times 10^7$ M^{-1} s^{-1}, Eq. 6.2.13), $^{\bullet}O_2^-$ ($k = 6.6 \times 10^{-1}$ M^{-1} s^{-1}, Eq. 6.2.14) and $HO^{\bullet}_2$ ($k = 3.0 \times 10^0$ M^{-1} s^{-1}, Eq. 6.2.15). Of the three ROS produced in the O_3/Cu-WET1 catalytic system, the $^{\bullet}OH$ radicals reached the highest concentration, promoting the degradation of CBZ and MET. However, the presence of H_2O_2 was a scavenger of these radicals, reducing their availability in the catalytic system, limiting the pollutants degradation. Also, it was important to consider the by-products reactions of the CBZ and MET degradation with O_3 since they could also be secondary reactions that would be taking place in parallel.

The H_2O_2 concentration of the model was affected by considering one of the three hypotheses of the O_3 decomposition by OH^- (Eq. 6.2.29 to 6.2.31). Therefore, the concentration of H_2O_2 was followed by UV-VIS spectrophotometry during all the reaction of the catalytic system O_3 /Cu-WET1, to check which of the three hypotheses had the best fitted to the experimental conditions; the results are shown in Figure 6.2.9.

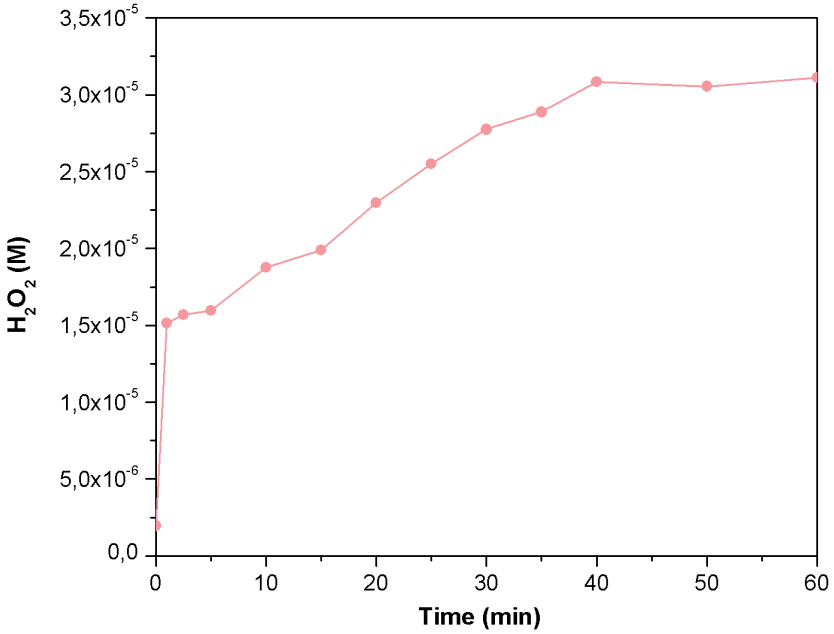


Figure 6.2.9. Hydrogen peroxide measured during the ozonationreaction , after 60 min in contact with 0.1 g of Cu-WET1, 0.25 mL of aqueous solution (only miliQ water).

From the H_2O_2 monitoring, the hydrogen peroxide concentration increased over the reaction time reaching a concentration close to $3x10^{-5}$ M in the solution after 60 min of treatment with ozone, the value obtained experimentally was lower than the model, which may be due to the generation of $^{\bullet}OH$ being also lower in the heterogeneous system with the Cu-WET1 material. Despite this, it could be concluded Eq. 6.2.29 (hypothesis I) was assumed due to the results obtained using Kintecus software allowed to identify the concentration of H_2O_2 measured in the ozonation reaction it was of the order of the model when Eq. 6.2.29 was considered (results will be described in more detail later). Additionally, Kintecus helped elucidate the ROS responsible for pollutant degradation.

When the ozone dose was high compared to the amount of catalyst, the O_3 decomposition was generated through complex chain reactions that cause hydroxyl radicals to get involved with various species of radicals, causing the production of more stable hydroxyl radicals, but in lower concentration due to the ozone autocatalytic decomposition [30].

As a result of the different values of the O_3/catalyst ratio, the appearance of Cu^{3+} species determined the catalysis of ozone. Similar values of the O_3/catalyst ratio promoted the Fenton-like process that finished entering the loop of Cu^{2+}/Cu^{+} reduction allowed by H_2O_2, finally ended up a scavenger specie (Figure 6.2.7). When the H_2O_2 concentration increased (scavenger of $^{\bullet}OH$), the same happens with the concentration of $^{\bullet}OH$ radicals. After reaching a maximum

production of hydroxyl radicals through the Fenton-like process, other secondary reactions appear in parallel attacking •OH, ending in process recombination which limited the hydroxyl radicals available to attack the contaminants of interest (Eq. 6.2.13). If the initial concentration of ozone did not exceed the concentration of hydrogen peroxide formed by kinetic competition, what was happening was a Fenton-like process.

6.2.4.4 Materials characterization after ozonation processes

The materials were characterized after being used in the catalytic degradation of CBZ and MET. Figure 6.2.10. shows the diffractograms of all the materials, in which two peaks at 2Θ = 17° and 22° were perceptible in all, attributed to the cellulose present in the fique fiber used as support. Additionally, for the materials with anchored MOFs, WET1-199 and SH-WET1-199, some small peaks at 2Θ = 11° related to the characteristic diffraction of the metal-organic framework HKUST-1 can be seen. Besides, the reaction with ozone caused the attack of some frame structural components, as can be confirmed by the destruction of the crystalline structure of the MOFs.

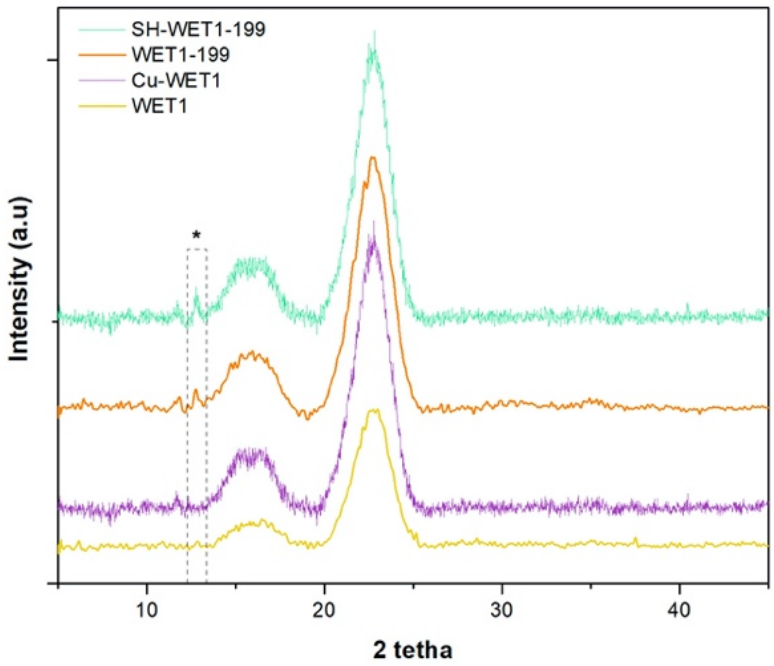


Figure 6.2.10. XRD diffractograms of WET1, Cu-WET1, WET1-199 and SH-WET1-199, after 120 min of reaction.

Additionally, the tested materials were analyzed by SEM microscopy (Figure 6.2.11) to study how their morphology changed after being used as catalysts of the ozonation reaction. Cu-WET1

preserved the morphology like a crust or fiber coating, a result of the impregnation of copper (II) on the material surface; there were no significant changes between the contaminants treated.

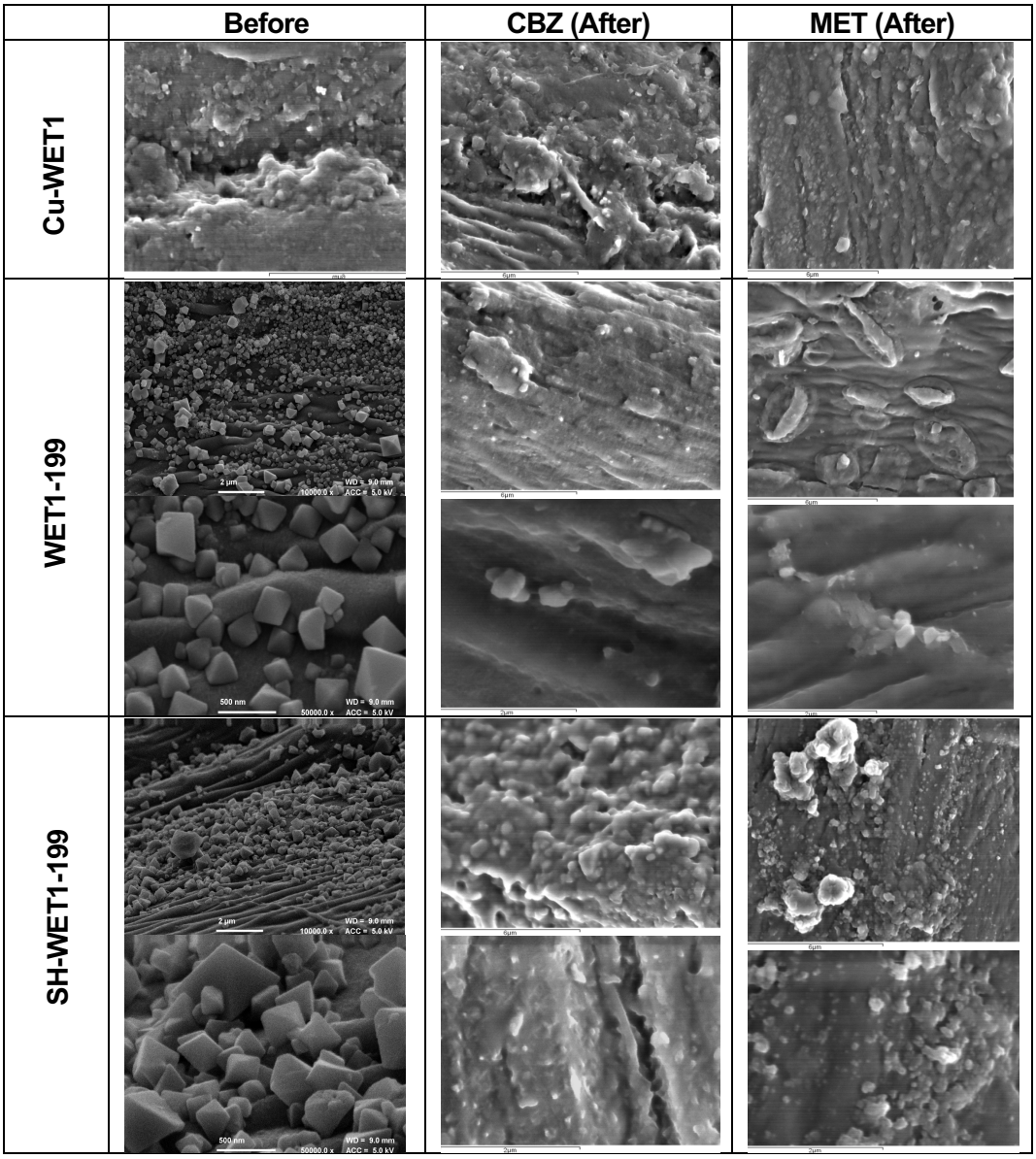


Figure 6.2.11. SEM micrographs of WET1, Cu-WET1, WET1-199 and SH-WET1-199, after 120 minutes to ozonation reaction and their initial condition.

On the contrary, the materials with metal-organic frameworks anchored onto the fiber surface corresponding to WET1-199 and SH-WET1-199 demonstrated changes before and after ozone treatment. Specifically, the material WET1-199 after reacted with CBZ created a coating on the fique fiber, as well as the deposit of certain lumps that seem to be what was the MOF structure. However, when the same material interacted with MET, the surface showed a different look, it

was like burst blisters belonging to what was a characteristic octahedron of the HKUST-1 frame morphology.

As for the other materials with metal-organic frameworks, the surface of SH-WET1-199 had an appearance very similar to Cu-WET1, corresponding to a rough surface related to copper, which covered the fique fiber. According to the micrographs after ozonation of WET1-199 and SH-WET1-199 (Figure 6.2.11), it can be suggested from the morphology description done before, the catalyst interaction with the two pollutant molecules was different due to the surface changes for each catalyst after ozonation.

Also, the material stability was analyzed at the end of each reaction with ozone employing ICP-OES. The amount of copper leached from each of the materials used as catalysts was summarized in Table 6.2.6. After 120 min of reaction, small concentrations of copper were detected in the solution of both contaminants using Cu-WET1. Regarding the materials with MOFs anchored on the surface, as was expected, WET1-199 evidenced the highest amount of copper leaching (between 1.04 and 1.27 mg L^{-1}, because of the hydrolytic instability described in chapter 5.2, while the frame modified with thiol groups of SH-WET1-199 reached concentrations of 0.71 and 0.95 mg L^{-1} ppm, with CBZ and MET, respectively.

Table 6.2.6. Copper leached from the catalysts used in the ozonation reaction of MET and CBZ, quantified by ICP-OES.

Material	Cu^{2+} anchored (mg L^{-1})	Cu leached with CBZ (mg L^{-1})	Cu leached with MET (mg L^{-1})
WET1	0.66	0.01 ± 0.02	0.02 ± 0.02
Cu-WET1	21.94	0.08 ± 0.03	0.15 ± 0.05
WET1-199	53.34	1.04 ± 0.29	1.27 ± 0.98
SH-WET1-199	35.85	0.71 ± 0.16	0.95 ± 0.33

Likewise, it was interesting to confirm a trend in the amount of copper leached by all the materials. When the catalyst reacted with MET, the concentration was always higher compared to the leaching values in the reaction with CBZ. These results confirm that these materials are not stable when subjected to extreme conditions such as ozonation, showing the need to rethink the MOFs synthesis and strategies to their anchoring on the materials, really constituted by strong and stable bonds to avoid being converted in vectors to contaminate the liquid effluents. In addition, the amounts of copper detected in the solution for all materials evaluated were always less than the standard established as the maximum limit (2 mg L^{-1}) for copper in water according to the WHO [52].

The use cycles of the Cu-WET1 material in the degradation of the CBZ and MET pollutants was analyzed, and the results were summarized in Figure 6.2.12. The Cu-WET1 catalyst proved to be stable after 4 runs, each run with a duration of 120 min, corroborating the results obtained by ICP in which a minimum amount of copper leached from the materials after the ozonation reaction (Table 6.2.6).

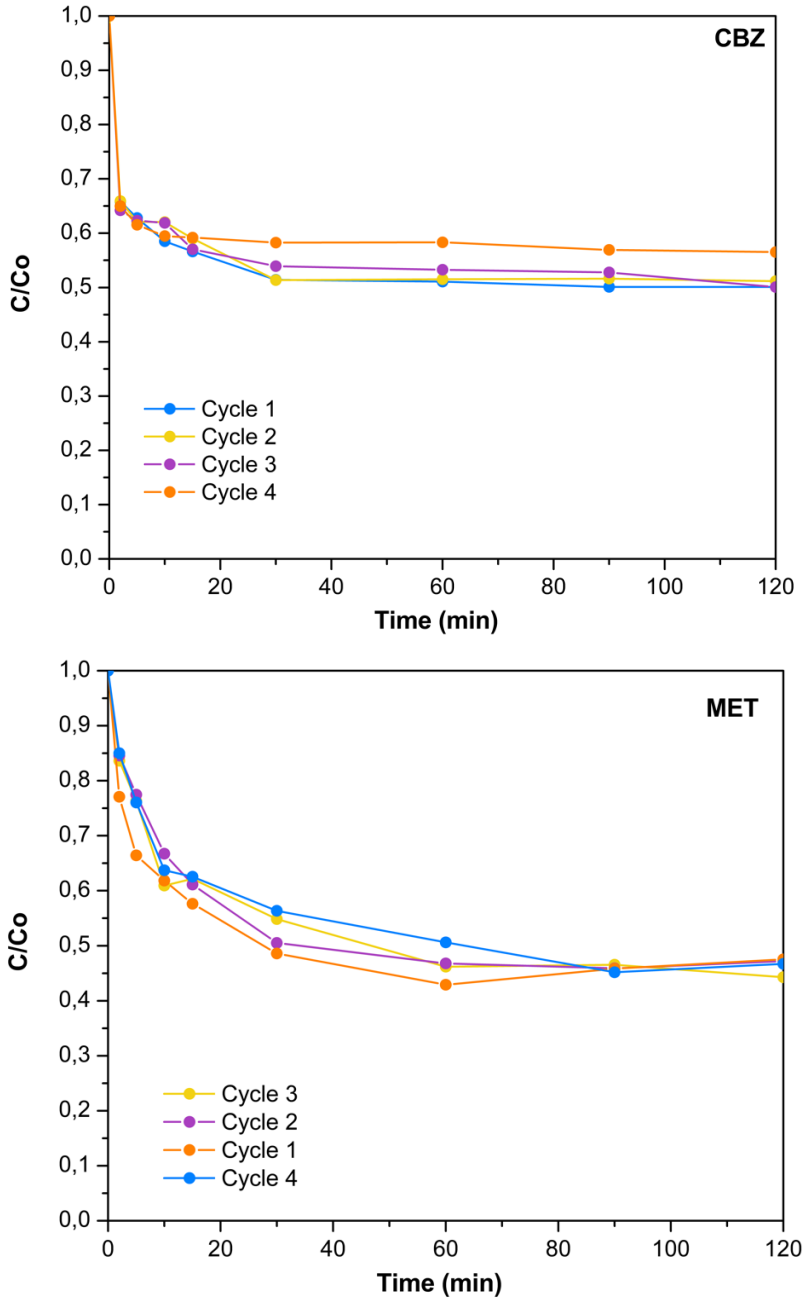


Figure 6.2.12. Cycle use of Cu-WET1 for degradation of CBZ and MET, after each run of 120 min in contact with 0.1 g of the catalyst material, room temperature and pH = 6.45, separately.

6.2.5 Conclusions

From the hybrid materials evaluation developed by the combination of natural fiber and copper either in Cu^{2+} form or coordinated as a metal center in metal-organic frameworks, it was evidenced transition metals such as copper can act as catalysts in advanced oxidation processes, such as ozonation. They promote the O_3 decomposition to generate more active radical species to contribute to the treatment of effluents contaminated with emerging pharmaceutical pollutants, for example, CBZ and MET.

Additionally, it was found the O_3 / Cu^{2+} ratio could affect the efficiency of the oxidation process. To control this reaction the amount of copper should prevail since the ozonation reaction is favored through the loop Cu^{2+} / Cu^{3+}, allowing the generation of radical species capable of attacking organic compounds. Otherwise, copper catalysis produces many oxidizing species such as $^{\bullet}OH$, H_2O_2 and ($^{\bullet}O_2^-$), which recombine by side reactions. When the concentration of H_2O_2 is high, it ends up suppressing the ozone reaction and carrying out a Fenton-like oxidation process. Furthermore, some operational factors as the reaction solution pH, class and concentration of the transition metal, and type of organic contaminant can also affect the catalytic process.

From the materials evaluated, Cu-WET1 was the material with the highest degradation and mineralization degrees of the emerging pharmaceutical pollutants studied. MET reached better results compared to CBZ, as expected, since it has in its chemical structure a larger number of functional groups prone to be attacked, reducing its refractory character. However, for the materials with anchored MOFs, their crystalline structure was destroyed after being subjected to conditions as strong as the reaction with ozone, and further improvements in their design are required to be applied in this type of applications. This was a preliminary study to open a new window to understand in more detail how hybrid materials with copper can act as catalysts in the ozonation reaction.

6.2.6 References

1. Barbosa, M., Moreira, N., Ribeiro, A., Pereira, M. & Silva, A. Occurrence and removal of organic micropollutants: An overview of the watch list of EU Decision 2015/495. *Water Res.* **94**, 257–279 (2016).

2. Mompelat, S., Le Bot, B. & Thomas, O. Occurrence and fate of pharmaceutical products and by-products, from resource to drinking water. *Environ. Int.* **35**, 803–814 (2009).

3. Coutu, S., Wyrsch, V., Wynn, H., Rossi, L. & Barry, D. Temporal dynamics of antibiotics in wastewater treatment plant influent. *Sci. Total Environ.* **458–460**, 20–26 (2013).

4. Ortiz de García, S., Pinto Pinto, G., García Encina, P. & Irusta Mata, R. Consumption and occurrence of pharmaceutical and personal care products in the aquatic environment in Spain. *Sci. Total Environ.* **444**, 451–465 (2013).

5. Belanger, S. *et al.* Aquatic risk assessment of alcohol ethoxylates in North America and Europe. *Ecotoxicol. Environ. Saf.* **64**, 85–99 (2006).

6. Hollender, J. *et al.* Elimination of organic micropollutants in a municipal wastewater treatment plant upgraded with a full-scale post-ozonation followed by sand filtration. *Environ. Sci. Technol.* **43**, 7862–7869 (2009).

7. Margot, J. *et al.* Treatment of micropollutants in municipal wastewater: Ozone or powdered activated carbon. *Sci. Total Environ.* **461**, 480–498 (2013).

8. Nakada, N. *et al.* Removal of selected pharmaceuticals and personal care products (PPCPs) and endocrine-disrupting chemicals (EDCs) during sand filtration and ozonation at a municipal sewage treatment plant. *Water Res.* **41**, 4373–4382 (2007).

9. Mathon, B., Coquery, M., Miege, C., Penru, Y. & Choubert, J. M. Removal efficiencies and kinetic rate constants of xenobiotics by ozonation in tertiary treatment. *Water Sci. Technol.* **75**, 2737–2746 (2017).

10. Wang, J. & Chen, H. Catalytic ozonation for water and wastewater treatment: Recent advances and perspective. *Sci. Total Environ*. **704**, 1-17 (2020).

11. Yu, D., Li, L., Wu, M. & Crittenden, J. C. Enhanced photocatalytic ozonation of organic pollutants using an iron-based metal-organic framework. *Appl. Catal. B Environ.* **251**, 66–75 (2019).

12. Li, X. *et al.* Water Contaminant Elimination Based on Metal-Organic Frameworks and Perspective on Their Industrial Applications. *ACS Sustain. Chem. Engin*. **7**, 4548–4563 (2019).

13. Yu, D. *et al.* Iron-based metal-organic frameworks as novel platforms for catalytic ozonation of organic pollutant: Efficiency and mechanism. *J. Hazard. Mater.* **367**, 456–464 (2019).

14. Wang, H. *et al.* An iron-containing metal-organic framework as a highly efficient catalyst for ozone decomposition. *Angew. Chemie Int.* **57**, 16416–16420 (2018).

15. Wanigarathna, D. K. J. A., Gao, J. & Liu, B. Metal organic frameworks for adsorption-based separation of fluorocompounds: a review. *Mater. Adv.* **1**, 310–320 (2020).

16. Ketchie, W. C., Fang, Y. L., Wong, M. S., Murayama, M. & Davis, R. J. Influence of gold particle size on the aqueous-phase oxidation of carbon monoxide and glycerol. *J. Catal.* **250**, 94–101 (2007).

17. Kintecus, Enzyme & Combustion Chemical Kinetics and Equilibrium Software. http://www.kintecus.com/ (2020).

18. Westerhoff, P., Yoon, Y., Snyder, S. & Wert, E. Fate of endocrine-disruptor, pharmaceutical, and personal care product chemicals during simulated drinking water treatment processes. *Environ. Sci. Technol.* **39**, 6649–6663 (2005).

19. Akpinar, I. & Yazaydin, A. O. Rapid and efficient removal of carbamazepine from water by UiO-67. *Ind. Eng. Chem. Res.* **56**, 15122–15130 (2017).

20. Naghipour, D., Amouei, A., Taher Ghasemi, K. & Taghavi, K. Removal of metoprolol from aqueous solutions by the activated carbon prepared from pine cones. *Environ. Heal. Eng. Manag.* **6**, 81–88 (2019).

21. Margot, J., Rossi, L., Barry, D. & Holliger, C. A review of the fate of micropollutants in wastewater treatment plants. *Wiley Interdiscip. Rev. Water* **2**, 457–487 (2015).

22. Rogers, K. & Cammarata, A. Superdelocalizability and charge density. A correlation with partition coefficients. *J. Med. Chem.* **12**, 692–3 (1969).

23. Pham, A. N., Xing, G., Miller, C. J. & Waite, T. D. Fenton-like copper redox chemistry revisited: Hydrogen peroxide and superoxide mediation of copper-catalyzed oxidant production. *J. Catal.* **301**, 54–64 (2013).

24. Ershov, B. G., Morozov, P. A. & Gordeeev, A. V. Effect of silver and copper ions on the decomposition of ozone in water. *Russ. J. Phys. Chem. A*. **86**, 1795–1799 (2012).

25. Barbosa, M., Ribeiro, A., Pereira, M. & Silva, A. Eco-friendly LC–MS/MS method for analysis of multi-class micropollutants in tap, fountain, and well water from northern Portugal. *Anal. Bioanal. Chem.* **408**, 8355–8367 (2016).

26. Ferguson, P., Bernot, M., Doll, J. & Lauer, T. Detection of pharmaceuticals and personal care products (PPCPs) in near-shore habitats of southern Lake Michigan. *Sci. Total Environ.* **458–460**, 187–196 (2013).

27. Virkutyte, J. *Treatment of Micropollutants in Water and Wastewater*. (Water Intelligence, 2010).

28. García, H. & Navalon, S. *Metal-Organic Frameworks : Applications in Separations and Catalysis*. (Wiley, 2018).

29. Beltrán, F. J., Álvarez, P. M. & Gimeno, O. Graphene-based catalysts for ozone processes to decontaminate water. *Molecules*. **24**, 1-30 (2019).

30. Eddy Zeng. *Persistent Organic Pollutants (POPs): analytical techniques, environmental fate and biological effects.* (Elsevier, 2015).

31. Faria, P. C. C., Órfão, J. J. M. & Pereira, M. F. R. Ozone decomposition in water catalyzed by

activated carbon: Influence of chemical and textural properties. (American Chemical Society , 2006).

32. Huber, M. M., Canonica, S., Park, G. Y. & Von Gunten, U. Oxidation of pharmaceuticals during ozonation and advanced oxidation processes. *Environ. Sci. Technol.* **37**, 1016–1024 (2003).

33. Benner, J. & Ternes, T. A. Ozonation of metoprolol: Elucidation of oxidation pathways and major oxidation products. *Environ. Sci. Technol.* **43**, 5472–5480 (2009).

34. Bourgin, M., von Gunten, U., McArdell, C. S., Hollender, J. & Hofman-Caris, R. Compilation of kinetics and mechanisms for the oxidative transformation of organic substances. (DORA Eawang, 2015).

35. Abdedayem, A., Guiza, M. & Ouederni, A. Copper supported on porous activated carbon obtained by wetness impregnation: Effect of preparation conditions on the ozonation catalyst's characteristics. *Comptes Rendus Chim.* **18**, 100–109 (2015).

36. Perez-Benito, J. F. Copper(II)-catalyzed decomposition of hydrogen peroxide: Catalyst activation by halide ions. *Monatshefte fur Chemie.* **132**, 1477–1492 (2001).

37. Staehelin, J. & Holgné, J. Decomposition of ozone in water: rate of initiation by hydroxide ions and hydrogen peroxide. *Environ. Sci. Technol.* **16**, 676–681 (1982).

38. Bühler, R. E., Staehelin, J. & Hoigné, J. Ozone decomposition in water studied by pulse radiolysis. HO2/O2- and HO3/O3- as intermediates. *J. Phys. Chem.* **88**, 2560–2564 (1984).

39. Elliot, A. J. & Buxton, G. V. Temperature dependence of the reactions OH + O2- and OH + HO2 in water up to 200 °C. *J. Chem. Soc. Faraday Trans.* **88**, 2465–2470 (1992).

40. Bielski, B. H. J., Cabelli, D. E., Arudi, R. L. & Ross, A. B. Reactivity of HO2/O−2 radicals in aqueous solution. *J. Phys. Chem. Ref. Data.* **14**, 1041–1100 (1985).

41. Field, R. J., Noyes, R. M. & Postlethwaite, D. Photoreduction of hydrogen peroxide by hydrogen. *J. Phys. Chem.* **80**, 223–229 (1976).

42. Forni, L., Bahnemann, D. & Hart, E. J. Mechanism of the hydroxide ion initiated decomposition of ozone in aqueous solution. *J. Phys. Chem.* **86**, 255–259 (1982).

43. Buxton, G. V., Greenstock, C. L., Helman, W. P. & Ross, A. B. Critical Review of rate constants for reactions of hydrated electrons, hydrogen atoms and hydroxyl radicals (·OH/·O− in Aqueous Solution. *J. Phys. Chem. Ref. Data.* **17**, 513–886 (1988).

44. Ferradini, C., Foos, J., Houee, C. & Pucheault, J. The reaction between superoxide anion and hydrogen peroxide. *Photochem. Photobiol.* **28**, 697–700 (1978).

45. Riley, D. P., Rivers, W. J. & Weiss, R. H. Stopped-flow kinetic analysis for monitoring superoxide decay in aqueous systems. *Anal. Biochem.* **196**, 344–349 (1991).

46. Hagiopol, C. & Johnston, J. W. *Chemistry of modern papermaking*. (CRC Press, 2012).

47. Pham, A. N., Rose, A. L. & Waite, T. D. Kinetics of Cu(II) reduction by natural organic matter. *J. Phys. Chem. A.* **116**, 6590–6599 (2012).

48. Moffett, J. W. & Zika, R. G. Reaction Kinetics of Hydrogen Peroxide with Copper and Iron in Seawater. *Environ. Sci. Technol.* **21**, 804–810 (1987).

49. Wang, Z. *et al.* Accelerated oxidation of 2,4,6-trichlorophenol in Cu(II)/H2O2/Cl- system: a unique “halotolerant” Fenton-like process. *Environ. Int.* **132**, 1-12 (2019).

50. Wols, B. A., Hofman-Caris, C. H. M., Harmsen, D. J. H. & Beerendonk, E. F. Degradation of 40 selected pharmaceuticals by UV/H2O2. *Water Res.* **47**, 5876–5888 (2013).

51. Weiss, J. Investigations on the radical HO2 in solution. *Trans. Faraday Soc.* **31**, 668–681 (1935).

52. EPA. Lead and Copper Rule | Drinking Water Requirements for States and Public Water Systems | US EPA. https://www.epa.gov/dwreginfo/lead-and-copper-rule (2020).

6.3. Antibacterial activity on *Escherichia coli* of metal-organic frameworks anchored onto fique fiber

6.3.1. Abstract

Natural fibers with surface modifications and hybrid materials based on metal-organic frameworks with copper metallic centers and cellulose fibers prepared in situ were evaluated in pathogens applications with Gram-negative bacteria, such as Escherichia coli, following the modified protocol of the ASTM standard- 2149-13A. The highest antibacterial properties were evidenced in the hybrid materials WET1-199 and SH-WET1-199, reaching 99.2 and 99.9% reduction of antibacterial activity in just 5 min. The contact death produced by the electrostatic interactions of WET1-199 and SH-WET1-199 materials surface and the bacteria cell membrane formed by peptidoglycans was proposed as a mechanism of *E. Coli* elimination. The evaluation of this type of application with hybrid materials opens doors for further exploration in future work in areas not only of treating water contaminated with pathogens but also with other biomedical applications.

Key words: *E. coli,* antibacterial activity, fique fiber, metal-organic frameworks, HKUST-1.

6.3.2. Introduction

Currently, water pollution has led to public health problems worldwide, where despite having the water supply, a large percentage of the world's population does not receive it in adequate sanitary conditions. It is estimated that around 2100 million people do not have a safe water supply, this fact influences that around 842000 people die every year from causes related to water quality [1]. In main urban centers, different types of pathogenic microorganisms have been identified in surface waters, such as *Pseudomonas*, *Aeromonas*, *Arcobacters*, *Legionella's* and *Enterobacteria,* among the most common [2].

Specifically*, Escherichia coli* has been defined as the most common indicator of microbial contamination in drinking water [3]. Therefore, the monitoring and control of this pathogen are necessary to comply with safety standards, allowing the design and implementation of strategies to ensure universal access to drinking water [3]. Besides, this pathogen occurs frequently in regions where optimal water sanitation systems are not available, leading to serious public health

problems [1]. Technologies of water sanitation have the challenge of design more effective processes and materials considering the pathogen resistance to traditional sanitation methods, which should provide green processes at moderate costs.

The traditional methods of drinking water sanitation include free chlorine, ozone, chloramines, and visible UV radiation, all of which have good antibacterial effectiveness and are relatively low in cost [4]. Alternatively, antibacterial nanomaterials (NMs) as well as chitosan, silver nanoparticles, photocatalytic titanium dioxide, fullerol, and carbon nanotubes, have also demonstrated strong antimicrobial properties [5]. The action mechanism of NMs include photocatalytic production of reactive oxygen species, damage to the bacterial cell envelope, disruption of energy transduction, and inhibition of enzymatic and DNA synthesis activity [5].

Metal-organic frameworks (MOF) are structured nanomaterials that have multiple advantage due to the wide range of molecular block building units (MBB) that can be structured. This particularity allows synthesizing MOFs with predetermined physicochemical properties for multiple applications [6]. MOFs with bactericidal properties have been synthesized using transition metals such as copper or silver, which have been widely studied for their high bactericidal activity [78].
One of the advantages of MOFs over other nanomaterials such as nanoparticles is the high surface area available in MOFs. Because nanoparticles are thermodynamically unstable, they tend to aggregate with each other decreasing the surface area, which results in a decrease of their antimicrobial activity [9]. It has also been shown that MOFs structures can be anchored to carboxymethylated fibers by creating coordinating links between the metal centers and the carboxylate groups of the fibers. As a result, the MOF structure is stabilized and the release of metals ions is more controlled, improving antimicrobial activity [9].

Lignocellulosic materials are characterized precisely by the many reactive sites (hydroxyl groups) onto the surface, which allows the surface functionalization with compounds such as carboxylic acids, aldehydes, and amines [10]. Consequently, carboxylic groups allow anchoring nanostructures of MOFs nanostructures, obtaining a hybrid material with a metallic surface. In this vein, copper and copper oxide surfaces have demonstrated greater antimicrobial effectiveness than other metals such as silver or cadmium due to their physicochemical properties [11]. Copper oxidation at moderate temperature and humidity conditions, together with the high solubility of these oxides, lead to high rate of ion release from the solid metal surface. Furthermore, the soft ionic character of the dissolved ions, according to Pearson's concept, leads

to a high toxicity for the bacteria [11]. These conditions are the key characteristics that explain copper´s superior performance over other transition metals.

A small number of reports have been shown to combine lignocellulosic materials with MOFs to be evaluated in antibacterial applications. For example, silk fibers have been used as a substrate for the assembly of copper and trimesic acid as Cu-BTC (MOF-199) nanostructures for antibacterial applications [12]. Nanocrystals of Cu-BTC have also been immobilized in cotton-based substrates and their bactericidal activity against *E. coli* was evaluated [13]. The present study was focused on the antibacterial activity evaluation of fique fiber base materials as cellulose platform. Specifically, five materials were tested on the bactericidal activity of *E. coli*: raw (R), pretreated (WE), functionalized (WET1), fique fiber with HKUST-1 anchored (WET1-199), and HKUST-1 modified with thiol groups anchored onto fique fiber (SH-WET1-199).

6.3.3. Materials and methods

6.3.3.1 Chemicals and materials

Lysogeny broth (LB), buffer solution of KH_2PO_4 (0.3 mM) and ampicillin were purchased from Sigma Aldrich, tryptic soy agar (TSA) was supplied by neogen products. The bacterial cultures *Escherichia coli* (DH5-Alpha) were collected from ATCC.

6.3.3.2 Experimental set-up and procedure

Microbial activity of *E. coli* was measured according to ASTM-2149-13A [14], which was implemented with some modifications (Figure 6.3.1). Cell culture was performed under sterile conditions adding 50 mL of *E. coli* in 5 mL of LB, where the incubation time was 18 h at 37 °C and 100 rpm agitation. Subsequently, the pre-culture was centrifuged at 400 rpm for 5 min, discarding the supernatant and resuspending the pellet in 10 mL of KH_2PO_4 buffer. This suspension was diluted in buffer solution until obtaining an absorbance of 0.28-0.3 at 475 nm, the bacterial concentration was adjusted in a range of 1.5 – 3.0 x 10^8 FUC mL^{-1}. Finally, this solution is diluted 1000 times with the buffer, obtaining the working solution.

The analysis of the microbial activity consisted of 7 tests: 5 of which corresponded to the materials, and 2 to the positive control where ampicillin was used (C+) and the growth control (CC). Therefore, 12.5 mL of working solution was added in 7 falcons of 50 mL, of which 1 g of

each material, previously sterilized, was added to 5 falcons and was left to incubate at 35 °C and 150 rpm for 1 h. Finally, the supernatant of each incubation sample was serially diluted (Figure 6.3.1), seeded on agar, and incubated at 37 °C and 150 rpm for 18 h.

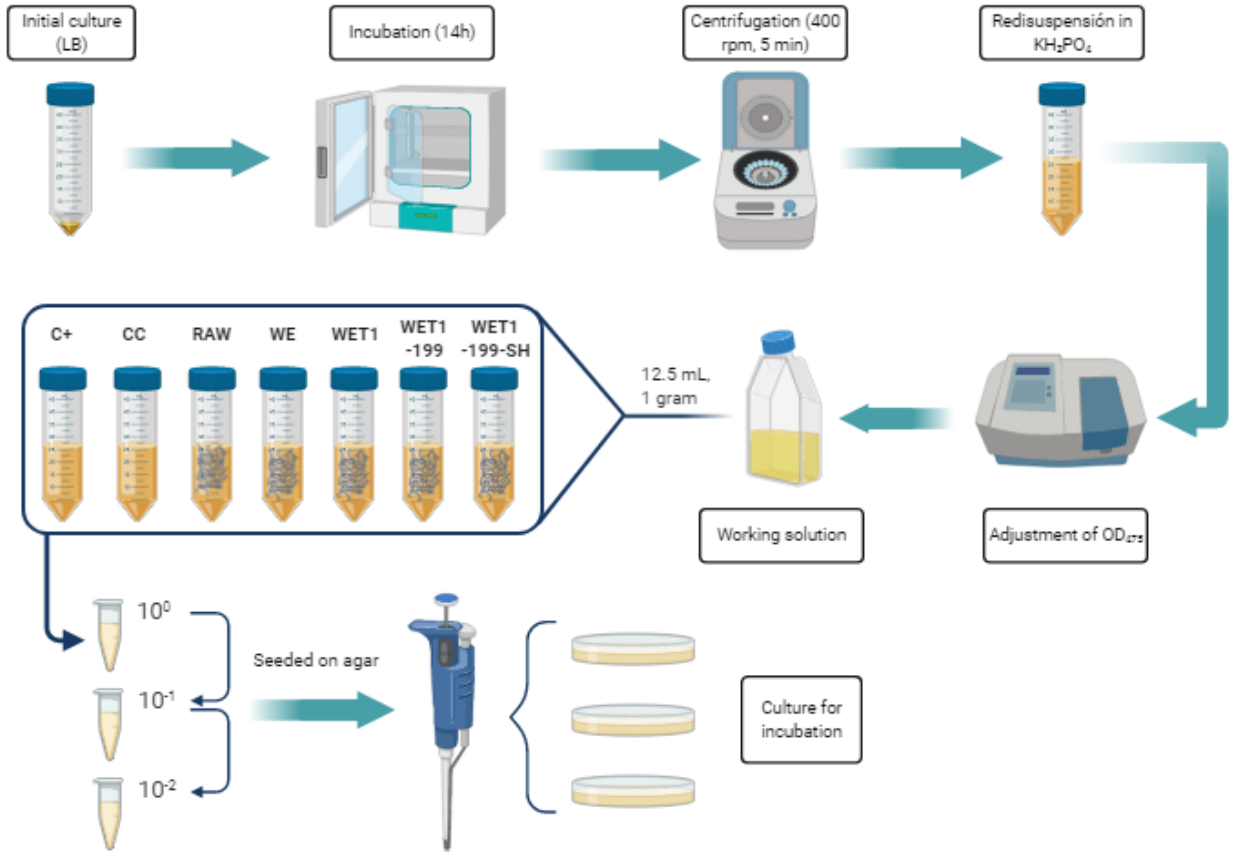


Figure 6.3.1. Modified ASTM-2149-13A procedure scheme.

According to ASTM-2149-13A [14], the percentage of bacteria reduction was determined by quantifying the colony forming units per milliliter CFU mL^{-1}. For this, the Eq. 6.3.1 was used:

$$Reduction\ \%\ (CFU/mL) = \frac{B - A}{B} * 100 \qquad \text{Eq. 6.3.1}$$

Where, *A* corresponds to *CFU* per milliliter for the treated substrate after the specified contact time, and *B* is related with CFU per milliliter for the growth control after the specified contact time.

6.3.3.3 Statistical Analysis

All the experimental results were performed in triplicate and the results were expressed as mean ± standard deviation (SD). The statistical significance between the groups was determined by one-way ANOVA followed by a test for trial trend. A p-value > 0.05 was considered statistically significant, the software Minitab ® was used to make the analysis.

6.3.4. Results and Discussion

The antibacterial activity of fibers with and without metal-organic frameworks anchored (MOFs) was evaluated following the percentage reduction of *E. Coli* (Eq. 6.3.1) in batch experiments. As shown in Figure 6.3.2, the inhibition bar with the highest value of colony-forming units (CFU) per mL was the growth control (CC), since it had no treatment. As a positive control (C+) was used the ampicillin antibiotic, as was expected after 18 h of incubation, no growth of *E. Coli* occurred.

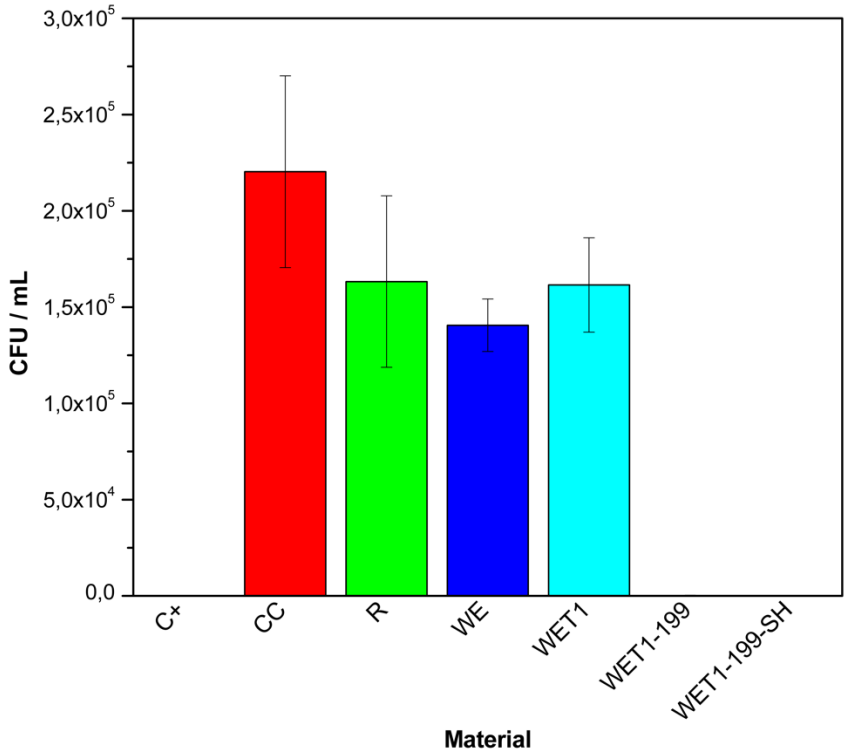


Figure 6.3.2. Reduction percentage of *E. Coli* using as positive control ampicillin (C+), growth control (CC), raw (R), pretreated (WE) and functionalized (WET1), HKUST-1 or SH-HKUST-1 MOFs anchored onto fique fibers, WET1-199 and SH-WET1-199, respectively.

The antibacterial activity On the other hand, among the fiber samples without MOFs (Figure 6.3.2), raw (R), pretreated (WE), and functionalized by TEMPO oxidation (WET1), similar

inhibition results were observed since the surface modifications of the fiber were not strong enough to change the physicochemical properties of the fibers. However, the antibacterial activity of the materials with MOFs anchored with metallic copper centers showed close minimum values of CFU / mL after 18 h of being in contact with *E. Coli*. As it has already been reported, copper ions promoted the damage to the bacterial enveloped [13], increasing the bactericidal effect of the hybrid materials surface analyzed. Figure 6.3.2 and Table 6.3.1 summarized the reduction percentages and the colony-forming units of each of the evaluated materials, respectively.

The data obtained in Table 6.3.1 were studied through an analysis of variance (ANOVA) in which no significant differences were observed in the reduction percentage of *E. Coli* between the different materials evaluated, the value of R^2 corresponded to 97.59%. According to the Tukey test, there were significant differences between the treatments since two types of them were statistically identified (materials with and without anchored MOFs), and there was also a significant difference between the treatments compared with the growth control (CC), values reported in Table 6.3.1.

Table 6.3.1. Reduction percentage of *E. Coli* using different materials. Using the Tukey method, means do not share a letter are significantly different (Tukey, $p<0.05$).

Material	**Label**	Reduction (%)
Ampicillin	C+	100 ± 0.00^{A}
Growth control	CC	0.00 ± 0.00^{C}
Raw	R	25.9 ± 12.3^{B}
Pretreated	WE	36.2 ± 10.8^{B}
Functionalized	WET1	26.7 ± 11.8^{B}
HKUST-1 and WET1	WET1-199	99.2 ± 0.06^{A}
SH-HKUST-1 and WET1	SH-WET1-199	99.9 ± 0.02^{A}

The antibiotic ampicillin, evaluated as C+ according to Table 6.3.1, completely inhibited the growth of *E.Coli* after 18 h. The R, WE, and WET1 fibers without MOFs showed similar antibacterial activity in the range of 25.9 to 36.2% (Table 6.3.1), the 25.9% reduction of the bacteria by the R material can be attributed to the presence of compounds such as sapogenins and hecogenins, which have been shown to have antibacterial activity [15]. Of the three materials, the pretreated fiber displayed, in comparison to the treatments of the same Tukey group, the highest elimination of *E. Coli* with 36.2%, probably because of the type of pretreatment carried out to the fiber utilizing Organosolv. This pretreatment included the first stage of liquid-solid extraction treatment with water, followed by an extraction stage with ethanol (for more details, check chapter 3); and, as it is known, ethanol has antibacterial properties [16], justifying an

approximate 10% increase in the reduction percentage compared to R, probably attributed to ethanol residues present on the fiber surface.

Regarding the WET1 fiber, the presence of sodium carboxylate functional groups (-COONa) resulted from the oxidation carried out to hydroxyl groups on the surface of the fique fiber through the TEMPO reaction. It has been shown in another study that carboxylate groups when in contact with *E. Coli* are reduced to aldehyde groups, which end up affecting the percentage reduction in the growth of this bacterium [17], a fact that explains the 26.7% reduction in the growth of *E. Coli* by this material. In addition, the two materials evaluated with anchored MOFs achieved the elimination of *E. Coli* of 99.2 and 99.9%, using WET1-1 and SH-WET1-199, respectively. The materials with anchored MOFs were superior compared to the fibers alone in terms of reduction percentages in the *E. Coli* growth, demonstrating the HKUST-1 crystals had a significant role in the inactivation of the bacteria and a high potential to be used for the bacteria removal from contaminated liquid effluents.

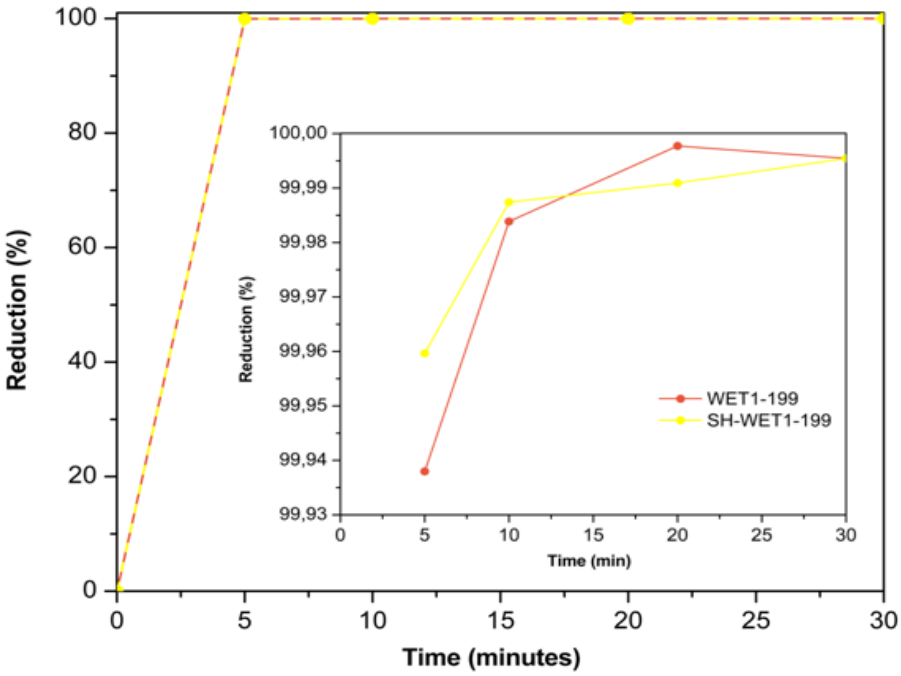


Figure 6.3.3. Reduction percentage of *E. Coli* using, HKUST-1 or SH-HKUST-1 MOFs anchored onto fique fibers, WET1-199 and SH-WET1-199, respectively.

To analyze the change in the percentage reduction of E. Coli using the materials WET1 and SH-WET1-199 over time, in Figure 6.3.3 the growth reduction kinetics of the analyzed bacteria were exposed. The materials with metal-organic frameworks are highly effective since in just 5 minutes

a 99.9% reduction in growth was achieved. There are reports in which it was confirmed that the constituent elements of the HKUST-1 frame, that is, the trimesic acid linker and the metal source (copper (II) acetate) can have bactericidal activity separately. However, Rodriguez *et al.* demonstrated the growth of *E. Coli* bacteria with the linker and salt solutions individually. Concluding that the compounds involved in the synthesis of HKUST-1 could not individually have bactericidal activity on *E. Coli* [13]. Even in another study, Zhitnitsky *et al.* revealed salts, organic acids, and transition metals have weak antibacterial activity when used individually [18].

In contrast, synergistic antibacterial approaches between organic acids and transition metals, which are widely used and highly available compounds, have been investigated. *E. Coli* has been revealed to be sensitive to divalent metals and hypersensitive to acetate ions in the medium, when complexed with transition metals [19], since the toxicity of organic acids modifies the cellular homeostasis pH, due to the acid diffusion in the cell where they were deprotonated and negatively charged. Potentially, under these conditions, being with positively charged transition metals, the complexes are electro-neutral, facilitating the permeation of these compounds into the bacterial cell membrane, to produce toxic effects such as induction of intracellular substance leakage, disruption of DNA structure, damage to vital enzymes, accumulation in cell Wall and decrease in its permeability [7]. The increase in the bactericidal effects of the transition metals made possible by organic acids was the result of synergistic and non-additive effects; it was found the sensitivity of organic acids was directly proportional to the concentration of metals released or accumulated[18].

The synergy between acetate and copper exhibited to have much stronger antibacterial properties than with zinc [18], due to stronger electrostatic interactions between the thin peptidoglycan layer and copper complexes [20]. According to several studies, copper metal oxides such as CuO and Cu_2O in nanoparticle forms have been described as potential biocidal agents, with their antibacterial activity being attributed to the formation of reactive oxygen species (ROS)[7].

Additionally, MOFs have also been demonstrated to have antibacterial properties, as a result of the presence of metal cations in the framework coordinated with linkers. Their application in this field is under development. Therefore, there are reports of antibacterial efficiency, but no defined attack mechanisms have been reported. Most of the times, the antibacterial properties are achieved in a matter of hours, and the experimental parameters are difficult to compare between studies due to the differences in the inoculation technique used (wet or per plate), incubation temperature, metal present in the frame, and the amount of MOFs used. For example, MOFs like

Ag_3(3-phosphonobenzoate) were exhibited to constrain the growth of bacterial strains *S. aureus, E. coli,* and *Pseudomonas aeruginosa* [21], Cu-BTC (on silk fibers) inhibited *E. coli and S. aureus* [22], ZIF-67 acted against *E. coli; Pseudomonas putida; S. cerevisiae* [23] and HKUST-1 was indicated to have antifungal activity against *S. cerevisiae* and *G. candidum* [24].

MOFs in comparison with other compounds such as natural or synthetic polymers loaded with metal ions take advantage of having the speciation uniformity and metal active site distribution. In general, in investigations related to the MOFs antibacterial activity, it has been proposed these compounds function as deposits of divalent metal ions such as Ag^{2+}, Zn^{2+}, Cu^{2+} or Ni^{2+}.Throughout the gradual degradation of the frame structures they are released gradually [21], being associated with physical damage to bacterial cells and not with the alteration of metabolic processes as occurs with antibiotics [7]. On the contrary, other authors attribute the bacterial elimination by the contact between the solid/liquid interface and not by the leached metal ions from the destruction of the MOF. This is a much more recent theory that is currently beginning to be understood in depth [20].

Properly, for HKUST-1 it has been suggested the antibacterial effect was related to the gradual degradation of the Cu-BTC structure, in which trimesic acid allowed the rupture of the cell wall and plasma membrane, promoting the slow release of Cu^{2+}, which acted as an oxidant for organic remains [7]. Of the two approaches, in this research, based on characterizations carried out in previous chapters, it was indicated the amount of copper leached from the materials WET1-199 and SH-WET1-199 was significant after being in contact with water for 3 and 48 h. However, for the experiments performed in this application as displayed in Figure 6.3.1, the materials were not more than one hour in contact with the working solution. So, the probability of copper release from the MOFs structures was not significantly high to be the possible mechanism by which the antibacterial activity of *E. Coli* occurred.

It is well known the antimicrobial mechanisms of copper metal-organic frameworks are complex and diverse. From the two most common proposed mechanisms of the MOFs antibacterial activity, in this research, it was assumed that *E. Coli* is sensitive to death by contact with the materials WET1-199 and SH-WET1-199, coinciding with other authors such as Rodriguez *et al.* [13]. It is important to confirm this mechanism, with complementary studies to support a more detailed molecular view of the mechanism with scientific evidence. However, the current state of the contact death mechanism will be described, for which some contributing factors have been

identified in other studies, mainly using surface moisture inoculation, as is the case in current research.

Until now, the death of *E. Coli* by contact with MOFs has been tentatively explained. Figure 6.3.4 presents a scheme of what would be the steps to be considered in the mechanism. First, the copper interaction with the cell wall resulted from a negative charge presented in the cells and positive charge from the metal centers of Cu^{2+} within the frame structure. Furthermore, the adhesion of MOFs to the bacterial surface could be influenced by the intrinsic properties of the materials WET1-199 and SH-WET1-1999, such as surface roughness, chemical composition, and hydrophobicity [20]. The union of copper and cell wall led to the copper agglomeration on the E. Coli cells surface until the copper ions began to penetrate into the cell membrane [25], causing the destruction of the bacterial cell wall by mechanisms such as endocytosis or direct diffusion [20], (Fig. 6.3.4a).

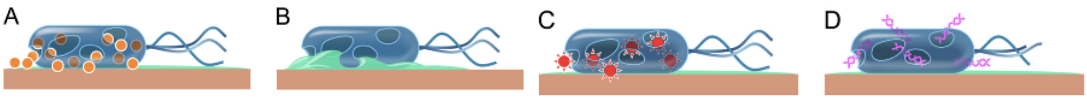


Figure 6.3.4. Schematic illustration of the antibacterial mechanism proposed by Rajeshkumar *et al.* [20].

Second, oxidative stress of the cell membrane proteins and fatty acids was caused (Figure 6.3.5) by the generation of ROS originated from the electron donating nature of the MOFs surface mediated by redox cycles of copper (Fenton type reaction). ROS species, such as hydroxyl radicals, participated in harmful reactions for cellular molecules such as oxidation of proteins and lipids (Figure 6.3.5), as well as the depletion of sulfhydryl, as in cysteines or glutathione [26]. Another species of ROS was the hydrogen peroxide generated by the recombination of hydroxyl ions, which end in lipid peroxidation [25]. The oxidation of the cellular active systems results in the loss of the transmembrane potential, propitiating the cell lysis and cytoplasm leakage (Figure 6.3.4b)[20].

Third, the incitement of cell death by the ROS produced (Figure 6.3.4 c) caused by increased cell permeability, leading to uncontrolled transport of ROS and even copper ions through the cytoplasmic membrane, triggering this way diverse biological responses that end in the collapse of the bacterial defense systems, inducing apoptosis in bacteria [25]. Finally, in the fourth stage, the degradation of DNA, RNA, or lipids occurs, which are secondary events produced after cell death (Figure 6.3.4d) [20].

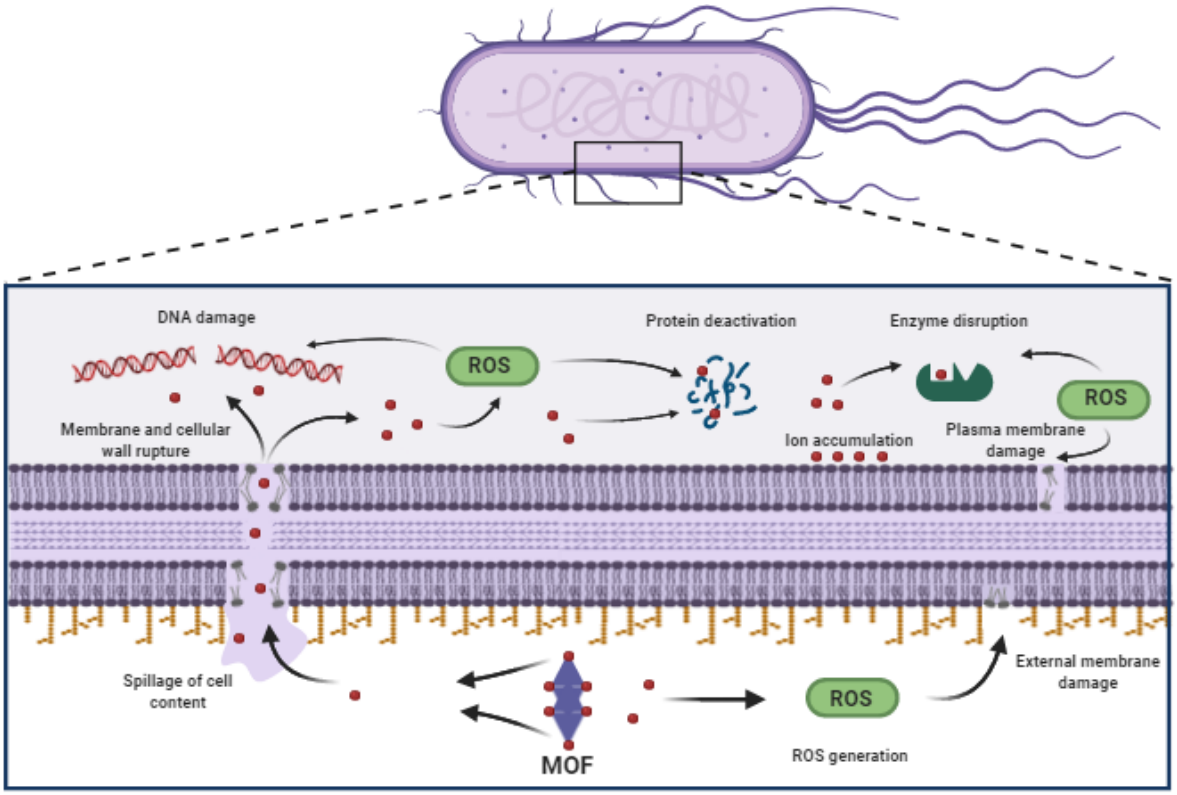


Figure 6.3.5. Illustration of the chemistry involved in cellular damage caused by oxidative stress in E. Coli bacteria during the antibacterial activity of materials with MOFs. Modified from [24].

6.3.5. Conclusions

The evaluation of the antibacterial activity of new materials, especially hybrid materials such as WET1-199 and SH-WET1-199, is an option that opened doors for new applications of this type of material. This study demonstrated the antibacterial activity of different chemically activated fique fibers, in which only those with metal-organic frameworks anchored onto fique fiber demonstrated high efficiency in the elimination of E. Coli bacteria with reduction percentages of 99.2 and 99.9% in less than 5 min, for the materials WET1-199 and SH-WET1-199, respectively.

From the monitoring of the antibacterial activity over time, no significant differences were confirmed between these two types of materials. It is believed the performance on the bacteria elimination was not affected by problems of copper leaching in MOFs. Contact death, due to electrostatic interactions of the bacterial cell wall and surface of the materials WET1-199 and SH-WET1-199, was suggested as a mechanism of antibacterial action, which largely depended on properties of the material as the type of metal used, roughness, among others. However, it is

important in future studies to examine the comprehensive evaluation of the mechanisms and hybrid materials cytotoxicity.

6.3.6. References

1. World Health Organization. *Investing in water and sanitation: increasing access, reducing inequalities.* (Sanitation and Water for All, 2014).

2. Jin, D. *et al.* Bacterial communities and potential waterborne pathogens within the typical urban surface waters. *Sci. Rep.* **8**, 1–9 (2018).

3. Charles, K. J., Nowicki, S. & Bartram, J. K. A framework for monitoring the safety of water services: from measurements to security. *Clean Water.* **3**, 1-6 (2020).

4. Shannon, M. A. *et al.* Science and technology for water purification in the coming decades. *Nature*. **452**, 301–310 (2008).

5. Li, Q. *et al.* Antimicrobial nanomaterials for water disinfection and microbial control: Potential applications and implications. *Water Res*. **42**, 4591–4602 (2008).

6. Furukawa, H., Cordova, K. E., O'Keeffe, M. & Yaghi, O. M. The chemistry and applications of metal-organic frameworks. *Science.* **341**, 1-8 (2013).

7. Wyszogrodzka, G., Marszałek, B., Gil, B. & Dorozyński, P. Metal-organic frameworks: Mechanisms of antibacterial action and potential applications. *Drug Discov. Today*. **21**, 1009–1018 (2016).

8. Firouzjaei, M. D., Shamsabadi, A. A., Sharifian Gh., M., Rahimpour, A. & Soroush, M. A novel nanocomposite with superior antibacterial activity: a silver-based metal organic framework embellished with graphene oxide. *Adv. Mater. Interfaces*. **5**, 1-7 (2018).

9. Duan, C. *et al.* Synthesis of novel cellulose- based antibacterial composites of Ag nanoparticles@ metal-organic frameworks@ carboxymethylated fibers. *Carbohydr. Polym.* **193**, 82–88 (2018).

10. Tavakolian, M., Jafari, S. M. & van de Ven, T. G. M. A Review on Surface-Functionalized Cellulosic Nanostructures as Biocompatible Antibacterial Materials. *Nano-Micro Lett*. **12**, 1-23 (2020).

11. Luo, J., Hein, C., Mücklich, F. & Solioz, M. Killing of bacteria by copper, cadmium, and silver surfaces reveals relevant physicochemical parameters. *Biointerphases*. **12**, 1-10 (2017).

12. Abbasi, A. R., Akhbari, K. & Morsali, A. Dense coating of surface mounted CuBTC Metal-Organic Framework nanostructures on silk fibers, prepared by layer-by-layer method under ultrasound irradiation with antibacterial activity. *Ultrason. Sonochem.* **19**, 846–852 (2012).

13. Rodríguez, H. S., Hinestroza, J. P., Ochoa-Puentes, C., Sierra, C. A. & Soto, C. Y. Antibacterial activity against *Escherichia coli* of Cu-BTC (MOF-199) metal-organic framework immobilized onto cellulosic fibers. *J. Appl. Polym. Sci.* **131**, 1-5 (2014).

14. ASTM. Standard Test Method for Determining the Antimicrobial Activity of Antimicrobial Agents Under Dynamic Contact Conditions, ASTM E2149-20.(ASTM International, 2020).

15. Arabski, M., Węgierek-Ciuk, A., Czerwonka, G., Lankoff, A. & Kaca, W. Effects of saponins

against clinical E. coli strains and eukaryotic cell line. *J. Biomed. Biotechnol.* **2012**, 1-6 (2012).

16. Somchit, M. N., Reezal, I., Elysha Nur, I. & Mutalib, A. R. In vitro antimicrobial activity of ethanol and water extracts of Cassia alata. *J. Ethnopharmacol.* **84**, 1–4 (2003).

17. Wu, C. N. *et al.* TEMPO-oxidized bacterial cellulose pellicle with silver nanoparticles for wound dressing. *Biomacromolecules* **19**, 544–554 (2018).

18. Zhitnitsky, D., Rose, J. & Lewinson, O. The highly synergistic, broad spectrum, antibacterial activity of organic acids and transition metals. *Sci. Rep.* **7**, 1–13 (2017).

19. Shock, E. L. & Koretsky, C. M. Metal-organic complexes in geochemical processes: Estimation of standard partial molal thermodynamic properties of aqueous complexes between metal cations and monovalent organic acid ligands at high pressures and temperatures. *Geochim. Cosmochim. Acta.* **59**, 1497–1532 (1995).

20. Rajeshkumar, S. *et al.* Antibacterial and antioxidant potential of biosynthesized copper nanoparticles mediated through Cissus arnotiana plant extract. *J. Photochem. Photobiol. B Biol.* **197**, 1-6 (2019).

21. Berchel, M. *et al.* A silver-based metal-organic framework material as a 'reservoir' of bactericidal metal ions. *New J. Chem.* **35**, 1000–1003 (2011).

22. Abbasi, A. R., Akhbari, K. & Morsali, A. Dense coating of surface mounted CuBTC Metal-Organic Framework nanostructures on silk fibers, prepared by layer-by-layer method under ultrasound irradiation with antibacterial activity. *Ultrason. Sonochem.* **19**, 846–852 (2012).

23. Aguado, S. *et al.* Antimicrobial activity of cobalt imidazolate metal-organic frameworks. *Chemosphere* **113**, 188–192 (2014).

24. Wyszogrodzka, G., Marszałek, B., Gil, B. & Dorozyński, P. Metal-organic frameworks: Mechanisms of antibacterial action and potential applications. *Drug Discov. Today*. **21**, 1009–1018 (2016).

25. Applerot, G. *et al.* Understanding the antibacterial mechanism of CuO nanoparticles: Revealing the route of induced oxidative stress. *Small.* **8**, 3326–3337 (2012).

26. Grass, G., Rensing, C. & Solioz, M. Metallic copper as an antimicrobial surface. *Appl. Environ. Microbiol*. **77**, 1541–1547 (2011).

7. Conclusions and perspectives

7.1 Conclusions

The development of new hybrid materials was achieved, between the combination of lignocellulosic fibers like fique fiber and metal-organic frameworks (MOFs) based in copper. These materials demonstrated to be active, physicochemically stable and selective, and with homogeneous properties considering the particle size and distribution after the MOFs anchoring onto the surface of lignocellulosic fibers. The properties synergy of each element in the hybrid materials corroborated to be potentially useful in remediation processes of aqueous liquid effluents contaminated with emerging contaminants.

From the conclusions presented in each of the chapters described previously, the main achievements of this work were:

- To establish a methodology for the modification of the physicochemical properties of the Fique fiber through a pretreatment and functionalization process, which creates suitable surface conditions to allow its use as a support for the anchoring of MOFs.
- Design a stepwise green synthesis of MOFs and its modification to include thiol groups in the frame structure. The synthesis methodology produced MOFs grafted onto functionalized fique fibers that ensures: i) stability in aqueous conditions, and ii) formation of a chemical interaction.
- The materials obtained were chemically, structurally, and physically characterized not only to follow the changes of the materials throughout the different modifications but also to know the weaknesses and strengths of each of the stages of the materials synthesis.
- The materials synthesized were tested and their efficiencies were analyzed on the removal of different types of emerging contaminants (inorganic, organic and bacteria).

The characterization presented in Chapter 2 allowed to evidence the fique fiber as great lignocellulosic biomass to take advantage of the cellulose present in its structure to be used as

potential support in hybrid materials. A comprehensive design of experiments developed in Chapter 3, demonstrated how pretreatments as acid and alkali in the lowest experimental conditions affected in a significant way its structural properties. The organosolv pretreatment modified the surface in a slightly different way from solvents like ethanol and water originating a more homogeneous and cleaner fiber.

Then, the pretreated fiber was chemically activated through a functionalization process to include functional groups on the fiber surface. For that, in Chapter 4, two chemical modifications were evaluated: carboxymethylation and oxidation mediated by TEMPO, which obtained degrees of substitution close to 11.3% of carboxymethyl ether groups and 9.32% of carboxylate, respectively. The main difference between these two types of functionalization was the selectivity when interacted with the hydroxyl groups (C6) of cellulose. In both types of functionalization, the importance of using pretreated fiber was established.

Regarding the MOFs synthesis of HKUST-1 from both methods evaluated, crystals with octahedral shapes and define crystallinity were obtained, which confirmed its identity according to simulated patterns. The green method gave rise yields of 85.7% while solvothermal method reached a maximum yield of 67.7%. In this way, it was shown that green synthesis turned out to be an innovative, simple, fast, affordable, and ecological method to prepare high-quality carboxylate-based MOF, as compared to those obtained under conventional conditions such as the solvothermal method.

Besides, as a consequence of the poor hydrolytic stability of HKUST-1, its modification by crystal poisons such as MBA (4-mercaptobenzoic acid) and TSA (thiosalicylic acid) to incorporate thiol groups in the linker that forms the metal-organic framework was performed. Particularly, MBA at 5 wt% did not show any distortion of the MOF crystallinity while it acted as steric impediment increasing hydrolytic stability from 6 to 48 h, for HKUST-1 and SH-HKUST-1 respectively. At the same time, new properties were developed with this functionalization, such as increased selectivity towards mercury without modifying its topology and composition.

The development of hybrid materials was reported combining functionalized fique fiber with MOFs. The immobilization of Cu-based MOFs like HKUST-1 and SH-HKUST-1 was evaluated via two methods: direct and secondary growth. During the direct method, the nucleation and crystals growth were done in the solution reducing the possibility to create real bound with the

functionalized surface. On the contrary, in the secondary growth copper metal ions were seeded on cellulose surfaces functionalized by ion exchange to create possible nucleation sites. The hybrid materials produced were formed approximately with 20 wt.% of metal organic-frameworks. Also, the hydrolytic stability improvement was achieved as a consequence of the linker modification using crystal poison and the grafting on lignocellulosic fibers used as substrates as supports. In addition, fiber functionalized by TEMPO oxidation revealed to be better as support compared to the CMC fiber, probably as a consequence of the bond length established between the support and the MOF anchored.

The materials produced were tested in different applications related to water treatment polluted with emerging contaminants. First, the materials were used to remove mercury. Comparing the materials with anchored MOFs, SH-WET1-199 demonstrated to be more selective for adsorption of Hg^{2+} ions than WET1-199, the adsorption capacities achieved in 30 min were 44.4 and 79.9 mg g^{-1}, respectively. From all the materials evaluated (raw, pretreated, functionalized fiber and both hybrid materials), the functionalized fiber showed the highest Hg^{2+} adsorption in water. This process was attributed to the interactions by stacking Π-Π, hydrogen bonds and electrostatic interactions.

In the second application, three hybrid materials based on copper were explored in the catalytic ozonation of organic contaminants in water like carbamazepine (CBZ) and metoprolol (MET). All the Cu-catalysts showed to have a better catalytic performance on the degradation of MET than CBZ. Moreover, the ozonation catalyzed by Cu-WET1 demonstrated the highest activity in terms of degradation percentage (43.4 ± 3.6 and 52.8 ± 1.4 % for CBZ and MET) and TOC removal (51.4 ± 12.3 and 63.5 ± 13.1 % for CBZ and MET), probably because of the copper availability onto the surface. Furthermore, a preliminary simulation was implemented to understand the O_3/Cu^{2+} catalytic interaction; a significant formation of radical oxygen species (ROS), like hydroxyl and hydrogen peroxide from ozone decomposition catalyzed by copper, was found. Also, the influence of the O_3/Cu^{2+} ratio was found to be an important parameter because it can affect the amount of hydrogen peroxide produced, determining which advanced oxidation process will happen.

The third application evaluated of the hybrid materials was their antibacterial activity. The elimination of E. Coli bacteria with reduction percentages of 99.2 and 99.9% in less than 5 min

for the materials WET1-199 and SH-WET1-199 were confirmed, respectively. Specifically, this application is an option that opened doors for new applications.

7.2 Perspectives

This work creates a whole of possibilities to explore the materials produced in different applications and approaches. Among these, the following can be highlighted:

- Analyze the composition of the liquor produced after the alkali or acid fiber pretreatment and identify other potential application of its by-products, taking in consideration that these liquids are rich in sugars like glucose, xylose, and some aromatic compounds.

- Test the anchoring of other types of materials like nanoparticles to take advantage of the active chemical groups developed on the fiber surface.

- Follow the MOF anchoring methodology developed to test other MOFs more stable in water, considering different metal centers focused on the possible potential application, and validate the methodology reproducibility.

- Evaluate the materials produced in other applications like sensors or take advantage of other additional properties of the new hybrid materials.

- Regarding the application for heavy metals removal, try to evaluate the selectivity of the materials with different ions. Also, scale or design a possible reactor configuration to remove heavy metals in continuous.

- Regarding the ozonation application, analyze a complete set of catalyst / oxidant agent to find the adequate ratio to move the reaction from Fenton to ozonation, and verify if this was a possible improvement to treat pharmaceuticals in water streams.

- In the antibacterial application, develop cytotoxicity studies to analyze the effect of the hybrid materials in human health.